Metallurgy and Design of Alloys with Hierarchical Microstructures

Krishnan K. Sankaran

Rajiv S. Mishra



Elsevier
Radarweg 29, PO Box 211, 1000 AE Amsterdam, Netherlands
The Boulevard, Langford Lane, Kidlington, Oxford OX5 1GB, United Kingdom
50 Hampshire Street, 5th Floor, Cambridge, MA 02139, United States

Copyright © 2017 Elsevier Inc. All rights reserved.

No part of this publication may be reproduced or transmitted in any form or by any means, electronic or mechanical, including photocopying, recording, or any information storage and retrieval system, without permission in writing from the publisher. Details on how to seek permission, further information about the Publisher's permissions policies and our arrangements with organizations such as the Copyright Clearance Center and the Copyright Licensing Agency, can be found at our website: www.elsevier.com/permissions.

This book and the individual contributions contained in it are protected under copyright by the Publisher (other than as may be noted herein).

Notices
Knowledge and best practice in this field are constantly changing. As new research and experience broaden our understanding, changes in research methods, professional practices, or medical treatment may become necessary.

Practitioners and researchers must always rely on their own experience and knowledge in evaluating and using any information, methods, compounds, or experiments described herein. In using such information or methods they should be mindful of their own safety and the safety of others, including parties for whom they have a professional responsibility.

To the fullest extent of the law, neither the Publisher nor the authors, contributors, or editors, assume any liability for any injury and/or damage to persons or property as a matter of products liability, negligence or otherwise, or from any use or operation of any methods, products, instructions, or ideas contained in the material herein.

Library of Congress Cataloging-in-Publication Data
A catalog record for this book is available from the Library of Congress

British Library Cataloguing-in-Publication Data
A catalogue record for this book is available from the British Library

ISBN: 978-0-12-812068-2

For information on all Elsevier publications visit our website at
https://www.elsevier.com/books-and-journals



Publisher: Nikki Levy
Acquisition Editor: Christina Gifford
Editorial Project Manager: Andrae Akeh
Production Project Manager: Susan Li
Designer: Christian Bilow

Typeset by TNQ Books and Journals

Preface

The continuously improved understanding of the physical mechanisms that govern the behavior of materials coupled with the availability of advanced characterization techniques and efficient computational modeling and simulation tools is rendering the accelerated design and insertion of alloys with targeted combination of properties possible. Significant progress is being made in this regard, for example, in the framework of the "Systems Approach" and "Integrated Computational Materials Engineering" and the infrastructure of the "Materials Genome Initiative". Our book aims to provide a description of the processing−microstructure−property relationships for alloys with hierarchical microstructures, essentially their physical metallurgy, which is necessary for the effective and judicious application of the state-of-the-art alloy design tools.

The book grew out of courses that we have taught over the years at Washington University in St. Louis (KKS), Missouri University of Science & Technology (RSM), and more recently at the University of North Texas (RSM). These courses were designed to satisfy the needs of students, academic researchers, and practicing engineers for the knowledge of how structural materials, with their ever-increasing microstructural complexity, are optimized and how they will behave in service. The focus of the book is on metallic materials used in airframe structures; however, these materials have sufficiently diverse microstructures that the underlying principles can be extended to other materials systems.

A question arises naturally regarding our stated need for this book because many publications dealing with aspects of the design of advanced materials and their selection are already available. In addition to the articles in ASM Handbook volumes and those continuously appearing in various journals, these include

- M.F. Ashby, "Materials Selection in Mechanical Design", 5th ed., 2017, Butterworth-Heinemann.
- Z.H. Barber, ed., "Introduction to Materials Modeling", 2005, Maney Publishing.
- M.F. Horstemeyer, "Integrated Computational Materials Engineering (ICME) for Metals", 2012, Wiley.
- I.J. Polmear et al., "Light Alloys", 5th ed., 2017, Butterworth-Heinemann.

Despite the availability of these publications, a gap needs to be filled for delineating the interrelationships of multiple microstructural and deformation mechanisms and applying the tools of designing microstructures for achieving desired combinations of engineering properties such as strength, corrosion resistance, durability, and damage tolerance in multicomponent materials used for critical structural applications. This is the gap that our book seeks to fulfill.

Alloy design is essentially microstructural design. Although the specific modulus values of the light alloys (based on magnesium, aluminum and titanium), high strength steels, and nickel base alloys used in propulsion systems are all about 25 MPa/(kg/m^3), the ability to manipulate their microstructure is what enables the

achievement of a wide range of desired property combinations for applications. This aspect is discussed in the introductory chapters with subsequent chapters dealing with individual classes of materials used in airframe structures.

A unique aspect of our book is the discussion of physical metallurgy and alloy behavior using state-of-the-art engineering alloys, the approach to understanding their behavior, and how new alloys can be designed and applied. Also included is a chapter on recent developments in complex concentrated alloys (such as high entropy alloys) and one on design of alloys amenable to state-of-the-art manufacturing methods such as friction stir welding and additive manufacturing. The goal is to provide sufficient knowledge to apply the concepts of microstructural design and integrated computational materials engineering in everyday practice.

The book can be used at the senior undergraduate or graduate level as a text or a reference in courses covering the physical metallurgy and mechanical behavior of alloy systems with emphasis on their design. These aspects are covered in sufficient detail with examples using alloys in commercial applications. Problem sets are also included. It should be emphasized that the book is not a text on basic physical metallurgy or on computational materials science but is a treatment of their application to alloy design. As such, it is also a suitable reference book for all engaged in the design and application of alloys.

Our learning and application of the subject matter of the book have been aided significantly not only by our experience but also by many excellent teachers and interactions with colleagues. We would like to mention a few who have made the most impact in this regard. KKS would like to acknowledge (the late) Professor M.B. Bever's "Structure and Properties of Metals" course at the Massachusetts Institute of Technology, which had a tremendous influence on the way he has approached physical metallurgy of alloys ever since. This course was itself based on the earlier writings on microstructural hierarchy by Professor Cyril Stanley Smith. KKS has also benefited significantly from continued interactions, since graduate student days, with Professor Krishna Rajan (Chair of the Department of Materials Design and Innovation, University at Buffalo, The State University of New York), who by the way was a graduate student instructor for Professor Bever's course. The notes and problem sets from this course, taken more than 40 years ago, are as relevant today as then, despite the advances in theory and the analysis and characterization tools.

RSM would like to acknowledge Professors G.S. Murty, G.W. Greenwood, H. Jones, and A.K. Mukherjee who shaped his early understanding of linkages among processing−microstructure and mechanical properties. He is indebted to Professor G.B. Olson for inspiring him to start teaching a course on "Advanced Materials by Microstructural Design". Professor Olson was very generous to share the way he introduced "Systems Approach" to undergraduate students. Many thanks to colleagues and students who have contributed to my understanding of the subject that is presented in this book.

We owe a special debt of gratitude to many colleagues who kindly spent enormous time and effort in thoroughly reviewing many chapters and providing

corrections and suggestions for improvement. We particularly acknowledge Professor Satyam Suwas of the Indian Institute of Science for critically reviewing the chapters on aluminum alloys and titanium alloys, Dr. Bob Bucci (retired from Alcoa, presently Arconic) for critically reviewing the chapter on aluminum alloys and their use, and Dr. Sesh Tamirisa (of RTI International, presently Arconic) for critically reviewing the chapter on titanium alloys. We also thank Charles Saff (retired from Boeing) for general discussions regarding the applications of materials to structures and for help with the problems. Although their reviews and input have greatly improved the book, we take sole responsibility for any errors and shortcomings.

Regarding the units of measurements used in the book, properties of most commercial alloys are reported in English units in the literature. In these instances, principally for chapters on Al-, Ti-, and Fe-based alloys and others where necessary, the properties are reported in the same units as the source along with the conversion. Otherwise, only SI units are used.

A final note of thanks is due to the staff at Elsevier: Christina Gifford, Acquisitions Editor, for facilitating the development of this book, Andrae Akeh, Editorial Project manager, for ensuring the timely submission of the manuscript, Anita Vethakkan for help with the copyright permissions and Susan Li, Production Project manager, for help with the production of the book.

Krishnan K. Sankaran
Rajiv S. Mishra
May 2017

CHAPTER

Introduction 1

CHAPTER OUTLINE

Synopsis 1
1.1 Structural Materials Evolution and Applications 2
1.2 Structural Materials Properties and Selection 5
1.3 Microstructures and Microstructural Hierarchy 6
1.4 Hierarchical Microstructures and Properties of Engineering Alloys 9
1.5 Alloy Design for Material Properties 12
1.6 Alloy Design for Material Manufacturability 15
1.7 Summary 17
1.8 Organization of the Book 18
References 19

SYNOPSIS

This chapter briefly traces the evolution of engineering structural materials with a focus on the selection of materials for use in airplane structures, which are designed to operate in complex and severe loading conditions in harsh environments. The approach to designing such materials with microstructural features necessary to achieve desired properties is discussed in the context of the "Systems Approach," [1] which in recent years has enabled the rapid design, qualification, and insertion of materials in structural applications at much lower cost, which was made possible by advances in computational modeling and simulation. The hierarchical nature of the microstructures in aluminum, titanium, and ultrahigh strength steel alloys used in airframe structures and the importance of understanding the interactions between composition, processing, microstructure, and properties are emphasized for designing alloys to meet performance targets and amenability to novel manufacturing techniques such as friction stir welding and additive manufacturing. Although the emphasis is on alloys used in airframes, the methods are applicable to other structures as in propulsion systems and automobiles.

Metallurgy and Design of Alloys with Hierarchical Microstructures. http://dx.doi.org/10.1016/B978-0-12-812068-2.00001-1

Copyright © 2017 Elsevier Inc. All rights reserved.

1.1 STRUCTURAL MATERIALS EVOLUTION AND APPLICATIONS

Materials have played a significant role in advancing technologies throughout human history. Fig. 1.1 illustrates the evolution and changing relative importance of various classes of engineering materials with the progression of time [2]. Although metallic materials became increasingly dominant over the past 2 millennia, polymer–matrix composite materials, which have lower density, are making significant inroads. For aerospace and automotive systems, new monolithic and composite materials based on metals, polymers, and ceramics continue to be developed at an accelerating pace to provide better fuel efficiency, enable operation in extreme environments, and meet stringent environmental regulations. Property improvements to meet these requirements, particularly in metallic materials, have been made possible by "tailoring" their "microstructure" using a combination of alloying and processing approaches. Iron-based alloys have evolved in this manner over a 1000 years and are among the most commonly used metallic materials. In contrast, aluminum alloys, developed only within the past century, became the dominant material used for airplane design, with titanium alloys and polymer-based composite materials finding increasing use more recently. The early dominance of aluminum alloys for airframe applications was aided significantly by designing alloys with continuous improvements in property combinations to keep pace with evolving

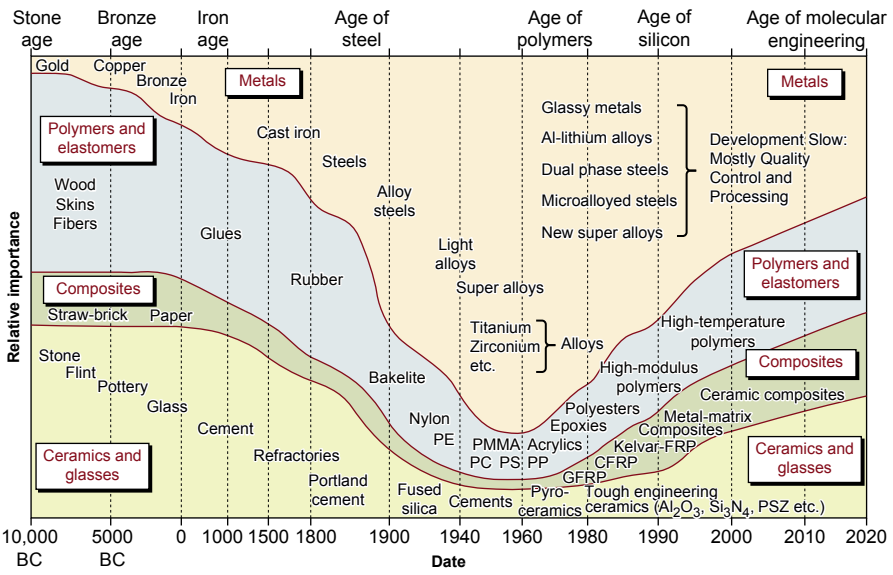


FIGURE 1.1

Evolution of engineering materials that emphasizes their relative importance [2].

airframe design requirements. Superalloys are used in aerospace propulsion systems and refractory metals are used in structures exposed to very high temperatures.

The loading conditions and environments experienced by materials used in aerospace vehicles are extreme and complex. Design of efficient and affordable systems requires the selection of materials that can meet multiple and often conflicting property and manufacturability targets to achieve maximum performance and lowest product and life cycle costs arising from their operation and in-service maintenance. The critical importance of materials selection can be illustrated by considering the loading types and the corresponding material property requirements for various components of the fuselage, wing, empennage, and supporting structures in a typical commercial airplane, shown in Fig. 1.2 [3].

For example, upper wing skins experience compression loading for which materials with high compression strength are required and lower wing skins experience tension loading for which materials with high-fatigue crack growth resistance are required. Of course, the materials need to possess acceptable levels of other properties. Landing gear structures (not shown in Fig. 1.2) are considered part of the airframe and require materials with very high strength. The materials used in the Boeing 777 airplanes currently in service are shown in Fig. 1.3 [4]. Some of these materials, which were developed specifically for this airplane, were chosen for their capability to meet challenging performance goals and include aluminum, titanium, and steel alloys as well as polymer-based materials. Use of new materials resulted in weight savings of 5800 pounds (2631 kg), a significant amount, for this airplane.

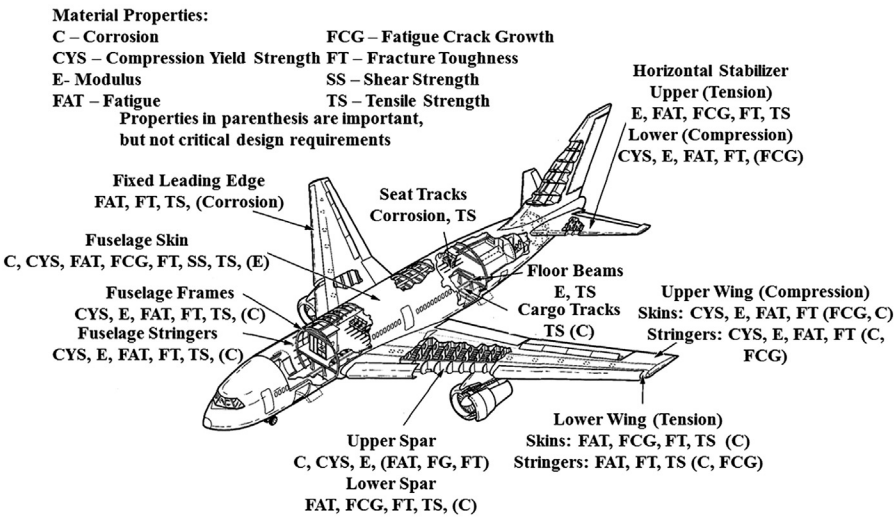


FIGURE 1.2

Property requirements for airplane structures [3]. Note the need to balance a combination of properties for any particular structure.

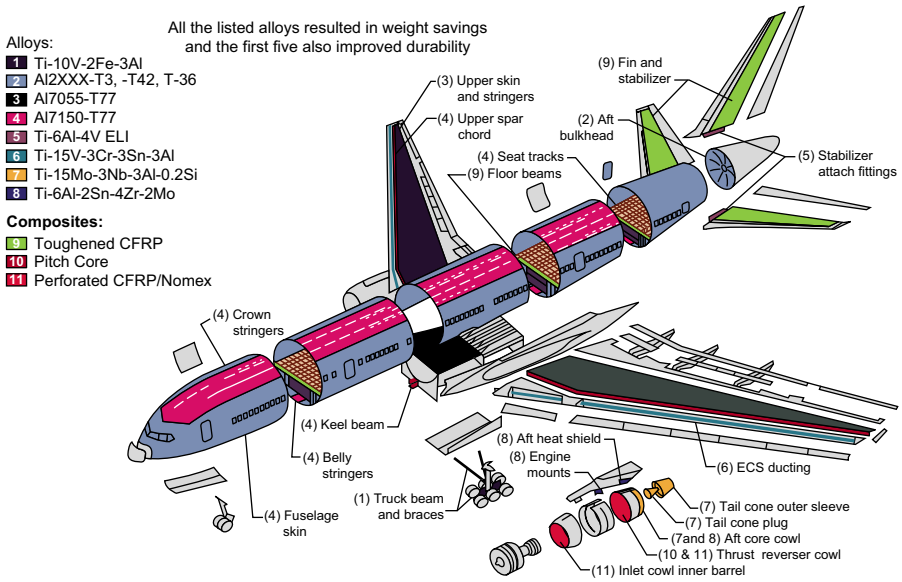


FIGURE 1.3

Materials used for the Boeing 777 [4].

Adapted and reprinted with permission of ASM International. All rights reserved. www.asminternational.org.

The increasing use of titanium alloys and polymer–matrix composite materials in the airframes (fuselage, wings, empennage, and landing gear and excluding the propulsion system) of commercial passenger airplanes is illustrated by the materials distribution shown in Table 1.1 [5–7]. The trend of replacing aluminum alloys with these materials started in the 1970s with high-performance military airplanes and more recently with the Boeing 787 and Airbus A350 commercial passenger airplanes. In the future, at least half the airframe weight can be expected to be made up of structures fabricated from combinations of aluminum, titanium, and steel alloys. Based on density alone, magnesium alloys are attractive, but their strength, corrosion resistance, manufacturability, and other attributes need to be improved further for them to be viable.

Table 1.1 Materials Usage in Boeing and Airbus Airplanes

Materials Distribution (wt%)							
	Boeing [5]					**Airbus [6,7]**	
Material	**747**	**757**	**767**	**777**	**787**	**A380**	**A350**
Aluminum	81	78	80	70	20	61	19
Titanium	4	6	2	7	15	10 (Ti and steel)	14
Steel	13	12	14	11	10		6
Composites	1	3	3	11	50	22	53
Other	1	1	1	1	5	7	8

All the metallic materials that are candidates for airframe design possess heterogeneous, hierarchical microstructures with interacting features at multiple length scales, designed for optimum combinations of properties like strength, toughness, and corrosion resistance. The physical metallurgy of these alloys encompasses the microstructure types and strengthening mechanisms commonly observed in all metallic alloys. Their description and understanding in the context of new materials design, the subject of this book, although essential for developing future materials to satisfy airframe performance goals, can also be extended to alloys used in propulsion systems, automobiles, and other demanding applications.

1.2 STRUCTURAL MATERIALS PROPERTIES AND SELECTION

Materials selected for use in load-bearing structures must possess an optimum combination of mechanical properties, ability to withstand harsh service environments without degradation, and be amenable to ease of fabrication into components. The best materials for specific applications are determined by detailed "trade" studies that consider all these attributes during design along with the estimation of the manufacturing and life cycle costs. The approach for materials selection for diverse design applications has been described in detail in several excellent text books and publications [2,8,9].

Materials selection for design occurs initially during the screening stage in which the absolute limits of the values of the properties are considered and no tradeoffs are made. For example, only aluminum alloys or polymer-based composites will generally be considered for wing skins in airplanes, as these will meet the performance requirements and give the lowest weight for a metallic or nonmetallic composite structure, respectively. Specific material selection will then be made by trading off the properties and attributes of individual materials, for example various aluminum alloys, and ranking them within the family of materials identified during the screening stage. With very few exceptions, density is the single most important material property that determines structural weight, followed by yield strength and elastic modulus. Table 1.2 shows the dependence of the weight of structures designed for various loading conditions as a function of these material properties.

Using a lower density material while maintaining the other properties will always reduce the weight in direct proportion, whereas the relative benefits of using higher modulus or higher strength materials will depend on the type of loading.

Table 1.2 Dependence of Structural Weight on Material Properties

Loading (Structural Element)	Stiffness	Strength
Tension (tie)	$(\rho)/(E)$	$(\rho)/(\sigma_y)$
Bending (beam)	$(\rho)/(E)^{1/2}$	$(\rho)/(\sigma_y)^{2/3}$
Bending (panel)	$(\rho)/(E)^{1/3}$	$(\rho)/(\sigma_y)^{1/2}$

ρ, *density;* E, *elastic modulus;* σ_y, *yield strength.*

Table 1.3 Relative Weight of Structure for Flat Plate Buckling Loading Using Various Materials

Material	Aluminum	Titanium	Iron	C/Epoxy
Density (g/cc)	2.7	4.5	7.3	1.3
Elastic modulus (GPa)	70	120	211	57
Relative weight of structure	1	1.39	2.03	0.71

Exceptions include landing gear components, for example, for which the strength of the material is critical and volume constraints preclude the use of lower density, lower strength alloys. Thus ultrahigh strength steel alloys with three times the density of aluminum alloys, but with about three times their strength, will be selected for landing gear components. However, for representative loading conditions encountered by airframe structures, the low density of aluminum alloys provides the lowest weight compared with other metallic materials, as shown in Table 1.3.

Once a material family is selected for a given application, some of the important mechanical properties used in trade studies for airframe structures are (1) tensile, compression, and shear strength, which are measures of the resistance to deformation under monotonic loading, and (2) resistance to fatigue crack initiation and propagation and fracture toughness, which are measures of durability and damage tolerance. To prevent degradation in service environments, materials also need to possess adequate resistance to various types of corrosion like general, galvanic, and exfoliation as well as stress corrosion cracking, which occurs under the simultaneous influence of mechanical loading and corrosive environments. Structural assemblies are typically made up of multiple parts fabricated from different types of materials and galvanic compatibility between these materials and their differential thermal expansion coefficients are also considered in materials selection.

The properties of a given alloy can be sensitive or insensitive to its "microstructure" (defined and discussed in the next section). Density is insensitive to the microstructure. Although elastic modulus is insensitive in the sense that it is not affected by the types of imperfections and is the same in the cold worked or annealed condition, it is a sensitive function of the texture or the preferred orientation of the grains. Mechanical properties and resistance to environmental degradation are sensitive to the microstructure. It is this aspect of the "microstructure—property relationships" that enables optimum and balanced combinations of properties to be achieved in materials by employing various processing methods to produce the corresponding microstructures.

1.3 MICROSTRUCTURES AND MICROSTRUCTURAL HIERARCHY

The chapter titled "Microstructure of Metals and Alloys" in "Physical Metallurgy" [10] defines the "microstructure" of metallic materials to consist of "the distribution

and topological arrangement of grains, phases, interfaces, and other defects in three dimensions. A metal microstructure is a direct result of the alloy chemistry and processing history, and it dictates the final properties and performance of the alloy, and/or any component made from it." The individual space-filling features of the microstructure, such as listed in Fig. 1.4 for representative alloy systems, constitute a spatial hierarchy across a range of length scales. The interactive response of these features to external loading and environments determines the properties of the materials.

Microstructures of materials, which are determined by their processing path, are rarely in thermodynamic equilibrium. Thus associated with the multilevel spatial hierarchy discussed earlier are relaxation times characteristic of each level of length scale (temporal hierarchy), which provide enabling processing pathways to achieve desired microstructures. The microstructural features amenable to manipulation by processing occupy the intermediate region of the total length scales ranging from electronic structure to continuum, as shown in Fig. 1.5 [11].

Fig. 1.6 shows the distinct, hierarchical modeling methods used to describe materials behavior across the length scales. Quantum mechanics and molecular dynamics (Newtonian mechanics) methods are used to model the behavior of electrons and atoms, respectively. Due to the difficulty of modeling (computational constraints) the behavior of large number of atoms, they are "coarse-grained" into cells containing features of interest, such as dislocations or grains, which are then

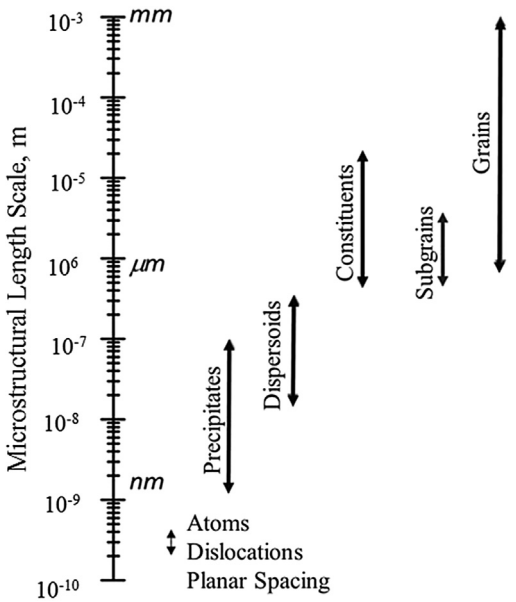


FIGURE 1.4

Spatial hierarchy of microstructural features for aluminum alloys.

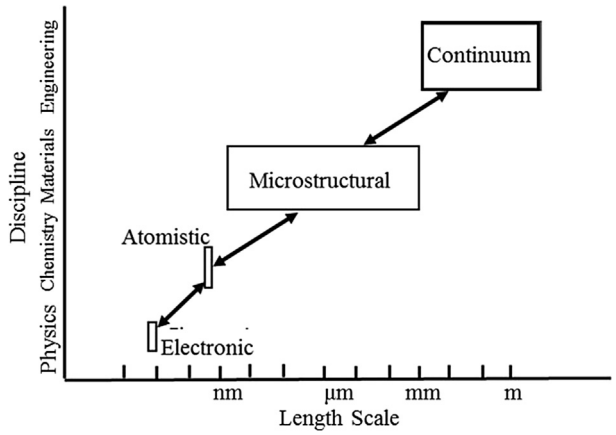


FIGURE 1.5

Association of various disciplines with spatial hierarchies.

Adapted from D.G. Pettifor, Controversial concepts in alloy theory revisited, The Science of Alloys for the 21st Century, A Hume-Rothery Symposium Celebration, TMS Fall Meeting, St. Louis, MO, 2000.

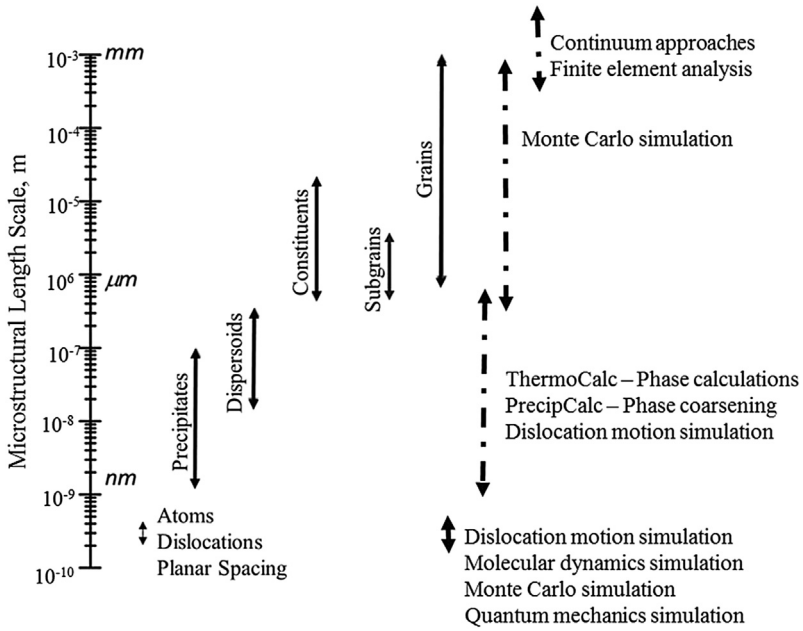


FIGURE 1.6

An example of various materials modeling approaches corresponding to spatial hierarchy.

modeled at the microstructural scale using Monte Carlo simulation or similar techniques. Finally, constitutive equations are used to model materials at the continuum level. Fig. 1.6 is illustrative and just gives examples of a few commonly used modeling tools. For each length scale, various integrated modeling approaches are also possible to combine the effects from different microstructural features.

1.4 HIERARCHICAL MICROSTRUCTURES AND PROPERTIES OF ENGINEERING ALLOYS

Hierarchical features, i.e., features of different sizes, can exist within each of these length scales. Structural alloys can be regarded as materials into which hierarchical microstructural features are "engineered" by synthesis and processing to achieve desired properties for applications. Such an approach is also useful for imparting the ability for special processing like superplastic forming of titanium alloys by producing a distribution of fine grains of two allotropic phases in roughly equal volume fractions. Structural elements such as foams, honeycombs, and cellular solids represent hierarchy at the macrostructural level [12].

Multicomponent aluminum and steel alloys contain second phases dispersed in the alloy matrix, whereas titanium alloys contain a distribution of two ductile phases. By processing the alloys to vary both the morphologies and characteristics of the matrix (degree of recrystallization, grain size distributions and texture) and the second phases (precipitates, dispersoids, and constituents), desired microstructures can be produced in aluminum alloys to achieve the property requirements for design. An example of these microstructural features can be seen in Fig. 1.7 for commercial wrought aluminum alloys. Fig. 1.7A shows the anisotropy of the grain structure, micrometer-sized coarse constituent particles, and intermediate-sized dispersoids in

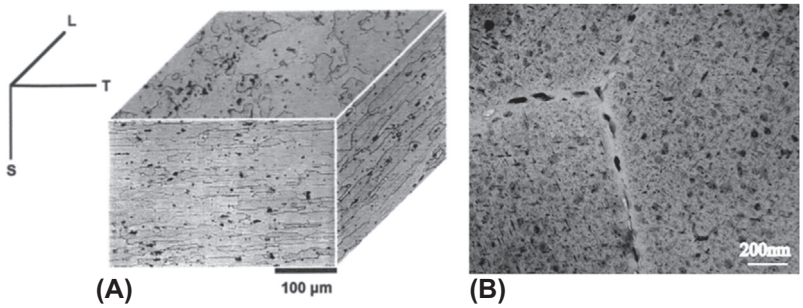


FIGURE 1.7

Microstructure of high-strength, precipitation-hardened, commercial aluminum alloys showing (A) grain shape anisotropy, dispersoids, and constituent particles in 7075-T6 sheet [13] and (B) precipitate-free zones and distribution of precipitates within the grains and along the grain boundaries in 7050-T651 plate [14].

7075-T6 sheet [13]. Fig. 1.7B shows fine (<50 nm) intragranular strengthening precipitates and precipitate-free zones along with coarse precipitates along the grain boundary in 7050-T651 plate [14]. Each of these features and their interactions determine the properties important for materials selection.

Occurrence of hierarchy within a given hierarchical scale of microstructure can often lead to beneficial effects as illustrated by several examples. The formation of disordered γ (matrix) particles within ordered γ' (Ni_3(Ti,Al)) precipitates during aging of a nickel-based superalloy was observed to eventually split and refine these particles resulting in increased strength [15]. Another example is the production of two distinct sizes of nanoscale defects in a severely plastically deformed aluminum alloy resulting in an exceptional strength level near 1 GPa [16].

From the perspective of engineering alloys, the properties of metallic materials that are relevant for design and manufacturing are determined by the large variety of the hierarchical features, their interactions, and the associated mechanisms that occur principally at the "microstructural" level, as schematically shown in Fig. 1.8. Table 1.4 compares the strength levels of the nominally pure matrix material with those of two corresponding high-strength airframe structural alloys, one of which is widely used and considered the benchmark for further alloy improvements and the other with better balance of properties that was developed and successfully implemented in structures to increase their performance. These improvements are a

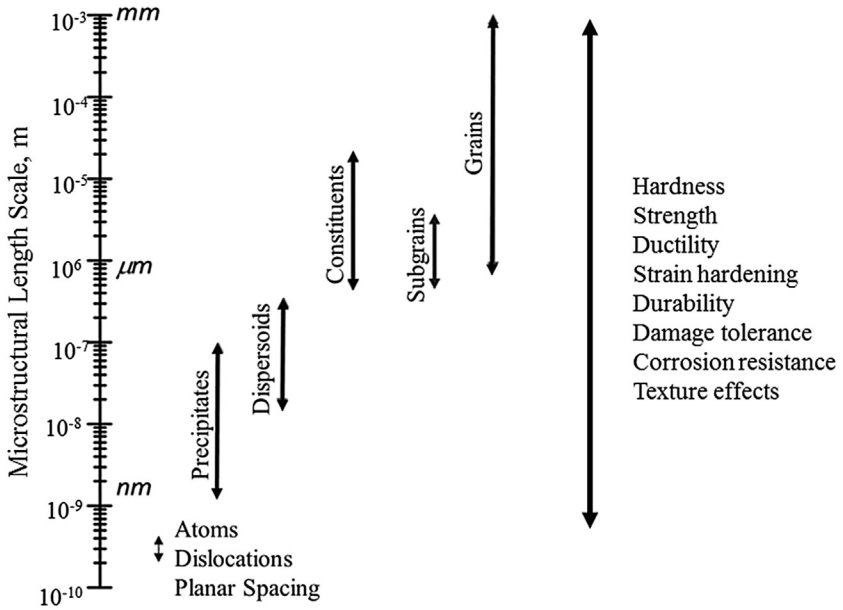


FIGURE 1.8

Linkage of hierarchical microstructural features with material properties.

Table 1.4 Comparison of Properties of Nominally Pure and Commercially Used High-Strength Alloys

Alloy Family	Alloy Type	Alloy and Condition	Density (Mg/m^3 (lb/in.^{3}))	Tensile Modulus (GPa (10^3 ksi))	Specific Modulus (GPa/Mg/m^3 or 10^3 ksi/lb/in.^{3})	Yield Strength (MPa (ksi))
Aluminum	Commercially pure grade	1100 (strain hardened)	2.71 (0.098)	69 (10.0)	25	115 (17)
	Common high strength alloy	7050 (T74—overaged)	2.83 (0.102)	70 (10.2)	25	450 (65)
	Alloy developed for higher strength	7055 (T77—retrogressed and reaged)	2.86 (0.103)	70 (10.2)	24	620 (90)
Titanium	Unalloyed titanium	Grade 1 (fabricated bar)	4.5 (0.163)	103 (14.9)	23	170 (25)
	Common alloy	Ti-6-4 (mill annealed)	4.43 (0.160)	110 (16.0)	25	825 (120)
	Higher strength alloy	Ti-10-2-3 (heat treated)	4.65 (0.168)	100 (14.5)	22	1100 (160)
Iron	Low carbon steel	AISI 1008 cold drawn bar	7.87 (0.284)	200 (29.0)	25	285 (41)
	Common landing gear alloy	300 M (quenched and tempered at 205°C)	7.83 (0.283)	200 (29.0)	26	2140 (310)
	High toughness alloy	Aermet 100 (quenched and aged at 480°C)	7.9 (0.285)	195 (28.3)	25	1970 (286)

Alloy Composition (wt%)

Al 1100: 99(min)Al–0.12Cu–1.0(max)Si + Fe
Al 7050: Al–6.2Zn–2.3Mg–2.3Cu-0.12Zr–0.12(max)Si–0.15(max)Fe
Al 7055: Al–8.0Zn–2.0Mg–2.3Cu–0.16Zr–0.10(max)Si–0.15(max)Fe
Unalloyed Ti Grade 1: 99.175(min) Ti–0.18(max)O
Ti-10-2-3: Ti–10V–2Fe–3Al
Ti-6-4: Ti 6Al–4V
AISI 1008: Fe–0.06C–0.38Mn
300M: Fe–0.42C–0.75Mn–1.65Si–1.80Ni–0.80Cr–0.40Mo–0.07V
Aermet 100: Fe–0.23C–13.4Co–11.1Ni–3.10Cr–1.2Mo

direct result of synthesis and processing that produced alloys with microstructural features for corresponding enhancements of properties and structural efficiency.

Although the specific modulus values of the light alloys (based on aluminum and titanium) and high-strength steel alloys are all between 22 and 25 GPa/(Mg/m^3), microstructural manipulation by processing can provide significant strength increases along with good combinations of toughness, corrosion resistance, and other important properties. An example of the "processing—microstructure—property" relationships used to develop an ultrahigh strength, corrosion-resistant steel alloy is shown Fig. 1.9 [17]. This "systems approach" clearly shows the multivariate relationships between the entire processing sequence for the alloy (from melt refining to final tempering) and the hierarchical microstructural features that must be optimized to produce target properties. These relationships and their underlying physical mechanisms for various materials of interest will be discussed in subsequent chapters using examples of alloys currently in use.

1.5 ALLOY DESIGN FOR MATERIAL PROPERTIES

Complete and accurate quantitative descriptions of the physical mechanisms that govern the relationships among composition, processing, microstructure, and properties of metallic materials have not always preceded or been necessary for their development and successful use. A good example is the discovery and use of aluminum alloys in airplane structures without a knowledge of their strengthening mechanisms. Development of the theory of precipitation hardening did not occur until later when techniques were available to characterize the microstructures. Much of alloy development throughout history has occurred in this way by chance discoveries aided by the accumulated empirical knowledge of materials behavior and how they are affected by processing.

It is now instructive to review the historical approaches to alloy design leading up to the present methods embodied in "Materials by Design" [17,18] and "Integrated Computational Materials Engineering (ICME)" [19] and grounded in the infrastructure of the "Materials Genome Initiative (MGI)" [20]. Over the past several decades, empirical alloy design has been aided by the concurrent advances in electron microscopy, fracture mechanics, and other materials characterization and analysis techniques. This in turn has enabled the further development and refinement of the theories and models of the mechanisms governing materials behavior, with which there is now the ability to "design" rather than "discover" new alloys [21].

All the alloys developed for structural applications have multiple alloying elements and second phases. An excellent discussion in this regard is the 1973 Institute of Metals Lecture by Decker [21], which, from the perspective of "alloy design," discussed in detail the design of second-phase morphologies and their use to control the matrix microstructures to optimize strength, ductility, toughness, and other properties along with the physical mechanisms underlying the processing—microstructure—property relationships. This was followed by the publication in

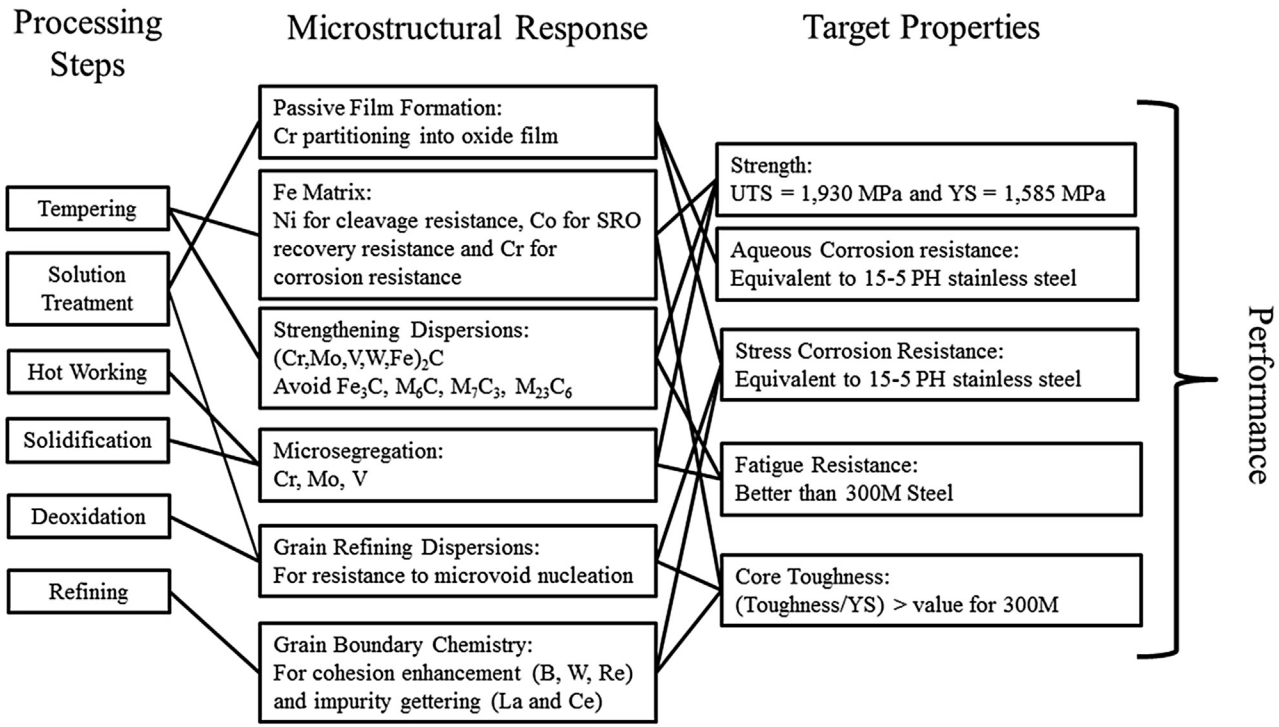


FIGURE 1.9

Processing—microstructure—property relations for an ultrahigh strength, corrosion-resistant steel. These charts illustrate the "Systems Approach" for materials design.

Adapted from G.B. Olson, Genomic materials design: the ferrous frontier, Acta Materialia, 61 (2013) 771–781.

1976 of "Alloy and Microstructural Design," describing the designing of alloys with the microstructures necessary to achieve individual properties like strength, fracture toughness, and creep resistance [22].

Olson's "Systems Approach" has perhaps been the first and most successful in model-based, computational design of alloys, many of which have been successfully commercialized [17]. This integrated approach considers the desired material as a system with target properties synthesized from the perspectives of material designers, suppliers, modelers, and structural designers. The material properties of interest are considered as subsystems and the performance goals for the alloys are achieved by employing processing methods (the means to achieve the target property goals, as illustrated for example in Fig. 1.9) that provide the optimum microstructures. A corresponding hierarchy of computational models (Fig. 1.6) and validation experiments are used to arrive at the final alloy composition and processing approach. This approach has the advantage of significantly reducing the cost and shortening the alloy development cycle. Although typical empirical alloy design approaches would require tens, if not more, of trial and error prototype compositions to be made and tested, the goals can be achieved with two or three prototypes with the systems approach [23]. Computational modeling itself can become very intensive and expensive. Spectral methods have been developed and applied to compress these requirements and to enable the inverse process of designing the "microstructure" for given performance [24].

The advances made in recent years in the ability to computationally model and simulate materials behavior across the entire length scales of materials phenomena have also increased the appeal of the systems approach to rapidly and inexpensively design alloys and processes to meet performance goals. The challenge in computational modeling and simulation arises from the range of length and time scales that govern materials response, as shown in Table 1.5 [25]. This problem is mitigated somewhat by the fact that most phenomena of interest in alloy design occur only in the "microstructural" regime in Fig. 1.5.

Computational materials science and engineering has also given rise to the field of ICME, mentioned earlier. ICME is usually defined as "the integration of materials information, captured in computational tools, with engineering product performance analysis and manufacturing-process simulation" [19]. The ICME approach has been applied successfully to many industrial problems [26], one of the earliest being the development of the "Virtual Aluminum Casting" process that links product design and manufacturing up front and provides a capability to predict product properties and durability that can then be used to adjust the processing, all virtually before components are fabricated [27]. The product development knowledge base for the "use cases", for example, castings, comprises all the legacy information such as microstructure−property relationships, manufacturing process, costs, etc., and could include the relevant associated analytical, computational, and statistical models.

The application of the systems approach to design alloys in the context of computational materials design and ICME, the modeling methods used, and the alloys that have been developed are shown in the framework of the materials genome

Table 1.5 Length and Time Scales in Materials Science and the Approach Used to Simulate Materials Behavior

Structural Feature		Length Scale (m)	Time Scale (s)	Applicable Mechanics
Mechanical structure	Assembly	10^{3}	10^{6}	Structural mechanics
	Component	10^{1}	10^{6}	Structural and continuum mechanics
	Element	10^{-1}	10^{0}	
Material structure	Grains	10^{-3}	10^{-3}	Crystal plasticity
	Second phases and defects	10^{-5}	10^{-6}	Crystal plasticity
	Single dislocation	10^{-7}	10^{-9}	Dislocation dynamics
	Atomic	10^{-9}	10^{-12}	Molecular dynamics
	Electronic orbitals	10^{-11}	10^{-15}	Quantum mechanics

Adapted from R. Lesar, Introduction to Computational Materials Science, Cambridge University Press, 2013.

timeline in Fig. 1.10 [28]. As depicted in this figure, the MGI traces its origin to the early work in the development of the Calculation of Phase Diagrams approach, which itself can be traced to the work of Kaufman and Cohen [29], the thermodynamics and kinetics models and software, including material databases (Thermocalc, Dictra, Pandat, Precipicalc) and their more recent integration with the density functional theory methods. The parallel development of computationally designed alloys (principally iron-based), advances in the integrated modeling methodologies under several government sponsored programs, and Ford's virtual aluminum castings program are also seen. These programs were also concurrently reported in workshops and documented in their proceedings [19,20,30].

The genomic systems approach to alloy design utilizing computational modeling and simulation across the relevant length scales is very powerful in accelerating the development and insertion of materials at lower cost for targeted applications. As described in the next section, this approach can also be applied readily to developing alloys that are amenable to many of the state-of-the-art, revolutionary manufacturing processes such as friction stir welding and additive manufacturing. However, to use these approaches successfully, the hierarchical relationships and the underlying physical metallurgy mechanisms for the processing/microstructure/property/performance interactions must be clearly understood for the alloy systems being developed.

1.6 ALLOY DESIGN FOR MATERIAL MANUFACTURABILITY

Materials developed for use in structures are fabricated into components by a variety of processes such as machining, forming, chemical milling, and the like. The

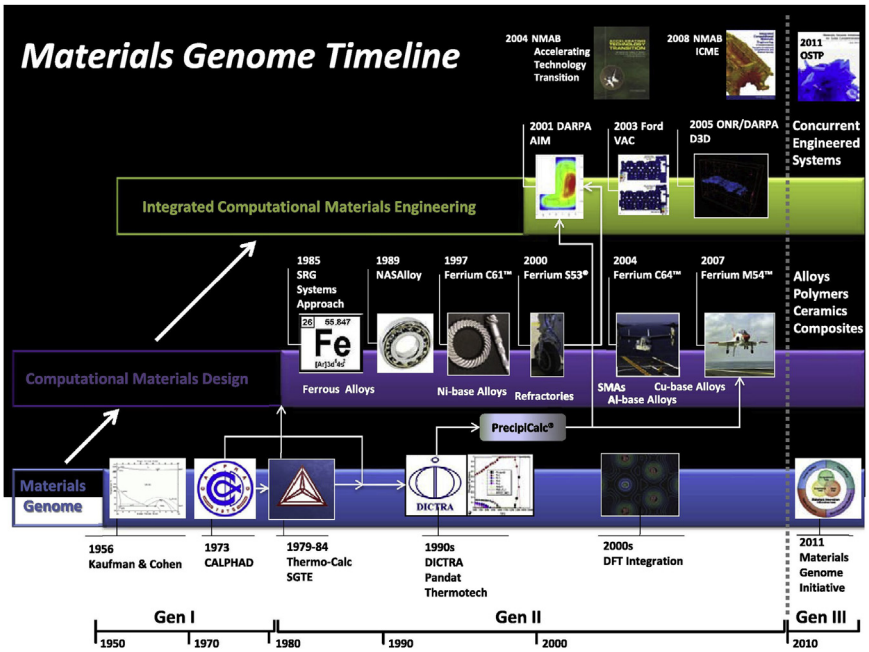


FIGURE 1.10

Materials genome timeline [28].

response of the materials to these processes is generally not considered during alloy design and the microstructures carefully tailored for achieving a balanced combination of optimum properties may be altered with negative consequences. Examples include the elimination of the preferential grain flow produced in the desirable direction in aluminum alloy forgings, by metal removal during subsequent machining and the distortion of machined components due to the development of residual stresses caused by material removal.

Product design is evolving rapidly to take advantage of new metal processing capabilities, such as superplastic forming [31] and more recently friction stir welding [32] to create integrated, unitized structures that simplify design, reduce the number of parts in an assembly, and eliminate large numbers of fasteners, all of which reduce weight and cost. These processes have the potential to economically fabricate structures that are otherwise not possible using traditional manufacturing methods. However, alloys as designed presently typically cannot be processed by these techniques without suffering a reduction in properties, such as the strength reduction in friction stir welded aluminum alloy 7050 (Fig. 1.11) that cannot be recovered by postweld treatments [33]. Hence, all too often, these processes do not find extensive use due to the negative effects on the properties of alloys with microstructures that were not initially designed to take advantage of them.

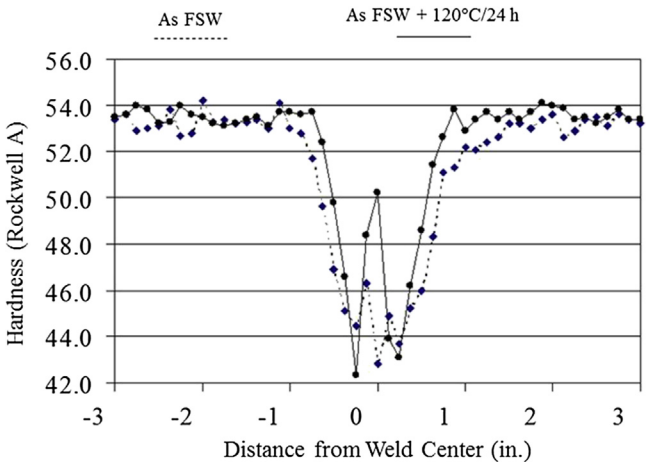


FIGURE 1.11

The hardness reduction in friction stir welded high-strength 7050 aluminum alloy [33].

Additive manufacturing is an emerging technology to revolutionize production of parts on demand with the potential to reduce cost and energy use [34]. Materials undergo complex thermal cycles during additive manufacturing that are different from those experienced during traditional processing of alloys, and the resulting microstructures may not be representative of those designed initially.

The underlying mechanisms of the processing—microstructure—property—performance interactions and hence the alloy design approaches are the same for designing hierarchical microstructures for properties or manufacturability or a combination of both.

1.7 SUMMARY

The central theme of this book is the discussion, in "Systems Approach" framework, of the processing—microstructure—property relations for aluminum, titanium, and steel alloys presently used in airframes and that of magnesium and "complex" alloys with potential for future use. This is a powerful method for understanding the metallurgical principles operating in alloys of increasing microstructural complexity that are in present use, thereby also providing methods for designing better alloys. Another advantage of this approach is the ability to design alloys with microstructures that are amenable to fabrication of structures by promising state-of-the-art processing approaches, for example, friction stir welding and additive manufacturing.

Alloys used in airframe applications provide a rich variety of microstructural features and encompass multiple strengthening mechanisms and deformation modes. A discussion of these alloys by comparing and contrasting their behavior in the

framework discussed earlier is an excellent way to understand their fundamental metallurgical behavior, which is necessary for the judicious selection and use of the existing alloys as well as for the application of integrated approaches for microstructural design for property targets and manufacturing operations for specific applications.

1.8 ORGANIZATION OF THE BOOK

The reminder of the book is organized as follows:

- Chapter 2 provides an overview of the mechanisms that govern the processing—microstructure—properties relationships, which form the basis of the "Systems Approach" for alloy and process design. Features of the material properties, hierarchical microstructures, and the sensitivities of the properties to the microstructure or lack thereof are discussed in terms of the ability to predictively model the properties. Emphasis is on aluminum, titanium, magnesium, and steel alloys with diverse and distinct microstructural features, which are compared and contrasted to describe alloy design for both properties and amenability to manufacturing.
- Chapter 3 reviews the state of alloy design evolving from the traditional, empirical methods, and trending toward the increasing use of theoretical, physics-based, and data-based models in the "Material by Design", ICME, and MGI framework.
- Chapters 4—8 discuss the physical metallurgy of aluminum, titanium, steel, magnesium, and "complex" alloys, respectively. Each of these chapters is generally divided into three sections, with the first section covering the metallurgical features unique to each alloy family that render them useful for particular structural applications, the second section discussing commercial alloys that are in current use and how unique combinations of various properties are achieved in them and the third section discussing future directions and approaches for alloy design.
- Chapter 9 covers alloy design for manufacturability focusing on three technologies:
  - superplastic forming, which is relatively well established,
  - friction stir welding, which is beginning to see increasing applications, and
  - additive manufacturing, which promises to be a breakthrough process for the future.
- Chapter 10 describes briefly the approaches to implementing alloys and processes in practice and provides a summary with concluding remarks on future outlook.
- Appendices cover various topics relevant for materials and processes modeling and for estimating properties from superposition of contributions to properties from hierarchical features.

REFERENCES

[1] G.B. Olson, Computational design of hierarchically structured materials, Science 277 (5330) (1997) 1237−1242.
[2] M.F. Ashby, Materials Selection in Mechanical Design, third ed., Elsevier, 2005, pp. 1−9. (Chapter 1).
[3] E.A. Starke Jr., J. Staley, Application of modern aluminum alloys to aircraft, Progress in Aerospace Science 32 (1996) 131−176.
[4] B. Smith, The Boeing 777, Advanced Materials and Processes 161 (9) (2003) 41−44.
[5] T. Dursun, C. Soutis, Recent developments in advanced aircraft aluminium alloys, Materials and Design 56 (2014) 862−871.
[6] Airbus Technical Digest FAST (Issue 32) (2013) 5.
[7] Airbus Technical Magazine FAST (2013) 7. Special Edition A350XWB.
[8] M.F. Ashby, Multi-objective optimization in material selection and design, Acta Materialia 48 (1) (2000) 359−369.
[9] M.F. Ashby, E. Cope, D. Cebon, Materials selection in engineering design (Chapter 10), in: K. Rajan (Ed.), Informatics for Materials Science and Engineering, Elsevier, 2013, pp. 219−244.
[10] G. Spanos, W.T. Reynolds, Microstructure of metals and alloys, in: Physical Metallurgy, fifth ed. vol. II, Elsevier, 2014, pp. 1073−1112.
[11] D.G. Pettifor, Controversial concepts in alloy theory revisited, The Science of Alloys for the 21st Century, in: A Hume-Rothery Symposium Celebration, TMS Fall Meeting, St. Louis, MO, 2000.
[12] R. Lakes, Materials with structural hierarchy, Nature 361 (1993) 511−515.
[13] K.K. Sankaran, R. Perez, K.V. Jata, Effects of pitting corrosion on the fatigue behavior of aluminum alloy 7075-T6: modeling and experimental studies, Materials Science and Engineering 297 (1−2) (1997) 223−229.
[14] J. Su, T.W. Nelson, R. Mishra, M. Mahoney, Microstructural investigation of friction stir welded 7050-T651 aluminum, Acta Materialia 51 (2001) 713−729.
[15] F. Vogel, N. Wanderka, Z. Balogh, M. Ibrahim, P. Stender, G. Schmitz, J. Banhart, Mapping the evolution of hierarchical microstructures in a Ni-based superalloy, Nature Communications 4 (Article 2955) (2013) 1−7.
[16] P.V. Liddicoat, X. Liao, Y. Zhao, Y. Zhu, M. Murashkin, E.J. Lavernia, R.Z. Valiev, S.P. Ringer, Nanostructural hierarchy increase the strength of aluminium alloys, Nature Communications 1 (63) (2010) 1−7.
[17] G.B. Olson, Genomic materials design: the ferrous frontier, Acta Materialia 61 (2013) 771−781.
[18] G.B. Olson, Designing a new materials world, Science 288 (5468) (2000) 993−998.
[19] Integrated Computational Materials Engineering: A Transformational Discipline for Improved Competitiveness and National Security, The National Academies Press, Washington, DC, 2008.
[20] Materials Genome Initiative for Global Competitiveness, Office of Science and Technology Policy, NSF, Washington, DC, 2011.
[21] R.F. Decker, Alloy design using second phases, Metallurgical Transactions 4 (11) (1973) 2495−2518.
[22] J.K. Tien, G.S. Ansell (Eds.), Alloy and Microstructural Design, Academic Press, 1976.

[23] C.E. Campbell, G.B. Olson, Systems design of high performance stainless steels I. Conceptual and computational design, Journal of Computer-Aided Materials Design 7 (2001) 145−170.
[24] D.T. Fullwood, S.R. Niezgoda, B.L. Adams, S. Kalidindi, Microstructure sensitive design for performance optimization, Progress in Materials Science 55 (2010) 477−562.
[25] R. Lesar, Introduction to Computational Materials Science, Cambridge University Press, 2013.
[26] M.F. Horstemeyer, Integrated Computational Materials Engineering (ICME) for Metals: Using Multiscale Modeling to Invigorate Engineering Design with Science, Wiley, 2012.
[27] J. Allison, M. Li, C. Wolverton, X. Su, Virtual aluminum castings: an industrial application of ICME, JOM 58 (11) (2006) 28−35.
[28] G.B. Olson, C.J. Kuehmann, Materials genomics: from CALPHAD to flight, Scripta Materialia 70 (2014) 25−30.
[29] L. Kaufman, M. Cohen, The martensitic transformation in the iron-nickel system, Transactions of the American Institute of Mining Metallurgical Engineers 206 (1956) 1393−1401.
[30] Accelerating Technology Transition, The National Academies Press, Washington, DC, 2004.
[31] E.J. Tegel, M.O. Pruitt, L.D. Hefti, SPF/DB takes off, Advanced Materials and Processes 136 (1) (1989) 36−41.
[32] R.S. Mishra, P.S. De, N. Kumar, Friction Stir Welding and Processing, Springer, 2014.
[33] K.V. Jata, K.K. Sankaran, J.J. Ruschau, Friction stir welding effects on microstructure and fatigue of aluminum alloy 7050-T7451, Metallurgical and Materials Transactions 31A (2000) 2181−2192.
[34] W.E. Frazier, Metal additive manufacturing: a review, Journal of Materials Engineering and Performance 23 (6) (2014) 1917−1928.

CHAPTER

Modeling of Processing–Microstructure–Properties Relationships

2

CHAPTER OUTLINE

Synopsis **22**
2.1 Properties of Structural Materials **22**
2.1.1 Physical Properties 22
2.1.2 Mechanical Properties 22
2.1.3 Electrochemical Properties 23
2.2 Microstructure–Properties Relationships **24**
2.2.1 Microstructural Features 24
2.2.2 Strength 24
2.2.3 Fracture Toughness 27
2.2.3.1 Aluminum Alloys 27
2.2.3.2 Steel Alloys 27
2.2.3.3 Titanium Alloys 28
2.2.3.4 Magnesium Alloys 29
2.2.4 Fatigue Properties 29
2.2.4.1 Aluminum Alloys 29
2.2.4.2 Steel Alloys 29
2.2.4.3 Titanium Alloys 31
2.2.4.4 Magnesium Alloys 31
2.2.4.5 Relationship of Fatigue Properties to Tensile Properties 31
2.2.5 Corrosion Resistance 32
2.2.5.1 Aluminum Alloys 32
2.2.5.2 Steel Alloys 33
2.2.5.3 Titanium Alloys 33
2.2.5.4 Magnesium Alloys 33
2.2.6 Effects of Anisotropy of Microstructural Features 34
2.3 Modeling of Microstructure–Property Relationships **34**
2.3.1 Strength 35
2.3.2 Fracture Toughness 35
2.3.3 Fatigue 36
2.3.4 Corrosion 36

Metallurgy and Design of Alloys with Hierarchical Microstructures. http://dx.doi.org/10.1016/B978-0-12-812068-2.00002-3
Copyright © 2017 Elsevier Inc. All rights reserved.

2.4 Modeling of Processing and Its Effects on Microstructure 37
2.5 Implications for Alloy and Process Design 38
2.6 Summary 39
References 39

SYNOPSIS

This chapter provides an overview of the mechanisms that govern the processing—microstructure—properties relationships, which form the basis of the "Systems Approach" for alloy and process design. Features of the material properties, hierarchical microstructures, and the sensitivities of the properties to the microstructure or lack thereof are discussed in terms of the ability to predictively model the properties. Methods used to model the effects of processing on microstructural development are also discussed briefly and related to the extent to which computational techniques can be applied for alloy and process design. Emphasis is on aluminum, titanium, magnesium, and steel alloys with diverse and distinct microstructural features and how they interact to provide combinations of properties important for mechanical design, which are compared and contrasted to describe alloy design for both properties and amenability to manufacturing.

2.1 PROPERTIES OF STRUCTURAL MATERIALS

The material properties, shown in Fig. 1.2, that determine airframe structural performance can be grouped into the following categories.

2.1.1 PHYSICAL PROPERTIES

Density is the most important physical property for material selection, unless precluded by constraints such as volume as in landing gear components, high cost, or lack of acceptable levels of other properties as in magnesium alloys. Physical properties such as heat and thermal conductivities and coefficients of thermal expansion become important considerations, particularly for structural assemblies made up of multiple material families. This is illustrated by the recent development of a high strength aluminum alloy with a higher value of electrical conductivity than those of current alloys, for compatibility with carbon-reinforced polymer composite materials in airframe structures [1].

2.1.2 MECHANICAL PROPERTIES

These include elastic properties (e.g., Young's, bulk, and shear modulus), strength (e.g., tension, compression, and shear), ductility, fracture toughness, and resistance to initiation and propagation of fatigue cracks. In addition to determining the

stiffness of structural members, as shown in Table 1.2, elastic properties also affect the stresses required to initiate plastic flow and thus the yield strength of the materials, as well as their fatigue and fracture behavior because the elastic energy release also contributes to the driving force for fracture.

2.1.3 ELECTROCHEMICAL PROPERTIES

Aluminum and steel alloys are susceptible to various types of corrosion and are always protected by surface treatments and coatings to prevent damage during service. Corrosion resistance of materials is measured in tests unique to each type of corrosion and the results are not always reported in quantitative terms. For example, susceptibility to exfoliation corrosion of high strength aluminum alloys is rated by the letters EA, EB, EC, and ED corresponding to the level of exfoliation ranging from superficial to very severe as determined by American Society for Testing and Materials (ASTM) tests. Resistance to stress corrosion cracking (SCC), which occurs in susceptible materials under load and environments specific to the material, is determined by loading smooth or precracked specimens. Electrochemical tests determine the corrosion susceptibility by measuring the corrosion and pitting potentials of second-phase particles. Thus the variety and the general lack of quantitative measures of resistance to the various types of corrosion coupled with a lack of knowledge of the anticipated service environments have thus precluded the use of electrochemical properties for structural design.

Materials are designed and developed for structures to perform at maximum possible efficiency for which density and mechanical properties are the primary considerations. However, the resistance of materials to corrosion, which increases maintenance costs during service and can also affect structural integrity, and their amenability to ease of operations such as machining and forming, which affect the manufacturing costs, are also important factors in materials selection. Table 2.1 lists the properties and attributes of materials that influence their selection for airframe structural applications. This is a general list and the required property

Table 2.1 Material Properties and Attributes That Influence Their Selection and Design

Physical properties	Density, thermal expansion, elastic moduli, Poisson's ratio
Static mechanical properties	Tensile, compressive, shear and bearing strength, ductility
Durability and damage tolerance	Fatigue strength and crack growth resistance, fracture toughness
Environmental resistance	Resistance to various types of corrosion and stress corrosion cracking
Producibility	Ingot casting and thermomechanical processability, machinability, chemical processing, inspectability

combinations and the need to possess additional attributes such as thermal and electrical conductivities will vary for each type of material and the application, such as shown in Fig. 1.2, for which it is considered.

2.2 MICROSTRUCTURE—PROPERTIES RELATIONSHIPS

Hierarchical nature of the microstructural features and their effects on material properties were discussed briefly in Section 1.3. This section provides a comparative overview of these features for specific alloy systems and how they affect the properties. The microstructures of wrought metallic alloys used in structural applications are the culmination of their evolution during processing that typically starts with ingot casting and proceeds through thermomechanical processing, heat treatments, and component fabrication by forming, machining, joining, and chemical processing. The morphologies of all the features constituting the microstructural hierarchy and their quantitative characterization enable modeling of the effects of processing on microstructure and material properties.

2.2.1 MICROSTRUCTURAL FEATURES

Aluminum, magnesium, titanium, and steel alloys possess distinct and diverse hierarchical microstructural features resulting from alloying with several elements and processing by various methods. Table 2.2 provides a representative listing and description of these distinguishing features in commonly used alloys in each family whose properties, except those for the magnesium alloy, are shown in Table 1.4.

The discussion is limited to wrought alloys as this product form accounts for most of the structural applications. The properties of the alloys are determined by the characteristics of the matrix phase(s), "second" phase(s), and the interactions between them. Titanium and iron exist in multiple allotropic forms providing opportunities for developing alloys with larger varieties of microstructures and properties compared with alloys of aluminum and magnesium, which exist in only one allotropic form. For airframe applications, this is particularly true of titanium alloys, which can be processed under a variety of conditions to produce a range of microstructures with corresponding property combinations.

2.2.2 STRENGTH

Aluminum, magnesium, and steel alloys designed for use in airframes are strengthened principally by precipitates, as shown in Fig. 2.1 [2—4]. In aluminum and magnesium alloys these precipitates form during aging of the supersaturated solid solution and in steels during the tempering of martensite. Two phase titanium alloys are strengthened by α—β interfaces shown in three microstructural variants in Fig. 2.2 [5]. The interfaces contribute to strength by acting as barriers to dislocation motion. Metastable and near-beta titanium alloys derive strength principally from the precipitation of α particles from the β phase, as shown in Fig. 2.3 [6].

Table 2.2 Hierarchical Microstructural Features in Structural Alloys

	Matrix	**Second Phases**
Aluminum (e.g., 7050 and 7055)	• Single phase (α-FCC) • Texture • Degree of cold work • Degree of recrystallization • Grain/subgrain size • Grain shape anisotropy • Grain boundary precipitate free zone	• Strengthening precipitates • Size, shape, orientation, volume fraction, distribution, degree of coherency with the matrix • Dispersoids • Size, volume fraction • Constituents • Size, volume fraction, distribution
Magnesium (e.g., AZ31)	• Single Phase (α-HCP) • Texture • Degree of cold work • Defects (e.g., twins) • Grain size	• Strengthening precipitates • Size, shape, orientation, volume fraction
Titanium (e.g., Ti—6Al—4V and near-β Ti—10V—2Al—3Fe)	**α—β alloys** • Two phases (α-HCP and β-BCC) • In alloys heat treated in the β region • Prior β grain size • Grain boundary α • Colony size • α lath thickness • β volume fraction and thickness • In alloys heat treated in the α + β region • β grain size • β volume fraction and size • Equiaxed α volume fraction and size • Secondary α volume fraction and size • α and β texture	• Typically no second phases • Silicide precipitates in some alloys for high-temperature properties
Iron (e.g., 300M and Aermet 100)	**Quenched/Tempered steels (300M)** **Secondary hardening steels (Aermet 100)** • Single phase (α-BCC) • Tempered martensite • Defect structure	• Strengthening precipitates • Size and volume fraction of carbides (alloy carbides in Aermet 100)

BCC, *body centered cubic;* FCC, *face centered cubic;* HCP, *hexagonal close packed.*

Although strengthening of structural alloys is typically attributed to one principal mechanism, additional mechanisms can also be effective. Some such examples for aluminum alloys are strengthening of the matrix by solid solution, cold work, and grain boundaries. Further, stacking faults and modulus misfit caused by the

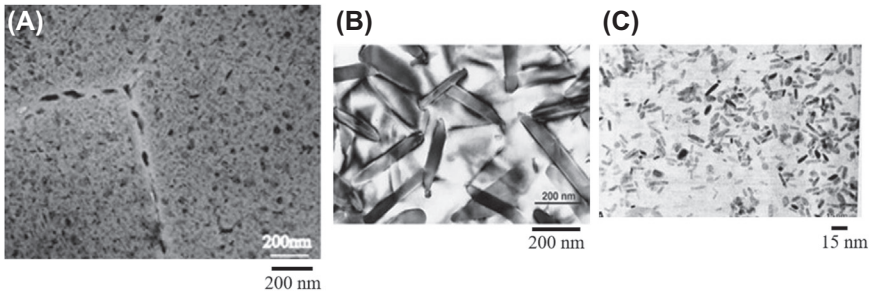


FIGURE 2.1

Precipitate microstructures (A) 7050 aluminum alloy showing η' and grain boundary precipitates [2]; (B) AZ 91 magnesium alloy showing β [3]; and (C) Aermet 100 showing M_2C alloy carbides [4].

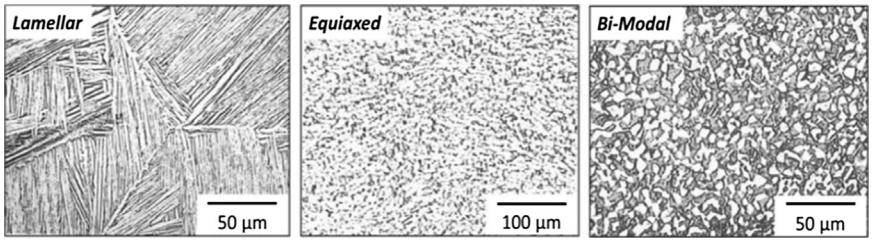


FIGURE 2.2

Lamellar, bimodal, and equiaxed microstructures for a representative α/β alloy [5].



FIGURE 2.3

Microstructure of aged Ti—10V—2Fe—3Al showing globular primary α and a high volume fraction of aged α precipitates in a β matrix [6].

difference in the properties between the matrix and the precipitates can also contribute to strength [7]. Similarly, the matrix phase in titanium alloys can be strengthened considerably by elements in solid solution, the most important of which is aluminum, and by oxygen, an interstitial solute element, which is also considered an impurity. The overall strength of the alloys then is a superposition of the contributions from all the operating mechanisms. The relative contribution from each mechanism will vary with the processing and heat treatments that produce various microstructures.

2.2.3 FRACTURE TOUGHNESS

The ability to resist fracture is a key characteristic for material selection for designing airframe structures. The critical stress intensity at which unstable crack propagation starts, the plane strain fracture toughness K_{Ic}, is an inherent material property used in the design of damage tolerant structures. As to be expected, the microstructural features and mechanisms that determine fracture toughness vary considerably with the alloy families.

2.2.3.1 Aluminum Alloys

The fracture toughness of high strength aluminum alloys is adversely affected by void nucleation at slip concentrations, constituent particles, coarse grain boundary precipitates, and precipitate free zones (PFZs) and the subsequent link up of these voids. In precipitation hardened alloys, slip accumulation and the resulting stress concentration and strain accumulation at obstacles, shown schematically in Fig. 2.4, provide sites for crack nucleation. Thus K_{Ic} will vary inversely with yield strength for a given alloy [8]. Although toughness can be improved by reducing the grain size to minimize the stress concentrations, an unrecrystallized microstructure is preferred in these alloys for optimum fracture and fatigue resistance. Using cleaner alloys to reduce the amount of constituents and controlling the heat treatment parameters to minimize or eliminate grain boundary precipitates and PFZs improve toughness without decreasing yield strength.

2.2.3.2 Steel Alloys

Similar to the behavior of aluminum alloys, the fracture toughness of ultrahigh strength, quenched, and tempered steels are also determined by the characteristics of the matrix and second phases. The chemistry and heat treatments of steel alloys are designed to eliminate any negative effects due to ductile—brittle transition and temper embrittlement. Fracture in these alloys occurs by the nucleation of voids at impurity particles, principally sulfides and oxides, and their subsequent coalescence. Modification of the types of the sulfide inclusions and increasing their spacing have a significant effect on increasing the fracture toughness [9,10]. Prior austenite grain size and the fine-scale structure of the tempered martensite matrix also affect fracture toughness. Austenitizing at a lower temperature to reduce the grain size must be balanced with the need to dissolve all the carbides prior to

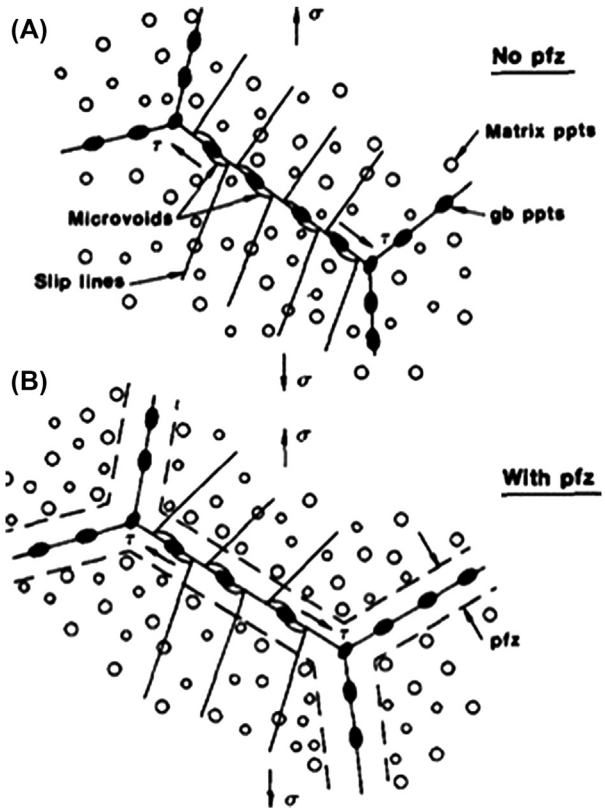


FIGURE 2.4

Schematic of slip localization in a precipitation hardened aluminum alloy: (A) precipitate shearing and (B) grain boundary precipitate free zones [8].

quenching from the austenite region, as undissolved carbides will decrease toughness. Similarly, the tempering temperature is balanced to achieve a fine-scale structure for good combinations of strength and fracture toughness.

2.2.3.3 Titanium Alloys

The use of triple arc melting practice and subsequent ingot processing ensure that titanium alloys are generally free of inclusions and pores that reduce the toughness of aluminum and steel alloys. In α/β titanium alloys, the highest toughness is achieved by processing in the high-temperature β region and transforming the β phase to produce a fully lamellar microstructure, shown in Fig. 2.2. This type of Widmanstatten structure features tortuous paths that increase the difficulty for cracks to proceed. Reducing oxygen and hydrogen impurities also increases the toughness of titanium alloys.

2.2.3.4 Magnesium Alloys

Very little information is available on the effects of microstructure on the fracture toughness of wrought magnesium alloys as they have not yet found applications in the design of critical structures. Both the texture and grain size affect the fracture toughness of these alloys. In an extruded magnesium alloy with a basal texture in which the basal planes in most of the grains were parallel to the extrusion direction, the toughness was higher in the direction perpendicular to the basal planes [11]. Grain refinement increases fracture toughness by preventing deformation twins, which are sources of microcracks, and by nucleating slip in basal and nonbasal planes [12].

2.2.4 FATIGUE PROPERTIES

Fatigue lives of components consist of crack initiation and propagation stages. Accordingly, the fatigue properties of materials used in design are characterized by their crack initiation lives and crack growth rates. The "Safe Life" approach to designing parts assumes that the total life of the component is consumed upon initiation of a crack in the material. The "Damage Tolerance" approach to design assumes the presence of flaws in the materials and that the life of the part is spent in the propagation of flaws to the critical size that initiates unstable fracture [13]. Crack initiation lives are characterized by the fatigue strength of the materials and are measured in stress-life (S—N) or strain-life (ε—N) tests. Crack growth rates are measured in tests that determine the crack extension per cycle (da/dN) as a function of the stress intensity at the crack tip (ΔK).

However, factors that increase the toughness of aluminum alloys are not always effective in reducing resistance to crack growth except at high rates approaching unstable propagation at stress intensities near the fracture toughness. At lower stress intensities and crack growth rates that represent stable crack growth and most of the fatigue life for damage-tolerant design of components, reduction of grain size and overaging have a detrimental effect as they reduce slip reversibility and crack tortuosity.

2.2.4.1 Aluminum Alloys

All the microstructural features that improve the fracture toughness of aluminum alloys by reducing strain localization will also increase their fatigue strength. As summarized in Table 2.3, homogenizing slip will mitigate the effects of shearable precipitates and modifying the grain structure and boundary morphologies will mitigate the effects of PFZs.

2.2.4.2 Steel Alloys

As with aluminum alloys, factors that increase the toughness such as reducing grain size and minimizing inclusions will also improve the fatigue strength of steel alloys. Except at rates approaching unstable crack propagation, microstructure has relatively little effect on fatigue crack growth [14].

Table 2.3 Influence of Microstructural Features on Properties

Property	Alloy Family	Microstructural Features for Property Enhancement	
		Matrix	**Second Phases**
Strength	Aluminum	• Solid solution, degree of cold work, and reduced grain size	• Precipitates with favorable size, shape, orientation, volume fraction, degree of coherency with the matrix and modulus misfit
	Magnesium	• Solid solution, texture, degree of cold work, and reduced grain size	
	Titanium	• α and β matrix phases (relative volume fractions, solid solution, texture, and grain size)	
	Steel	• Solid solution, degree of recovery, and grain size	• Carbide precipitates with favorable size and volume
Fracture Toughness	Aluminum	• Grain size reduction	• Reduce constituents and shearable precipitates that localize strain
	Titanium	• Increase proportion of lamellar microstructure	
	Steel	• Grain size reduction and elimination of impurities	• Reduction of inclusions
	Magnesium	• Grain size reduction and elimination of impurities	
Fatigue	Aluminum	• Grain size reduction for crack initiation resistance • Unrecrystallized matrix for crack growth resistance	• Reduce constituents and shearable precipitates for crack initiation resistance • Reduce constituents and overaged precipitates for crack growth resistance
	Titanium	• Reduce primary and lamellar α size for crack initiation resistance • Increase proportion of lamellar microstructure for crack growth resistance	
	Steel	• Grain size reduction and elimination of impurities for fatigue initiation resistance	
	Magnesium	• Grain size reduction for fatigue initiation resistance	
Corrosion	Aluminum	• Reduce grain shape anisotropy for exfoliation resistance • Reduce precipitate free zones (PFZs) for stress corrosion cracking (SCC) resistance	• Eliminate constituents for pitting and exfoliation resistance • Eliminate grain boundary precipitates for SCC and exfoliation resistance
	Steel	• Grain size reduction and elimination of impurities for SCC resistance	
	Magnesium	• Eliminate impurities for SCC resistance	

2.2.4.3 Titanium Alloys

For each of the three types of microstructures possible in two-phase titanium alloys (Fig. 2.2), the fatigue properties are affected principally by the morphologies and distribution of the alpha and beta phases. In fully equiaxed microstructures, fatigue cracks nucleate at slip bands within the alpha grains and reducing the alpha grain size will increase the fatigue strength. For fully lamellar structures, cracks nucleate at slip bands within the alpha lamellae or at alpha zones along prior beta grain boundaries. For bimodal microstructures, cracks can nucleate within the lamellar matrix, within the primary alpha grains or at the interface between the lamellar matrix and the primary alpha phase [14]. In all these cases, reducing the size of the primary alpha grains and the width of the alpha lamellae will increase the fatigue strength. Alloys with equiaxed grains will exhibit higher fatigue crack growth rates than those with fully lamellar microstructures. The crack growth rates for alloys with bimodal microstructures will fall between those for the equiaxed and lamellar microstructures.

2.2.4.4 Magnesium Alloys

As with fracture toughness, not much information is available on the fatigue properties of wrought magnesium alloys. In these alloys, fatigue crack initiation is related to slip in preferentially oriented grains and micropores. Crack growth mechanisms can be brittle or ductile and transgranular or intergranular [15].

2.2.4.5 Relationship of Fatigue Properties to Tensile Properties

Fatigue strength of structural alloys, typically defined as the maximum stress amplitude for a life of 10^7 or 10^8 cycles, generally increases with increasing tensile strength, although the proportional increase is different for each alloy family. The fatigue strength to tensile strength ratios for ultrahigh strength materials is not always as high as to be expected but may even decrease beyond certain strength levels [16]. This ratio is high and generally close to 0.5 for nonheat treatable Al alloys and steels tempered to low strength levels and is about 0.3 for precipitation hardened Al alloys. Such behavior is attributed to the mechanisms of fatigue deformation in materials with different microstructural features. Slip localization and the possible removal of precipitates from certain slip bands in precipitation hardened Al alloys causes softening and further accumulation of slip leading to crack nucleation [17]. In general, for alloys in which crack nucleation occurs internally at pores or particles, as in aluminum alloys, the ratio will be lower compared with those for alloys in which cracks nucleate only at the surface. Fatigue crack growth rates are relatively insensitive to the microstructure in the stable region as is evident from the crack growth curves for various aluminum alloys falling into one narrow scatter band shown in Fig. 2.5A [18]. The band includes growth rates for both heat treatable and nonheat treatable alloys with yield strength values ranging from 37 to 65 ksi (~250–450 MPa). The growth rates for different families of alloys are also similar when the stress intensity is normalized to the elastic modulus, as shown in Fig. 2.5B for Ni, Al, Fe, and Ti alloys [15].

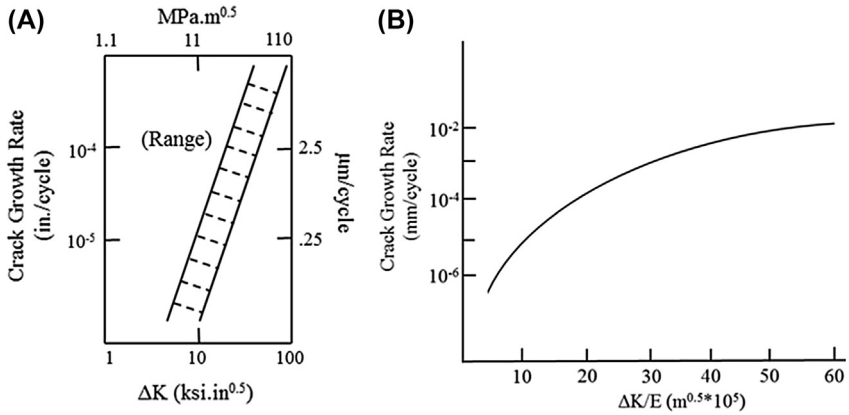


FIGURE 2.5

(A) Fatigue crack growth behavior for aluminum alloys and (B) fatigue crack growth rate curve as a function of stress intensity normalized by modulus for several materials, in vacuum and $0 < R < 0.1$.

(A) Adapted from Fatigue life of aluminum alloys, in: Fatigue and Fracture, in: ASM Metals Handbook, vol. 19, ASM International, 1996, pp. 785–800. (B) Adapted from Fatigue and fracture resistance of magnesium alloys, in: Fatigue and Fracture, in: ASM Metals Handbook, vol. 19, ASM International, 1996, pp. 874–881.

Permission of ASM International. All rights reserved. www.asminternational.org.

2.2.5 CORROSION RESISTANCE

Among the many types of corrosion observed in service, microstructure has a strong influence on the susceptibility to pitting, exfoliation, and intergranular corrosion, which cause localized attack and to SCC and corrosion fatigue, which occur in conjunction with loading. Other types of corrosion such as crevice corrosion and filiform corrosion are initiated in structural details in crevices, recessed areas, and under protective coatings with further attack proceeding in the forms of localized corrosion. Many of these forms of corrosion types are also specific to the types of materials and not all occur in every structural material family.

2.2.5.1 Aluminum Alloys

The heterogeneous microstructure of aluminum alloys (Fig. 2.1), tailored for acceptable mechanical properties renders them susceptible to localized corrosion due to the presence of second-phase particles with electrochemical characteristics that differ from those of the matrix [19]. Breakdown of surface passive film in the vicinity of intermetallic constituent particles in a corrosive environment initiates pitting in these alloys. Once formed, intermetallic constituent particles cannot be eliminated from the alloy and the pitting resistance cannot be improved by heat treatments. Intergranular corrosion proceeds selectively along grain boundaries and exfoliation corrosion proceeds beneath the surface along grain boundaries (intergranular corrosion) or along stringers of intermetallic particles. Thick plate products of aluminum alloys, which have highly elongated grain structures and are precipitation hardened

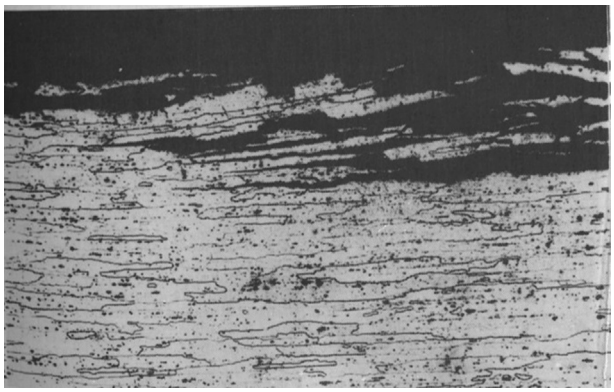


FIGURE 2.6

Exfoliation in the high strength aluminum alloy 7178-T651 showing how exfoliation corrosion develops along thin, elongated grains [20].

Reprinted with permission of ASM International. All rights reserved. www.asminternational.org.

to peak strength, show maximum susceptibility to exfoliation corrosion resulting in grain lift out, as shown in Fig. 2.6 [20]. SCC occurs in susceptible aluminum alloys under tensile loading and in specific environments. The resistance to both exfoliation and SCC can be improved significantly by overaging, however, at the expense of strength.

2.2.5.2 Steel Alloys

SCC is the most important consideration for selection of ultrahigh strength steels for airframe applications. The threshold stress intensity for a specific environment (K_{Iscc}) generally decreases with increasing yield strength and the SCC fracture path is typically along prior austenite grain boundaries. Attempts to increase the resistance to SCC have focused on refining the grain size and mitigating the effects of impurity elements that segregate to the grain boundaries [9].

2.2.5.3 Titanium Alloys

Titanium alloys have excellent corrosion resistance. They do not pit and corrosion is not a consideration for their selection and use in airframe applications [21]. SCC can occur in α/β alloys with high aluminum contents when heat treatment produces the ordered Ti_3Al phase, due to the susceptibility of the α phase.

2.2.5.4 Magnesium Alloys

Corrosion behavior of magnesium alloys is severely degraded by small amounts of impurity elements such as Fe, Cu, and Ni and the amounts of these elements must be less than their solubility limits [22]. The susceptibility of magnesium alloys to SCC increases with Al content, is the greatest in alloys with Zn and Al as the alloying elements, and is lower in alloys with rare earths and Zr [15].

2.2.6 EFFECTS OF ANISOTROPY OF MICROSTRUCTURAL FEATURES

Directional variations in the properties of wrought products of structural materials can arise both from texture and from the anisotropy of the microstructural features. There is necessarily no correlation between these factors. For example, materials exhibiting grain shape anisotropy as shown in Fig. 1.7 may not exhibit texture. Texture will have a major effect on the deformation behavior and mechanical properties of alloys with limited slip systems such as hexagonal close packed (HCP) magnesium alloys and titanium alloys with significant HCP α phase content. On the other hand, even without any texture, properties of alloys with anisotropic grain shapes and distribution of second-phase particles as stringers along the primary thermomechanical working direction (e.g., rolling direction) will be higher in this direction than in the short transverse direction (shown as L and S directions, respectively, in Fig. 1.7). All these factors are important in alloy design as will be discussed subsequently.

The discussion thus far shows the complex nature of the microstructure—property relationships, summarized in Table 2.3, for the structural alloys by relating the effects of the various hierarchical features on properties. The difficulty, if not the impossibility, of achieving maximum possible values of every property in a single alloy is immediately obvious. However, this complexity also opens up opportunities for tradeoffs by enabling multiple combinations of properties in a single alloy by processing it variously to achieve different microstructures. The latter fact is very important in the context of reducing the cost of developing and qualifying new materials as there will be no need to design a new alloy composition to meet every single property requirement.

2.3 MODELING OF MICROSTRUCTURE—PROPERTY RELATIONSHIPS

The purpose of modeling in the context of design of alloys is to understand the physical mechanisms responsible for their properties and performance. Quantitative modeling of the cause-and-effect relationships from processing-to-microstructure-to-properties-to-performance will provide the capability to design the microstructures and processing to develop materials that will meet property and performance goals. However, predictive models are not available to describe every cause-and-effect aspect of the microstructure—property relationships shown in Table 2.3. As stated recently by Rollett (as attributed in Ref. [23]), "it is presently feasible to model yield strength, challenging to model strain hardening, ductility and fatigue and very challenging to model corrosion." Significant progress continues to be made in this regard aided by the accumulation of empirical data and the advances in materials characterization techniques. The increasing computing capabilities also enable the mining of these data to uncover relationships, further advancing the development of physical models. Following is a brief discussion of the extent to which microstructure-sensitive properties of airframe structural alloys can be modeled.

2.3.1 STRENGTH

Strength of structural alloys is the result of the superposition of contribution from several mechanisms, with one being typically the dominant as in precipitation hardening for aluminum alloys. The contributions from each of the mechanisms are a function of one or more of the microstructural features that can be measured and used to model the strength. Fraser and Collins [24] have comprehensively reviewed the current state of modeling of the tensile properties of metallic materials. Among the mechanical properties, other than elastic modulus, yield strength is the easier one to model, particularly for aluminum, magnesium, and quenched and tempered steel alloys with a single matrix phase. For these alloys, the upper limit of precipitation hardening is given by the modified Orowan equation [25]:

$$\Delta\sigma_p \approx \frac{Gb}{S_p} \approx \frac{Gb(f)^{0.5}}{d}$$

where $\Delta\sigma_p$ is the contribution to the yield strength from the particles, G is the shear modulus, S_p is the interparticle spacing, d is the particle diameter, f is the volume fraction of the particles, and b is the magnitude of the Burgers vector, for $S_p >>$ the particle diameter. For aluminum alloys with G of 26 GPa and b of 0.284 nm, containing 0.05 volume fraction of 2-nm-diameter particles, the upper limit of yield strength is ~825 MPa (125 ksi). By comparison, the maximum yield strength of commercial aluminum alloys such as 7055 with multiple strengthening mechanisms is about 600 MPa (~90 ksi). This value has been calculated to be made up of about 300 MPa (~45 ksi) solely from precipitation hardening and the remainder due to contributions from grain boundaries and matrix–precipitate interactions including modulus misfit and stacking faults [7]. This example points to the tradeoffs in microstructures necessary to achieve acceptable combination of multiple properties.

In two-phase lamellar microstructures such as in Ti–6Al–4V, interphase interfaces form barriers to dislocation motion. These microstructures are characterized by features whose individual contributions cannot be separated and modeled easily. Mining of the large amount of available data on the tensile properties of this alloy using neural network approach has shown that solid solution strengthening of both the α and β phases along with the volume fraction of the α phase contribute to the strength [26].

2.3.2 FRACTURE TOUGHNESS

The fracture of aluminum alloys is controlled principally by the three types of second-phase particles and their effects on the matrix microstructure, yield strength, and work hardening behavior. Available models consider one or more of these features with the use of a specific model depending on the context in which it is being applied, as shown in the following.

- $K_{Ic}\ \alpha\ (f_v)^{1/6}$ for alloys with otherwise identical microstructures, where f_v is the volume fraction of the void-nucleating second-phase particles [27].

- $K_{Ic} \propto n(\sigma_y \sigma_c \lambda)^{1/2}$ for alloys with identical distribution of second-phase particles, where n is the work hardening exponent, σ_y is the yield stress, and σ_c and λ are the decohesion stress and the spacing of the particles [28].
- K_{Ic} values for alloy 7050 reported in the literature agree with the values predicted by [7].

$$K_{Ic} \approx \left[\frac{\sigma_{ys}}{(1-2\nu)} \left\{ \pi(1+n) l_o \left(\frac{\varepsilon_{yy}^p \; E}{\sigma_{ys}} \right)^{1+n} \right\}^{\frac{1}{2}} \right]$$

where n is the work hardening exponent, l_0 is the inclusion spacing, ε_{yy}^p is the plane strain fracture strain $= 0.25$, $\varepsilon_f = 0.25 \ln (1/(1-\text{RA}))$ (ε_f is the tensile fracture strain and RA is the reduction in area).

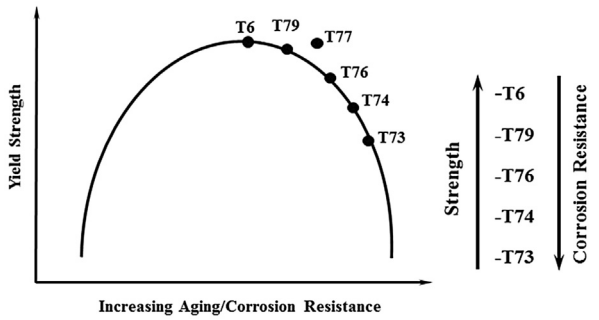
Although significant empirical data and knowledge on the toughness of titanium and steel alloys are available, predictive models encompassing all the relevant microstructural parameters have not been developed.

2.3.3 FATIGUE

Quantitative models relating fatigue properties to microstructural parameters are generally not available for use in alloy design. Fatigue strength usually scales with tensile strength and crack growth rates are relatively insensitive to the microstructure. Alloys are typically designed to meet strength targets and the heat treatments are subsequently modified to achieve balanced combination of strength and fatigue resistance. A recent experimental and polycrystal plasticity modeling study of two-phase titanium alloys has suggested the importance of $\alpha-\beta$ interfaces and β-phase volume fraction on the fatigue behavior and has indicated the effort required for tailoring microstructures to reach target properties [29].

2.3.4 CORROSION

As with fatigue, quantitative models relating corrosion to microstructural parameters are generally not available for use in alloy design. However, extensive knowledge exists on features that are either beneficial or detrimental to corrosion resistance of aluminum and steel alloys and a tradeoff is made to achieve the acceptable strength and corrosion resistance. Fig. 2.7 illustrates this approach for a high performance alloy such as 7055. As the alloy is overaged beyond the peak strength condition, the resistance to corrosion increases with a concomitant decrease in strength. Retrogression/reaging (RRA) treatment is a special aging treatment designed to produce acceptable corrosion resistance without much loss of strength. RRA treatment consists of aging the alloy already in the peak strength condition at a higher temperature to dissolve the strengthening precipitates followed by rapid cooling and reaging. The resultant distribution of strengthening precipitates is similar to that in the peak aged condition but the grain boundary precipitates are conducive to providing SCC resistance [30].



-T6	Peak Aged
-T77	Retrogression and Overaging
-T79	Very Limited Overaging
-T76	Overaged to Achieve Enhanced Exfoliation Resistance
-T74	Overaged to Achieve Enhanced Exfoliation and SCC Resistance
-T73	Overaged to Achieve Optimum Exfoliation and SCC Resistance

FIGURE 2.7

Heat treatment schemes for strength—corrosion resistance tradeoff.

2.4 MODELING OF PROCESSING AND ITS EFFECTS ON MICROSTRUCTURE

Models describing the microstructural evolution of alloys have been classified into (1) material models that describe grain growth, precipitation, and similar phenomena that occur within the material and (2) process models that describe the effects of manufacturing resulting in macroscopic changes in the component such as in forging or friction stir welding [31]. The distinction into materials and process models is somewhat arbitrary with the goal being the ability to model the evolution of the microstructure and predict its final state, which can then be used for predicting the properties. These models can be phenomenological in which the underlying physical mechanisms are not fully known or they can be mechanistic. For example, the Avrami equations describing recrystallization kinetics are phenomenological models, whereas the Hall—Petch equations relating grain size to strength are mechanistic models. A key difficulty in modeling the evolution of microstructure is the treatment of the interfaces such as between the matrix and precipitates. Phase field methods overcome this problem by representing the entire microstructure continuously by a single variable, the order parameter. In the case of a system with matrix and precipitates, the order parameter will be 1 for the precipitate, 0 for the matrix, and between 0 and 1 for the interface [32].

Prediction of microstructure is valuable in many different situations such as for achieving critical properties, e.g., fracture toughness or when optimizing processes (e.g., welding speed or extrusion rate) or for coupling multistage processes for alloy and process development (e.g., effect of homogenization on grain growth after

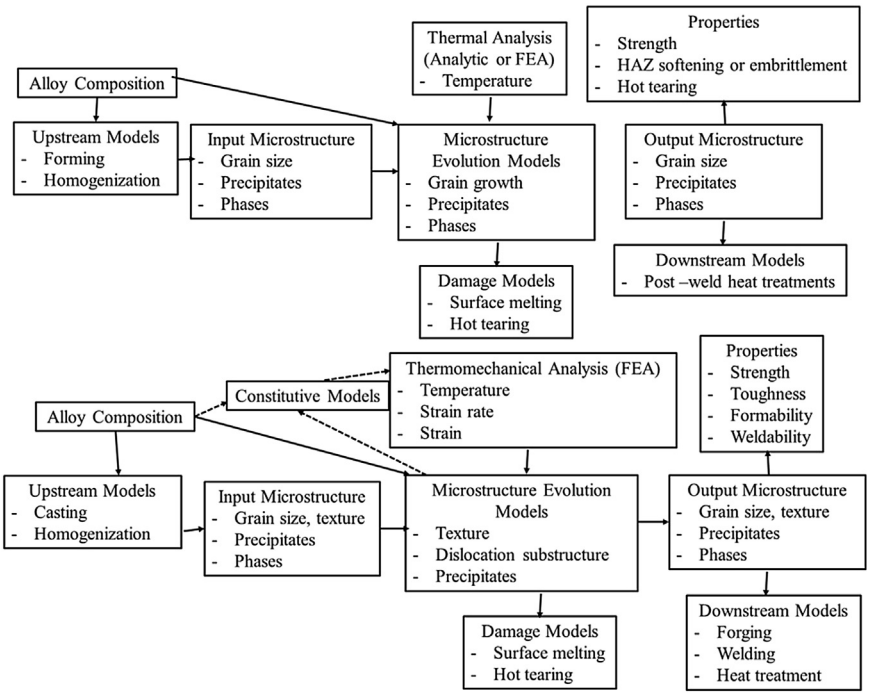


FIGURE 2.8

Schematic diagram showing the components of process models for welding (top) and hot rolling (bottom) [33].

forming). Fig. 2.8 [33] depicts the interplay between different components of material and process models and illustrates its applicability to alloy and process design.

Detailed descriptions of material and process modeling and simulation for structural alloys are included in the ASM Metals Handbook Volume 22A, *Fundamentals of Modeling for Metals Processing* and Volume 22B, *Metals Process Simulation*. Information from these volumes and other available sources will be used to describe specific alloy systems in subsequent chapters.

2.5 IMPLICATIONS FOR ALLOY AND PROCESS DESIGN

Quantitative, mechanistic understanding of the processing—microstructure—property schemes for alloys with hierarchical microstructures is evolving rapidly. Coupled with this, the development of computational capabilities and accumulated empirical knowledge has rendered alloy design for properties and manufacturability feasible. Many successes have already been reported. These range from the modeling and validation of a simple, nonheat treatable aluminum alloy to reduce

its cost by increasing use of scrap in the melt [34] to the computational design of aluminum sheet alloy for formability for auto components [35] and the flight of the first fully computationally designed and qualified steel [36], which all will be discussed in the third chapter. This trend, which can be expected to continue, bodes well for alloy design to keep pace with the development of revolutionary manufacturing processes and for reducing the cost and time for their qualification and insertion in critical applications.

2.6 SUMMARY

This chapter provided a brief overview of the important features of the processing and microstructures that determine the properties of structural alloys for selection and use in mechanical design. The ability or otherwise to model the relationships among these features in terms of gaps in their understanding was discussed in the framework of alloy and process design. The discussion will serve as a basis for the detailed review of specific alloy families in subsequent chapters.

REFERENCES

[1] B.L. Reichlinger, B.J. McElroy, Iulian Gheorghe, Aluminum Zinc Magnesium Silver Alloy, US Patent 8557062, October 15, 2013.
[2] J. Su, T.W. Nelson, R. Mishra, M. Mahoney, Microstructural investigation of friction stir welded 7050-T651 aluminum, Acta Materialia 51 (2001) 713−729.
[3] J.-F. Nie, Precipitation hardening in magnesium alloys, Metallurgical and Materials Transactions A 43 (2012) 3891−3939.
[4] R. Ayer, P. Machmeier, Transmission electron microscopy examination of hardening and toughening phenomena in Aermet 100, Metallurgical Transactions A 24 (1993) 1943−1953.
[5] S. Tamirisakandala, P. Russo, 60 years of microstructure development in titanium alloy technology development, in: Proceedings of 13th World Conference on Titanium − 2015, TMS-Wiley, 2016, pp. 713−716.
[6] J.D. Cotton, R.D. Briggs, R.R. Boyer, S. Tamirisakandala, P. Russo, N. Shchetnikov, J.C. Fanning, State of the art in beta titanium alloys for airframe applications, JOM 67 (6) (2015) 1281−1303.
[7] M. Dixit, R.S. Mishra, K.K. Sankaran, Structure−property correlations in Al 7050 and Al 7055 high-strength aluminum alloy, Materials Science and Engineering A 478 (2008) 163−172.
[8] A.K. Vasudevan, R.D. Doherty, Grain boundary ductile fracture in precipitation hardened aluminum alloys, Acta Metallurgica 35 (1987) 1193−1219.
[9] W.M. Garrison, Ultrahigh-strength steels for aerospace applications, JOM 42 (5) (1990) 20−24.
[10] Y. Tomita, Improved fracture toughness of ultrahigh strength steel through control of non-metallic inclusions, Journal of Materials Science 28 (1993) 853−859.

[11] H. Somekawa, T. Mukai, Effect of texture on fracture toughness in extruded AZ31 magnesium alloy, Scripta Materialia 53 (2005) 541−545.
[12] H. Somekawa, A. Singh, T. Mukai, High fracture toughness of extruded Mg−Zn−Y alloy by the synergistic effect of grain refinement and dispersion of quasicrystalline phase, Scripta Materialia 56 (2007) 1091−1094.
[13] M.P. Kaplan, T.A. Wolff, Life extension and damage tolerance of aircraft, in: Fatigue and Fracture, ASM Metals Handbook, vol. 19, ASM International, 1996, pp. 559−565.
[14] F.C. Campbell, Fatigue and fracture of engineering alloys, in: F.C. Campbell (Ed.), Fatigue and Fracture − Understanding the Basics, ASM International, 2012, pp. 209−261.
[15] Fatigue and fracture resistance of magnesium alloys, in: Fatigue and Fracture, ASM Metals Handbook, vol. 19, ASM International, 1996, pp. 874−881.
[16] J.C. Pang, S.X. Li, Z.G. Wang, Z.F. Zhang, General relation between tensile strength and fatigue strength of metallic materials, Materials Science and Engineering A 564 (2013) 331−341.
[17] I. Polmear, Aluminium alloys, in: Light Alloys, Elsevier, 2005, pp. 29−96.
[18] Fatigue life of aluminum alloys, in: Fatigue and Fracture, ASM Metals Handbook, vol. 19, ASM International, 1996, pp. 785−800.
[19] N. Birbilis, R.G. Buchheit, Electrochemical characteristics of intermetallic phases in aluminum alloys an experimental survey and discussion, Journal of the Electrochemical Society 152 (4) (2005) B140−B151.
[20] E.H. Hollingsworth, H.Y. Hunsicker, Corrosion of aluminum and aluminum alloys, in: Corrosion, ninth ed. ASM Handbook, vol. 13, ASM International, 1987, pp. 583−609.
[21] R.R. Boyer, Attributes, characteristics and applications of titanium and its alloys, JOM 62 (5) (2010) 21−24.
[22] B.A. Shaw, R.C. Wolfe, Corrosion of magnesium and magnesium-base alloys, in: Corrosion: Materials, ASM Handbook, vol. 13B, ASM International, 2005, pp. 205−227.
[23] K. Feldman, S.R. Agnew, The Materials Genome Initiative at the National Science Foundation: a status report after the first year of funded research, JOM 66 (3) (2014) 336.
[24] P.C. Collins, H.L. Fraser, Modeling of tensile properties, in: Fundamentals of Modeling for Metals Processing, ASM Handbook, vol. 22A, ASM International, 2009, pp. 377−399.
[25] E. Hornbogen, E.A. Starke Jr., Theory assisted design of high strength low alloy aluminum, Acta Materialia 41 (9) (1993) 1−16.
[26] P.C. Collins, S. Koduri, B. Welk, J. Tiley, H.L. Fraser, Neural networks relating alloy composition, microstructure and tensile properties of α/β-processed TIMETAL 6-4, Metallurgical and Materials Transactions A 44 (2013) 1441−1453.
[27] D. Dumont, A. Deschamps, Y. Brechet, A model for predicting fracture mode and toughness in 7000 series aluminium alloys, Acta Materialia 52 (2004) 2529−2540.
[28] G.G. Garrett, J.F. Knott, The influence of compositional and microstructural variations on the mechanism of static fracture in aluminum alloys, Metallurgical Transactions A 9 (1978) 1187−1201.
[29] B.D. Smith, D.S. Shih, D.L. McDowell, Cyclic plasticity experiments and polycrystal plasticity modeling of three distinct Ti alloy microstructures, International Journal of Plasticity (2013). http://dx.doi.org/10.1016/j.ijplas.2013.10.004.
[30] N.C. Danh, K. Rajan, W. Wallace, A TEM study of microstructural changes during retrogression and reaging in 7075 aluminum, Metallurgical Transactions A 14 (1983) 1843−1850.

[31] D.U. Furrer, S.L. Semiatin, Introduction to fundamentals of modeling for metals processing, in: Fundamentals of Modeling for Metals Processing, ASM Handbook, vol. 22A, ASM International, 2009, pp. 3–6.
[32] R.S. Qin, H.K. Bhadeshia, Phase field method, Materials Science and Technology 26 (7) (2010) 803–811.
[33] O. Grong, H.R. Shercliff, Microstructural modeling in materials processing, Progress in Materials Science 47 (2) (2002) 163–282.
[34] I.J. Polmear, J.E. Tibballs, B. Rinderer, Modeling composition/processing/property relationships in a cold-rolled aluminum alloy, JOM 51 (11) (1999) 51–54.
[35] P.E. Krajewski, L.G. Hector Jr., Y. Qi, R.K. Mishra, A.K. Sachdev, "Atoms to autos": a multiscale approach to modeling aluminum deformation, JOM 63 (11) (2011) 24–32.
[36] G.B. Olson, Genomic materials design: the ferrous frontier, Acta Materialia 61 (2013) 771–781.

CHAPTER

Alloy Design Approaches 3

CHAPTER OUTLINE

Synopsis 43
3.1 Alloys for Airframe Structures 43
3.2 Traditional Approaches for Alloy Design 44
3.3 Model-Based Approaches for Alloy Design 47
3.4 Examples of Model-Based Alloy and Product Design 50
3.5 Microstructure Representation for Model-Based Alloy Design 52
3.6 Summary 54
References 55

SYNOPSIS

This chapter reviews the state of alloy design evolving from the traditional, empirical methods and trending toward the increasing use of theoretical, physics-based models in the "Materials by Design", Integrated Computational Materials Engineering (ICME), and Materials Genome Initiative (MGI) framework. Use of models and computational methods is made possible by the increasing quantitative understanding of the multivariate nature of the microstructure−property relations responsible for materials behavior. This, in turn, is aided by the ability to rapidly characterize and digitally represent microstructural features and the use of materials informatics to statistically assess the large amounts of materials data being accumulated for inputs into model development and alloy design.

3.1 ALLOYS FOR AIRFRAME STRUCTURES

Very few of the 62 metals in the periodic table possess the right combinations of density, cost, availability, stability, and the feasibility for alloying and processing for them to be considered as base metals for structural alloy design. To date, only monolithic alloys based on aluminum, titanium, and iron have been used successfully and extensively in airframe structures. Aluminum- and titanium−matrix composite materials generally possess superior modulus and strength compared with the monolithic alloys and have found limited applications in aerospace structures [1] but their

Metallurgy and Design of Alloys with Hierarchical Microstructures. http://dx.doi.org/10.1016/B978-0-12-812068-2.00003-5

Copyright © 2017 Elsevier Inc. All rights reserved.

widespread use has been limited by high cost and manufacturing limitations. Considerable research is presently underway in the development of high-entropy alloys with high-strength, low-density, and high-temperature capabilities [2]. Unlike traditional alloys, they are based on more than four and typically five elements in equal amounts [3] and are in the early stages of development with the promise for future use.

Airplanes are designed, deployed, and maintained to remain in service for at least two, if not more, decades. Entirely new airplanes such as the Boeing 787 and Airbus A350 are developed rather infrequently and once in service, continue to be reintroduced as derivative models with limited scope for new materials substitution. Thus opportunities for the insertion of new materials do not arise often enough due to the long service lives of airplanes. On the other hand, when a new airplane is being designed, the time interval for materials selection is short and improved materials are not considered unless they are ready with properties that can be used for structural design. Further, given the large amounts of processing, manufacturing, and properties data along with the service experience already available for established alloys, new alloys with marginal improvements in the properties typically will not be selected for design. Materials selection involves consideration of both performance improvements and cost of insertion, as will be shown with specific examples in later chapters on individual alloys.

Until the introduction of polymer–matrix composites in the Boeing 787 and Airbus A350, aluminum alloys were the principal materials used for airframes except for landing gear structures, which use ultrahigh strength steel alloys. The Boeing 777X presently under development will use metallic alloys for the fuselage and polymer–matrix composites for the wings [4]. The continuous improvements in the property combinations for the metallic materials used in airframes, shown for selected alloys in Figs. 3.1–3.3 [5], despite occurring only incrementally, have enabled significant increases in the performance of structures.

3.2 TRADITIONAL APPROACHES FOR ALLOY DESIGN

In the present alloy development and insertion schemes, a newer alloy can trace its lineage to all of the earlier ones it has replaced and revolutionary changes from traditional alloying and processing strategies typically do not occur [6]. Nevertheless, alloys having better combinations of properties continue to be developed and have been inserted successfully in the design of every new airplane. Some of the new aluminum, titanium, and steel alloys introduced this way are shown in Figs. 3.1–3.3. They serve to illustrate the traditional, semiempirical approaches to alloy design, based principally on experience and the known processing–microstructure–property relationships.

All the aluminum alloys presently used in airframe structures have evolved from the accidental discovery of precipitation hardening in 1901 and the identification of its causes in 1919 [7]. These alloys contain either copper or a combination of zinc

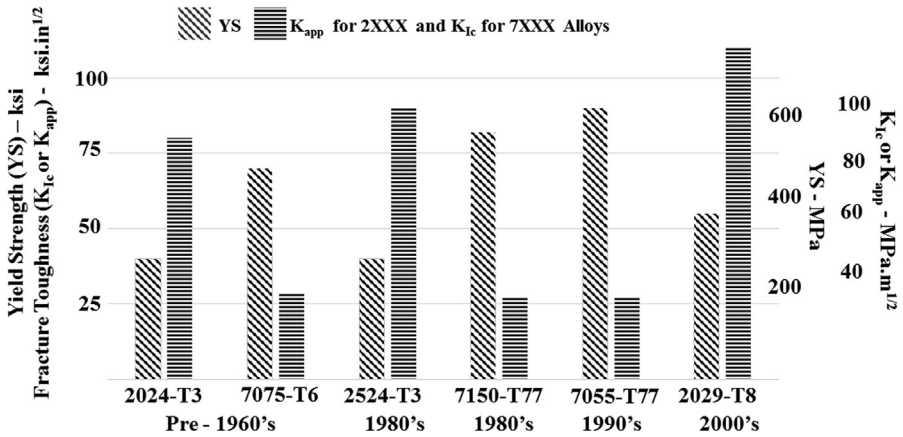


FIGURE 3.1

Evolution of aluminum alloys with varying property combinations.

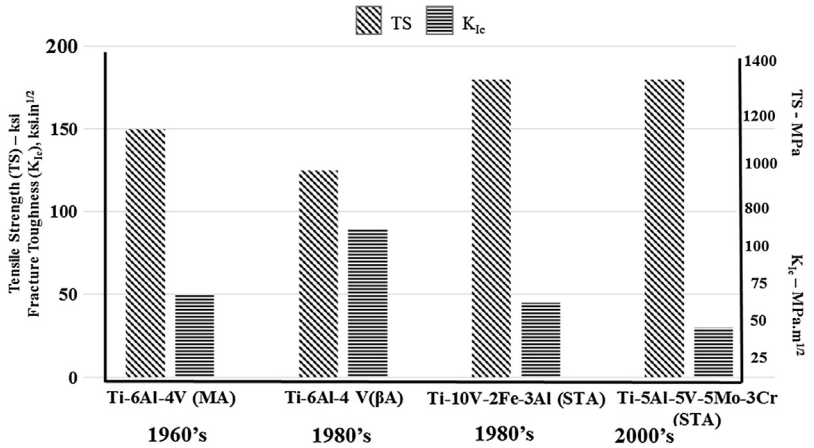


FIGURE 3.2

Evolution of titanium alloys with varying property combinations.

and magnesium as the primary alloying elements for precipitation hardening, respectively, resulting in better damage tolerance for fuselage skins or higher strength for upper wing skin applications. Tailoring of these alloys for particular property improvement has been based on applying the microstructure—property relationships listed in Table 2.3. Alloy 7055 was developed this way in the 1990s for the upper wing structures of the Boeing 777 [8]. Both alloys 7050 and 7055 have the same alloying elements (Table 1.4), but the use of higher amounts of the precipitation hardening solute elements combined with the retrogression and reaging heat

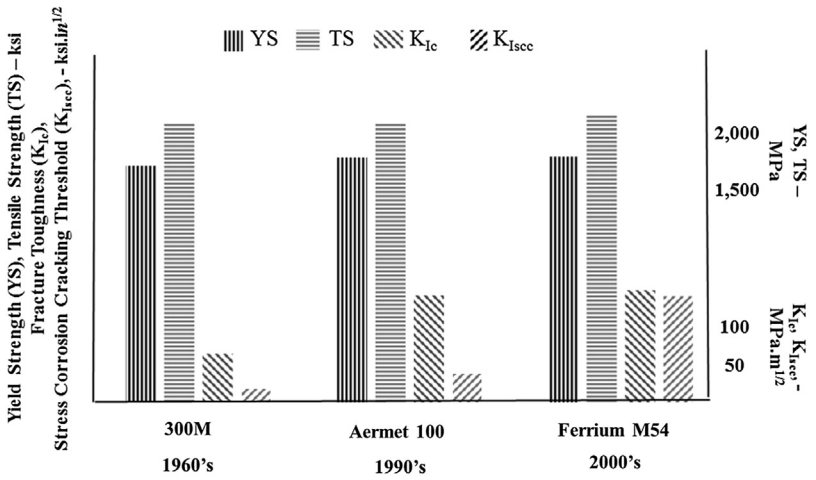


FIGURE 3.3

Evolution of ultrahigh strength steels with varying property combinations.

treatment (T77 temper shown in Fig. 2.7) for alloy 7055 provided higher strength and a balanced combination of toughness and corrosion resistance contributing to considerable weight savings. Alloy 7050 itself had been developed in the 1970s for better property combinations in thick sections compared with alloys such as 7075 developed in the 1940s. Development and insertion of alloy 2524 with lower impurity (Fe and Si) content than in alloy 2024 used in earlier airplanes increased the durability of fuselage structures. New alloys developed using similar approaches have been implemented in the Airbus A380 [9].

The basis for the development of titanium alloys used in aerospace structures is the manipulation of the volume fractions and morphologies of α and β phases by varying the amounts of the elements stabilizing these phases and thermomechanical processing. Applications for titanium alloys have grown with their development guided by the "enlightened empiricism" covering all aspects of their production [10]. Ti−6Al−4V, the most widely used titanium alloy, can be heat treated to achieve different strength and toughness combinations (Fig. 3.2). Metastable β titanium alloys are used for applications requiring higher strength than provided by Ti−6Al−4V (Table 1.4). Alloy Ti−10V−2Al−3Fe is replacing steel alloys in landing gear parts resulting in considerable weight savings [11].

Quenched and tempered, medium carbon 4340 and its variant 300M are the principal ultrahigh strength steels used for landing gear structures. The need for alloys with higher toughness and resistance to stress corrosion cracking without reducing strength was driven by the US Navy for airplanes operating in a carrier environment [12]. The alloy development approaches to meet these requirements were to increase the carbon content of the secondary-hardening, high-alloy steel AF 1410 (Fe−0.16 C−14Co−10Ni−2Cr−1Mo) from 0.16 to 0.20 wt% for increased strength and to

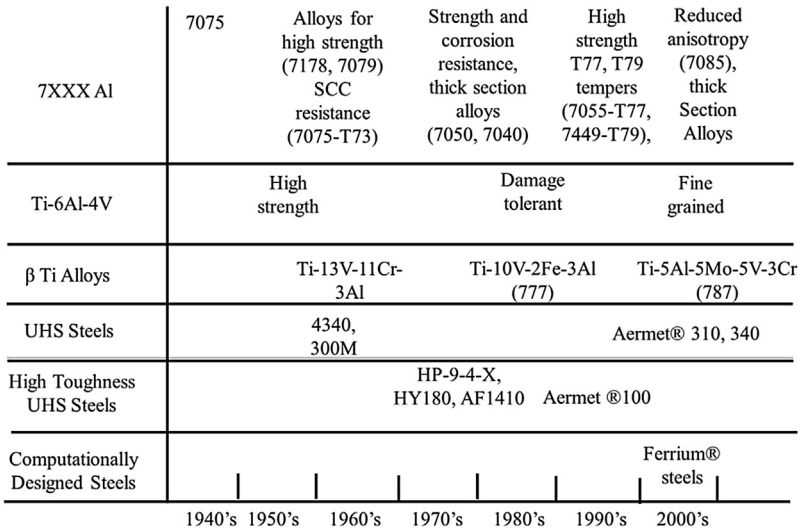


FIGURE 3.4

Timeline for the development of key alloying and processing strategies for representative structural alloys.

develop alloy Aermet 100 by increasing the carbon level to 0.23 wt% and adjusting the relative amounts of the other elements, as shown in Table 1.4.

Alloys in use today, shown in the above examples, have been designed using considerable trial and error experiments, with the need for empiricism and extensive testing reduced somewhat by the increased understanding of the physical mechanisms from prior experience. Fig. 3.4 provides a timeline of these developments wherein key changes were made in the alloying and processing approach, each of which had a positive impact on property combinations.

3.3 MODEL-BASED APPROACHES FOR ALLOY DESIGN

Traditional alloy design also uses models of materials behavior, although they are mostly empirical in nature with a few aspects such as precipitation hardening based on mechanistic models. However, physical mechanisms of materials behavior are being developed and validated at an accelerating pace enabling the use of theory in the design of alloys. This approach was used to determine that the features necessary for high strength and good fracture resistance in aluminum alloys should consist of ultrafine dispersion of noncoherent phases, in contrast with the coherent/semicoherent phases in traditional alloys, along with the addition of solute that decreases the stacking fault energy of the matrix and promotes planar slip [13]. The increasing use of models is further illustrated by the example of the combined use of first

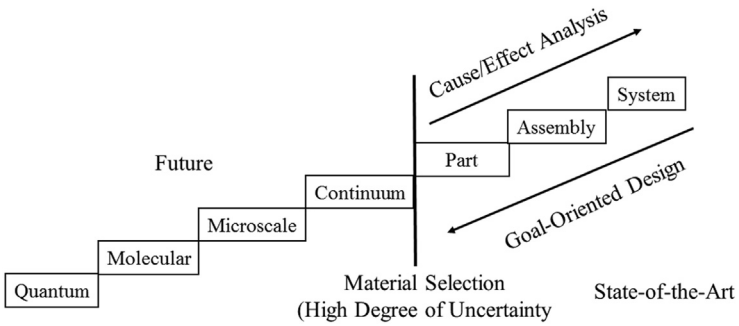


FIGURE 3.5

Hierarchy of levels from atomic scale to system level in concurrent materials and product design [15].

principles atomistic and phase diagram calculations, quantitative analysis, and empirical models to provide an approach to designing age hardenable, wrought aluminum alloy for moderate temperature applications, as will be discussed in the next chapter [14].

The ability to computationally design alloys will ensure that the optimum material is available within the typically short window for selection during product design. It will also eliminate the need to continuously develop alloys with incremental improvements in anticipation of future opportunities for which the timing and the requirements cannot be predicted with certainty. The goal of the "Materials by Design" and ICME approaches discussed briefly in the first chapter is to accelerate materials design targeting product design requirements by using material models, simulations, and databases. In this context, McDowell and Olson [15] have discussed the approaches to the "concurrent design" of materials and products. Referring to Fig. 3.5, materials design (left of the vertical solid line) presently occurs independent of product design (right of the vertical solid line). The challenge according to these authors is to "develop methods that employ bottom-up modeling and simulation, calibrated and validated by characterization and measurement to the extent possible, facilitated by top-down, requirements-driven exploration of the hierarchy of material length scales."

Materials design targeting specific products and performance requirements necessarily involves modeling across the length scales, as properties of materials are affected by phenomena occurring at each length scale. This is handled by multiscale modeling using either the concurrent approach in which one universal description of the system valid at all length scales is constructed or the hierarchical approach in which modeling is carried out at each scale from which information is extracted for use in the adjoining scale [16]. The book by Horstemeyer [17] discusses in detail the hierarchical multiscale modeling of an automotive component addressing the issues and methods used for bridging the various length scales.

This approach is also applicable to alloy design for airframes and other applications.

Materials databases are key to the success of model-based approaches to alloy design, from the point of view of both developing and validating models. Structural alloys contain multiple phases with some typically in metastable equilibrium. The modeling of the evolution of phases and hence that of the microstructure and properties and their quantitative prediction is aided by the CALPHAD (CALculation of PHAse Diagrams) tools and databases of thermodynamic properties [18]. Continued development of higher-accuracy CALPHAD tools had a significant effect in the development of the "Materials by Design" approach shown in the "Computational Materials Design" line in Fig. 1.10.

One consequence of all alloy development efforts is the generation over time of large amounts of data on composition−processing−microstructure properties relationships both for alloys in service and those from the experimental trials leading up to them. These data are of value in helping to develop, refine, and validate the physical models and mechanisms of materials behavior, thereby providing new directions for alloy design. However, much of the data, especially those generated in the development of commercial alloys, are proprietary to material suppliers and users and are not readily available. Open literature data are dispersed widely and the methods and assumptions used in the experiments or computer simulations are typically not described clearly and adequately. Despite these problems, statistical techniques have been used to analyze whatever data are available and the output has been applied in model development and alloy design. A promising discipline in this respect is the emerging field of materials informatics, which advantageously utilizes data mining methods and computational capabilities to identify and interpret multivariate correlations among the many variables that determine materials behavior [19].

Adaptive numeric modeling, defined as the extraction by empirical mathematical means of system relationships from observed data and thereby predicting the response of the system [20,21], has been used to examine data from many materials to determine correlations, not otherwise evident, in complex data sets. These correlations can be used to construct models for alloy design. A simple, early example of this approach is shown by the modeling of the effects of compositional variations on the properties of the nonheat treatable aluminum alloy 3105 (Al−0.55Mn−0.5Mg) from an analysis of the published properties of the alloys 1100, 3003, and 3004 [22]. Fig. 3.6 shows the compositional relationships among these alloys and compares the experimental and predicted values of the tensile strength of alloy 3105. The results provide guidance for the use of larger amounts of scrap into the melt, which although resulting in compositional variations also provides cost savings.

Adaptive numeric models have predicted the strength and electrical conductivity of Al−Zn−Mg−Cu alloys, the latter property being an indication of the stress corrosion cracking resistance, which is difficult and expensive to measure in production conditions [20]. The Bayesian neural network modeling of results from virtual experiments on α/β-processed Ti−6Al−4V determined that the most significant

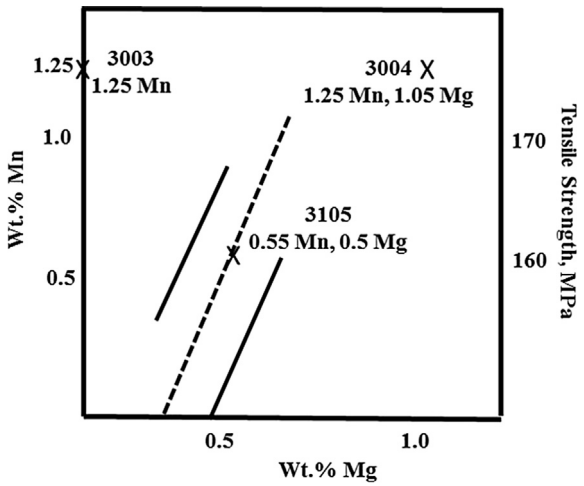


FIGURE 3.6

A schematic relationship of alloy 3105 and related aluminum alloys 1100, 3003, and 3004. The predicted strength of industrially processed 3105 is within the band of that measured for alloys with varying Mg content between 0.35 and 0.63 wt%.

Adapted from I.J. Polmear, J.E. Tibballs, B. Rinderer, Modeling composition/processing/property relationships in a cold-rolled aluminum alloy, JOM 51 (11) (1999) 51–54.

contribution to strength came from the volume fraction of the equiaxed α particles and the solid solution hardening of the α phase by aluminum and oxygen and, unexpectedly, of the β phase by iron to some extent [23].

3.4 EXAMPLES OF MODEL-BASED ALLOY AND PRODUCT DESIGN

Efforts by industry to model the entire length scales for materials design are illustrated by initiatives such as "Atoms to Airplanes" [24] and "Atoms to Autos" [25]. This section will briefly highlight a few examples of model-based alloy and product design undertaken to meet a variety of processing and property requirements. Although some of these are for applications other than airframes, they do point to the possibilities of the model-based approaches to reduce the empiricism, cost, and cycle time for the development of alloys and processes.

Alloy systems currently in use will form the basis for new alloy development and insertion at least in the near future. However, the advances in computational modeling for predicting materials behavior and the availability of commensurate computing power and infrastructure have opened up the possibility to rapidly evaluate nontraditional alloy concepts, such as the high-entropy alloys (HEA). In the search for useful compositions, high-throughput computations can use first principle

methods to create databases for a large number of alloys for screening [26], thereby eliminating the need for expensive experiments. Approaches to the design of HEAs using a combination of computational materials science, combinatorial materials synthesis, and design of experiments coupled with the traditional alloy design principles have been discussed in detail [27].

Nickel-based superalloys strengthened by the intermetallic phase γ' are used extensively in turbine blades and their operating temperatures have been increased by using thermal barrier coatings. Significant effort has been underway to model the behavior of these alloys with the objective of determining strategies to further improve their performance. Using first-principles and phase-field modeling, Zhou et al. [28] successfully predicted the composition−microstructure relationships for Ni−Al binary and Ni−Al−Mo ternary alloys that can then be used for targeted alloy design. In another investigation [29], a multistage hierarchical modeling method was used to design alloys that can operate beyond the limits of nickel-based alloys. By performing semiempirical thermodynamic calculations for the rapid, initial screening of the 26 transition elements followed by accurate ab initio calculations, a few alloys in the Mo−Ni−Al system combined with doping of platinum group metals were found promising for further investigation.

The "Virtual Aluminum Castings" (VAC) project has perhaps been the first and most publicized success of applying ICME and implementing its results by industry [30]. The overall process entails the simulation of the thermal history during casting and prediction of the resulting microstructures at all locations in the casting, the corresponding properties, and finally the casting durability. The cycle is repeated until the component is optimized. The simulation is completed prior to casting and testing the actual component in an engine. The metallurgical length scales showing the microstructural features of the casting and the properties that they affect are shown in Fig. 3.7. One advantage of this approach is the ability to account for the local variations in the mechanical properties and residual stresses and their effects on the casting performance. The implementation of the VAC is estimated to have resulted in significant cost savings and cost avoidance.

Multiscale approaches have also been used for improving the formability of aluminum sheet for automobile components by modeling the effects of composition and microstructure on strength and deformation characteristics [25]. The predictions were made for Al−Mg alloys already in use in the auto industry by performing calculations across electronic, atomistic, microstructure, and continuum scales. Another example of a multiscale modeling approach is the redesign of the control arm of an automobile, discussed in detail by Horstemeyer [17].

Among the airframe structural alloys, Ferrium S53 steel, developed as a drop-in replacement for ultrahigh strength steels currently in use, is the first computationally designed alloy to reach flight qualification [31]. The alloy with a composition of Fe−0.21C−14Co−10Cr−5.5Ni−2Mo−1W−0.3V is a corrosion resistant, secondary hardening steel strengthened by M_2C carbide precipitates and contains sufficient Cr to provide corrosion resistance and eliminate the need for cadmium plating. The alloy was designed and processed to achieve the microstructure−property combinations

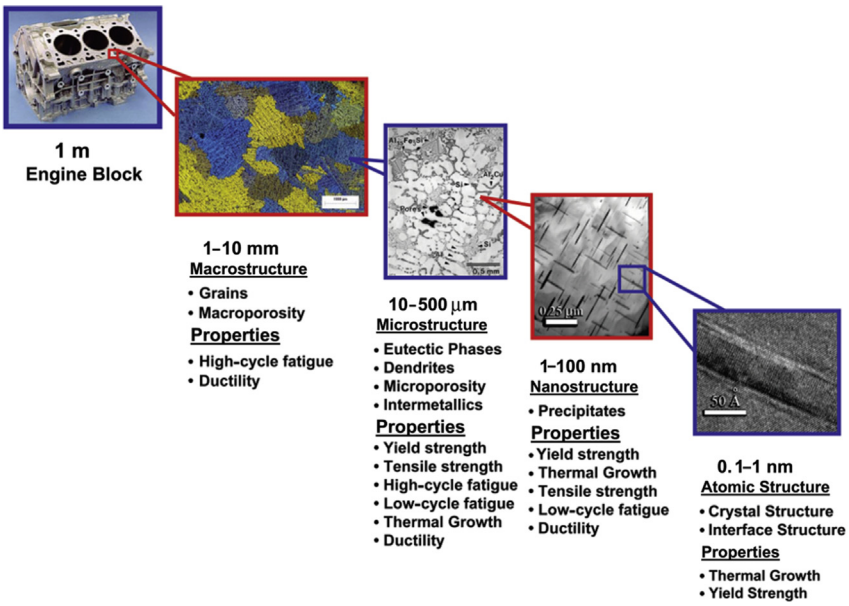


FIGURE 3.7

Microstructure—properties relationships across the length scale in aluminum casting [30].

shown in Fig. 1.9. This approach also eliminated the need for a large number of prototypes to be designed and tested, as in the empirical approach, thus reducing cost and cycle time, as shown in Fig. 3.8 [15]. The design of Ferrium S53 and other steels will be discussed in detail in a later chapter.

3.5 MICROSTRUCTURE REPRESENTATION FOR MODEL-BASED ALLOY DESIGN

It should be clear from the discussion thus far that most properties of importance in alloy design are sensitive to the microstructure. Accordingly, quantitative characterization and mathematical representation of features such as grains, particles, and defects are important for modeling both the effects of processing on their evolution and for their effects on properties. The geometrical representation of these features, including all spatial correlations along with the constitutive equations for the individual phases and interfaces, and a multiscale modeling and simulation framework are all essential for alloy design in the ICME framework [32].

Microstructures of materials are stochastic in nature and must be described in statistical terms [33]. Most microstructural observations are made in two-dimensional (2D), planar sections of materials. Classical stereological methods described in many textbooks [34,35] can be used to construct three-dimensional (3D) descriptions

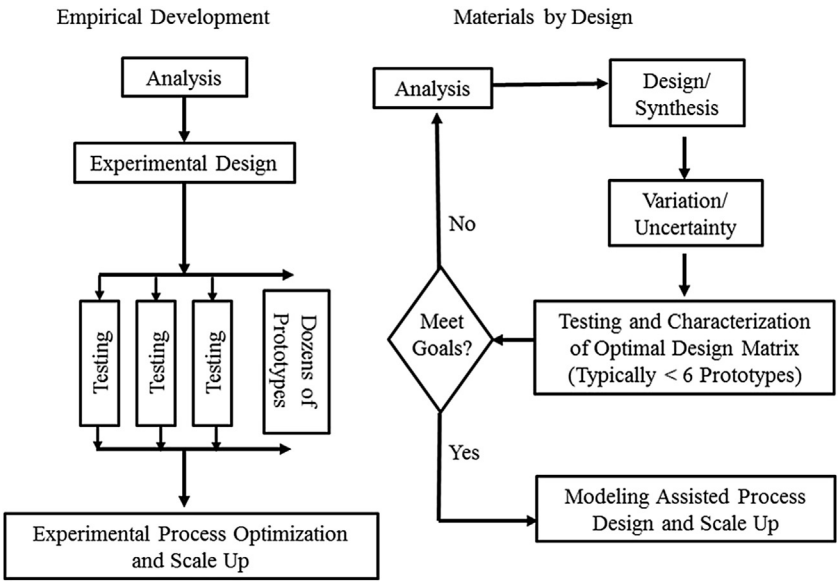


FIGURE 3.8

Comparison of experiment intensive traditional approach with analysis intensive materials by design approach [15].

of features from 2D observations. However, they do not capture the true complexity of the microstructural morphologies, which can only be obtained by 3D characterization. A variety of techniques such as 3D atom probe tomography and serial sectioning mechanically or by focus ion beam are presently available to obtain true 3D representations of the microstructure [36]. Fig. 3.9 is an example of 3D representation

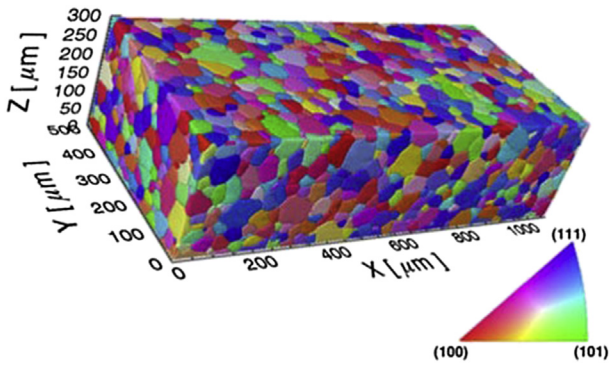


FIGURE 3.9

Microstructure of β-stabilized polycrystalline titanium alloy containing 4300 grains, generated by three-dimensional reconstruction [37].

of a β stabilized titanium alloy reconstructed from serial sectioning, optical microscopy with intermittent electron backscatter diffraction, image segmentation, and processing algorithms [37]. The 3D spatial distribution of crystal lattice orientations shown in this figure is essential for relating texture to properties.

The mathematical description of all the hierarchical features (Table 2.2) in structural alloys is extremely complex and requires a very high dimensional representation. For microstructures such as those in α/β titanium alloys, it is very difficult and often impossible to determine the effects of each of the large number of microstructural parameters on any one property, although statistical modeling provides some insight and discovers unexpected correlations, as discussed earlier [22]. For applications such as these, automatic classification and organization of large datasets available from 3D characterization can be powerful in the investigation of microstructure–property relationships [38].

3.6 SUMMARY

The theoretical design of structural alloys has come a long way in the last three decades since the publication of an article by Pettifor [39] stating that quantum theory was just beginning to be useful in the design of alloys. Based on the examples discussed in this chapter, ongoing advances in theory and computing capabilities can be expected to sustain the accelerating trend toward efficient model-based design of alloys with complex, hierarchical microstructural features. This should not, however, underestimate the value of empiricism, which when used judiciously, will continue to be a very valuable complement for theory-based alloy design. The ability to digitally represent and analyze all aspects of the data representing the multivariate correlations among composition, processing, microstructure, and properties will provide a knowledge of the invertible relationships among these factors, as shown in Fig. 3.10 [37]. This will enable the composition and processing means to be identified for attaining the goals of alloy design (Fig. 1.9). The trend is also underscored by the recent launching of a new open access journal *Integrating Materials and*

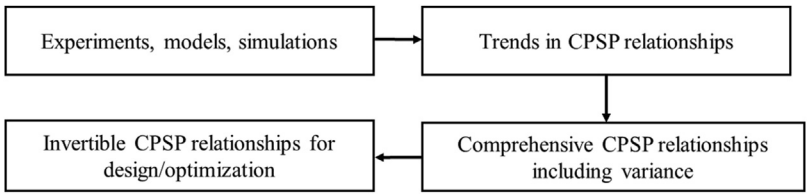


FIGURE 3.10

Schematic descriptions of the envisioned transformations for materials data. *CPSP*, composition–processing–structure–properties.

Adapted from S.R. Kalidindi, Data science and cyberinfrastructure: critical enablers for accelerated development of hierarchical materials, International Materials Reviews 60 (3) (2015) 150–168.

Manufacturing Innovation [40] focusing on global collaboration, integrated design teams, digital data, computational modeling, and more complex and high-throughput experimentation.

REFERENCES

[1] D.B. Miracle, Aeronautical Applications of Metal-Matrix Composites, in Composites ASM Handbook 21, ASM International, 2001, pp. 1043−1049.

[2] D.B. Miracle, J.D. Miller, O.N. Senkov, C. Woodward, M.D. Uchic, J. Tiley, Exploration and development of high entropy alloys for structural applications, Entropy 16 (1) (2014) 494−525.

[3] J.-W. Yeh, S.-K. Chen, S.-J. Lin, J.-Y. Gan, T.-S. Chin, T.-T. Shun, C.-H. Tsau, S.-Y. Chang, Nanostructured high-entropy alloys with multiple principal elements: novel alloy design concepts and outcomes, Advanced Engineering Materials 6 (5) (2004) 299−303.

[4] A. Jacob, Boeing launches 777X, features 787 Dreamliner composite wing technology, Materials Today, Elsevier 20 (November 2013).

[5] Data for 2524, 7150, 7055 and 2029 Are From Various Alcoa Data Sheets, for Ti-10V-2Al-3Fe, and Ti-5Al-5V-5Mo-3Cr From JOM, vol. 67 (6) (2015) 1281−1303, for Aermet 100 From Carpeneter Technology Data Sheet, for Ferrium M54® From QuesTek Data Sheet and for Other Common Alloys From ASM Handbooks.

[6] D.G. Pettifor, Computer−aided materials design: bridging the gaps between physics, chemistry and engineering, Physics Education 32 (3) (1997) 164−168.

[7] E. Hornbogen, Hundred years of precipitation hardening, Journal of Light Metals 1 (2001) 127−132.

[8] B. Smith, The Boeing 777, Advanced Materials and Processes 161 (9) (2003) 41−44.

[9] P. Lequeu, P. Lassince, T. Warner, Aluminum alloy development for the Airbus 380, Advanced Materials and Processes 165 (2007). Part 1 (June) 33−35; Part 2 (July) 41−44.

[10] D. Banerjee, J. Williams, Perspectives on titanium science and technology, Acta Materialia 61 (2013) 844−879.

[11] R. Boyer, R. Briggs, The use of β titanium alloys in the aerospace industry, Journal of Materials Engineering and Performance 14 (6) (2005) 681−685.

[12] W.M. Garrison Jr., Ultrahigh strength steels for aerospace applications, JOM 42 (5) (1990) 20−24.

[13] E. Hornbogen, E.A. Starke Jr., Theory assisted design of high strength low alloy aluminum, Acta Materialia 41 (1993) 1−16.

[14] A.W. Zhu, B.M. Gable, G.J. Shiflet, E.A. Starke, The intelligent design of age hardenable wrought aluminum alloys, Advanced Engineering Materials 4 (2002) 839−846.

[15] D.L. McDowell, G.B. Olson, Concurrent design of hierarchical materials and structures, in: S. Yip, T.D. Rubia (Eds.), Scientific Modeling and Simulations, Springer, 2009, pp. 207−240.

[16] R.M. Nieminen, From atomistic simulation towards multiscale modelling of materials, Journal of Physics: Condensed Matter 14 (2002) 2859−2876.

[17] M.F. Horstemeyer, Integrated Computational Engineering (ICME) for Metals, TMS Wiley, 2012.

[18] G.B. Olson, C.J. Kuehmann, Materials genomics: from CALPHAD to flight, Scripta Materialia 70 (2014) 25−30.

[19] K. Rajan, Materials informatics, Materials Today 8 (10) (2005) 38−45.
[20] M.J. Starink, I. Sinclair, P.A.S. Reed, P.J. Gregson, Predicting the structural response of heat-treatable Al alloys, Materials Science Forum, Trans Tech Publications 331 (2000) 97−110.
[21] P.A.S. Reed, M.J. Starink, S.R. Gunn, I. Sinclair, Adaptive numerical modeling of hybrid physically based ANM approaches in materials engineering − a survey, Materials Science and Technology 25 (2009) 488−503.
[22] I.J. Polmear, J.E. Tibballs, B. Rinderer, Modeling composition/processing/property relationships in a cold-rolled aluminum alloy, JOM 51 (11) (1999) 51−54.
[23] P.C. Collins, S. Koduri, B. Welk, J. Tiley, H.L. Fraser, Neural networks relating alloy composition, microstructure and tensile properties of α/β-Processed TIMETAL 6-4, Metallurgical and Materials Transactions A 44 (2013) 1441−1453.
[24] S.C. Christensen, A. Browning, J. Gosse, Computational methods for new materials development: the "Atoms to Airplanes" concept, in: 1st World Congress on Integrated Computational Materials Engineering, July 10−14, 2011. Seven Springs, PA.
[25] P.E. Krajewski, L.G. Hector Jr., Y. Qi, R.K. Mishra, A.K. Sachdev, "Atoms to Autos": a multiscale approach to modeling aluminum deformation, JOM 63 (11) (2011) 24−32.
[26] M. Asta, Computational materials discovery and design, JOM 66 (3) (2014) 364−365.
[27] J.-W. Yeh, Alloy design strategies and future trends in high entropy alloys, JOM 65 (12) (2013) 1759−1771.
[28] S.H. Zhou, Y. Wang, J.Z. Zhu, T. Wang, L.Q. Chen, R.A. MacKay, Z.K. Liu, Computational tools for designing Ni-based superalloys, Superalloy (2004) 969−975.
[29] P.K. Ray, T. Brammer, Y.Y. Ye, M. Akinc, M.J. Kramer, A multistage hierarchical approach to alloy design, JOM 62 (10) (2010) 25−29.
[30] J. Allison, M. Li, C. Wolverton, X. Su, Virtual aluminum castings: an industrial application of ICME, JOM 58 (11) (2006) 28−35.
[31] G.B. Olson, Genomic materials design: the ferrous frontier, Acta Materialia 61 (2013) 771−781.
[32] D.L. McDowell, S. Ghosh, S.R. Kalidindi, Representation and computational structure-property relations of random media, JOM 63 (3) (2011) 45−51.
[33] A.M. Gokhale, Quantitative characterization and representation of global microstructural geometry, in: Metallography and Microstructures, ASM Handbook, ASM International, 2004, pp. 428−447.
[34] R.T. DeHoff, F.N. Rhines, Quantitative Microscopy, McGraw Hill, 1968.
[35] E.E. Underwood, Quantitative Stereology, Addison Wesley, 1970.
[36] M.C. Uchic, M.A. Groeber, A.D. Rollett, Automated serial sectioning methods for rapid collection of 3-D microstructure data, JOM 63 (3) (2011) 25−29.
[37] S.R. Kalidindi, Data science and cyberinfrastructure: critical enablers for accelerated development of hierarchical materials, International Materials Reviews 60 (3) (2015) 150−168.
[38] S.R. Kalidindi, S.R. Niezgoda, A.A. Salem, Microstructure informatics using higher-order statistics and efficient data-mining protocols, JOM 63 (4) (2011) 34−41.
[39] D. Pettifor, New alloys from the quantum engineer, New Scientist 11 (1510) (1986) 48−53.
[40] C.H. Ward, Integrating Materials and Manufacturing Innovation: a new forum for the exchange of information to integrate materials, manufacturing and design engineering innovations, Integrating Materials and Manufacturing Innovation 1 (1) (2012). Springer Open Access Journal.

CHAPTER

Aluminum Alloys

4

CHAPTER OUTLINE

Synopsis **58**
4.1 Aluminum Alloys for Airframe Structures **58**
4.2 Classification of Wrought Aluminum Alloys **62**
4.3 Physical Metallurgy of Wrought, PH Aluminum Alloys **65**
4.3.1 Alloying for Precipitation Hardening 67
4.3.1.1 Phase Equilibria Considerations 69
4.3.1.2 Precipitation Reactions 74
4.3.1.3 Mechanisms and Modeling of Precipitation Hardening 91
4.3.1.4 Integrated Process Modeling for Precipitation Hardening 94
4.3.1.5 Effects of Precipitation Hardening on Property Combinations 97
4.3.2 Alloying for Control of Matrix Microstructure 99
4.3.2.1 Matrix Microstructure Development and the Effects of Dispersoids 99
4.3.2.2 Specific Alloy Systems 100
4.3.2.3 Quench Sensitivity 102
4.3.2.4 Modeling of Matrix Microstructure Evolution 103
4.3.2.5 Effects of Matrix Microstructure on Property Combinations 104
4.3.3 Effects of Impurity Elements 104
4.4 Processing–Microstructure–Property Relations in Wrought, PH Aluminum Alloys **107**
4.4.1 Modeling of Strength 111
4.4.2 Ductility and Strain Hardening Behavior 116
4.4.3 Durability and Damage Tolerance Properties 117
4.4.3.1 Fracture Toughness 117
4.4.3.2 Fatigue Properties 122
4.4.3.3 Corrosion Behavior 128
4.5 Commercial Aluminum Alloys **138**
4.5.1 2XXX Series Alloys 139
4.5.2 6XXX Series Alloys 142
4.5.3 7XXX Series Alloys 142
4.5.3.1 Strength Improvements Relative to 7075-T6 143
4.5.3.2 Development of T73 Temper 145
4.5.3.3 Higher Purity Alloys for Controlled Toughness 145

Metallurgy and Design of Alloys with Hierarchical Microstructures. http://dx.doi.org/10.1016/B978-0-12-812068-2.00004-7

Copyright © 2017 Elsevier Inc. All rights reserved.

4.5.3.4 Development of Alloys With High Strength and SCC Resistance 146
4.5.3.5 Elimination of Mid-Plane Defects 146
4.5.3.6 Improvements in Thick Products Beyond 7050 147
4.5.3.7 Ultrahigh Strength Alloys 148
4.5.3.8 Minimizing of Anisotropy 149
4.5.3.9 Summary of 7XXX Series Alloy Development 149
4.5.4 Al–Li Alloys 150
4.5.5 Summary 155
4.6 Aluminum Alloy and Product Design 155
4.6.1 Aluminum Alloy Design 155
4.6.1.1 Work Hardening and Grain Refinement 156
4.6.1.2 Solid Solution Strengthening 157
4.6.1.3 Dispersion Strengthening 157
4.6.2 New Alloy Design in the Traditional Composition Space 158
4.6.2.1 Rapid Solidification Processed Alloys 158
4.6.2.2 Computational Alloy Design 159
4.6.3 New Alloy Design With Alternative Compositions 161
4.6.4 Modeling for New Alloy Design 164
4.6.5 Integrated Aluminum Alloy/Product Design 165
4.7 Summary 166
References 167
Further Reading 175

SYNOPSIS

This chapter describes the metallurgy of wrought, precipitation hardenable aluminum alloys used in airframe structures. Their composition–processing–microstructure–properties relationships and the ability or lack thereof to modeling these are used as the framework for the discussion. Alloying elements are added to aluminum for two reasons, namely precipitation hardening and control of matrix microstructure. The individual and combined effects of these sets of alloying elements and the impurities that are always present on the microstructure and properties are discussed in detail. This is followed by a review of the overall behavior of the various classes of aluminum alloys and those of specific alloys used commercially. The chapter concludes with a discussion of the status and possible directions for new alloy design and approaches to their insertion.

4.1 ALUMINUM ALLOYS FOR AIRFRAME STRUCTURES

Aluminum alloys have been the dominant materials used for airframe structures until the increasing trend in the use of polymer–matrix composites, as shown in

Table 4.1 Materials Usage in Commercial Airplanes

Materials Distribution (wt%)							
	Boeing [1]					Airbus [2]	
Material	747	757	767	777	787	A380	A350
Aluminum	81	78	80	70	20	61	19
Titanium	4	6	2	7	15	10 (Ti and steel)	14
Steel	13	12	14	11	10		6
Composites	1	3	3	11	50	22	53
Other	1	1	1	1	5	7	8

Table 4.1 [1,2]. The Boeing 787 and Airbus A350 are built with about 50% of these materials, which are lighter than aluminum alloys and possess better resistance to degradation by corrosion and fatigue. The cost premium for composite structures is also offset by the lower operation and in-service maintenance costs compared with those for metallic structures and by continuous improvements in their manufacturing efficiency. In response, by focusing on an integrated approach to working with the users, the aluminum suppliers have continued to develop alloys with better mix of properties (Alcoa has developed 65 new specifications for aluminum alloys since 2000) and manufacturing characteristics, resulting in structures that are less expensive than those made from titanium and composites while also being up to 10% lighter at the system level [3]. Although both the fuselage and wing skins of 777 and A350 principally used composite materials, the fuselage of the Boeing 777X, launched in 2013 and expected to enter into service in late 2019, will use metallic materials [4]. In the future, methods such as friction stir welding and additive manufacturing, described in a subsequent chapter, can be expected to transform the way alloys are developed and manufactured into components.

The historical development of aluminum alloys for airframe structural applications has also been responsive to meeting the evolving criteria for airplane design, as shown in Table 4.2 [5,6]. The early effort was on developing alloys with as high a strength as possible, which, however, resulted in corresponding reductions of toughness and corrosion resistance. With the advent of fracture mechanics-based design philosophy and the use of thicker product forms, durability, damage tolerance, and resistance to stress corrosion cracking (SCC), particularly in the short transverse direction, became important considerations for eliminating degradation by fatigue and corrosion and for reducing in-service maintenance costs. The high fuel cost in the 1980s provided the added impetus for the development of alloys with lower density achieved through the addition of lithium as an alloying element. The overall goal of alloy development presently is to reduce the cost of manufacturing, operation, and maintenance of airplane systems without sacrificing property combinations and structural performance.

Table 4.2 Evolution of Design Drivers for Commercial Aircraft

Time Frame	Principal Design Drivers
Pre-1930s	Static strength
1930s–1960s	Static strength, corrosion resistance, fatigue
1960s–1970s	Static strength, corrosion resistance, stable elevated temperature properties, durability, damage tolerance, good properties in thick sections
1980s	All the above and dramatic weight savings
1990s	Static strength, corrosion resistance, durability, damage tolerance, good properties in thick sections, highly balanced properties, low manufacturing, acquisition and maintenance (ownership) costs, high level of safety
2000s–present	Above as for 1990s and amenability to revolutionary processing such as additive manufacturing.
Future	Above plus breakthrough structural weight and cost savings, extended maintenance/inspection intervals, passenger comfort, green aerostructures

Adapted from J. Liu, M. Kulak, A new paradigm in the design of aluminum alloys for aerospace application, Materials Science Forum 331–337 (2000) 127–140; R.J. Bucci, M.A. James, M. Kulak, M.B. Heinimann, H. Sklyut, J.R. Brockenbrough, Material and structural simulation methodology advancements for fatigue and damage tolerant critical aircraft structures – an aluminum supplier perspective, Fatigue and Fracture Toughness Symposium, 13th International Conference on Aluminum Alloys (ICAA – 13), Carnegie Mellon University, Pittsburgh, Pennsylvania, June 3–7, 2012.

The importance of aluminum alloys in the development of modern aviation can be appreciated in the context of the evolution of engineering materials outlined in the first chapter. It did not take many years after the discovery of precipitation hardening, coincidentally using aluminum alloys, and indeed also not long after the discovery of the process to economically extract aluminum with the development of the Hall–Heroult process in 1886, that alloys were being designed and produced for airframe applications. Of course, airframe design and applications for aluminum alloys took off soon after the historic flight by Wright brothers in 1903.

Although precipitation hardenable aluminum alloys were rapidly being developed and used, the basic alloy systems, Al–Cu–Mg and Al–Zn–Mg–Cu and the narrow choice of compositions on which they are based have remained the same to date. Despite this limitation, the improvements in properties enabling significant performance gains in airframes are due to the microstructural diversity that can be achieved by alloying and processing. This has been helped in no small measure by the overall development of the theories and understanding of the strengthening mechanisms in metals aided by the availability of continuously improving testing and characterization methods and more recently by computational modeling.

Only the precipitation hardened (PH) alloys based on the Al–Cu and the Al–Zn–Mg systems provide sufficient strength for use in airframes, with the former

used for structures for which damage tolerance is critical and the latter where strength is critical. The tensile strength of pure, annealed aluminum is about 10 MPa (~1.5 ksi). All aluminum alloys contain iron and silicon as impurities, although silicon is also added deliberately to certain alloy families for strengthening. The yield strength of the commercially pure wrought aluminum alloy 1100 with a combined total maximum of 1 wt% Fe and Si is about 30 MPa (~4 ksi) in the annealed condition. The improvement in the yield strength of this alloy over that of pure aluminum can be attributed to very limited solid solution strengthening and wrought processing effects. In wrought aluminum alloys, most of the Fe and Si are present in the form of constituent particles in a size range greater than about 1 μm that makes them ineffective for strengthening. The yield strength of alloy 1100 can be increased to about 150 MPa (~20 ksi) by work hardening. Alloys with Mn and Mg as the principal alloying elements can be work hardened to achieve yield strength levels of about 250 and 300 MPa (~35–40 ksi), respectively. Only precipitation hardening can provide higher strength levels in aluminum alloys.

The development and metallurgy of wrought, PH aluminum alloys have been treated in detail in many readily available review papers and books (see list for "Further Reading" at end of chapter). These publications provide excellent coverage of the effects of processing and microstructure on properties such as strength, toughness, and corrosion behavior, typically individually and separately. This chapter will emphasize the effects of composition, processing, and microstructure in the context of achieving a balanced and targeted combination of these properties, using examples from the historic evolution of aluminum alloys in service that can then be applied for new alloy design.

As shown in Table 4.2, static strength is always the principal consideration for the selection of aluminum alloys. Tradeoffs between strength and other properties, for example fracture toughness, resistance to degradation by fatigue, and various types of corrosion are considered only to the extent that the alloys possess the minimum strength required for structural performance. Over the past decades, aluminum alloys have been developed with significant, concurrent improvements to both strength and other properties, as shown in Figs. 3.1 and 3.2. These alloys are all PH systems in which the desired microstructures are produced and properties are optimized by a combination of secondary alloying additions, mitigating the effects of impurity elements and using the processing sequence shown schematically in Fig. 4.1.

The importance of all the processing steps is evident from the fact that precipitation hardening (solution heat treatment, quenching, and aging), which is key to achieving the strength, is just the last one prior to which many of the matrix microstructural features that affect the properties have already evolved. This scheme along with the ability to model the effects of composition, processing, and microstructure on properties will be used as a roadmap to gain an understanding of the underlying physical metallurgy of heat treatable aluminum alloys pertinent for alloy design.

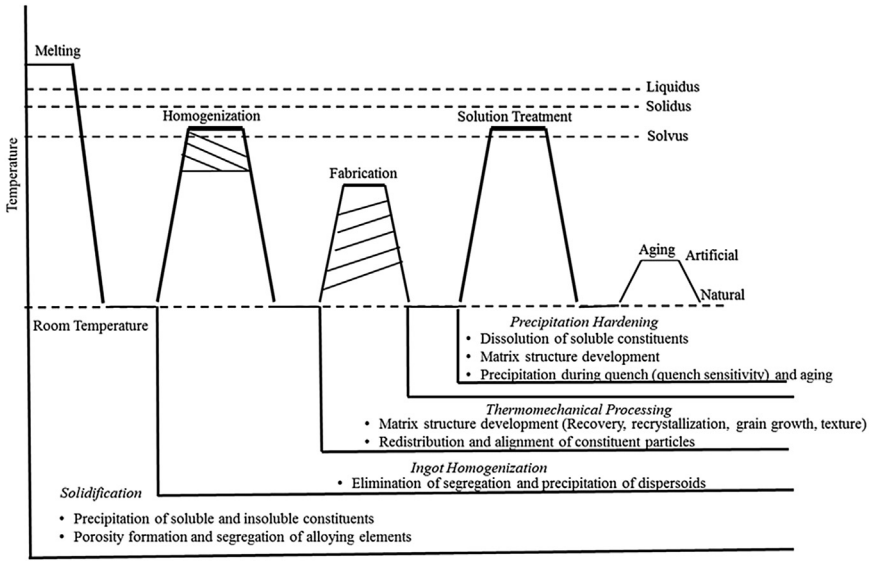


FIGURE 4.1

Sequence of processing steps and microstructure development for commercial PH aluminum alloys.

4.2 CLASSIFICATION OF WROUGHT ALUMINUM ALLOYS

Classification of the principal aluminum alloys based on the alloying additions is shown in Fig. 4.2 [7]. Wrought alloys strengthened by work hardening and age hardening are classified as "nonheat treatable" and "heat treatable," respectively. This chapter will be limited to discussing the precipitation (age) hardening alloys in wrought form, although the possibilities of increasing the strength of other alloys will be considered as potential approaches for alloy design. Lithium has also been used as an alloying element to lower the density of aluminum alloys containing Cu and Mg either singly or in combination. PH Al—Cu—Li alloys are presently in limited service in airplanes and will be included in the discussion. The wrought, heat treatable aluminum alloys based on the alloying additions are shown in Fig. 4.3.

Wrought aluminum alloys are designated by the Aluminum Association's numbering system, as shown in Table 4.3. The ASM Handbook volumes provide detailed information on the alloys and their classification schemes [8]. The first digit denotes the principal alloying element, the second indicates modifications to the original alloy, and the last two indicate the specific alloy. Based on this classification, aluminum alloys used in airframes belong to the 2XXX, 6XXX, or 7XXX series. Al—Li—Cu—Mg alloys with Li as the principal alloying element and classified in the 8XXX series have also been developed. Compositions of representative alloys that will be used to illustrate the physical metallurgy of wrought precipitation hardenable Al alloys are shown in Table 4.4. Additional alloys will be listed and discussed in detail in the section on commercial alloys.

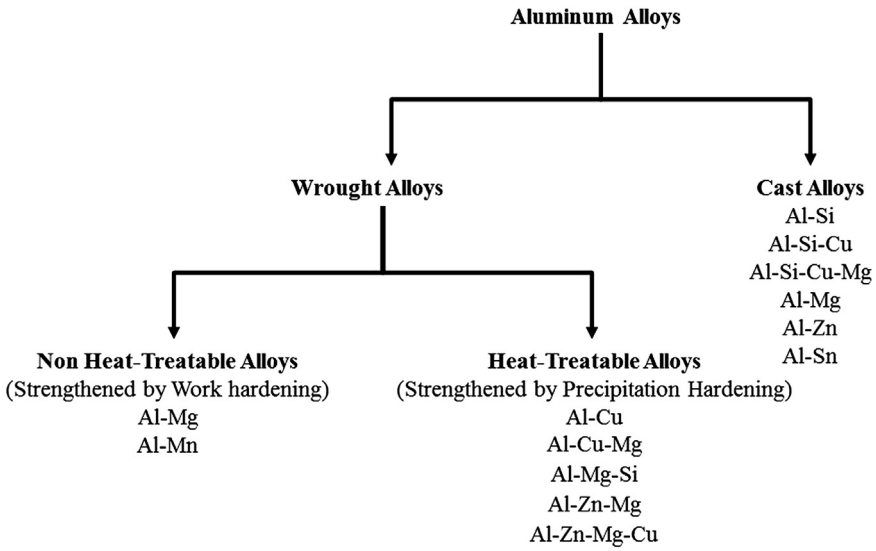


FIGURE 4.2

Principal aluminum alloys based on alloying additions.

Adapted from J.R. Davis, Introduction to aluminum and aluminum alloys, in: Aluminum and Aluminum Alloys, ASM Specialty Handbook, ASM International, 1993, pp. 31–46.

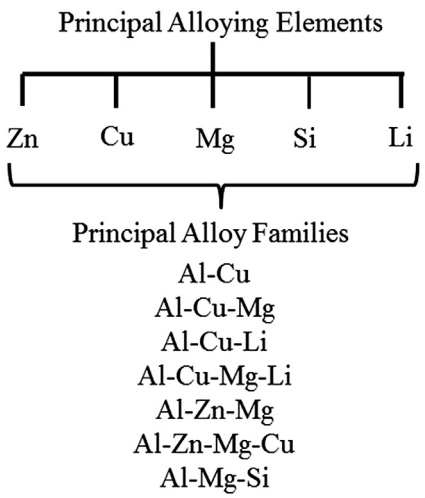


FIGURE 4.3

Wrought precipitation hardenable aluminum alloy families based on alloying additions.

Table 4.3 Numbering System Designation for Wrought Aluminum Alloys

Principal Alloying Element(s)	Alloy Designation
At least 99.00% aluminum	1XXX
Copper	2XXX
Manganese	3XXX
Silicon	4XXX
Magnesium	5XXX
Magnesium and silicon	6XXX
Zinc	7XXX
Other elements	8XXX

Table 4.4 Nominal Compositions of Representative Wrought Aluminum Alloys (wt%)

7XXX Series Alloys

Alloy	Zn	Mg	Cu	Zr	Cr	Si (Max)	Fe (Max)	Mn (Max)	Ti (Max)
7075	5.6	2.5	1.6	–	0.23	0.40	0.50	0.30	0.20
7175	5.6	2.5	1.6	–	0.23	0.15	0.20	0.10	0.10
7475	5.7	2.2	1.6	–	0.22	0.10	0.12	0.06	0.06
7178	6.8	2.8	2.0	–	0.23	0.40	0.50	0.30	0.20
7050	6.2	2.3	2.3	0.12	<0.04	0.12	0.15	0.10	0.06
7040	6.2	2.1	2.9	0.10	<0.04	0.10	0.13	0.04	0.06
7449	8.1	2.3	1.0	[a]	<0.04	0.20	0.15	0.20	0.06
7055	8.0	2.0	2.3	0.16	<0.04	0.10	0.15	0.05	0.06
7085	7.5	1.5	1.6	0.12	<0.04	0.06	0.08	0.04	0.06

2XXX Series Alloys

Alloy	Cu	Mg	Mn	Zr	Si (Max)	Fe (Max)	Zn (Max)	Cr (Max)	Ti (Max)
2024	4.3	1.5	0.6	–	0.50	0.50	0.25	0.10	0.15
2124	4.3	1.5	0.6	–	0.20	0.30	0.25	0.10	0.15
2524	4.3	1.4	0.6	–	0.06	0.12	0.25	0.05	0.10
2029[b]	3.6	1.0	0.3	0.12	0.12	0.15	–	–	0.10

Al–Li Alloys

Alloy	Cu	Li	Mg	Zr	Mn	Ag	Zn	Si (Max)	Fe (Max)
2198	3.2	0.95	0.5	0.11	<0.5	0.4	<0.35	0.08	0.10
2199	2.6	1.6	0.2	0.08	0.3	–	0.6	0.05	0.07

For all alloy families, other elements not shown—each <0.05 and total <0.15.

[a] *For alloy 7449 — Ti + Zr < 0.25.*

[b] *2029 has 0.4 Ag.*

Table 4.5 Temper Designation System for Wrought Aluminum Alloys

Temper Designation	Sequence of Heat Treatment
F	As fabricated condition (variable strength)
O	Annealed (lowest strength state)
W	Solution treated—applies to alloys that age significantly at room temperature
T	All conditions except F, O, and W, which produce stable tempers
T1	Cooled from elevated temperature shaping process and naturally aged to stable temper
T2	Cooled from elevated temperature shaping process, cold worked, and naturally aged to stable temper
T3	Solution treated, cold worked, and naturally aged to stable temper
T4	Solution treated and naturally aged to stable temper
T5	Cooled from high temperature shaping process and artificially aged
T6	Solution treated and artificially aged
T7	Solution treated and artificially aged beyond maximum strength
T8	Solution treated, cold worked, and artificially aged
T9	Solution treated, artificially aged, and cold worked
T10	Cooled from elevated temperature shaping process, cold worked, and artificially aged

Table 4.5 lists the Aluminum Association's "temper" designations, which denote the specific mechanical and thermal processing paths that wrought aluminum alloys undergo to control their properties and characteristics. These are also covered in detail in ASM handbook volumes [8]. The W temper applies to alloys that age spontaneously at room temperature after solution treatment and quenching. It is always followed by the time of natural aging. The T temper is always followed by one or more digits. As an example, alloy 7150-T7751 is a 7XXX series alloy derived from 7050 and heat treated to an overaged T77 temper to provide a certain level of resistance to corrosion. The last two digits denote that the product has received a certain amount of stretch after solution treatment.

4.3 PHYSICAL METALLURGY OF WROUGHT, PH ALUMINUM ALLOYS

Aluminum alloys for airframe structures are designed primarily for strength for which addition of elements that give rise to precipitation hardening is both necessary and sufficient. However, to achieve adequate toughness and fatigue properties, it is also necessary to control the microstructure of the matrix and prevent excessive grain growth during processing for which dispersoid forming elements are necessary. The

effects of the matrix and the second phase particles (strengthening precipitates, dispersoids, and constituent particles) on the properties of aluminum alloys were discussed briefly in Chapter 2 (Tables 2.2 and 2.3). Fig. 4.1 shows how these microstructures evolve during processing. On this basis, the metallurgy of aluminum alloys underlying their design can be described by modeling the effects of the various factors, shown in Table 4.6, that determine the individual and combined effects of the alloying additions, impurities, and processing on the microstructure and properties. Accordingly, the remainder of the chapter is organized as follows.

Section 4.3 describes the role of precipitation hardening elements, dispersoid forming elements, and the impurities separately. Alloying for precipitation hardening discusses in detail the phase relationships, precipitation reactions and their modeling, the effects of defects and trace elements on the precipitation kinetics, the phases that form in specific alloy systems and the resulting hardening mechanisms including effects on properties. Alloying for control of matrix microstructure describes the effects of dispersoid forming elements, particularly on quench sensitivity. Impurity elements are described in terms of their effects, particularly on fracture toughness. Section 4.4 integrates this information for describing the overall processing—microstructure—properties relationships with emphasis on modeling, particularly strength and toughness. Finally, the metallurgy of commercial alloys and the possible directions for new alloy design and their integration with product design are discussed.

Prior to discussing the physical metallurgy of aluminum alloys, it will be helpful to review the production and thermomechanical processing of wrought products. Aluminum mill products are considered as *those … that have been subjected to plastic deformation by hot- and cold-working mill processes (such as rolling, extruding,*

Table 4.6 Modeling the Effects of Composition and Processing on the Microstructure and Properties of Aluminum Alloys

	Alloying for Precipitation Hardening	**Alloying for Matrix Microstructural Control**	**Impurity Elements**
Microstructure	• Phase diagrams • Thermodynamics and kinetics of precipitation reactions • Stability of phases	• Dispersoid precipitation • Substructure and texture evolution • Quench sensitivity and precipitate free zones • Texture	• Soluble and insoluble constituent formation • Constituent redistribution and alignment
Properties	• Precipitation strengthening • Toughness • Fatigue • Corrosion resistance	• Substructure strengthening • Toughness • Fatigue • Corrosion resistance • Anisotropy of properties	• Toughness • Fatigue • Corrosion resistance • Anisotropy of properties

and drawing, either singly or in combination), so as to transform cast aluminum ingot into the desired product form. The microstructural changes associated with the working and with any accompanying thermal treatments are used to control certain properties and characteristics of the worked, or wrought, product or alloy [9].

The various wrought forms of aluminum alloys are flat-rolled products (sheet, plate, and foil), rod, bar, wire, tubular products, shapes, and forgings. Flat-rolled and tubular products, rod, bar and wire are considered mill products. Plate refers to flat-rolled products with thickness greater than 6.3 mm (0.25 in.), sheet to those in the range of 0.15−0.63 mm (0.006−0.249 in.) and foil to thinner material. A variety of shapes can be obtained by forging of aluminum alloys. These are not considered as mill products.

Referring to Fig. 4.1, processing begins with melting of aluminum and the alloying additions followed by casting the melt into an ingot. The cast ingot is scalped, if necessary, to remove surface irregularities and then homogenized by heating at a temperature high enough to eliminate the segregation of alloying elements, dissolve the low melting eutectic compounds formed during solidification and for precipitation of dispersoids. Following homogenization, the ingot is hot worked to break down the cast structure and fabricated into wrought products such as plate and sheet. Rolling can be performed "hot," at temperatures where restoration processes such as recovery and recrystallization occur or "cold," at temperatures where strain hardening occurs. The maximum temperature for hot rolling and forgings is typically about 50°C (80°F) below the solvus. These products are solution heat treated at a temperature above the solvus to dissolve the precipitation hardening elements, rapidly cooled to room temperature to retain the solute in a supersaturated solid solution (SSSS) and aged at room or slightly elevated temperature for the precipitation reactions to occur. The solution treated alloy may be cold worked prior to aging to generate defects that promote heterogeneous nucleation and enhance the kinetics of precipitation.

4.3.1 ALLOYING FOR PRECIPITATION HARDENING

The precipitation hardening step is shown schematically for a binary alloy in Fig. 4.4 [10]. In this scheme, the alloy is solution treated at a temperature T_0, which is above the solvus followed by quenching to room temperature and aging at T_1, which can be room or slightly elevated temperature. The alloy quenched from the solution treatment temperature may also be cold worked prior to aging. The figure also shows the solvus lines and the time−temperature−transformation (TTT) diagrams for the sequence of metastable and stable precipitates that typically form in Al−Cu alloys.

The requirements for aluminum alloys to be precipitation hardenable were identified soon after the discovery of this phenomenon. Investigations on the first commercial alloy, Duralumin (alloy 2017 in the present system of designation) identified them as follows [11].

- The alloy should contain elements in sufficient concentration and fully soluble at an elevated temperature, but exceeding the equilibrium solubility at room or moderately elevated temperature.

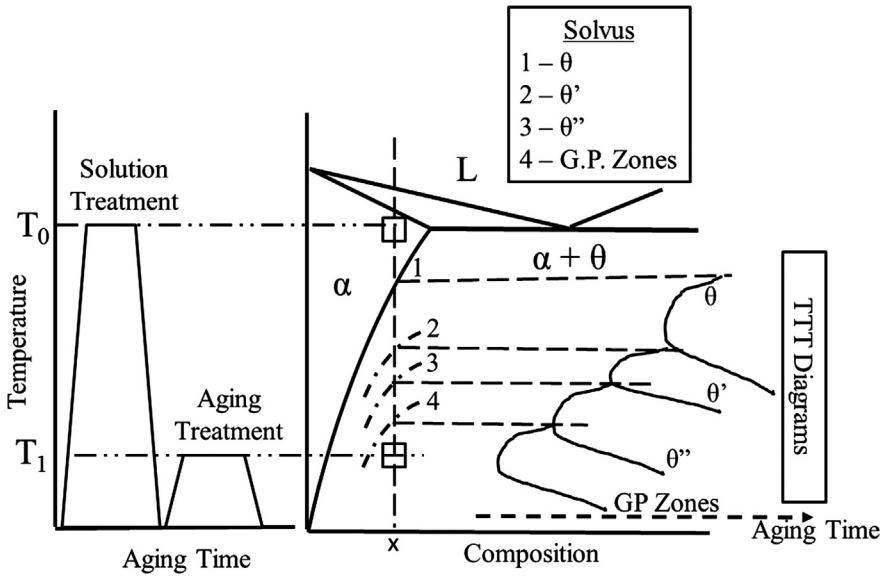


FIGURE 4.4

Schematic figure showing part of a binary phase diagram for precipitation hardenable alloys, heat treatment schemes for age hardening an alloy of solute content "x" and time–temperature–transformation diagrams for the stable and metastable precipitate phases.

Adapted from J.-F. Nie, Physical metallurgy of light alloys, in: Physical Metallurgy, fifth ed., D.E. Laughlin, K. Hono (Eds.), vol. III, Elsevier, 2015, pp. 2009–2156.

- The alloy should be heated at a high temperature (solution treatment) to dissolve the elements and should be rapidly cooled to a low temperature to retain the elements in solid solution.
- The rapidly cooled alloy should be aged at room (or moderately elevated) temperature to precipitate a second phase that increases hardness.

These requirements, discovered without the benefit of modern characterization and analysis techniques, still form the basis for all PH alloys in use or in development. Duralumin had a yield strength of 280 MPa (40 ksi). Subsequent alloy development to improve the strength further was mostly empirical by addition of various elements with the dictum that "if a little is good, add more until something bad happens" [12]. The five age hardenable alloy systems identified in Fig. 4.2 emerged out of these developments. The maximum solid solubilities of the alloying elements for these systems in the corresponding binary alloys are shown in Table 4.7 [13].

Having a high solid solubility and a sloping solvus, as shown in Fig. 4.4, is a necessary but not a sufficient condition for precipitation hardenability in practice. Despite the high solid solubility of Mg (5XXX alloys), the difficulty of nucleating precipitates in the Al–Mg system has precluded their use as heat treatable alloys

Table 4.7 Solid Solubilities of Alloying Elements in Aluminum

Element	Reaction Type	Maximum Solid Solubility (wt%)	Reaction Temperature, °C (°F)
Cu	Eutectic	5.7	548 (1018)
Mg	Eutectic	17.4	450 (842)
Zn	Eutectic	82.2	382 (720)
	Monetectic	31.6	275 (527)
Li	Eutectic	4.2	601 (1114)
Si	Eutectic	1.65	577 (1071)

unless they contain sufficient Cu (2XXX alloys), Si (6XXX alloys), or Zn (7XXX alloys). Thus thermodynamics and kinetics, which determine the equilibrium phase diagrams and the rates of the precipitation reactions, respectively, are both important considerations for alloy design.

4.3.1.1 Phase Equilibria Considerations

For each of the principal alloying elements in aluminum alloys, the highest strength is achieved by adding additional elements that also participate in the precipitation reactions. Corresponding ternary, quaternary, and higher-order phase diagrams are therefore necessary to determine the maximum amounts of the solute elements that can be added and the temperature at which the alloys can be solution heat treated. Multicomponent phase diagrams are generally not available readily and even when available do not account for the additional effects of the impurity and dispersoid forming elements on the solubilities and phase equilibria, particularly for compositions representative of commercial alloys. A comprehensive collection of available phase diagrams in the composition spaces of interest for commercial aluminum alloys has been published [14,15]. An example of such a diagram for the solidus in the Al−Cu−Mg system is shown in Fig. 4.5.

As seen in this figure, the invariant reaction of interest for Al−Mg−Cu (2XXX) alloys, which contain up to about 5 wt% Cu and 2 wt% Mg, occurs at 507°C (945°F), not accounting for the effects of the dispersoid forming and impurity elements. As will be discussed subsequently, the solvus can be very close to this temperature, which can potentially cause localized melting during solution treatment. The objective in aluminum alloy design is to maximize precipitation hardening by adding as much solute as can be dissolved completely by solution treatment at as low a temperature as possible (to minimize grain growth) within the narrow range between the solvus and solidus, for which accurate representations of phase equilibria are necessary.

Within the limited number of available aluminum alloy systems with potential for age hardening, many useful alloys have been developed with combinations of properties for targeted applications. Although this activity has mostly been empirical, significant progress continues to be made in developing methods for thermodynamic

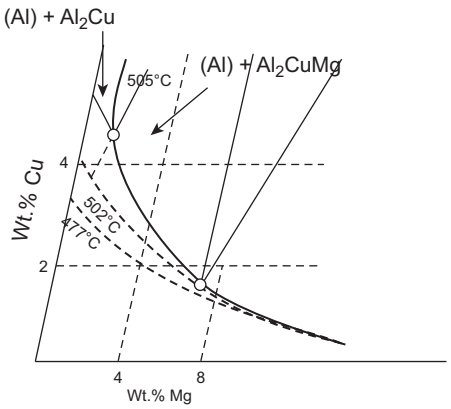


FIGURE 4.5

Solidus lines in the Al—Cu—Mg system.

Adapted from N.A. Belov, D.G. Eskin, A.A. Aksenov, Alloys of the Al—Cu—Si—(Mg, Fe) system, in: Multicomponent Phase Diagrams—Applications for Commercial Aluminum Alloys, Elsevier, 2005, pp. 83—132.

modeling of multicomponent phase equilibria [16] and calculation of phase diagrams [17], which can be used for alloy design. In this respect, the increasing availability of thermodynamic databases coupled with first principles calculations enables the CALPHAD (CALphad of PHAse Diagrams) approach possible for the calculation of multicomponent phase equilibria and phase diagrams [18].

Intermetallic constituent particles form by eutectic reaction during the solidification of aluminum alloys. Constituent particles containing the impurity elements Fe and/or Si (Si is also an alloying element in 6XXX series alloys) are insoluble. Intermetallic particles containing only the precipitation hardening elements may be highly soluble or sparsely soluble depending on the total solute content [19]. In commercial practice, it is impossible to consistently produce alloys containing elements in the exact desired amounts and the compositions are specified to be within an achievable nominal range. Phase diagrams can provide guidance regarding the upper limits of the specified range that should not exceed the maximum combined solid solubilities of the alloying elements at the solution treatment temperature. They can also predict the types of intermetallic phases that can form during solidification. For example, the specified composition range for the Al—Cu—Mg alloy 2024 is such that depending upon the actual composition, the solution treated alloy may contain both Al_2Cu (θ) and Al_2CuMg (S), only θ, only S, or neither of these two phases. The undissolved particles tie up solute that would otherwise be available for precipitation hardening and reduce the toughness.

The need for phase diagrams for alloy design can be appreciated from recent investigations to identify composition and processing conditions to eliminate and mitigate the effects of intermetallic particles in aluminum alloys. For example, from the quaternary Al-6 wt% Zn—Mg—Cu phase diagram at 460°C (860°F)

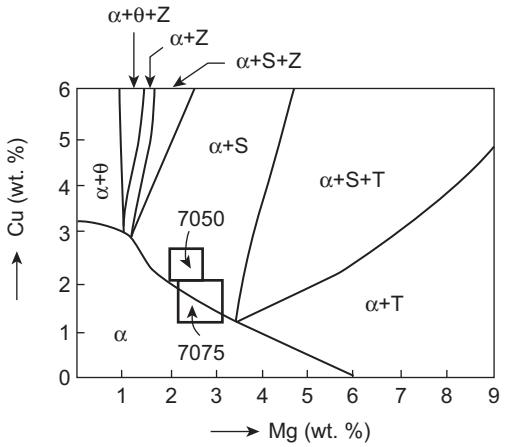


FIGURE 4.6

Phase relationships for Al-6 wt% Zn—Mg—Cu alloys at 460°C (860°F).

Adapted from X.M. Li, M.J. Starink, The effect of compositional variations on the characteristics of coarse intermetallic particles in overaged 7xxx Al alloys, Materials Science and Technology 17 (11) (2001) 1324–1328.

(Fig. 4.6) it is seen that the S phase will be present in alloy 7050 at this temperature and that solution treatment at a higher temperature is necessary for its complete dissolution [20]. Z and T phases contain Al, Cu, Mg, and Zn and are solid solutions of compounds formed in the ternary Al—Cu—Mg and Al—Zn—Mg systems.

The presence or full dissolution of the S phase in 7075 will depend on the actual amounts of Cu and Mg in the alloy. In commercial practice, alloy 7050 is solution treated in the range of 475 ± 6°C (887 ± 11°F) and 7075 at a temperature between 465 ± 6°C (869 ± 11°F) and 480 ± 6°C (896 ± 11°F) depending on the product form. Further, within the specified range for Zn, 6 wt% Zn is in the middle for 7050 and near the maximum for 7075. Thus as with the example of 2024 mentioned earlier, the presence or absence of the intermetallic S phase in 7XXX series alloys will depend on the exact composition and the temperature at which the alloy is solution treated.

Fig. 4.7 shows the solvi for the S phase in the Al-6 wt% Zn—Mg—Cu alloy that has been estimated from the data available at 460°C (860°F) (Fig. 4.6) using a regular solution model for its formation [20]. The range of Cu and Mg content for 7075 and 7050 is superimposed in Figs. 4.6 and 4.7 and shows that for alloys with 6% Zn, the S phase will dissolve completely in 7050 at 475°C or higher.

An additional constraint for alloy design arises from the progressive narrowing with increasing solute content of the single phase field in which alloys are solution treated, as seen for example in Fig. 4.8 for Al-4 wt% Cu—Mg alloys [21].

Again, as with composition, due to the difficulty of precisely controlling processing temperatures in industrial operations, a range is specified for solution treatment.

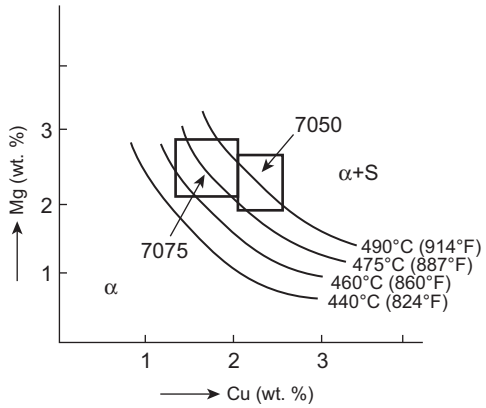


FIGURE 4.7

Estimated solvi for the S Phase in Al-6 wt% Zn—Mg—Cu alloy at 440—490°C (824—914°F).

Adapted from X.M. Li, M.J. Starink, The effect of compositional variations on the characteristics of coarse intermetallic particles in overaged 7xxx Al alloys, Materials Science and Technology 17 (11) (2001) 1324—1328.

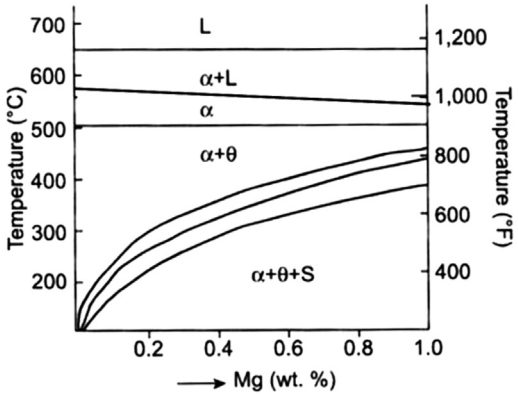


FIGURE 4.8

Series of calculated isopleths for the Al-rich corner of the Al-4 wt% Cu—Mg ternary system based upon three different databases.

Adapted from B.M. Gable, A.W. Zhu, G.J. Shiflet, E.A. Starke Jr., Assessment of the aluminum-rich corner of the Al—Cu—Mg—(Ag) phase diagram, CALPHAD 32 (2008) 256—267.

This is of importance for the 2XXX series Al—Cu—Mg alloys for which the solidus is only a few degrees above the maximum specified solution temperature [22]. For the commonly used alloy 2024, the nominal solution temperature is 495°C (923°F) with a specified range of ±6°C (±11°F) and the solidus is 502°C (936°F), which is just 1 degree above the maximum specified. The melting temperature could be

reduced locally within the ingot if the composition is not uniform. Thus the composition limits and solution treatment temperature range should be carefully specified and temperature must be controlled precisely during processing to ensure that all the solute can be dissolved at as low a temperature as possible within the single phase field range while avoiding incipient melting and minimizing coarsening of the substructure and grains.

Fig. 4.8 also shows the boundary of $\alpha + \theta$ and $\alpha + \theta + S$ phase fields for Al-4 wt % Cu−Mg alloy, calculated from different databases. Despite the differences in the three estimates, S phase will be present as an equilibrium precipitate in most of the Al−Cu−Mg alloys. Thus phase diagrams for the metastable strengthening phase are also necessary for designing precipitation hardening treatments and for avoiding the formation of equilibrium phases. These will be discussed in detail in the section on precipitation reactions.

From the foregoing discussion, although commercial aluminum alloys are always in a metastable condition while in service, a knowledge of both the equilibrium and metastable phase diagrams and phase relationships is critical for the design of alloys and their processing schemes.

Multicomponent phases containing only the precipitation hardening elements that form during ingot casting and processing should dissolve completely during solution treatment, if their amounts are less than their maximum combined solid solubilities in aluminum. However, as mentioned earlier, these elements form intermetallic compounds with the dispersoid forming elements (Mn, Cr, and Zr) and the impurities (Fe and Si), and once formed are insoluble. The liquid to solid transformation for Al with these elements is either eutectic or peritectic. Table 4.8 lists the type and temperature of the reactions, the concentration of the second element and its maximum solid solubility in Al for the various elements [13].

The amount of dispersoid forming elements added to commercial aluminum alloys is well below their maximum solid solubilities and they remain in solid solution after ingot casting and subsequently precipitate as intermetallic particles during postsolidification treatments. A small fraction of these elements is also present in constituent particles. Due to the very low maximum solid solubility, intermetallic

Table 4.8 Characteristics of Binary Phase Diagrams

Element	Type of Reaction	Concentration of the Second Element (wt%)		Reaction Temperature (°C)
		Maximum Solid Solubility	Eutectic or Peritectic	
Cr	Peritectic	0.72	0.4	661
Mn	Eutectic	1.8	1.9	658.5
Zr	Peritectic	0.28	0.11	660.5
Fe	Eutectic	0.05	1.8	655
Si	Eutectic	1.65	12.7	577

particles containing Fe, which are insoluble, are always present in aluminum alloys. They tie up the alloying elements and reduce toughness. Phase diagrams for Al with multiple precipitation hardening, dispersoid forming and impurity elements are not available and cannot be easily calculated or experimentally determined. All the alloy development has relied largely on an empirical understanding of the combined effects of these elements and processing, developed by the aluminum alloy suppliers.

4.3.1.2 Precipitation Reactions

The fundamental nature and mechanisms of solid state precipitation of second phase particles and their effects on properties have been studied extensively over the past century. Many ferrous and nonferrous alloys strengthened by precipitation are being developed continuously and used successfully for critical applications, particularly in aerospace. This trend is also enabled by the increasing sophistication of techniques such as high-resolution scanning transmission electron microscopy and atom probe tomography providing fundamental understanding of the mechanisms of the metallurgical transformations. A vast amount of literature has been published in this time frame. Among these, the chapter on the physical metallurgy of light alloys by J.-F. Nie [10] provides an excellent overview of the metallurgy of precipitation reactions and hardening in aluminum, magnesium, and titanium alloys. For an extensive description of the fundamentals of phase transformations and the background in thermodynamics, kinetics, diffusion theory, and the structure and properties of interfaces necessary to understand them, the reader is referred to the popular text book "Phase Transformations in Metals and Alloys" [23].

Processing, such as shown in Fig. 4.1, seldom, if at all, occurs under conditions necessary to attain equilibrium. With respect to precipitation, the desired strength is achieved by the formation of phases in metastable equilibrium (Fig. 4.4), which, nevertheless, are stable during the service lives of commercial alloys. The rate of cooling from the solution treatment temperature to room temperature (quench rate) must be sufficiently high to prevent precipitate nucleation during the quench, both to avoid undesirable phases and to prevent loss of solute to these phases that would otherwise be available for the precipitation of the desired phases. The minimum rate that will prevent precipitate nucleation during quench can be obtained from the TTT (time−temperature−transformation) curves, shown schematically in Fig. 4.4 for a sequence of precipitates in binary Al−Cu alloys. Typically, these curves do not fully account for the effects of features such as defects, grain and subgrain boundaries, dispersoids, and constituent particles that are already present in the alloy and act as heterogeneous sites for precipitate nucleation during the quench. These effects are described by the sensitivity of the alloy properties to the quench and play a significant role in the combination of properties that can achieved.

From the perspective of understanding and modeling the processing−microstructure relationships for optimizing the combination of properties, it is essential to delineate the effects of the following factors.

1. **Precipitate characteristics**: Precipitates can nucleate homogeneously or heterogeneously. Nucleation is enhanced by heterogeneous sites such as defects introduced by cold work, although the resulting effects on properties are not always beneficial, as will be discussed by a comparison of 2XXX and 7XXX alloys. Nucleation, growth, and coarsening of precipitates overlap to some extent, but these stages are distinguished by increase in number density, increase in size, and decrease in number density of the precipitates, respectively. The composition, crystal structure, degree of coherency, size distribution, volume fraction, and the morphological features of the precipitates, which are determined by the aging conditions, affect the deformation behavior and properties of the alloys.
2. **Secondary alloying additions and impurity elements**: Dispersoid forming elements (Cr, Mn, and Zr) and impurities (Fe and Si) form intermetallic particles that tie up solute and act as heterogeneous nucleation sites during the quench producing coarser precipitates. Elements, principally Ag, are added to commercial alloys to enhance nucleation and beneficially alter precipitate characteristics.
3. **Precipitate-free zones (PFZs)**: PFZs are regions in the matrix devoid of precipitates and occur principally along grain boundaries. They are caused by solute depletion due to heterogeneous precipitate nucleation at these sites. PFZs can also be caused by the depletion of vacancies, which are critical for precipitate nucleation. The dispersoid particles affect the degree of recrystallization and the grain size and thus play an indirect role in the development of PFZs.

Precipitation and its effects on properties are affected by many interdependent factors, not all of which are amenable to modeling. Much of the aluminum alloy development over the past century has relied on empirical approaches, although, as discussed in Chapter 2, advances are being made in the modeling of the effects of processing and microstructure on individual properties such as strength and toughness.

4.3.1.2.1 Precipitation Mechanisms

All PH aluminum alloys contain a distribution of one or more precipitate phases whose composition, crystal structure, degree of coherency with the matrix phase, shape, size distribution, and volume fraction are determined by the alloy composition and heat treatment conditions. The goal of the precipitation hardening treatment is to achieve targeted combination of properties in alloys by optimizing the heat treatment conditions to produce the desired microstructures.

Referring to Fig. 4.4, quenching of the alloy from the solution treatment temperature, T_0, to room temperature will initially result in a SSSS of the α phase with the same solute content. Aging of the alloy will result in the precipitation of a second phase from the α phase, and the phase (Guinier–Preston or GP zones, θ'', θ', or θ) that nucleates will be determined by the aging temperature relative to the solvi for

these phases. The salient aspects of the nucleation, growth, and coarsening of precipitates and their characteristics are briefly described here.

1. **Homogeneous nucleation**: Nucleation of a second phase particle, say θ'', from the α-SSSS entails the formation of an α/θ'' interface and generation of a misfit between the phases due to the differences in their specific volumes. The total free energy of the system will be reduced by the formation of a certain volume of the relatively more stable θ'' phase, and will be increased by the surface energy of the α/θ'' interface and the misfit strain energy. For a spherical nucleus of diameter d, the total free energy change is

$$\Delta G = \left(\frac{\pi}{6}\right) d^3 \left(\Delta Gv - \Delta Gs\right) + \pi d^2 \gamma \tag{4.1}$$

   where ΔGv, ΔGs, and γ are the free energy change per unit volume, misfit strain energy per unit volume, and the interfacial energy per unit area, respectively [10]. Although the reduction in the free energy drives the nucleation reaction, the creation of the interface and the misfit provides a resistance. The variation of ΔG with d is such that nuclei with a size less than a certain critical diameter, d*, will not be stable as the total free energy of the system can be lowered by their dissolution. Nuclei with a diameter greater than d* will grow due to the continuous reduction of the total free energy.
2. **Heterogeneous nucleation**: Although every atom in the SSSS is a potential site for homogeneous nucleation, heterogeneous sites such as grain boundaries facilitate precipitation by reducing the activation energy barrier. Precipitate nucleation in aluminum alloys is almost always heterogeneous for which the sites include vacancies, dislocations, grain boundaries, and interphase boundaries between the matrix and preexisting particles such as dispersoids. However, they also act as nucleation sites during the quench resulting in coarser equilibrium precipitates and PFZs.
3. **Degree of coherency of the precipitate/matrix interface**: At a coherent precipitate/matrix interface, the atomic positions of the two phases match perfectly. The corresponding interatomic spacing in the two phases is usually different resulting in lattice distortion and coherency strains at the interface. The total free energy of the system is increased by the interfacial strain energy. If the energy increase is sufficiently large, a semicoherent interface results in which the lattice mismatch is accommodated by dislocations. An incoherent interface results when the lattice mismatch is too large or the corresponding interatomic spacing between the phase is more than 25% [24]. The precipitates (GP zones) that form in aluminum alloys in the very early stages of aging have the same crystal structure and little lattice misfit resulting in fully coherent precipitates with low energy interfaces. The phases that precipitate subsequently will have different crystal structures. In this case, the precipitates will be semicoherent if identical planes in the two phases can be oriented in a way to provide a low energy interface and will be incoherent otherwise.

4. **Precipitate shape**: Precipitates will take the shape that will minimize the sum of the interfacial and misfit strain energies. For fully coherent precipitates (GP zones), the shape will be spherical (the most compact shape) when the misfit energy is small. With increasing misfit strain energy, the shape will be flattened in the elastically soft direction of the precipitate. In binary Al−Ag, Al−Zn, and Al−Cu alloys in which zones containing 50%−100% solute can be formed, the shape changes to disk at high misfit, as shown in Table 4.9 [24]. When the matrix and the precipitate have different crystal structures but contain an identical plane, partially coherent precipitates form. These have both coherent or semicoherent and incoherent interfaces and take on plate, lath (elongated plate), or needle shapes.
5. **Precipitate Growth**: Precipitates grow by the diffusion of solute atoms in the matrix to their interface, followed by transfer of atoms across this interface. The relative rates of these two processes will determine whether growth is controlled by the rate of diffusion of solute in the matrix or the rate of its transfer across the interface. This is of importance to the growth (thickening) of partially coherent, plate-shaped precipitates. Transfer of atoms across a coherent or semicoherent interface is much more difficult than across an incoherent interface. These precipitates can grow by a mechanism wherein incoherent ledges form in otherwise planar coherent/semicoherent interfaces [10]. Solute atoms migrate to and transfer across the ledges resulting in precipitate thickening by the lateral movement of ledges.
6. **Precipitate coarsening**: Coarsening occurs by the dissolution of the smaller precipitates and diffusion of the solute across the matrix to the larger particles that then increase in size. The coarsening rate at a given temperature decreases with decreasing equilibrium solute solubility and diffusion rate and by having a coherent/semicoherent interface. The upper limit of service temperature for commercial, PH aluminum alloys is low enough that coarsening is generally not of concern. However, even a short time, accidental exposure to moderately elevated temperatures during service or maintenance operations could result in precipitate coarsening and affect the properties deleteriously.

4.3.1.2.2 Effects of Defects and Trace Elements

Precipitate nucleation in aluminum alloys is almost always heterogeneous and is aided by the presence of intrinsic (vacancies, grain boundaries, etc.) and extrinsic (trace elements in solid solution) defects and second phase particles such as dispersoids. Although all these sites promote nucleation by reducing the activation energy barrier, there is a wide variation in their effects on the precipitate morphologies and

Table 4.9 Shapes of Guinier−Preston Zones in Al Alloys

Atomic Radius (nm)	Al-1.43	Ag-1.44	Zn-1.38	Cu-1.28
Zone misfit (%)	–	+0.7	−3.5	−10.5
Zone shape	–	Spherical	Spherical	Disk

resulting alloy properties. Vacancies and dislocations enhance nucleation and diffusion rates generally resulting in a finer distribution of precipitates, which, with few exceptions, provides a better combination of properties. Trace elements alter the interface character and frequently also the precipitate type. Grain boundaries and dispersoids also promote nucleation but result in the formation of PFZs and coarse precipitates in adjacent areas with deleterious effects on properties.

Vacancies play a crucial role in aiding the nucleation and growth of precipitates from the SSSS. The equilibrium vacancy concentration in metals decreases exponentially with decreasing temperature and just as the solute atoms, vacancies in equilibrium during solution treatment are retained in supersaturation upon quenching. These nonequilibrium, quenched-in vacancies form clusters that grow spontaneously and reduce the energy of the system [25]. Clusters can also collapse into dislocation loops and provide sites for precipitate nucleation. Although vacancies cannot be imaged and observed directly, their important role was known very early during the development of precipitation hardening. For example, it has been observed that for samples quenched from different solution treatment temperatures but aged at the same temperature, the precipitation rate will be the highest in the sample quenched from the highest temperature due to the higher concentration of quenched-in vacancies [10]. For samples quenched at different rates from a given solution treatment temperature, the concentration of quenched-in vacancies will decrease with decreasing quench rate and affect the precipitation rates accordingly. This is due to the increasing loss of vacancies during the quench with decreasing rates. This is significant in commercial practice where it is impossible to achieve uniform quench rates and thus correspondingly uniform properties, across parts with high cross-sectional area.

In many alloys based on the Al−Cu and Al−Cu−X (X = Mg or Li) systems, intermediate precipitates that follow GP zones in the precipitation sequence provide higher strength and property combinations, but cannot readily nucleate from the quenched in vacancies alone. Dislocations are introduced by a small amount of cold work in these alloys following solution treatment to promote the nucleation of these intermediate phases by reducing the misfit strain energy barrier.

Trace elements are often added in small amounts to aluminum alloys to alter the nucleation and growth characteristics of precipitates. Their beneficial effects had been known as early as the 1950s when additions of Cd, In, or Sn were found to significantly alter the precipitation sequence in Al−Cu alloys [26]. The addition of a small amount of Sn was found to suppress the formation of GP zones and promote a finer and uniform dispersion of the semicoherent, intermediate θ' phase resulting in higher hardness. More recently Ag has been the principal trace element of choice, particularly for Al−Li alloys based on the 2XXX series.

Trace elements affect the precipitation process in many ways as follows [10,27,28]:

- interactions with vacancies and altering the precipitation kinetics,
- changing the interfacial energy of the clusters and precipitates by segregating to the interface,

- raising the GP zone solvus and altering the temperature range of stability of the precipitate phases,
- promoting the nucleation of new phases,
- affecting the stability of phases by changing the electron-to-atom ratio, and
- stimulating precipitation in general.

Trace elements can also be used potentially in lieu of cold working for alloys in product forms and shapes that may not be amenable to deformation.

4.3.1.2.3 Formation and Effects of PFZs

A review of the causes and effects of PFZs was first published in 1970 considering the prevailing theories to explain the observations regarding precipitation [29]. These observations included the temperatures for precipitate nucleation, role of excess vacancies, occurrence of PFZs at grain boundaries, sensitivity of the alloys to changes in heat treatments, response to double aging treatments, and the effects of trace elements. The study of PFZs was also of interest as they adversely affected the properties of commercial alloys.

Precipitate nucleation at vacancies comes closest to being homogeneous and the behavior of vacancy-assisted PFZs can be explained by the heat treatment temperatures and the quench rates. The driving force for precipitate nucleation increases with decreasing temperature for a given alloy, and as shown in Fig. 4.9 [29], there is a temperature T_c below which homogeneous nucleation is possible without excess, quenched-in vacancies. In other words, below T_c, nucleation can occur at vacancies with just their equilibrium concentration at the aging temperature. With the

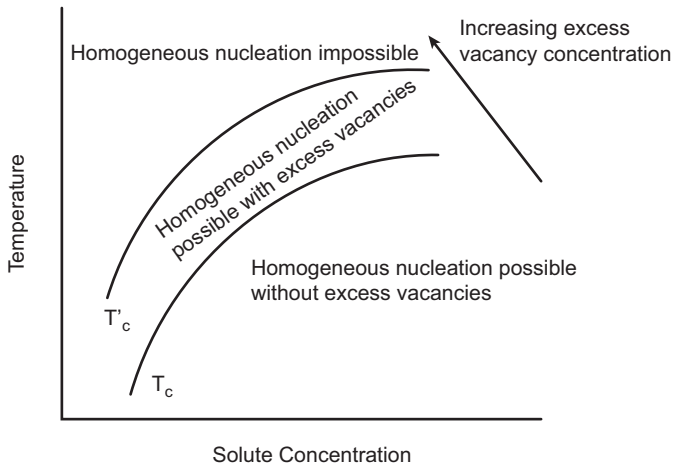


FIGURE 4.9

Critical temperature for homogeneous nucleation of precipitates.

Adapted from E.A. Starke Jr., The causes and effects of denuded or precipitate-free zones at grain boundaries in aluminum alloys, JOM 22 (1) (1970) 54–63.

availability of quenched-in vacancies, homogeneous nucleation at vacancies is possible in a range of temperatures above T_c and up to T'_c.

Grain boundaries act as sinks for vacancies causing their depletion during and following quenching of the alloy. The resulting vacancy concentration profile adjacent to the grain boundaries is such that solution treating at a higher temperature, quenching at a faster rate, and aging at a lower temperature will all decrease the width of PFZs. During quenching, grain boundaries can also act as sites for heterogeneous nucleation of precipitates that then grow into coarse particles. The resulting depletion of solute near the grain boundaries causes the formation of "solute-depleted PFZs" during subsequent aging. These PFZs are accompanied by the presence of coarse precipitates at the grain boundaries, as shown in Fig. 4.10 for alloy 7050 [30]. Like grain boundaries, dispersoid particles can also nucleate precipitates and cause solute-depleted PFZs. Once formed, the effects of these PFZs cannot be reversed by subsequent aging treatments.

PFZs are softer than the surrounding matrix and hence are areas for strain localization and paths for easy crack nucleation and propagation under both monotonic and cyclic loading in normal and corrosive environments. Aging at lower temperatures and introduction of dislocations by cold work to nucleate precipitates in competition with grain boundaries are some approaches to mitigate the effects of PFZs. Over the years, new alloying approaches and processing practices have also been developed to minimize the deleterious effects of PFZs and achieve concurrent improvements in strength, fracture, and corrosion resistance in commercial alloys. One example is the use of Zr as the dispersoid forming element instead of

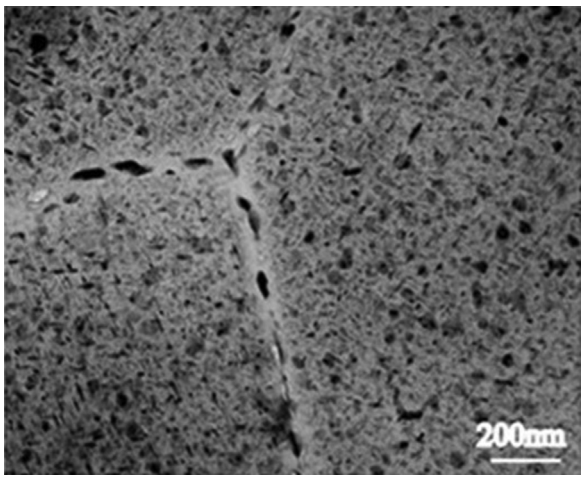


FIGURE 4.10

Microstructure of alloy 7050-T7451 showing precipitate free zones and coarse grain boundary precipitates [30].

Cr in 7XXX series alloys starting with 7050 developed in the 1970s. Zr containing dispersoids are coherent and through their effect on matrix recovery, promote unrecrystallized microstructures. The resulting reduction in grain boundary areas provides better combinations of strength and corrosion resistance, particularly in thick sections. These will be discussed in the section on quench sensitivity.

4.3.1.2.4 Precipitation in Specific Alloy Systems

In the framework of the precipitation reactions and mechanisms described previously, this section will describe their sequences of formation and characteristics in systems that form the basis for structural aluminum alloys in current use. These systems are Al−Cu, Al−Cu−Mg, Al−Cu−Li and Al−Cu−Mg−Li (2XXX series), Al−Mg−Si (6XXX series), and Al−Zn−Mg−Cu (7XXX series).

4.3.1.2.4.1 Al−Cu Alloys Precipitation hardening was discovered nearly a century ago using Al−Cu samples. Because of this unique position, it is not surprising that Al−Cu alloys have perhaps been the most studied to understand and apply PH alloys. Although most of the Al−Cu alloys in service for demanding structural applications contain ternary additions for property enhancement, a review of the precipitation processes in binary Al−Cu alloys is very helpful in delineating the effects of the various factors that control this process and affect the properties of other systems.

Precipitation from the SSSS in Al−Cu alloys follows the sequence

$$\alpha\ (\text{Al SSSS}) \rightarrow \text{GP Zones} \rightarrow \theta'' \rightarrow \theta' \rightarrow \theta$$

with Fig. 4.4 showing the solvus for the equilibrium phase θ and the metastable phases GP zones, θ″ and θ′. Even though the volumetric free energy decrease (ΔGv) will be the lowest for the formation of the equilibrium phase θ, the nucleation barrier will be lower for the intermediate phases. GP zones will be the first to nucleate when an alloy is aged below its solvus. GP zones are fully coherent with the Al matrix and will have the lowest interfacial energy (ΔGs) and misfit strain energy γ. θ″ has a tetragonal crystal structure with (010) and (100) planes similar to that in α and forms as plates that are fully coherent with the matrix. Although θ′ is semicoherent, it needs dislocations or secondary particles for nucleation.

Fig. 4.4 shows that the phases can overlap as precipitation proceeds with formation of those of higher stability. This is seen in the aging response of Al−Cu alloys with varying Cu content shown in Fig. 4.11 [10]. At 130°C (266°F), which is below the GP zone solvus for all the compositions shown in the plots, this phase will nucleate first and eventually transition sequentially to θ″ and θ′. The two stages of hardening exhibited by alloys with 4 and 4.5 wt% Cu is due to the stability of the GP zones after they reach the critical size and prior to transition to θ″ and θ′. Maximum hardness is achieved at a shorter time with increasing Cu content and increasing aging temperature. Aging times of 24 h or less are preferred in commercial practice and the aging temperature will be selected to provide the maximum hardness within reasonable aging times.

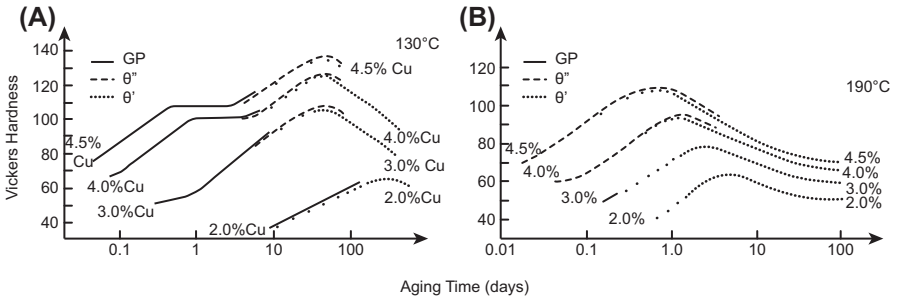


FIGURE 4.11

Effects of alloy composition and aging temperature on the maximum hardness achievable in Al–Cu binary alloys. (A) 130°C (266°F) and (B) 190°C (374°F) [10].

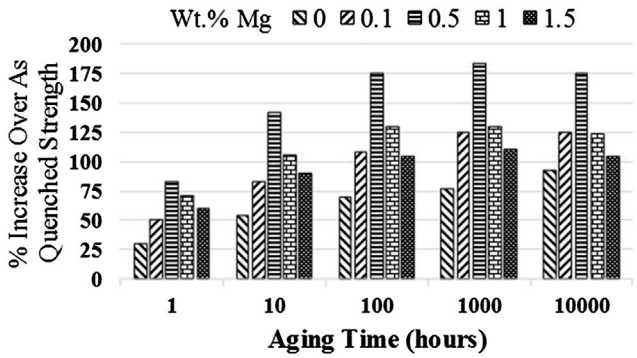
For alloys with 4–4.5 wt% Cu, typical of 2XXX series alloys, maximum hardness is achieved at 190°C (374°F) at aging times of 24 h or less. However, the relatively coarse distribution of θ' limits the maximum value that is possible. Although refinement of θ' precipitates by trace addition elements such as Sn increases hardness of Al–Cu alloys, better combinations of properties are achieved with Mg or Li additions. The strength of Al–Cu–Mg and Al–Cu–Li can also be increased further by cold work and trace element additions.

4.3.1.2.4.2 Al–Cu–Mg Alloys Most 2XXX series alloys developed for commercial use are based on the Al–Cu–Mg system. Among these, alloy 2024 and its derivatives, e.g., 2124 and 2524, are used widely. The nominal compositions of these alloys are given in Table 4.4. The 2X24 alloys contain 4–4.5 wt% Cu and 1.5 wt% Mg as the solute elements. In the earlier discussion on phase equilibria, it was observed that the S (Al_2CuMg) phase will be present as the equilibrium phase in most 2XXX series, Al–Cu–Mg alloys. The relative amounts of Cu and Mg will determine if θ will also be present. 2X24 alloys with Cu:Mg weight ratio between two and three contain both θ and S as the equilibrium phases. Precipitation in these alloys follows the sequence

$$\alpha\ (\text{Al SSSS}) \rightarrow \text{Solute clusters} \rightarrow \theta'' + \text{GPB (Guinier–Preston–Bagaryatsky)}$$
$$\text{Zones} \rightarrow \theta' + \Omega \rightarrow \theta + \text{S}$$

GPB zones are the precursors to the S phase in Al–Cu–Mg alloys, as are GP zones to θ'' in binary Al–Cu alloys. The Ω phase forms at the expense of θ' in Al–Cu–Mg alloys, but its nucleation is facilitated by the addition of Ag. In this range of the amounts of Cu and Mg, the hardness of the alloys increases with increasing Mg content, as shown in Fig. 4.12 [31], forming the basis for the development of 2024 and its derivatives. Cold work after solution treatment will also increase the strength considerably by providing dislocations for nucleation, which results in a finer distribution of precipitates.

Ag additions increase the age hardening response of all aluminum alloys containing Mg [19]. Additions of 0.4–0.5 wt% Ag cause a uniform and dense distribution of



Mg (Wt.%)	As-Quenched Yield Strength ksi	MPa
0	13	90
0.1	12	83
0.5	12	83
1	17	117
1.5	20	138

FIGURE 4.12

Effect of Mg content on the strength of Al–4Cu–Mg (wt%) alloys aged at 20°C (68°F).

Plotted from data in C.R. Brooks, Aluminum-base alloys, in: Heat Treatment Structure and Properties of Nonferrous Alloys, ASM International, 1982, pp. 115–137.

the Ω phase, which increases the hardness considerably, as shown in Fig. 4.13 [10]. This has been the basis for the development of Al–Cu–Mg–Ag alloy 2029 (composition shown in Table 4.4). The crystal structure of Ω is related to that of θ. The beneficial effect of Ag additions is attributed to the formation of Ag–Mg

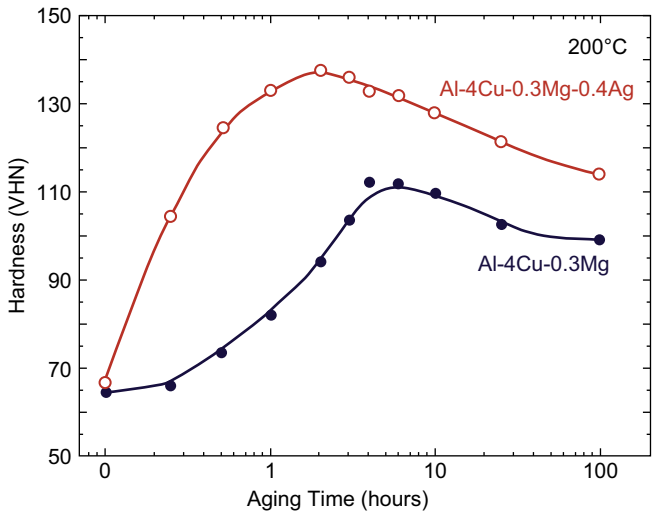


FIGURE 4.13

Age hardening response of Al–4Cu–0.3Mg and Al–4Cu–0.3Mg–0.4Ag (wt%) alloys at 200°C (392°F) [10].

clusters early in the decomposition of the Al SSSS and the modification of the precipitation process by the preferred Ag–Mg interactions.

4.3.1.2.4.3 Al–Cu–Li Alloys and Al–Cu–Mg–Li Alloys Addition of each wt% of Li to Al alloys results in a 3% reduction in density and 6% increase in modulus. Although binary Al–Li alloys are precipitation hardenable, they do not exhibit the required combinations of strength and toughness. Li is much more attractive through its effects on increasing the properties of Al–Cu and Al–Cu–Mg alloys while also lowering their density, and much of the recent alloy development has focused on these alloy families. A review by Rioja and Liu [32] provides a comprehensive description of the evolution, key microstructural features, and properties of Al–Li alloys with a focus on application specific product forms.

The metastable phase δ' (Al_3Li) precipitates as spherical, fully coherent particles that strengthen binary Al–Li alloys. The phases that precipitate in Al–Cu–Li alloys depend on the relative levels of Cu and Li, as shown in Table 4.10 [33], and include the ternary phase T_1 (Al_2CuLi) in addition to those that form in the respective binary alloys. The nucleation of T_1 is difficult in Al–Cu–Li alloys and, as with θ' in the binary Al–Cu alloy, cold working prior to aging provides sites for its heterogeneous nucleation and results in a more uniform distribution. Maximum strength from T_1 is achieved at deformation levels of 3%–6% [19].

The strengthening contribution by the T_1 phase can be increased considerably by the addition of Mg and Ag, forming the basis for the current (third) generation Al–Li alloys (e.g., 2198 and 2199 shown in Table 4.4). The main strengthening precipitates in these alloys are T_1, θ', and δ', depending on the amounts of Cu and Li, and Ω, which is isomorphous and isostructural with T_1. Addition of Mg promotes the homogeneous nucleation of T_1 from prior GP zones of Cu and Li atoms providing a highly dense distribution of these precipitates. Ag segregates to the precipitate–matrix interface, similar to its role in Al–Cu–Mg alloys without Li, and in combination with Mg accelerates T_1 nucleation while retarding its growth. As with Al–Cu–Li alloys, cold work prior to aging is very beneficial in promoting the heterogeneous precipitation of T_1, as shown in Fig. 4.14, thereby increasing the strength considerably [10].

4.3.1.2.4.4 Al–Mg–Si Alloys The 6XXX series alloys possess lower strength properties than the 2XXX and 7XXX series alloys and are used in secondary

Table 4.10 Precipitation Sequence in Al–Cu–Li Alloys

Cu:Li Ratio	Precipitation Sequence
>4	α (SSSS) $\rightarrow$ GP zones $\rightarrow \theta'' \rightarrow \theta'$
2.5–4	α (SSSS) $\rightarrow$ GP zones $\rightarrow$ GP zones $+ \delta' \rightarrow \theta'' + \theta' + \delta' \rightarrow \delta' + T_1 \rightarrow T_1$
1–2.5	α (SSSS) $\rightarrow$ GP zones $+ \delta' \rightarrow \theta' + \delta' \rightarrow \delta' + T_1 \rightarrow T_1$
1	α (SSSS) $\rightarrow \delta' + T_1 \rightarrow T_1$

GP, *Guinier–Preston.*

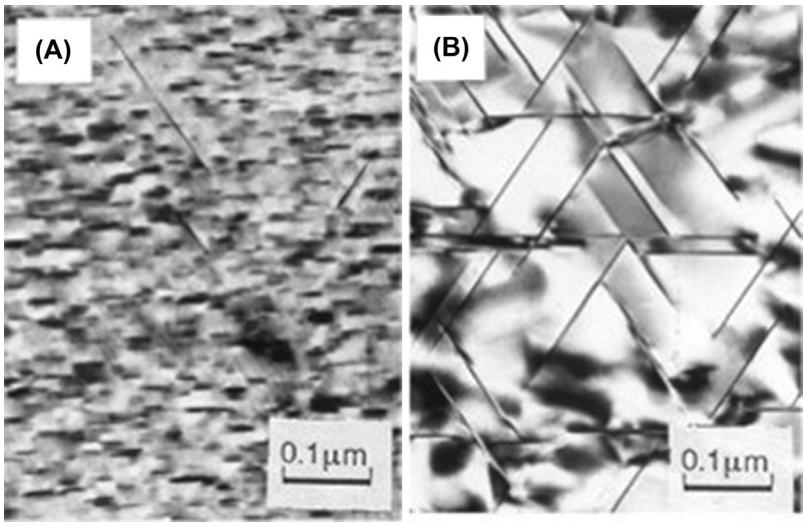


FIGURE 4.14

Microstructure of Al–5.3Cu–1.3Li–0.4Mg–0.4Ag–0.16Zr (wt%), quenched and aged 8 h at 160°C (320°F) (A) (diamond pyramid hardness number-146) showing GP zones and occasional plates of T_1 and (B) cold worked 6% prior to aging (diamond pyramid hardness number-200) showing a uniform dispersion of T_1 plates having high aspect ratios [12].

applications and in welded assemblies. Representative alloys are shown in Table 4.11. The equilibrium phases in these alloys are Si and β (Mg_2Si) and their precipitation sequences are very complex. Current understanding indicates that the sequence is as follows [19]:

$$\alpha\ (\text{Al SSSS}) \rightarrow \text{Independent clusters of Mg and Si, coclusters of Mg and Si} \rightarrow \text{GP Zones} \rightarrow \text{Si-rich phase} \rightarrow \beta'' \rightarrow \beta' \rightarrow \beta$$

The clusters and the transition phases β″ and β′ contribute to strength. Increasing the level of Cu increases the number of possible phases and the complexity of precipitation sequence, improves the age hardening response and further increases the strength.

4.3.1.2.4.5 Al–Zn–Mg–Cu Alloys The Al–Zn–Mg–Cu system forms the basis for alloys with the best combination of properties for use in critical airframe structures. Both Zn and Mg have significant solid solubility in Al, but neither of the

Table 4.11 Nominal Compositions of Representative 6XXX-Series Alloys

Alloy	Mg	Si	Cu	Cr	Mn	Fe	Zn
6061	1.0	0.6	0.28	0.2	0.5	0.7 Max	0.25 Max
6013	1.0	0.8	0.85	0.1	0.6	0.5 Max	0.25 Max

respective binary alloys are useful as PH alloys in practice. The large combined solid solubilities of Zn and Mg in Al, the ability to precipitation harden to the highest strength levels and the possibility to obtain a range of property combinations have all resulted in the continuing development of commercial aluminum alloys based on the Al−Zn−Mg−Cu system.

Equilibrium phases in the Al-rich corner of the Al−Zn−Mg system are T ($Mg_{32}(Al,Zn)_{49}$), η ($MgZn_2$) and β (Al_3Mg_2). In compositions representative of commercial alloys, the precipitation sequence is [19].

$$\alpha \text{ (Al SSSS)} \rightarrow \text{GP Zones} \rightarrow \eta' \rightarrow \eta$$

GP zones start as spherical clusters of Zn atoms with vacancy-assisted diffusion of Mg into them. η′ is a transition precipitate and a precursor to η. Unlike in Al−Mg−Cu alloys, the GP zones in Al−Zn−Mg alloys continue to grow for several years with increasing strength, as shown in Fig. 4.15 [34] and never attain the required microstructural stability for service. These alloys are therefore not used in the naturally aged condition. Another difference between the Al−Cu−Mg and the Al−Zn−Mg−Cu systems is that the GP zones in the latter have very low coherency strains and deformation prior to aging does not have any beneficial effect. Rather, heterogeneous nucleation sites alter the proportion of the various phases reducing the strength. Al−Zn−Mg−Cu alloys are used only in the T6 and the T7 tempers.

Artificial aging conditions can be altered in Al−Zn−Mg−Cu alloys to provide varying combinations of strength and corrosion resistance. The formation of PFZs

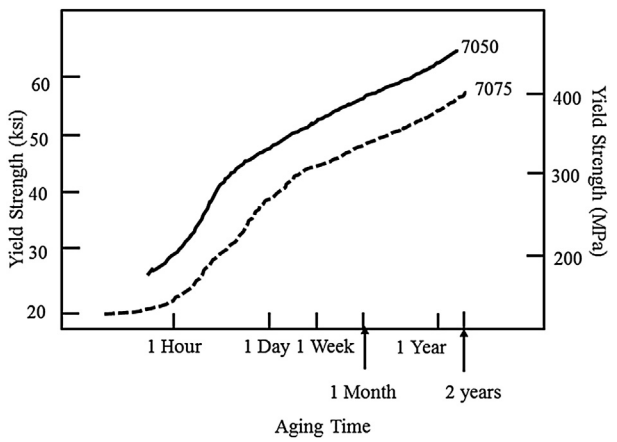


FIGURE 4.15

The effect of natural aging on the properties of Al−Zn−Mg−Cu alloys 7075 and 7050 sheet.

Adapted from J.T. Staley, Aging kinetics of aluminum alloy 7050, Metallurgical Transactions, 5 (1974) 929−932.

and the anisotropy of microstructure in these alloys render them susceptible to SCC in thick sections and exfoliation corrosion (EC) in relatively thin products. This susceptibility is the highest in the peak aged T6 temper in which the alloys are strengthened primarily by η'. Corrosion resistance can be improved by overaging beyond peak strength to a T7X temper in which the alloys are strengthened by η' and η. Overaging decreases the relative volume fraction of the shearable precipitates thereby reducing stress concentrations at grain boundaries and improving the resistance to SCC.

Recent Al−Zn−Mg−Cu alloy development effort has focused on increasing the strength of overaged alloys while maintaining acceptable corrosion resistance. These developments include two-step aging, Cu additions and the use of retrogression and reaging (RRA) treatment. Strength loss can be minimized if a single step overaging at the higher temperature is preceded by aging at the lower peak aging temperature. Cu partitions into all precipitates increasing strength and further minimizing the strength loss. In the RRA treatment, the peak aged alloy is quenched to room temperature, heated in the range of 200−280°C (392−536°F) to dissolve the precipitates (retrogression) and reaged to peak strength. Reaging after retrogression results in a higher volume fraction and more uniform distribution of η' resulting in strength levels near the peak values with acceptable corrosion resistance [35].

Table 4.12 lists the crystallographic and morphology information for some precipitates occurring in the Al alloy systems discussed above [10]. These precipitates typically form with simple orientation relationships such as for example $(001)_{\theta''} \parallel (001)_{\alpha}$ and $[100]_{\theta''} \parallel [100]_{\alpha}$ for Θ''. As increasingly sophisticated techniques are used for their characterization, a tremendous potential exists for the further elucidation of their nature and for the design and development of alloys with better combinations of properties.

4.3.1.2.5 Modeling of Precipitation

PH Al alloys can contain several metastable phases with varying and complex features (Table 4.12). Predictive and quantitative modeling of the thermodynamics and kinetics of the nucleation, growth and coarsening of these phases will enable the design of optimum alloys and processing conditions. However, the complexity of precipitates poses a significant challenge in this regard. The approaches and the various aspects of modeling of precipitation have been discussed in detail in many reviews [37−39], from which salient aspects with examples from recent efforts are described briefly in the following.

The objective of modeling of precipitation is to obtain all the information required for predicting the effects of the types and morphologies (composition, crystal structures, degree of coherency, shape, size distribution, and volume fraction) of the precipitates on properties. Nucleation, growth, and coarsening can all overlap during precipitation. These stages are distinguished by the number density of precipitates increasing with time during nucleation, their size increasing with time during growth, and by their number density decreasing with time during coarsening. Nucleation and coarsening will overlap when the precipitate/matrix interfacial energy is

Table 4.12 Characteristics of Metastable and Equilibrium Phases in Precipitation Hardened Aluminum Alloys

System	Phase	Crystal Structure	Lattice Parameter (nm)	Composition	Shape	Habit Plane
Al–Cu, Al–Cu–Mg	GP zones			Single/multilayer Cu atoms	Disk	$\{100\}_\alpha$
	Θ''	Tetragonal	a—0.404 c—0.768	Two layers of Cu separated by three Al layers	Plate	$\{100\}_\alpha$
	Θ'	Body centered tetragonal	a—0.404 c—0.58	Al_2Cu	Plate	$\{100\}_\alpha$
	Ω	Face centered orthorhombic	a—0.496 b—0.859 c—0.848	Al_2Cu	High aspect ratio plate	$\{111\}_\alpha$
Al–Cu–(Mg)–Li	T_1	Hexagonal	a—0.496 c—1.391	Al_2CuLi	High aspect ratio plate	$\{111\}_\alpha$
Al–Zn–Mg–Cu	η'	Hexagonal	a—0.496 c—1.402	Various reported	Thin plate	$\{111\}_\alpha$

below a critical value or the solute supersaturation is above a critical value. In most cases in practice, precipitation can be assumed to occur without overlap of nucleation and coarsening.

Several factors increase the difficulty of modeling precipitation in Al alloys [37]. Some of these are the competition for solute by the concurrent precipitation of phases containing the same solute (e.g., θ' and T_1 in Al−Cu−Li alloys), concurrent precipitation in the matrix and at grain boundaries, PFZ formation, varying shapes and chemistries of transition phases, multimodal distribution of precipitate sizes and their nonhomogeneous spatial distribution. It is difficult and often impossible to account for all these factors in practice. Accordingly, many simplifying assumptions are made, as illustrated in the modeling of the precipitation kinetics in an Al−Zn−Mg alloy, which considered only the mean particle size of one type of spherical, homogeneously distributed precipitate [40]. Precipitation was assumed to occur in two stages, that of overlapping nucleation and growth and of overlapping growth and coarsening, with no overlap of nucleation and coarsening. The approach to this effort, adapted from its description by Hutchinson [37], is qualitatively described below.

- During the nucleation and growth stage, the model describes the precipitate nucleation rate, N', in terms of the activation barrier, ΔG^*, and critical nucleus size, R^* (described earlier and which both incorporate the interfacial energy γ) and the solute diffusivity and concentration in the matrix. The temporal evolution of the mean precipitate size, R_m is described in terms of its diffusional growth rate.
- During the growth and coarsening stage, the evolution of N' and R_m is described by combining their evolution in the respective individual stages. During growth, N does not change ($N' = 0$) and R_m increases in accordance with its diffusional growth rate. During coarsening, N decreases and R_m increases as determined by the reduction in the interfacial energy.
- When the decrease in N due to coarsening is greater than that due to nucleation, the integration of the equations to evaluate N' and R_m changes from the one for the nucleation and growth stage to that corresponding to the growth and coarsening stage.

The model was used to calculate the temporal evolution of N, R_m, critical precipitate radius, and solute content for an Al−6.1Zn−2.35Mg−0.1Zr (wt%) alloy isothermally aged at 160°C (320°F). Results were compared with the values obtained experimentally [41], and despite the simplifying assumptions, the predicted mean precipitate radius values agree well with the values obtained from small angle neutron scattering and transmission electron microscopy, as shown in Fig. 4.16 [40] for one of the cases that were modeled.

The calculation of the nucleation rates requires a knowledge of the free energy terms associated with the formation of the new phase (ΔGv) and the corresponding interfacial energy γ for each of the possible phases that can precipitate in a given alloy system. The Gibbs free energy data required for the calculation of ΔGv for phases in Al alloy systems are available in many databases developed by the

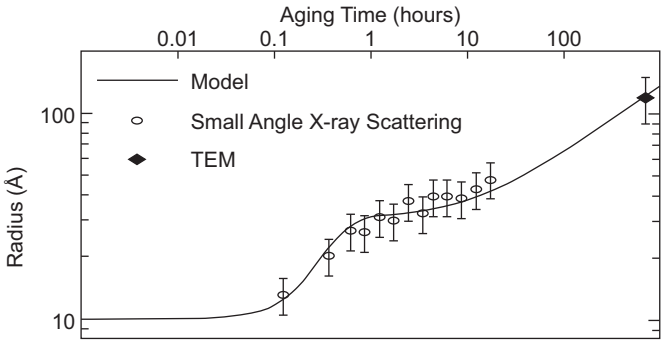


FIGURE 4.16

Comparison of predicted and measured values of mean radius of precipitates for aging of Al–6.1Zn–2.35Mg–0.1Zr (wt%) alloy isothermally aged at 160°C (320°F) [40].

CALPHAD community. The nucleation rate is very sensitive to even small changes in γ and the lack of availability of accurate values for this parameter is a major drawback of this "mesoscale" modeling approach. Atomistic approaches do not have this drawback, but are limited to only short aging times for coherent precipitates.

Following is a list of additional complexities that can arise in treating the precipitation in Al alloys and how some can be addressed [37]:

- Multiple phases forming simultaneously and a single phase nucleating both in the matrix and at grain boundaries can be treated by the same approach as for each of the phases and each type of nucleation site. The individual equations can be coupled.
- Precipitate sizes can occur in multiple distributions such as the bimodal distributions in retrogression and reaged alloys with coarse and fine precipitates, each with their own distribution. A single value for the mean precipitate size is obviously not representative of such distributions. These can be addressed by discretizing the size distribution into classes and monitoring the precipitation density in each class.
- Nonspherical precipitates constitute most of the phases in Al alloys, but sufficient progress has not been made in modeling their behavior. Precipitate shape is determined by the anisotropy in the interfacial and strain energies. Shape evolution depends on the anisotropy of interface motion, which is controlled by the interface "mobility." Differences in the mobility of interfaces cause precipitate shapes to change as for example the change in length of precipitates without change in thickness. Phase field approaches can model the growth and coarsening of nonspherical particles, but not their nucleation, which must be introduced separately.
- In commercial practice, many Al alloys are deformed following solution treatment prior to aging. The defects introduced by deformation provide heterogeneous sites for nucleation, as described earlier, accelerate growth and coarsening, modify their spatial distribution and also alter the precipitate type

and shapes. Defects such as dislocations reduce the activation barrier for nucleation and increase the diffusion rates for the growth and coarsening of precipitates. These effects can be accounted for by using modified values for γ, which again is not known with accuracy.

Modeling of precipitation requires a knowledge of thermodynamic (free energy, interfacial energy, etc.) and kinetic parameters (mobility, diffusivity, etc.) for the components and phases in the alloy systems and how they are affected by defects and precipitate morphologies. These parameters, either calculated or measured, are being generated at a rapid pace and incorporated in commercial or open databases thus overcoming the difficulties of the classical approaches. Software packages use these data and model the evolution of matrix composition, size distribution, number density, and volume fraction of precipitates and other quantities that can be used for property prediction. In a recent study, stable and metastable phases in Al−Cu, Al−Cu−Mg, Al−Mg−Si, and Al−Mg−Zn systems were modeled using the CALPHAD approach and the results were incorporated into software packages that were then used to predict the optimum processing temperatures and the evolution of the precipitate characteristics [42]. This trend can be expected to accelerate with the increasing availability of data, computational capabilities, and refinement of the modeling approaches.

4.3.1.3 Mechanisms and Modeling of Precipitation Hardening

As discussed in the earlier chapters, a significant fraction of the strength of PH alloys arises from various mechanisms by which precipitates act as obstacles to dislocation motion. These alloys also derive a portion of their strength from matrix microstructural features such as grain boundaries and dislocation substructures. This section will focus only on the mechanisms that contribute to the flow (yield) stress from the precipitates. Contributions from other sources, their superposition on strengthening arising from precipitates and the effects on toughness, fatigue, and corrosion behavior will be discussed later.

Precipitation hardening has been investigated extensively and the theories and understanding of the mechanisms as they have evolved over the years have been thoroughly reviewed in general [43−45] and specifically for Al alloys [10,27]. Models for precipitation hardening must quantitatively describe the effects of all precipitate features, which from the perspective of commercial aluminum alloys are those present in them after aging and prior to placement in service. Depending on the specific system and its final aging condition, the alloy will have one or more fully or partially coherent precipitates of various shapes, sizes, and volume fractions. Dislocations can shear coherent and semicoherent precipitates. They bypass incoherent precipitates by the Orowan bowing mechanism leaving loops in their wake. The resistance of the precipitates to dislocation motion contributes to alloy strength.

Some of the key parameters used to characterize the precipitates are the size, volume fraction, particle spacing, and shape. The first three of these are related by the fact that given any two, the third parameter can be calculated readily, at least for

uniform particles homogeneously distributed in the matrix, i.e., of constant size and spacing. For varying particle sizes and nonhomogeneous distributions, mean values can be calculated from a knowledge of their distribution. Shape is represented by aspect ratios such as *l*/*d* for rods and *d*/t for circular plates, where *l*, *d*, and t are the length, diameter, and thickness, respectively. Further, the particle size, spacing and cross-sectional shape as projected on the slip plane, not their absolute values, should be used. Within this framework, the parameters that are used by the models discussed in the following sections are those that most clearly describe the operating mechanisms.

4.3.1.3.1 Hardening by Shearable Precipitates

When precipitates are sheared, the mechanisms that can operate to increase the strength of alloys are as follows [19,27].

- Interfacial (chemical) strengthening due to the creation of an interface in the sheared particle
- Order strengthening due to the creation of antiphase boundaries in an ordered precipitate
- Stacking fault strengthening arising from differences in the stacking fault energies between the matrix and the precipitate
- Modulus strengthening arising from differences in the moduli between the matrix and the precipitate
- Coherency strengthening arising from the elastic stresses due to misfitting coherent precipitates such as, for example, the tetragonally distorted and nonspherical particles in Al—Cu alloys

Strengthening from precipitates that are sheared can be expressed by [27] the following:

$$\tau = cf^m r^p \tag{4.2}$$

where τ is the critical resolved shear stress (CRSS), f and r are the volume fraction and radius of the precipitates, and c is a constant determined by which combination of the above mechanisms operates. The exponents m and p are always positive and the overall strength increases with increasing f and r. However, there are differences among the different mechanisms in their dependence on f and r and the conditions under which each is effective. Each of these mechanisms has been studied in detail and several of the reviews [10,19] have extensive references to the original investigations.

4.3.1.3.2 Hardening by Orowan Mechanism

With increasing resistance to shearing, dislocations bypass particles beyond a certain size. The CRSS for hardening by bypassing can be expressed by [27] the following:

$$\tau = \frac{0.8Gbf^{0.5}}{2\pi[2(1-\nu)r]^{0.5}} \ln(1.6r/r_0) \tag{4.3}$$

where G is the shear modulus, b is the Burgers vector, ν is the Poisson's ratio, and r_0 is the inner cutoff radius of the dislocation. In this case, the strengthening decreases with increasing particle size.

Based on the above relations, Fig. 4.17A–D illustrates the dependence of CRSS (τ) and thus the yield stress of the alloy on the precipitate characteristics. Fig. 4.17A schematically shows the relationship between CRSS and size when a single particle is sheared, for which case the volume fraction need not be considered explicitly. In practice, in the early stages of aging of alloys, both the volume fraction (f) and the radius (r) of the particles increase and the CRSS particle size relationship will be as shown in Fig. 4.17B. Beyond a certain size, the CRSS for bypass of particles by the Orowan mechanism will be lower than that for shearing, as shown in Fig. 4.17C and at peak strength, dislocations will start bypassing particles with the CRSS decreasing subsequently in accordance with Eq. (4.3).

Al alloys can have multiple precipitate types each with different size distributions and thus varying contribution to strengthening. The effect of particle size distribution on the CRSS is shown in Fig. 4.17D [19]. Peak strength during aging will occur immediately after the size of the largest, but not the average, precipitate

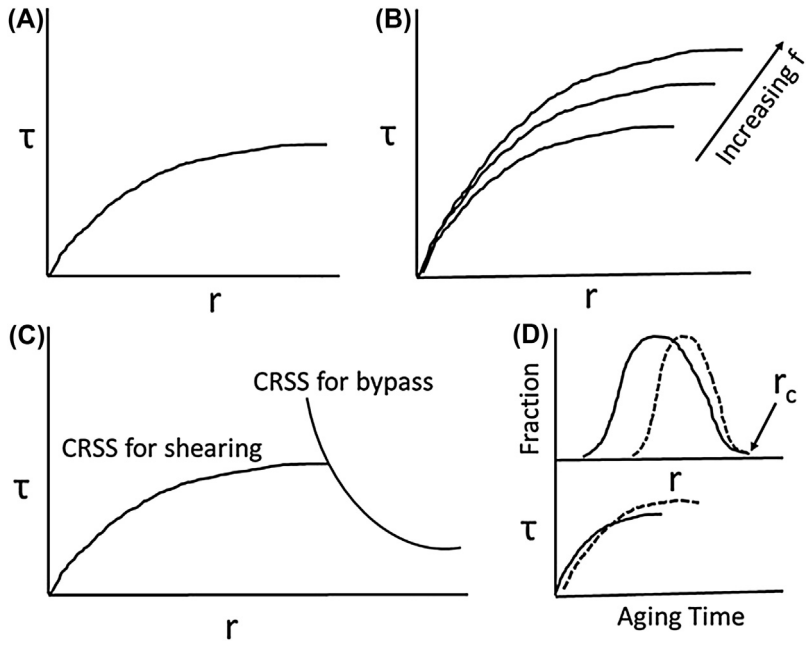


FIGURE 4.17

Dependence of critical resolved shear on the precipitate characteristics.
(A) dependence on radius (r) for shearing of a single particle (B) effect of simultaneously increasing radius and particle volume fraction (C) dependence on particle radius for shearing and bypass mechanisms (D) dependence on particle size distribution.

(D) Adapted from M. Tiryakioglu, J.T. Staley, Effect of alloying additions in aluminum alloys, in: G.E. Totten and S. Mackenzie (Eds.), Handbook of Aluminum, Physical Metallurgy and Processes, vol. 1, CRC Press, 2003, pp. 81–210.

reaches the critical value, r_c, as shown in this figure. However, the contribution to strength will be higher from narrower particle size distributions as these will have effectively higher average particle size. As seen in Fig. 4.17B, the critical precipitate size also depends on the volume fraction of the precipitates and thus is not a constant even for a given alloy system. In comparing Fig. 4.17B and D, it should be noted that in the initial stages of aging of aluminum alloys both f and r increase concurrently until the particle size reaches the critical value, r_c, corresponding to the transition from shearing to bypass, after which f is constant, but r increases. Each successive point in the rising portion of the curves in Fig. 4.17D corresponds to successively higher value of f. Strengthening by cutting of precipitates is effective at high volume fractions of relatively small precipitates up to about 20 nm in size.

4.3.1.3.3 Effects of Precipitate Shape

Precipitates also form in many shapes and orientations (Table 4.12) and the effective dimensions to be used for modeling will be determined by their projection on the slip plane. The volume fraction and the size of the precipitates determine the spacing between them, which for spherical particles can be measured as their center-to-center or surface-to-surface distances. The effective diameter of these particles in the slip plane in which the dislocations move will be a fraction of their true diameter and will depend on how the particles are distributed in the slip plane and how it intersects them. To determine the effectiveness of nonspherical precipitates, comparison can be made of the incremental increase in CRSS from these particles with that from spherical particles at constant volume fraction and number densities.

The review of the effects of the precipitate features indicates that maximum strength will be achieved with plate shaped precipitates of high aspect ratios forming in $\{100\}_\alpha$ and $\{111\}_\alpha$ planes [10]. High strength alloys in the Al−Cu−Li/Al−Cu−Mg−Li−Ag systems and 7XXX series are strengthened by plate shaped T_1 and η', respectively, forming in $\{111\}_\alpha$ planes. Higher solute content can increase strength further by increasing the precipitate volume fraction, as was observed in the early development of 7XXX alloys. However, this approach has limitations as the strength increase was accompanied by decreases in toughness and corrosion resistance. Similarly, the Li content in third generation Al−Li alloys has been reduced to improve toughness and minimize anisotropy. Another promising method to increase strength is to add elements such as Ag that change the interface characteristics and promote nucleation of alternative phases such as Ω. The promise of methods such as introducing ultrafine dispersions of hard particles [46] and development of PH Al−Mg−Sc alloys will be discussed later.

4.3.1.4 Integrated Process Modeling for Precipitation Hardening

With the continuous generation and refinement of the relevant thermodynamic and kinetic parameters, both from experiments and first-principle calculations, the capability to model precipitation reactions and hardening in Al alloys is improving significantly. For alloy design, currently available software packages can perform integrated simulations and accurately predict the precipitation behavior and

resulting hardening for many of the Al (and other) alloy systems. However, from the perspective of industrial operations, it is also important to predict the effects of processing where conditions deviate from that typically used in developing the models. For example, various quenching media (warm water, glycol, etc.) are used in practice to reduce the cooling rates from the solution treatment temperature so as to minimize distortion of thin parts and residual stresses in thick parts. Decreasing the cooling rates will increase precipitate nucleation at heterogeneous sites (e.g., grain boundaries and dispersoids) during quench, reduce the solute available for aging and consequently decrease the alloy strength.

The "quench factor analysis" (QFA) method was developed to predict the effects of the quench path (cooling curve) on the properties of the alloys after aging [47]. Use of QFA requires the generation of time–temperature–property (TTP) or C curves. These curves are determined for each alloy–temper combination using samples quenched to various temperatures between the solvus and the aging temperature, isothermally holding for various times, quenching to room temperature, aging, and measuring the desired properties. A given C curve represents the critical hold time at each temperature to which the sample is quenched that will result in the same value of the measured property after aging. As an example, Fig. 4.18 shows C-curves for Al alloy 7075-T6 with each curve representing the critical hold times at different quench temperatures that resulted in the same fraction of the yield or tensile strength of the alloy after aging under conditions that will nominally achieve T6 properties [48].

It is clearly seen that the strength after aging decreases with increasing hold time, at any temperature, beyond the maximum necessary to achieve the T6 strength. The critical time for achieving 100% of the property is the incubation time for the nucleation of the precipitates. In this sense the C or TTP curves are such as the TTT curves

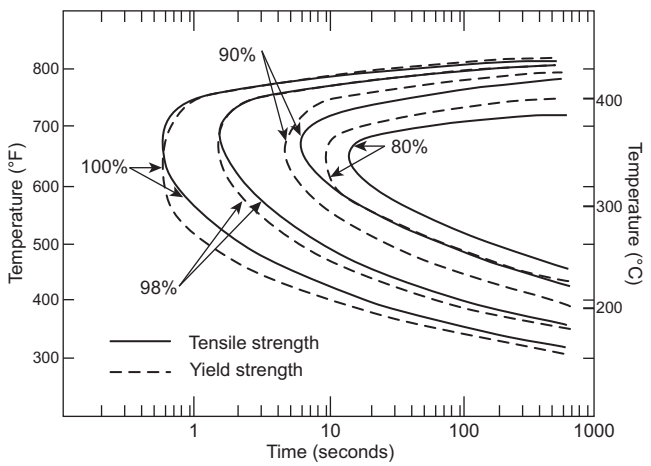


FIGURE 4.18

Time–temperature–property diagrams for 7075-T6 for various levels of strength [48].

commonly used to determine the incubation times for the initiation of the transformation at any temperature. Increasing time at any temperature beyond the critical values results in higher precipitation during quench with correspondingly lower strength after aging.

A series of C curves such as shown in Fig. 4.18 can be constructed for any final aging condition for any property of interest. In the case of a property such as yield strength, its value, σ, measured after solution treatment, quenching and aging, is related to the "Quench Factor," Q, by the following equation.

$$\sigma = \sigma_{\max} \exp(k_1 Q) \tag{4.4}$$

where $\sigma_{\max}$ is the strength attainable with infinite quench rate, $k_1 = \ln(\sigma_x/\sigma_{\max})$, and σ_x is the strength represented by the C curve. This relationship assumes that the minimum strength attainable after a very slow quench is much less than $\sigma_{\max}$ [47]. This minimum value is the value of the strength achieved after annealing the alloy to its softest condition. For a given continuous cooling curve during quench and for the C curves for the material, Q is defined by the following:

$$Q = \int_{t_0}^{t_f} dt/c_t \tag{4.5}$$

where dt is the time increment from the quench (cooling) curve, t_0 and t_f are time at start and end of quench, respectively and C_t is the critical time (a function of temperature).

The theories and methods for the construction of C curves have been discussed in several publications [47–50] and refinements have been made to these models [51]. Fig. 4.19 shows a series of C curves corresponding to 99.5% of the maximum

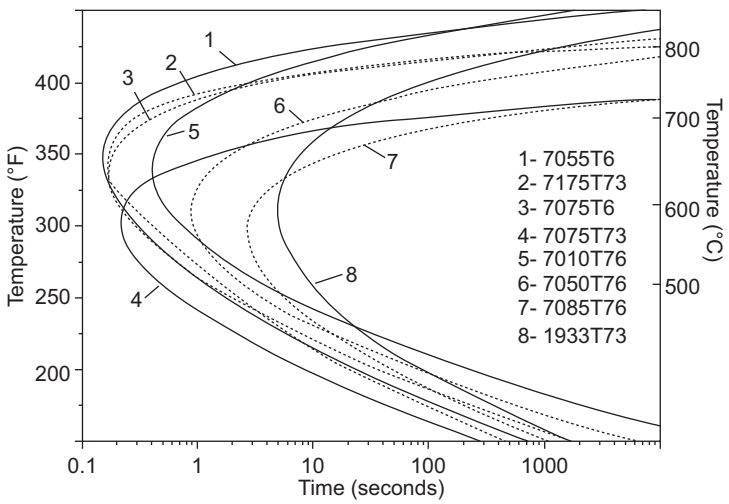


FIGURE 4.19

C curves for commercial Al–Zn–Mg alloys [52].

achievable hardness (loss of 0.5% due to lower quenching rate) for several commercial, 7XXX Al−Zn−Mg−Cu alloys and the Russian alloy 1933 [52]. These measurements are consistent with the fact that among the 7XXX series alloys, 7085 is the least susceptible to loss of strength due to slower cooling and that 7085 is used in thicker sections compared with 7055, which develops higher strength in relatively thinner sections.

In industrial applications, Al alloys undergo thermal exposure during many operations such as forming, curing of adhesives, and welding, often under nonisothermal conditions. Some of these operations occur after solution treatment, quenching, and aging, which irreversibly and severely overage the alloys and deleteriously affect the properties. The interplay of many materials and process models needs to be considered for predictively describing the effects of these operations. Process models for the precipitation hardening of Al alloys have been developed and validated by relating process variables (e.g., alloy, heat treatment parameters) and properties (e.g., hardness, strength) [53,54]. These were used successfully to predict the effects of subsequent thermal exposure of the alloys under nonisothermal conditions. Models necessary for integrating the evolution of microstructure under isothermal conditions and its effects on yield stress, strain hardening and fracture toughness have been developed with the potential for extension to nonisothermal treatments [55]. These will be discussed in the chapter on designing alloys for specific manufacturing processes. Integration such as discussed here will also enable the use of integrated computational materials engineering (ICME) approach, described in Chapter 1, to embed manufacturing operations and part characteristics in alloy design.

4.3.1.5 Effects of Precipitation Hardening on Property Combinations

Chapter 2 discussed how both the matrix and second phase features affect all the properties important for alloy design. Generally, these features do not act in isolation and the properties are a result of the interactions and superposition of their effects. For example, the precipitate types, morphologies, and distributions optimized for peak strength will generally lead to maximum slip localization and loss of toughness. Adding elements to form dispersoids that tailor the matrix microstructure may cause precipitates to nucleate on these particles during quench and reduce the strength. Nevertheless, it is necessary to understand the mechanisms of actions of individual features so that their combined effects can be predicted. This section will briefly consider the effects of only the precipitates and the superposition of all other features will be discussed later.

The effects of strengthening precipitates on the properties of Al alloys were discussed briefly in Chapter 2 (Table 2.3) and that on strength in detail earlier in this chapter. Precipitates affect toughness and fatigue properties based on whether dislocations shear or bypass them. Once sheared, the resistance to further dislocation motion is reduced and the resulting slip concentration (Fig. 2.3) will cause void nucleation and reduce toughness. Slip is more uniformly dispersed when precipitates are bypassed. This is reflected in the relationship between yield strength and toughness as a function of the aging condition for alloy 7050

quenched from the solution treatment temperature at different rates, as shown in Fig. 4.20 [56].

The reason for the reduction of strength with decreasing cooling rate has been discussed already. Irrespective of the quench rate, toughness (measured in this example by the unit initiation energy) decreases as the alloy is progressively aged to peak strength following which it increases with overaging. However, the toughness of overaged alloys is always lower than that of the underaged alloys at the same strength level.

The observed relationships between yield strength and toughness as a function of the aging treatment is, at least in part, a result of the superposition of the effects of the interaction between precipitates and dislocations (shearing or bypass) and the strain hardening rates. As aging progresses from the quenched condition to peak strength, the continuous increase in the volume fraction and size of the shearable precipitates along with the reduction of the solute content in the matrix increases slip localization and decreases the strain hardening rate. Toughness decreases continuously as a result. During continued aging past peak strength, the solute content in the matrix remains constant and precipitates that coarsen at constant volume fraction are bypassed by dislocations, which increases the strain hardening rate and toughness. It should be noted that PFZ's and grain boundary precipitates have a significant influence on the toughness. Fracture in high strength Al alloys follows a combination of transgranular and intergranular paths and is determined by the effects of intragranular and grain boundary precipitates and the presence of PFZs. Depending on the relative contributions of these features to the fracture process, the toughness of the alloys can remain the same or decrease further when aged past peak strength.

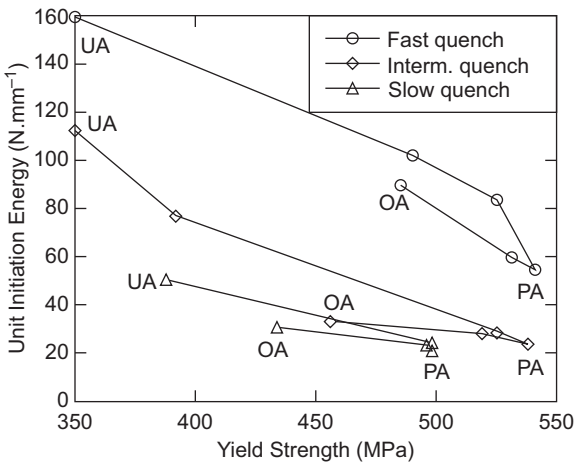


FIGURE 4.20

Toughness—yield strength relationships for Al alloy [56]. *OA*, overaged; *PA*, peak aged; *UA*, underaged.

Precipitate characteristics that reduce toughness and resistance to fatigue crack initiation, however, improve the resistance to fatigue crack growth (FCG). This is due to slip being more reversible when precipitates are sheared during deformation under cyclic loading. As with toughness, resistance to SCC decreases as aging progresses with the least resistance in the peak aged condition. Resistance to SCC and exfoliation can be improved by overaging to promote a more uniform precipitation near the grain boundaries to mitigate the effects of the PFZ's.

4.3.2 ALLOYING FOR CONTROL OF MATRIX MICROSTRUCTURE

Features of the Al matrix such as its grain structure, substructure, degree of recrystallization, and texture affect the alloy properties, particularly its toughness and fatigue behavior. The evolution of the matrix microstructure is influenced by the properties of Al such as its stacking fault energy (SFE) and the presence of $\sim$20–500 nm sized dispersoid particles, which control recovery, recrystallization, and grain growth during the thermomechanical processing sequence shown schematically in Fig. 4.1. Among the elements that have very limited solid solubility but full solubility in molten Al, Mn, Cr, and Zr are used in commercial alloys to form dispersoids. These elements are added in amounts ranging from about 0.1–0.5 wt%, remain in solution during solidification and precipitate as second phase particles during ingot homogenization. Due to the very low solid solubility and diffusivity of these elements in the Al matrix, once formed, the particles are stable and resist coarsening and dissolution.

4.3.2.1 Matrix Microstructure Development and the Effects of Dispersoids

The very high SFE ($\sim$200 mJ/m^2) of Al enables easy cross-slip of dislocations. This results in dynamic recovery and polygonization during deformation at relatively low temperatures wherein dislocations arrange themselves into cellular networks. At higher temperatures, dynamic recovery leads to formation of subgrains. With continued deformation, subgrain boundaries can evolve into high angle boundaries by the process of continuous dynamic recrystallization (CDRX). When present, dispersoids pin subgrain boundaries preventing their coalescence and retarding CDRX. With the formation of a stable, dynamically recovered substructure, there is limited, if any, driving force for subsequent static recrystallization during solution treatment.

In addition to the possibility of CDRX, recrystallization can occur discontinuously by "particle stimulated nucleation" of new grains at constituent particles (>1 μm) resulting from accumulation of dislocations and strain. Dispersoids also retard such discontinuous recrystallization (DRX) and grain growth by pinning migrating boundaries by the Zener mechanism, which is described by [27].

$$R_{(crit)} = \left(\frac{3\beta}{4}\right)\left(\frac{r}{f}\right) \tag{4.6}$$

The volume fraction, f, and radius, r, of the dispersoid particles determine the critical radius, $R_{(crit)}$, of the grains at which they will cease to grow. The value of the constant β in the equation is approximately 1. Thus a high volume fraction

(i.e., small interparticle spacing) of small dispersoid particles is effective in retarding both dynamic and static DRX and grain growth.

4.3.2.2 Specific Alloy Systems

Historically, Mn and Cr have been added to 2XXX and 7XXX series alloys, respectively. Mn was present in the first Al–Cu alloy developed nearly a century ago. A combination of Mn and Cr is used in 6XXX series alloys. Dispersoids that form in alloys containing Mn, Cr, or both are all incoherent with the Al matrix. Zr replaced Cr in alloy 7050, introduced in the 1970s, and has been added to all the 7XXX series alloys developed since. Zr has also been used in 2XXX series alloys such as 2029. Third generation Al–Li alloys contain Zr and Mn, which in combination provide a more uniform dispersoid distribution for improving resistance to recrystallization and grain growth and increasing toughness [32,57]. Dispersoids in Zr containing alloys are coherent. Dispersoid compositions in Al alloys are listed in Table 4.13 [19].

All the processing steps shown in Fig. 4.1 contribute to varying degrees in determining the matrix microstructure. In this regard, changes occurring during thermomechanical processing and how they are affected by the dispersoids have the most influence. The effects of dispersoids depend on their size, volume fraction, distribution, and coherency or lack thereof with the matrix. The thermomechanical processing conditions such as temperature, strain rate, and total strain vary with alloys and product forms, which in conjunction with the dispersoids determine the microstructure of the matrix. The evolution of microstructure can accordingly be described with reference to specific combinations of alloys, product forms, and nature of the dispersoids.

Majority of the Al alloy parts used in airframes are fabricated from sheet, plate, and extrusions of 2XXX and 7XXX series alloys. The grain structure is typically elongated in the working direction (rolling and extrusion directions) giving rise to anisotropy of properties. Many applications also use forgings, for which the grain direction in the interior is related to their shape, whereas near-surface grain flow is along the external contour. Plate products were typically restricted to less than about 150 mm (6 in.) in thickness because of the development of anisotropy of properties in the short transverse direction. In addition, due to the difficulty to uniformly

Table 4.13 Dispersoid Compositions in Al Alloys

Alloy Type (Examples of Alloys)	Dispersoids
2X24 (2024, 2124, 2324, 2524)	$Al_{20}Cu_2Mn_3$
6013	$Al_{12}Mn_3Si$
7X75 (7075, 7175, 7475)	$Al_{12}Mg_2Cr$
7X50 (7050, 7150), 7055	Al_3Zr
Al–Li alloys with Zr (second generation alloys, e.g., 2090)	Al_3Zr
Al–Li alloys with Zr and Mn (third generation alloys)	Al_3Zr and $Al_{20}Cu_2Mn_3$

impart deformation through the product thickness during rolling, the remnants of the cast structure such as porosity in the mid-plane of thick plate could not be eliminated completely, which degraded the fatigue properties. More recently, improved ingot casting and processing practices have eliminated many of these limitations and made thicker plate products possible.

For sheet fabrication, Al alloy ingots are rolled to larger levels of strain at relatively lower temperatures and often cold rolled, compared with those for thick plate products. These processing conditions promote recrystallization with grain growth restricted by the pinning of boundaries by dispersoids. As a result, sheet and relatively thin plate products exhibit elongated, pancake-shaped grains in the rolling direction, as shown in Fig. 4.21 [58].

The alloy dynamically recovers during rolling at higher temperatures with recrystallization being prevented by the dispersoids. Coherent dispersoids are more effective in retarding recrystallization than the incoherent dispersoids. A recent study of several Al−Zn−Mg−Cu alloys found that the extent of recrystallization on average were 39% and 65% for Zr and Cr containing alloys, respectively [59]. Both recrystallized and unrecrystallized areas containing subgrains retained from dynamic recovery will be elongated in the rolling direction. Extruded products, particularly those with large aspect ratios, tend to develop an elongated grain structure along the direction of extrusion.

The texture that develops in flat rolled products and extrusions with high aspect ratio is similar to those observed in pure face centered cubic metals with high SFE. The effects of both texture and grain shape anisotropy in Al alloys are reflected in the anisotropy of their mechanical properties. The effects of texture are more important for nonheat treatable alloys as they affect the formability and quality of the products.

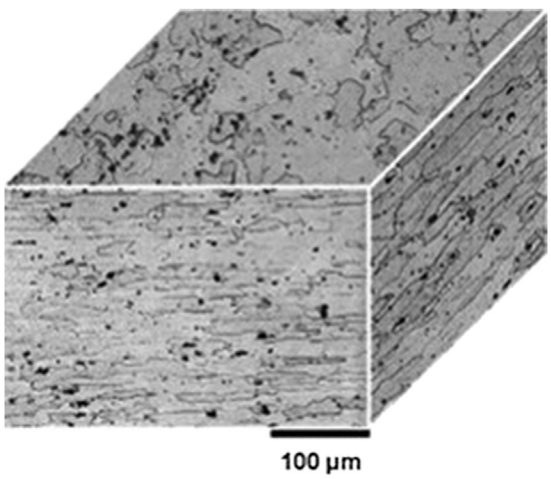


FIGURE 4.21

Microstructure flat rolled Al alloys showing grain shape anisotropy [58].

Al–Li alloys are an exception, as the texture in conjunction with the morphologies of the strengthening phases has a strong influence on the anisotropy of properties and the manufacturing characteristics.

Both in-plane and through-thickness anisotropy in recrystallized, second generation Al–Li alloys resulted from strong texture [32]. For example, strength in the plane of the sheet was significantly lower in the direction 45° from the longitudinal. The anisotropy was also accentuated in the aged alloys [60]. The extent of anisotropy has been reduced by introducing an annealing step to recrystallize the microstructure at an intermediate processing stage prior to final deformation thereby preventing recrystallization and strong texture development during solution treatment. Microstructure of representative third generation Al–Li alloys processed in this manner is shown in Fig. 4.22 [32].

All third generation Al–Li alloys contain Zr for controlling recrystallization and Mn for controlling grain growth and texture. Combination of Zr and Mn also counteracts their opposing microsegregation patterns during solidification, which results in a nonuniform distribution of each type of dispersoid. Together, the Zr and Mn containing dispersoids provide uniform coverage across the matrix and improve recrystallization resistance. However, the effectiveness of Zr is reduced in the presence of Mn due to the incorporation of some Zr in the Mn-containing dispersoids, thereby reducing the volume fraction of the coherent dispersoids and slightly decreasing the resistance to recrystallization [57].

4.3.2.3 Quench Sensitivity

The sensitivity of the properties of PH Al alloys to rate of quench from the solution treatment temperature and the method for its measurement by the QFA method were discussed earlier. The C curves indicate only the effects of cooling rates on the

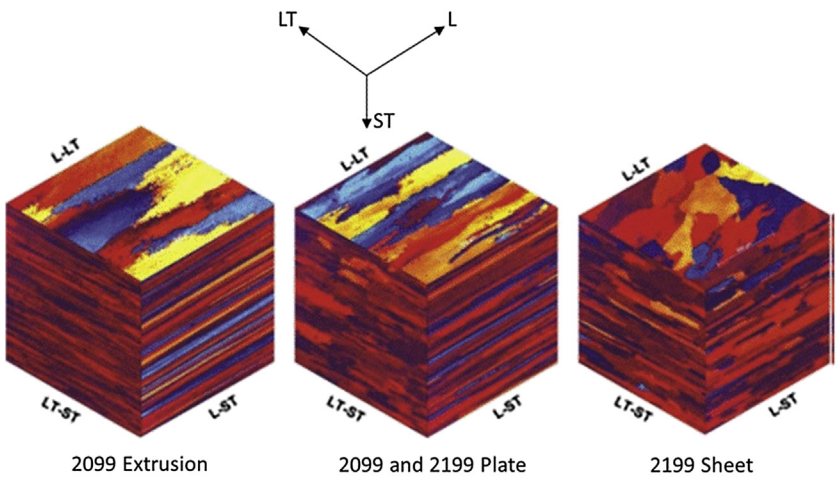


FIGURE 4.22

Microstructure of Al–Li alloys [32].

properties of a given alloy and aging condition and do not provide the relative contributions of the metallurgical factors such as dispersoids and grain/subgrain boundaries to precipitation during the quench.

Quench sensitivity is particularly important for the 7XXX series alloys, as they are exclusively used for applications requiring plate and forging products thicker than about 75 mm (3 in.), which require a slower quench to minimize distortions and residual stresses in the quenched parts. The cooling rates in the center of a 200 mm (8 in.) thick forging in the range from ~400 to 275°C (~750–525°F) have been measured to be about 3, 2, and 0.3°C/s (~5, 4 and 0.6°F/s) in cold, 70°C (158°F) and boiling water, respectively [61]. This is the critical temperature range in which precipitate nucleation occurs and gives rise to quench sensitivity. Isothermal aging of an Al–5.5 Zn–2.5 Cu–1.6 Cu (all wt%) alloy at 60°C (108°F) after solution treatment and quenching at three different rates showed that the resistivity loss, associated with transition phase formation, was the highest for the alloy with Cr, followed by that with Zr and, the least for the baseline alloy without addition of any dispersoid forming elements [62].

Dispersoid forming elements that have been added to all 7XXX series alloys starting with 7075 to control the recrystallization and grain growth are also the principal reason for increasing the quench sensitivity. Without these elements, the η phase would nucleate only at grain/subgrain boundaries during the quench. The quench sensitivity has been decreased by replacing Cr with Zr, which precipitates as coherent particles that promote dynamic recovery and reduce the extent of recrystallization and grain boundaries from which precipitates can nucleate. Alloy design must balance the need for high strength achieved by the fastest quench rates with that for minimizing residual stresses and maintaining adequate levels of toughness and corrosion resistance.

4.3.2.4 Modeling of Matrix Microstructure Evolution

Matrix microstructural features that affect properties are subgrain size, degree of recrystallization, grain size, and texture, which evolve dynamically during deformation and statically during anneals and solution treatment. Cold working, if performed prior to aging, also will increase the defect density. Unlike PH alloys, properties of nonheat treatable (NHT) alloys are determined primarily by the matrix microstructure. Accordingly, most, if not all, of the methods for studying the evolution of matrix microstructure have focused on NHT alloys, whereas those for precipitation has been the focus for PH alloys.

During thermomechanical processing, the microstructures of both NHT and PH alloys are similar in the sense that matrix deformation occurs in the presence of a relatively small volume fraction of nondeformable second phase particles (dispersoids and constituents). The PH alloys will also contain precipitates whose amount is determined by the excess solute remaining at the processing temperature. Thus the methods used for NHT alloys could in principle be used for PH alloys. The dynamics of recovery and CDRX are based on dislocation annihilation and can be modeled using crystal plasticity. DRX is based on nucleation and growth processes and needs

a knowledge of nucleus density, orientations, and spatial distribution, which are typically not available [63,64]. Grain size can be predicted from the size and spatial distribution of the dispersoid particles, if available. Alloys in the same family such as the 2XXX or 7XXX series and the same product form are typically processed similarly. Although physics-based approaches are being developed, sufficient empirical knowledge has been accumulated on the effects of processing on the microstructure that can be used to aid in alloy design.

4.3.2.5 Effects of Matrix Microstructure on Property Combinations

The effects of matrix and second phase particles on the properties of Al alloys are interrelated by their combined actions in determining the microstructure. Still, a knowledge of the individual contributions is necessary to predict the overall property values resulting from their superposition. In the case of the matrix, substructure, grain size and shape, degree of recrystallization, and texture contribute to the magnitude and anisotropy of properties and are briefly described qualitatively. Quantitative descriptions are included in the treatment of overall processing−microstructure−property relationships.

Strengthening by subgrains in the unrecrystallized areas and the recrystallized grains can be described by the Hall−Petch equation:

$$\sigma_y = \sigma_o + kd^{-1/2} \tag{4.7}$$

where σ_o is the frictional stress and k is a constant. Thus increasing the degree of recrystallization will decrease strength by decreasing the volume fraction of subgrains, which due to their smaller size, are more effective than grains. However, the contribution to the total strength by boundaries is relatively small compared to that from precipitation. Finer grains are more effective when slip is localized as in underaged alloys than when slip is dispersed as in overaged alloys [19].

Texture is very effective in strengthening products such as large aspect ratio extrusions in the forming direction and contributes to the anisotropy of mechanical properties. Predicting its effects on strength anisotropy requires a knowledge of Taylor factor for the loading direction. Recrystallization decreases strength by eliminating the deformation texture. Toughness and resistance to FCG decrease with increasing recrystallization and commensurate increase in intergranular fracture. Fully unrecrystallized microstructures possess the highest toughness and FCG resistance [65].

Dispersoids, added solely for controlling the matrix microstructure, increase the quench sensitivity. They also reduce toughness and resistance to crack propagation by nucleating microvoids that link up with the voids initiated by the constituent particles, as shown in Fig. 4.23 for the Al−Cu−Mg alloy 2024.

4.3.3 EFFECTS OF IMPURITY ELEMENTS

Impurity elements carried over from the metal extraction steps are unavoidable in Al alloys. In specifications of compositions for Al alloys, each impurity element is

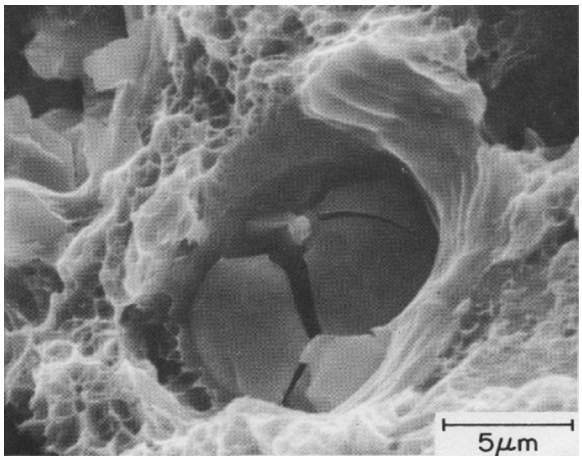


FIGURE 4.23

Crack nucleation at a constituent particle and fracture by void linkup in alloy 2024.

limited to less than 0.05 wt% and the total of these elements to less than 0.15 wt%, as seen for example in Table 4.4. Fe and Si are the exceptions, as they are present in amounts of about 0.5 wt% each in commercial alloys of nominal purity, unless they are added deliberately as alloying elements. The impurity elements combine with each other, the other alloying additions and with aluminum to form a variety of complex intermetallic constituents during solidification, with Table 4.14 listing the compositions of those observed in 2XXX and 7XXX series [19].

Once formed, constituent particles cannot be dissolved and remain in the alloy. These particles of irregular shape are typically a few to 30 μm in size, may be broken up and aligned as stringers in the direction of deformation during ingot processing, fracture at relatively low strains and affect the toughness and fatigue properties. They are also found in higher concentrations in recrystallized areas indicating their role in particle stimulated nucleation of grains. Constituent particles initiate fracture by nucleating voids, as shown in Fig. 4.23, which are then linked by the rupture of the intervening ligaments due to precipitate deformation and microvoid nucleation

Table 4.14 Constituents in Aluminum Alloys

Alloy Type (Examples of Alloys)	Constituents
2X24 (2024, 2124, 2324, 2524)	Al_7Cu_2Fe, $Al_{12}(Fe, Mn)_3Si$, Al_2CuMg, Al_2Cu
6013	$Al_{12}(Fe, Mn)_3Si$
7X75 (7075, 7175, 7475)	Al_7Cu_2Fe, $Al_{12}(Fe, Mn)_3Si$, Mg_2Si
7X50 (7050, 7150)	Al_7Cu_2Fe, Mg_2Si, Al_2CuMg
7055	Al_7Cu_2Fe, Mg_2Si
Al-Li alloys	Al_7Cu_2Fe, Al_2CuLi, Al_6CuLi_3

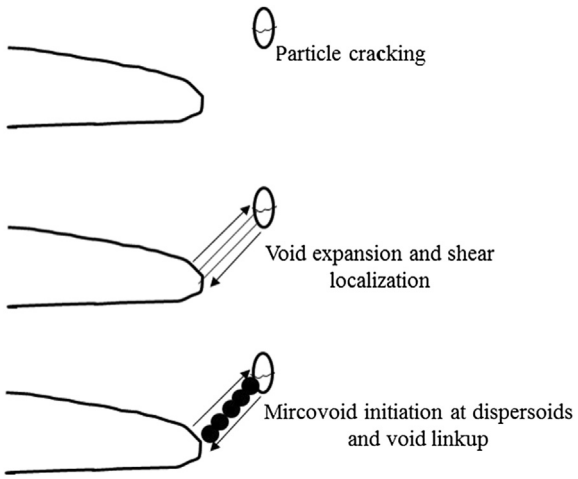


FIGURE 4.24

Schematic of the fracture process in aluminum alloys by void nucleation and linkup.

Adapted from J.F. Knott, Fracture resistance in aluminium, in: R. Lumley (Ed.), Fundamentals of Aluminium Metallurgy, Woodhead Publishing, Cambridge, UK, 2011, pp. 538–573.

around the dispersoid particles within the shear bands. A schematic depiction of the linking process is shown in Fig. 4.24 [66].

In addition to tying up solute elements that would otherwise be available for precipitation hardening, the most important and deleterious effects of the constituents are in reducing toughness and fatigue properties and in initiating corrosion pits. The only way to mitigate these effects is to use alloys with lower Fe and Si levels, which would reduce their volume fraction and increase the interparticle spacing.

Although several microstructural variables affect the fracture toughness of Al alloys, the effects of constituent particles can be considered independently. This is suggested by the observations in a study [67] that the area fractions of the constituent particles measured in the fracture surfaces were

1. higher than those measured on polished surfaces indicating their role in initiating fracture, and
2. the same under all quench rates and aging conditions that were tested for a given alloy,
3. greater in alloy 7050 than in 7040 of slightly higher purity.

Although the models that have been proposed for the fracture toughness of Al alloys have different dependencies on the volume fraction and spacing of the constituent particles, increasing the purity of the alloys by reducing Fe and Si always increases toughness. Constituent particles increase FCG rates in the region beyond stable growth when the crack tip stress intensity rapidly approaches the fracture toughness of the alloy. In this region, fracture is increasingly controlled by void nucleation

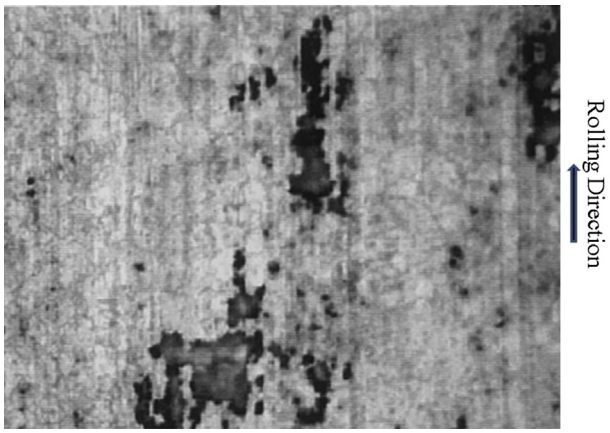


FIGURE 4.25

Localized corrosion in 7075-T6 proceeding along the direction of distribution of constituent particles in 7075-T6 [58].

at the constituent particles and the mean spacing of the voids is approximately equal to the cyclic plastic zone size width in the crack plane [68]. However, under conditions of variable amplitude loading involving high tensile loads, secondary crack nucleation at the constituents can delay the growth of the primary crack [19].

Constituent particles can initiate localized corrosion due to the widely varying electrochemical characteristics among different types of particles and with the matrix. Despite the ubiquitous presence of oxide films on the surface of Al alloys providing protection from environmental attack, the relative differences in the corrosion and pitting potentials among the constituents and with the Al matrix renders the alloys susceptible to localized corrosion [69]. For example, pitting in Al alloys is always associated with a fraction of the constituent particles present. Localized corrosion also tends to follow the direction of distribution of the particles, as shown in Fig. 4.25. The constituents are aligned in the rolling direction along which pit growth takes place [58].

4.4 PROCESSING—MICROSTRUCTURE—PROPERTY RELATIONS IN WROUGHT, PH ALUMINUM ALLOYS

In the framework of the processing scheme shown in Fig. 4.1, the preceding sections described, to the extent possible, the effects of individual features of the matrix microstructure and second phase particles on the properties of PH aluminum alloys. It is evident that many processing and microstructural variables interact to determine each property, whose discussion is the subject of this section. Features that affect properties include the dislocation density, degree of recrystallization, grain size, and subgrain size for the matrix and the degree of coherency, size distribution, shape,

and volume fraction for the second phase particles. Typical values for these parameters are given in Table 4.15. They are generally measured in two-dimensional planar sections from which their volumetric attributes are calculated using stereological relationships. With the availability of automated specimen sectioning tools and data analysis software, three dimensional representations of the material can be generated readily and are increasingly being used for modeling of microstructure and properties.

In reviewing the processing–microstructure–properties relationships using data from published literature, mention must be made of the differences in the way alloys are processed commercially and in the laboratory, even under nominally similar conditions. Commercial practice uses optimized conditions, within the nominal range, that are proprietary to each alloy producer. For example, rate of cooling of the ingot after homogenization and the stretching of large plate for stress relief, both affect microstructure and properties, but cannot be accurately reproduced in the laboratory. The properties reported for commercial alloys are statistically determined from measurements on several lots representative of production sizes and are guaranteed to be within a specified range. All these factors must be considered in designing alloys for potential commercialization.

Designations for aluminum alloys specify their composition limits and the thermal and mechanical processes that they undergo. Many key aspects of processing and microstructure are not evident from these designations. They include, for example, porosity, effects of variations in processing within that specified nominally, and the kinetics and quantitative description of microstructural evolution. It is important to have a knowledge of the influence of processing on all microstructural features that affect properties, as illustrated by the following examples using the evolution of porosity, constituent particles, recrystallization, and precipitates.

Table 4.15 Typical Microstructural Features

Microstructural Feature	Description
Sub grain size	≈1–5 μm, equiaxed
Degree of recrystallization	≈25% with coherent dispersoids ≈65% with incoherent dispersoids ≈100% for cold rolled products
Grain size and shape	≈10–100 μm, elongated in the working direction
Dispersoids	≈20–50 nm, coherent, spherical particles (volume fraction <1%) ≈20–500 nm, incoherent, irregular particles (volume fraction <1%)
Constituents	≈1–30 μm, incoherent, irregular particles (volume fraction <1%)
Precipitates	≈1–20 nm (volume fraction ≈3%–5%)

During thermomechanical processing, it is difficult to impart deformation uniformly through the cross section of large ingots and consequently products such as thick plate exhibit porosity and remnants of the cast structure in their center. Advances in processing have largely eliminated these problems. Pores nucleate fatigue cracks from the first loading cycle even before their nucleation at constituent particles. Results of a detailed characterization of the pores and constituent particles in 6 in. (150 mm) thick 7050-T7451 plate, with two levels of porosity, are shown in Fig. 4.26 [70]. The area and volume fractions of porosity are higher in the center than in the quarter depth and surface for both plates, whereas the constituent particles tend to be more evenly distributed. The dimensions and distributions of these features can be used as inputs for probabilistic fatigue life prediction models.

Cooling rates from ingot homogenization and intermediate processing temperatures are as important as that from solution treatment, which was discussed in the section on quench sensitivity. Most processing occurs nonisothermally during which precipitates may dissolve, form or coarsen. It is generally assumed that these particles will dissolve during solution treatment. However, slow cooling of alloy 7050 from homogenization at 480°C (896°F) to room temperature under conditions representative of commercial practice resulted in particles, 7 μm in diameter, which were coarse enough to cause particle stimulated nucleation during subsequent thermal exposure. The degree of recrystallization under these conditions was four times larger than for the alloy cooled rapidly after homogenization [71].

The continuous evolution of the precipitates with the aging of representative 7XXX series alloys is shown in Fig. 4.27, from data on a study of alloy 7449 [72]. The alloy was solution treated at 474°C (885°F), quenched to room temperature, held for 4 days, heated to 120°C (248°F), at a controlled rate, aged for 6 h, heated to 160°C (320°F), and aged continuously. The decrease in the number density of precipitates during heating to 120°C (248°F) is due to the reversion of GP zones that form at room temperature. Precipitate growth occurs at 120°C (248°F) at nearly constant number density and increasing size and volume fraction to about 0.06. GP zones transition to η' during the heat up to 160°C (320°F) with a substantial decrease in number density, a small decrease in volume fraction and a large increase in radius. Continued aging at 160°C (320°F) results in precipitates coarsening at constant volume fraction.

The multivariate nature of the hierarchical relationships among processing, microstructure and properties for PH aluminum alloys is shown schematically in Fig. 4.28, which follows the framework introduced and being used by Olson with great success for alloy development [73]. Although it is impossible to capture every individual dependency among the variables, the scheme serves to illustrate important relationships that are not evident otherwise. It is also a convenient reference that can be used to describe the mechanisms and develop models for the properties of PH aluminum alloys for alloy design. It should also be noted that some forming operations and cold working are conducted following quenching and prior to aging, which are not explicitly shown in the figure. Residual stress, shown as a

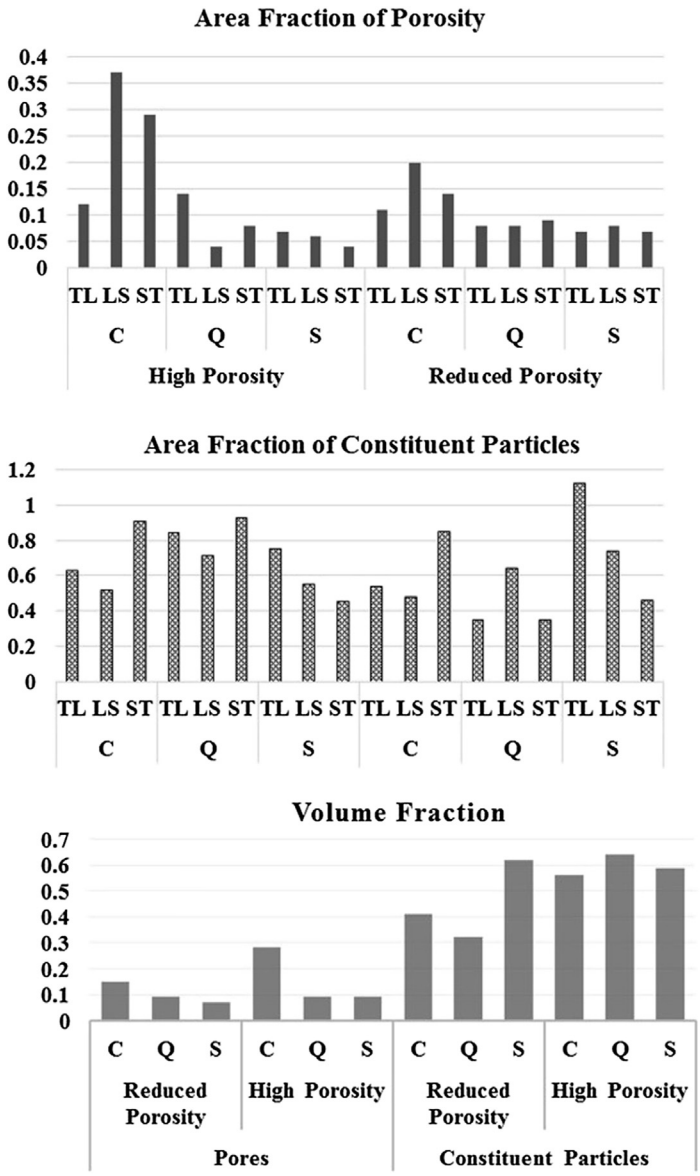


FIGURE 4.26

Porosity and constituent particles in 7050-T7451. *C*, center; *Q*, quarter thickness; *S*, surface. TL, LS, and ST are planes normal to short transverse (thickness), long transverse (width) and longitudinal (rolling direction) directions, respectively.

Plotted from data in J. Zhang, M.A. Przystupa, A.J. Luévano, Characterizations of pore and constituent particle populations in 7050-T7451 aluminum plate alloys, Metallurgical and Materials Transactions A 29 (1998) 727–737.

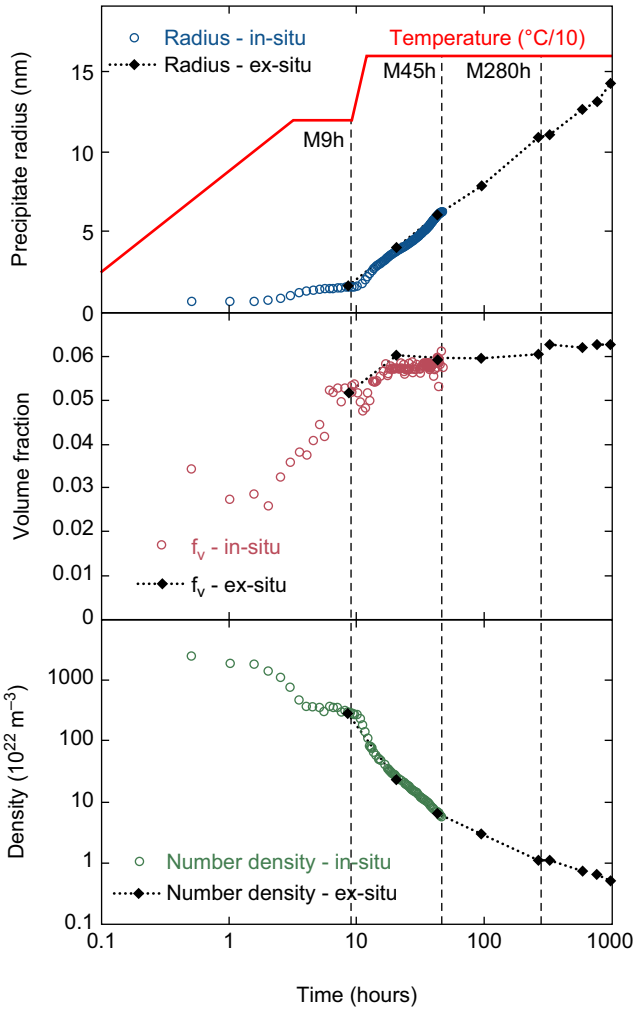


FIGURE 4.27

Precipitate evolution in 7XXX series alloys—MXH refers to hours of artificial aging starting with the ramp up from room temperature [72].

microstructural feature, has a significant influence on product attributes such as dimensional stability and ease of assembly of components.

4.4.1 MODELING OF STRENGTH

The yield strength of wrought PH aluminum alloys is determined by the superposition of contributions from all the microstructural features that act as obstacles

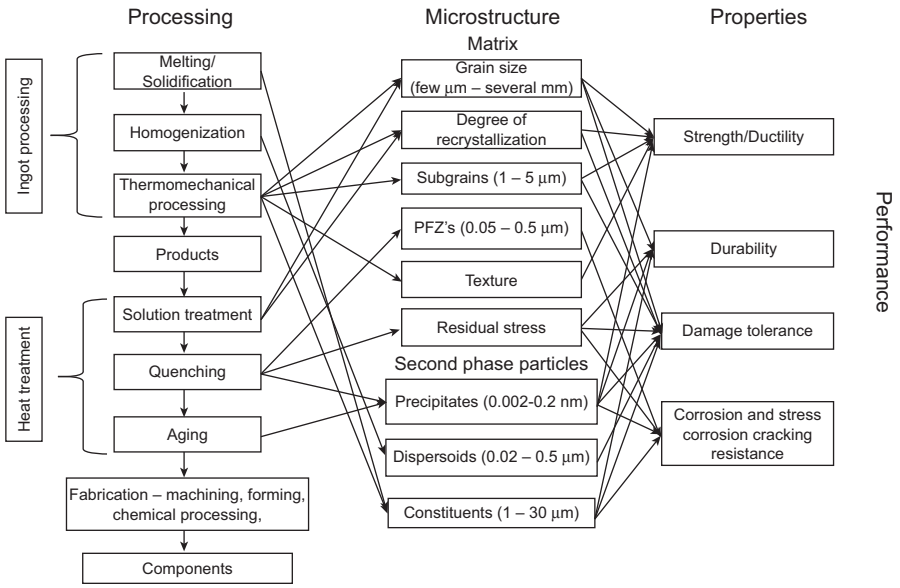


FIGURE 4.28

Processing—microstructure—properties relationships for wrought precipitation hardened aluminum alloys.

to dislocation motion. Table 4.16 shows the evolution of these features through all stages of processing and how they affect strength, all of which must be included in the models for yield strength.

The laws describing the total contributions to strength are determined by the nature of the interactions between obstacles and dislocations. The superposition of strengthening from two obstacles is expressed by [74] the following:

$$\Delta\tau^q = \Delta\tau_1^q + \Delta\tau_2^q \tag{4.8}$$

where $\Delta\tau_1$ and $\Delta\tau_2$ are the respective contributions from the two obstacles, $\Delta\tau$ is their combined contribution and the exponent q is between 1 and 2. The value of q is determined by the relative strengths of the obstacles and is 1, for example, for the superposition of strengthening from a high density of weak obstacles (GP zones) and a low density of dislocations, as in the early stages of aging of aluminum alloys. As aging proceeds, both precipitates and dislocations will have equal strength and q will be 2 in this case [75]. Additional contributions to strength are treated similarly. Considering the superposition of strengthening from the intrinsic CRSS of aluminum ($\Delta\tau_0$), solid solution ($\Delta\tau_{ss}$), dislocations ($\Delta\tau_d$) and precipitates ($\Delta\tau_{ppt}$), the total strength (τ_{tot}) is given by [59]

$$\tau_{tot} = \Delta\tau_0 + \Delta\tau_{ss} + \left(\Delta\tau_d^2 + \Delta\tau_{ppt}^2\right)^{1/2} \tag{4.9}$$

Table 4.16 Processing–Microstructure–Properties Relationships for Wrought Precipitation Hardened Aluminum Alloys Containing Zr

Processing Parameters	Microstructure	Effect on Strength
Solidification and rate of cooling	Formation of constituents containing solute elements, e.g., Al_7Cu_2Fe	Negative due to loss of solute that would otherwise be available for precipitation
Homogenization and subsequent rate of cooling	Precipitation of fine, coherent, dispersoids	Positive due to pinning of subgrains and preventing recrystallization during subsequent thermomechanical processing
	Coarsening of dispersoids at slow cooling rates to sizes that can stimulate nucleation of grains	Negative due to reduction in subgrain volume during subsequent thermomechanical processing
Thermomechanical processing	Dynamic recovery and formation of stable subgrain structure	Positive
	Recrystallization (dynamic or particle stimulated)	Negative
Solution treatment	Static recrystallization and grain growth	Negative
Quenching	Nucleation of precipitates depending on quench rate	Negative due to loss of solute that would otherwise be available for precipitation
Aging	Precipitation of strengthening phases	Positive

The macroscopic yield strength (σ_y) of the alloy is then given by

$$\sigma_y = \Delta\sigma_{gb} + M\tau_{tot} \tag{4.10}$$

where $\Delta\sigma_{gb}$ is the strengthening due to grain/subgrain boundaries and M is the Taylor factor ~ 3, with its actual value depending on the texture. The term $\Delta\sigma_{gb}$ includes the frictional stress σ_o (from Eq. 4.7). The equations can also be modified to include contributions from stacking faults, ordering, and interfaces and from multiple strengthening precipitates. Such a model described by the following equation has been used to predict the yield strength for Al–Zn–Mg–Cu alloys using microstructural parameters reported in the literature [76].

$$\sigma_y = \Delta\sigma_{gb} + M\left(\Delta\tau_{ss}^2 + \Delta\tau_d^2 + \Delta\tau_{ppt}^2 + \Delta\tau_{sf}^2 + \Delta\tau_{mod}^2\right)^{1/2} \tag{4.11}$$

where $\Delta\tau_{sf}$ and $\Delta\tau_{mod}$ are the contributions from stacking faults and modulus, respectively, and the other terms are as defined before. It predicted a value of 436 MPa (63 ksi) for the yield strength of 7050-T7451, whereas the measured value

was 490 MPa (71 ksi). It should be noted that $\Delta\tau_{ss}$ is included along with the terms for strong obstacles. Using solid solution strengthening as an additive term along with that from grain boundaries would increase the predicted strength making it closer to the measured value.

In another example, the individual contributions to yield strength for an Al−2.5 Li−1.2Cu−0.7Mg−0.1Zr alloy were calculated from the known values for the corresponding Al−Li, Al−Li−Zr, and Al−Cu−Mg alloys. The estimated value of strengthening from precipitates was then compared to the measured value, as shown in Table 4.17 [77].

The strength of the solution treated binary alloy is the sum of the contributions from the friction stress, which for pure aluminum is 10 MPa, and solid solution. The strength of the solution treated Al−Li−Zr alloy is the superposition of contributions from friction stress, solid solution, and grain refinement. After aging, the strength increase in this alloy is solely due to δ′ precipitation, because the low volume fraction of Zr containing dispersoids does not contribute to strengthening. For the Al−2.5Li−1.2Cu−0.7Mg−0.1Zr alloy, strength after aging is from both δ′ and S′, which is 47 MPa when calculated using Eq. (4.8), with a value of 2 for q. Using 1.5 for q results in an estimate for this value of 51 MPa, which is closer to the measured value of 55 MPa [19]. Order strengthening expected from δ′ and the stacking fault, coherency and modulus effects expected from S′ are included in the precipitation strengthening and are not calculated separately. Despite some of the assumptions made in estimating the contributions, the example does illustrate the usefulness of these approaches in delineating the effects of multiple contributions to the strength of PH aluminum alloys.

The models described earlier can predict the yield strength of alloys with known microstructural parameters and material properties such as interfacial and stacking fault energies that are necessary to compute the individual contributions. However, the effects of all the variables shown in Table 4.16 must also be known quantitatively to predict the strength of alloys solely from a knowledge of their compositions and

Table 4.17 Estimation of Contributions to Strengthening in Al−Li−Cu−Mg−Zr Alloy From Binary and Ternary Systems

Alloy	Measured Strength (MPa)			Estimated Strengthening Contribution (MPa)
	Solution Treated	Aged	Increment due to Aging	
Al−2.5Li	30 (A)			Friction stress = 10 Solid solution = 20
Al−2.5 Li−0.1 Zr	55 (B)	100 (C)	45 (D = C − B)	(Sub) grain boundary (B−A) = 25 δ′ precipitates (D) = 45
Al−1.2Cu−0.6Mg			15 (E)	S′ precipitates (E) = 15
Al−2.5Li−1.2Cu −0.7Mg−0.1Zr			55 (F)	δ′ and S′ = $(D^2 + E^2)^{0.5}$ = 47

processing conditions. In this context, Starink and Wang [59] have developed and validated a model for overaged Al–Zn–Mg–Cu alloys by accounting additionally for the solute lost to insoluble constituents, influence of solute supersaturation on the rate of precipitation, varying recrystallization fractions with Cr and Zr, and texture. It predicted yield strength values to within 14 MPa (2 ksi) of that measured for several experimental and commercial alloys. It also predicted the aging time at various temperatures that will result in specified strength values, as a function of the degree of recrystallization and the total solute content.

Incorporation of texture in strength models is important from the perspective of predicting anisotropy of mechanical properties of aluminum alloys. Anisotropy can occur in the plane of rolling for plate and sheet and through the thickness for plate and thick extrusions. Anisotropy manifests differently in alloys with and without Li additions, as shown in Fig. 4.29 [32].

Referring to Fig. 4.30, which defines the various directions in flat rolled products, the yield strength is lowest for alloy 2024 in the transverse direction ($\theta = 90°$) and for second generation Al–Li alloy 8090 in the $\theta = 45°$ direction. Although the third generation Al–Li alloy 2199 also has the lowest strength when $\theta = 45°$, the degree of anisotropy is considerably lower. Alloy 8090 also exhibits greater through thickness anisotropy than does 2199, with the strength of 8090 progressively increasing from near the plate surface to mid-thickness for both the L (longitudinal, $\theta = 0°$) and LT (long transverse, $\theta = 90°$) directions.

Mechanical anisotropy arises from crystallographic texture, grain shape anisotropy, and, particularly for alloys with Li, precipitate orientation, and distribution. It should be noted that grain shape anisotropy does not necessarily imply the presence of texture, although it usually does, and the lack of anisotropy does not rule out texture. An investigation of the through thickness anisotropy for the second generation Al–Li alloy 2090 plate showed a direct correlation between strength and texture [78]. The maximum strength occurred at mid-thickness and correlated with the peak intensities of the crystallographic texture components corresponding to hot deformation and the maximum calculated value of the Taylor factor, *M*.

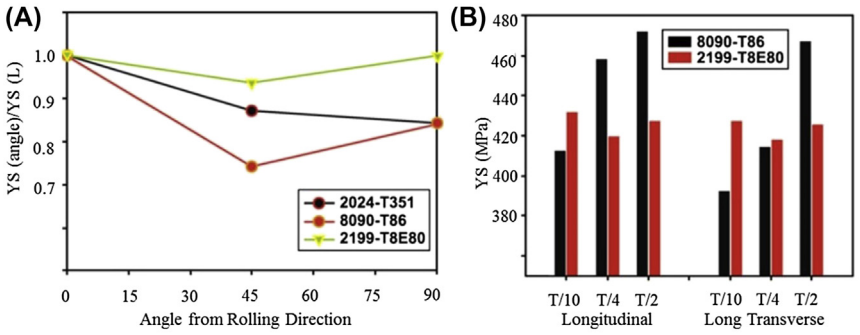


FIGURE 4.29

Anisotropy of properties in aluminum alloys, (A) in-plane and (B) through thickness [32].

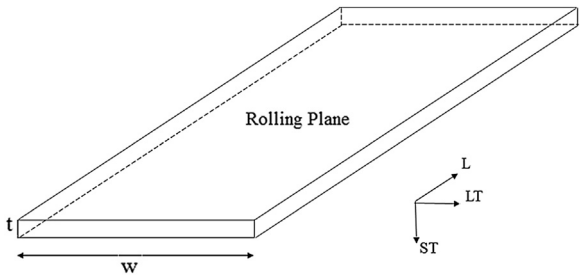


FIGURE 4.30

Orientations in flat rolled products. *L*, longitudinal (rolling); *LT*, long transverse; *ST*, short transverse directions; *T*, product thickness; *W*, product width.

However, similar trend in the anisotropy was also observed for yield strength normalized for *M*, suggesting that anisotropy did not result solely from crystallographic texture. Additional experiments suggested that the strengthening phase T_1 was partly responsible for the observed anisotropy. As discussed earlier, the deformation processing sequences were subsequently altered to reduce the anisotropy in third generation Al−Li alloys. For optimum properties in these alloys, extrusions and plate are processed to be unrecrystallized and sheet to be in the recrystallized condition, as shown in Fig. 4.21.

The discussion has focused only on yield strength, which is the easiest to predict among the properties that affect the deformation behavior of PH aluminum alloys. Tensile strength is always specified, measured, and reported for these alloys, but generally not used for design purposes and typically serves for assuring the quality of materials. Models do not exist for predicting tensile strength in a manner similar to that for yield strength and those being developed are empirical and rule based.

4.4.2 DUCTILITY AND STRAIN HARDENING BEHAVIOR

Besides strength, other important tensile properties are ductility and strain hardening behavior. They affect fracture toughness and play a key role in determining the formability of alloys during manufacturing operations. As for the effects of second phase particles, yield strength is affected directly by precipitates and indirectly by dispersoids and constituent particles through their effects on tying up of solute, quench sensitivity, and recrystallization behavior. However, all second phase particles directly affect ductility.

Ductility of PH aluminum alloys decreases with increasing strength during aging and exhibits anisotropic behavior in products. For thick, rolled products, its typical value ($\sim$10%) as measured by the percent elongation is the highest in the rolling direction and lowest ($\sim$3%) in the normal, through thickness direction. Fracture in these alloys occurs in a ductile manner by the linking up of voids initiating at the larger constituent particles with their linkup aided by the deformation of the precipitates and the microvoid nucleation at the smaller dipsersoid particles in the ligament,

as shown by the fracture surface of an aluminum alloy in Fig. 4.23. Ductility is thus controlled by the combined effects of all the second phase particles, and a multiscale model has been developed to quantitatively describe their individual and coupled effects [79]. Ductility can be increased by the reduction of the volume fraction of all these types of particles. However, reducing the amounts of precipitate and dispersoids must be balanced with the need to maintain strength and toughness. Capability also does not exist to predict the ductility of PH aluminum alloys.

The strain hardening behavior of PH aluminum alloys containing second phase particles is determined by whether they are sheared or bypassed by dislocations. The stress necessary for deforming a shearable particle does not increase and may decrease with continued shearing. However, for particles that are bypassed, stress necessary to continue deformation will increase due to the presence of loops around the particles effectively decreasing the interparticle spacing. Thus in PH aluminum alloys, the strain hardening behavior is determined essentially by the matrix (solid solution effects) and the nature of the strengthening precipitates.

The effect of the matrix and precipitates is seen in the changing values of the strain hardening rates with the progress of aging in PH aluminum alloys, as observed in the behavior of alloy 7449 whose precipitation evolution (Fig. 4.27) was discussed earlier. As aging proceeds from the quenched condition, the strain hardening rate decreases with increasing volume fraction of shearable precipitates and the depletion of solute in the matrix, reaching the lowest value at peak strength. With continued aging, strain hardening rate increases corresponding with the transition from precipitate shearing to bypassing [72].

4.4.3 DURABILITY AND DAMAGE TOLERANCE PROPERTIES

The tensile properties of alloys, although the principal criteria for alloy design, do not provide measures of resistance to deformation and failure in the presence of defects in the material and/or in corrosive environments. As shown in Table 4.2, properties such as fracture toughness and fatigue resistance have become important considerations for airframes and consequently for alloy design since the 1960s. Resistance to failure under fatigue loading and in a corrosive environment (durability) and the load carrying capability of the material in the presence of defects (damage tolerance) are measured by properties such as fracture toughness, fatigue strength, FCG rates, residual strength, and resistance to various types of corrosion. Their relative importance depends on the component location in the airframe, as shown in Fig. 1.2. All the properties that determine the durability and damage tolerance (DADT) are sensitive to the microstructure and much of the aluminum alloy development in the past 50 years or so has focused on improving them while generally maintaining strength.

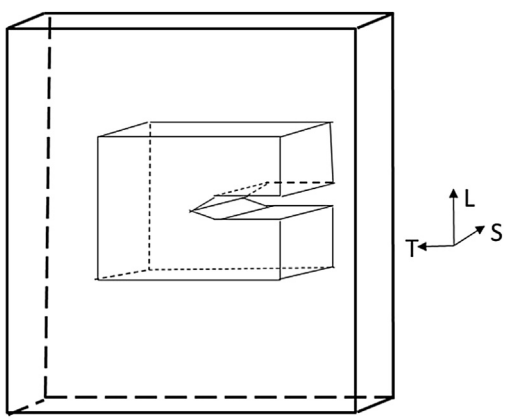
4.4.3.1 Fracture Toughness

Fracture toughness provides a measure of the resistance of the material to crack extension. Methods available to characterize fracture toughness are discussed in

detail in many handbooks. For PH aluminum alloys, the commonly used measure is the plane-strain fracture toughness, K_{Ic}, which is a material property. Under conditions that deviate from plane strain, such as for sheet and relatively thin plate material undergoing slow, stable crack growth characteristic of aluminum alloys, fracture toughness can be measured using R curves, which record crack extension as a function of stress intensity. Measures for plane stress fracture toughness, K_{app} or K_c, can be obtained from R curves by calculating the stress intensity at maximum load using the initial, precrack length or an effective crack length (physical crack length plus the plastic zone size), respectively. Plane stress fracture toughness is not an inherent material property and needs to be determined as a function of material thickness. K_{Ic} is the limiting value of decreasing K_c with increasing material thickness until plane strain conditions prevail.

As with the tensile properties, fracture toughness also exhibits anisotropy. It is particularly important for thick products for which K_{Ic} values are a function of the orientation of the crack plane and the direction of crack propagation. Thus there will be six values of K_{Ic} for thick products corresponding to the six configurations (L-T, L-S, T-L, T-S, S-T, and S-L) of the test specimens. The specimen configuration identifies the fracture plane and the direction of crack propagation with the geometry of the product, as shown in Fig. 4.31, for the L-T specimen orientation. For this orientation, the crack will grow in the transverse direction in a plane normal to the longitudinal direction.

Fracture in wrought, PH aluminum alloys is always ductile and occurs by a mixture of transgranular and intergranular modes, which is a consequence of their



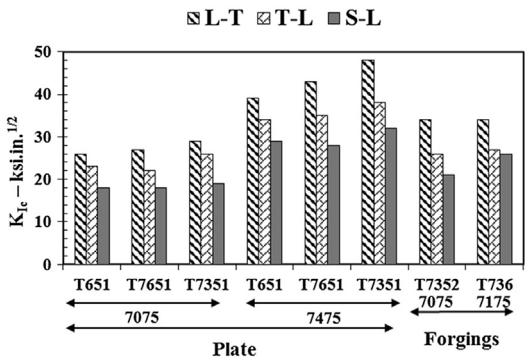
L – Longitudinal direction (length, rolling/extrusion direction, forging axis)
T – Long transverse direction (width)
S – Short transverse direction (thickness)

FIGURE 4.31

Orientations of K_{Ic} specimens.

heterogeneous and hierarchical microstructures. Recrystallization, precipitation in the grain boundaries and PFZs can be minimized but not eliminated in commercial alloys. Intergranular fracture occurs by strain localization in the PFZs and by crack nucleation at coarse precipitate particles and its propagation along the grain boundaries. In the grain interior, breakup, or decohesion of the constituent particles will initiate voids. Transgranular fracture occurs in the ligament by their link up from the failure due to the shear deformation of the precipitates and subsequent microvoid formation at dispersoid particles in the shear bands (Figs. 4.23 and 4.24). The effects of processing variables and microstructural features on fracture toughness can be explained on this basis, as follows:

1. Constituent particles that form during solidification always reduce toughness. All alloys developed after the 1970s have lower Fe and Si impurities to reduce their volume fraction for improving toughness as shown in Fig. 4.32 [80].
2. Toughness decreases with increasing degree of recrystallization. This is due to the increase in high angle grain boundary volume and PFZ's. Processing, particularly for thick products, is designed to produce a fully unrecrystallized microstructure to mitigate these effects, although recrystallization cannot be completely prevented.
3. Coherent dipersoids containing Zr will prevent or at least reduce the amount recrystallization and minimize grain boundary volume.
4. Reduced quench rates from solution treatment will reduce toughness by promoting coarse grain boundary precipitates with accompanying PFZ's, as shown in Fig. 4.10.
5. Increasing shear localization from increasing volume fraction of shearable precipitates during aging to peak strength will progressively reduce toughness, as shown in Fig. 4.20.



Alloy	Maximum Level (wt.%)	
	Fe	Si
7075	0.50	0.40
7175	0.20	0.15
7475	0.12	0.10

FIGURE 4.32

Toughness of aluminum alloys with various impurity levels.

Plotted from data in R.J. Bucci, E.A. Starke Jr., Selecting aluminum alloys to resist failure by fracture mechanisms, ASM Handbook, Fatigue and Fracture, vol. 19, ASM International, 1996 pp. 771–812.

The dependence of toughness on composition, processing, and microstructural variables as listed above and on yield strength, as shown in Figs. 4.20 and 4.32, provides a challenge for its prediction for alloy design. Models have been developed by considering the effects of constituent particles, degree of recrystallization, strain localization in the matrix, and void nucleation at grain boundary precipitates as affected by PFZs, either individually or in some combination. A few of these were briefly mentioned in the second chapter and are elaborated in the following.

Hahn and Rosenfield developed a model for toughness considering the voids nucleated at the constituents. These are linked by the shear deformation and secondary voids formed by the decohesion of dispersoids within them in the ligament [81]. It predicted toughness as

$$K_{Ic} \approx \left[2\sigma_{ys}E\left(\frac{\pi}{6}\right)^{1/3}D\right]^{1/2} f_c^{-1/6} \tag{4.12}$$

where σ_{ys} is the yield strength, E is the Young's modulus, and D and f_c are the diameter and volume fraction of constituent particles. This relationship is based on the critical step in fracture being the growth of voids in the ligament between cracked particles. It agrees with the observations of increasing toughness at similar strength levels with decreasing f_c, but contradicts the observations of increasing toughness with decreasing particle size.

The model developed by Chen and Knott considered dipsersoid decohesion within the large shear bands in the ligament as the controlling step. It predicted toughness as [82]

$$K_{Ic} \approx \left[\left(\frac{mb}{10A}\right)\sigma_c\sigma_{ys}En^2\lambda d^{-1}\right]^{1/2} \tag{4.13}$$

where m is a constant in the relationship between toughness and crack opening displacement, σ_c is the stress at which decohesion occurs, n is the strain hardening exponent and λ and d are the spacing and size of the disperoids, respectively. A is a constant of the order of $Gb/2\pi$ with G being the shear modulus. This relationship suggests that dispersoids with a high matrix/interface strength, small size, and large spacing are beneficial for toughness. The smaller size and higher interfacial strength of coherent Zr containing dispersoids provide higher toughness than in otherwise similar alloys, but with Cr additions.

Although these relationships generally agree with the trends in measured properties for many alloys, they predict increasing toughness with increasing strength, which is opposite of that observed when alloys are aged to peak strength. Further, most 7XXX series alloys are used in the overaged condition where dislocations by pass precipitates thereby dispersing slip and reducing stress concentrations. The models also do not explicitly account for recrystallization or the relative amounts of transgranular and intergranular failure modes. As such, they can be used for predicting toughness for varying amounts of

constituents or dispersoid particles in alloys with otherwise equivalent microstructures.

Several models for fracture toughness have attempted to account for the various micromechanisms associated with fracture processes. One of these related toughness to the degree of recrystallization, size and orientations of recrystallized grains and constituent particles, thus accounting for anisotropy of toughness in thick products [83,84]. Toughness was related to the orientation of the surfaces of constituent particles and grain boundaries through the angles θ_p and θ_r, respectively, defined as the angle between their normals and the loading direction. Toughness was predicted to increase with decreasing values of $<\cos\theta_p>$ and $<\cos\theta_r>$, which are the averages of the cosine values of the respective angles. In rolled plate, the constituents are distributed as stringers of particles elongated in the rolling direction. The high angle boundaries of the flat, pancake shaped, recrystallized grains are also oriented similarly. The surfaces of these features are thus generally parallel to the rolling direction and the rolling plane. Toughness will increase with decreasing areas of the grains and constituent particles oriented parallel to the fracture plane. For the L-T orientation, both θ_p and θ_r will be high and near 90° and thus the toughness will be maximum and for the S-L orientation, the angles will be zero and the toughness will be minimum, as observed in practice. The model also predicted increasing toughness with decreasing degree of recrystallization and increasing grain size, both of which will decrease the grain boundary volume. Further, this also explains increasing toughness with increasing particle size in the Hahn and Rosenfield model discussed earlier. The effective particle size will be higher for the S-L orientation resulting in a reduction of stress for void nucleation and a consequent reduction of toughness suggesting that the critical step for fracture is void initiation and not void growth [85].

The relative amounts of competing intergranular and transgranular failure modes in the fracture process have been accounted for by calculating the energy dissipation during these processes [67]. The model correctly correlated the relationship between yield strength and toughness for alloys 7050 (Fig. 4.20) and 7040 that were quenched at two rates. Predictions agreed with measurements in terms of the (1) variations between the fast and slow quenched alloys, (2) larger variation in the fast quenched alloys compared with the slowly quenched, (3) minimum toughness in peak aged condition, and (4) lower toughness in the overaged material compared to underaged material of same strength.

A good correlation between the predicted and measured toughness for alloys 7150 and 7449 was obtained by using Ashby's theory of work hardening resulting from nonshearable precipitates and grain structure [86]. This theory describes strain hardening as

$$\sigma = \sigma_{ys} + M\left[0.35G\left(\frac{b}{d_g}\right)^{0.5} + 0.25G\left(\frac{bf_{ns}}{2r_{ns}}\right)^{0.5}\right]\varepsilon_p^{0.5} \tag{4.14}$$

$$= \sigma_{ys} + K_A\varepsilon_p^{0.5} \tag{4.15}$$

where d_g is the grain size, f_{ns} and r_{ns} are the volume fraction and radius of the nonshearable particles (η' for these alloys) and K_A accounts for strain hardening. It predicted fracture toughness as

$$K_{Ic} = C_1 \left(\frac{2CE\varepsilon_c^*}{1-\nu^2} \right) K_A^{\gamma} \, \sigma_{ys}^{\gamma-0.5} \tag{4.16}$$

where C and C_1 are constants, ν is the Poisson's ratio and γ is about 0.85 for aluminum alloys. ε_c^* is the strain for critical crack tip conditions. The predictions agreed well with the measured values.

The fracture toughness models highlighted above have focused on one or a few of the many processes that occur during fracture. The plane stress toughness, K_c and K_{app}, will be discussed subsequently with respect to crack growth resistance of specific alloys. All the matrix and second phase features that affect toughness are interrelated through their dependencies on the processing parameters. Although a comprehensive relationship for toughness that includes all components of the fracture process is yet to be developed, those available and validated for specific conditions can be used advantageously to understand material behavior, optimize microstructural features and provide guidance for alloy design.

4.4.3.2 Fatigue Properties

Fatigue strength, life, and crack growth rates are the properties of interest for the application of aluminum alloys for airframes. The structural design philosophy will determine which of these properties is applicable. The safe-life and damage tolerance approaches to fatigue design can be found in many publications (e.g., Ref. [87]). The safe-life approach to designing for infinite life, characterized as "High Cycle Fatigue," requires that no cracks will initiate during service for which the stress-life (S–N) properties of the material are required. In practice, the definition of "no crack" implies a crack size below that which can be detected reliably. Safe-life approach to designing for finite life, characterized as the "Low Cycle Fatigue," uses strain-life (ε-N) properties. Damage tolerance approach to design assumes the presence of cracks, which are monitored by planned inspections. This approach uses FCG rate, da/dN, measured as a function of the stress intensity factor, ΔK, where a is the crack length and N is the number of cycles. Fatigue life is composed of the life to initiate a crack, small crack growth, stable crack growth, and fast fracture. All these properties vary with the stress amplitude, stress ratio, stress concentration factor, and the environment. They are also measured under variable amplitude loading using specimen configurations representative of service conditions. The discussion that follows will be limited to data from S–N tests, which provide a measure of the fatigue life/strength, and da/dN – ΔK tests, which provide crack growth rates.

4.4.3.2.1 Fatigue Strength/Life

Fatigue behavior in the high cycle fatigue regime is characterized by fatigue strength, which is the stress at which failure does not occur in a specified number of cycles or fatigue life, which is the number of cycles to failure at a given stress

level. Unlike steel alloys, aluminum alloys do not exhibit an endurance limit, but the S—N curves tend to flatten at about 500 million cycles and the stress corresponding to this life is reported as the endurance limit [80].

A significant fraction of the fatigue lives measured in S—N tests is comprised of the number of cycles to initiate a crack. Hence, features that improve fracture toughness of aluminum alloys by reducing strain localization and retarding crack initiation will also increase fatigue strength, as already discussed in the second chapter. Beneficial features include nonshearable precipitates for slip homogenization and reduced volume fraction of constituents. Fatigue cracks in 7075-T651 have been shown to nucleate exclusively at constituent particles located near the surface [88]. Nucleation occurred only at a few particles whose surface normal was in the short transverse direction and which intersected the fewest grain boundaries. Due to grain shape anisotropy, not all similarly oriented particles intersected the same number of grain boundaries. These observations are consistent with the beneficial effects of reduced volume fraction of constituents and finer grain size on fatigue crack initiation.

Reducing the degree of crystallization and grain size will benefit alloys with shearable precipitates and retard nucleation at PFZs. However, overaging will not mitigate the effects of solute-depleted PFZs, as there will be no precipitates in this region to homogenize deformation [80]. A comparison of the fatigue lives of specimens taken from the mid-thickness regions of 7050 alloy with two levels of porosity that were otherwise identical (Fig. 4.26), showed that the cumulative fatigue lives were substantially longer for the alloy with lower porosity. Cumulative fatigue lifetime distributions, shown in Fig. 4.33, for three 150-mm (6 in.) 7050-T6 plates with different levels of porosity and one 25-mm (1 in thick) plate of the same alloy clearly depict this effect [89]. The fatigue stress levels are higher for the low porosity and thin materials.

As discussed in the second chapter, the ratio of the fatigue strength to the tensile strength for PH aluminum alloys is about 0.3, which is lower than for alloys strengthened by work hardening. The fatigue lives for the PH aluminum alloys are limited by the presence of potential crack nucleating sites. Processing and microstructural modifications to eliminate these sites can improve fatigue lives to some extent.

Fatigue strength and lives of alloys will decrease in the presence of corrosive environments including moisture in the ambient atmosphere. The effects will become increasingly pronounced at lower stress amplitudes and longer lives, as shown schematically in Fig. 4.34 based on the results of many investigations [90]. In a given environment, the fatigue lives can be improved in 2XXX and 7XXX series alloys by overaging to the more corrosion resistant T8 and T7 tempers, respectively. However, this will result in the loss of toughness and increased FCG rates for the 2XXX series alloys.

4.4.3.2.2 Fatigue Crack Growth

FCG behavior of aluminum alloys can be described in the context of the damage tolerance approach to design of structures. In this framework, crack growth can be divided into four regimes, as shown schematically in Fig. 4.35 [91].

Alloy	Thickness in. (mm)	Microstructural feature	Maximum Stress ksi (MPa)
Old	5.7 (145)	Coarse porosity	35 (241)
Now	5.7 (145)	Porosity	35 (241)
Low porosity	6.0 (152)	Small porosity, constituent particles	40 (276)
Thin	1.0 (25)	Constituent particles, refined grain size	45 (310)

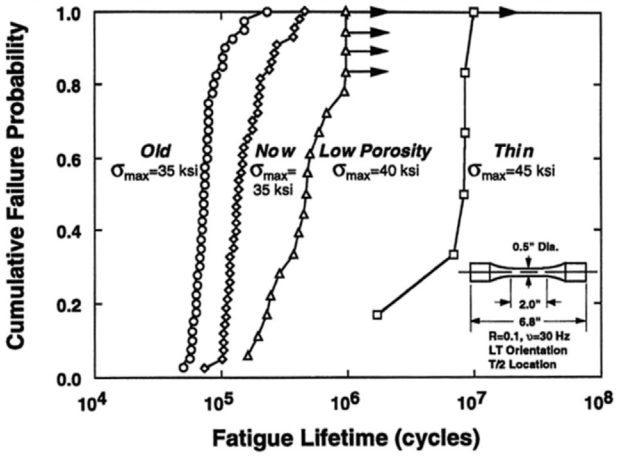


FIGURE 4.33

Cumulative fatigue lives distributions for alloy 7050-T7451 plate with four levels of porosity.

Adapted from P.E. Magnusen, R.J. Bucci, A.J. Hinkle, J.R. Brockenbrough, H.J. Konish, Analysis and prediction of microstructural effects on long-term fatigue performance of an aluminium aerospace alloy, International Journal of Fatigue 19 (1997) 275–283.

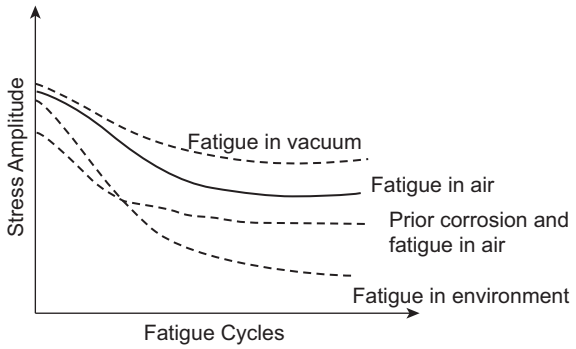


FIGURE 4.34

Effect of environment on fatigue lives.

Adapted from R.J.H. Wanhill, Aircraft corrosion and fatigue damage assessment, US Air Force ASIP Conference Proceedings, 1995, pp. 983–1027.

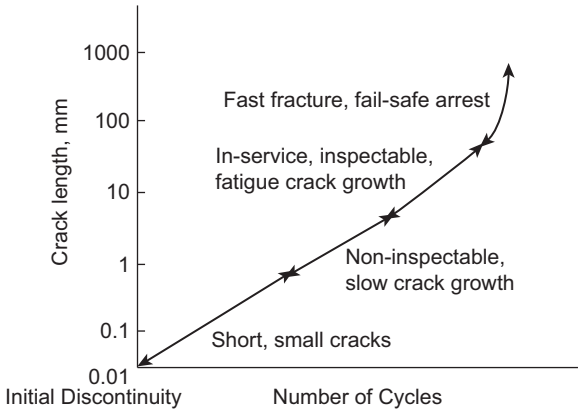


FIGURE 4.35

Four regimes of fatigue crack growth.

Adapted from R.J.H. Wanhill, G.H. Bray, Fatigue crack growth behavior of aluminum lithium alloys, in: N. Eswara Prasad, A.A. Gokhale, R.J.H. Wanhill (Eds.), Aluminum-Lithium Alloys: Processing, Properties and Applications, Elsevier, 2014, pp. 381–412.

Fatigue begins with the nucleation of a crack and its growth in the small crack regime that transitions into the slow growth period followed by the region where long cracks (LCs) can be inspected and finally by the fast fracture region. The transition from the noninspectable to inspectable region varies with the crack sizes that can be reliably detected. The first two regimes are used to assess durability and the last two for damage tolerance. The FCG behavior of PH aluminum alloys can be described in this framework, although the properties of alloys are measured and compared principally in the last two regimes.

In the LC growth regime, crack growth curves for aluminum alloys generally fall within a band, as shown in Fig. 4.36 for 2XXX including the first generation Al—Li alloy 2020 and 7XXX series alloys [91]. Generally, crack growth in 2XXX series alloys is slower than in 7XXX series alloys, with Al—Li alloys having superior resistance. Within each alloy family, factors that promote higher toughness also provide higher resistance to crack growth, with the effect increasing with increasing stress intensity factors approaching fracture toughness. This behavior is illustrated by the superior crack growth resistance observed in 2124 and 7475, which are higher toughness alloys with a smaller volume fraction of constituents, compared with 2024 and 7075, respectively.

The effects of second phase particles on FCG behavior are related to their size range, as shown schematically in Fig. 4.37 [80]. Constituents influence crack growth only at rates approaching fast fracture. A detailed characterization of the fatigue fracture surfaces of three 7075-T6 aluminum alloys with different volume fractions of constituent particles that were otherwise identical, has shown that fracture by void nucleation at these particles are important only when their mean spacing is

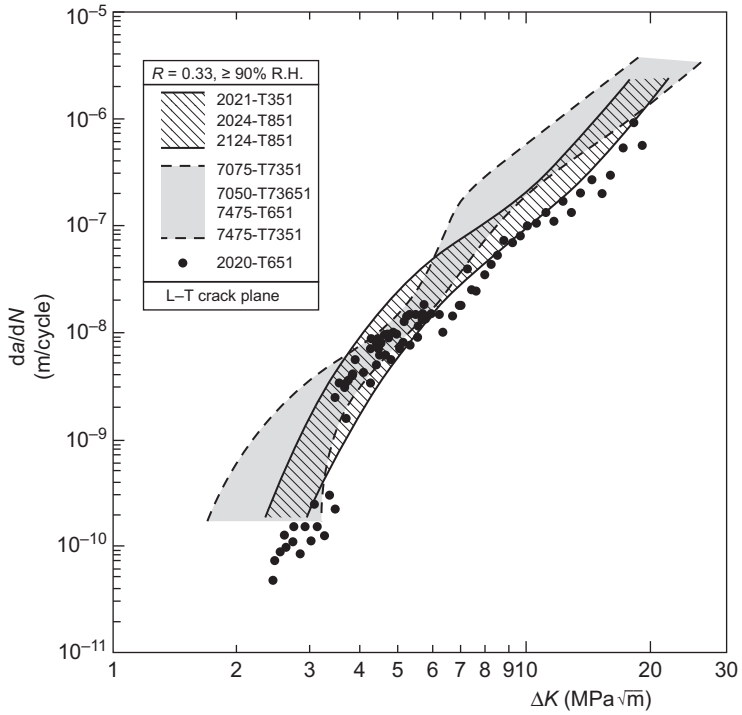


FIGURE 4.36

Fatigue crack growth curves for aluminum alloys [91].

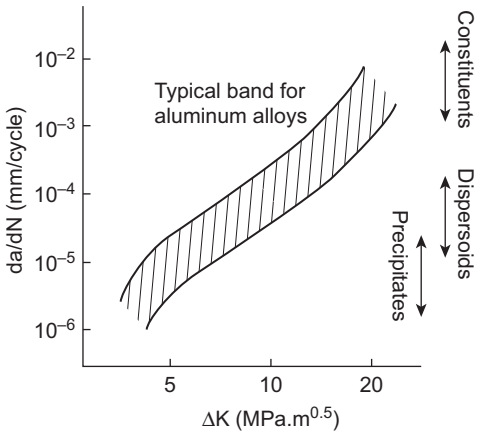


FIGURE 4.37

Relationship of particle size to fatigue crack growth rate for aluminum alloys.

Adapted from R.J. Bucci, E.A. Starke Jr., Selecting aluminum alloys to resist failure by fracture mechanisms, ASM Handbook, Fatigue and Fracture, vol. 19, ASM International, 1996, pp. 771–812.

approximately the same as the width of the cyclic plastic zone [68]. This occurs only at growth rates corresponding to fast fracture. Dispersoids have only a minor direct influence, but affect growth rates through their effects on recrystallization and grain sizes. Factors such as fine grain sizes and overaged precipitates that improve toughness will increase crack growth rates. Growth of cracks is slowed by increasing tortuosity in their path, which can be accomplished by shearable precipitates and large grain sizes, which, however, contribute to a reduction in toughness. Slip is more reversible in alloys with shearable precipitates, which coupled with large grain sizes increases crack tortuosity resulting in zig and zag and branched cracking thereby reducing the overall crack growth. As with fatigue lives, corrosive environments including ambient humidity will increase crack growth rates compared to that in vacuum and will be a factor of about two to four higher in the standard neutral salt water environment used in the laboratory to characterize crack growth behavior.

4.4.3.2.3 Modeling of Fatigue Behavior

The effects of processing and microstructure on the fatigue properties of PH aluminum alloys have been studied for a long time and significant knowledge has been accumulated, enabling the development of models that describe many aspects of the relationships. For example, fatigue lives can be predicted by using the size of the crack nucleating feature, such as a pore or constituent particle, as that of an initial flaw and then calculating the growth rate using known $da/dN - \Delta K$ relationship for the alloy. The performance capability and probability of failure of a material under given loading conditions can then be estimated from a knowledge of the size distribution of the crack nucleating features. The models that have been developed have been empirical and parametric and do not account for the underlying microstructural mechanisms responsible for fatigue.

From the perspective of predicting the effects of microstructures on fatigue behaviors, the total life, N_t, which is the sum of initiation, N_i, and propagation, N_p, lives, is further decomposed as follows [92]:

$$N_i = N_{nucl} + N_{\mathrm{MSC}} + N_{\mathrm{PSC}'} \tag{4.17}$$

$$N_p = N_{\mathrm{PS}''} + N_{\mathrm{LC}} \tag{4.18}$$

where N_{nucl} is the number of cycles to form a crack nucleus and N_{MSC}, N_{PSC}, and N_{LC}, are the number of crack growth cycles in the microstructurally small (MSC), physically small (PSC), and LC regimes. Growth of PSCs is the sum of their growth cycles attributable to the initiation ($N_{\mathrm{PSC}'}$) and the propagation ($N_{\mathrm{PSC}''}$) regimes. The size of MSCs is such that their nucleation and growth are affected by microstructural features such as grains and second phase particles. PSCs are not strongly affected by microstructure. The stages of nucleation and growth of MSC, PSC, and LCs can be superimposed approximately with the crack growth regimes shown in Fig. 4.35. The growth of LCs corresponds to the last two regimes and that of MSCs with the short crack regime.

Fatigue behavior of PH aluminum alloys can, in principle, be treated as a multistage process, with each stage affected by one or more features of the hierarchical

scale of microstructures. Nucleation and growth of MSCs are affected by the nature of the precipitates, degree of recrystallization, grain size, and constituent particles. The LC growth regime is relatively insensitive to the microstructure except at rates approaching fast fracture where constituents affect growth. Stress concentrations at features such as PFZs, grain boundaries, and particles nucleate cracks, but the underlying mechanisms such as dislocation activity and slip are difficult to incorporate. Unless such mechanistic understanding is developed at all relevant length scales, predicting the effects of microstructure on fatigue properties will be difficult. The status of microstructure sensitive modeling of fatigue including the present shortcomings and scope for future work has been treated in several reviews [92,93].

4.4.3.3 Corrosion Behavior

Aluminum alloys are generally protected from uniform corrosion by a naturally occurring surface oxide skin. However, heterogeneities in the microstructure of wrought, PH aluminum alloys render them susceptible to several localized types of corrosion and SCC. Although these alloys are never used without elaborate corrosion protection schemes for airplane service, corrosion can still occur due to deterioration of the protective coatings, internal environments, and structural design, manufacturing and maintenance details [36]. Continuing advances being made in the (1) development and use of more corrosion resistant materials, (2) procedures to control corrosion, and (3) improve inspection and maintenance procedures, have significantly reduced the incidents of corrosion in practice. Some of the corrosion mechanisms occurring in PH aluminum alloys require the presence of residual stresses in the material or superimposed external stress. Almost all the processing and microstructural features that increase the strength of PH aluminum alloys will reduce their resistance to corrosion. Similarly, those that improve toughness, and DADT will generally improve corrosion resistance, particularly for SCC. The types of corrosion affected predominantly by the composition, processing, and microstructure of PH aluminum alloys are pitting, intergranular corrosion (IGC), exfoliation, and SCC.

4.4.3.3.1 Pitting Corrosion

Pitting occurs in aluminum alloys due to the electrochemical differences between the matrix and second phase particles. Particles that are more noble and cathodic relative to the Al matrix cause its dissolution resulting in pitting. Particles that are anodic relative to the Al matrix will dissolve themselves. A detailed investigation of the electrochemical characteristics of the constituents and dispersoids found in PH aluminum alloys has provided their classification as follows [69]:

- Noble particles with high electrochemical activity (Al_2Cu, Al_7Cu_2Fe) that cause pitting.
- Noble particles with low electrochemical activity (Al_3Zr). These dispersoid particles are also too small to cause pitting.
- Active particles with high dissolution rates ($MgZn_2$).

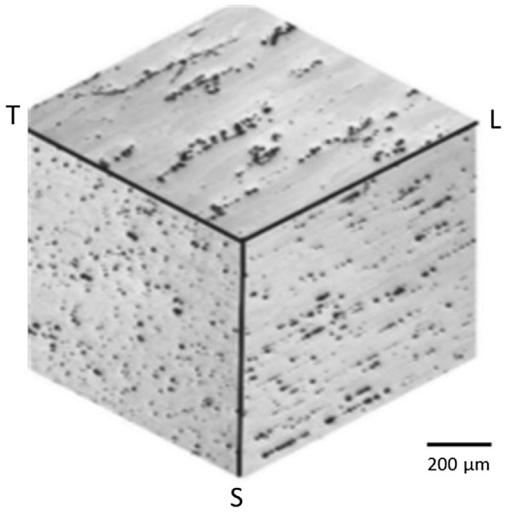


FIGURE 4.38

Constituent particles that cause pitting in 7075-T6 [94].

- Active particles with low dissolution rates, not commonly observed in alloys of interest.
- Active particles with compound containing a relatively noble element such as Cu (Al_2CuMg). Dealloying of Al and plating of Cu onto the more noble particles can cause pitting. 2XXX series alloys with Cu as the principal alloying element are thus less resistant to pitting and general corrosion than other alloys. In these alloys, decreasing Cu will improve resistance to corrosion.

Most of the constituent particles tend to be cathodic and will cause pitting. Their distribution in alloy 7075-T6 is shown in Fig. 4.38 [94]. The areal number density was measured to be 2000 particles/mm^2. Fig. 4.39 shows a distribution of these

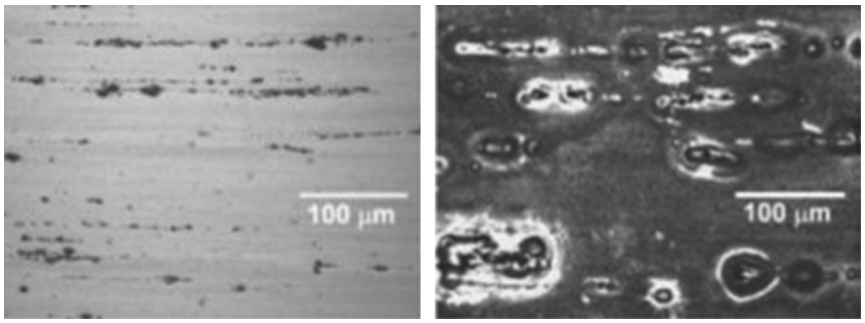


FIGURE 4.39

Constituent particles on the surface (left) and pitting (right) [94].

particles in the LS plane with pits formed around them. Pits tend to nucleate at clusters of particles and their geometries vary widely.

Pits can cause stress concentrations, nucleate fatigue cracks and reduce fatigue life. Their effects can be quantified by considering them as preexisting flaws. The size and geometric (width, depth) shape distributions of pits can be characterized quantitatively and analyzed statistically for use in the probabilistic assessment of fatigue lives, in a manner similar to that discussed earlier for determining the effects of porosity. In a given environment, presence of prior pitting corrosion will reduce fatigue lives of alloys, as schematically shown in Fig. 4.34. For example, despite the higher purity of alloy 2524 compared with 2024, prior pitting corrosion reduced the fatigue strength of both alloys at 10^5 cycles by about 40% [95].

Fig. 4.40 shows the measured lives of 7075-T6 aluminum alloy specimens with and without prior corrosion damage [58]. The corroded specimens contained varying amounts of pitting corrosion damage caused by exposing for varying durations in a prohesion salt spray test (ASTM Standard G85 Annex 5). The measured lives are also compared with the lives for alloys without any prior corrosion damage but with two levels of stress concentrations, K_t. As expected, a continuous decrease of fatigue lives is observed with increasing corrosion damage. Interestingly, these lives are bounded by the lives for the alloys with no prior corrosion damage and with K_t values of 1 and 2, respectively, suggesting that the effects of varying levels of corrosion damage can be attributed to correspondingly equivalent stress concentration factors.

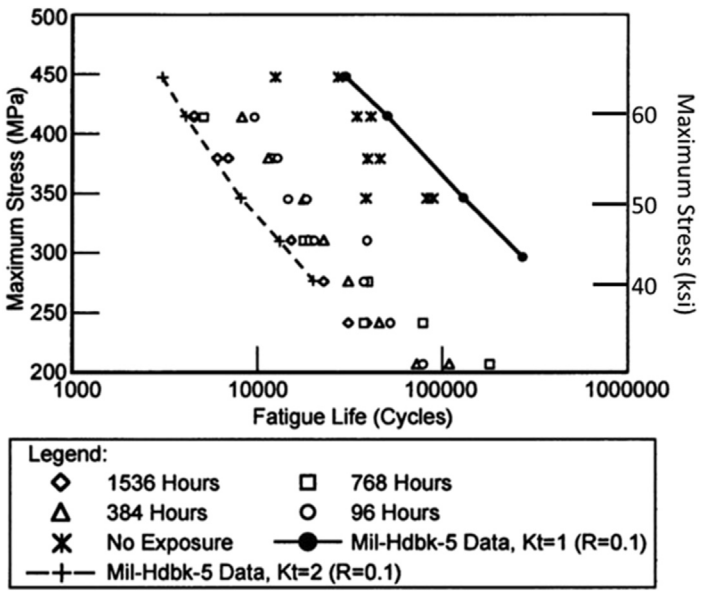


FIGURE 4.40

Fatigue lives of 7075-T6 as a function of pitting corrosion damage [58].

Effects of corrosive environments on fatigue crack nucleation can be modeled by the testing of pristine specimens in the environments during which fatigue and corrosion damage accumulate simultaneously. Corrosion pits are considered as surface cracks whose growth rates are determined by the pitting kinetics. A fatigue crack nucleates from the pit either when the pit grows to a critical size at which the stress intensity factor reaches the threshold for fatigue cracking or when the FCG rate exceeds the pit growth rate [96]. Studies on alloy 2024-T3 have shown that both these criteria are needed for adequately describing the transition from pitting to FCG [97].

Compared to the vast amount of available information on the effects of constituent particles on pitting, that on the effects of precipitates is very sparse. The number and area density of pits in 7075-T6 have been reported to be higher than in 7075-T73, although their distributions shifted to larger sizes with increasing exposure for the latter alloy [98]. The observations have been explained by the differences in the size and density of the anodic precipitates in both tempers. Their high volume fraction in the T6 temper causes higher amounts of peripheral pitting at the cathodic constituents near the anodic precipitates. With lower number of precipitates in the T73 temper due to their coarsening, growing pits will increase in size without any new sites for nucleation, explaining their shifts to larger sizes. The effects of pitting on fatigue lives showed that the alloy had higher value of absolute lives in the T73 temper than in the T6 temper, but the lives were lower when the fatigue stress was normalized to the yield strength [99]. The material in the T73 temper has lower absolute strength than that in the T6 temper, but better intrinsic crack initiation resistance due to the homogenization of deformation. This advantage is lost in the corroded T73 material where cracks nucleate exclusively at pits and further propagation is easier than in the T6 alloy, in which crack path is tortuous.

4.4.3.3.2 Intergranular Corrosion

If the quench rate from the solution heat treatment temperature is slow enough to cause the precipitation of Cu-rich precipitates in the grain boundaries, the adjacent matrix region is depleted of this element and rendered anodic relative to the grain interior [100]. Preferential attack of this region will cause corrosion to proceed along the grain boundaries. Both 2XXX and 7XXX series alloys are susceptible to IGC in the underaged tempers. With progress of precipitation during aging to peak strength, the amount of Cu in solution will be reduced continuously and the susceptibility to IGC will be reduced. The C curve approach discussed earlier can be used to identify the quench rates necessary to eliminate IGC [47].

4.4.3.3.3 Exfoliation Corrosion

EC occurs in PH aluminum alloys having highly elongated grain structures, as found in rolled products and extrusions. Solute depleted regions adjacent to grain boundaries and precipitates aligned along their length cause corrosion to proceed along these regions. In practice, EC occurs in areas where water can concentrate in riveted or similar joints from where corrosion can proceed inward along the subsurface region of the alloy [97]. Accumulation of sufficient corrosion products, which can

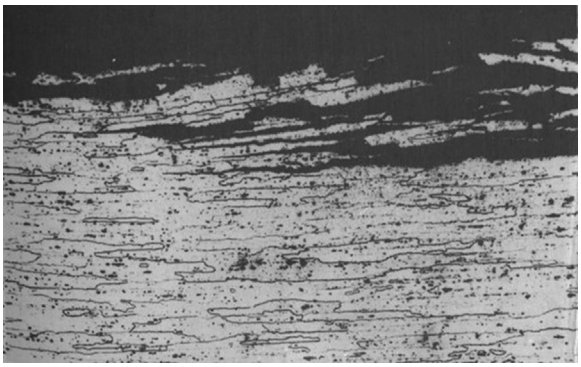


FIGURE 4.41

Exfoliation corrosion in aluminum alloy 7178-T651. Corrosion develops along thin, grain boundaries, as seen in the cross section [101].

Reprinted with permission of ASM International. All rights reserved. www.asminternational.org.

cause up to a sixfold increase in volume, acts as a wedge to lift grains, as shown in Fig. 4.41 [101], and cause the "pillowing" of joints. Thus EC can be considered as an extreme form of IGC.

Although the exact mechanisms underlying EC are still not settled, precipitation of Cu containing phases in the grain boundaries, for example, η ($Mg(Zn, Cu, Al)_2$) in 7XXX series alloys, and depletion of solute in adjacent regions cause galvanic coupling. From a study of 7XXX series alloys, two mechanisms have been proposed for EC. Both start as IGC, which transitions in the first mechanism into EC by the lifting of grains and in the second into intergranular fracture due to hydrogen penetration into the material from the corrosion reaction [102]. The resistance to EC can be improved by overaging to T76 temper, which eliminates the continuous grain boundary precipitates by their coarsening. This will be discussed in more detail with respect to improving the resistance of the alloys to SCC.

Galvanostatic measurements of an experimental 7XXX series alloy aged to T6 and T76 tempers showed that the number of transients (fluctuations greater than 2 mV) recorded in 24 h decreased continuously as the aging time increased beyond peak strength. With the mechanism of EC found to be intergranular fracture, the transients were attributed to crack propagation [103]. As discussed in the second chapter, with no quantitative measures available for ranking the susceptibility of alloys to EC, the electrochemical measurements as described here could potentially be developed for this purpose.

Compared with pitting corrosion, the modeling of EC has received much less attention, which may be partly due to the difficulty of geometrically describing the EC morphologies as equivalent initial flaws and partly to the complex interactions of loading with the corrosion damage [97]. In tests conducted on alloy 7178-T6 specimens, prepared from wing skins that had seen 15 years of actual service, introduction of EC was found to reduce the toughness slightly and increase the FCG rates in both dry and wet air [104].

The fatigue lives of 7075-T6511 specimens prepared from wing skins that had natural exfoliation occurring in service, agreed with those predicted from a simplified model in which the exfoliation damage was treated as a surface crack with a depth that was obtained from nondestructive measurements [105]. One purpose of modeling the effects of corrosion damage on properties is to develop the ability to predict the behavior of materials in service, which needs measures for damage that accurately represents that occurring naturally. Areas damaged by EC have multiple features such as grain boundary particles, IGC and several other discontinuities. Attempts have been made to identify a "corrosion process" zone associated with EC and to relate the fatigue lives to the dimensions of this zone. It predicted the lives of artificially corroded 7075-T6 specimens well, but overestimated the lives of those corroded naturally in service.

4.4.3.3.4 Stress Corrosion Cracking

SCC occurs in susceptible alloys by the joint action of a corrosive environment and sustained tensile stress. The source of stress can be from externally applied loading or internal residual stresses in the material resulting from manufacturing operations. Wrought PH aluminum alloys with grain boundary precipitates and adjacent PFZs are susceptible to SCC, which therefore follows an intergranular path. As with EC, the mechanisms proposed for SCC are anodic dissolution of the solute-free zones or the grain boundary precipitates and hydrogen assisted cracking. Alloy composition, heat treatment, product form, and orientation all determine the SCC behavior of PH aluminum alloys. The microstructural features that promote SCC, i.e., continuous grain boundary precipitates and PFZs, are caused by the same processing conditions that also affect fracture toughness, fatigue behavior, IGC, and EC. Thus SCC behavior exhibits anisotropy and dependence on product forms and orientations similar to those for toughness. The resistance to SCC failure is the least in the short transverse direction and in the S-L orientation.

SCC behavior is characterized by conducting tensile tests in corrosive environments on smooth specimens under constant load or displacement or strain rate. Environmental exposure can be continuous or alternate with the ambient. Constant load tests provide time to failure as a function of initial applied stress, similar to the lives measured from S—N tests for fatigue. The stress below which failure does not occur is designated as the threshold stress, σ_{th}, for the alloy and temper in the specific environment, as shown in Fig. 4.42 for alloy 7075-T6 plate [101]. The effect of the direction of loading is very clear with the threshold stress the lowest in the short transverse direction. The threshold stress normalized to the yield strength is often used to compare and rank different alloy and temper combinations for SCC resistance. The threshold stress can also be measured as a function of exposure time, i.e., whether failure does or does not occur in a specified exposure time.

Precracked specimens are used to measure stress corrosion crack velocities in specific environments as a function of the stress intensity factor. Details of the test methods, their advantages, shortcomings, and modifications are available from several publications [106,107]. These tests measure stress corrosion crack velocity

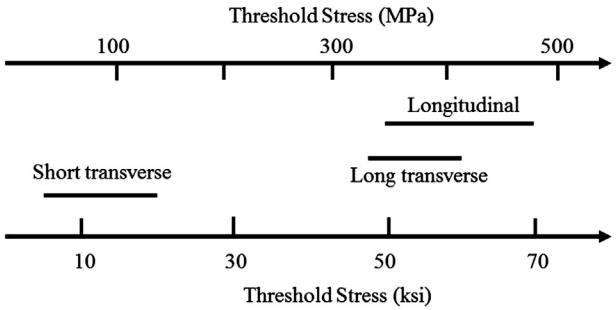


FIGURE 4.42

The relative resistance to stress-corrosion cracking of 7075-T6 plate, 6.4–76 mm (0.25–3 in.) thick, as influenced by direction of stressing. Samples alternately immersed in 3.5% NaCl.

Adapted from J.G. Kaufman, Corrosion of aluminum and aluminum alloys, in: Corrosion: Materials, ASM Handbook, vol. 13B, ASM International, 2005, pp. 95–124.

(v) as a function of the stress intensity (K_I), as shown schematically in Fig. 4.43 [108]. The stress intensity at which measurable crack growth begins, K_{Iscc}, is designated as the threshold stress intensity. Two regions where v increases with K_I are separated by a plateau in which v is independent of K_I. When K_I approaches the fracture toughness, K_{Ic}, of the material, the specimen fails by fast fracture.

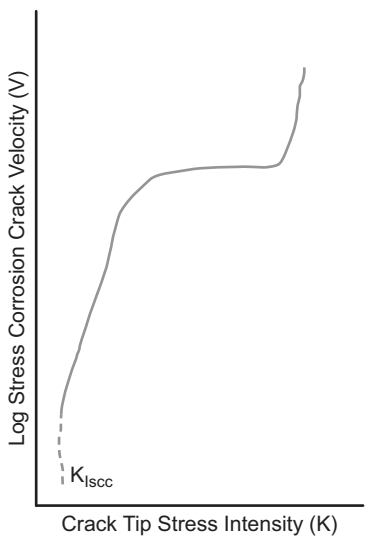


FIGURE 4.43

Schematic of stress intensity versus growth rate curves.

Adapted from M.O. Speidel, Stress corrosion cracking of aluminum alloys, Metallurgical Transactions A 6A (1975) 631–651.

The v-K curves for several PH aluminum alloys are shown in Fig. 4.44 [108]. 7XXX series alloys are predominantly used for applications requiring high strength, particularly in thick sections. Accordingly, much of the work on SCC and developing more resistant alloys has focused on these systems. Fig. 4.45 shows the general trend in SCC susceptibility and strength as a function of aging time for PH aluminum alloys [108]. Susceptibility is low in the SSSS and rises with increasing aging time reaching a peak, often before the maximum strength, and decreases with continued aging. However, broad and systematic correlations between strength and σ_{th} or between and K_{Ic} and K_{Iscc} are not possible. Overaged alloys possess better resistance to SCC than do underaged alloys of the same strength.

Almost all 7XXX series alloys are used in the overaged condition for improved corrosion performance. For sheet and relatively thin plate applications for which SCC is not a concern, alloys are used in the peak aged, T6 condition. Peak strength is achieved in 7075-T6 by aging in one step at 120°C (248°F) for 24 h. The alloy is strengthened by GP zones in the underaged condition and leading up to peak strength. As discussed in earlier sections, these precipitates are sheared by dislocations. The resulting slip concentrations in the coarse slip bands increase the stress on the PFZs, which coupled with the anodic dissolution of PFZs or the continuous η ($MgZn_2$ type) precipitates in the grain boundaries cause SCC under the combined action of stress and corrosive environments.

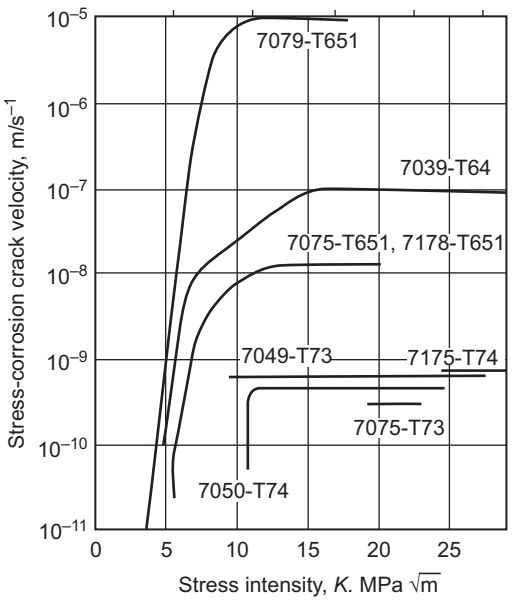


FIGURE 4.44

Crack propagation rates in stress-corrosion tests using precracked specimens of various product forms of 7XXX-series alloys.

Adapted from M.O. Speidel, Stress corrosion cracking of aluminum alloys, Metallurgical Transactions A 6A (1975) 631–651.

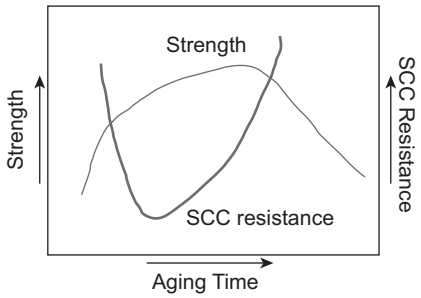


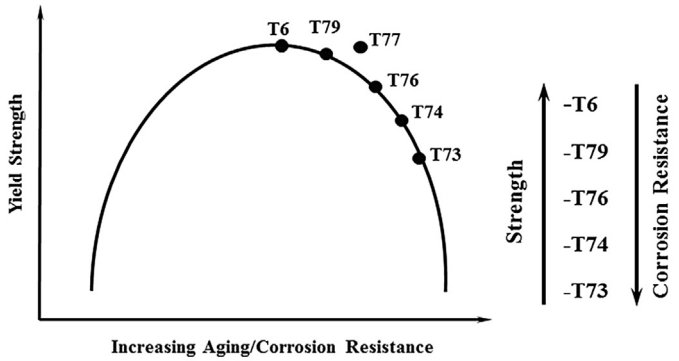
FIGURE 4.45

Schematic of variation of strength and stress corrosion cracking resistance with aging time.

Adapted from M.O. Speidel, Stress corrosion cracking of aluminum alloys, Metallurgical Transactions A 6A (1975) 631–651.

Overaging increases resistance to SCC by homogenizing slip thereby reducing stress concentrations and by the coarsening of grain boundary precipitates which eliminates their continuous occurrence as films along grain boundaries. Overaging by aging in one step at a temperature above about 150°C (302°F) can increase SCC resistance, but the loss of strength relative to the peak aged condition is much more than if it were performed in two steps. The dissolution of GP zones above 150°C (302°F) and the direct nucleation of η' from the solid solution results in a coarser distribution of the strengthening precipitates and lower strength than if η' nucleated from preexisting GP zones. Thus aging at about 100°C (212°F) for a short time to produce GP zones followed by aging above 150°C (302°F) for nucleation of η' from GP zones results in its finer distribution and good combinations of strength and SCC resistance. This requires the aging time and temperature of the first step and the heating rate to the second step to be controlled to ensure that the GP zones do not dissolve prior to nucleating η'. Resistance to EC can be achieved with shorter second step aging times than required for resistance to SCC. Fig. 4.46 schematically shows the relationship between the extent of overaging and the resulting combination of strength and resistance to various types of corrosion. RRA treatments discussed earlier can provide acceptable corrosion resistance in relatively thin products while retaining high strength levels.

Addition of Cu in sufficient amounts to Al–Zn–Mg alloys increases both strength and SCC resistance. Cu substitutes for Zn in the grain boundary phase η ($MgZn_2$ type) reducing its dissolution and decreasing the crack velocity during SCC. Cu also remains in solution during the first step aging and promotes the precipitation of the semi coherent phase during the second step resulting in overall improvements to strength and SCC resistance. A detailed analysis of investigations conducted over an extended period showed the critical dependence of SCC behavior



-T6	Peak Aged
-T77	Retrogression and Overaging
-T79	Very Limited Overaging
-T76	Overaged to Achieve Enhanced Exfoliation Resistance
-T74	Overaged to Achieve Enhanced Exfoliation and SCC Resistance
-T73	Overaged to Achieve Optimum Exfoliation and SCC Resistance

FIGURE 4.46

Heat treatment schemes for strength—corrosion resistance trade-off.

on Cu content, Zn/Mg ratio, and excess Mg [109]. Excess Mg is that amount remaining after accounting for the stoichiometric amounts of Mg, Cu, and Zn to precipitate completely. Optimum resistance to SCC is found in peak aged and overaged alloys with <8% Zn, <1% excess Mg, Zn/Mg ratio between 2 and 3, and Cu either <0.2% or between 1.3% and 2% (all wt%). Overaging is beneficial only for alloys with Cu > 0.8%. Table 4.18 lists the nominal compositions of selected 7XXX series alloys along with the values for these parameters.

The compositions of alloys 7075, 7050, and 7010 fall within the range for optimum SCC resistance in the overaged conditions. The Zn/Mg ratio and Cu content were increased in 7010 and 7050 compared to that in 7075 to obtain higher strengths on overaging while simultaneously increasing SCC resistance as close as possible to

Table 4.18 Nominal Compositions of Selected 7XXX Series Alloys (wt%)

Alloy	Zn	Mg	Cu	Cr	Mn	Zr	Zn/Mg	Excess Mg
7075	5.6	2.5	1.6	0.30			2.24	0.86
7079	4.3	3.3	0.6	0.20	0.20		1.30	2.38
7010	6.2	2.3	1.7			0.12	2.70	0.49
7050	6.2	2.3	2.3			0.12	2.70	0.16
7055	8.0	2.0	2.3			0.16	4.00	0.06

Excess Mg amounts from N.J. Henry Holoyd, G.M. Scamans, Stress corrosion cracking in Al—Zn—Mg—Cu aluminum alloys in saline environments, Metallurgical and Materials Transactions A 44A (2013) 1230—1253.

that of 7075-T73. 7055 with a very high Zn/Mg ratio was designed to provide high strength while maintaining acceptable corrosion resistance. 7079, developed before the use of Zr began, was designed to provide higher strength than 7075-T6 and had good resistance to SCC initiation but poor resistance to its growth. These aspects will be discussed in detail in the next section focusing on the development of commercial PH aluminum alloys.

The SCC susceptibility of 2XXX series, Al−Cu−Mg alloys results from the precipitation of the S phase (Al_2CuMg) in grain boundaries. Susceptibility is the highest in the underaged condition, which decreases as the alloys are aged to peak strength. The cold work imparted prior to aging results in a higher density of intragranular precipitate nucleation in the T8 temper providing the highest combination of strength and SCC resistance in these alloys. In the family of alloys containing Li additions, the SCC and exfoliation resistance of third generation alloys have been improved significantly over that of the earlier alloys. This has been achieved by reducing the total solute content, addition of Zn and aging to a certain threshold duration at which corrosion resistance is highest and remains unchanged with further aging [32].

4.5 COMMERCIAL ALUMINUM ALLOYS

The processing−microstructure−properties relationships schemes provide an excellent framework to discuss the historical and ongoing development of wrought, PH aluminum alloys for commercial use. The Al−Cu−Mg and Al−Zn−Mg−Cu systems, which still form the basis for most of the 2XXX and 7XXX alloys, have been known from not long after precipitation hardening was discovered. Although the compositions of these alloys have stayed within a narrow range over the years, step changes in property combinations have been achieved by optimizing secondary alloying additions (e.g., use of Zr in 7XXX series alloys), aging treatments (e.g., RRA) and modified processing technologies, to name a few. The latter has also resulted in the introduction of thicker product forms and alloys with reduced property anisotropy. The ability to achieve unique properties within the narrow composition space is largely due to innovative processing proprietary to suppliers, but published information, particularly pertaining to patents and supplier data sheets, provides excellent descriptions and insight into the problems and the approach used by the new products to their solution. Mention should also be made of Russian alloys [110,111] many of which contain Sc as a secondary addition for controlling recrystallization and grain size and for increasing the weldability.

Required combinations of properties in materials for structural components were discussed in the first chapter. Generally, one property will have the largest effect in determining performance assuming that all other properties meet their targeted minimum values. These key material properties are compression yield strength for use in upper wing and DADT for lower wing components and fuselage skins. As schematically shown in Fig. 4.47, durability in terms of resistance to corrosion

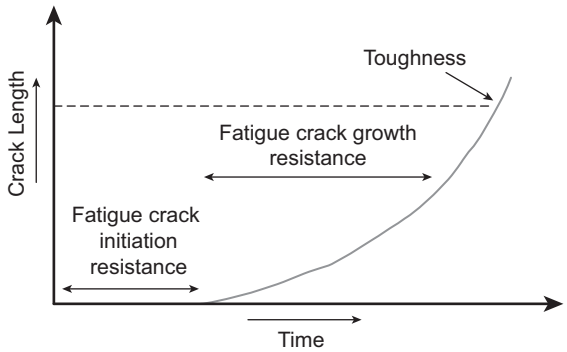


FIGURE 4.47

Schematic of the influence of durability and damage tolerance on life time.

Adapted from T. Warner, R. Dif, J.C. Ehrstrrom, P. Lassince, Improved Durability Aluminium Alloys for Airframe Structures, RTO AVT Workshop on "New Metallic Materials for the Structure of Aging Aircraft", Corfu, Greece, 19–20 April 1999, RTO MP-25, 10–1; 10–6.

and fatigue crack initiation determines the time for nucleation of a crack following which damage tolerance affects its resistance to growth [112]. Once the critical crack length is reached, toughness controls failure.

The 2XXX series alloys are generally chosen for applications requiring DADT and the 7XXX series alloys for strength and for thick section requirements. Al–Li alloys are being developed as low density alternatives for both the systems. In handbooks and supplier data sheets, properties are reported for alloys as a function of temper, product form, orientation, thickness and as typical, minimum, or guaranteed values based on statistical evaluations. Data for representative alloys discussed here have been adapted from many sources that are referenced where necessary. Publications from the Aluminum Association show ongoing registration of new alloys designed for targeted properties to meet airplane design requirements. Registration of the alloy and temper is usually the first step in its commercialization. Commercial alloys discussed in this section are representative of the state-of-the-art and only a snapshot in time. Although modifications, improvements, and new alloys are reported continuously, the following discussion is nevertheless illustrative of their metallurgy.

4.5.1 2XXX SERIES ALLOYS

The first precipitation hardening alloy was discovered in 1906 and patented in 1909. It was based on the Al–Cu–Mg system, contained about 4% Cu, 1% Mg, and 0.7% Mn (all wt%) and formed the basis for the commercial alloy 2017 (Duralumin). Table 4.19 shows the compositions of commercial 2XXX series alloys discussed in this section. Alloys containing Li exhibit distinguishing features and are discussed separately. Alloy 2024, the first to have a yield strength approaching 345 MPa

Table 4.19 Compositions of Commercial 2XXX Series Alloys (wt%)

Alloy	Cu	Mg	Mn	Zr	Fe	Si	Zn	Cr	Ti
2024	4.35	1.50	0.60		0.50	0.50	0.25	0.10	0.15
2024A	4.10	1.35	0.48		0.20	0.15	0.25	0.10	0.15
2124	4.35	1.50	0.60		0.30	0.20	0.25	0.10	0.15
2224	4.10	1.50	0.60		0.15	0.12	0.25	0.10	0.15
2324	4.10	1.50	0.60		0.12	0.10	0.25	0.10	0.15
2524	4.25	1.40	0.58		0.12	0.06	0.25	0.10	0.15
2026	3.95	1.30	0.55	0.15	0.07	0.05	0.10		0.06
2027	4.40	1.25	0.85	0.10	0.15	0.12	0.20		0.08

Cu, Mg, Mn, and Zr are nominal and Fe, Si, Zn, Cr, and Ti are maximum values.Other elements are limited to 0.05 each and 0.15 total maximum.

(50 ksi), was introduced in 1931 and replaced 2017 for general use in airframes. Alloy 2124, with composition similar to 2024, except for lower levels of Fe and Si, was developed subsequently. The higher purity and resulting lower volume fraction of constituent particles improved toughness and enabled thick section plate products with good ductility in the short transverse direction, as shown in Fig. 4.48 [113]. Alloy 2124 in the peak aged T8 temper also has good strength at moderately elevated temperatures. Alloy 2024A was developed in Europe.

Al−Cu−Mg alloys are strengthened by GPB zones in the T3 and T4 tempers and by θ' and Ω (in Ag containing alloys) in the T8 and T6 tempers. Shearable precipitates such as GPB zones slow crack growth by increasing tortuosity and provide high damage tolerance. Thus alloy 2024-T3 with adequate strength and toughness, but high resistance to crack growth was the material of choice for fuselage skins until improved alloys were developed. Alloy 2524 was subsequently developed and selected for the fuselage skin material for Boeing 777 [114]. Compared with 2024-T3, 2524-T3 had similar strength levels but combined both higher toughness and lower crack growth rates resulting from lower levels of crack nucleating particles, as shown in Table 4.20 [95]. Such a combination of properties was achieved by a tight control of composition that included significantly lowering the impurity levels and adjusting the amounts of Cu and Mg in relation to the amounts of Mn, Fe, and Si. By keeping Cu and Mg to their combined level of maximum solubility and by minimizing insoluble constituents containing these elements, both toughness and FCG behavior were improved relative to 2024 [115]. Alloy 2024A, a modification of 2024 with lower levels of Fe and Si and tighter chemical composition, also exhibits higher toughness compared with 2024 [112].

Improved plate and extrusion products for lower wing components include 2324 and 2027 plate alloys and 2224, 2026, and 2027 extrusion alloys. Alloy 2324 is used on the Boeing 777 [114] and 2027 was selected for A380 [116]. Coupled with the much lower Fe and Si than in 2024 and 2124, tight composition

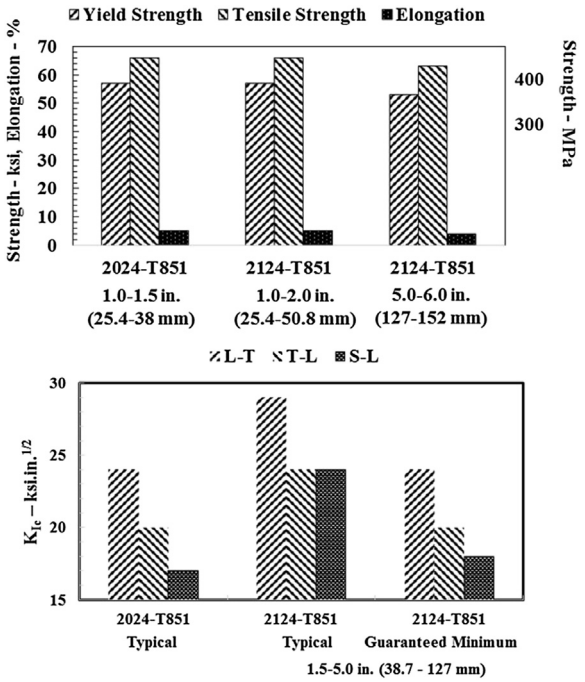


FIGURE 4.48

Properties of commercial 2024-T851 and 2124-T851 plate alloys. (A) Tensile properties (minimum values in the long transverse direction), (B) fracture toughness.

Plotted from data in Alloy 2124 Plate – Technical Data, Alcoa data sheet.

control and improved processing, these alloys possess generally higher strength, toughness and fatigue properties compared with 2024. It should be noted that alloys 2026 and 2027 were the more recently developed among these alloys and have a combination of both Mn and Zr typical of the third generation Al–Li alloys. As discussed earlier in this chapter, a combination of these two elements ensures uniform dispersoid coverage. The importance of tight compositional controls to minimize or eliminate excess solute is also seen in the tighter limits on the elements Ti and Zn. Russian alloy development shows a similar trend by reducing the amounts of Fe and Si and adjusting the chemistry of alloys containing Zr additions [117]. Reducing Fe and Si levels increased strength, toughness,

Table 4.20 Typical Properties of 2524-T3 versus 2024-T3 Sheet

% Increase in Toughness (K_c)	% Decrease in Fatigue Crack Growth Rate (da/dN)
23	61

fatigue life, and resistance to crack growth. The toughness was increased further without lowering other properties by adding Zr and adjusting the levels of Cu and Mg.

4.5.2 6XXX SERIES ALLOYS

The strength of Al−Mg−Si alloys can be increased by the addition of Cu. Compositions of alloys that are used in airframe applications is shown in Table 4.21. The precipitation hardening phases in these alloys are based on β (Mg_2Si) and λ ($Al_5Cu_2Mg_8Si_6$). The alloys have excellent resistance to exfoliation and SCC. Addition of Cu increases IGC susceptibility, which can be reduced by overaging to a T7 type temper. Alloy 6156 has lower Fe than 6056 and was selected for fabricating components by laser beam welding for use in the A380 [116]. For corrosion protection, a clad alloy was developed specifically for 6156 for use in the T6 temper with a 10% higher toughness than bare 6056-T78.

4.5.3 7XXX SERIES ALLOYS

As PH aluminum alloys became preferred materials for airplane structures in the 1930s and 1940s, 2XXX series alloys did not possess sufficient strength to meet airframe design requirements. Development studies in the Al−Zn−Mg−Cu system in the 1940s identified an alloy with the nominal composition Al−6.5Zn−1.8 Mg−1.5Cu (wt%), which is within the range of many of the current commercial alloys [109]. The first alloy that was continuously produced from 1940 had the composition Al−7.5Zn−1.6Mg−0.7Cu (wt%), which was registered as 7076 in 1954.

Alloy 7075 was introduced in 1943 and registered in 1954. It contains Cr that precipitates as the E phase ($Al_{12}Mg_2Cr$) and stabilizes the dynamically recovered substructure in plate, extrusions, and forgings. Recrystallization occurs in sheet due to the cold work during processing, but the dispersoids pin grain boundaries resulting in flat, pancake shaped grains elongated in the rolling direction, as discussed in detail earlier. Alloys containing Cr are quench sensitive and susceptible to SCC in the peak aged temper. All subsequent alloy development in the Al−Zn−Mg−Cu system has been aimed at achieving the highest possible strength with

Table 4.21 Compositions of Commercial 6XXX Series Alloys (wt%)

Alloy	Mg		Si		Cu		Mn		Cr	Zn		Ti	Fe
6013	0.8	1.2	0.6	1	0.6	1.1	0.2	0.8	0.1	0.25		0.1	0.5
6056	0.6	1.2	0.7	1.3	0.5	1.1	0.4	1	0.25	0.1	0.7	–	0.5
6156					0.7	1.1	0.4	0.7				0.2[a]	0.2

Values given as specification range. A single value indicates the maximum allowed.
[a] *Zr + Ti.*

optimum corrosion resistance and durability/damage tolerance properties in thick sections while minimizing anisotropy of properties. Many alloy compositions have been registered and most of the alloys are available in multiple product forms and tempers. The resulting diversity of microstructures and the way property data is reported preclude a comprehensive comparison of all the alloys. Properties are reported in many formats such as typically expected or guaranteed minimum or based on statistically derived design allowable values. Often, the direction and the product form for which the property is reported are not always specified. In the following comparisons of the alloys, their properties and the underlying metallurgical mechanisms, every effort is made to ensure that data of similar pedigree are compared.

Following the introduction of alloy 7075-T6, development of 7XXX series alloys and related processing to meet the needs for airframe design has progressed in the approximate and often overlapping sequence described below. The compositions of these alloys are shown in Table 4.22.

- Alloys for higher strength in the T6 temper, resulting in 7079 and 7178.
- Overaged tempers to increase SCC resistance, resulting in 7075-T73.
- Higher purity alloys for controlled toughness, resulting in 7175 for forgings and 7475 for all products.
- Alloys with the strength of 7075-T6 and SCC resistance of 7075-T73, resulting in 7010 and 7050 that can also be produced in thick sections.
- Elimination of mid-plane porosity in thick alloys, resulting in 7050 that can be fabricated in thicknesses up to about 250 mm (10 in.).
- Alloys with better properties in thick sections than 7050, resulting in 7040 (up to 9 in., 225 mm), 7140 (up to 10 in., 250 mm), and 7065 and 7099 (up to 6 in., 150 mm).
- Heat treatments for higher strength while maintaining other properties at adequate levels, resulting in 7449-T79 and the retrogression and reaged 7150-T77 and 7055-T77 in extrusion and plate.
- Thick alloy with very low through-thickness anisotropy, resulting in 7085.
- Very high strength extrusion alloys, resulting in 7136-T76.

Each of the above developments will be discussed briefly using properties of commercial alloys and the processing and microstructures responsible for achieving them. A historical review published in 1976 described how evolution of aircraft design concepts, size, and manufacturing methods influenced the development of Al–Zn–Mg–Cu alloys [118]. This review stated that if strength were the only criterion for alloy selection without the requirements of having to consider stress concentrations and environmental effects, compositions that were available 40 years earlier would have been adequate.

4.5.3.1 Strength Improvements Relative to 7075-T6

Higher strength compared with 7075-T6 was achieved by increasing the amounts of Zn, Mg, and Cu while maintaining the levels of all other elements. Strength of alloy

Table 4.22 Compositions of Commercial 7XXX Series Alloys (wt%)

Alloy	Zn		Mg		Cu		Cr		Zr		Mn	Ti	Fe	Si
7075	5.1	6.1	2.1	2.9	1.2	2	0.18	0.28			0.3	0.2	0.5	0.4
7175	5.1	6.1	2.1	2.9	1.2	2	0.18	0.28			0.1	0.1	0.2	0.15
7475	5.2	6.2	1.9	2.6	1.2	1.9	0.18	0.25			0.06	0.06	0.12	0.1
7178	6.3	7.3	2.4	3.1	1.6	2.4	0.18	0.28			0.3	0.2	0.5	0.4
7010	5.7	6.7	2.1	2.6	1.5	2	0.05		0.1	0.16	0.1	0.06	0.15	0.12
7050	5.7	6.7	1.9	2.6	2	2.6	0.04		0.08	0.15	0.1	0.06	0.15	0.12
7150	5.9	6.9	2	2.7	1.9	2.5	0.04		0.08	0.15	0.04	0.06	0.15	0.12
7040	5.7	6.7	1.7	2.4	1.5	2.3	0.04		0.05	0.12	0.04	0.06	0.13	0.1
7140	6.2	7	1.5	2.4	1.3	2.3	0.04		0.05	0.12	0.04	0.06	0.13	0.1
7065	7.1	8.3	1.5	1.8	1.9	2.3	0.04		0.05	0.15	0.04	0.06	0.08	0.06
7085	7	8	1.2	1.8	1.3	2	0.04		0.08	0.15	0.04	0.06	0.08	0.06
7081	6.9	7.5	1.8	2.2	1.2	1.8	0.04		0.06	0.15	0.25	0.06	0.15	0.12
7055	7.6	8.4	1.8	2.3	2	2.6	0.04		0.08	0.25	0.05	0.06	0.15	0.1
7449	7.5	8.7	1.8	2.7	1.4	2.1			0.05	0.15	0.2	0.08	0.15	0.12
7056	8.5	9.7	1.5	2.3	1.2	1.9					0.2		0.12	0.1
7136	8.4	9.4	1.8	2.5	1.9	2.5	0.05		0.1	0.2	0.05	0.1	0.15	0.12
7099	7.4	8.4	1.6	2.3	1.4	2.1	0.04		0.05	0.15	0.04	0.06	0.15	0.12
7042	6.5	7.9	2	2.8	1.3	1.9	0.05				0.3		0.2	0.2

Values given as specification range. A single value indicates the maximum allowed.

7178-T6 was about 10% higher than that of 7075-T6 due to the higher volume fraction of the strengthening precipitates. However, as to be expected, the toughness of this alloy was lower and the alloy is no longer selected for new designs.

4.5.3.2 Development of T73 Temper

Al–Zn–Mg–Cu alloys aged to the peak strength, T6 temper, are susceptible to SCC. Optimization of the two step aging treatment, initially used to reduce the total aging cycle time for manufacturing, resulted in the T73 temper, which produced the best SCC resistance in alloy 7075, as shown in Table 4.23 [80]. High resistance to SCC is achieved, albeit with a concurrent strength reduction, by aging first at a low enough temperature to precipitate GP zones and then at a higher temperature to nucleate η' from these zones and coarsen the grain boundary precipitates.

The SCC ranking in the ST direction is improved in 7075-T73 over 7075-T6. The progressive increase in SCC resistance can be seen in the better ranking for 7050-T74 than for 7050-T76, which has adequate resistance to EC.

4.5.3.3 Higher Purity Alloys for Controlled Toughness

Along with poor resistance to SCC, 7075-T6 products also exhibited anisotropy of mechanical properties. Alloy 7175 was initially developed to increase the ductility in the short transverse direction by maintaining the same levels of the precipitation hardening elements but lowering Fe, Si, and Mn to reduce the undesirable second phases. In related studies, alloys with a given level of solute elements were observed to possess higher toughness at peak strength compared with alloys with higher solute that were underaged or overaged to the same strength level. This indicated that the partially coherent precipitates provided the best combination of strength and toughness. Based on this, alloy 7475 was developed by a further reduction of impurity

Table 4.23 SCC Ratings for 7075 and 7050 Alloys

Alloy	Test Direction	Rolled Plate	Extrusions
7075-T73	L	A	A
	LT	A	A
	ST	A	A
7075-T6	L	A	A
	LT	B[a]	B[a]
	ST	D	D
7050-T76	L	A	A
	LT	A	A
	ST	C	C
7050-T74	L	A	A
	LT	A	A
	ST	B	B

A, *very high;* B, *high;* C, *intermediate;* D, *low;* L, *longitudinal;* LT, *long transverse;* ST, *short transverse.*
[a] *Rating will be C for thicker sections.*

elements and slight adjustments to Zn, Mg, and Cu. The strength and toughness of alloys 7075 and 7475 plate and for 7075 and 7475 forgings are shown in Fig. 4.32. 7475 has better toughness than 7075 plate in all tempers and orientations and 7175 in the LT and SL orientations for forgings.

4.5.3.4 Development of Alloys With High Strength and SCC Resistance

Demand for restoring the strength level of 7075-T6 combined with its SCC resistance in T73 temper spurred the development of alloys that led to the introduction of 7010 and 7050. Alloy development efforts included varying Zn/Mg ratios, amount of Cu, type and amount of dispersoid forming elements and control of impurities. Addition of 0.3−0.4 wt% of Ag was also considered, but the benefits did not warrant the added cost [118]. Compared to 7075, the resulting alloy 7050 had higher Zn/Mg ratio, higher level of Cu, Zr instead of Cr, and lower levels of impurities. The mechanism of achieving higher strength after the second step aging was later attributed to the effects of higher amount of Cu close to the limit of its combined solid solubility with Zn and Mg. Cu remains in solution during the first aging step, raises the GP zone solvus and participates in the precipitation reaction during the second step [34]. Alloy 7050 possessed superior combination of strength, toughness, and SCC resistance resulting from higher solute, hardening effect from Cu, decrease in the degree of recrystallization due to Zr, which reduced quench sensitivity and along with reduced impurities also increased toughness, particularly for thick sections. These improvements are shown in Fig. 4.49 and Table 4.24 [119]. The minimum fracture toughness values for all orientations for alloy 7050, shown in Table 4.24, are better than those for alloy 7075 in all tempers, shown in Fig. 4.32. Alloy 7010 developed with the same goals, had lower levels of Cu to improve ingot fabricability.

4.5.3.5 Elimination of Mid-Plane Defects

The generally higher properties of 7050 and its lower quench sensitivity enabled the development of thick sections. However, the pattern of segregation of alloying elements during solidification and the inability to impart the full effects of

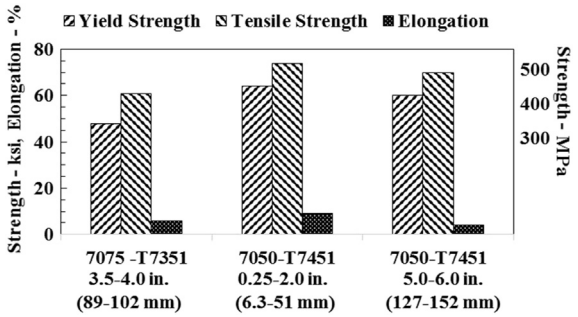


FIGURE 4.49

Tensile properties of alloys 7075 and 7050 (properties are minimum values in the LT direction).

Plotted from data in Alloy 7050 Plate and Sheet—Technical Data, Alcoa data sheet.

Table 4.24 Minimum Fracture Toughness of Alloy 7050 [119]

Fracture Toughness, K_{Ic} ksi.in.$^{1/2}$ (MPa.m$^{1/2}$)			L-T	T-L	S-L
7050-T7451	1–2 (25.42–50.80) 5–6 (127.03–152.40)	Guaranteed minimum values	29 (31.96) 24 (26.4)	25 (27.5) 22 (24.2)	– 21 (23.1)

thermomechanical processing in the mid-thickness regions resulted in both through thickness anisotropy and lower properties with increasing thickness. The effects of porosity were eliminated by improved processing, as shown in Figs. 4.26 and 4.33, enabling the production of plate products up to about 250 mm (10 in.) thick.

4.5.3.6 Improvements in Thick Products Beyond 7050

Further alloy development focused on increasing strength in thick products beyond that of 7050 while maintaining other properties. Alloy 7040 with lower Mg and Cu and tighter control of Zr and impurities has lower quench sensitivity compared with 7010 and 7050, resulting in higher strength and toughness [120]. Residual stresses in thick products cause manufacturing issues such as distortions during machining. Control of residual stresses in 7040 plate products mitigates this effect. 7040 was selected for fuselage frames and wing spars on A380 [116]. Properties of recently developed alloys for thick plate products are shown in Fig. 4.50 [120–122]. Alloy 7040 is produced in thicknesses up to 9 in. (225 mm) and 7140 up to 10 in. (250 mm).

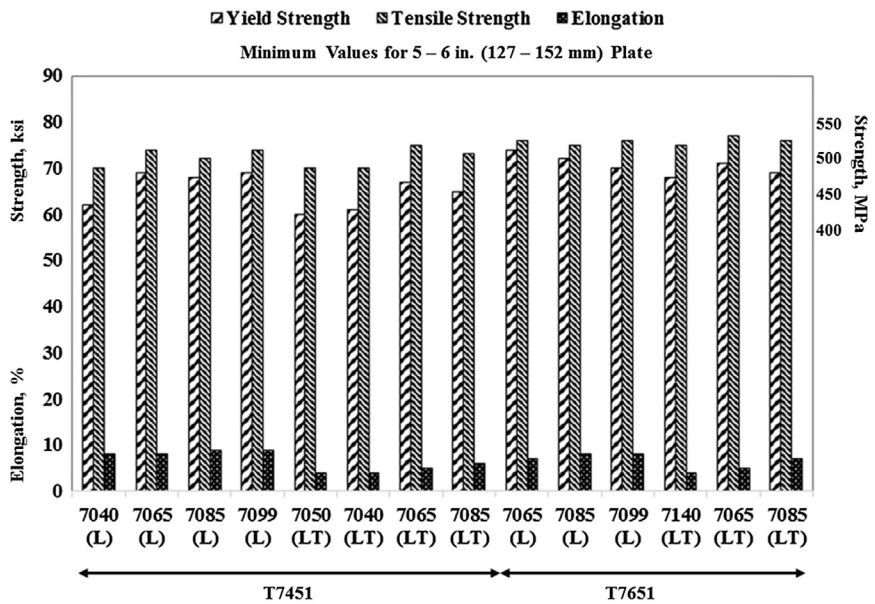


FIGURE 4.50

Properties of higher strength 7XXX alloys in thick gauges.

4.5.3.7 Ultrahigh Strength Alloys

The development of the RRA treatment resulted in a significant increase in the yield strength of 7XXX series alloys. Application of this treatment to alloy 7150 plate and extrusion resulted in combining the corrosion resistance of the overaged temper with the strength achievable by peak aging. The benefits of this treatment, specified as the T77 temper, are shown by the property data in Fig. 4.51, which compare the properties of 7150-T7751 plate with those of 7075 and 7050 in various tempers [123]. The improvement in the EC resistance of 7150 by aging to the T7751 temper is not accompanied by loss of strength.

Increasing the Zn/Mg ratio and Cu content resulted in the development of alloy 7055, which in the T77 temper is stronger than 7150 while maintaining other properties, as shown in Table 4.25 [124]. 7055-T7751 was selected for the upper wing panels for Boeing 777. A very slight overaging, designated as the T79 temper, was applied to alloy 7449 and selected for the Airbus A380. Alloys such as 7056 and 7136 with much higher strength have been developed for plate and extrusion, respectively, by increasing the Zn content further.

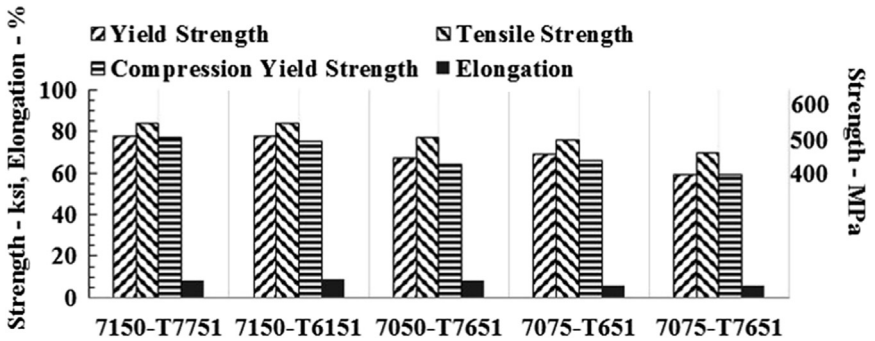


FIGURE 4.51

Properties of 7075, 7050, and 7150 plates: 1 in. (25.4 mm) gauge (minimum values in the L direction).

Table 4.25 Typical Properties of 7150-T7751 and 7055-T7751 Plate 1 in. (25.4 mm) Gauge (Long Transverse Direction)

Alloy and Temper	Yield Strength ksi (MPa)	Tensile Strength ksi (MPa)	Compression Yield Strength ksi (MPa)	Elongation (%)
7150-T7751	82 (565)	88 (607)	87 (600)	11
7055-T7751	89 (614)	93 (641)	94 (648)	10

4.5.3.8 Minimizing of Anisotropy

Alloys exhibiting very high strength such as 7055 are presently limited in product thickness due to special heat treatment requirements. Further, the strength of alloys in heavy sections decreases with increasing thickness due to the unavoidable quench sensitivity. Segregation of alloying elements during solidification and some recrystallization also cannot be avoided, which further contributes to anisotropy. However, unlike other alloys, strength of 7085 plate is essentially the same in the thickness range from about 100−175 mm (4−7 in.). The strength of overaged 7085 in the L and LT directions are also 70 and 55 MPa (10 and 8 ksi) higher, respectively, than for comparable 7050 products. Alloy 7085 is based on US patent 6972110, which describes a composition range of 6−10 Zn, 1.2−1.9 Mg, 1.2−2.2 Cu, and Mg $\leq$ (Cu + 0.3) (all in wt%) [125]. Only alloys 7065 and 7085 satisfy these requirements. The unique properties of 7085 have been rationalized in a study by Boselli et al., as follows [126].

- Based on thermodynamic modeling, equilibrium temperature for the onset of melting increases and the solvus for M ($MgZn_2$) and S (Al_2CuMg) phases decreases in the direction of increasing Zn content, i.e., from 7050 to 7085. These factors result in a wider single phase region and reduced quench sensitivity that allows for a slower quench for 7085 compared with 7050, as also shown in Fig. 4.19. The resulting lack of S phase precipitation in grain boundaries also results in higher toughness in 7085.
- The higher quench sensitivity of 7050 causes some GP zone precipitation during quench. Thus the strength of as-quenched 7050 will be higher after slower cooling. As aging proceeds, the higher concentration of quenched-in vacancies and higher solute available for precipitation in the faster quenched alloy result in higher peak strength than in the slower quenched alloy. In contrast, the lack of quench sensitivity in 7085 results in peak strength values that is near-identical and only slightly higher in the fast quenched alloy.
- Untransformed clusters of solute atoms have been observed to persist with growing η' precipitates during aging of 7050. The concentration of vacancies bound to these clusters would be higher in the higher solute alloy 7085. As aging proceeds past peak strength, the increase in coarsening kinetics due to release of these vacancies is higher in 7085 than in 7050. This effect will be more pronounced with decreasing plate thickness explaining the decreasing yield strength at quarter-thickness in 7085 plate below about 3 in. and the relative lack of variation in such properties in the higher thickness range.

4.5.3.9 Summary of 7XXX Series Alloy Development

Referring to the representative compositions listed in Table 4.22, the metallurgy of Al−Zn−Mg−Cu system has enabled the development of alloys with many combinations of properties within the narrow composition space bounded by 5.1−9.7 Zn, 1.2−2.9 Mg, and 1.2−2.5 Cu (all wt%) with control of secondary and impurity elements and use of improved processing approaches. Fig. 4.52 provides a timeline

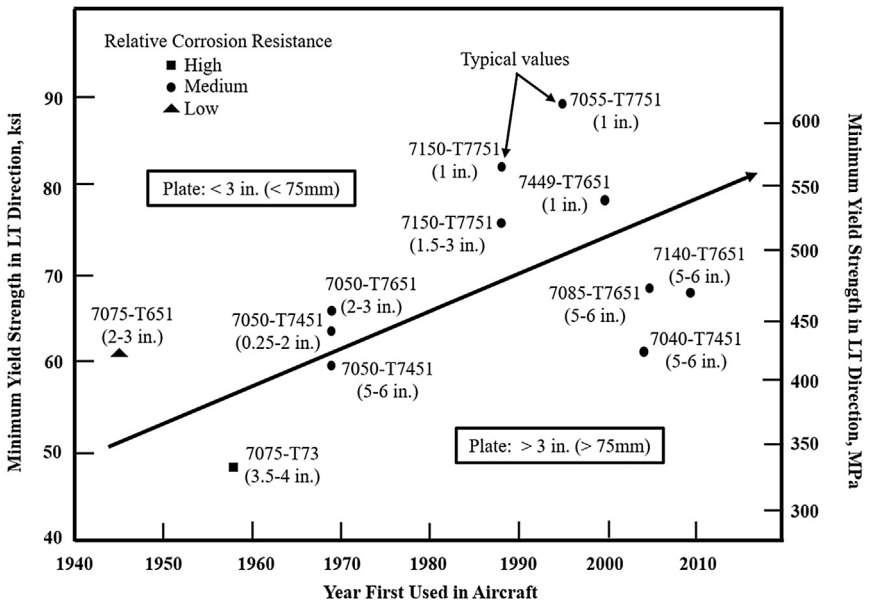


FIGURE 4.52

Evolution and service insertion of 7XXX series plate alloys.

of the property improvements in 7XXX plate alloys and the year of their insertion in service.

The scope for further alloy development is promising, particularly using computational modeling tools guided by advanced characterization techniques and by alloying with elements such as Sc. Alloys have been developed in Russia by adding combinations of Ag and Sc to Al−Zn−Mg−Cu−Zr alloys [127]. Ag accelerates the kinetics of overaging, increases the volume fraction of η and size of the grain boundary precipitates, and reduces the PFZ zone width. Sc substitutes for Zr in Al_3Zr and along with Ag improves strength, toughness, and fatigue resistance. A US developed Sc containing alloy designated as 7042 has been registered. The discussion in this section was focused on the metallurgy as it principally applies to flat rolled sheet and plate products. The grain flow characteristics of forgings provide substantial benefits, but the availability of thicker, high quality plate, enables machining of large components. However, the same metallurgy applies to other products.

4.5.4 AL−LI ALLOYS

Table 4.26 lists the compositions of the current Al-Li alloys (third-generation), available product forms and the non-Li alloys that they can potentially replace [128,129]. Lower density Al−Li alloys are attractive for aerospace use, particularly for space applications for which weight reduction is critical. Alloy 2195 replaced 2219 on

Table 4.26 Compositions, Product Forms, and Potential Applications for Third Generation Al—Li Alloys

Alloy	Li		Cu		Mg		Zr		Mn		Ag		Zn		Ti	Fe	Si
2050	0.7	1.3	3.2	3.9	0.2	0.6	0.06	0.14	0.2	0.5	0.2	0.7	0.25		0.1	0.1	0.08
2055	1	1.3	3.2	4.2			0.05	0.15	0.1	0.5	0.2	0.7	0.3	0.7		0.l	0.07
2060	0.6	0.9	3.4	4.5	0.6	1.1					0.05	0.5	0.3	0.5		0.07	0.07
2065	0.8	1.5	3.8	4.7	0.25	0.8			0.15	0.5	0.15	0.5	0.3			0.1	0.1
2076	1.2	l.8	2	2.7	0.2	0.8	0.05	0.16			0.15	0.4				0.1	0.1
2195	0.8	1.2	3.7	4.3	0.25	0.8	0.08	0.16	0.25		0.25	0.6	0.25			0.15	0.12
2196	1.4	2.1	2.5	3.3			0.04	0.18	0.35				0.35				
2296	1.3	1.9	2.1	2.8	0.2	0.8			0.05	0.5			0.25				
2297	1.1	1.7	2.5	3.1	0.25		0.08	0.15	0.l	0.5			0.05		0.12	0.1	0.1
2397													0.05	0.15			
2098	0.8	1.3	3.2	3.8	0.25	0.8	0.04	0.18	0.35		0.25	0.6	0.35		0.1	0.15	0.12
2198	0.8	1.1	2.9	3.5					0.5		0.l	0.5				0.1	0.08
2099	1.6	2	2.4	3	0.l	0.5	0.05	0.12	0.1	0.5			0.4	1		0.07	0.05
2199	1.4	l.8	2.3	2.9	0.05	0.4							0.2	0.9			
Product forms	Sheet and plate				2198, 2060, 2098, 2199												
	Plate				2050, 2055, 2099, 2195, 2297, 2397												
	Extrusions				2055, 2065, 2076, 2099, 2196, 2296												
	Forgings				2050, 2060												

Product	Alloy/Temper	Substitute for
Sheet	2098-T851, 2198-T8, 2060-T8E30 (damage tolerant/medium strength)	2024-T351, 2524 T3/T351
Plate	2199-T86, 2050-T84, 2060-T8E86 (damage tolerant)	2024-T351, 2324-T39, 2624-T351, 2624-T39
	2297-T87, 2397-T87 (medium strength)	2124-T851
	2099-T86 (medium strength)	7050-T7451, 7X75-T7XXX
	2050-T84, 2055-T8X, 2195-T82 (high strength)	7150-T7751, 7055-T7751, 7055-T7951, 7255-T7951
	2050-T84 (medium strength)	7050-T7451
Forgings	2050-T852, 2060-T8E50 (high strength)	7175-T7351, 7050-T7452
Extrusions	2099-T81, 2076-T8511 (damage tolerant)	2024-T3511, 2026-T3511, 2024-T4312
	2099-T83, 2099-T81, 2196-T8511, 2055-T8E83, 2065-T8511 (medium/high strength)	7075-T73511, 7075-T79511, 7150-T76511, 7175-T79511, 7055-T77511, 7055-T79511

the Space Shuttle external tank reducing its weight by 7500 pounds (3400 kg). Alloy 2196 is used in the floor beams of the A380 airplane. Following the introduction of the first-generation alloys, development in the 1980s focused on maximizing the amount of Li to achieve as low a density as possible concomitant with maintaining the other properties. Some of these alloys nominally had more Li than Cu or Mg, and with Li being the principal alloying element, were classified as 8XXX series alloys. Although these second-generation alloys exhibited up to about 10% lower density than state-of-the-art 7XXX series alloys, they suffered from in-plane and through-thickness anisotropy of properties and low values of fracture toughness and found only very limited applications. Processing modifications to alter the matrix microstructures in these alloys have largely eliminated the problems of the earlier alloys. The recent publication "Aluminum-Lithium Alloys: Processing, Properties and Applications" [130] provides a detailed review of the history of Al–Li alloy development, phase diagrams, processing, microstructures, properties, and applications. The compositions of the representative first and second generation Al–Li alloys are shown in Table 4.27. Included for comparison are the 014XX alloys developed in the Soviet Union, some of which have Mg or Li as the principal alloying element, contain Sc, and as such can be classified in the 5XXX or 8XXX series, respectively.

All third-generation Al–Li alloys have less than 2% Li, <1% Mg, and varying Cu up to 4.2% (all wt%). Most also contain Ag. They are primarily strengthened by T_1 with additional contributions from θ' or δ' depending on the relative levels of Cu and Li. Mg and Ag affect precipitation kinetics. High strength is developed only after cold work prior to aging and all these alloys are used in the T8 temper. With a few exceptions, all contain both Zr and Mn for forming dispersoids. Impurities are very tightly controlled to achieve better toughness. In this framework, the

Table 4.27 Nominal Compositions (wt%) of Li-Containing Alloys

	Alloy	Li	Cu	Mg	Zr	Mn	Other
First generation	2020	1.2	4.5			0.5	0.2 Cd
	VAD23[a]	1.15	5.15			0.6	0.18 Cd
	01420[a]	2.1	5.2		0.11	0.5	
	01421[a]	2.1	5.2		0.11		0.17 Sc
Second generation	2090	2.1	2.7		0.11		
	2091	2.0	2.0	1.3	0.11		
	8090	2.4	1.2	0.8	0.11		
	8091	2.6	2.0	0.8	0.11		
	01430[a]	1.7	1.6	2.7	0.11		
	01440[a]	2.4	1.5	0.8	0.11		
	01450[a]	2.1	2.9		0.11		
	01460[a]	2.25	2.9		0.11		0.1 Sc

The levels of the impurity elements Fe and Si are maintained at less than 0.1%.
[a] *Russian alloys.*

properties of 2099 and 2199 are attributed to the following factors, with the mechanism of their actions shown schematically in Fig. 4.53 [32]:

- Strengthening by T_1 (Al_2CuLi), θ' (Al_2Cu type), and δ' (Al_3Li)
- Presence of equilibrium T_1 and T_2 (Al_6CuLi_3), β' (Al_3Zr), and $Al_{20}Cu_2Mn_3$, which all improve toughness
- Grain boundary precipitation of T_1 and T_2 will reduce toughness
- Control of recrystallization by β'
- Control of grain size and texture by $Al_{20}Cu_2Mn_3$ and dispersoids
- Improvement of fatigue properties by incoherent $Al_{20}Cu_2Mn_3$ and coherent δ'
- Improvement of corrosion resistance by Zn, which remains in solid solution

Alloy 2060 is strengthened only by T_1. Alloys 2060, 2198, and 2199 in sheet form are all candidates for fuselage skin applications. 2060 in the T8 temper is superior to 2524-T3 in terms of strength, toughness, and crack growth rates. As shown in Table 4.26, there are several candidate alloys for plate applications. These alloys also exhibit much lower through thickness and in-plane anisotropy of properties compared with the second-generation alloys. The effect of the type of strengthening precipitates on the anisotropy is seen by comparing the properties of alloys 2060 and 2199, shown in Table 4.28. The thin T_1 phase in 2060 results in higher anisotropy than in 2199, although it is much lower than in second generation Al–Li alloys [131].

Most of the third generation Al–Li alloys have been developed only in slightly more than a decade, which is a relatively short time compared to the long history

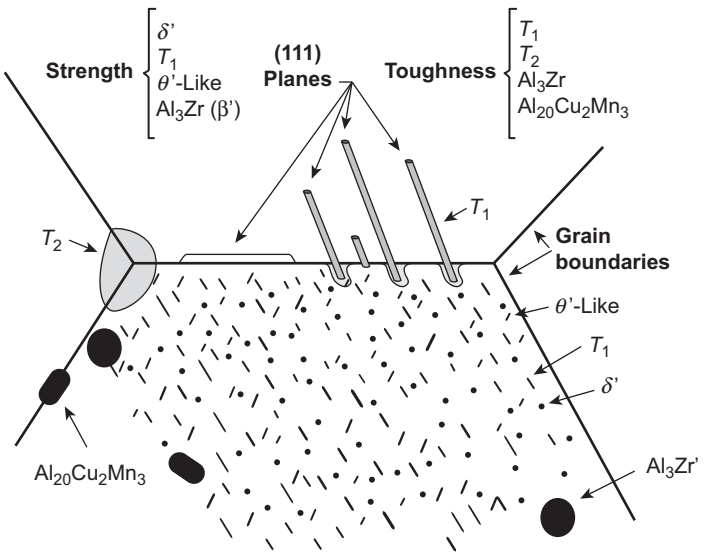


FIGURE 4.53

Microstructure schematic in Al–Li alloys 2099 and 2199 [32].

Table 4.28 Properties of 2060 and 2199

Alloy	Gauge, mm (in.)	Yield Strength, MPa (ksi), Anisotropy (%)				Tensile Strength, MPa (ksi), Anisotropy (%)			
		L	LT	45°	Anisotropy	L	LT	45°	Anisotropy
2199-T86	19–31.7 (0.75–1.25)	424 (61)	420 (61)	385 (56)	5.2	461 (67)	467 (68)	436 (63)	1.9
2060-T8E86	30–36.8 (1.18–1.45)	520 (75)	488 (71)	454 (66)	9.4	544 (79)	545 (79)	510 (64)	3.1

% YS anisotropy = $\{[2 \times YS(L) - YS(LT) - YS(45°)]/2 \times YS(L)\} \times 100$
% TS anisotropy = $\{[2 \times TS(L) - TS(LT) - TS(45°)]/2 \times TS(L)\} \times 100$

Alloy	Gauge (mm)	t/2 Plane			t/4 Plane			Through-Thickness Gradient, $Value_{t/2} - Value_{t/4}$	
		YS, MPa (ksi)	TS, MPa (ksi)	Elongation (%)	YS, MPa (ksi)	UTS, MPa (ksi)	Elongation (%)	YS, MPa (ksi)	UTS, MPa (ksi)
2199-T86	19–31.7 (0.75–1.25)	414 (60)	451 (65)	12.7	409 (59)	445 (65)	13.4	5 (1)	6 (1)
2060-T8E86	30–36.8 (1.18–1.45)	510 (74)	534 (77)	14.4	532 (77)	553 (80)	12.4	−22 (−3)	−19 (−3)

L, *longitudinal;* LT, *long transverse. Data for 2199 and 2060 are averages of 10 and 6 lots of plates, respectively.*

of (non-Li) 2XXX and 7XXX series alloys. As such, data in handbooks and published literature is sparse. With further development and implementation, data are expected to be available for the comprehensive understanding of the metallurgy of these alloys.

4.5.5 SUMMARY

Despite the limitations imposed by the number of available alloy systems, narrow composition spaces, and choice of processing approaches, a remarkable number of wrought PH aluminum alloys continue to be developed. This is also spurred in part by the increasing use of competing materials. In response, the availability and ease of application of computational modeling coupled with the vast data generated to date can be expected to drive the alloy development trend. Possibilities for using both traditional and nontraditional approaches for this goal are discussed in the next section.

4.6 ALUMINUM ALLOY AND PRODUCT DESIGN

The status of designing new alloys for airframe applications using semiempirical and physics-based approaches was discussed in brief in the third chapter. Much of new aluminum alloy design has relied on the former approach. Although computational models are increasingly used to optimize alloy compositions and processing parameters, PH aluminum alloys lag steels in their application across the entire length scale of materials behavior (at least as discerned from published information). However, even in steels, computational alloy design is still generally based on existing composition and processing spaces. Referring to Table 4.6 and Fig. 4.28, models for solidification (segregation of alloying elements) and homogenization (dispersoid precipitation) are well developed. For thermomechanical processing (microstructure and texture evolution), NHT aluminum alloys have received more emphasis, mainly due to their reliance on work hardening for strength and the importance of texture on forming operations. With the continuous generation of thermodynamic databases, ability to predict phase diagrams and precipitation reactions is improving. The challenges to modeling the latter were described in detail earlier. Yield strength, fracture toughness, and the effects of some forms of corrosion such as pitting can also be predicted.

This section discusses the approaches to both new aluminum alloy design and the current integrated modeling and simulation efforts to "tailor" structures that satisfy many of the design "drivers" listed in Table 4.2 [6]. A successful example of the latter is the design and manufacture of unitized, damage tolerant structures while mitigating the undesirable effects residual stresses [132,133].

4.6.1 ALUMINUM ALLOY DESIGN

Historic development of aluminum alloys for high performance structures has proceeded along two independent paths, the first focusing on improvements to wrought

PH aluminum alloy families already in use and the second on alternative alloy systems. Both approaches have also attempted to benefit from nontraditional processing with mixed success. This section discusses the progress made to date in these areas emphasizing the underlying metallurgy and concludes with remarks on the prospects for future alloy design. A later chapter is devoted to alloy design taking advantage of the manufacturing and performance efficiencies offered by techniques such as additive manufacturing, friction stir welding, and related hybrid processes.

Nontraditional processing approaches have been used to develop new alloys not possible by traditional methods and for imparting novel microstructures to existing alloys. In this regard, significant research and development have been carried out to increase the strength and other properties of aluminum alloys by mechanisms other than precipitation hardening. Examples include producing ultrafine grains by severe plastic deformation (SPD), high volume fractions of fine scale dispersions by rapid solidification processing, reinforcement with ceramic particles, and nanophase alloys by cryomilling. Property improvements achievable by some of these methods can be estimated from models for strengthening, as follows.

4.6.1.1 Work Hardening and Grain Refinement

The strength of pure Al can be increased by work hardening and grain refinement. Increasing the dislocation density, ρ, to $\approx 10^{14} - 10^{16}/\text{m}^2$ by severe cold working would increase the yield stress, $\Delta\sigma_\rho$, by about 1 GPa, based on the following:

$$\Delta\sigma_\rho = MGb\alpha\rho^{0.5} \tag{4.19}$$

where M is the Taylor factor ≈ 3, α is about 0.33, G is the shear modulus for Al $\approx$ 25.5 GPa and b is the Burgers vector for Al $\approx$ 0.28 nm.

The grain size of Al can be reduced to less than 100 nm by SPD [134]. Using the Hall–Petch relationship (Eq. 4.7) and assuming a value of 0.1 MPa $\text{m}^{0.5}$ for k, strength increase due to grain size reduction to 100 nm is estimated to be $\approx$300 MPa. SPD can be applied to all alloys in principle, as has been reported for several Al alloys including 7075 whose strength was increased to about 1 GPa with a ductility of nearly 5% following SPD of the solution treated and quenched alloy by high pressure torsion [134]. The strength increase to 1 GPa, which cannot solely result from the average 26 nm grain size, was attributed to a hierarchy of the nanostructures in the material experimentally observed by a combination of advanced X-ray, electron microscopy, and atom probe tomography. The microstructural hierarchy consisted of high dislocation density, subnanometer intragranular solute clusters, two geometries of intergranular nanostructures, and grains tens of nanometers in size. The strength of these alloys was attributed to interactions of dislocations with the nanostructural hierarchy. Intragranular solute clusters, each with a few solute atoms, contribute to strengthening similar to that observed in the early stages of aging of traditional PH aluminum alloys. These clusters may also stabilize the dislocation structure. The intergranular clusters can stabilize the grain boundaries in the nanostructure and resist embrittlement. Ultrafine grain sizes can also

be produced by techniques such as by friction stir processing and the properties of these structures will be discussed in a subsequent chapter.

4.6.1.2 Solid Solution Strengthening

Among the alloying elements with appreciable solid solubility in Al (Table 4.7), Mg provides the highest strengthening. Increase in yield strength, $\Delta\sigma_{ss}$, provided by 2 wt % Mg (solubility limit at room temperature) in solid solution is estimated as 75 MPa from

$$\Delta\sigma_{ss} = \left(MG\varepsilon c^{0.5}\right)/700 \tag{4.20}$$

where c is the concentration in at.% of Mg in solid solution and the constant ε is experimentally determined to be 0.38 for Mg.

4.6.1.3 Dispersion Strengthening

The basis for current PH aluminum alloys is the precipitation from SSSS obtained by quenching from the single phase region below the solidus. A SSSS can also be obtained by rapidly cooling the alloy from the liquid state, which enables the retention in solution of otherwise insoluble elements such as Fe. This "rapid solidification processing" (RSP) approach is the basis for producing Al alloys strengthened by 0.25–0.35 volume fraction of dispersed particles, with average diameter of about 50 nm [135]. The intermetallic dispersions form during aging at a temperature above that used for precipitation hardening. Their volume fraction is also much higher than that of the precipitates in traditional alloys, which is about 0.05. The alloys possess submicrometer grain sizes that when superimposed with dispersion strengthening provide good strength at room temperature. For an Al–Fe–V–Si alloy with a dispersion volume fraction, f, of 0.27 in a size range of 40–80 nm [136], the interparticle spacing, L, is estimated to be $\approx$100 nm from the following

$$L = 1.25r\left(\frac{2\pi}{3f}\right)^{0.5} \tag{4.21}$$

where f is the volume fraction and r is the particle radius, for which the average value of 30 nm is used. The Orowan strengthening from this dispersion is estimated from Eq. (4.5) to be 360 MPa. The strengthening from 500 nm grains is estimated from Eq. (4.7) to be about 140 MPa. The superposition of these two contributions is obtained from Eq. (4.11) as their sum, which is 500 MPa. If the fine grains were to be considered as strong obstacles, the superposition will be given by the square root of the sum of the squares of the individual contributions. In this case, the strength is 385 MPa. Due to the extremely low diffusivity of elements such as Fe in Al, the intermetallic dispersions are resistant to coarsening. Thus these alloys retain a substantial fraction of their strength at elevated temperatures where PH alloys lose their strength rapidly.

Other past developments include the use of rapid solidification to improve the properties of PH 7XXX series alloys by using elements such as Co and Ni to

form dispersoids. Alloys with high modulus and strength levels comparable to PH Al alloys have been developed by reinforcing Al with dispersions of particulate, principally SiC. These approaches have been successful in meeting the needs for limited applications requiring, for example, higher stiffness or higher strength at cryogenic and moderately elevated temperatures. The ability to scale up to producing alloys with the combination of properties in the size range of mill products required for large structures has only been possible with wrought, ingot metallurgy aluminum alloys for which significant manufacturing infrastructure, knowledge base, and application experience exist.

4.6.2 NEW ALLOY DESIGN IN THE TRADITIONAL COMPOSITION SPACE

The previous section discussed the metallurgical basis for property improvements made to 2XXX and 7XXX alloys including those containing Li. In PH Alloys, peak strength occurs at the point of transition from dislocation shearing to bypass of plate shaped precipitates having a habit plane of $\{111\}_\alpha$ (η' in Al−Zn−Mg−Cu, Ω in Al−Cu−Mg and T_1 in Al−Cu−Mg−Li alloys) or $\{100\}_\alpha$ (θ'' in Al−Cu−Mg alloys). From a prediction of strengthening contributions, which agrees well with measured values, it has been suggested that strength can be improved further by increasing the number density and aspect ratio of these plate shaped particles oriented on rational planes [137]. This is generally achieved by increasing the amounts of solute elements. Trace elements can be beneficial in this respect, as currently used by adding Ag to improve the strength of Al−Cu−Mg alloys with or without Li. High strength and resistance to fracture under static loading can also be achieved by producing a small volume fraction of very fine hard particles whose critical size for transition to a less coherent state can be reduced by trace element additions [46]. Such a microstructure would have to be tailored for imparting resistance to fatigue loading.

A patent application has been filed for an 7XXX alloy comprising, about 5.8−6.8 Zn, 2.5−3 Mg, 1.5−2.3 Cu, less than 0.2 Sc, and 0.2 Zr and optionally less than about 0.5 Ag (all wt%) [138]. The investigation that led to this application developed an index to quantify the susceptibility of the alloy to SCC. The SCC Index is computed as $2 \times$ wt% Zn + wt% Mg − wt% Cu where these values are the equilibrium amounts of the respective solutes in solution in the Al matrix at the aging temperature, calculated after accounting for the precipitation of the phases. The expectation was that alloys with reduced SCC index will have less elemental Zn in the matrix that would segregate to grain boundaries.

4.6.2.1 Rapid Solidification Processed Alloys

Significant progress was made in the 1980s in developing Al−Zn−Mg−Cu alloys with compositions similar to traditional 7XXX series alloys that were processed by rapid solidification of the melt at high rates. The cooling rates that were two to four orders of magnitude higher than for conventional ingot castings refined the

microstructure by extending solid solubilities, reducing segregation and refining the size of the constituent phases and grain size [135]. The compositions of two 7XXX series alloys developed this way are shown in Table 4.29.

Rapid solidification enabled the addition of about 1.5 wt% Co, which precipitated as nonshearable Co_2Al_9 dispersoids. Coupled with the absence of coarse constituents and fine grain size, these dispersoids provided higher toughness, fatigue strength, and better resistance to SCC. Powder particles invariably contain an oxide layer that gets hydrated. The powder degassing temperature needs to be carefully selected to ensure complete dehydration and to prevent release of hydrogen from the reaction between the released water and alloying elements. During thermomechanical processing, the oxide particles get broken up and redistributed in much the same way as constituent particles in conventional alloys and deleteriously affect properties. The oxygen content in the alloys can be as high as about 0.5 wt%. Still, the alloys provided overall property improvements and were amenable to mill processing and manufacturing with existing infrastructure. However, they did not find use due to the cost of processing of billets to produce sufficiently large mill products.

Rapidly solidified alloys processed by melt spinning and with higher amounts of solute than in traditional alloys having yield strength exceeding 700 MPa ($\sim$100 ksi) are commercially available for selected applications [139]. Similar levels of high strength have been achieved in alloy 7075 by adding an extra cryomilling step to process the powders prior to consolidation. The production of ultrafine grain sizes increased strength by about 100 MPa ($\sim$15 ksi) over that of alloys without cryomilling, although strengthening in both alloys was principally from Orowan mechanism due to precipitation of η' [140]. Elemental and alloy powder have also been used to produce alloys by mechanical alloying, which again have not found many applications.

4.6.2.2 Computational Alloy Design

The goal of computational alloy design is to reduce both empiricism and the need for extensive trial and error experiments for identifying alloy compositions and processing windows. Experiments cannot be completely avoided, at least not yet. One example of the model-based approach to develop aluminum alloys with targeted properties is the attempt at the "intelligent" design of wrought, age hardenable Al–Cu–Mg–Ag alloys for moderate temperature applications [141]. Initial alloy selection was based on a review of available empirical and literature data from which the Al–Cu–Mg system with high Cu:Mg ratio was chosen due to the superior thermal stability of the θ' phase. Addition of Ag as a trace element was considered due to its effect on enhancing the hardening response by the formation of Ω in this system. The Al–Cu–Mg–Ag phase diagram was then developed using the CALPHAD approach to identify compositions that would place the alloy in the equilibrium ($\alpha + \theta$) field in which Ω would form. Following the determination of crystal structure and interfacial energies for the desired precipitates, thermal simulation would identify the processing parameters to produce the creep resistant microstructure. The stability of the Ω phase in alloys with high levels of Ag and moderate amounts

Table 4.29 Compositions of Aluminum Alloys 7090 and 7093 (wt%)

Alloy	Zn	Mg	Cu	Co	Ni	Zr	O	Fe (Max)	Si (Max)	Others Each (Max)	Others Total (Max)
7090	7.3–8.7	2.0–3.0	0.6–1.3	1.0–1.9	–	–	0.20–0.50	0.15	0.12	0.05	0.15
7093	8.3–9.7	2.0–3.0	1.0–1.9	–	0.04–0.16	0.08–0.12	0.05–0.50	0.15	0.12	0.05	0.15

of Mg was demonstrated in an Al−Cu−Mg−Ag alloy development study [142]. The chemistry of the α/Ω phase boundary plays a key role in determining its resistance to coarsening and hence the ability to optimize the properties of the alloy by aging. The chemistry was estimated using experimentally measured characteristics of the Ω precipitates and thermodynamic data for the relevant portion of the multicomponent phase diagram, from which Ag was identified as the limiting species in maintaining the desirable interface. Computational analysis has also been used subsequently to identify trace elements that would promote clusters to act as precursors for enhancing Ω formation and suppressing those based on the θ and S phases [143].

4.6.3 NEW ALLOY DESIGN WITH ALTERNATIVE COMPOSITIONS

Rapid solidification processing has also been used to develop Al alloys with high levels of Fe along with elements such as V and Si to produce high volume fractions of dispersoids, discussed earlier and amorphous aluminum alloys that can be processed into nanocrystalline alloys with potential for developing ultrahigh strength [144]. Again, these alloys have the same limitations regarding processing and scale up for wrought products for large scale structures and are presently limited to niche applications.

A promising approach to develop alloys with the combination of properties required for airframes is the use of Sc for precipitation hardening. The Al-rich end of the binary Al−Sc alloy phase diagram exhibits a eutectic reaction at 0.47 wt% Sc and a sloping solvus with a maximum solid solubility of 0.38 wt% Sc in Al, thus providing a path for precipitation hardening [145]. The strengthening phase is ordered Al_3Sc, a few nm in size, which forms by nucleation from the SSSS upon aging in the range of 250−350°C (482−662°F). This phase forms directly from the solid solution without any precursor phases. Aging at higher temperatures results in the cellular precipitation of coarse Al_3Sc particles that do not contribute to strength. Increasing the solidification rate can extend the solid solubility of Sc thereby increasing the Al_3Sc volume fraction and extent of precipitation hardening.

The beneficial effects of adding Sc to Al alloys include grain refinement in the melt, recrystallization and grain size control and precipitation hardening [146]. Other than the two 7XXX series alloys mentioned earlier, Sc additions to commercial alloys have been made principally to nonheat treatable Al−Mg and Al−Mg−Li alloys developed in Russia, the purpose being to control the grain structure and improve weldability [147]. These alloys also contain Zr, which substitutes for the Sc in Al_3Sc, forming $Al_3(Sc, Zr)$. The composition and properties of a recently registered commercial 5XXX series alloy containing Sc, designated 5028, is shown in Table 4.30. This alloy can be laser beam or friction stir welded and develops properties comparable to 2024-T3 [148]. It is nonheat treatable and thus has advantages in terms of reducing processing and minimizing microstructural heterogeneities.

The properties of Al−Mg−0.5 wt% Sc alloys containing varying amounts of Mg up to 6 wt% are shown in Table 4.31 [149]. The alloys were solidified at a moderately rapid rate that was sufficient to retain the Sc in solution in the as-cast material

Table 4.30 Composition (wt%) and Tensile Properties of 5028 in the H116 Temper

Mg	Mn	Sc	Zr	Ti	Cr	Zn	Cu (Max)	Fe (Max)	Si (Max)	Others Each (Max)	Others Total (Max)
3.2–4.8	0.30–1.0	0.02–0.40	0.05–0.15	0.05–0.15	0.05–0.15	0.05–0.50	0.20	0.40	0.30	0.05	0.15

	Yield Strength				Tensile Strength				Elongation (%)	
	L		LT		L		LT			
Thickness mm (in.)	MPa	ksi	MPa	ksi	MPa	ksi	MPa	ksi	L	LT
2.3 (0.09)	330	48	345	50	402	58	405	59	12	13
5 (0.20)	325	47	330	48	400	58	400	58	12	13

L, longitudinal; LT, *long transverse.*

Table 4.31 Properties of Al–Mg–Sc Alloys

Mg Content (wt%)	Yield Strength, MPa (ksi)	Tensile Strength, MPa (ksi)	Elongation (%)	Strain Hardening Exponent	Tear Strength/ Yield Strength	Unit Propagation Energy, kJ/m^2 (in.-lb/in.^{2})
Rolled at 288°C (550°F) and aged at 288°C (550°F) for 4 hours (All Alloys Had 0.5 wt% Sc)						
0	286 (41)	297 (43)	14.5	0.020	1.74	319 (1822)
2	341 (49)	370 (54)	13.5	0.051	1.95	317 (1811)
4	381 (55)	443 (64)	14.5	0.072	1.93	278 (1588)
6	381 (55)	467 (68)	10.5	0.107	1.2	84 (480)
Rolled at 288°C (550°F), cold rolled and aged at 288°C (550°F) for 4 hours (All Alloys Had 0.5 wt% Sc)						
0	298 (43)	319 (46)	10.5	0.008	1.59	193 (1102)
2	376 (55)	401 (58)	8.5	0.052	1.74	123 (703)
4	414 (60)	460 (67)	9.5	0.064	1.68	114 (651)
6	433 (63)	503 (73)	10.5	0.074	1.33	100 (571)

and then warm rolled and aged at 288°C (550°F) for 4 h with and without cold rolling prior to aging. Strength of the binary Al−Sc alloy after aging is a superposition of the strength from the matrix friction stress, dislocations, grain structure, and Al_3Sc precipitates. Sc was retained in solution after solidification, and Al_3Sc precipitation occurs independently of Mg. Therefore, the precipitation strengthening will be the same in all the alloys except for the effects of mechanical working, particularly in the cold rolled alloy.

If microstructural parameters were available, the properties can be quantitatively analyzed in terms of the superposition of strengthening from all the features. As such, the properties under both sets of processing (with and without cold rolling) indicate that the strengthening is predominantly from precipitation. Cold work has a small influence on strength, but does not appear to further increase the contribution from precipitation. The strain hardening exponent increases with increasing Mg with a corresponding increase in the crack initiation toughness indicated by the ratio of the tear strength to yield strength. The precipitation of Al_8Mg_5 particles in the alloy with 6 wt% Mg provides void nucleation sites and reduces the toughness. The combination of strength and toughness in the alloy with 4 wt% Mg was found to be in the range of values for 2024-T3 and 7075-T73. In Al−1 wt% Sc alloy with 0 and 4 wt% Mg, Al_3Sc increased strength by 240 and 310 MPa (35 and 45 ksi), respectively, confirming the significant contribution by precipitation strengthening [150]. These alloys must be solidified at a sufficiently rapid rate to retain the Sc in solution in the as-cast condition. The amount of Sc exceeding its maximum equilibrium solid solubility cannot be dissolved subsequently.

The solidification rates needed to retain excess Sc in solid solution are not as high as those in rapid solidification, thus avoiding the need for powder degassing and consolidation into billet. However, faster rates than traditional ingot casting are required thereby limiting the product forms to thin sheet as can be produced by continuous twin roll casting, which is a commercially viable process. The contributions to strengthening from the various microstructural features were estimated for a twin roll cast alloy with a nominal composition of Al−4Mg−0.8Sc−0.08Zr (all wt %). The superposition of the contributions was estimated for the alloy after aging the as-cast material and after friction stir processing the aged alloy to produce ultrafine grains [151]. The commonly used additivity rules, such as Eq. (4.11), over predicted the strength of ultrafine grained alloys due to the negative deviation of the Hall Petch slope at very small grain sizes in this material.

4.6.4 MODELING FOR NEW ALLOY DESIGN

Computational design of new alloys, e.g., the creep resistant Al−Cu−Mg−Ag discussed earlier, requires thermodynamic data for phases that form during solidification, thermomechanical processing, and heat treatment. Such data are either experimentally measured or estimated from first principles calculations, as done for the precipitate phases in Al−Cu−Mg alloys [152]. The activation energy for precipitate nucleation in these alloys can be reduced by increasing the driving force or

by creating heterogeneous sites. In Al–Cu–Mg alloys, the trace element Ag promotes formation of clusters of Mg and Cu atoms on the {111} plane of the matrix, which is also the habit plane for nucleation of the desirable Ω phase. On the other hand, Si promotes clusters on the {100} plane, which is not favorable for Ω phase formation. In addition to providing guidelines for alloy design, these types of calculations also point out the effects of impurity elements such as Si in affecting precipitation behavior in addition to their roles in forming constituent particles and reducing toughness.

Large amounts of data are being generated across the length scales of materials behavior. The ability to digitally represent microstructural parameters and the computational capabilities to mine, analyze and provide insight into processing–microstructure–properties data are also increasing rapidly. All of these developments bode well for the rapid design of new alloys. Examples of numerical modeling to develop alloys were discussed briefly in the third chapter. However, these techniques are not an end in themselves and their real power lies in the ability to apply them advantageously to accelerate design using physics-based methods. This can be appreciated by referring to the scheme shown in Fig. 4.28. The number of relationships among any two, three, or more of these variables controlling the processing–microstructure–properties behavior is large and requires multidimensional representations. Experiments to generate data by systematically varying each parameter, for optimizing a given property even for just one alloy composition, is practically impossible. In this case, physics-based models and accumulated experience can provide insight into reducing the amount of needed data.

Data for mining can be obtained from publications in the literature and from organized data bases available in handbooks and in materials specifications. The latter typically will have less scatter. Strictly from a numerical approach, these data bases are amenable to discerning correlations in processing–microstructure–properties that may not otherwise be evident. Alloy design is essentially an optimization problem aimed at meeting multiple property objectives within the physical and practical constraints of alloying and processing combinations. The data based methods can be used at various levels to provide insight into alloy behavior. Many examples of applying these techniques are available in the literature. These include the use of genetic algorithms to identify the solute content and particle radius and volume fraction to optimize strength and ductility of Al–Mg–Sc–Zr alloys [153] and creating multidimensional response surfaces for property objectives as a function of alloy compositions and temper to identify parameters for optimizing SCC resistance of 7XXX series alloys [154].

4.6.5 INTEGRATED ALUMINUM ALLOY/PRODUCT DESIGN

Historically, Al alloy development has kept pace with the evolving airplane design drivers (Table 4.2), as shown as an example for 7XXX series alloys in Fig. 4.52. Although the improved properties of the alloys are beneficial by themselves, there is significant added value in their integration into high performance product

concepts aided by using advanced computational design and structural analysis tools. As mentioned in the introduction to this chapter, the aluminum suppliers are actively working with the airplane manufacturers and end users in the pursuit of these opportunities. It enables the suppliers to contribute to optimum design solutions by identifying performance advantages for the new alloys beyond that solely based on their improved properties. In addition, it also renders aluminum alloys, given their cost advantages and manufacturing knowledge base, competitive with alternative materials such as polymer–matrix composites. The many recent advances made in virtual product design and analytical tool capabilities also facilitate richer engagement between the original equipment manufacturers (OEM) and their material suppliers, as for example shown in the Alcoa/OEM trade study approach taken to efficiently (more rapidly and with less testing, consistent with the goals of computational approaches) asses the weight saving and durability/damage tolerance safety margin benefit potential of different new alloy combinations [6].

Another recent successful example of the integrated approach is the manufacture of critical structures free of residual stresses that was mentioned earlier. Unitizing of structures by consolidating parts has the advantage of lowering weight and cost by reducing part count. One way of unitizing parts is to use forgings that are traditionally designed to near-net shape. Availability of high quality plate in thick gauges and the advances in high speed machining offer another means for achieving unitization. Although forgings provide significant benefits in terms of cost, weight and properties, the development of bulk residual stresses and the resulting issues and variances with sizing and life of forged components have been major roadblocks to their wide use. Alcoa has developed processes to selectively impart cold work for stress relief in strategic locations throughout forgings. These locations are determined by using analysis capabilities to simulate and map residual stress states that arise during processing [6]. In recent studies [132,133], the processing steps (from forging through heat treatment, cold working and machining) were modeled and three dimensional maps of residual stresses in the forging and the machined parts were created. This enabled location-specific crack-initiation and growth analyses to be conducted while accounting for residual stresses and resulted in adjustments to the forging design until the desired component life was achieved. These examples serve to illustrate the ability of modeling and simulation tools in the frame work of ICME, not only to design alloys for property targets but also to help implement alloys such as 7085 for maximum benefit.

4.7 SUMMARY

It should be clear from the discussion of the metallurgy of wrought precipitation hardenable aluminum alloys that their processing–microstructure–properties relations are complex with many interdependent variables whose combined effects are very difficult to completely quantify. This complexity also offers a wide scope for new alloy development through understanding of their effects and judicious

control of these variables. It is remarkable that the ongoing development of improved 2XXX and 7XXX series alloys is based on compositions not too different from 2024 and 7075, respectively, commercialized nearly seven decades ago. This has been made possible by the continued understanding of their metallurgy, which is aided by accumulating empirical data and advanced characterization techniques. The information on precipitation hardening in general and for aluminum alloys in particular that are still being published will help create databases for model development and validation. Of course, aluminum alloy suppliers will continue proprietary development ensuring steady improvements in products as evidenced by the steady registrations of new alloys and tempers. Although one property may increase only incrementally, it may still be enough in combination with other properties to open new enabling applications.

The limits of precipitation hardening in aluminum alloys are well understood and further enhancements can be expected from the identification and use of trace elements for which first principle calculations can be very beneficial. With the development of revolutionary materials processing techniques such as friction stir welding and additive manufacturing, their integration into the manufacturing stream for airframe is not too distant. In this context, development of alloys can be expected to occur concurrently with these processes to maximize the benefits through their synergy. This aspect is described in a later chapter. Aluminum alloy development has had longer history of development than any other structural material for airframes. As other materials, particularly polymer based composites, begin to dominate the mix of airframe structural materials, aluminum alloys with continuously improving property combinations and the ability to be inserted in critical, "tailored" structures, will maintain their important role.

REFERENCES

[1] T. Dursun, C. Soutis, Recent developments in advanced aircraft aluminium alloys, Materials and Design 56 (2014) 862−871.
[2] Airbus Technical Digest FAST, 32, 5 (A380) and Airbus Technical Magazine FAST (July 2003). Special Edition A350 XWB (June 2013) 7 (A350).
[3] H. Canaday, Composites vs. Metals, Aerospace America, The American Institute of Aeronautics and Astronautics, May 2015, pp. 19−23.
[4] A. Jacob, Boeing launches 777X, features 787 Dreamliner composite wing technology, Materials Today, Elsevier 20 (November 2013).
[5] J. Liu, M. Kulak, A new paradigm in the design of aluminum alloys for aerospace application, Materials Science Forum 331−337 (2000) 127−140.
[6] R.J. Bucci, M.A. James, M. Kulak, M.B. Heinimann, H. Sklyut, J.R. Brockenbrough, Material and structural simulation methodology advancements for fatigue and damage tolerant critical aircraft structures − an aluminum supplier perspective, Fatigue and Fracture Toughness Symposium, 13th International Conference on Aluminum Alloys (ICAA − 13), Carnegie Mellon University, Pittsburgh, Pennsylvania, June 3−7, 2012.
[7] J.R. Davis, Introduction to aluminum and aluminum alloys, in: Aluminum and Aluminum Alloys, ASM Specialty Handbook, ASM International, 1993, pp. 31−46.

[8] R.N. Caron, J.T. Staley, Effects of composition, processing and structure on properties of nonferrous alloys, in: Nonferrous Alloys, Materials Selection and Design, ASM Handbook, vol. 20, ASM International, 1997, pp. 383−415.
[9] J.W. Bray, Aluminum mill and engineered wrought products, properties and selection, in: Nonferrous Alloys and Special-Purpose Materials, ASM Handbook, vol. 2, ASM International, 1990, pp. 29−61.
[10] J.-F. Nie, Physical metallurgy of light alloys, in: fifth ed., in: D.E. Laughlin, K. Hono (Eds.), Physical Metallurgy, vol. III, Elsevier, 2015, pp. 2009−2156.
[11] C.R. Simcoe, The discovery of strong aluminum, Advanced Materials and Processes 169 (August 2011) 35−36.
[12] I.J. Polmear, Aluminium alloys−a century of Ag hardening, in: J.-F. Nie, A.J. Morton, B.C. Muddle (Eds.), Materials Forum 28, Institute of Materials Engineering Australasia Ltd., 2004, pp. 1−14.
[13] N.A. Belov, D.G. Eskin, A.A. Aksenov, Characteristics of binary phase diagrams, in: Multicomponent Phase Diagrams − Applications for Commercial Aluminum Alloys, Elsevier, 2005, pp. 379−381.
[14] N.A. Belov, D.G. Eskin, A.A. Aksenov, Alloys of the Al-Cu-Si-(Mg, Fe) system, in: Multicomponent Phase Diagrams − Applications for Commercial Aluminum Alloys, Elsevier, 2005, pp. 83−132.
[15] N.A. Belov, D.G. Eskin, A.A. Aksenov, Alloys with a high content of zinc, in: Multicomponent Phase Diagrams − Applications for Commercial Aluminum Alloys, Elsevier, 2005, pp. 193−222.
[16] U. Kattner, The thermodynamic modeling of multicomponent phase equilibria, JOM 49 (12) (1997) 14−19.
[17] S.-L. Chen, F. Zhang, F.-Y. Xie, S. Daniel, X.-Y. Yan, Y.A. Chang, R. Schmid-Fetzer, W.A. Oates, Calculating phase diagrams using PANDAT and panengine, JOM 55 (12) (2003) 48−51.
[18] Y. Wang, S. Shang, L. Chen, Z. Liu, Density functional theory-based database development for CALPHAD automation, JOM 65 (11) (2013) 1533−1539.
[19] M. Tiryakioglu, J.T. Staley, Effect of alloying additions in aluminum alloys, in: G.E. Totten, S. Mackenzie (Eds.), Handbook of Aluminum, Physical Metallurgy and Processes, vol. 1, CRC Press, 2003, pp. 81−210.
[20] X.M. Li, M.J. Starink, The effect of compositional variations on the characteristics of coarse intermetallic particles in overaged 7xxx Al alloys, Materials Science and Technology 17 (11) (2001) 1324−1328.
[21] B.M. Gable, A.W. Zhu, G.J. Shiflet, E.A. Starke Jr., Assessment of the aluminum-rich corner of the Al−Cu−Mg−(Ag) phase diagram, CALPHAD 32 (2008) 256−267.
[22] R. Howard, N. Bogh, D.S. MacKenzie, Heat treating processes and equipment, in: G.E. Totten, S. Mackenzie (Eds.), Handbook of Aluminum, Physical Metallurgy and Processes, vol. 1, CRC Press, 2003, pp. 881−970.
[23] D.A. Porter, K.E. Easterling, M.Y. Sharif, Phase Transformations in Metals and Alloys, third ed., CRC Press, 2009.
[24] D.A. Porter, K.E. Easterling, M.Y. Sharif, Crystal interfaces and microstructure, in: Phase Transformations in Metals and Alloys, third ed., CRC Press, 2009, pp. 111−180.
[25] H. Numakura, Defects in metals, in: fifth ed., in: D.E. Laughlin, K. Hono (Eds.), Physical Metallurgy, vol. III, Elsevier, 2015, pp. 561−637.
[26] G. Sha, R.K.W. Marceau, S.P. Ringer, Precipitate and solute clustering in aluminium: advanced characterization techniques, in: R. Lumley (Ed.), Fundamentals of

Aluminium Metallurgy − Production, Processing and Applications, Woodhead Publishing Ltd., 2011, pp. 344−366.
[27] E.A. Starke Jr., in: J.L. Walter, M.R. Jackson, C.T. Sims (Eds.), Alloying of Aluminum: Development of New Aluminum Alloys, in: Alloying, ASM International, 1988, pp. 165−197.
[28] D.L. Gilmore, E.A. Starke Jr., Trace elements on precipitation processes and mechanical properties in a Al-Cu-Li Alloy, Metallurgical and Materials Transactions A 28 (1997) 1399−1415.
[29] E.A. Starke Jr., The causes and effects of denuded or precipitate-free zones at grain boundaries in aluminum alloys, JOM 22 (1) (1970) 54−63.
[30] J. Su, T.W. Nelson, R. Mishra, M. Mahoney, Microstructural investigation of friction stir welded 7050-T651 aluminum, Acta Materialia 51 (2001) 713−729.
[31] C.R. Brooks, Aluminum-base alloys, in: Heat Treatment Structure and Properties of Nonferrous Alloys, ASM International, 1982, pp. 115−137.
[32] R.J. Rioja, J. Liu, The evolution of Al-Li products for aerospace and space applications, Metallurgical and Materials Transactions A 43A (2012) 3325−3337.
[33] N. Eswara Prasad, T.R. Ramachandran, Phase diagrams and phase reactions in Al-Li alloys, in: N. Eswara Prasad, A.A. Gokhale, R.J.H. Wanhill (Eds.), Aluminum-Lithium Alloys: Processing, Properties and Applications, Elsevier, 2014, pp. 61−97.
[34] J.T. Staley, Aging kinetics of aluminum alloy 7050, Metallurgical Transactions 5 (1974) 929−932.
[35] N.C. Danh, K. Rajan, W. Wallace, A TEM study of microstructural changes during retrogression and reaging in 7075 aluminum, Metallurgical Transactions A 14 (1983) 1843−1850.
[36] A. Adjorlolo, Corrosion in commercial aviation, in: ASM Handbook, Corrosion: Environment and Industries, vol. 13C, ASM International, 2006, pp. 598−612.
[37] C.R. Hutchinson, Modeling the kinetics of precipitation in aluminum alloys, in: R. Lumley (Ed.), Fundamentals of Aluminium Metallurgy, Woodhead Publishing, Cambridge, UK, 2011, pp. 422−467.
[38] J.D. Robson, Modeling the overlap of nucleation, growth and coarsening during precipitation, Acta Materialia 52 (2004) 4669−4676.
[39] B. Rheingan, E.J. Mittemeijer, Modelling precipitation kinetics: evaluation of the thermodynamics of nucleation and growth, CALPHAD 50 (2015) 49−58.
[40] A. Deschamps, Y. Brechet, Influence of predeformation and aging of an Al-Zn-Mg Alloy − II. Modeling of precipitation kinetics and yield stress, Acta Materialia 47 (1998) 293−305.
[41] A. Deschamps, F. Livet, Y. Brechet, Influence of predeformation and aging of an Al-Zn-Mg Alloy − I. Microstructure evolution and mechanical properties, Acta Materialia 47 (1998) 281−292.
[42] H.-L. Chen, Q. Chen, J. Bratberg, A. Engstrom, Prediction of stable and metastable formation in aluminum alloys, Materials Today: Proceedings 2 (2015) 4939−4948.
[43] A. Kelly, R.B. Nicholson, Precipitation hardening, Progress in Materials Science 10 (1963) 151−391.
[44] A.J. Ardell, Precipitation hardening, Metallurgical Transactions 16 (1985) 2131−2165.
[45] B. Reppich, Particle strengthening, in: H. Mughrabi (Ed.), Materials Science and Technology-A Comprehensive Treatment, Plastic Deformation and Fracture of Materials, vol. 6, VCH, 1993, pp. 331−358.

[46] E. Hornbogen, E.A. Starke Jr., Theory assisted design of high strength low alloy aluminum, Acta Materialia 41 (1993) 1−16.
[47] J.W. Evancho, J.T. Staley, Kinetics of precipitation in aluminum alloys during continuous cooling, Metallurgical Transactions 5 (1974) 43−47.
[48] J. Staley, M. Tiryakioglu, The use of TTP curves and quench factor analysis for property prediction in aluminum alloys, in: M. Tiryakioğlu (Ed.), Advances in the Metallurgy of Aluminum Alloys, Proceedings of the James T. Staley Honorary Symposium on Aluminum Alloys, TMS, 2001, pp. 6−15.
[49] R.J. Flynn, J.S. Robinson, The application of advances in quench factor analysis property prediction to the heat treatment of 7010 aluminium alloy, Journal of Materials Processing Technology 153−154 (2004) 674−680.
[50] G.P. Dolan, R.J. Flynn, D.A. Tanner, J.S. Robinson, Quench factor analysis of aluminium alloys using the Jominy end quench technique, Materials Science and Technology 21 (2005) 687−692.
[51] P.A. Rometsch, M.J. Starink, P.J. Gregson, Improvements in quench factor modelling, Materials Science and Engineering A 339 (2003) 255−264.
[52] S. Liu, Q. Zhong, Y. Zhang, W. Liu, X. Zhang, Y. Deng, Investigation of quench sensitivity of high strength Al−Zn−Mg−Cu alloys by time−temperature-properties diagrams, Materials & Design 31 (2010) 3116−3120.
[53] H.R. Shercliff, M.F. Ashby, A process model for age hardening of aluminium alloys—I. The model, Acta Metallurgica et Materialia 38 (1990) 1789−1802.
[54] H.R. Shercliff, M.F. Ashby, A process model for age hardening of aluminium alloys—II. Applications of the model, Acta Metallurgica et Materialia 38 (1990) 1803−1812.
[55] A. Deschmps, D. Dumont, Y. Brechet, C. Sigli, B. Dubost, Process modeling of age-hardening aluminum alloys: from microstructure evolution to mechanical and fracture properties, in: M. Tiryakioğlu (Ed.), Advances in the Metallurgy of Aluminum Alloys, Proceedings of the James T. Staley Honorary Symposium on Aluminum Alloys, TMS, 2001, p. 289.
[56] D.A. Dumont, D.A. Deschamps, Y. Brechet, On the relationship between microstructure, strength and toughness in AA7050 aluminum alloy, Materials Science and Engineering: A 356 (2003) 326−336.
[57] D. Tsivoulas, J.D. Robson, C. Sigli, P.B. Prangnell, Interactions between zirconium and manganese dispersoid-forming elements on their combined addition in Al−Cu−Li alloys, Acta Materialia 60 (2012) 5245−5259.
[58] K.K. Sankaran, R. Perez, K.V. Jata, Effects of pitting corrosion on the fatigue behavior of aluminum alloy 7075-T6: modeling and experimental studies, Materials Science and Engineering A 297 (2001) 223−229.
[59] M.J. Starink, S.C. Wang, A model for the yield strength of overaged Al−Zn−Mg−Cu alloys, Acta Materialia 51 (2003) 5131−5150.
[60] R.J. Rioja, Fabrication methods to manufacture isotropic Al-Li alloys and products for space and aerospace applications, Materials Science and Engineering A 257 (1998) 100−107.
[61] D.S. Thompson, B.S. Subramanya, S.A. Levy, Quench rate effects in Al-Zn-Mg-Cu alloys, Metallurgical Transactions 2 (1971) 1149−1160.
[62] M. Conserva, P. Fiorini, Interpretation of quench sensitivity in Al-Zn-Mg-Cu alloys, Metallurgical Transactions 4 (1973) 857−862.
[63] B. Radhakrishnan, G. Sarma, C.H.J. Davies, Modeling of microstructural evolution during processing of aluminum alloys, in: G.E. Totten, S. MacKenzie (Eds.),

Handbook of Aluminum, Alloy Production and Materials Manufacturing, vol. 2, CRC Press, 2003, pp. 221−276.
[64] G. Gottstein, Though process modeling of materials fabrication: philosophy, current state and future directions, in: D.A. Molodov (Ed.), Microstructural Design of Advanced Engineering Materials, Wiley, 2013, pp. 3−17.
[65] F.D.S. Marquis, Evolution of microstructure, fracture toughness and fatigue resistance during processing of 7X50 aluminum alloys, in: E.W. Lee, W.E. Frazier, N.J. Kim, K.V. Jata (Eds.), Light Weight Alloys for Aerospace Applications IV, TMS, 1997, pp. 61−72.
[66] J.F. Knott, Fracture resistance in aluminium, in: R. Lumley (Ed.), Fundamentals of Aluminium Metallurgy, Woodhead Publishing, Cambridge, UK, 2011, pp. 538−573.
[67] D. Dumont, A. Deschamps, Y. Brechet, A model for predicting fracture mode and toughness in 7000 series aluminium alloys, Acta Materialia 52 (2004) 2529−2540.
[68] S.M. El-Soudani, R.M. Pelloux, Influence of inclusion content on fatigue crack propagation aluminum alloys, Metallurgical Transactions 4 (1973) 519−531.
[69] N.G. Birbillis, R.G. Buchheit, Electrochemical characteristics of intermetallic phases in aluminum alloys—an experimental survey and discussion, Journal of the Electrochemical Society 152 (2005) B140−B151.
[70] J. Zhang, M.A. Przystupa, A.J. Luévano, Characterizations of pore and constituent particle populations in 7050-T7451 aluminum plate alloys, Metallurgical and Materials Transactions A 29 (1998) 727−737.
[71] J.D. Robson, Microstructural evolution in aluminium alloy 7050 during processing, Materials Science and Engineering A 382 (2004) 112−121.
[72] G. Fribourg, Y. Brechet, A. Deschamps, A. Simar, Microstructure-based modelling of isotropic and kinematic strain hardening in a precipitation-hardened aluminium alloy, Acta Materialia 59 (2011) 3621−3635.
[73] G.B. Olson, Genomic materials design: the ferrous frontier, Acta Materialia 61 (2013) 771−781.
[74] A. deVaucorbeil, W.J. Poole, C.W. Sinclair, The superposition of strengthening contributions in engineering alloy, Materials Science and Engineering A 582 (2013) 147−154.
[75] L.M. Cheng, W.J. Poole, J.D. Embury, D.J. Lloyd, The influence of precipitation on the work-hardening behavior of the aluminum alloys AA6111 and AA7030, Metallurgical and Materials Transactions A 34A (2003) 2473−2481.
[76] M. Dixit, R.S. Mishra, K.K. Sankaran, Structure−property correlations in Al 7050 and Al 7055 high-strength aluminum alloys, Materials Science and Engineering A 478 (2008) 163−172.
[77] D.J. Lloyd, Precipitation hardening, in: Strength of Metals and Alloys, ICSMA 7, vol. 3, 1985, pp. 1745−1778.
[78] A.K. Vasudevan, W.G. Fricke, R.C. Malcolm, R.J. Bucci, On through thickness crystallographic texture gradient in Al-Cu-Li-Zr Alloy, Metallurgical Transactions 19A (1988) 731−732.
[79] G. Liu, G.J. Zhang, X.D. Ding, J. Sun, K.H. Chen, The influences of multiscale-sized second-phase particles on ductility of aged aluminum alloy, Metallurgical and Materials Transactions A 35A (2004) 1725−1734.
[80] R.J. Bucci, E.A. Starke Jr., Selecting aluminum alloys to resist failure by fracture mechanisms, in: ASM Handbook, Fatigue and Fracture, vol. 19, ASM International, 1996, pp. 771−812.

[81] G.T. Hahn, A.R. Rosenfield, Metallurgical factors affecting fracture toughness of aluminum alloys, Metallurgical Transactions A 6A (1975) 653−668.
[82] C.Q. Chen, J.F. Knott, Effects of dispersoid particles on toughness of high-strength aluminium alloys, Metal Science 15 (1981) 357−364.
[83] N.U. Deshpande, A.M. Gokhale, D.K. Denzer, J. Liu, Relationship between fracture toughness, fracture path, and microstructure of 7050 aluminum alloy: Part I. Quantitative characterization, Metallurgical and Materials Transactions A 29A (1998) 1191−1201.
[84] A.M. Gokhale, N.U. Deshpande, D.K. Denzer, J. Liu, Relationship between fracture toughness, fracture path, and microstructure of 7050 aluminum alloy: Part II. Multiple micromechanisms-based fracture toughness mode, Metallurgical and Materials Transactions A 29A (1998) 1203−1210.
[85] R.H. Van Stone, J.A. Psioda, Discussion of metallurgical factors affecting fracture toughness of aluminum alloys, Metallurgical Transactions A 6A (1975) 668−670.
[86] N. Kamp, I. Sinclair, M.J. Starink, Toughness-strength relations in the overaged 7449 Al-based alloy, Metallurgical and Materials Transactions A 33A (2002) 1125−1136.
[87] D.W. Cameron, D.W. Hoeppner, Fatigue properties in engineering, in: ASM Handbook, Fatigue and Fracture, vol. 19, ASM International, 1996, pp. 15−26.
[88] Y. Xue, H. El Kadiri, M.F. Horstemeyer, J.B. Jordon, H. Weiland, Micromechanisms of multistage fatigue crack growth in a high-strength aluminum alloy, Acta Materialia 55 (2007) 1975−1984.
[89] P.E. Magnusen, R.J. Bucci, A.J. Hinkle, J.R. Brockenbrough, H.J. Konish, Analysis and prediction of microstructural effects on long-term fatigue performance of an aluminum aerospace alloy, International Journal of Fatigue 19 (1997) 275−283.
[90] R.J.H. Wanhill, Aircraft corrosion and fatigue damage assessment, in: US Air Force ASIP Conference Proceedings, 1995, pp. 983−1027.
[91] R.J.H. Wanhill, G.H. Bray, Fatigue crack growth behavior of aluminum lithium alloys, in: N. Eswara Prasad, A.A. Gokhale, R.J.H. Wanhill (Eds.), Aluminum-lithium Alloys: Processing, Properties and Applications, Elsevier, 2014, pp. 381−412.
[92] D.L. McDowell, Microstructure-sensitive modeling and simulation of fatigue, in: ASM Handbook, Fundamentals of Modeling for Metals Processing, vol. 22A, ASM International, 2009, pp. 408−418.
[93] D.L. McDowell, F.P.E. Dunne, Microstructure-sensitive computational modeling of fatigue crack formation, International Journal of Fatigue 32 (2010) 1521−1542.
[94] D.G. Harlow, M.G. Wang, R.P. Wei, Statistical analysis of constituent particles in 7075-T6 aluminum alloy, Metallurgical and Materials Transactions A 37 (2006) 3367−3373.
[95] G.H. Bray, R.J. Bucci, E.L. Colvin, M. Kulak, Effect of prior corrosion on the S/N fatigue performance of aluminum sheet alloys 2024-T3 and 2524-T3, in: Effects of the Environment on the Initiation of Crack Growth, ASTM International, 1997, pp. 89−106.
[96] G.C. Chen, K.C. Wan, M. Gao, R.P. Wei, Transition from pitting to fatigue crack growth—modeling of corrosion fatigue crack nucleation in a 2024-T3 aluminum alloy, Materials Science and Engineering A 219 (1996) 126−132.
[97] K.K. Sankaran, R. Perez, H. Smith, Military aircraft corrosion fatigue, in: ASM Handbook, Corrosion: Environment and Industries, vol. 13C, ASM International, 2006, pp. 195−204.
[98] S. Dey, M. Gunjan, I. Chattoraj, Effect of temper on the distribution of pits in AA 7075 alloy, Corrosion Science 50 (2008) 2895−2901.

[99] S. Dey, S.K. Raj, A. Basumallick, I. Chattoraj, The effect of pitting on fatigue lives of peak-aged and overaged 7075 aluminum alloys, Metallurgical and Materials Transactions A 41A (2010) 3297−3307.
[100] J. Moran, Effects of metallurgical variables on the corrosion of aluminum alloys, in: ASM Handbook, Corrosion: Fundamentals, Testing and Protection, vol. 13A, 2003, p. 275.
[101] J.G. Kaufman, Corrosion of aluminum and aluminum alloys, in: Corrosion: Materials, ASM Handbook, vol. 13B, ASM International, 2005, pp. 95−124.
[102] T. Marlaud, B. Malki, C. Henon, A. Deschamps, B. Baroux, Relationship between alloy composition, microstructure and exfoliation corrosion in Al-Zn-Mg-Cu alloys, Corrosion Science 53 (2011) 3139−3149.
[103] T. Marlaud, B. Malki, A. Deschamps, B. Baroux, Electrochemical aspects of exfoliation corrosion of aluminum alloys: the effects of heat treatment, Corrosion Science 53 (2011) 139−1400.
[104] J.P. Chubb, T.A. Morad, B.S. Hockenhull, J.W. Bristow, The effect of exfoliation corrosion on the fracture and fatigue behavior of 7178-T6 aluminium, International Journal of Fatigue 17 (1995) 49−54.
[105] M.G. Renaud, N.C. Bellinger, Fatigue modeling for aircraft structure containing natural exfoliation corrosion, International Journal of Fatigue 29 (2007) 677−686.
[106] G.H. Koch, Tests for stress-corrosion cracking, AM&P (August 2001) 36.
[107] W. Dietzel, P. Bala Srinivasan, A. Atrens, Testing and evaluation methods for stress corrosion cracking in metals, in: V.S. Raja, T. Shoji (Eds.), Stress Corrosion Cracking: Theory and Practice, Woodhead Publishing Ltd., UK, 2011, pp. 133−166.
[108] M.O. Speidel, Stress corrosion cracking of aluminum alloys, Metallurgical Transactions A 6A (1975) 631−651.
[109] N.J. Henry Holoyd, G.M. Scamans, Stress corrosion cracking in Al-Zn-Mg-Cu aluminum alloys in saline environments, Metallurgical and Materials Transactions A 44A (2013) 1230−1253.
[110] I.N. Fridlyander, Advanced high-strength aluminum-base materials, Metal Science and Heat Treatment 47 (2005) 269−275.
[111] V.V. Zakharov, Structurally strengthened aluminum alloys, Metal Science and Heat Treatment 51 (2009) 74−81.
[112] T. Warner, R. Dif, J.C. Ehrstrrom, P. Lassince, Improved Durability Aluminium Alloys for Airframe Structures, RTO AVT Workshop on "New Metallic Materials for the Structure of Aging Aircraft", Corfu, Greece, 19−20 April 1999, RTO MP-25, 10−1; 10−6.
[113] Alloy 2124 Plate − Technical Data, Alcoa data sheet.
[114] B. Smith, The Boeing 777, Advanced Materials and Processes 161 (9) (2003) 41−44.
[115] E.L. Colvin, J.J. Petit, R.W. Westerlund, P.E. Magnusen, Damage Tolerant Aluminum Alloy Products Useful for Aircraft Applications Such as Skin, US Patent 5213639, May 25, 1993.
[116] P. Lequeu, P. Lassince, T. Warner, Aluminum alloy development for the Airbus 380, Advanced Materials and Processes 165 (2007). Part 1 (June) 33−35; Part 2 (July) 41−44.
[117] V.V. Zakharov, T.D. Rostova, High-resourse high-strength aluminum alloys, Metal Science and Heat Treatment 37 (1995) 203−207.
[118] H.Y. Hunsicker, Development of Al-Zn-Mg-Cu alloys for aircraft, Philosophical Transactions of the Royal Society of London. Series A, Mathematical and Physical Sciences 282 (1307) (1976) 359−376. Rosenhain Centenary Conference: The Contribution of Physical Metallurgy to Engineering Practice.

[119] Alloy 7050 Plate and Sheet − Technical Data, Alcoa data sheet.
[120] ALCAN 7040-T651, ASM Alloy Digest. Filing Code Al-418, ASM International, 2008.
[121] Aluminum Alloy 7065, Alcoa data sheet.
[122] KaiserSelect Plate Alloy 7099-T7451, High strength for light weight structures, Kaiser Aluminum data sheet.
[123] Alcoa 7150-T7751 and T77511, ASM Alloy Digest, Filing Code Al-442, ASM International, 2015.
[124] 7055 Alloy-T7751 Plate and-T77511 Extrusion, Alcoa Technical data Sheet.
[125] D.J. Chakrabarti, Aluminum Alloy Products Having Improved Property Combinations and Method for Artificially Aging Same, US Patent 6972110, December 2005.
[126] J. Boselli, D.J. Chakrabarti, R.T. Shuey, Aerospace applications: metallurgical insights into the improved performance of aluminum alloy 7085 thick products, in: J. Hircsh, B. Skrotzki, G. Gottstein (Eds.), Aluminium Alloys: Their Physical and Mechanical Properties vol. 1, Wiley, 2008, pp. 202−208.
[127] I.N. Fridlyander, A.V. Dobromyslov, E.A. Tkachenko, O.G. Senatorova, Advanced high-strength aluminum-base materials, Metal Science and Heat Treatment 47 (2005) 269−275.
[128] R.J.H. Wanhill, Aerospace applications of aluminum-lithium alloys, in: N. Eswara Prasad, A.A. Gokhale, R.J.H. Wanhill (Eds.), Aluminum-Lithium Alloys: Processing, Properties and Applications, Elsevier, 2014, pp. 503−535.
[129] G. Jagan Reddy, R.J.H. Wanhill, A.A. Gokhale, Mechanical working of aluminum-lithium alloys, in: N. Eswara Prasad, A.A. Gokhale, R.J.H. Wanhill (Eds.), Aluminum-Lithium Alloys: Processing, Properties and Applications, Elsevier, 2014, pp. 187−219.
[130] N. Eswara Prasad, A.A. Gokhale, R.J.H. Wanhill (Eds.), Aluminum-Lithium Alloys: Processing, Properties and Applications, Elsevier, 2014.
[131] L.M. Karabin, G.H. Bray, R.J. Rioja, G. Venema, Al-Li-Cu-Mg-(Ag) products for lower wing skin applications, in: H. Weiland, A.D. Rollett, W.A. Cassada (Eds.), 13th International Conference on Aluminum Alloys Proceedings, Wiley-TMS, 2012, pp. 529−534.
[132] M.A. James, R. Watton, R.J. Rucci, An integrated approach to manage the impact of bulk residual stress on the design-build-sustain process for primary aircraft structures, Aircraft Structural Integrity Program Conference, November 30−December 2, 2010, San Antonio, TX.
[133] R. Dutton, P. Kobryn, D. Ball, J. Castle, M. James, P. Yavari, From integrated computational materials engineering to integrated computational structures engineering, in: W. Poole, S. Christensen, S. Kalidindi, A. Luo, J.D. Madison, D. Raabe, X. Sun (Eds.), Proceedings of the 3rd World Congress on Integrated Computational Materials Engineering, TMS-Wiley, 2015, pp. 99−106.
[134] P.V. Liddicoat, X.Z. Liao, Y. Zhao, Y. Zhu, M. Murashkin, E.J. Lavernia, R.Z. Valiev, S.P. Ringer, Nanostructural hierarchy increases the strength of aluminium alloys, Nature Communications 1 (6) (2010) 63−69.
[135] E.J. Lavernia, J.D. Ayers, T.S. Srivatsan, Rapid solidification processing with specific reference to aluminium alloys, International Materials Reviews 37 (1) (1992) 1−44.
[136] A.P. Reynolds, Elevated temperature fatigue of P/M aluminum alloy 8009, Scripta Metallurgica et Materialia 28 (1993) 201−206.
[137] J.F. Nie, B.C. Muddle, Microstructural design of high strength aluminum alloys, Journal of Phase Equilibria 19 (6) (1998) 543−551.

[138] A. Misra, J.A. Wright, Aluminum Alloys, United States Patent Application Publication No. US 2012/0291926 A1, November 22, 2012.
[139] RSP Alloys Data Sheets, RSP-Technology, The Netherlands, 2016. http://www.rsp-technology.com/site-media/user-uploads/rsp_overview_2016-4-1_low.pdf.
[140] K. Ma, H. Wen, T. Hu, T.D. Topping, D. Isheim, Mechanical behavior and strengthening mechanisms in ultrafine grain precipitation-strengthened aluminum alloy, Acta Materialia 62 (2014) 141−155.
[141] A.W. Zhu, B. Gable, G.J. Shiflet, E.A. Starke Jr., The intelligent design of age hardenable wrought aluminum alloys, Advanced Engineering Materials 4 (2002) 839−846.
[142] B.M. Gable, G.J. Shiflet, E.A. Starke Jr., Alloy development for the enhanced stability of Ω precipitates in Al-Cu-Mg-Ag alloys, Metallurgical and Materials Transactions A 37 (2006) 1091−1105.
[143] A. Zhu, B.M. Gable, G.J. Shiflet, E.A. Starke Jr., Trace element effects on precipitation in Al-Cu-Mg-(Ag, Si) alloys: a computational analysis, Acta Materialia 52 (2004) 3671−3679.
[144] J.H. Perepezko, R.J. Hebert, Amorphous aluminum alloys-synthesis and stability, JOM 54 (3) (2002) 34−39.
[145] E.A. Marquis, D.N. Seidman, Nanoscale structural evolution of Al_3Sc precipitates in Al(Sc) alloys, Acta Materialia 49 (2001) 1909−1919.
[146] J. Royset, Scandium in aluminium alloys: physical metallurgy, properties and applications, Metallurgical Science and Technology 25 (2) (2013) 11−21.
[147] Yu.A. Filatov, V.I. Yelagin, V.V. Zakharov, New Al-Mg-Sc alloys, Materials Science and Engineering A280 (2000) 97−101.
[148] Aerospace Aluminum AA5028, AlMgSc, Aleris International Inc., 2015.
[149] R.R. Sawtell, C.L. Jensen, Mechanical properties and microstructures of Al-Mg-Sc Alloys, Metallurgical Transactions A 21 (1990) 421−430.
[150] B.A. Parker, Z.F. Zhou, P. Nolle, The effect of small additions of scandium on the properties of aluminum alloys, Journal of Materials Science 30 (1995) 452−458.
[151] N. Kumar, R.S. Mishra, Additivity of strengthening mechanisms in ultrafine grained Al−Mg−Sc alloy, Materials Science and Engineering A580 (2013) 175−183.
[152] A.W. Zhu, G.J. Shiflet, E.A. Starke Jr., First principles calculation for alloy design of moderate temperature age-hardenable Al alloys, Materials Science Forum, Trans Tech Publications 519 (2006) 35−44.
[153] A.J. Kulkarni, K. Krishnamurthy, S.P. Deshmukh, R.S. Mishra, Microstructural optimization of alloys using a genetic algorithm, Materials Science and Engineering A 372 (2004) 213−220.
[154] S. Bhargava, G.S. Dulikravich, G.S. Murty, A. Agarwal, M. Colaco, Stress corrosion cracking resistant aluminum alloys: optimizing concentrations of alloying elements and tempering, Materials and Manufacturing Processes 26 (2011) 363−374.

FURTHER READING

[1] R. Lumley (Ed.), Fundamentals of Aluminium Metallurgy, Woodhead Publishing, Cambridge, UK, 2011.
[2] A.E. Hughes, N. Birbillis, J.M.C. Mol, S.J. Garcia, X. Zhou, G.E. Thompson, High-strength Al-Alloys: microstructure, corrosion and principles of protection, in:

Z. Ahmad (Ed.), Recent Trends in Processing and Degradation of Aluminum Alloys, InTech Publishers, 2011, pp. 223−262.

[3] J.C. Williams, E.S.A. Starke Jr., Progress in structural materials for aerospace systems, Acta Materialia 51 (2003) 5775−5799.

[4] G.E. Totten, S. Mackenzie (Eds.), Handbook of Aluminum: vol. 1 − Physical Metallurgy and Processes, vol. 2 − Alloy Production and Materials Manufacturing, CRC Press, 2003.

[5] E.A. Starke, J.T. Staley, Application of modern aluminum alloys to aircraft, Progress in Aerospace Science 32 (1996) 131−172.

[6] J.E. Hatch, Aluminum: Properties and Physical Metallurgy, ASM International, 1984.

CHAPTER

Titanium Alloys

5

CHAPTER OUTLINE

Synopsis **178**
5.1 Titanium Alloys for Airframe Structures **179**
5.2 Classification, Characteristics, and Historical Development of Titanium Alloys **181**
5.2.1 Classification of Titanium Alloys 182
5.2.2 Characteristics of Titanium Alloys 189
5.2.3 Historical Development of Titanium Alloys 191
5.2.4 Summary 192
5.3 Physical Metallurgy of Titanium Alloys **194**
5.3.1 Alloying of Titanium 194
5.3.1.1 Phase Stability 195
5.3.1.2 Solid Solubility of Alloying Elements 195
5.3.1.3 Alloying of Near-α Alloys 195
5.3.1.4 Alloying of α/β Alloys 196
5.3.1.5 Alloying of β Alloys 196
5.3.1.6 Phases and Phase Relationships 197
5.3.2 Processing of Titanium Alloys 207
5.3.2.1 Primary Working of Titanium Alloys 208
5.3.2.2 Secondary Working of Titanium Alloys 211
5.3.2.3 Heat Treatment of Titanium Alloys 212
5.3.2.4 Modeling of Thermomechanical Processing 215
5.3.2.5 Processes for Cost-Affordable Titanium Alloys 217
5.3.3 Microstructure of Titanium Alloys and its Relationship to Processing 220
5.3.3.1 Microstructure and Texture of Titanium Alloys 221
5.3.3.2 Effects of Processing on Microstructure and Texture 226
5.3.3.3 Modeling of Microstructure and Texture 232
5.4 Properties of Titanium Alloys and Their Relationships to Composition, Processing, and Microstructure **238**
5.4.1 Strength 241
5.4.1.1 α/β Alloys 241
5.4.1.2 β Alloys 244
5.4.2 Ductility 246
5.4.3 Durability and Damage Tolerance Properties 249
5.4.3.1 Fatigue Strength/Life 249

Metallurgy and Design of Alloys with Hierarchical Microstructures. http://dx.doi.org/10.1016/B978-0-12-812068-2.00005-9
Copyright © 2017 Elsevier Inc. All rights reserved.

5.4.3.2 FCG Behavior 253
5.4.3.3 Fracture Toughness 253
5.4.4 Stress Corrosion Cracking 257
5.4.5 High Temperature Properties 257
5.4.6 Summary of Composition—Processing—Microstructure—Properties Relationships 258
5.4.7 Modeling of Composition—Processing—Microstructure—Properties Relationships 259
5.4.7.1 Modeling of Strength 260
5.4.7.2 Modeling of Fracture Toughness 262
5.4.7.3 Integrated Modeling 263
5.5 Commercial Titanium Alloys 264
5.5.1 Ti—6Al—4V and Ti—6Al—4V ELI 264
5.5.2 α/β Alloys 265
5.5.2.1 TIMETAL 62S 266
5.5.2.2 Ti—6Al—6V—2Sn 266
5.5.2.3 Ti—6Al—2Sn—2Zr—2Mo—2Cr—0.15Si (Ti-6-22-22) 267
5.5.2.4 α/β Alloys for Improved Formability 267
5.5.2.5 α/β Alloys for Intermediate Temperature Applications 269
5.5.3 Near-α Alloys 269
5.5.4 Near-β and Metastable β Alloys 274
5.5.4.1 Near-β Alloys 274
5.5.4.2 Metastable β Alloys 276
5.6 New Alloy Design 278
5.7 Summary 280
References 280

SYNOPSIS

This chapter describes the metallurgy of titanium alloys used in aerospace structural applications. These alloys are unique in that their microstructures contain two ductile phases whose volume fractions, sizes, and morphologies can be manipulated by processing to achieve a wide range of property combinations across a range of temperatures. The diversity of microstructural features and the mechanisms of deformation also result in significant complexity to their understanding, which, however, has not prevented the empirical development and insertion of these alloys for critical applications. As with the chapter on aluminum alloys, the composition—microstructure—properties—relationships schemes and the ability or lack thereof to model the various aspects of the behavior of titanium alloys within this framework, aided by the continuing evolution of the understanding of underlying mechanisms, will form the basis for the description. The chapter will conclude with a discussion of the status and prospects for new alloy design and the barriers to their qualification and insertion.

5.1 TITANIUM ALLOYS FOR AIRFRAME STRUCTURES

Titanium alloys possess higher absolute and specific strength values than the lighter aluminum alloys and lower density and higher specific strength than steel and superalloys at temperatures up to about 550°C. Combined with their excellent corrosion and oxidation resistance, these attributes render Ti alloys attractive for structural applications in both airframes and propulsion systems. The principal barrier to the widespread use of Ti alloys is their high cost, which results from the need to process the melt in batches in vacuum to produce the primary metal and the difficulty of subsequent fabrication into mill products and structural components. Accordingly, much of the initial development of Ti alloys was for military applications requiring significantly higher, enabling structural performance that was made possible by substituting for steel and superalloys in propulsion systems and for Al alloys in airframe parts experiencing temperatures beyond their service capability.

The first extensive use of Ti alloys for airframes was as early as in the 1960s for the SR-71 Blackbird reconnaissance aircraft whose Mach 3 cruising speed and high skin temperatures ruled out aluminum alloys. Steels and superalloys capable of operating at these high temperatures could not also be used due to excessive weight penalty. Ti alloys were ideal for this application and about 93% of SR-71 was fabricated from them [1]. The first commercial β Ti alloy, Ti−13V−11Cr−3Al was developed specifically for this purpose. Subsequently, Ti alloys continued to be used in substantial amounts in military aircraft, as shown in Table 5.1 [2].

Although the amount of Ti alloys in airframe structures in commercial airplanes increased steadily, their total use was rather limited until the introduction of Boeing 787, as shown in Fig. 5.1 [3]. Use of large amounts of polymer−matrix composite materials in highly tension loaded structures of this airplane resulted in the selection of Ti alloys for areas where metals were preferred [4]. Al alloys perform well under compression loading, but Ti alloys are better in tension while also having better corrosion resistance and galvanic and stiffness compatibility with carbon-reinforced polymer composites.

Applications for Ti alloys in the examples cited earlier are enabled by their unique metallurgy and combination of properties that compare with those of Al and steel alloys used in airframes, as follows.

Table 5.1 Structural Materials Distribution (wt%) in Military Aircraft [2]

	Aircraft			
Material	**F-15E**	**F/A-18C/D**	**F/A-18E/F**	**F-22**
Aluminum	49	49	31	16
Titanium	32	13	21	39
Composites	2	10	19	24
Other (including steel)	17	28	29	21

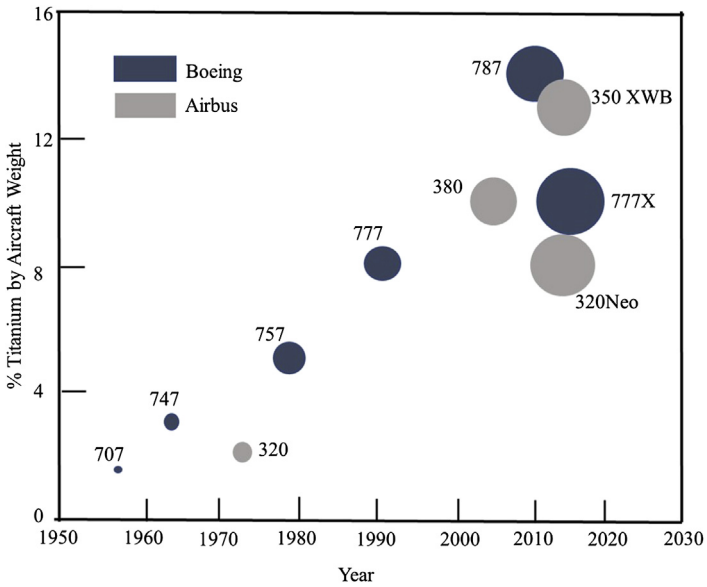


FIGURE 5.1

Usage of titanium alloys in commercial airplanes [3].

Adapted and reprinted with permission of ASM International. All rights reserved. www.asminternational.org.

- Ti occurs in two allotropic forms, hexagonal close packed (HCP) α and body centered cubic (BCC) β, which can coexist in alloys in equilibrium over a range of temperatures. Hence, Ti alloys can be processed either in the high temperature single phase β or the two phase $\alpha + \beta$ regions and then cooled at different rates thereby providing the ability through controlled alloying and processing to achieve varying volume fractions, sizes, and morphologies of these two ductile phases. In contrast, alloying of Al is limited by the need to obtain a single phase supersaturated solid solution by solution treatment within a narrow temperature range followed by rapid quenching to room temperature.
- Solid solution and precipitation hardening of both α and β phases, either of which could be the matrix phase as determined by alloy composition and processing, along with additional strengthening from the presence of α/β interfaces and the refinement of these phases enable a broader range of property combinations possible in Ti alloys compared with other airframe alloys. In contrast, Al alloys used for fuselage and wings and steel alloys used for landing gear are strengthened principally by precipitation hardening of a single phase, face centered cubic (FCC) α-Al or BCC α-Fe, with only limited contributions from other mechanisms.
- The high temperature β phase in Ti alloys undergoes a martensitic transformation upon rapid quenching, like the austenite, γ phase in steel alloys. This transformation by itself does not provide adequate strengthening in Ti alloys. However, the two-phase α/β morphology can be altered by varying the

processing temperatures and subsequent cooling rates to produce equiaxed or lamellar or a mixture of both microstructures to achieve targeted combinations of strength, toughness, and fatigue properties.

- Significant amounts of the β phase can also be retained at room temperature by quenching of certain Ti alloys in which the martensite start temperatures (M_s) are lowered sufficiently. Aging of the retained, metastable β produces a fine dispersion of the secondary α phase, which increases strength considerably. This is in contrast with steel alloys where strengthening results from the formation of martensite, toughness is improved at the expense of strength by its tempering (aging), and any retention of the high temperature austenite phase is generally deleterious for properties.
- Wrought structural Al alloy compositions are not amenable for processing into cast products and wrought and cast Al alloys are classified separately, but structural Ti alloys can be processed into both product forms. Enabled by the ability to heal and repair casting defects by hot isostatic pressing and welding, properties equivalent to that of wrought products have been achieved in Ti castings for selected compositions and heat treatments. Near net shape castings can be designed to unitize multiple wrought parts providing cost savings and expanding the applicability of Ti alloys.
- The sizes, morphologies, and volume fractions of the α and β phases can be tailored to render Ti alloys superplastically formable with the potential to design unitized structures for significant reduction of weight and manufacturing cost. This aspect of Ti alloys is discussed in the chapter focused on alloy design for processing attributes.

Desirable combinations of properties are achieved in Ti alloys by optimizing the various processing paths and the resulting microstructures rendered possible by combinations of alloying elements that stabilize either the α or β phase, which also provides a convenient basis to classify these alloys. This classification scheme along with the effects of composition, processing, and microstructure on properties will be used in subsequent sections as a roadmap to gain an understanding of the underlying physical metallurgy of Ti alloys pertinent for their design and use in airframe structures.

5.2 CLASSIFICATION, CHARACTERISTICS, AND HISTORICAL DEVELOPMENT OF TITANIUM ALLOYS

Ti alloys are classified based on the phases present in them at room temperature. The different crystal structures, physical properties, and deformation characteristics of the α and β phases also impart distinguishing processing characteristics and property attributes to the various classes of Ti alloys. Compared with the BCC β phase, the HCP α phase exhibits higher resistance to plastic deformation, lower ductility, higher anisotropy of properties, lower diffusion rates by at least two orders of magnitude, and higher creep resistance [5].

5.2.1 CLASSIFICATION OF TITANIUM ALLOYS

Alloying elements that raise, lower, or have a very small effect on the allotropic transition temperature of Ti (882°C for the pure element) are designated as α stabilizers, β stabilizers, or neutral elements, respectively. In Ti alloys, the single phase α and β fields are separated by the two-phase α + β region. The minimum temperature at which a Ti alloy is comprised fully of β as the equilibrium phase is termed the beta transus temperature (T_β), which can be lowered to room temperature or below by the addition of sufficient amounts of β stabilizers. Thus depending on the composition, Ti alloys can consist fully of α or β or a mixture of α and β in equilibrium at room temperature. However, as stated earlier, β can still be retained at room temperature in metastable equilibrium by rapid quenching of alloys in which the M_s is below room temperature.

Al is the principal α stabilizing element added to Ti alloys. It is a readily available, low cost, lower density element soluble in both α and β and provides solid solution hardening. It is the only substitutional solute with such attractive attributes for alloying Ti. Other α stabilizers include the interstitial elements O, N, and C, whose levels are controlled for achieving good property combinations, and B, Ga, Ge, and rare earth elements, which are not used in commercial alloys.

The phase diagrams, related transformations, and their use for classifying Ti alloys are covered in detail in many publications [6–11]. The salient features germane to understanding commercial alloys are discussed briefly in this section. Ti alloys used in structural applications contain α and β stabilizers and the neutral elements in various relative amounts, which require multicomponent phase diagrams for analysis. However, with the lack of availability of such diagrams, binary, and pseudobinary diagrams are used to illustrate the principles of alloying. As with Al alloys, these diagrams do not account for transformation kinetics in terms of effects on such factors as hardenability that have a significant effect on properties.

Fig. 5.2A and B [6,8] shows schematic phase diagrams commonly used to describe the individual and combined effects of alloying elements and the way they are used to classify Ti alloys. As shown in Fig. 5.2A, increasing the amounts of β stabilizing elements lowers T_β and expands the two-phase α + β region. The commonly used alloying elements of this type have varying levels of solid solubility in both α and β phases and are further classified as β-isomorphous (e.g., Mo, Nb, and V) or β-eutectoid (e.g., Cr, Fe, and Si) elements. Under equilibrium conditions, the β phase undergoes a simple transformation in alloys with the isomorphous elements or a eutectoid transformation in which it decomposes into α and an intermetallic compound. However, the kinetics of the eutectoid reaction in alloys with commonly used β-eutectoid elements is very sluggish and in practice they behave as β-isomorphous elements. The formation of embrittling intermetallic compounds during service has been observed in Ti–13V–11Cr–3Al used in the SR-71. The elements Zr and Sn are β-isomorphous and β-eutectoid, respectively, but are classified as neutral elements because of their limited effect on T_β. Si is added for forming silicides to stabilize α/β boundaries in alloys designed for high-temperature use.

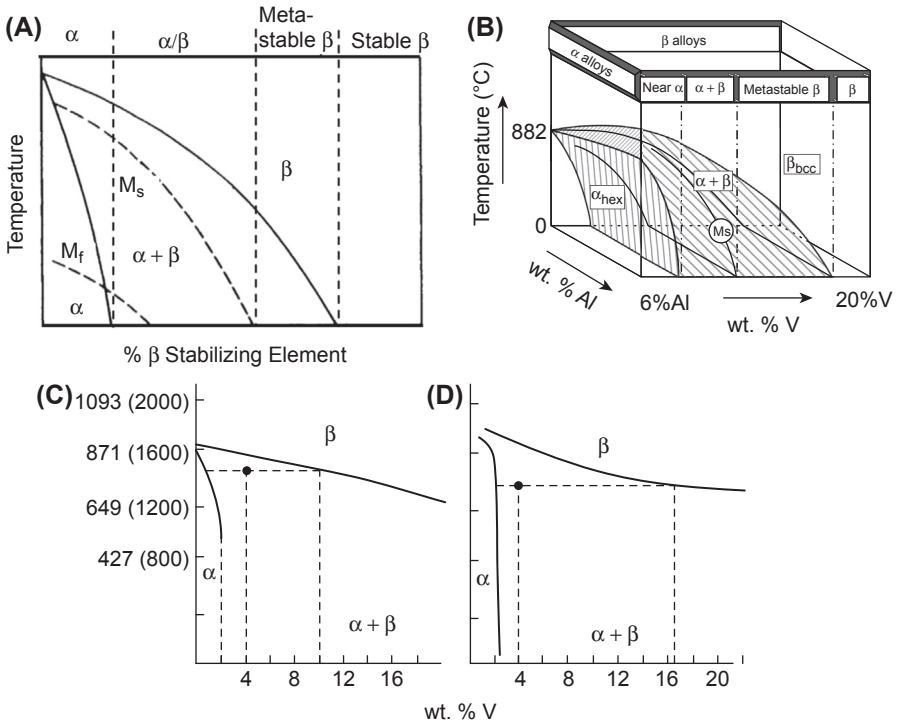


FIGURE 5.2

Schematic phase diagrams for Ti alloys. (A) Binary alloy with a β stabilizer, (B) three-dimensional depiction of alloys with α and β stabilizers [8], (C) binary Ti–V [11] and (D) pseudobinary Ti–6Al–xV [11].

(A) Adapted from I. Polmear, D. St. John, Titanium alloys, in: Light Alloys: From Traditional Alloys to Nanocrystals, Elsevier, 2006, pp. 299–365. (C) and (D) Reprinted with permission of ASM International. All rights reserved. www.asminternational.org.

Referring to Fig. 5.2A, the Ti alloy remains as single phase α at a given temperature until the limit of solid solubility of the β stabilizer in the α phase is reached, following which, the relative volume fraction of the β phase increases continuously until the alloy is comprised fully of this phase. Alloys with compositions that render them fully α or β or a mixture of these phases under equilibrium at room temperature are classified as α or β or α/β Ti alloys, respectively. This designation is unlike that for wrought Al alloys, in which only one matrix phase is present.

Fig. 5.2B is a schematic three-dimensional phase diagram depicting the effects of individual and combined additions of Al and V. Two-dimensional vertical sections of this diagram can be used as pseudobinary diagrams to depict the effects of varying β (or α) stabilizer additions for an alloy with a fixed amount of α (or β) stabilizer, as in the front face showing the Ti–6Al–xV diagram. Binary (Ti–V) and pseudobinary (Ti–6Al–V) phase diagrams are shown as examples

in Fig. 5.2C and D [11]. For a given V level, the addition of Al raises T_β and for a given temperature it increases both the volume fraction of the α phase and the V content of the remaining β phase, illustrating the ability to tailor the microstructure and properties through processing.

The effects of varying amounts of α and β stabilizers and the neutral elements in terms of stabilizing these phases in Ti alloys can be represented qualitatively by converting them to equivalent Al and Mo concentrations, respectively, as follows [5,7]:

$$[\mathrm{Al}]_{eq} = [\mathrm{Al}] + [\mathrm{Zr}]/6 + [\mathrm{Sn}]/3 + 10[\mathrm{O} + \mathrm{C} + 2\mathrm{N}], \text{ and}$$

$$[\mathrm{Mo}]_{eq} = [\mathrm{Mo}] + [\mathrm{Ta}]/5 + [\mathrm{Nb}]/3.6 + [\mathrm{W}]/2.5 + [\mathrm{V}]/1.5 + 1.25[\mathrm{Cr}] + 1.25[\mathrm{Ni}] + 1.7[\mathrm{Mn}] + 1.7[\mathrm{Co}] + 2.5[\mathrm{Fe}],$$

where [X] is the concentration of element "X" in wt% in the alloy.

These empirical relations, different versions of which are available in the literature, are generally useful in classifying and comparatively assessing alloys in terms of the formation and relative stabilities of their constituent phases. The concept of $[\mathrm{Al}]_{eq}$ was used originally to provide a measure of the combined effects of α stabilizer elements and thereby to determine an upper limit for the alloying additions to high temperature alloys that will prevent embrittlement following creep exposure [12].

Al and O are strong α stabilizers in terms of raising the $\alpha/(\alpha + \beta)$ boundary. Although Sn and Zr are β stabilizers with very small effects on T_β, Sn acts as an α stabilizer in the presence of Al. Zr may substitute for Ti and add to the effects of other α stabilizers. The $[\mathrm{Mo}]_{eq}$ can be used to estimate the relative β stabilizing tendency upon quenching of multicomponent alloys compared with that of a binary Ti−Mo alloy in which this phase can be retained at about 10 wt% of Mo [13]. The $[\mathrm{Al}]_{eq}$ and $[\mathrm{Mo}]_{eq}$ will progressively decrease and increase, respectively, with relative increases in the amount of the β stabilizer additions.

The commonly used terminologies for commercial Ti alloys differ from their classification into α, α/β, and β alloys in accordance with the phases present in equilibrium at room temperature. As mentioned earlier, at high quenching rates the β phase transforms martensically into nonequilibrium variants of the α phase, with the M_s temperature decreasing with increasing alloying additions. Alloys in which the untransformed β phase can be retained completely by quenching to room temperature are designated as metastable β alloys. Alloys with T_β at or below room temperature consist fully of equilibrium β and are designated as stable β alloys.

All the aerospace alloys designated in practice as "β alloys" are in fact highly β stabilized α/β alloys close to the $(\alpha + \beta)/\beta$ boundary and designated as near-β alloys or metastable β alloys, which has been shown separately in Fig. 5.2A. Similarly, among the α/β alloys, those close to the $\alpha/(\alpha + \beta)$ boundary that have less than about 10% by volume of the β phase in equilibrium are also termed as near-α alloys. Thus all the representative structural alloys shown in Table 5.2 are in principle α/β alloys, but in common practice are designated as near-α, α/β, or β (to include both near-β and metastable β) alloys, which will be used in the remainder of this chapter. Some of these alloys, e.g., SP-700, are not produced currently, but are included for

Table 5.2 Representative Structural Titanium Alloys

Alloy		Composition (wt%)—Nominal or Range. When One Value Is Shown for Fe and O, It Is the Maximum												T_β		Maximum Service Temperature	
	Nominal Composition (Common/Commercial Names)	Al	Zr	Sn	Mo	Nb	V	Cr	Fe	Si	O	$[Al]_{eq}$	$[Mo]_{eq}$	(°C)	(°F)	(°C)	(°F)
Alpha + beta	Ti–6Al–4V (Ti-6-4)	5.5–6.75					3.5–4.5		0.4		0.20	6.0	2.7	995	1823	400	752
	Ti–6Al–4V ELI (Ti-6-4 ELI)	5.5–6.5					3.5–4.5		0.25		0.13	6.0	2.7				
	Ti–6Al–1.7Fe–0.1Si (Timetal 62S)	5.5–6.5							1.3–2.0	0.07–0.13	0.15–0.20	6.0	4.3	1015	1859		
	Ti–6Al–6V–2Sn (Ti-6-6-2)	5.0–6.0		1.5–2.5			5.0–6.0		0.35–1.0		0.20	6.7	4.0	945	1733		
	Ti–6Al–2Sn–2Zr–2Mo–2Cr–0.15Si Ti-6-22-22)	5.25–6.25	1.75–2.25	1.75–2.25	1.75–2.25			1.75–2.25	0.25	0.12–0.2	0.14	7.0	4.5	960	1760		
	Ti–4.5Al–3V–2Mo–2Fe (SP700)	4.0–5.0			1.8–2.2		2.5–3.5		1.7–2.3		0.15	4.5	9.0	900	1652		
	Ti–4Al–2.5V–1.5Fe (ATI 425)	3.5–4.5					2.0–3.0		1.2–1.8		0.20–0.30	4.0	5.4				
	Ti–5Al–4V–0.6Mo–0.4Fe (TIMETAL 54M)	5			0.7		4		0.5			5.0	4.3	950	1742		
	Ti–5Al–4Cr–4Mo–2Sn–2Zr (Ti-17)	4.5–5.5	1.6–2.4	1.6–2.4	3.5–4.5			3.5–4.5			0.20	6.0	9.0	890	1634	400	752
	Ti–6Al–2Sn–4Zr–6Mo Ti-6-2-4-6)	5.5–6.5	3.6–4.4	1.75–2.25	5.5–6.5				0.15		0.15	7.3	6.0	940	1724	450	842
Near-alpha	Ti–6Al–2Sn–4Zr–2Mo–0.1Si (Ti-6-2-4-2)	5.5–6.5	3.6–4.4	1.8–2.2	1.8–2.2				0.25	0.06–1.3	0.15	7.3	2.0	995	1823	565	1049
	Ti–6Al–2.7Sn–4Zr–0.%Mo–0.45Si (TIMETAL 1100)	5.5–6.5	3.5–4.5	2.4–3.0	0.35–0.5				0.03	0.35–0.5	0.09	7.6	0.4	1015	1859	600	1112
	Ti–5.6Al–3.5Sn–3Zr–1Nb–0.25Mo–0.3Si (TIMETAL 829)	5.2–5.7	2.5–3.5	3.0–4.0	0.2–0.35	0.7–1.3				0.2–0.5	0.09–0.15	6.7	0.3	1015	1859	540	1004

Continued

Table 5.2 Representative Structural Titanium Alloys—cont'd

Alloy		Composition (wt%)—Nominal or Range. When One Value Is Shown for Fe and O, It Is the Maximum												T_β		Maximum Service Temperature	
	Nominal Composition (Common/Commercial Names)	Al	Zr	Sn	Mo	Nb	V	Cr	Fe	Si	O	$[Al]_{eq}$	$[Mo]_{eq}$	(°C)	(°F)	(°C)	(°F)
	Ti–5.8Al–4Sn–3.5Zr–0.7Nb–0.5Mo–0.35Si–0.06C (TIMETAL 834)	5.5–6.1	3.0–5.0	3.0–5.0	0.25–0.75	0.5–1.0				0.2–0.6	0.075–0.15	7.6	0.7	1045	1913	600	1112
	Ti–8Al–1Mo–1V (Ti-8-1-1)	7.35–8.3			0.75–1.25		0.75–1.25		0.15		0.06–0.12	8.0	1.7	1040	1904	455	851
Near-beta	Ti–10V–2Fe–3Al (Ti-10-2-3)	2.6–3.4					9.0–11.0		1.6–2.2		0.13	3.0	11.7	800	1472		
	Ti–5Al–5Mo–5V–3Cr (Ti-5553)	4.4–5.7			4.0–5.5		4.0–5.5	2.5–3.5	0.3–0.5			5.0	13.3	850	1562		
	Ti–5.5Al–5Mo–5V–2.3Cr–0.8Fe–0.14O (TIMETAL 18, Ti-18)	5.3–5.5			4.6–5.0		4.8–5.0	2.0–2.3	0.7–0.8		0.12–0.14	5.5	13.2	850	1562		
Metastable beta	Ti–13V–11Cr–3Al (Ti-13-11-3)	3					13	11				3.0	33.4	700	1292		
	Ti–3Al–8V–6Cr–4Zr–4Mo (Ti Beta C)	3.0–4.0	3.5–4.5		3.5–4.5		7.5–8.5	5.5–6.5	0.3			3.7	16.8	730	1346		
	Ti–15V–3Cr–3Sn–3Al (TIMETAL 15-3)	2.5–3.5		2.5–3.5			14.0–16.0	2.5–3.5	0.25		0.13	4.0	13.8	760	1400		
	Ti–15Mo–3Nb–3Al–0.2Si (TIMETAL 21S)	2.5–3.5			14.0–16.0	2.4–3.2			0.4	0.15–0.25	0.11–0.17	3.0	15.8	810	1490		

Ti-6-6-2 has 0.35–1.0 Cu. Each other element not indicated has a specified maximum and the total of these elements have specified maximum.

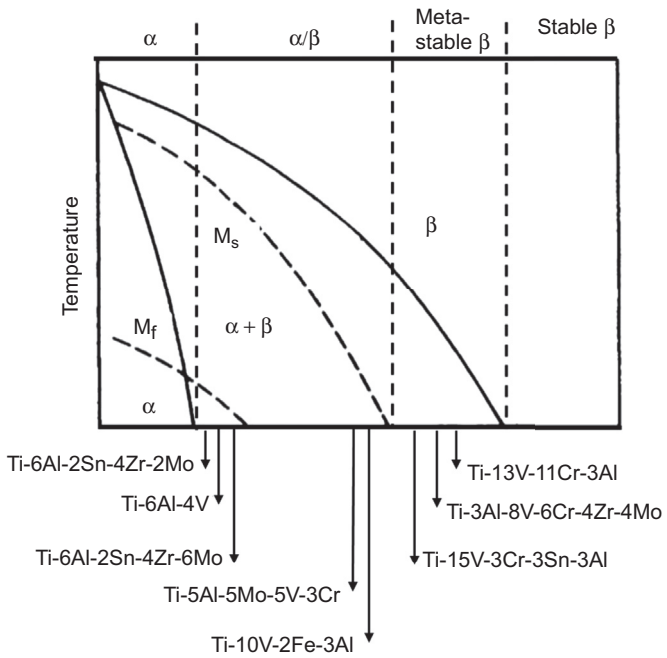


FIGURE 5.3

Mapping of commercial Ti alloys onto the pseudobinary diagram for the Ti-β stabilizer element system.

Adapted from I. Polmear, D. St. John, Titanium alloys, in: Light Alloys: From Traditional Alloys to Nanocrystals, Elsevier, 2006, pp. 299–365.

illustrating the range of compositions and for discussing the underlying metallurgy. Fig. 5.3 maps the compositions of some of these commercial alloys onto the pseudobinary phase diagram by grouping them into their common designations and giving an indication of the extent of β stabilization [6].

A brief description of the approaches to processing commercial Ti alloys and the resulting microstructural morphologies will be beneficial to understanding the distinguishing characteristics of the various alloy types. Starting with sponge, for which the Kroll process is still the principal source, the steps involved in the production of Ti alloy mill products and components are shown schematically in Fig. 5.4.

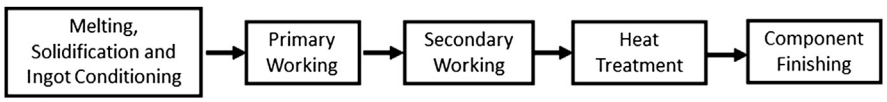
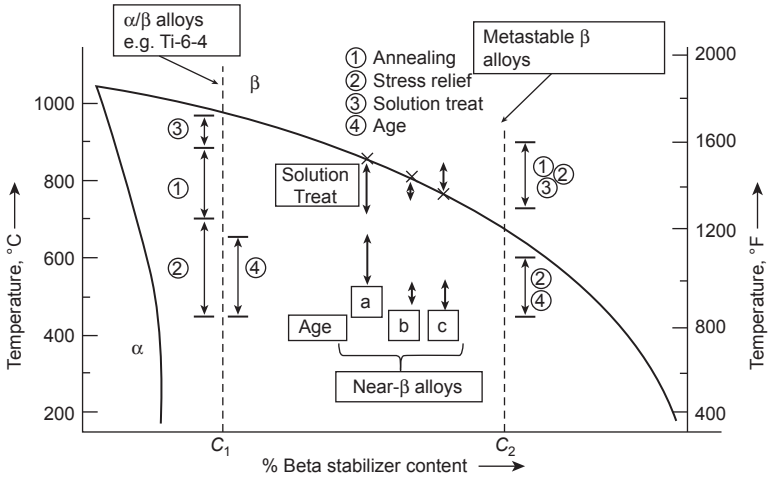


FIGURE 5.4

Processing steps for Ti alloys.

The first step is the melting of sponge and the alloying elements and solidifying the melt into ingots, which are then conditioned and homogenized to improve their compositional uniformity for subsequent working. Primary working involves ingot breakdown typically first above and through T_β, where the required forces lower. Working through T_β is necessary to promote recrystallization during the subsequent anneal in the β field. This is followed by working below T_β in the two-phase field to prevent microstructural coarsening. This step results in mill products such as billet, bar, plate, and sheet. In the secondary working stage, mill products are converted to components by forging, ring rolling, or extrusion of bar and billet and by the forming of sheet and plate. The heat treatment of components includes processes such as stress relief, annealing, solution heat treatment, and aging to achieve the desired microstructures. Manufacturing operations like final machining to shape and chemical milling are performed by the users. Detailed descriptions of these steps are available from several textbooks and ASM International publications. Although this is a general description of the overall processing of Ti alloys, significant variations exist in the thermomechanical processing steps and parameters for individual types of alloys. However, the principal focus of this chapter is on the effects of thermomechanical processing and heat treatments.

The general approach to heat treating Ti alloys is shown in Fig. 5.5 [11] along with a superposition of the temperature ranges for these operations for the various classes of Ti alloys. The α/β and near-β alloys are solution treated slightly below



(a – Ti-5Al-5Mo-5V-3Cr, b – Ti-10V-2Fe-3Al and c - Ti-15V-3Cr-3Sn-3Al
Points marked X are the mid-point of the range of T_β for the alloys [13])

FIGURE 5.5

Temperature ranges for various heat treatment operations for Ti alloys.

Adapted from F.H. Froes, Principles of beta transformation and heat treatment of titanium alloys, in: Titanium – Physical Metallurgy, Processing and Applications, ASM International, 2015, pp. 75–94. With permission of ASM International. All rights reserved. www.asminternational.org.

T_β and the metastable β alloys slightly above this temperature. Aging is conducted in a range depending on the desired final properties.

The process of solution heat treatment (SHT) and aging is only one among the many final "tempers" that are used for Ti alloys. The M_f temperature for Ti−6Al−4V is above room temperature (Fig. 5.3) and the β phase should transform to martensite upon water quenching from above T_β. However, for α/β alloys, SHT is typically performed slightly below T_β and thus the quenched alloy will have some "primary" α phase whose volume fraction will increase with decreasing SHT temperature. This temperature also determines the composition of the β phase, which will transform to martensite until it reaches a level where its M_s is below room temperature, in which case it will be retained in metastable equilibrium.

For Ti−6Al−4V quenched from its SHT temperature, the product of transformation of β will change with decreasing cooling rate from martensite to α formed by nucleation and growth. The morphology of the latter will change from acicular to plate like with further decrease in the cooling rate and a corresponding decrease in the response to aging. It should be noted that the term "aging" is a misnomer for an alloy like Ti−6Al−4V in which metastable β cannot be retained even at typically rapid cooling rates. The lower temperature anneal should rather be referred to as "tempering", although the term aging is used in common practice. In contrast, SHT of metastable β alloys is performed above T_β and the quenched alloys, in which β is retained in metastable equilibrium, are "aged" to precipitate "secondary" α and provide hardening. Near-β alloys are quenched from below T_β, but due to the high solute supersaturation of β, sufficient amount is retained in metastable equilibrium for subsequent age hardening. The diversity of processing, microstructures, and properties achievable in Ti alloys will be discussed in detail subsequently.

5.2.2 CHARACTERISTICS OF TITANIUM ALLOYS

The general characteristics of commercial Ti alloys are listed in Table 5.3. The α alloys include commercially pure (CP) Ti. Although CP Al alloys have Fe and Si as the impurity elements with no beneficial effects on properties, Ti alloys contain interstitial elements such as O, N, and C, which are considered as impurities in the sense that they deleteriously affect toughness. However, these α stabilizers, particularly O, are also used in controlled amounts for solid solution strengthening. The minimum yield strength of CP Ti increases from 172 to 483 MPa (25−70 ksi) with increasing oxygen from 0.18% to 0.40% [14]. The strength of α alloys, which are not heat treatable, can be increased further by adding substitutional solute elements like Al and Sn and by grain refinement. These alloys also contain small additions of Fe resulting in a dispersion of β to prevent coarsening of the microstructure. CP Ti alloys are used mostly in nonaerospace applications, although the alloy Ti−5Al−2.5Sn with its good weldability and low temperature properties is used for cryogenic applications in space systems.

Progressively increasing the amount of β stabilizers expands the α + β field and increases strength by increasing the amount of β that can be subsequently aged. The

Table 5.3 Typical Characteristics of Commercial Titanium Alloys

α Alloys	**α/β Alloys (Including Near-α Alloys)**	**Near-β and Metastable β Alloys**
• Not heat treatable • May contain small amount of β for microstructure refinement • Satisfactory room temperature strength • Good creep resistance • Good toughness • Weldable • Poor fabricability	• Heat treatable • At equilibrium α + β • Increasing room temperature strength, decreasing creep resistance and deceasing fabricability with increasing β stabilization • Good toughness • Weldable at β $V_f < 20\%$ • Good producibility	• Heat treatable • At equilibrium α + β • High room temperature strength • Low creep resistance • Good toughness • Poor weldability • Excellent fabricability

As discussed in the text, metastable β alloys are α/β alloys in which β can be retained in metastable equilibrium by quenching.

increase in strength and fabricability is accompanied by a decrease in creep resistance. The processing conditions for a given α/β alloy can also be varied to produce various microstructures for different combinations of strength, toughness, and fatigue properties. Within this context, this chapter will focus on the physical metallurgy of the two classes of Ti alloys used in airframes, namely α/β alloys, an example of which is Ti−6Al−4V, the most commonly used alloy for these applications, and β alloys, an example of which is Ti−5Al−5Mo−5V−3Cr, the high strength alloy used in the Boeing 787 landing gear. The near-α alloys, used in engines and the relatively hot structures of the airframes such as nacelles, the most common of which is Ti−6Al−2Sn−4Zr−2Mo−0.08Si, will be discussed to the extent necessary to illustrate the metallurgy of α/β alloys.

Depending on processing, minimum yield strength of Ti−6Al−4V can vary between about 850 and 1050 MPa (∼125−150 ksi) and that of Ti−5Al−5Mo−5V−3Cr between about 800 and 1200 MPa (∼115−175 ksi). The maximum use temperatures for Ti−6Al−4V and Ti−6Al−2Sn−4Zr−2Mo−0.1Si are about 400 and 565°C (∼750 and 1000°F), respectively. The processing−microstructure−property schemes for these types of alloys exhibit sufficient variety and complexity to be illustrative of the metallurgical principles of the approach to designing Ti alloys with hierarchical microstructures. Unlike Al alloys, which need to be solution treated to dissolve all the precipitation hardening elements, Ti alloys can be heat treated in either the single-phase β field or the two-phase α + β field, giving wide latitude in selecting processing conditions for optimizing individual properties.

At amounts of Al beyond that typically added to commercial alloys, the Ti−Al system exhibits ordered intermetallic compounds α_2 (Ti_3Al) and γ (TiAl), which

have better high temperature properties and lower densities than near-α alloys. Intermetallics based on γ TiAl are beginning to find use in jet engines. Stable β alloys with low modulus and biocompatibility are used in biomedical applications. These alloys are not used in airframes and will not be discussed further.

5.2.3 HISTORICAL DEVELOPMENT OF TITANIUM ALLOYS

A review of the evolution of Ti alloys will be helpful in setting the framework for understanding their complex physical metallurgy. As with other structural alloy systems, the knowledge of the composition−processing−microstructure−properties relationships for Ti alloys evolved concurrently with their development, insertion, and accumulation of service experience. With the development of computational materials science and availability of materials models, this experience is currently enabling the physics and data-based design of Ti alloys for targeted applications.

The development of Ti alloys has some similarities with that of Al alloys. The elements Ti and Al were discovered in 1791 and 1825, respectively. However, development of structural Al alloys did not begin until the introduction of the Hall−Heroult process in 1886 to economically produce Al metal and the discovery of precipitation hardening in 1906. Similarly, development of structural Ti alloys did not begin until the patenting of the Kroll process in 1940 and its demonstration to economically produce Ti metal in 1946. Following these milestones, the recognition of the unique properties of Ti alloys spurred significant research in studying the effects of alloying elements and processing on their microstructure and properties. Within a decade, the workhorse Ti−6Al−4V, still the most widely used Ti alloy, had been patented. The history of the evolution of Ti alloys and their early applications are summarized very well in recent publications [15,16].

Following demonstration of the commercial feasibility of the Kroll process, the 1950s and 1960s witnessed many research programs aimed at elucidating the phase equilibria, strengthening mechanisms and the processing−microstructure−properties relationships for Ti alloys. A list of these early programs is provided in the review by Abkowitz [15]. The initial emphasis of Ti alloy development was on applications for high temperature service to increase the efficiency of engines and the performance of military systems. This was prompted by the expectation of superior high temperature stability for Ti alloys based on the melting point of Ti (1668°C, 3034°F), which is higher than that of Fe and Ni on which superalloys are based. However, susceptibility to oxidation limited the usefulness of Ti alloys to below about 600°C (∼1100°F). An additional constraint was the embrittlement caused by the ordering reaction and precipitation of α_2 intermetallic compound in alloys containing high amounts of α stabilizing elements, which was avoided in alloys with $[Al]_{eq}$ less than 9 [6,12]. The strength of α/β alloys with higher β stabilization was also found to decrease more slowly with increasing temperature up to about 400°C rendering alloys such as Ti−6Al−2Sn−4Zr−6Mo useful at temperatures slightly above that for Ti−6Al−4V (Table 5.2).

Among these early studies was an investigation of a series of ternary Ti−Al−V alloys with Al initially restricted to 4 wt% and V to 12 wt% with the objective of meeting certain targeted properties and fabricability. The Ti−6Al−4V alloy resulted from this study following the finding that an expected loss of ductility did not occur between 2 and 4 wt% Al. The amount of Al was then increased to 6 wt% and that of V restricted to 4 wt% to ensure that the alloy was weldable [15]. Ti−6Al−4V continues to be the most widely used to date and serves as the basis to compare subsequently developed alloys.

Because of the adequacy of Ti−6Al−4V for most aerospace applications, the number of new structural Ti alloys developed over the past five decades has been limited. An extensive compilation of the properties of alloys current as of the early 1990s is available in *ASM's Materials Properties Handbook* [17] from which representative alloys are shown in Table 5.2 along with their $[Al]_{eq}$, $[Mo]_{eq}$, and T_β as well as the maximum use temperature for many of the alloys. It should be noted that although these alloys contain both α and β stabilizers, the $[Al]_{eq}$ and $[Mo]_{eq}$ values have been calculated independently based solely on the respective α and β stabilizer content. However, as will be discussed subsequently, the effectiveness of β stabilizers will be reduced by the α stabilizers and vice versa.

It is interesting that only ATI 425, TIMETAL 54M, TIMETAL 18, and Ti-5553 are not found in the list published in 1994. The β alloy Ti−13V−11Cr−3Al is in very limited use for secondary applications use but is included for reference. The list includes only the alloys developed in the United States and United Kingdom, although many alloys were also developed in the former Soviet Union. It should also be noted that all these alloys contain some level of interstitials, whose amounts are controlled but not accounted for in the calculation of $[Al]_{eq}$ and the effect of Si is not included in $[Mo]_{eq}$.

5.2.4 SUMMARY

The general attributes and status of structural Ti alloys are summarized below.

- Unlike Al alloys that have standardized classifications and designations from the Aluminum Association, which also maintains cross-references between alloys developed globally, Ti alloys are referred to variously by their compositions (e.g., Ti-64 or Ti−6Al−4V) or common names (e.g., Ti-1100 denoting a temperature capability of 1100°F, Beta C, etc.). Many alloys are single source and are typically procured to AMS specifications or in their absence, such as for the proprietary alloy Ti−5Al−5Mo−5V−3Cr, to user specifications.
- The values of $[Al]_{eq}$ are the highest for near-α alloys and range from 6.8 to 8.0 for those shown in Table 5.2. The maximum service temperature for these alloys generally increases with increasing $[Al]_{eq}$. The Ti−8Al−1Mo−1V alloy, developed in the early 1950s, is an exception due its lack of additional solid solution strengthening by Zr and Sn. All these alloys have small amounts of β

stabilizers to impart heat treatment capability for tailoring the microstructural morphologies of the phases to meet target properties.

- The values of $[Mo]_{eq}$ are the highest for β alloys and range from 11.7 to 22.4. All these alloys have small amounts of Al added to enable hardening of the β phase by the precipitation of α. Among the three classes, these alloys develop the highest strength levels at room temperature.
- The $[Al]_{eq}$, $[Mo]_{eq}$, strength levels, and temperature capabilities for the α/β alloys are intermediate to those of the α/β and β classes. Most of these alloys are capable of service up to about 400°C.
- The temperature capability of the near-α alloys is increased by reducing the $[Mo]_{eq}$ and thus the volume fraction of the β phase, increasing the amount of Sn and Zr, adding the slower diffusing Mo and Nb instead of V as the β stabilizers and adding sufficient Si for silicide precipitation [18]. Although α_2 precipitation is avoided in α/β alloy by processing above the solvus for this phase (∼550−600°C for Ti−6Al−4V), near-α alloys are aged below the solvus to precipitate this phase for improving high temperature strength.
- Development of α/β alloys has focused generally on achieving improvements relative to Ti−6Al−4V. For example, compared to Ti−6Al−4V, Ti−6Al−6V−2Sn develops higher strength from the higher V and Sn additions, Ti−62S develops similar properties at lower cost due to replacement of V by Fe and SP-700 is superplastically formable at a lower temperature.
- An example of β alloy development is the recent introduction of Ti−5Al−5V−5Mo−3Cr, used in Boeing 787, designed for better processability relative to Ti−10V−2Fe−3Al used in the Boeing 777.
- Finally, unlike Al alloys, Ti alloys do not have standardized temper designations. Processing temperatures for individual Ti alloys are specified in relation to their T_β. Although for Al alloys, these temperatures are related to the equilibrium solvus, the actual values and ranges are specified for each alloy−temper combination. Solution treatment and aging, particularly of α/β alloys, do not denote precipitation hardening treatments in the strict sense, but typically involve heating at a high temperature in the two-phase region to increase the volume fraction of the β phase followed by aging at a lower temperature to decompose the excess β phase for strengthening by its transformation products [19].

The earlier discussion is intended to provide an overview of the types of Ti alloys and the approaches to alloying as a prelude to the detailed discussion of their composition−processing−microstructure−properties relationships. The next section on the physical metallurgy of Ti alloys will describe the alloying approaches, the individual and combined effects of the alloying elements, and the processing paths that are available and necessary to achieve the microstructures for desirable properties. The diversity of microstructural morphologies that make Ti alloys attractive also adds significant complexity in delineating the interactions among the hierarchical features that affect the deformation mechanisms and determine the properties.

5.3 PHYSICAL METALLURGY OF TITANIUM ALLOYS

The overall approach for alloying Ti was discussed earlier in some detail in relation to the classification of Ti alloys and their commonly used designations. In the following sections, the physical metallurgy of Ti alloys is discussed in the framework of this distinction and the distinguishing composition—processing—microstructure—properties relationships.

5.3.1 ALLOYING OF TITANIUM

A review of the compositions of structural Ti alloys (Table 5.2) shows that in practice only a few elements are used for alloying Ti. Some of the attributes considered for their selection are cost, density, solid solubilities, and diffusivities in the α and β phases and the extent of hardening. Commercial alloys have multiple alloying elements whose combined effects on phase stabilities (in terms of expanding the $\alpha + \beta$ field to provide an adequate window for processing and the ability to control the amounts of primary phases) are also equally important.

Al is the only substitutional solute used for α stabilization. The interstitial elements play an important role in Ti alloys. For example, the levels of O are kept very low to improve toughness or within a controlled range to adjust T_β for favorable processing windows or imparting strength. Only Sn and Zr are the neutral elements used for solid solution hardening. Alloying elements used as β stabilizers are Mo, V, Nb, Cr, and Fe. Si is added in small amounts to selected alloys.

The properties of Ti alloys are controlled not only by the volume fractions of the α and β phases, which are determined by the composition but also by their morphologies and the way they are distributed, which are determined by processing and the final heat treatments. The early focus of Ti alloy development was on raising their operating temperature limits by increasing the amounts of α stabilizers and thus T_β. It was soon realized that addition of β stabilizers, which imparted the ability to heat treat the alloys and manipulate the microstructures, was necessary to achieve optimum combinations of properties. Following the introduction of Ti—6Al—4V in the early 1950s, further alloy development has generally proceeded in three directions: (1) increasing the temperature capability for use in engines, (2) increasing the strength for use in structures at ambient and more moderate temperatures, and (3) imparting attributes such as lowering cost and ability to process at lower temperatures.

Although the number of new structural alloys developed over the past two to three decades has been rather limited, the composition and processing of each alloy are uniquely tailored to achieve combinations of attributes such as fabricability, hardenability (ability to achieve adequate properties in thick sections), and the mix of properties. The alloying of Ti alloys is described only briefly in this section with more details provided in the discussion of individual alloys.

5.3.1.1 Phase Stability

The effects of alloying elements on the phase stability of Ti have been studied from both electronic structure and thermodynamic considerations [6,7]. Ti is a group IV transition metal (TM) with an unfilled 3d orbital. When it is alloyed with Al, the s-p electrons occupy lower energy levels and the d electrons occupy the Fermi level in the conduction band. Thus alloying with "simple" (nontransition) metals like Al preserves the HCP structure and stabilizes the α phase [20]. With increasing levels of the α stabilizer, the solid solution is terminated by the formation of an intermetallic compound, e.g., α_2 (Ti_3Al).

The most commonly used alloying elements added to Ti to stabilize the β phase are the group V (V and Nb) and group VI (Cr and Mo) TM. From group IV to VI, the *e/a* ratio for these TM increases from 4 to 6 and the crystal structures change from HCP (group IV) to BCC (groups V and VI). The effectiveness of β stabilization by the TM increases with increasing *e/a* ratio of the alloying element, which for these metals is the group number, as indicated by the progressively increasing value of $[Mo]_{eq}$ from V to Fe. Additionally, for retention of metastable β by quenching, the *e/a* ratio of the alloy should be at least 4.2. From the perspective of thermodynamics, regular solution models of Ti alloys indicate short range ordering of alloys with simple metal solute (α stabilizers) and clustering with TM solute (β stabilizers), with the strength of the interaction between Ti and the solute atoms being higher for the former. The values of the interaction parameters with Ti have been measured as 0.96, 0.62, 0.35, 0.29, and 0.28 $(eV)^{0.5}$ for Sn, Al, Mo, Cr, and V, respectively [21].

5.3.1.2 Solid Solubility of Alloying Elements

Contribution from solid solution hardening is an important component of the strength of Ti alloys and hence the extent of solid solubility of alloying elements is a key consideration for their selection. Equally importantly, the temperature dependence of their solubility limits in both the α and β phases affects the shapes of the phase diagrams. These factors in turn determine the processing window, the extent of solute partitioning between the α and β phases, and the ability to achieve the desired distributions and morphologies of these phases for optimizing properties.

For complete mutual solid solubility between two elements, the empirical Hume–Rothery rules require that the crystal structures of the two elements be identical, their atomic diameters not differ by more than 15%, and that their electronegativities not be too different. The atomic diameters of all the alloying elements are within 15% of that of Ti. In addition, the substitutional solutes Mo and V (both BCC) are fully soluble in β Ti, whereas Zr (HCP and BCC) is fully soluble in both α and β. The solid solubility of FCC Al is higher in α than in β Ti. The elements O, N, H, and C with atomic diameters less than 60% of that of Ti readily form interstitial solid solutions.

5.3.1.3 Alloying of Near-α Alloys

Other than Ti–8Al–1Mo–1V, all near-α alloys contain up to 6% Al, 3%–5% Zr, with a few exceptions of about 2%–3.5% Sn and very small amounts of Si (Table 5.2). Most contain only small amounts of Mo although a few also use Nb

as β stabilizer. The Al_{eq} is greater than 7 for alloys with the highest temperature capability. It will be higher in alloys in practice, considering the effects of O, even with its limited presence as an impurity. The rate of diffusion of alloying elements is higher in the β phase whose amount is hence reduced by limiting the Mo_{eq} for all the alloys to less than 2. Among the available β stabilizers, the slower diffusing elements Mo and Nb are used. The amount of Fe, although not used as an alloying element in near-α alloys, is still restricted due to its high diffusivity [18]. The effects of alloying on the phase diagrams, in terms of processing windows (e.g., by using C as a minor addition to TIMETAL 834) and the reduction of the amounts of β in commercial alloys, are discussed in later sections.

5.3.1.4 Alloying of α/β Alloys

The composition of Ti−6Al−4V is closer to that of near-α alloys (Fig. 5.3), since it was developed for moderate to high temperature applications. Limiting the amount of β improves weldability. Compared with Ti−6Al−4V, subsequently developed α/β alloys all have higher levels of β stabilization and use alloying elements in varying combinations for different purposes as follows. For each alloy, the composition is adjusted to provide a processing path that will create the right scales and distributions of the microstructural features for the required properties.

- Higher strength at room and elevated temperatures is achieved in Ti−6Al−6V−2Sn by the addition of Sn, which strengthens both α and β phases. Addition of Cu and Fe improves heat treatability.
- The composition of Ti−6Al−2Sn−2Zr−2Mo−2Cr−0.1Si provides better combinations of strength and damage tolerance.
- With compositions tending toward near-β alloys, Ti-17 and Ti−6Al−2Sn−4Zr−6Mo have improved forgeability and hardenability, develop higher strength in thicker sections, and have slightly higher temperature use capability.
- V is replaced by Fe in TIMETAL 62S resulting in a lower cost alloy with comparable properties.
- SP-700 and the more recently developed alloys ATI 425 and TIMETAL 54M have lower $[Al]_{eq}$ and use Fe with its higher diffusivity for enhancing formability in terms of lowering the optimum superplastic forming temperature and for improved machinability, respectively.

5.3.1.5 Alloying of β Alloys

The β alloys as a class have higher $[Mo]_{eq}$ and lower $[Al]_{eq}$ than the other classes of Ti alloys. They exhibit higher strength at moderate temperatures than the near-α and α/β alloys owing to their strengthening by the precipitation of fine α from a supersaturated β solid solution. Among these alloys, those with lower β stabilization (Ti−10V−2Fe−3Al and Ti−5Al−5Mo−5V−3Cr) develop higher strength because of the higher amounts of α that can be precipitated, whereas those with higher β stabilization (TIMETAL 15-3 and TIMETAL 21S) have better formability and were developed mainly for sheet and foil applications.

5.3.1.6 Phases and Phase Relationships

All Ti alloys used in aerospace structures contain both the α and β phases in relative equilibrium when placed in service. This is unlike precipitation hardenable (PH) Al alloys, which always contain metastable, precipitate phases that provide the needed strength. Ti alloys also exhibit metastable phases, which, however, may act only as intermediate precursors for nucleating equilibrium phases with varying morphologies to achieve optimum property combinations. This section will describe the phases that can be present and the conditions for their formation in structural Ti alloys, which will be followed by a discussion of the effects of processing on the evolution of microstructures containing these phases and the alloy properties.

5.3.1.6.1 Equilibrium Phases

In addition to the α and β phases, the equilibrium phases of importance that occur in Ti alloys are the intermetallic compounds α_2 (Ti_3Al) and Ti_5Si_3. Compounds based on β eutectoid elements typically do not occur in Ti alloys due to the sluggishness of the reactions and the limited amounts of the alloying elements. The exception is the formation of $TiCr_2$ in Ti−13V−11Cr−3Al after prolonged exposure in service, as in the SR-71 [9]. Although the properties of Ti alloys are influenced principally by the morphologies of the α and β phases, their relative volume fractions and the partitioning of the alloying elements between them, which can be estimated from phase diagrams, play a significant role in the way processing affects the microstructure and properties.

From Fig. 5.2D it is seen that as the temperature decreases below T_β for an alloy such as Ti−6Al−4V, there is an increase in the volume fraction of the α phase and a rapid increase in the amount of V partitioning to the β phase (Figs. 5.2C,D and 5.5). The equilibrium α, also termed primary α (α_p), present at this temperature does not transform during subsequent cooling and aging. However, the composition of the β phase in conjunction with the processing parameters will determine how much of it is retained and the nature of the transformation products and thus the microstructure and properties.

The Ti−Al system exhibits the intermetallic compound α_2 (Ti_3Al) with a DO_{19} crystal structure. Fig. 5.6 shows the $\alpha/(\alpha + \alpha_2)$ phase boundary reported by several investigators [22]. Also shown is the region of occurrence of short range order. The α Ti matrix is precipitation hardened by α_2, which, being an ordered compound, also promotes planar slip that can reduce toughness. As mentioned earlier, $[Al]_{eq}$ is limited to nine in commercial alloys to avoid the possibility of ordering and α_2 precipitation. The stability of α_2 is increased by O and Sn, both of which raise its solvus, whereas Sn also substitutes for Al. The α_2 solvus for Ti−6Al−4V, Ti−6Al−2Sn−4Zr−2Mo−0.1Si, and Ti−5.8Al−4Sn−3.5Zr−0.7Nb−0.5Mo−0.35Si−0.06C (TIMETAL 834) are approximately 550−600, 650, and 750°C (1022−1112, 1202, and 1382°F), respectively [18].

The aging time needed for precipitation of α_2 decreases with increasing temperature. Upon aging at 550°C (1022°F), α_2 was observed in Ti−6Al−4V after 28 days and in a binary Ti−7Al alloy only after 84 days [23]. Correlations from atom probe

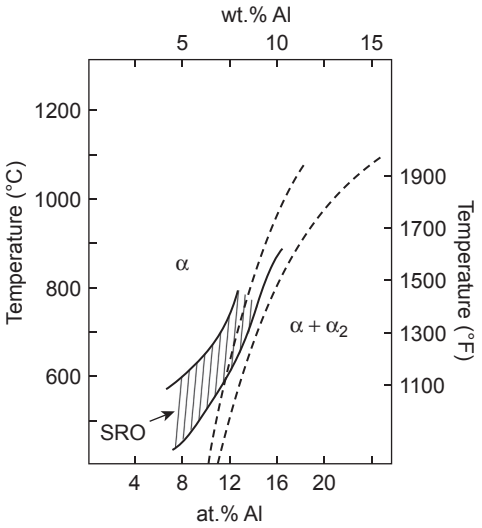


FIGURE 5.6

$\alpha/(\alpha + \alpha_2)$ phase boundary reported by several investigators. Also shown is the region of occurrence of short range order [22].

tomography and transmission electron microscopy showed that α_2 was preceded by the formation of clusters of Al atoms. The clusters occurred earlier in Ti−6Al−4V than in Ti−7Al, suggesting that the V in solution in α accelerates their formation by promoting vacancies thus increasing diffusivity and reducing the energy for formation of α_2. This is similar to the formation of clusters that transition to GP zones and θ' precipitates in Al−Cu alloys. The silicides Ti_5Si_3 or $(Ti,Zr)_5Si_3$ are present in alloys containing Si. Silicides are incoherent and precipitate at grain or phase boundaries and act as obstacles to dislocation motion [18].

5.3.1.6.2 Nonequilibrium Phases

Nonequilibrium phases play an important role in enabling optimum microstructures to be achieved for the desired properties in Al-, Ti-, and Fe-based alloys. The difference among these alloys is that metastable phases are generally only pathways to the final microstructure in Ti- and Fe-based alloys but are present in fully processed Al alloys in service during which they are stable for all practical purposes. The reliance of precipitation hardened Al alloys on metastable phases limits their usefulness to relatively low service temperatures.

The properties of Ti alloys are a superposition of the contributions from the individual constituent phases, their morphologies and how they interactively respond to deformation and environment. The microstructure of Ti alloys generally contain primary α, if processed in the $\alpha + \beta$ field prior to cooling and aging, and the products of transformation of the β phase, which themselves contain α and β in a variety of

morphologies. The composition and cooling rates from the processing temperature will determine whether and which of the metastable phases, martensite or omega (ω), will form. Martensites form in alloys with lower β stabilization such as Ti−6 Al−4V and the ω phases in near-β and metastable β alloys. The transformation of β phase to martensite is displacive and occurs with the cooperative movement of the atoms forming a new crystal structure. The composition of the parent phase is retained and thus the martensite is supersaturated with the solute elements. Two types of martensites, designated α' (hexagonal) and α'' (orthorhombic), occur in Ti alloys with the latter forming in alloys with higher β stabilization and thus higher solute concentration in the parent β phase. Both the martensite phases exhibit characteristic M_s and M_f temperatures, which are functions of alloy content. In addition, α'' can also form by deformation of the retained metastable β phase.

Fig. 5.7 shows the phases that will be present at room temperature upon quenching of alloys with increasing β stabilization [11]. Compositions C_1 and C_2 correspond respectively to the alloy content for which M_f and M_s occur at room temperature. Only the formation of the α' phase is shown in this figure. For an alloy with a total solute content less than C_1, the β phase composition will also be C_1 or lower at all solution treatment temperatures above T_2 and accordingly, all of this phase will transform to α'. Similarly, for an alloy with a concentration of alloying elements greater than C_2, the concentration of alloying elements in the β phase is always C_2 or higher at all solution treatment temperatures and accordingly, all this phase will be retained in the metastable state. Primary α will be present in alloys solution treated below T_β. No α' will form in any alloy quenched from below the

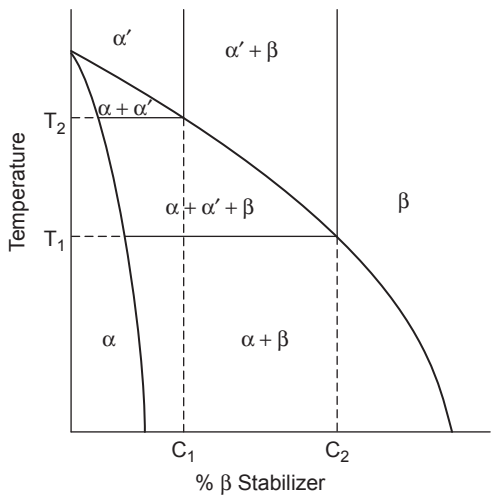


FIGURE 5.7

Schematic representation depicting the phases present after quenching from the indicated temperature regions [11].

Reprinted with permission of ASM International. All rights reserved. www.asminternational.org.

temperature T_2 because the β phase composition will always be greater than C_2. For alloys with total solute between C_1 and C_2 and solution treated between T_1 and T_2, the relative amounts of martensite and retained, metastable β will depend on the actual composition and solution treatment temperature.

With increasing β stabilization, the ω phase can form athermally (ω_a) during quenching or isothermally (ω_{iso}) upon aging of metastable β at relatively low temperatures. In alloys, such as, for example, Ti−10V−2Fe−3Al, in which ω_a forms, it is believed to compete with α″ formation. β phase separation occurs during aging of alloys with β stabilization sufficient to suppress formation of both martensites and the ω phases. In this reaction, very fine, uniformly dispersed coherent β′ phase precipitation is accompanied by solute partitioning that enriches the matrix and depletes the precipitate. The range of compositions for the formation of these phases is shown schematically in the pseudobinary phase diagram in Fig. 5.8A [13]. Fig. 5.8B [6] schematically shows the occurrence of the martensite phases α^m (α′ or α″) as a function of the *e/a* ratio for binary Ti-TM alloys. The phases present in selected commercial alloys are shown in Fig. 5.9 [11].

With their low modulus and biocompatibility, β Ti alloys are receiving significant attention for biomedical applications. Aided by modern experimental and analytical techniques, considerable research is being undertaken to understand and gain new insights into the mechanisms of formation of ω and α phases in these alloys [24]. In alloys used in aerospace structures, the metastable phases transform to equilibrium phases during subsequent processing and are thus not present in the final product.

5.3.1.6.3 Phase Relationships

The importance of a precise knowledge of phase diagrams and the kinetics of phase transformations for multicomponent systems representative of commercial alloys

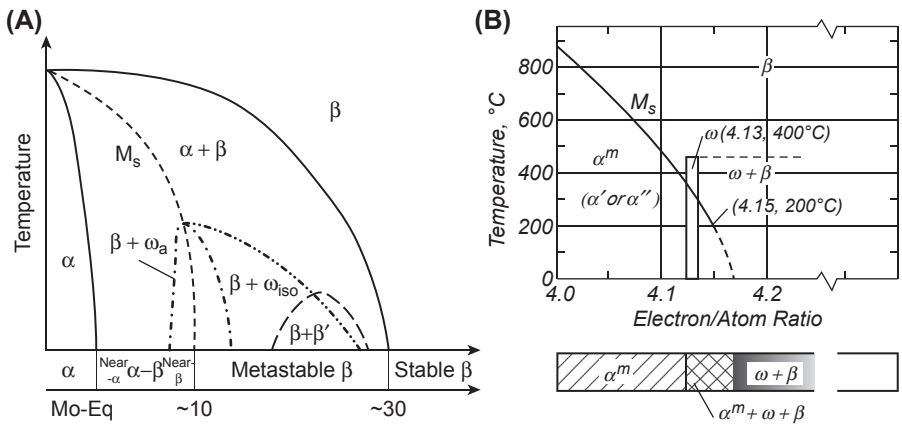


FIGURE 5.8

(A) Pseudobinary phase diagrams [13] and (B) schematic representation of the martensite and omega phases as a function of *e/a* ratio [6].

(B) Adapted and reprinted with permission of ASM International. All rights reserved. www.asminternational.org.

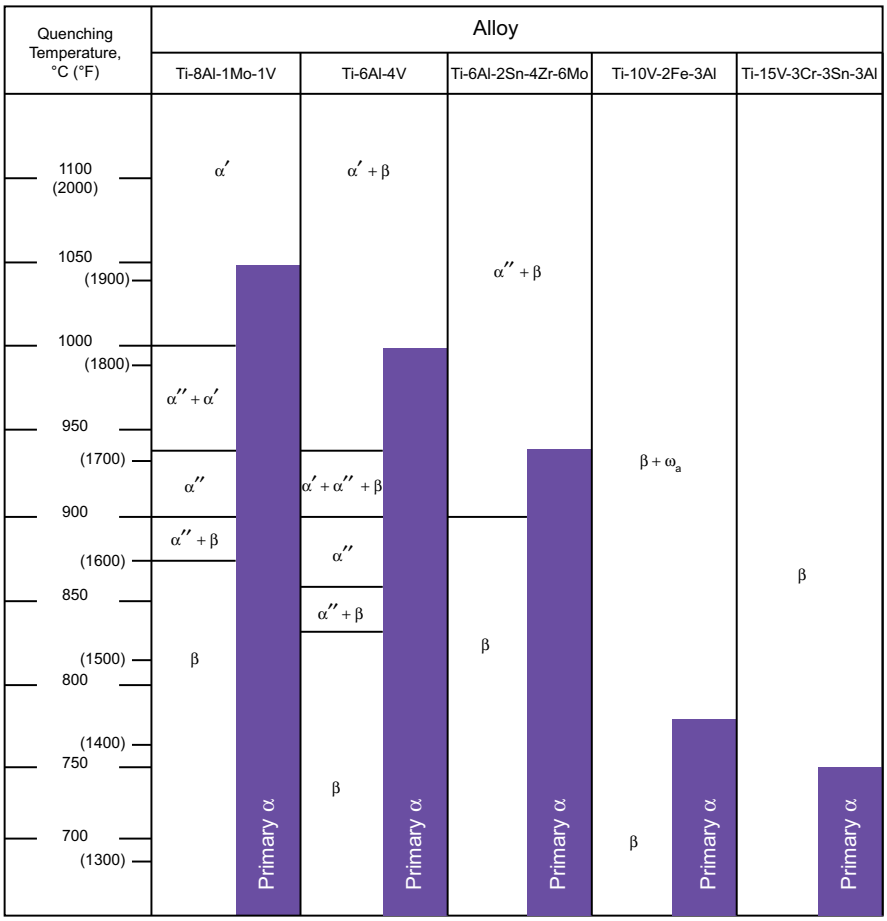


FIGURE 5.9

Phases present in various commercial alloys after quenching from the indicated temperatures [11].

Reprinted with permission of ASM International. All rights reserved. www.asminternational.org.

used in airframes has already been discussed in detail in the chapter on Al alloys. One advantage for Ti alloys relative to Al alloys is that their processing temperatures are much lower than the solidus and there is no possibility of localized melting. Ti alloys also offer a wider processing space compared with Al alloys, whose compositions need to be controlled to avoid localized melting, minimize grain coarsening, and ensure complete dissolution of solute all within the very narrow solidus-solvus temperature range available for solution treatment. However, the processing of Ti alloys still requires a knowledge of the phase relationships and transformations.

The most common and convenient way to represent the phase relationships for ternary and multicomponent Ti alloys is the use of isopleths, which are

vertical sections of the phase diagram for a fixed amount of one of the constituent elements. For example, the amount of Al is kept constant at 6% in the diagram shown in Fig. 5.2D and the phase relationships are shown as a function of V content and temperature. Fig. 5.2C, in which the amount of Al is 0, is just the binary Ti−V phase diagram. For alloys with more than three elements, the isopleths can still be used to represent phase relationships by combining the effects of all β stabilizers into a single value, as in the generic approach used in Fig. 5.3 to map commercial alloys in terms of the extent of their β stabilization.

Being the most widely used alloy, Ti−6Al−4V has been studied in considerable detail. Fig. 5.10A and B shows isopleths for Ti−Al−V alloys with constant levels of Al (with varying V) and V (with varying Al) for 2 and 4 concentrations, respectively [6]. The effect of Al on raising T_β and that of V on expanding the $\alpha + \beta$ field can be clearly seen. Fig. 5.10C shows isothermal sections for the Ti−Al−V system at four temperatures. Ti−6Al−4V is single phase β until slightly below 1000°C (1832°F) and lies in the two phase $\alpha + \beta$ field until 600°C (1112°F), as seen from both the isopleths and the isothermal sections.

One of the most important characteristics of Ti alloys in terms of selecting processing parameters is their T_β. Initial ingot homogenization and breakdown are conducted at temperatures between about 150 and 400°C (302 and 752°F) above T_β, whereas any subsequent processing in the single-phase field is performed within about 50°C (90°F) of this temperature to avoid excessive grain growth. Temperatures for processing (e.g., deformation processing and solution heat treatment) in the two-phase field are selected based on the required relative volume fractions of the two phases. This is particularly important for alloys designed for high creep resistance in which the amount of primary α needs to be limited to 5%−10%. As shown in Fig. 5.11, a shallower β approach curve allows for a wider and thus more practical temperature range for processing to obtain the controlled amount of this phase in IMI 834 (TIMETAL 834) than in IMI 829 (TIMETAL 829) [5,25] and in Ti-5553 than in Ti-10-2-3 [26]. Although the data for the change in volume fraction are plotted as a straight line in Fig. 5.11A, the β approach is not linear, as seen in Fig. 5.11B. The rate of change of volume fraction of the β phase increases with decreasing temperature below T_β.

Compositions of alloys cannot be precisely controlled in practice and the amounts of alloying elements are specified to be within an achievable range. Because alloying elements and interstitial impurities affect T_β significantly, it can vary widely within a range for different heats of a given alloy depending on their chemistry, as observed for Ti−6Al−4V for which it can be between 900 and 1000°C (1652 and 1832°F). This type of variation requires that T_β be measured and reported for every heat of Ti alloy supplied to industry [27]. With respect to β approach, the isothermal phase diagrams such as in Fig. 5.10C cannot be used to calculate the volume fractions and the compositions of each of the constituent phases. These must be measured experimentally or estimated using modeling of the phase relationships, as described next.

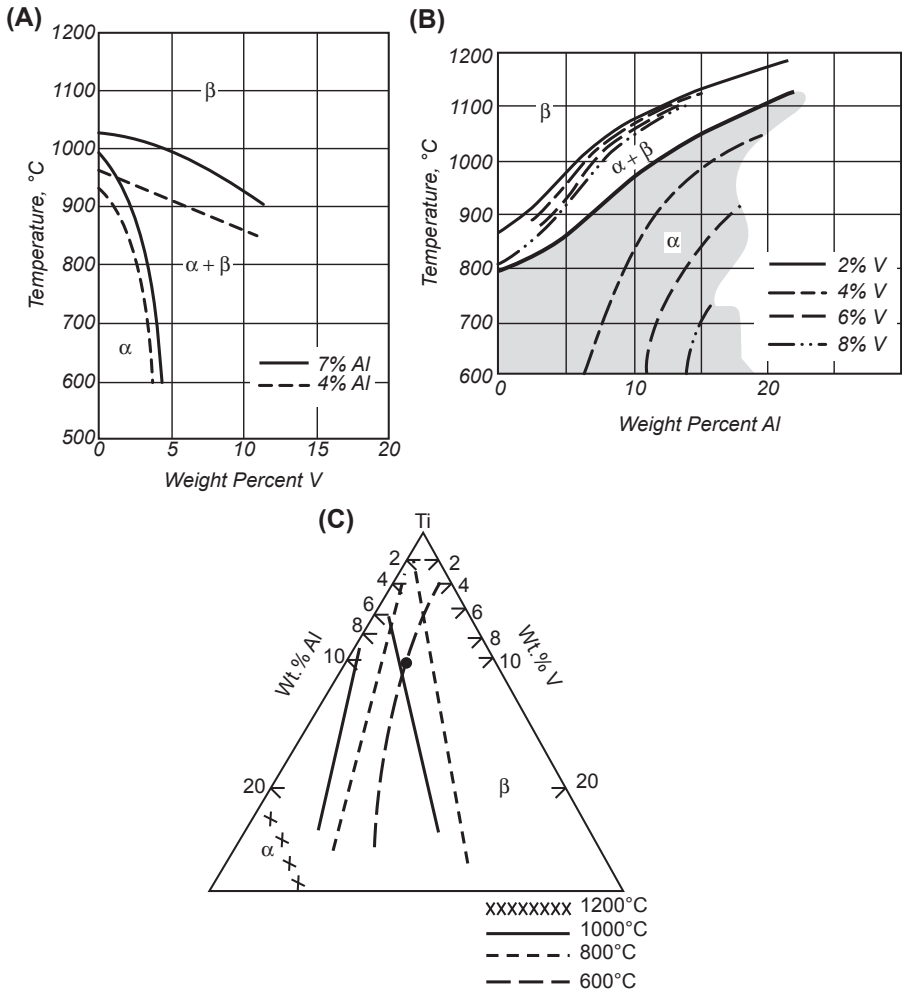


FIGURE 5.10

(A) and (B) Vertical [6] and (C) horizontal sections of the Ti–Al–V phase diagram.

Adapted from E.W. Collings, Introduction to titanium alloy design, in: J.L. Walter, M.R. Jackson, C.T. Sims (Eds.), Alloying, ASM International, 1988, pp. 257–370. With permission of ASM International. All rights reserved. www.asminternational.org.

5.3.1.6.4 Modeling of Phase Relationships

Both thermodynamic [27–29] and neural network modeling [30,31] methods have been used to predict phase relationships for Ti alloys. Modeling software performs calculations to predict phase diagrams and related quantities such as T_β, the phase proportions and the partitioning of alloying elements between them. As discussed earlier, these parameters are important for determining favorable processing conditions. For example, the optimum condition for superplastic forming of Ti–6Al–4V

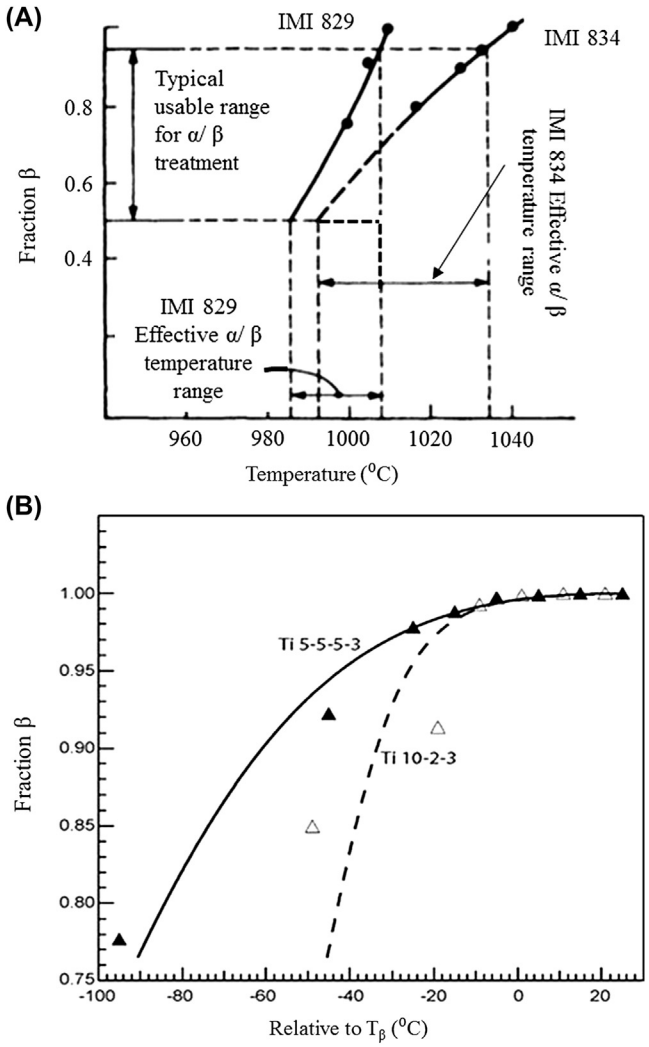


FIGURE 5.11

Beta approach curves for (A) TIMETAL 829 (IMI 829) and TIMETAL 834 (IMI 834) [5] and (B) Ti–5Al–5Mo–5V–3Cr and Ti–10V–2Fe–3Al [26].

is achieved when the volume fraction of the β phase is about 25% [32]. Thus it is important to know the temperature at which this condition occurs. Thermodynamic data needed for modeling are developed separately and available for alloy systems of interest.

Ability to accurately predict T_β for a Ti alloy of a specified composition is of great value in terms of reducing the time and cost involved in its experimental

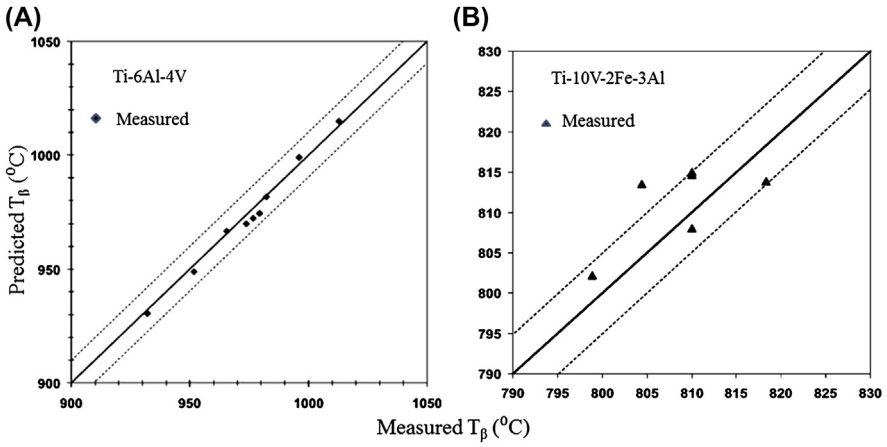


FIGURE 5.12

Comparison of predicted values of T_β with measured values for several heats of (A) Ti–6Al–4V and (B) Ti–10V–2Fe–3Al with different chemistries [27].

measurement for every heat. The "phase disappearance" method for measuring T_β involves heating of samples containing precipitated α phase at progressively higher temperatures separated by 15°C, holding for 15 min and water quenching [30]. T_β is then at most 15°C above the highest temperature for which α is still detected. The accuracy of the measurements can be improved by reducing the temperature interval, however, with additional time and cost.

Fig. 5.12 compares the predicted values of T_β with measured values for several heats of Ti–6Al–4V and Ti–10V–2Fe–3Al with different chemistries [27].

The predictions were made from calculations using the commercial software Pandat for multicomponent phase equilibrium calculations and the PanTitanium database for Ti alloys. The two values are in very good agreement with the average difference between them being within 3°C (~5°F) for Ti–6Al–4V and slightly higher for Ti-10-2-3. The significant influence of alloying elements on T_β, particularly for Ti–6Al–4V is seen from the measured values falling in a wide range of about 915–1010°C (1679–1850°F) for alloys with different compositions. Adding 10 ppm, each of O, C, and N was calculated to increase T_β of the baseline Ti–6Al–4V alloy by 0.27, 0.43, and 1.03°C, respectively. Predictions of T_β for several alloys in the Ti–Al–V and Ti–Al–Sn–Zr–Si systems have been found to agree well with that from thermodynamic modeling using ThermoCalc [30].

The slope of the β approach curve and the relative volume fractions of the α and β phases as a function of temperature are important for determining feasible processing windows for Ti alloys. Fig. 5.13 shows these values calculated using ThermoCalc for a Ti–6Al–4V alloy of a specified composition [29]. Also shown are the partitioning of Al and V to the two phases. V partitions rapidly to the β phase with decreasing temperature below T_β and the correspondingly increasing volume

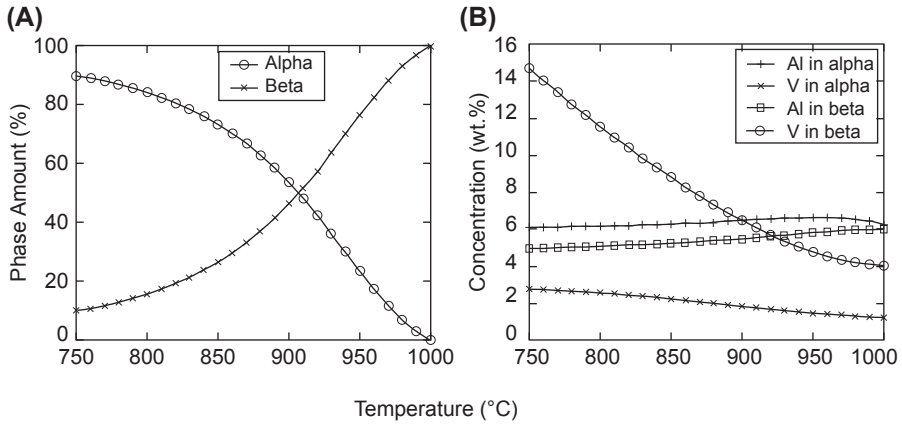


FIGURE 5.13

Calculated phase equilibria as a function of temperature (A) equilibrium α and β volume fractions and (B) equilibrium Al and V amounts in α and β for Ti–6Al–4V–0.2Fe–0.15O–0.03N–0.01C (all in wt%) [29].

fraction of α. Fig. 5.14 compares the calculated volume fraction of α with the measured values for one heat of Ti–6Al–4V and shows good agreement between the two [27]. The differences in the relative volume fractions of the two phases at a given temperature shown in Figs. 5.13 and 5.14 can be attributed to the varying alloy chemistries.

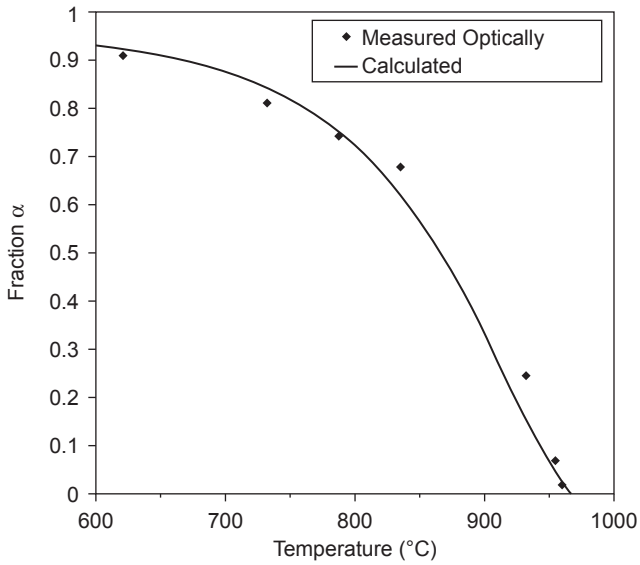


FIGURE 5.14

Calculated and measured fraction of α phase in Ti–6Al–4V as a function of temperature [27].

The accuracy of experimental measurements, reliability of thermodynamic databases, and availability of sufficient measured data to construct neural network models all determine the effectiveness and the predictive capabilities of the models. The continuing accumulation of such data, the refinement of databases, and the development of informatics methods can be expected to accelerate the future use of modeling, particularly for multicomponent commercial alloys.

5.3.2 PROCESSING OF TITANIUM ALLOYS

The general sequence of steps in the processing of Ti alloys starting from ingot casting through component finishing was outlined briefly earlier (Fig. 5.4). Ingot conditioning produces a surface smooth enough for its working without cracking and homogenization ensures uniformity of its composition. Following initial working above T_β, subsequent deformation processing (primary and secondary working) and heat treatment steps can be performed above or below this temperature using varying cooling rates after each operation. A diversity of microstructures can be produced this way for achieving a range of desired property combinations. Although the details of these microstructures and how they affect properties will be discussed later, a few key aspects are discussed here to help describe the effects of processing.

Highest strength is achieved in α/β alloys (including metastable β alloys) by solution heat treatment and aging. The achievable level of strength generally increases with increasing levels of β stabilizers in alloys. However, it is the distribution, morphologies, and arrangements of the α and β phases that determine properties such as toughness and resistance to creep and fatigue crack growth (FCG). Microstructures that are important in this regard are the lamellar, equiaxed, and bimodal (or duplex, which is a mixture of lamellar and equiaxed morphologies) types.

Lamellar microstructures are produced by slow cooling from the β field. It is always the first microstructure type produced in Ti alloys as they slowly cool from the β field after solidification. As discussed earlier, β can transform to martensite (α' or α'') by a displacive transformation or to α by nucleation and growth. The critical cooling rate for avoiding the latter in common α/β alloys such as Ti−6Al−4V is about 1000°C/min [33], achievable only in thin products by water quenching. Thus during the slow cooling of an α/β alloy from above T_β, the α phase nucleates initially at the prior β grain boundaries obeying the following crystallographic orientation relationship, of which there are 12 variants:

$$\{110\}_\beta \parallel \{0001\}_\alpha \text{ and } <1\bar{1}1>_\beta \parallel <11\bar{2}0>_\alpha$$

Parallel plates of α with one of the possible orientations, constituting a colony, then grow into the β grains until they impinge upon plates with a different orientation from another growing colony. Such a microstructure consisting of plates of α "lamellae" with retained β phase in between is shown for slowly cooled Ti−6Al−4V in Fig. 5.15 in which a few colonies and colony boundaries can be seen. The morphology changes to finer, needle-like, acicular α with increasing cooling rate

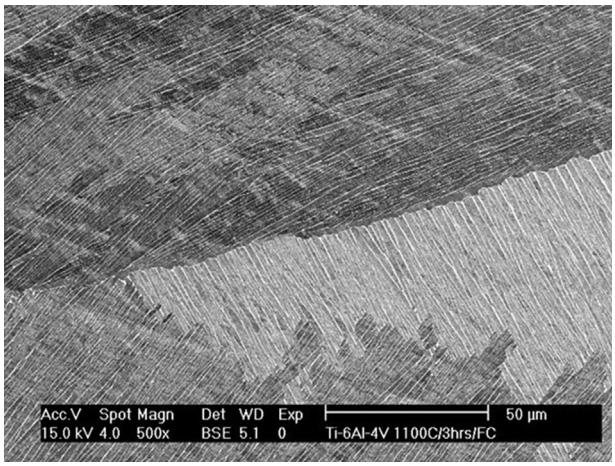


FIGURE 5.15

Microstructure of Ti–6Al–4V after cooling from 1100°C (2012°F).

Courtesy, Professor Raj Banerjee, University of North Texas.

from the β field. The large variety of microstructures that can be obtained in Ti alloys is documented in detail by Gammon et al. [34].

Achieving an equiaxed microstructure requires deformation and recrystallization in the $\alpha + \beta$ field. The typical sequence of processing used for Ti–6Al–4V and the lamellar and equiaxed microstructures that can result are shown in Fig. 5.16 [35]. This framework will be used to describe the processing of Ti alloys. Being used in critical applications, significant effort is also undertaken to eliminate various defects that could be introduced in these alloys during melting and subsequent processing.

5.3.2.1 Primary Working of Titanium Alloys

During the primary working stage, Ti alloy ingots are thermomechanically processed by a combination of upset, cogging, and rotary forging operations to break down the cast structure and produce mill products with uniform composition and microstructure. The principal mill products are billet, bar, and flat rolled plate and sheet, with casting electrodes constituting a very small percentage [36]. Billet is a semifinished product used for component shaping, for example, by forging, whereas bar, plate, and sheet are finished products. Plate and sheet are fabricated by rolling of slabs that are themselves rolled from forged blooms. Flat rolled products less than 0.187 in. (4.75 mm) thick are designated as sheet and those that are 0.1875 in. (4.75 mm) and thicker as plate. Bar is fabricated by rolling of billet using shaped rolls. The finished mill products may subsequently be machined or formed to shape.

Fabrication of mill products involves a series of heating, hot working, and cooling cycles. Working is performed both above and below T_β to refine the macro- and microstructure. After initial breakdown by hot working at about 150°C (270°F) above T_β, the ingot is worked at 35–50°C (60–90°F) below T_β for recrystallization.

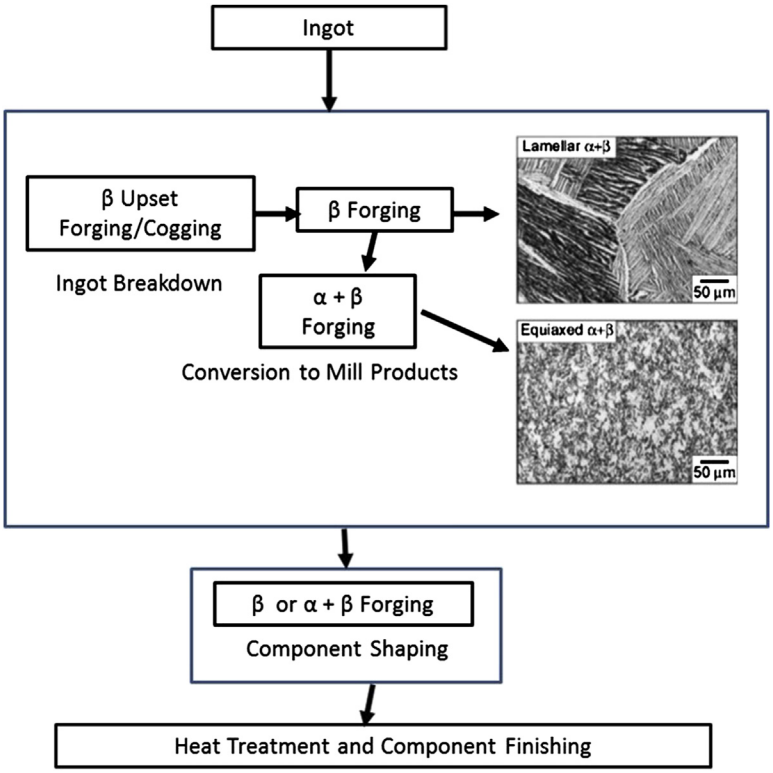


FIGURE 5.16

Typical thermomechanical processing sequence for Ti–6Al–4V forged component.

Micrographs from S. Tamirisakandala, B. Vedam, R.R. Bhat, Recent advances in the deformation processing of titanium alloys, Journal of Engineering Materials and Performance 12 (6) (2003) 661–673.

This is followed by working at about 50°C above T_β to complete the recrystallization process and then by final working in the $\alpha + \beta$ field. The typical range of hot working temperatures for ingot breakdown and finishing operations along with the rolling temperatures for bar, plate, and sheet is listed in Fig. 5.17 for selected alloys [37–39]. This figure clearly illustrates the typical working temperatures in relation to T_β. Although the maximum hot working temperatures for all the alloys listed are between 1050 and 1200°C (~1900–2200°F), those for commercial near-α and α/β alloys are no higher than about 150°C (270°F) above T_β, whereas for near-β and metastable β alloys they are about 350–450°C (~625–800°F) higher. This is because of the relative temperature dependence of the flow stress behavior of α/β and β alloys. Compared to the flow stress values for Ti–10V–2Fe–3Al and Ti–15V–3Al–3Cr–3Sn that for Ti–6Al–4V are higher but fall more rapidly with increasing temperature. When these values are compared in terms

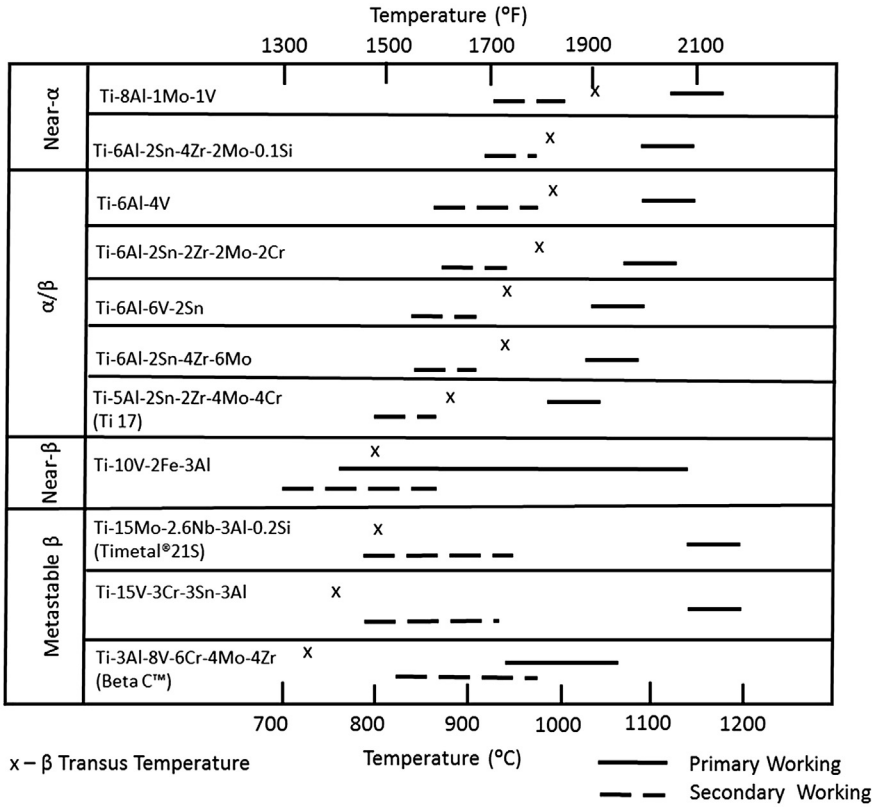


FIGURE 5.17

Temperature ranges for the primary and secondary working of representative titanium alloys.

of T_β, they are higher for β alloys at all temperatures due to the solid solution hardening resulting from higher solute levels in these alloys. With alloying content of 24 wt%, Ti−15V−3Al−3Cr−3Sn exhibits the highest flow stress. However, higher β phase content renders this alloy more formable than α/β alloys and strip/coil is often fabricated by cold rolling.

Hot working temperatures for Ti alloys are in the range of 0.65−0.75 of the solidus [37], which is lower than those for other material systems. The resulting high flow stress values coupled with their rapid increase with decreasing temperature narrow the useful range for hot working Ti alloys and render them difficult to process. Mill products are subjected to further processing by additional working (e.g., forging of billets), forming (e.g., superplastic forming), and heat treatment to optimize microstructures, which are influenced by the microstructures resulting from primary working. Significant advances are being made in the modeling and simulation of these processes to develop optimum processing schedules and elucidate processing−microstructure relationships.

5.3.2.2 Secondary Working of Titanium Alloys

During the secondary working of Ti alloys, the mill products are converted to useful component shapes by forging, extrusion, and ring rolling of bar and billet [40] and by forming of plate, sheet, strip, and tubing [41]. Forged Ti components are used widely in aerospace and other applications. Forgings generally exhibit superior properties compared with other similarly heat-treated mill products. However, despite the potential for fabricating close to final shape, significant portions of Ti forgings are typically machined away and "buy-to-fly" ratios of about 10–20 are not uncommon. The inability to achieve net shapes is due to a combination of factors such as the need for removing material to create deep pockets for weight reduction, which cannot be designed into the forging and for producing shapes that will ensure inspectability. The forging equipment, process, and parameters are similar to that for primary working. As shown in Fig. 5.16, forging can be performed in the $\alpha + \beta$ or β field depending on the property requirements in the finished component. Forging in the β field requires special care in terms of control of hold time at temperature to prevent excessive grain growth.

Presence of both α and β in Ti alloys provides inherent resistance to grain growth during forming in the $\alpha + \beta$ field. The high sensitivity of the flow stress of Ti alloys to strain rate, as measured by the index,

$$m = \partial\,(ln\,\sigma)/\partial\,(ln\,\dot{\varepsilon})$$

where σ is the flow stress and $\dot{\varepsilon}$ is the strain rate, coupled with the ability to produce a starting microstructure with a fine grain size by deformation in the $\alpha + \beta$ field, renders these alloys superplastically formable. The value of m for Ti–6Al–4V is shown for a range of temperatures, the corresponding volume fraction of the equilibrium α phase and for various strain rates in Fig. 5.18 [37]. The grain size is very stable

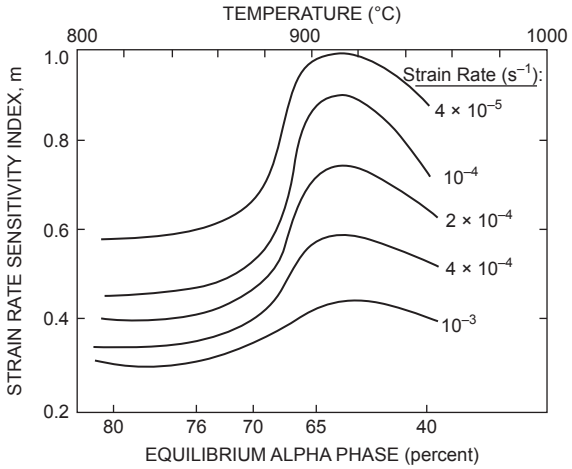


FIGURE 5.18

Dependence of m on temperature and volume fraction of α for Ti–6Al–4V [37].

during superplastic deformation of this alloy at 915°C (1680°F) growing from about 12 to less than 15 μm at a true thickness strain of 2 [42].

With alloys considered superplastically formable at values of *m* greater than 0.5, the temperature and deformation rate combinations for optimum forming can be obtained from this and similar plots. Superplastic forming of Ti alloy sheet with and without concurrent diffusion bonding has been used advantageously to design and fabricate components with fewer detail parts thus eliminating the need for fasteners and reducing cost and weight [43].

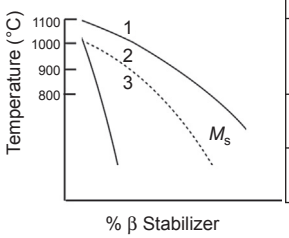
Die temperature is kept below 540°C (1000°F) in the conventional forging of Ti alloys, which can result in chilling and cause variations in temperature and the microstructure across the forging. This can be mitigated somewhat in "hot die" forging in which dies are heated to 650−815°C (1200−1500°F). Isothermal forging in which the dies are kept at higher temperatures takes advantage of the superplastic characteristics of Ti alloys. This enables forging at slow strain rates and reduced flow stresses without the problems of temperature loss and without the need to compromise between strain rate and die temperature, as with conventional forging.

Titanium alloys can be formed using methods such as brake, stretch, and hydro forming that are used for aluminum and steel alloys. Forming is carried out at temperatures up to about 500°C (932°F). The formability is generally the highest for metastable β alloys and decreases with decreasing β content in the alloy. Although not considered a forming process as such, machining, despite its relative difficulty, is a key process for fabricating Ti components, although large amounts of material are machined away from mill products. Microstructure affects machinability and processes have been developed for its improvement [44].

5.3.2.3 Heat Treatment of Titanium Alloys

Ti alloys are heat treated for relief of residual stresses following fabrication, improving attributes such as machinability and dimensional stability and for optimizing properties. The term annealing is used for many of these operations and Ti−6Al−4V, the most widely used alloy is used in service mostly in an "annealed" condition, although there are several types of this treatment. This is in contrast with Al alloys, which are always used in the solution heat treated, quenched, and aged condition, and for which annealing is a state in which the alloy is in its softest condition to facilitate forming operations. Although Ti alloys are also solution heat treated, quenched, and aged for achieving the highest possible strength, the parameters can vary widely depending on the alloy and the desired properties.

The range of temperatures for various heat treatment operations for Ti alloys is shown in Fig. 5.5. α/β alloys, from near-α to near-β, are typically solution heat treated below T_β. The exact temperature will determine the amount of β phase available for transformation following quenching and aging. The response to aging will depend on the cooling rate, which determines the nature of the transformation products. For a given alloy such as Ti−6Al−4V, which is closer to near-α alloy compositions, response to aging will increase with increasing cooling rates because of the formation of phases with solute supersaturation. It will also increase with increasing



Solution Treatment Temperature (°C)	Water Quenched	Air Cooled	Furnace Cooled
1065 (1)	$\alpha' + \beta$ + Prior β grain boundaries	Acicular $\alpha + \beta$ + Prior β grain boundaries	Plate-like $\alpha + \beta$ + Prior β grain boundaries
955 (2)	Primary $\alpha + \alpha' + \beta$	Primary α + Acicular $\alpha + \beta$	Equiaxed α + Intergranular β
845 (3)	Primary α + Metastable β	Primary $\alpha + \beta$	Equiaxed α + Intergranular β

FIGURE 5.19

Phases present in Ti–6Al–4V at room temperature after quenching from various temperatures at different rates [45].

solution treatment temperatures, if the cooling rates are sufficiently high, due to higher amounts of the β transformation products.

Solution treatment above T_β will result in a single-phase β solid solution, whereas below T_β, the alloying elements are just redistributed to their equilibrium values in the two phases. Fig. 5.19 lists the phases that will be present in Ti–6Al–4 V after solution treatment at various temperatures and cooling at different rates [45]. Compare this with Fig. 5.7, which depicted the phases present at room temperature after rapid cooling.

The nature of the transformation products of β will depend on its solute content at the SHT temperature.

- For alloys solution treated above T_β (1) prior β grain boundaries will be outlined for all cooling rates, (2) water quenching results in α' with some β being retained if the martensite transformation is not completed, and (3) lamellar α will become increasingly coarser with decreasing cooling rates.
- For alloys solution treated between T_β and M_s (1) primary α will be present for all cooling rates with its morphology becoming more equiaxed with decreasing cooling rates and (2) water quenching will result in α' with some β being retained, as earlier.
- For alloys solution treated below M_s (1) primary α will be present for all cooling rates with its morphology becoming more equiaxed with decreasing cooling rates and (2) water quenching will not result in α' but metastable β may be present if the M_s temperature of the solute-enriched β phase is below room temperature.

Fig. 5.15 shows the microstructure obtained by slow cooling in furnace from 1100°C (2012°F). Fig. 5.20 shows the corresponding representative microstructures after cooling from between T_β and M_s for a Ti–4Al–4Mo–2Sn alloy. The proportion of phases present in Ti–6Al–4V after quenching from various temperatures is shown in Fig. 5.21 [46].

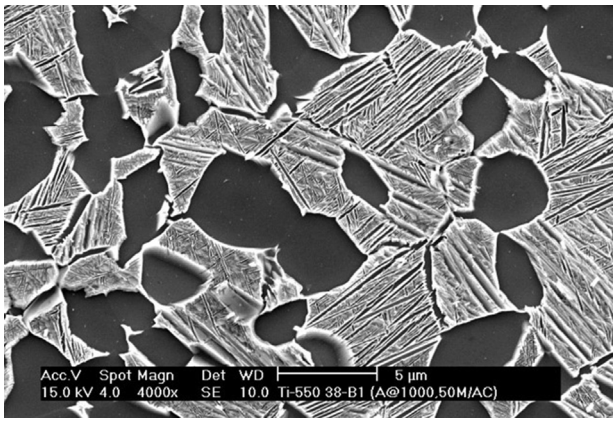


FIGURE 5.20

Microstructure of Ti–4Al–4Mo–2Sn cooled from below T_β showing equiaxed/globular α and transformed β.

Courtesy, Professor Raj Banerjee, University of North Texas.

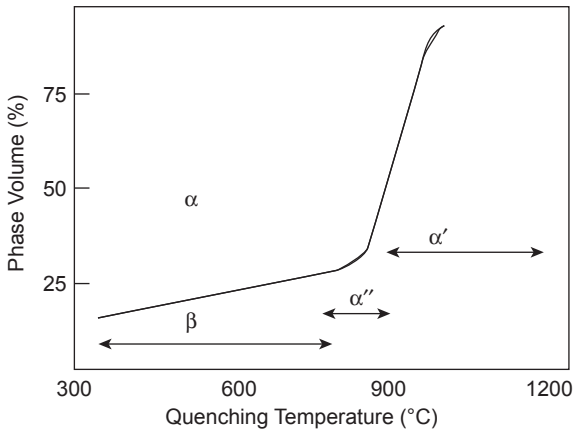


FIGURE 5.21

Volume fraction of phases present in Ti–6Al–4V at room temperature after rapid quenching from various temperatures [46].

Adapted and reprinted with permission of ASM International. All rights reserved. www.asminternational.org.

The volume fraction of primary α increases with decreasing quench temperature, as also shown in the α approach curve in Fig. 5.14, with a corresponding decrease in the amounts of the β transformation products. The yield and tensile strengths of quenched and aged Ti−6Al−4V were observed to decrease from 1055 to 980 MPa (152−142 ksi) and 1140 to 1025 MPa (165−149 ksi), respectively, as the solution treatment temperature was reduced from 940 to 845°C (1725−1550°F) [19]. This is also the temperature range in which the volume fraction of primary α increases rapidly with a corresponding decrease in the amounts of phases available for strengthening by aging. It should be noted that aging of martensite results in equilibrium α by the redistribution of the alloying elements and contributes to strength increase, which, however, is not as high as that provided by precipitation of α from metastable β, the principal source of strength for highly β stabilized alloys. Precipitation of α_2 by aging below its solvus and that of silicides was already discussed.

Highest strength is obtained in α/β alloys by solution treatment and aging. Special thermal treatments have been developed to modify the microstructures for enhanced combinations of other important properties. For example, recrystallization annealing and beta annealing are used for improved damage tolerance and fracture toughness but at the expense of fatigue strength. Several variations of annealing and aging treatments have also been developed for specific alloy compositions. These treatments will be discussed subsequently for individual alloys.

As with Al alloys, hardenability or the ability to achieve full property in thick sections is an important consideration in the heat treatment of Ti alloys. α/β alloys generally do not possess good hardenability due to poor thermal conductivity, with Ti−6Al−4V achieving full property only in sections less than about 1 in. (25 mm) thick [47]. Quench delay also needs to be minimized in alloys with low hardenability. The yield and tensile strengths of Ti−6Al−4V were observed to decrease from about 1100 to 950 MPa (160−138 ksi) and 1200 to 1050 MPa (174−152 ksi), respectively, as the quench delay increased from about 20 to 80 s [19]. The hardenability of highly β stabilized alloys, with a few exceptions, is sufficient to permit air cooling. For the near-β and metastable β alloys, quenching should be rapid enough to suppress both the formation of α′ and precipitation of α. Time-temperature-transformation (TTT) diagrams for these alloys, shown in Fig. 5.22, are useful in determining the maximum quench delay that can be tolerated [13]. Important considerations during heat treatment and other high temperature processing operations include the formation of an α case on the surface of Ti alloys due to their reactive nature and pick up of oxygen and nitrogen. The brittle surface layers must be removed completely following heat treatments.

5.3.2.4 Modeling of Thermomechanical Processing

Optimum thermomechanical processing (TMP) is key to the development of desired microstructures in defect free Ti alloy products. These alloys are unique in the complexity and diversity of their microstructures, which evolve during the series of steps combining varying sequences of hot working and thermal processing. The cost of the starting material and the difficulty of processing Ti alloys also

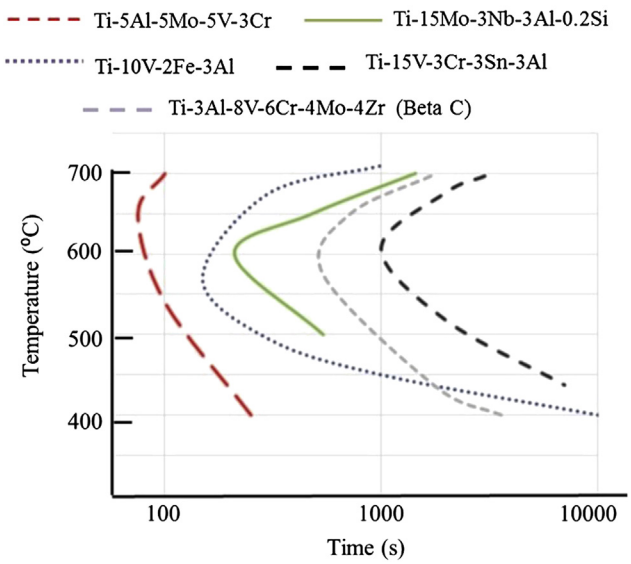


FIGURE 5.22

Time-temperature-transformation curves for α precipitation in selected β alloys. Ti-5553 and Ti-10-2-3 are solution treated below T_β [13].

underscore the importance of ensuring quality controls to avoid waste by rejection of defective parts. TMP involves interactions among many materials phenomena such as phase transformations, work hardening, and recrystallization. Although physics-based models that predict microstructures under these coupled conditions are generally not available, empirical models relating process parameters such as temperature and strain rate to microstructural evolution are being used successfully to fabricate Ti parts [37].

A critical step in the TMP of α/β alloys is the transformation of the lamellar α phase present in the alloy after forging in the β field during ingot breakdown to globular or equiaxed morphology by working in the α + β field, as shown in Fig. 5.16, which provides additional microstructural variability for property control [48]. The prior β grain size and thickness of the grain boundary α layer in the lamellar structure, shown in Fig. 5.16, have a significant effect on the subsequent workability in the α + β field and α globularization. Grain boundary α is deleterious for workability and finer grain sizes enhance globularization kinetics [37]. Deformation of Ti−6Al−4V samples with Widmanstatten structures and prior β grain sizes of 100 and 500 μm at a strain rate of 10^{-3}/s resulted in structures that were 90% and 40% globularized, respectively.

Among all the TMP steps, it is most time consuming to deform and convert the lamellar microstructure to an equiaxed type, in addition to being critical to achieving optimum properties. This step is also susceptible to the introduction of defects,

which can be related to fracture, shear localization, or metal-flow in the material [37]. Fracture-related defects or strain-induced porosity arise from microscopically inhomogeneous deformation and include wedge cracking arising from microcracking initiating at prior β grain boundary triple points and cavitation due to microvoid formation at edges. Shear localization defects include shear bands and cracks arising from inhomogeneous deformation across the work piece. Given the importance of this step in the overall TMP of Ti alloys and the potential for defects, "processing maps" have been developed to identify optimum processing conditions. These maps are developed from flow stress data over a wide range of temperature, strain rate, and strain to identify regions where various mechanisms of damage and microstructural evolution are active [32]. They identify "safe" spaces where desirable microstructural changes such as dynamic recovery and recrystallization, globularization, and superplasticity operate.

Processing maps for the deformation processing of several Ti alloys have been compiled and discussed comprehensively [35]. Selected findings from this study are presented and discussed to illustrate their utility in designing approaches for processing. Fig. 5.23A–C shows the processing map, variation of ductility with temperature, and variation of grain size with temperature compensated strain rate, respectively, for Ti–6Al–4V with a lamellar $\alpha + \beta$ microstructure and Fig. 5.24 shows selected micrographs from corresponding processing regions.

Hot working of the alloy with the microstructure shown in Fig. 5.24A in the "globularization" region results in the equiaxed microstructure shown in Fig. 5.24B. Working in the β recrystallization region results in the microstructure shown in Fig. 5.24G. Working in other regions result in defects shown in other corresponding micrographs. The alloy exhibits good ductility in the recommended region for hot working, as shown in Fig. 5.23B.

The Zener–Holloman, Z parameter combines the effects of temperature (T) and strain rate, $\dot{\varepsilon}$, on the flow stress by the equation

$$Z = \dot{\varepsilon} \exp\left(\frac{Q}{RT}\right)$$

where Q is the activation energy for deformation (445 kJ/mol for globularization) and R is the gas constant. The α grain size after globularization, predicted for various deformation conditions as a function of Z, is shown in Fig. 5.23C. Similar process maps for Ti–6Al–4V with a starting equiaxed microstructure can identify regions for superplastic forming. A deformation mechanism map at lower strain rates identifying regions for superplastic forming of Ti–6Al–4V is shown in Fig. 5.25 [49].

5.3.2.5 Processes for Cost-Affordable Titanium Alloys

The reasons for the high cost of Ti alloys are apparent from the definition of "low-cost titanium products" adapted in a "Low-Cost Titanium Workshop" as follows: Useful titanium alloy products whose production path involves processing that lowers costs, including reduction processes, electron beam and plasma arc single melt processes, optimized thermomechanical processing, and near net shape

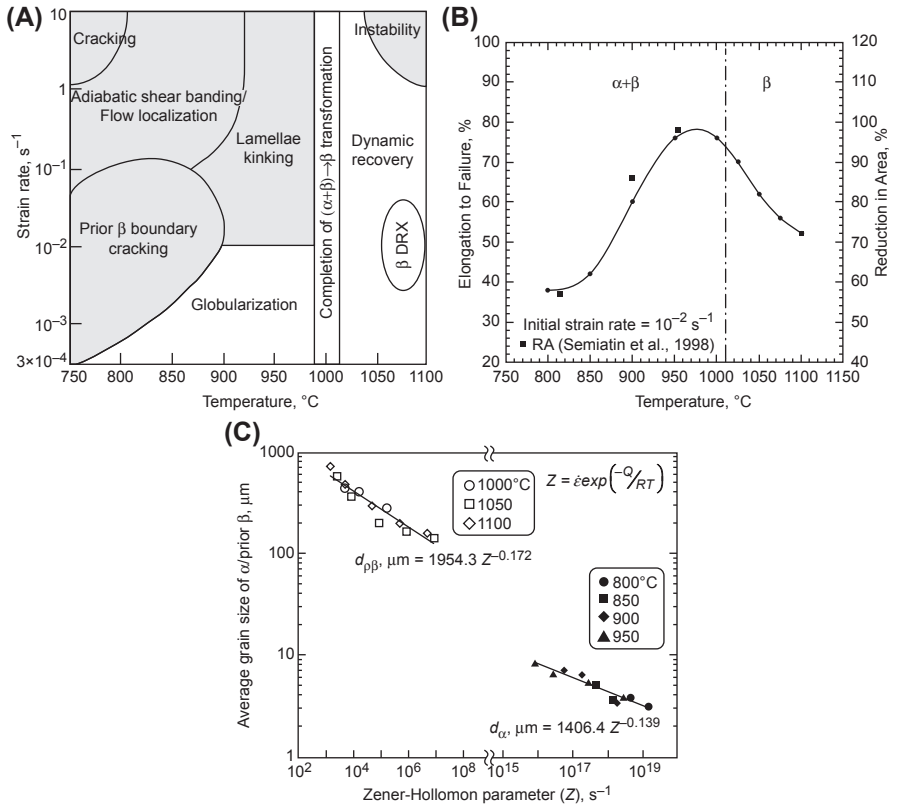


FIGURE 5.23

(A) Process map for Ti—6Al—4V with a lamellar microstructure, (B) ductility as a function of temperature, and (C) variation of grain size with temperature-compensated strain rate parameter (Z) [35].

fabrication. Some processes allow higher impurity levels (e.g., resulting from melting low-cost scrap) to be tolerated while enabling products to have good properties [50].

The approaches to reducing the cost of using Ti alloys include the development of methods to produce sponge directly from ore as a replacement for the current Kroll and Hunter processes, electron beam, and plasma arc melting to replace vacuum arc melting, and the use of net shape processes such as castings, powder metallurgy, superplastic forming, and additive manufacturing to reduce buy-to-fly ratios [36,51—53]. Improvements to the efficiency of presently used processes are also being made through the increased applications of modeling and simulation. At least for critical applications in airframes and engines, the properties and performance of lower-cost products need to equal that of current wrought products.

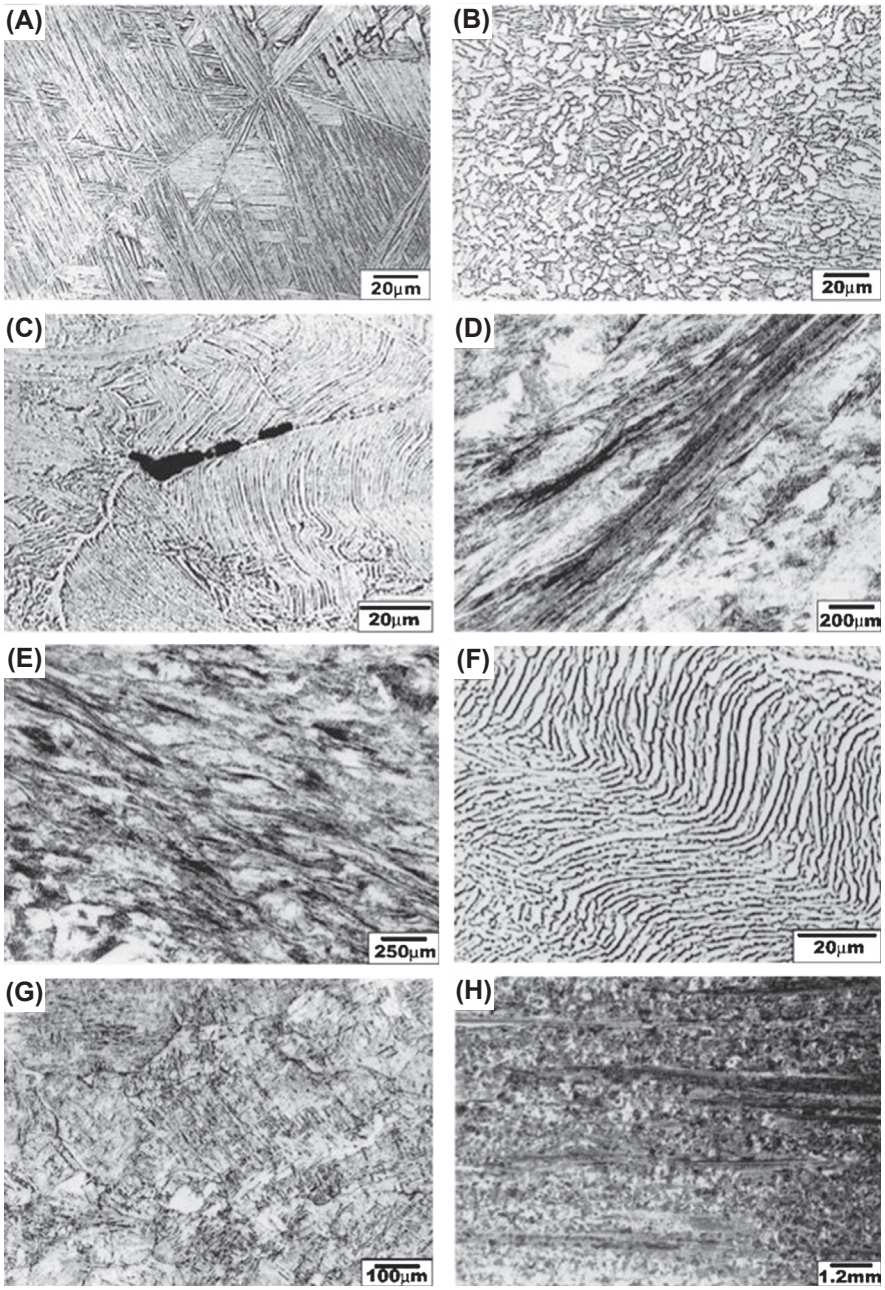


FIGURE 5.24

Microstructure of Ti—6Al—4V. (A) Lamellar microstructure, (B) globularization, (C) prior β boundary cracking, (D) adiabatic shear banding and cracking, (E) flow localization, (F) lamellar kinking, (G) dynamic recrystallization, and (H) β instability [35].

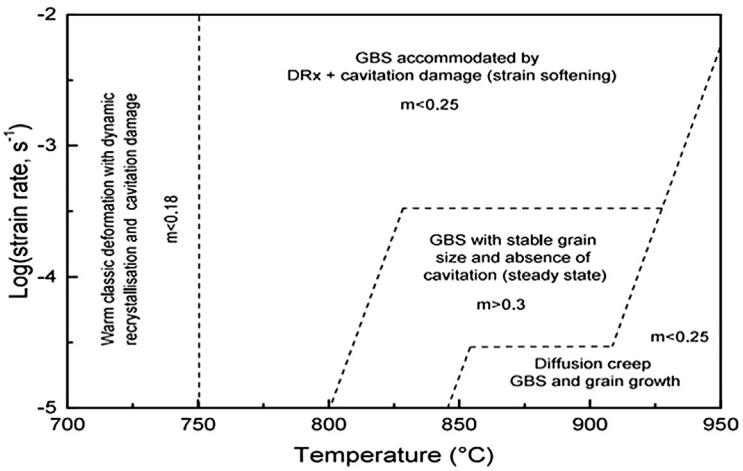


FIGURE 5.25

Process map for Ti—6Al—4V identifying dominant deformation mechanisms at slow strain rates [49].

Existing wrought alloy compositions are being used to develop and demonstrate the lower-cost processes. Since the physical metallurgy is the same for Ti alloys made and processed into shapes by various methods, these processes are not discussed further. Metallurgy and design of alloys that could take advantage of processes such as additive manufacturing are covered in Chapter 9.

5.3.3 MICROSTRUCTURE OF TITANIUM ALLOYS AND ITS RELATIONSHIP TO PROCESSING

Features of the complex microstructural characteristics of Ti alloys and their effects on properties were outlined briefly in Chapter 2 and in earlier sections of this chapter. Among the structural alloys used in critical aerospace applications, Ti alloys are unique in their reliance on a combination of two ductile phases in the microstructure and the advantageous manipulation of their morphologies by processing. The resulting inevitable complexity of the microstructure and its influence on properties and performance have also been a stimulus in the "creative learning process" enabling the advance of the technology of these alloys in a relatively short time span of 60 years [54]. This development span, shown in Fig. 5.26, started with the establishment of melting practices, which were themselves challenging owing to the reactivity of titanium, continued with the development of the various classes of Ti alloys, identifying and eliminating defects introduced during processing, addressing unique deformation mechanisms and more recently the development and application of computational modeling tools. This section will describe the key features of the microstructure of Ti alloys including defects, and their evolution, quantitative characterization, and modeling. Emphasis will be on the types of microstructures that determine the properties of importance for the application of commercial alloys.

The property combinations for PH Al alloys are determined principally by the precipitate microstructure, which evolves during aging of the supersaturated solid

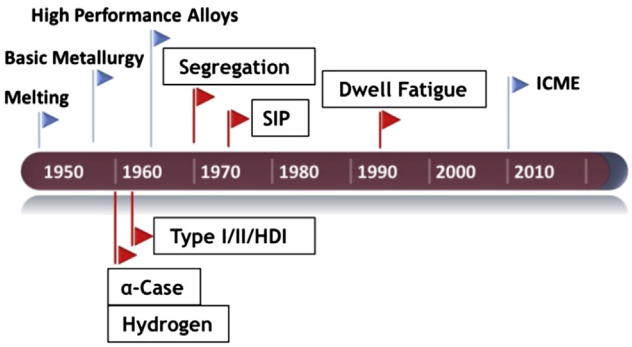


FIGURE 5.26

Timeline of titanium microstructure voyage [54].

solution obtained by solution heat treatment and quenching. Accordingly, the effects of processing on the microstructure and properties of these alloys could be discussed to a certain extent by the superposition of the results of independent analysis of the effects of TMP and heat treatment. The same is generally not true for Ti alloys due to the variety of microstructural morphologies that can result from the interactions between TMP and heat treatment. To provide a clear and detailed description of the processing−microstructure relationships, the features of the individual α and β phases will be described first. This will be followed by the discussion of the evolution and description of the important types of microstructure in Ti alloys. The discussion will use examples of Ti−6Al−4V (the most common α/β alloy), Ti−6Al−2Sn−4Zr−2Mo−0.1Si (the predominant high temperature alloy), Ti−10V−2Fe−3Al, and Ti−5V−3Cr−5Mo−5Al (high strength alloys used for landing gear components) and other alloys as relevant.

The microstructural characterization of Ti alloys also involves quantitative measurements of a larger number of morphological features than for other structural alloys. Although this poses a challenge in terms of being able to develop physical mechanisms of deformation based on many interacting variables, advances in characterization tools and the application of statistical and informatics methods have been very useful in this regard.

5.3.3.1 Microstructure and Texture of Titanium Alloys

The phases present in Ti alloys are α, β, and, depending on the composition and heat treatments, α_2 and silicides. The properties of these alloys are optimized for various applications principally by varying the volume fraction and morphology of the α phase by TMP and heat treatments. In addition, the development of texture during processing also affects the properties of Ti alloys.

5.3.3.1.1 Microstructure of Titanium Alloys

α can occur as a primary or secondary phase. Primary α (α_p) is present during hot working in the α + β field and persists through heat treatment, whereas secondary α

is a product of β transformation at a lower temperature [34]. Primary α can form by nucleation and growth during slow cooling of the alloy from above T_β, in which case the microstructure will be fully lamellar or from a high temperature in the α + β field. At slow cooling rates from the β field, secondary α nucleates preferentially at the β grain boundaries forming an almost continuous layer and upon further cooling, can also form by precipitation during the aging of supersaturated martensite or metastable β retained by rapid quenching of the alloy. For alloy Ti−6Al−4V, rapid cooling results in martensite, rather than metastable β. Thus during low temperature annealing, tempering of martensite occurs rather than precipitation by aging. However, metastable β can form in the near-α alloy, Ti−6Al−2Sn−4Zr−2Mo, which is made possible by the Mo addition. α_p grains can exhibit shape anisotropy in the direction of working. An equiaxed morphology will result from hot working and/or annealing above the recrystallization temperature. The lamellar morphology of secondary α can be converted to an equiaxed structure by its globularization, as discussed earlier.

At room temperature, a certain amount of equilibrium β phase is always present in α/β Ti alloys. It occurs as ribs separating α lamellae or as the intergranular phase in an equiaxed microstructure. β can be the matrix phase in alloys in which it is retained in a metastable state by quenching, which is then followed by aging to form secondary α by its intragranular precipitation.

Representative microstructures illustrating features of the α and β phases in α/β alloys for various heat treatments are shown in Fig. 5.27 [48]. This figure also lists the attributes of these phases, which need to be measured quantitatively to understand how they evolve during processing and affect the properties, particularly to aid in modeling the effects of composition and processing on the microstructure and properties [55]. Aided by the availability of advanced characterization tools, rapid, stereological procedures have been developed for their quantification [55,56].

5.3.3.1.2 Texture in Titanium Alloys

Ti alloys solidify into the BCC β phase. As described earlier, following initial breakdown of the ingot in the β field and through T_β, the alloys are generally hot worked in the α + β field and subjected to various TMP and heat treatment steps. From a recent review [57] of the effects of processing on microstructure and texture, the sequence of their evolution in alloys such as Ti−6Al−4V, schematically shown in Fig. 5.28 [48], can be summarized as follows, with A, B, and C 1−4 denoting the various possibilities.

- Initial processing in the β field (ingot breakdown and β anneal) results in a texture characteristic of BCC materials (A).
- Cooling from the β field results in a lamellar microstructure. Texture in the α laths in this microstructure inherits some of the β deformation texture and those resulting from the β to α transformation obeying crystallographic relationships and variant selection principles (B).
- Subsequent subtransus processing of α/β with starting lamellar microstructure results in globularization of the α laths by several mechanisms depending on the

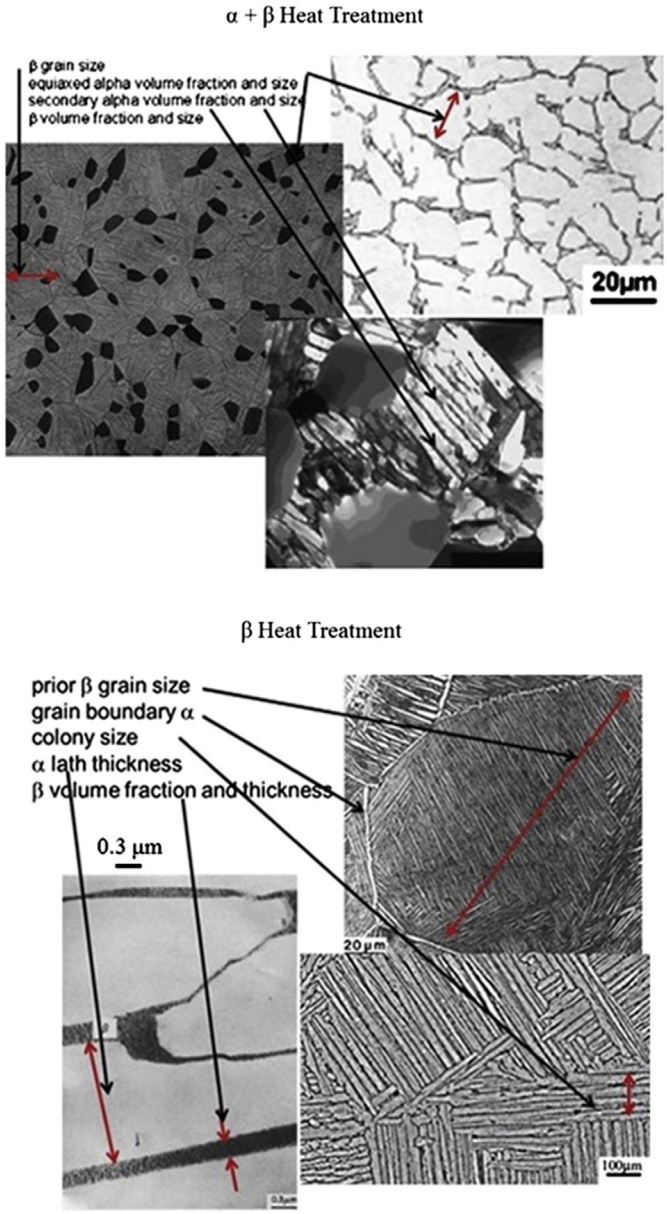
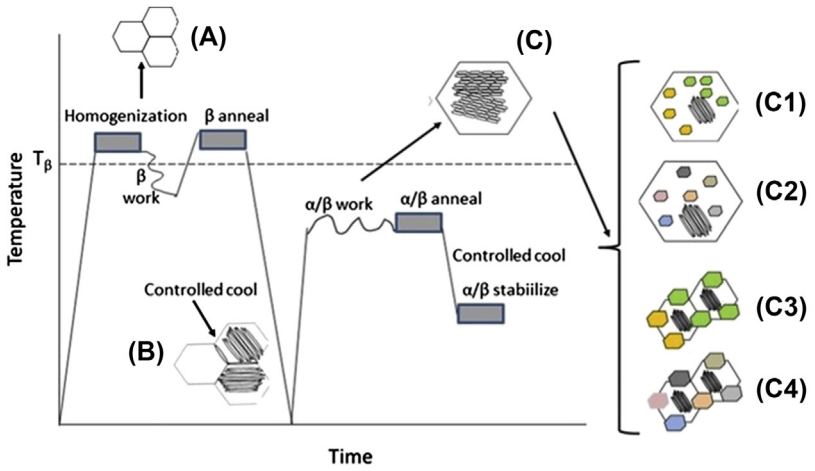


FIGURE 5.27

Microstructural parameters in various classes of microstructures in α/β alloys [48].



(The colors represent various primary α grain orientations)

(A) β recrystallization texture

(B) α lath texture depends on parent β texture, transformation texture and variant selection.

(C) Lath rotation and break-up breakup during subtransus processing

(C1) α globularization and no β recrystallization – Primary α texture from colony texture and β deformation texture.

(C2) α recrystallization and no β recrystallization - α deformation and recrystallization texture, β deformation texture, secondary α texture from parent β texture.

(C3) No α recrystallization and β recrystallization with special boundaries - secondary α texture from parent β texture.

(C4) α recrystallization and β recrystallization with special boundaries - secondary α texture from parent β texture.

FIGURE 5.28

Schematic representation of the processing paths and texture development in titanium alloys.

Adapted from D. Banerjee, J.C. Williams, Perspectives on titanium science and technology, Acta Materialia 61 (2013) 844–879.

temperature, strain rate, and amount of strain. Laths can plastically kink and bend or the α/β interfaces can roughen and groove. Slip bands may also shear the α laths. The result is the breakdown of laths into several α particles and rounding of their edges resulting in globularization.

- Globularization is not associated with the phenomenon of classic recrystallization, but similar to the process of geometric dynamic recrystallization that occurs by the "pinching" off of α particles from the lamellae by the mechanisms mentioned above. The globularized α (α_p) retains its original texture if the processing strains are relatively low, leading to macrozones of similarly oriented equiaxed α (C1). The size of these zones is determined by the starting colony size.

- In addition, the recovery and recrystallization of the β phase (C3) and conventional dynamic recrystallization of α (C4), as distinct from globularization, can also occur. These various possibilities are denoted by C 1–4 in Fig. 5.28. Also shown in this figure is the formation of secondary α that forms during the cool down from the α/β annealing temperature. This secondary α has the conventional transformation texture, discussed earlier.

Texture thus develops in the α and β phases in Ti alloys at all stages of processing with its evolution affected by the processing parameters, as shown in Fig. 5.28.

5.3.3.1.3 Defects in Titanium Alloys

The reactive nature, presence of multiple alloying elements with varying diffusivities causing segregation, and the difficulty of processing alloys containing two ductile phases with different deformation characteristics, all can result in the introduction of defects of various types in Ti alloys. Four types of melt-related defects can be found in Ti alloys [34]. These are high interstitial defects (HID or Type I), high aluminum defects (HAD or Type II), beta flecks and high density inclusions (HDI) such as W introduced into the melt with the raw material. Type I and Type II defects are high in the interstitials (O and N) and Al, respectively, which stabilize the α phase. Beta flecks are regions rich in beta stabilizer elements caused by segregation, particularly of the β eutectoid elements, Cr and Fe, and lower the T_β locally compared with the surrounding region in the microstructure.

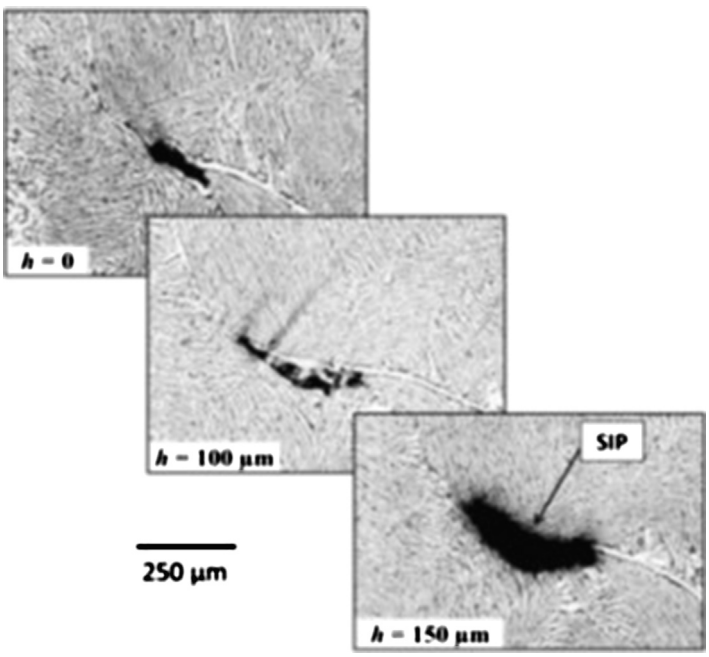


FIGURE 5.29

The origin of strain-induced porosity in Ti alloys as revealed by serial sectioning [54].

Defects introduced during processing such as strain induced porosity, wedge cracking, and shear banding (Figs. 5.24 and 5.29 [35]) were discussed earlier. Absorption of H in amounts above its solubility limit results in the precipitation of hydrides and of O results in a hard, brittle, α-stabilized surface layer. As with PH Al alloys, thick section products of highly β stabilized Ti alloys are prone to nonuniform response to heat treatments. The mechanisms of formation of these defects and effects to eliminate them are well understood and practiced.

5.3.3.2 Effects of Processing on Microstructure and Texture

The effects of processing on the development of microstructure and texture have already been discussed in earlier sections in broad terms in the context of describing their basic features. This section will focus on the processing sequences needed to impart specific microstructures and texture components in Ti alloys for various targeted property combinations. Structural Ti alloys of interest for aerospace applications are all in the α/β family in the sense that they all have both phases present in equilibrium at room temperature. In the continuum of increasing β stabilization, the maximum temperature capability decreases and the maximum achievable strength increases progressively generally from near-α through near-β alloys. Because of the narrowing of the processing window due to the extent of lowering of T_β and the resulting limited range for aging, the metastable β alloys do not have the potential to develop as high a strength as the near-β alloys. However, the processing for these alloys is similar enough that they will be treated as β alloys. Accordingly, the effects of processing are discussed separately for α/β alloys (including near-α) and the β alloys.

5.3.3.2.1 α/β Alloys

The many processing paths and the resulting features and morphologies of the α and β phases (Fig. 5.27) provide the opportunity to obtain a very large number of microstructure–property combinations in Ti alloys. However, the three important microstructure types in commercial alloys are lamellar, bimodal, and equiaxed, as mentioned earlier. The paths to achieve these microstructures and the effects of process parameters on their key features, which affect properties, have been described in detail [33,58] and will be summarized in this section. There is also a large amount of published literature on various aspects of the processing–microstructure relations for Ti alloys, from which selected information will be used.

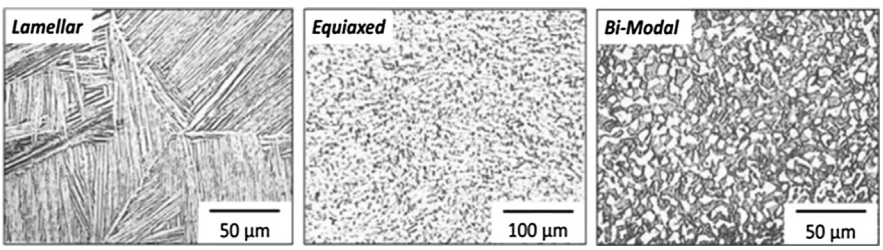


FIGURE 5.30

Lamellar, bimodal, and equiaxed microstructures for a representative α/β alloy [54].

Lamellar, bimodal, and equiaxed microstructures for a representative α/β alloy are shown in Fig. 5.30 [54]. In the framework of primary working and TMP of Ti alloys, these microstructures are achieved using varying sequences involving homogenization, deformation, recrystallization, and annealing, as shown in Table 5.4. The recrystallization and annealing temperatures are generally in the range of those for solution heat treatment and aging, respectively. The need for cooling at a controlled rate following any given processing operation will depend on the desired effects on subsequent processing and the final microstructure.

The formation of the lamellar microstructures at slow cooling rates from the β field was already discussed and shown in Fig. 5.15. With increasing cooling rate, the colony size and the width of the individual lamellae decrease. Colonies nucleating at grain boundaries cannot grow rapidly enough to fill the β grains. Colonies then nucleate at other colonies and the lamellae grow perpendicularly, which along with the decreasing colony size results in the characteristic "basket weave" microstructure. Further increases in the cooling rate produces, the needle-like, acicular α microstructure. Intermediate cooling rates will produce the Widmanstatten (basket weave) type structure shown in Fig. 5.30. Grain boundary α can be seen in all the "β-annealed" microstructures, with its width decreasing with increasing cooling rate. In "β-processed" materials in which the recrystallization step is omitted, the grain boundary α layers are not continuous, as they follow the shape of the deformed, unrecrystallized β grains. If the cooling rate is sufficiently high, secondary α will precipitate from the β phase for both β-annealed and β-processed materials.

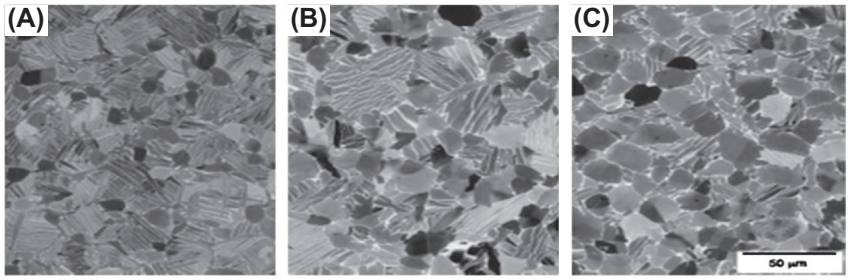
Bimodal microstructures are produced by deformation and recrystallization in the $\alpha + \beta$ field. The cooling rate after homogenization from the β field will determine the width of the α lamellae, which in turn will affect the size of the recrystallized α_p grains. Penetration of the β grains into the α lamellae separates them into α_p grains. The recrystallization temperature and cooling rate after this step will determine the volume fraction of α_p and the width of the α lamellae that form in the recrystallized β grains, respectively. The effects of the process parameters on the size and volume fraction of α_p are shown in Fig. 5.31 [56]. The solution heat treatment temperature and cooling rate have a significant influence on the volume fraction of primary α and the α lath, which in turn influence the mechanical properties.

Equiaxed microstructures can be produced in two ways. Cooling at a slow enough rate following the recrystallization step in the process to produce bimodal microstructures described earlier, will prevent the formation of α lamellae and only coarsen the α_p grains. In the other approach, performing the recrystallization treatment at a low enough temperature where a sufficiently high equilibrium α volume fraction exists will result in the formation of α_p directly from the deformed lamellae by its penetration into the β grains. This is the reverse of the mechanism that occurs in the production of bimodal structures. Because of alloying element partitioning between the α and β phase during recrystallization, secondary α can form during the final annealing treatment.

The mill annealed condition is produced by annealing the alloy directly after the deformation step without recrystallization. The deformation parameters in this

Table 5.4 Sequence of Processing Steps to Produce Various Microstructures in α/β Alloys

Microstructure Type	Processing Sequence			
	Homogenization	Thermomechanical Processing	Heat Treatment	
			Recrystallization	Annealing
Lamellar (β annealed)	Above T_β	β working followed by $\alpha + \beta$ working	β field followed by controlled cooling	~550–750°C for various time periods. Intermetallics (α_2 and silicides) will precipitate if annealed below the respective solvi.
Lamellar (β processed)	Above T_β	β working followed by controlled cooling	—	
Bimodal	Above T_β followed by controlled cooling	$\alpha + \beta$ working	$\alpha + \beta$ field followed by controlled cooling	
Equiaxed	Above T_β followed by controlled cooling	$\alpha + \beta$ working	$\alpha + \beta$ field followed by controlled, slow cooling $\alpha + \beta$ field at a low temperature	
Mill annealed	Above T_β followed by controlled cooling	$\alpha + \beta$ working followed by controlled cooling	—	



Specimen	Forging Strain	Solution Heat Treatment Temperature °C (°F) (Recrystallization)	Cooling Rate °C/s (°F/s)	Aging (Annealing)	
				Temperature °C (°F)	Time (Hours)
a	0.4	985 (1800)	3.7 (6.7)	704 (1300)	2
b	0.8	968 (1775)	0.37 (0.67)	593 (1100)	8
c	0.4	968 (1775)	0.37 (0.67)	704 (1300)	2

a - low volume fraction of small equiaxed α
b - small volume fraction of large equiaxed α
c - large volume fraction of large equiaxed α

FIGURE 5.31

Bimodal microstructure of Ti–6Al–4V forged at 968°C as a function of heat treatment conditions [56].

treatment are not tightly controlled and the microstructural changes that occur during annealing are not reproducible.

The microstructure and texture evolution for Ti alloys described earlier are controlled by the strain, strain rate, and temperature of deformation, diffusion coefficients, and the time and temperature of thermal treatments. From the self-diffusion coefficients of Ti in α and β, the approximate diffusion distances in these phases has been estimated as 0.8 and 0.9 μm for 50 h at 500°C and 4 and 40 μm for 1 h at 1000°C, respectively [46]. Thus microstructural changes will be very slow far below T_β. For $\alpha + \beta$ treated materials (bimodal, equiaxed, and mill annealed), the presence of two phases retards microstructural coarsening. If recrystallization (solution treatment) is conducted above M_S, the β phase will transform like that when it is conducted above T_β resulting in the bimodal structure. Fully equiaxed structure results if this treatment is performed below the M_S.

The important relationships between processing and the features of these microstructures are shown in Table 5.5. The processing and the evolution of microstructure, particularly of the various α phase morphologies, in Ti alloys is complex and a knowledge of many of the underlying phenomena and mechanisms of their evolution are still being developed.

5.3.3.2.2 β Alloys

These alloys include the near-β (e.g., Ti–10V–2Fe–3Al and Ti–5Al–5Mo–5V–3Cr) and the metastable-β (e.g., Ti–15V–3Cr–3Sn–3Al) alloys. Although both types of alloys contain α and β phases in equilibrium, the potential for strengthening

Table 5.5 Processing–Microstructure Relationships for α/β Alloys

Microstructure Type	Important Processing Parameters	Effects on Microstructure
Lamellar (β annealed)	Cooling rate after β recrystallization	• Increasing cooling rates decrease α colony size, α lamellae width, and grain boundary α width
Lamellar (β processed)	β deformation parameters	• Minimized time to prevent recrystallization • Mode (rolling, forging, etc.) determines β grain shape and geometry of grain boundary α • Strain determines β grain width (maximum α colony size) and morphology of grain boundary α
	Cooling rate after deformation	• Prevent recrystallization • Increasing cooling rate decreases α colony size and α lamellae width
Bimodal	Cooling rate after β homogenization	• α lamellae width determining maximum α_p size
	α + β deformation parameters	• Temperature determines texture type • Degree determines texture intensity and dislocation density • Mode determines texture symmetry
	Recrystallization temperature	• Volume fraction of α_p and β grain size • Solute partitioning
	Cooling rate after recrystallization	• α lamellae width
Equiaxed	Cooling rate after β homogenization	• α lamellae width and α grain size
	α + β deformation parameters	• Temperature determines texture type • Degree determines texture intensity and dislocation density • Mode determines texture symmetry
	Slow cooling rate after recrystallization or low recrystallization temperature to produce equiaxed structure	
Mill annealed	Cooling rate after β homogenization	• α lamellae width determining maximum α_p size
	α + β deformation parameters	• Degree of recrystallization, texture intensity and symmetry

For all microstructures, final annealing (aging) temperature will control the formation of secondary α and determine whether or not α_2 and silicides precipitate.

is higher in the former due to the higher volume fractions of α that can precipitate during aging. α precipitation in these alloys is no different from that in the α/β alloys, but one important difference is the role of the ω and β′ phases that may occur as precursors. Due to the lower T_β, these alloys can be processed at lower

temperatures than the α/β alloys. The important microstructure types and the processing paths to achieve them have been described in detail as β-annealed, β-processed, through transus processed and bimodal [59] and are briefly summarized. The principal steps are essentially like those for α/β alloys described earlier, particularly for the higher strength, near-β alloys, except that β alloys must be aged in the final step. Depending on the temperature difference between the recrystallization and the annealing steps, secondary α precipitation also occurs in α/β alloys, which could be considered an aging treatment.

The sequence of processing steps to obtain the various microstructure types in β alloys is shown in Table 5.6. In Ti alloys, the formation of an α layer at β grain boundaries cannot be avoided as these act as heterogeneous nucleation sites. The effects of this layer on the wokability of alloys in the context of globularization of the α phase were discussed already. Because β alloys rely on α precipitation for strengthening, the grain boundary layer and the accompanying precipitate free

Table 5.6 Sequence of Processing Steps to Produce Various Microstructures in β Alloys

Microstructure Type	Processing Sequence Following Homogenization Above T_β			
	Deformation	Recrystallization	Annealing	Aging
β annealed (metastable β alloys)	Above T_β or cold	Above T_β		Controlled heating rate to aging temperature or final aging preceded by preaging
β-Annealed (near-β alloys)	Above or below T_β	Above T_β followed by controlled cooling	Below T_β followed by controlled cooling	Single-step aging
β processed	Above T_β followed by controlled cooling		Below T_β followed by controlled cooling	Single-step aging
Through transus processed	Start above T_β and continue through transus		Below T_β followed by controlled cooling	Single-step aging
Bimodal (homogenization followed by controlled cooling)	Below T_β	Below T_β	Below T_β followed by controlled cooling	Single-step aging

zone (as in PH Al alloys) are much more harmful for the near-β than for the α/β and metastable β alloys. Processing steps are designed to mitigate their effects.

β-annealed microstructures are produced in metastable β alloys (some of which can be deformed cold) after deformation and recrystallization in the β field followed by aging to precipitate the α phase. To facilitate precipitation of α during aging, the alloys are either heated at a controlled rate or aged initially at a lower temperature to form the metastable phases ω and β′ that will act as precursors. For near-β alloys, following working above or below T_β, recrystallization below this temperature is followed by controlled cooling to minimize grain boundary α width. Next, an intermediate annealing treatment precipitates α and controlled cooling minimizes its volume fraction and coarsening. Precipitation of fine α occurs during final aging.

β-Processed microstructures are produced by deformation above T_β followed by controlled cooling to minimize the width of grain boundary α. The recrystallization step is omitted, as in the treatment for α/β alloys, to retain the deformed microstructure in which the grain boundary α is broken up. The annealing and aging steps are similar to the β-annealed materials. If the deformation in the β field is continued through the transus with a short time below this temperature, α precipitates at the deformed β grain boundaries, which is then also deformed and globularized. The effect is to break up the continuous α layer to globular particles and distribute them along the grain boundaries producing what is termed a "necklace" structure [59].

Bimodal structures have smaller β grain sizes that can mitigate the effects of the α layer, but the cooling rate after homogenization needs to be controlled to minimize its width. The intermediate annealing and aging treatments are performed as for other microstructures.

The importance of rapid quenching of these alloys to retain the metastable β phase for subsequent aging was already discussed with respect to the TTT diagrams (Fig. 5.22). The number of β alloys in commercial production is very small and their processing will be discussed later in relation to specific alloys. All these alloys are used in the solution heat treated and aged condition and a representative microstructure for Ti−10V−2Fe−3Al is shown in Fig. 5.32 [13]. Specific relationships between the processing parameters and the features of these microstructures in β alloys are shown in Table 5.7.

5.3.3.3 Modeling of Microstructure and Texture

Presence of α and β, and their crystallographic relationships and interactions during TMP introduce significant complexity to model the evolution of microstructure and texture in Ti alloys. Modeling of these alloys for identifying the processing space and parameters for globularization of α and production of defect free products was described earlier. The evolution of different microstructure types and the accompanying texture in these alloys are affected by phenomena occurring at all stages of processing from solidification through heat treatments, as shown in Fig. 5.28 and Table 5.8. Comprehensive reviews have described the modeling of microstructure [60] and texture [61] in Ti alloys. A subsequent review [57] has described phase transformations and mechanical behavior emphasizing the effects

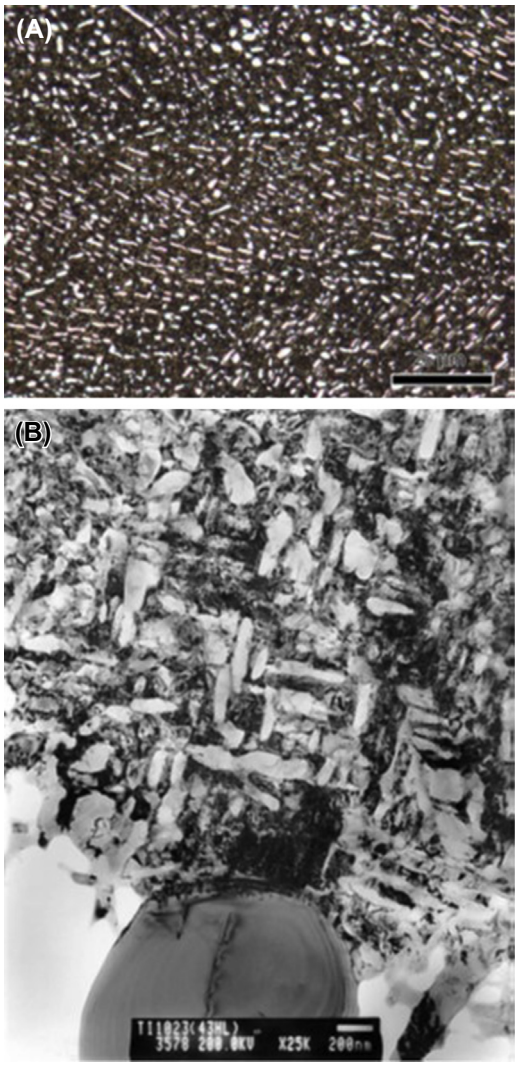


FIGURE 5.32

Microstructure of solution heat treated and aged Ti—10V—2Fe—3Al forging. (A) Light optical micrograph showing elongated primary α in an aged β matrix and (B) bright field, transmission electron micrograph image showing globular primary α and a high volume fraction of aged α precipitates [13].

of processing while delineating the challenges for achieving predictive capabilities using computational modeling tools. Evolving the understanding of the mechanisms and concurrent development of models continue to be published, particularly for specific commercial alloys, and selected, key aspects are described in this section.

Table 5.7 Processing—Microstructure Relationships for β Alloys

Microstructure Type	Important Processing Parameters	Effects on Microstructure
β annealed (metastable β alloys)	β-recrystallization Temperature	• Controls β grain size
	Heating rate to aging temperature or preaging temperature	• Controlled, homogeneous distribution of α precipitates
β annealed (near-β alloys)	Cooling rate after recrystallization	• Controls grain boundary α layer and "side plates"
	Annealing temperature and cooling rate	• Controls size and volume fraction of coarse α
β processed	β deformation parameters	• Minimized time to prevent recrystallization • Mode (rolling, forging, etc.) determines β grain shape and geometry of grain boundary α • Strain determines β grain width (maximum α plate size) and morphology of grain boundary α
	Cooling rate after deformation	• Prevent recrystallization • Controls grain boundary α layer and "side plates"
	Annealing temperature and cooling rate	• Controls size and volume fraction of coarse α
Through transus processed	β deformation parameters	• Minimized time to prevent recrystallization • Mode (rolling, forging, etc.) determines β grain shape and geometry of grain boundary α • Strain determines β grain width (maximum α size) and morphology of grain boundary α
	α + β deformation parameters	• Necklace microstructure
	Temperature of annealing and subsequent rate of cooling	• Controls size and volume fraction of coarse α
Bimodal	Cooling rate after β homogenization	• Controls grain boundary α layer
	α + β deformation	• Degree determines dislocation density
	Recrystallization temperature	• α_p volume fraction affecting β grain size and subsequent α amounts
	Annealing temperature and cooling rate	• Controls size and volume fraction of coarse α

For all microstructure types, temperature of final aging determines size and volume fraction of secondary α precipitates.

Table 5.8 Metallurgical Phenomena Occurring During Processing of Titanium Alloys

Processing Step	Metallurgical Phenomena
Solidification	β phase solidification texture
Initial ingot breakdown in β field	β texture evolution
β recrystallization and cool down	Static recrystallization and texture evolution of β Microstructure of transformed β (α variant selection and plate thickness)
α + β working	Coarsening of lamellar α Globularization (spheroidization) of lamellar α Coarsening of primary α Texture evolution in α and β
Heat treatment	Secondary α formation Coarsening of primary α β grain growth and texture evolution (β alloys)

Microstructural changes occur in Ti alloys both dynamically during deformation processing and statically during annealing, with the kinetics of these processes determined by the temperature, strain rate, and imparted strain level. The globularization of colony α, with the goal to produce fine, uniform, equiaxed grains for subsequent processing, has been described by two mechanisms [62]. It occurs statically by diffusion driven by the gradient in the solute concentration between the curved edge of the α plate and the flat, α−β interphase boundary of the same or an adjacent plate. The result is either thickening or spheroidization of the lamellae, with the former dominating at larger aspect ratios. Under dynamic conditions, spheroidization occurs by fragmentation of the lamellae, with the newly formed, equiaxed α grains coarsening at sufficiently high working temperatures. Spheroidization has been modeled phenomenologically using experimental data, as shown by an example for Ti−6Al−4V in Fig. 5.33A and B [63], in which the effect of the levels of prior strain and aspect ratio, respectively, can be clearly seen. Such data provide directions for choosing process parameters that produce a fully spheroidized microstructure of equiaxed α grains.

Static coarsening of equiaxed α occurs by a diffusion mechanism and has been modeled using a modified Lifshitz, Slyozov, and Wagner theory [64]. Dynamic coarsening of equiaxed α occurs at a rate about an order of magnitude higher than that under static conditions [65]. It occurs principally at strain rates typical of superplastic flow with the mechanism being sliding of the α/β interphase boundaries. Static coarsening of lamellae occurs by diffusion and has implications for globularization because the size of the equiaxed α can be no smaller than the plate thickness. Coarsening by diffusion between adjacent lamellae can be modeled readily, but that of aggregates of lamellae has not been modeled.

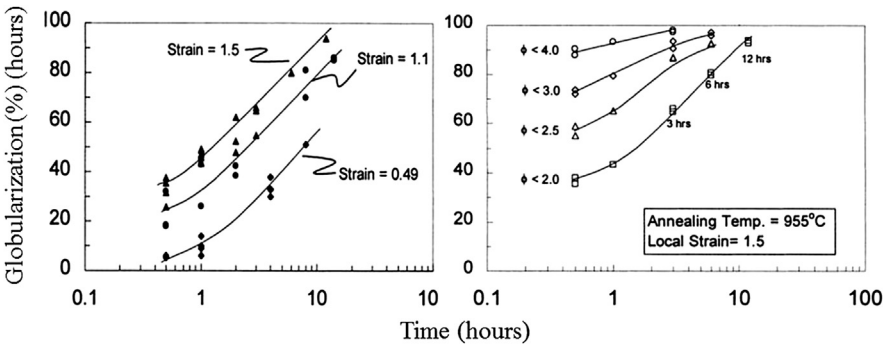


FIGURE 5.33

Volume fraction of spheroidized α in Ti—6Al—4V as a function of annealing time at 955°C and (A) amount of prestrain and (B) prestrain of 1.5 [63].

During the final heat treatment process, e.g., to produce bimodal microstructures, α/β alloys are annealed (solution heat treatment or recrystallization) at a temperature high in the two-phase field, cooled at a rapid rate, and annealed (aged) at a lower temperature. The principal microstructural changes are the coarsening of the primary α and the transformation of β by the formation of secondary α. Transformation kinetics during the continuous cooling from the solution treatment temperature has been modeled phenomenologically using the Johnson—Mehl—Avrami—Kolmogorov relationship to predict the fraction transformed as a function of time and cooling rate [66]. The formation of α lamellae has been modeled using phase field methods [28].

The final texture present in Ti products is the culmination of its evolution through all stages of processing (Fig. 5.28). Texture resulting from solidification, deformation, recrystallization, and phase transformation affects behavior at each succeeding step and the material properties. At intermediate stages of processing, texture can affect the response to subsequent operations such as forging or rolling. Deformation texture can affect microstructure evolution during phase transformations such as by influencing variant selection by the α phase. The amount of work done in modeling and simulation of texture in HCP materials is limited compared to that for FCC and BCC materials. This is a challenge particularly because of the strong tendency for Ti alloys to develop texture given the lower crystallographic symmetry of HCP α. The problem is compounded by the presence of two phases and interactions between them in terms of factors such as their response to deformation and partitioning of strain. In addition, evolution of texture and microstructure are coupled for phenomena such as recrystallization, grain growth, and phase transformations.

Recrystallization and grain growth of the β phase have been modeled using Monte Carlo and cellular automata methods [61]. In commercial practice, it is important to achieve a uniform recrystallized β grain size during annealing following ingot breakdown and during solution heat treatment following deformation processing. In the

former case, nonuniformity of store energy within grains results in simultaneous recrystallization and grain growth in different areas of the material, whereas in the latter, the starting texture and its evolution during grain growth affect the kinetics.

Two-phase Ti alloys deform heterogeneously accompanied by large local grain rotations and the formation of intragranular deformation bands. A model based on an analysis of microstructural observations of these phenomena occurring during hot working of Ti−6Al−4V showed that Taylor factor was inversely related to globularization efficiency, which would increase with the operation of both basal and prismatic slip simultaneously in all grains [67]. Deformation texture introduces anisotropy of properties in the final product. It is also important for subsequent operations, e.g., forming of sheet. Basal or near-basal texture, shown schematically in Fig. 5.34A, results in isotropic properties in the plane of the sheet, compared with transverse (prismatic) texture in Fig. 5.34B [68]. Fig. 5.34C [8] shows schematically the texture developed in Ti−6Al−4V as a function of the degree, mode, and temperature of deformation and how it is influenced by the phases during deformation. Using Taylor analysis, texture in primary α during deformation of Ti−6Al−4V has been predicted and shown to be in reasonable agreement with the measured texture [61]. Transformation texture manifests itself in the variant selection of the α phase during heat treatment, which has been modeled assuming random or biased selection.

Modeling of microstructure and texture evolution in Ti alloys is key to the computational design of alloy compositions and processing approaches. Enabled by the availability of sophisticated analysis and characterization methods, rapid progress is being made in their understanding and application. An example is the use of data from electron backscatter diffraction (EBSD) characterization of deformed materials to construct three-dimensional microstructures using the open source software "Digital Representation Environment for the Analysis of

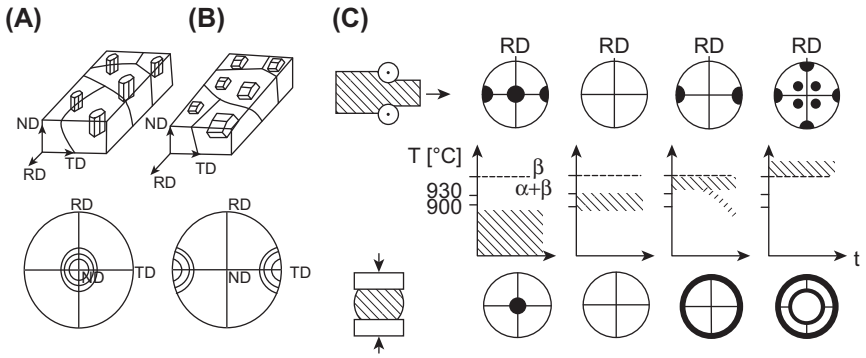


FIGURE 5.34

Schematic of texture in Ti with corresponding (0002) pole figure. (A) Sheet—basal orientation, (B) sheet—prismatic orientation [68], and (C) influence of deformation mode and temperature [8].

Microstructure in 3D" (DREAM.3D), which "presents an environment for processing, segmenting, quantifying, representing and manipulating digital microstructure data" [65]. A recent example of its use is the reasonably good replication of real microstructures for the near-β alloy Ti−5Al−5V−5Mo−3Cr from EBSD data [69].

5.4 PROPERTIES OF TITANIUM ALLOYS AND THEIR RELATIONSHIPS TO COMPOSITION, PROCESSING, AND MICROSTRUCTURE

The processing schemes used for Ti alloys produce complex microstructures with many features (Fig. 5.27) most of which are not amenable to quantitative modeling of their individual effects on properties. This is principally because of the inability to vary each feature systematically and independently of the others [48]. It is also unlike PH Al alloys for which the effects of each microstructural feature could be estimated and superposed to determine their combined effects on many of the properties, as was discussed in the previous chapter. Nevertheless, for Ti alloys these effects are well understood qualitatively for the microstructure types of interest and have been described in detail [5,8,18,33,70−74] and reviewed comprehensively, particularly in the framework of the mechanisms of deformation and modeling of properties including existing gaps therein [48]. Neural network models have also been used to delineate the contribution of each microstructural feature to properties to determine those that have the most impact [75]. These virtual models have the advantage of the ability to vary one microstructural feature while keeping all others fixed.

This section will describe the effects of processing and the resulting microstructures on the properties of importance for selection of commercial Ti alloys for applications. The length scale of the hierarchical microstructural features in α/β processed alloys that affect the properties range from few nanometers to several millimeters, as listed in Table 5.9 [76]. The multivariate relationships among the properties and various microstructural features will be emphasized with consideration of the ability or lack thereof to their modeling. The properties include strength, ductility, fracture toughness, fatigue strength, and FCG rates. Corrosion resistance is not discussed in detail as it is generally not an issue for selection and application of Ti alloys for airframe applications. These alloys do not have the constituent particles and other microstructural heterogeneities that promote electrochemical differences and initiate corrosion, as in PH Al alloys. The difficulty and expense of machining of Ti alloys coupled with its extensive use in the manufacture of parts with high buy-to-fly ratios have motivated studies to understand the effects of microstructures on machinability and to develop processing to improve this attribute. Many of the details pertaining to specific alloys will be discussed in the next section.

Table 5.9 Size Range of Microstructural Features in α/β Processed Ti Alloys [76]

Microstructural Feature	Approximate Size Range (μm)
α_2 (Ti_3Al)	0.005–0.05
Secondary α lath thickness	0.01–1
α lath thickness	0.1–10
β rib thickness	0.05–5
α particles	2–20
Secondary α colonies	1–50
α colonies	50–10,000
Microtextured regions	100–10,000
β grains (wrought processed)	100–10,000
Ghost (prior) β grains	100–10,000

It should be noted that although the focus of this book is on alloys for airframe structures for which Ti alloys are being increasingly used, at least for commercial airplanes, a significant fraction of the available properties data is on Ti–6Al–4V developed initially for its use in high temperature applications in engines. Still, this alloy has been characterized extensively and, along with the properties data available for β alloys developed for use in high strength applications in landing gears, provides a representative description of the relevant metallurgy. The discussion will be supplemented by reviewing the properties of specific Ti alloys developed for airframe applications.

The deformation behavior of Ti alloys containing α and β phases is determined by their individual characteristics and the interactions between them. Twinning, a key mechanism of deformation in pure HCP α Ti and dilute alloys, does not operate in α/β alloys representative of commercial compositions. Although solid solution hardening of α and β contributes to strength, its principal source is the resistance to dislocation motion by their interfaces. The volume fraction and morphologies of primary and secondary α control the amount and nature of the interfaces and along with texture have a significant influence on strength and other properties such as toughness, as shown for example in Figs. 3.2 and 5.35 [48]. Although these figures plot the variation of toughness with tensile and yield strength, respectively, the correlation between the properties and the alloy, heat treatment, and microstructure data in the respective plots is clear. In addition, when comparing the behavior of Ti alloys and PH Al alloys, as shown in Figs. 3.1, 3.2, 4.40, and 5.35, a parallel can be seen in the trends in the variation of toughness with strength for different alloy types (2XXX vs. 7XXX and α/β vs. β) and microstructures within given alloy types (underaged, peak aged, and overaged for Al alloys vs. lamellar, equiaxed, and bimodal for Ti alloys).

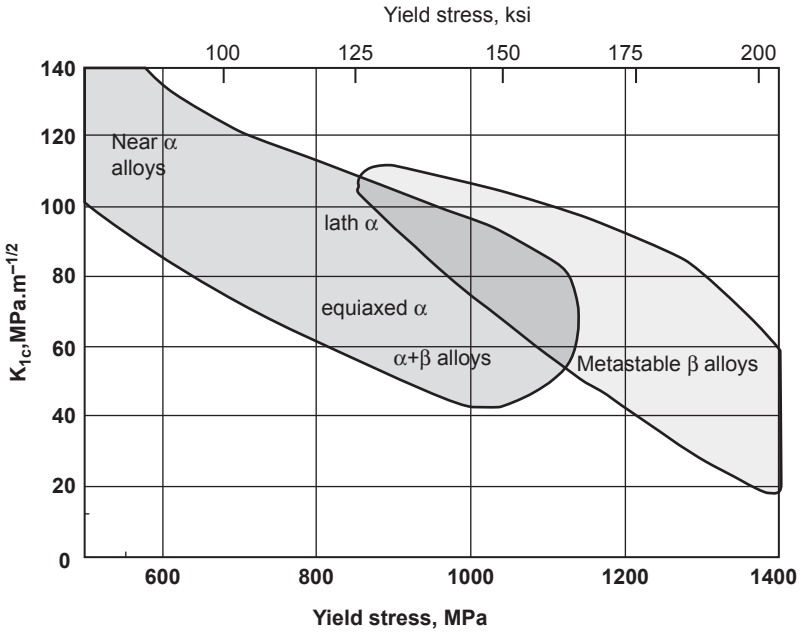


FIGURE 5.35

Yield strength—toughness relationships for Ti alloys with various microstructures [48].

The effective slip length, an important feature of deformation that determines the properties, is based on different features for the various microstructure types of Ti alloys. The crystallography of slip and plasticity in these alloys have been reviewed [48]. For fully lamellar structures, the slip length is represented by the size of colonies with similarly oriented α lamellae. As the cooling rate increases, the colonies become smaller and turn into the characteristic basket weave structure and finally into acicular laths of the martensitic structure. Slip in these microstructures initiates in the α phase and is anisotropic, even within a single colony, effectively considered an α grain, due to the difference in the ease of slip transfer across the interfaces for the various slip systems. Slip transfer becomes more complex for microstructures with increasing number of multiply oriented small colonies and for bimodal microstructures with a mixture of α_p and colonies. Given the complexity of the mechanisms of plastic deformation, properties of Ti alloys are not amenable to prediction by superposition of the effects of individual microstructural features estimated from relevant mechanistic models, which in most cases are not available, nor by simple "rules of mixtures". A review of various analytical models for the plastic deformation of alloys with two ductile phases including Ti alloys has been published [77].

It has been pointed out earlier in several contexts that processing of Ti and indeed all structural alloys is optimized to achieve microstructures for desired combinations

of multiple properties. This makes it difficult to discuss the effects of processing and microstructure on each property individually without reference to their impact, beneficial or otherwise, on other properties. Still, each property will be considered separately and will be followed by the consideration of integrated modeling of processing—microstructure—properties relationships in the framework of the systems approach described in the first chapter. An additional consideration, particularly for Ti alloys given their complexity, is the necessity to carefully distinguish the effects on the properties of varying the features for a specific versus multiple microstructure types. Nevertheless, despite the very limited number of structural Ti alloys in production and commercial use, large amounts of data have been generated to provide at least a qualitative understanding of their metallurgy.

5.4.1 STRENGTH

That all commercial Ti alloys used in aerospace structures are essentially "α/β" alloys, classified further as near-α, α/β, near-β, and metastable β in the continuum of increasing β stabilization, can be seen from Fig. 5.36 [5], which schematically shows how strength varies with composition and heat treatment after cooling from above T_β. The strength of the annealed alloys increases continuously with increasing solute content. The strength of as-quenched alloys reaches a peak at the composition at which the martensite transformation is complete. Following this, the strength continues to decrease with increasing retention of metastable β with increasing solute content. Aging of the quenched alloys increases strength significantly due to precipitation of α from metastable β. However, as discussed previously, the properties of Ti alloys can be varied widely by solution heat treatment above or below T_β and by aging at various temperatures to allow the formation of secondary α from the transformed β or by precipitation from metastable β.

5.4.1.1 α/β Alloys

The effects of heat treatment on the tensile properties of Ti—6Al—4V, shown in Fig. 5.37 (data from Ref. [78]), serve to illustrate the relative contributions of various microstructural features to the strength of α/β Ti alloys and set the framework for their detailed discussion. The as-quenched microstructures resulting from SHT at three different temperatures followed by cooling at various rates, shown in Fig. 5.19, were discussed earlier. These microstructures are similar for SHT temperatures of 955 (1750) and 900°C (1650°F).

The measured tensile properties show that as the SHT temperature is reduced to slightly below T_β (955°C), the strength of water-quenched alloys stays nearly the same. With further lowering of this temperature, strength decreases as the amount of α_p increases. Water quenched alloys also provide the highest response to aging. The strength of aged alloys exhibits a similar trend with decreasing SHT temperature. Increasing α_p amounts decrease the β available for transformation. Quenching from 845°C possibly produces orthorhombic α″ (see Fig. 5.9), which although soft provides significant strengthening upon aging. Compared with water quenched

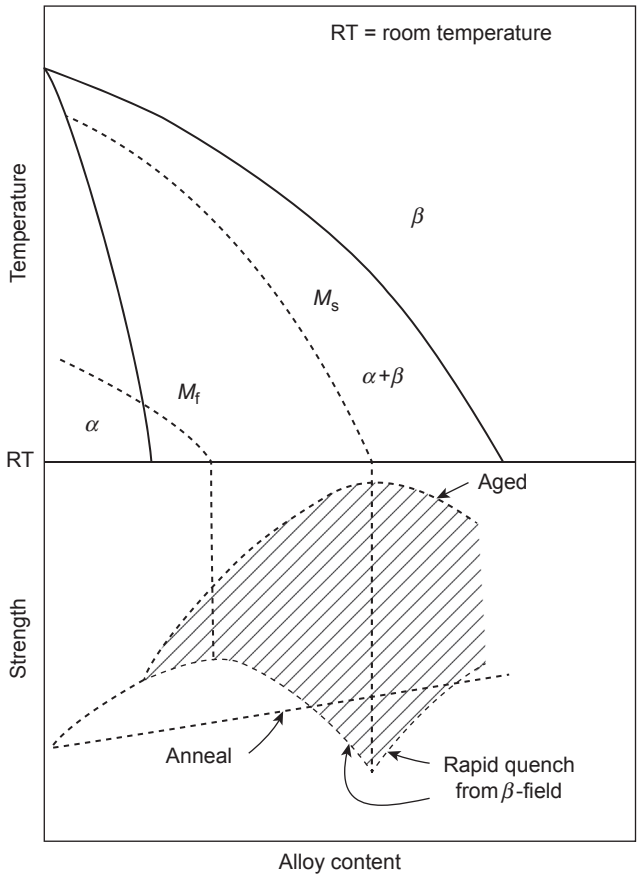


FIGURE 5.36

Schematic representation of variation of strength with alloy content and heat treatment [5].

alloys, response to aging and the corresponding strength are lower and the least for air-cooled and furnace-cooled alloys, respectively. However, SHT below T_β produces a higher response to aging for the slowly cooled alloys. As discussed in detail earlier, Ti alloys undergo complex sequences of TMP prior to heat treatment, which influences strength additionally through its dependence on the microstructure, characterized, for example, by the various features shown in Figs. 5.27 and 5.31.

As with most structural alloys, the beneficial effects of certain processing parameters on properties of Ti alloys were observed and advantageously utilized in commercial applications even prior to the characterization and understanding of the effects of microstructures. Increased strength was thought to be due to the "number and fineness" of α/β boundaries, which, for a fixed α_p content, could be increased

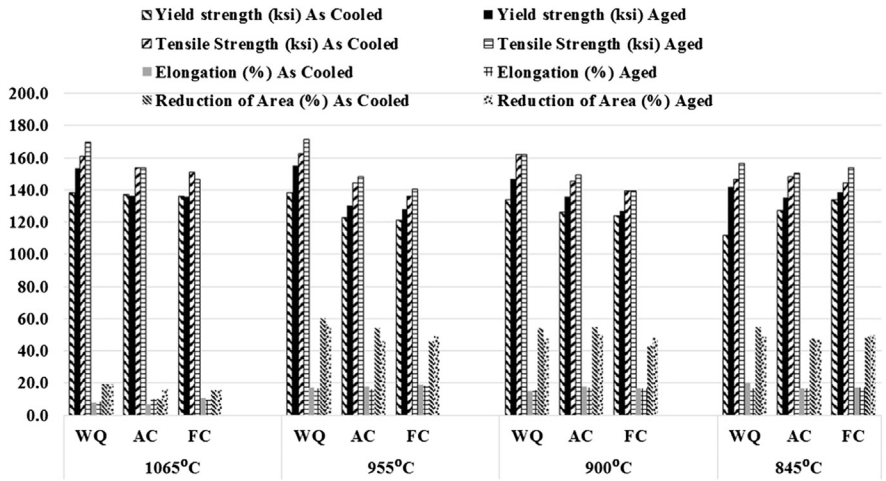


FIGURE 5.37

Typical tensile properties of Ti–6Al–4V, 0.625 in. bar, as a function of heat treatment (solution treated at the temperatures indicated, *WQ*, water quench; *AC*, air cool; *FC*, furnace cool and aged at 540°C for 4 h).

Data from Metallography, RMI Titanium Company Publication.

significantly by SHT, rapid cooling, and aging [47]. From the critical microstructural features and their many possible correlations with process parameters for α/β alloys, the relationships among cooling rate, colony size, and slip length are considered the most important in affecting the properties [58]. In this framework, the effects of the different microstructure types on strength are as follows.

1. For fully lamellar microstructures, colony size, individual lamellae width, and slip length all decrease with increasing cooling rates (Table 5.5), with a consequent increase of strength. The effect is only moderate in the range of commercial cooling rates (less than about 1000°C/s), as seen in the strength values trend in Fig. 5.37, but is large at higher cooling rates [33]. The yield strength increases only slightly although a larger increase is observed for the tensile strength.

The strength of alloys with lamellar microstructures can be enhanced by producing "bilamellar" microstructures through controlled precipitation of secondary α lamellae in the β phase [33,79]. Such a microstructure is beneficial for products such as castings that cannot be hot worked to refine the coarse lamellar microstructure. Bilamellar microstructures are produced by adding an intermediate annealing (termed intercritical) between solution and final annealing. During rapid cooling from the intercritical step, very fine, secondary α lamellae form in the V enriched β ribs. The slip length is effectively reduced in such a microstructure with beneficial effects on properties. This is demonstrated by intercritical annealing of Ti–6Al–4V,

initially processed by β annealing at 1050°C (1925°F) for 30 min and furnace cooling to produce a fully lamellar structure followed by solution annealing at 970°C (1780°F) for 4 h and furnace cooling to stabilize the microstructure. The strength of this alloy increased from 650 MPa to 677, 750, 828, 805, and 750 MPa (94 to 98, 109, 120, 117 and 109 ksi) by intermediate annealing at 800, 840, 880, 920, and 960°C (1470, 1545, 1615, 1690 and 1760°F), respectively, for 1 h and air cooling [80]. The peak strength occurring for annealing at 880°C (1615°F) was attributed to solute partitioning effects, whereby the coarse α lamellae are depleted of solute at high temperatures by its redistribution into the secondary lamellae. Decreasing cooling rate after intermediate annealing increased the size of the secondary α lamellae and reduced the strength. This approach is, however, not practical in thick section commercial product due to the low thermal conductivity and quench sensitivity of Ti−6Al−4V.

2. For bimodal microstructures, the strength is determined by the superposition of the effects for the fully lamellar microstructures and solute partitioning between α and β at the SHT temperature. Deformation and SHT in the two-phase field results in smaller β grain sizes and correspondingly smaller colony sizes and lamellar width upon quenching. The β grain size is determined by the volume fraction of α_p, which depends on the SHT temperature and its size, which is determined by the cooling rate from the β field prior to α + β processing. Thus based on colony size alone, for identical cooling rates, the strength of alloys with bimodal microstructures will be higher than those with fully lamellar microstructures. During solute partitioning, α_p is enriched by Al and O and β by V, which is a factor when SHT is between T_β and about 850°C (1560°F). The yield stress reaches a maximum at an α_p volume fraction between 0.1 and 0.2 [33]. This is illustrated by its variation with the SHT temperature for Ti−6Al−4V [81]. The strength values for this alloy reach a maximum between the SHT temperature of about 900 (1650) and 950°C (1740°F) and decrease with further increase in the amount of α_p when solute partitioning has a greater effect, reaching a minimum at about 815°C (1500°F). Upon aging, a continuous reduction of strength is observed with decreasing SHT temperature.
3. For equiaxed microstructures, the slip length is determined by the grain size of the α phase. Its influence on strength is identical to that of colony size for fully lamellar microstructures.

In addition to the effects of TMP and heat treatments, the properties of Ti alloys are also affected by texture, particularly for sheet and oxygen content. Properties of Ti−6Al−4V, illustrating these effects for the various microstructure types discussed above, are shown in Figs. 5.38 and 5.39 [46,82]. Fig. 5.38 shows the dependence of the strength on the size of the α lamellae for the fully lamellar and bimodal and the α_p particle size for the equiaxed microstructures. Fig. 5.39 shows the dependence of strength on the various commercial processing practices.

5.4.1.2 β Alloys

Irrespective of the prior processing steps (Table 5.6), all β Ti alloys are used after solution heat treatment and aging, during which secondary α (α_s) precipitates. In

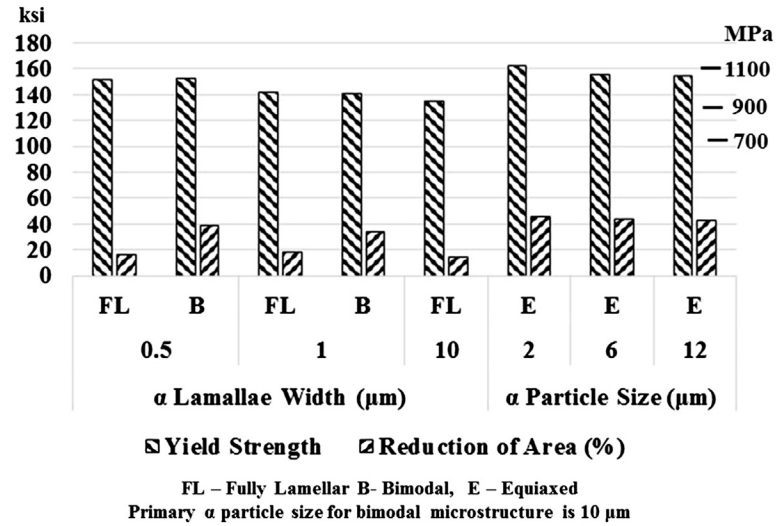
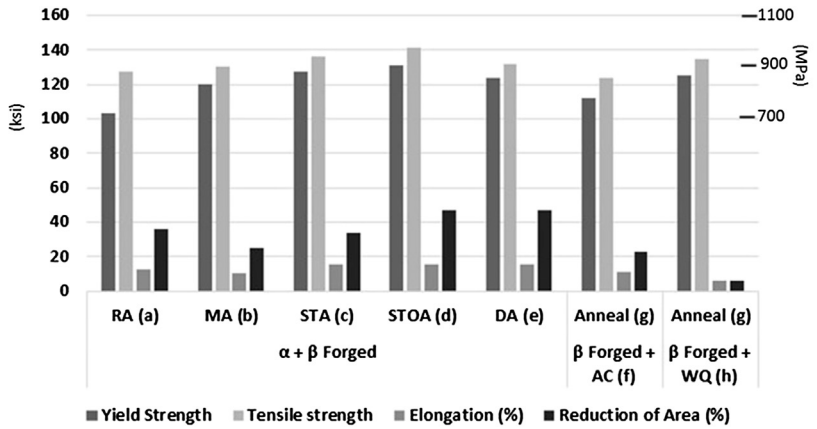


FIGURE 5.38

Yield strength and ductility of Ti—6Al—4V as a function of microstructure type and size of key features.



(a) RA - Recrystallization Anneal: 925°C/4h, Air Cool at 50°C/h to 760°C, Air Cool
(b) Mill Annealed
(c) Solution Treat and Age (594°C/4h)
(d) Solution Treat and Overage (594°C/24h)
(e) DA - Duplex Anneal: 870°C/2h, Air Cool + 705°C/2h, Air Cool
(f) AC - Air Cool
(g) 705°C/2h, Air Cool
(h) WQ - Water Quench

FIGURE 5.39

Effect of thermomechanical processing and heat treatment on the tensile properties of Ti—6Al—4V.

addition, α_p will be present in alloys processed below T_β. Thus, among the microstructural features that affect the properties of these alloys, namely β grain size, size, morphology, and volume fractions of α_p and α_s, and grain boundary α [71], whose dependence on processing are shown in Table 5.7, α that precipitates during aging has the most effect on strength. In this sense, these alloys are similar to PH Al alloys in the superposition of the contributions to strength from various microstructural features. The β grain size and grain boundary α have only a marginal effect on strength, whereas affecting other properties significantly. However, the α_s particles are incoherent with the matrix and in stable equilibrium, whereas precipitates in Al alloys are metastable and either coherent or semicoherent.

The general principles of precipitation hardening apply to the aging of β Ti alloys. The peak strength decreases with increasing aging temperature due to the decreasing volume fraction of equilibrium α and is achieved in shorter durations. The volume fraction of α_s that can precipitate is dependent on the amount of α_p as the total amount of α is fixed by equilibrium considerations. Desired values of yield strength can be achieved to balance other properties by varying the aging parameters and increasing the volume fraction of coarse α by decreasing the cooling rate from the processing temperature prior to aging [59]. Strengthening is by the Orowan mechanism of particle bypassing and increases with decreasing interparticle spacing, d. The yield strength can be estimated from the following relation [13], where d is in μm:

$$\text{Yield Strength (MPa)} = 850 + 70/\text{d}$$

The tensile properties of Ti−10V−2Fe−3Al, shown in Table 5.10 [83], illustrate the general effects of microstructural features for β alloys. Conditions 5 and 7 are processed above T_β and have no α_p present. The increase in strength from finer α_s precipitates for identical α_p amounts can be seen by comparing conditions 2 with 1 and 4 with 3. The decrease in strength from higher amounts of α_p for similar α_s morphologies can be seen by comparing conditions 1 with 3 and 2 with 4. The effects of elongated α_p morphologies, which improve toughness but reduce ductility, will be described later. Cold work has a beneficial effect on precipitation during aging, as shown in Fig. 5.40, for the metastable β alloy Ti−15V−3Cr−3Al−3Sn [84].

5.4.2 DUCTILITY

Ti alloys do not contain crack nucleating second phase particles such as the constituent particles in PH Al alloys or sulfides and carbides in steels. Cracks can nucleate in Ti alloys at interphase interfaces due to strain incompatibility or at localized slip bands that arise from intense planar slip [48]. Many types of interfaces occur in Ti alloys like those between the grain boundary α or equiaxed α and the transformed β matrix or between the α laths and β in the lamellar structure. Planar slip can result in the presence of short range ordering and in alloys containing age hardening phases (e.g., α_2 or ω). Interstitial elements (O, N, C, and H) in excessive amounts reduce ductility while increasing strength [74].

Table 5.10 Tensile Properties of Ti–10V–2Fe–3Al for Various Processing Conditions

	Condition	Heat Treatment	Microstructure	Yield Strength		Tensile Strength		Elongation (%)	Strain to Fracture
				ksi	MPa	ksi	MPa		
Primary α	1	725°C/20 h, WQ + 500°C/1 h (salt)	30% Primary α + large secondary α	154	1062	160	1103	17.7	0.99
	2	725°C/100 m, WQ + 370°C/ 1000 m	30% Primary α + small secondary α	181	1248	206	1420	7.6	0.19
	3	780°C/3 h, WQ + 500°C/1 h (salt)	10% Primary α + large secondary α	174	1200	181	1248	10.3	0.63
	4	780°C/3 h, WQ + 500°C/1 h (air)	10% Primary α + small secondary α	209	1441	224	1544	2.4	0.09
	5	850°C/2 h, WQ + 500°C/4 h (salt)	Grain boundary α + large secondary α	181	1248	190	1310	3.9	0.16
Elongated primary α	6	700°C/100 m, WQ + 200°C/ 6800 m	35% Primary $\alpha + \omega$	176	1214	184	1269	0.5	0.02
	7	850°C/2 h, WQ + 500°C/4 h (salt)	Grain boundary α + large secondary α	171	1179	183	1262	3.8	0.17
	8	760°C/75 m, WQ + 500°C/1 h (salt)	10% Primary α + large secondary α	188	1296	200	1379	4.6	0.23
	9	700°C/75 m, WQ + 350°C/ 1000 m	30% Primary α + small secondary α	180	1241	202	1393	3.9	0.11

WQ, *water quench.*

Data used with permission of ASM International. All rights reserved. www.asminternational.org.

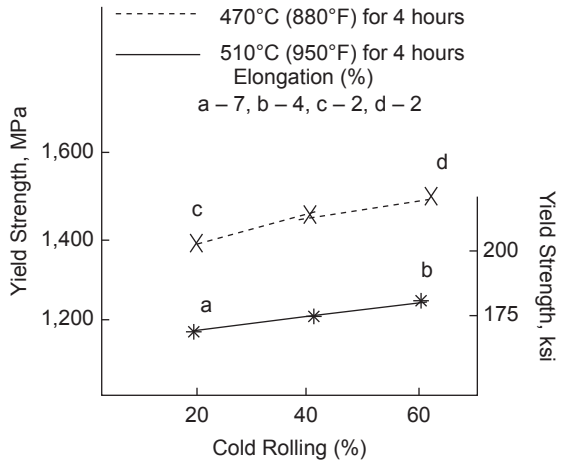


FIGURE 5.40

Effect of prior cold work on strength after aging for Ti—15V—3Cr—3Al—3Sn [84].

Adapted and reprinted with permission of ASM International. All rights reserved. www.asminternational.org.

Ductility of Ti alloys generally decreases with increasing strength but exceptions exist that are based on microstructural features, slip length, and the relative strength of the phases on either side of the interfaces. For example, as the cooling rate increases, both strength and ductility increase with decreasing colony size and slip length until the ductile dimple fracture mode changes from transcrystalline to intercrystalline type. In alloys cooled at higher rates, whereas matrix strength continues to increase, cracks nucleate and propagate along the soft, grain boundary α layer resulting in low ductility [33]. For identical cooling rates, both strength and ductility will be higher for bimodal than for lamellar, and for smaller α grain sizes in equiaxed microstructures.

Grain boundary α layer has a stronger effect on the ductility of β alloys due to the higher strength of the age hardened matrix. With the slip length being the distance between grain boundary triple points, bimodal microstructures with characteristically smaller grain sizes will exhibit higher ductility compared with that for β annealed condition. β processed alloys with their characteristic unrecrystallized microstructure and elongated β grains exhibit anisotropy with ductility being the highest in the longitudinal (L) loading direction, lower in the short transverse (ST) direction, and the lowest in the loading direction with an angle 45—60 degrees between both the L and ST directions. The behavior can be explained by the geometry of the grains and the grain boundary α layer in relation to the slip length and the stresses on them as determined by the loading direction [33]. This observation is somewhat like the anisotropy exhibited by thick section PH Al alloy products containing pan cake shaped grains and precipitate free zones along the grain boundaries. Also, as observed with PH Al alloys, ductility of β alloys will decrease with increasing age hardening due to increasing strength difference between the matrix and the soft grain boundary α layer. This effect will be mitigated by reducing the β grain size.

Considering the effects of interstitial content, texture, and the many microstructural features that affect the ductility of Ti alloys, those processed in the β region generally possess lower ductility than those processed in the two-phase region. For the latter, ductility increases with increasing amounts of α_p up to a certain level beyond which it will decrease. The morphology of α_p affects ductility with the values being lower in alloys with unrecrystallized microstructures containing elongated grains (conditions 6–9 in Table 5.10). For similar strength levels, globular α_p provides higher ductility. Microstructure generally has more of an effect on the ductility of β alloys due to their reliance on age hardening for strengthening. Alloys containing the ω phase exhibit very low ductility (condition 6 in Table 5.10) and the ductility increases with decreasing strength beyond peak aging (compare conditions 1 with 2 and 3 with 4 in Table 5.10).

5.4.3 DURABILITY AND DAMAGE TOLERANCE PROPERTIES

The previous chapter described in detail the fracture toughness and fatigue behavior that characterize the durability and damage tolerance of PH Al alloys and the way these properties are used in various approaches to structural design. This section describes the effects of processing and microstructure on these properties for Ti alloys. Unlike PH Al alloys, Ti alloys do not contain crack nucleating second-phase particles and their deformation is controlled principally by the interfaces between the two ductile phases α and β. As will be discussed, this results in key differences in the way strength, ductility, toughness, and fatigue behavior vary with each other for these alloy systems. Generally, for Ti alloys of a given family such as α/β alloys, fatigue strength and crack growth rates show similar trends as yield strength and fracture toughness, respectively. However, the sizes of various microstructural features have distinct and seemingly contradictory effects on many aspects of these properties such as high cycle fatigue (HCF) strength, low cycle fatigue (LCF) strength, FCG in the microcrack, and macrocrack regimes and fracture toughness.

The phenomenon of dwell fatigue results in a significant reduction of the fatigue life of Ti alloys with high α content (high temperature near-α alloys) [85]. It is caused by a sustained hold at the maximum stress at ambient temperatures, is of concern for engines and as such is not discussed in this chapter. The compositions and microstructural conditions susceptible to this phenomenon have been discussed in detail [18] and a crystal plasticity model has been used to explain its occurrence in the near-α alloy Ti–6Al–2Sn–4Zr–2Mo and not in the α/β alloy, Ti–6Al–2Sn–4Zr–6Mo [86].

5.4.3.1 Fatigue Strength/Life

Fatigue life in the high cycle regime is controlled by resistance to crack nucleation, which is measured by the HCF strength (stress for a fatigue life of 10^7 cycles). Life in the low cycle regime is controlled both by nucleation and propagation of "microcracks" (small cracks initiating at microstructural features) as distinct from "macrocracks" (large through-thickness cracks) [33].

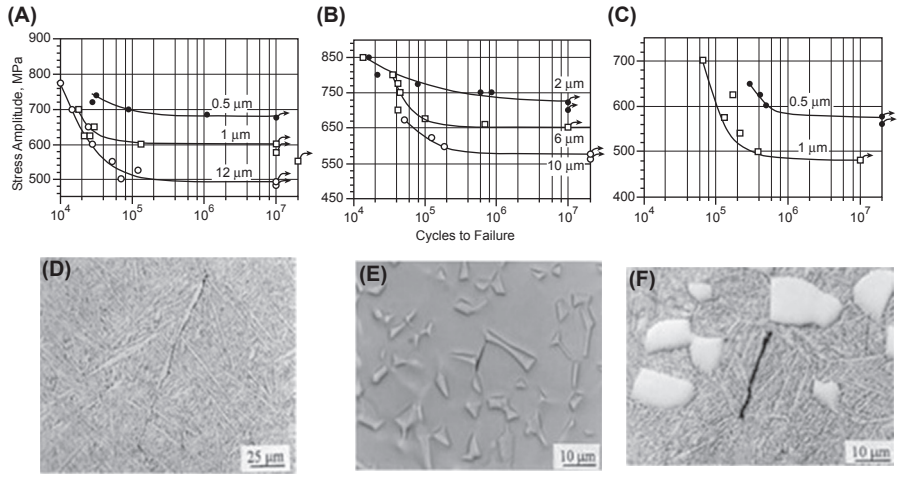


FIGURE 5.41

S–N curves for Ti–6Al–4V (A) fully lamellar (effect of lamellar width), (B) equiaxed (effect of grain size), and (C) bimodal (effect of lamellar width) with the corresponding crack nucleation sites shown in (D–F), respectively [72].

5.4.3.1.1 High Cycle Fatigue Behavior

For a given microstructure, features that increase the yield strength, shown in Fig. 5.38, also increase the HCF strength, as illustrated in Fig. 5.41A–C for Ti–6Al–4V [72]. Fatigue lives and particularly HCF strength increase with decreasing lamellar size for the fully lamellar and bimodal microstructures and with decreasing grain size for the equiaxed microstructure. Crack nucleation sites for these materials are shown in the corresponding microstructures in Fig. 5.41D–F. For the colony microstructure, fatigue cracks nucleate either within slip bands extending across the colony or within individual lamellae, for the equiaxed microstructure within the α grains and for the bimodal structure in the lamellar matrix, α grains or at their interfaces [33,71]. For a given microstructure type, the final heat treatment can affect the HCF strength. For Ti–6Al–4V with a coarse lamellar microstructure, the HCF strength values were 500 MPa (73 ksi) for the heat-treated alloy (solution heat treated at 800°C (1472°F) for 1 h/water quenched/aged at 500°C (932°F) for 24 h) compared with 350 MPa (51 ksi) for the alloy stress relieved at 650°C (1200°F) and air cooled. The yield stress values for these alloys were 930 and 830 MPa, (135 and 120 ksi), respectively [33]. Similarly, as the yield stress for Ti–6Al–4V with a fine lamellar microstructure increased from 910 to 990 MPa (132 to 137 ksi) with increasing O content from 0.08 to 0.19 wt%, the HCF strength increased from 480 to 580 MPa (70 to 84 ksi).

The HCF behavior of β alloys has been reviewed comprehensively [87]. The HCF strength of β alloys is generally influenced by grain size, degree of age hardening, grain boundary α, precipitate free zones, and the size and volume fraction of α_p.

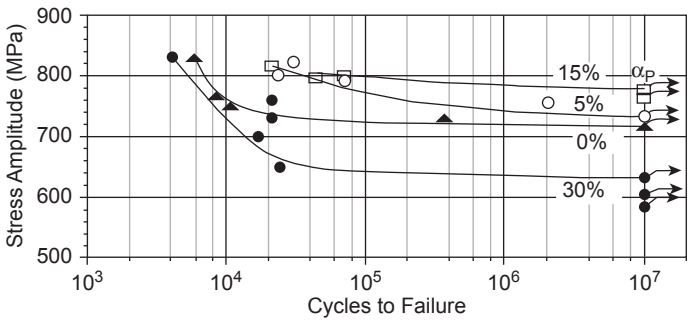
The relative importance of these factors differs between the near-β and metastable β alloys and the microstructure types. The microstructure of near-β alloys such as Ti−10V−2Fe−3Al can be varied to a greater degree than that of the metastable β alloys by processing to produce different amounts of α_p, like the α/β alloys. As the strength of β alloys is increased by aging, fatigue cracks nucleate in the soft grain boundary region due to the increasing strength difference between this region and the matrix, thereby placing an upper limit on the HCF strength. Like the effects on tensile ductility, bimodal microstructures provide better HCF performance than β annealed (fully lamellar) microstructures, with improvements occurring up to certain amounts of α_p, as seen in Fig. 5.42 for Ti−10V−2Fe−3Al [72].

The reduction in the strength of the age hardened β matrix with increasing levels of α_p reduces the yield stress and the corresponding HCF strength. Reduction of grain size and thus the deleterious effects of the grain boundary α layer, particularly for the metastable β alloys has a beneficial effect on improving HCF. The ratio of HCF strength to yield strength increases with decreasing grain size, as seen by its increase from 0.50 to 0.65 (for 10^6 cycles) when the grain size decreased from 122 to 40 μm for Beta C alloy [71].

High cycle fatigue behavior depends on many microstructural features, which have different effects depending on the alloy class and microstructure type. It can generally be improved by aging to the optimum level, small grain size, suppressing grain boundary α, and producing a homogeneous distribution of secondary α.

5.4.3.1.2 Low Cycle Fatigue Behavior

Length scale of the microstructural features plays a larger role in affecting LCF compared with that of HCF behavior [73]. This is because of the relatively low



Primary α (Volume)	Yield Strength MPa (ksi)	Failure Strain
0	1555 (226)	0.02
5	1370 (199)	0.09
15	1330 (193)	0.11
30	1195 (173)	0.25

FIGURE 5.42

Yield stress and S−N curves for Ti−10V−2Fe−3Al as a function of primary α [72].

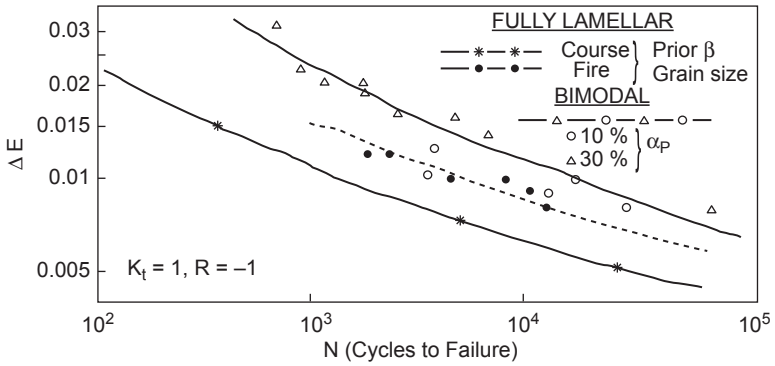


FIGURE 5.43

Strain-life curves for Ti–6Al–4V as a function of microstructure [73].

values of stresses in the HCF regime wherein resistance to dislocation motion in the lattice controls slip and the HCF strength generally increases with yield strength. In the LCF regime, cracks nucleate early under the relatively high maximum stresses. Again, as with HCF, for fully lamellar structures, LCF life will increase with decreasing colony and lamellar size resulting from higher cooling rates as well as lower prior β grain size. The LCF life is also higher for bimodal structures with their typically smaller β grain sizes than for fully lamellar structures, with the effect increasing with amount of α_p up to about 30%. These observations are shown in the strain-life plots for Ti–6Al–4V in Fig. 5.43 [73]. However, at higher α_p volume fractions, the weakening of the β matrix and the subsequently transformed β microstructure caused by solute partitioning result in lower LCF lives for the bimodal microstructure causing the crossover of the curves, as shown in Fig. 5.44 [73].

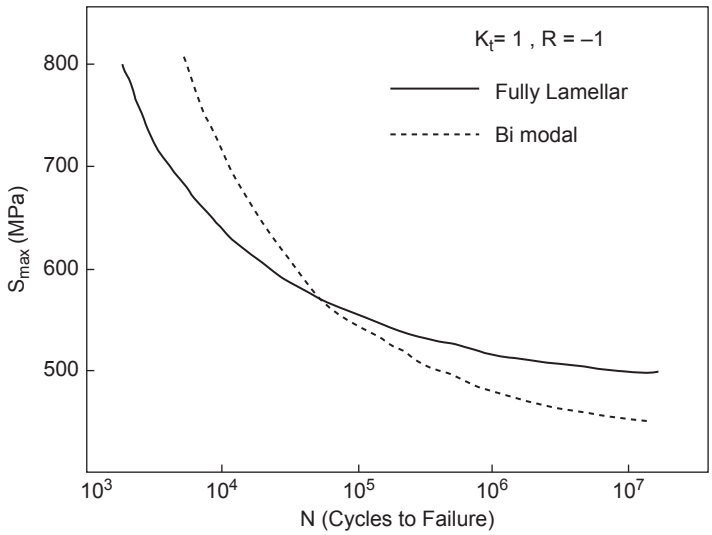


FIGURE 5.44

Stress-life curves for Ti–6Al–4V as a function of microstructure [73].

Similar crossover can occur in comparing the effects of aging and O content, as they act in opposing ways. Fig. 5.42 shows the convergence of the S−N curves in the LCF regime for Ti−10V−2Fe−3Al, for which the grain boundary α plays a more important role.

5.4.3.2 FCG Behavior

Microstructural effects on FCG for PH Al alloys were discussed for short and long cracks. For Ti alloys, FCG and its dependence on microstructure have been reported for short/small and long/large cracks [73] and for corresponding microcracks and macrocracks [33,72]. Microstructurally short/small cracks initiate and grow into mechanically short/small cracks, which exhibit irregular growth, coalesce and transition into long/large cracks. The effects of variables such as R ratio, texture, β grain size and age hardening have been discussed in detail for relevant alloy classes and microstructure types [33,59,71−73]. The following discussion will focus briefly only on the features of importance for the common microstructure types discussed earlier.

For α/β alloys, FCG resistance for microcracks is superior in fine than in coarse lamellar microstructures. In the size range for these cracks, individual, α plates provide more obstacles and stronger resistance in the fine lamellar microstructure. For macrocracks, the colony and prior β grain boundaries in the coarse microstructure provide numerous barriers and higher resistance for growth. A bimodal structure with its characteristically smaller colony size has a better FCG resistance for microcracks than the lamellar microstructure, whereas the opposite holds for macrocracks. Comparing equiaxed with coarse lamellar microstructures, the former is more resistant to FCG in the microcrack and the latter in the macrocrack regime.

Resistance to FCG depends on the scale of the microstructural features that act as barriers and increase the tortuosity of the crack path explaining the opposing trends for small and long crack behavior. Coarse, fully lamellar and fine, equiaxed microstructures generally provide the most and least resistance, respectively, to FCG in the long crack regime (macrocracks), with the bimodal structures in between, as shown schematically for Ti−6Al−4V in Fig. 5.45 [46]. The opposite is generally true for microcracks.

In contrast with α/β alloys such as Ti−6Al−4V, the higher strength levels of β alloys result in smaller plastic zone sizes that encompass only a few of the strengthening α_s particles. This renders the FCG for the β alloys relatively insensitive to the microstructure in the long crack regime as shown in Fig. 5.46 for several of these alloys and for several processing parameters for Ti−10V−2Fe−3Al [71].

5.4.3.3 Fracture Toughness

For α/β Ti alloys, coarse, fully transformed microstructures, which promote crack tortuosity, provide the highest fracture toughness followed by bimodal (produced at the same cooling rates as the lamellar) and the equiaxed types. Within each microstructure type, fracture toughness increases with increasing coarseness of the relevant microstructural feature (e.g., colony size, α lamellae width and α grain size).

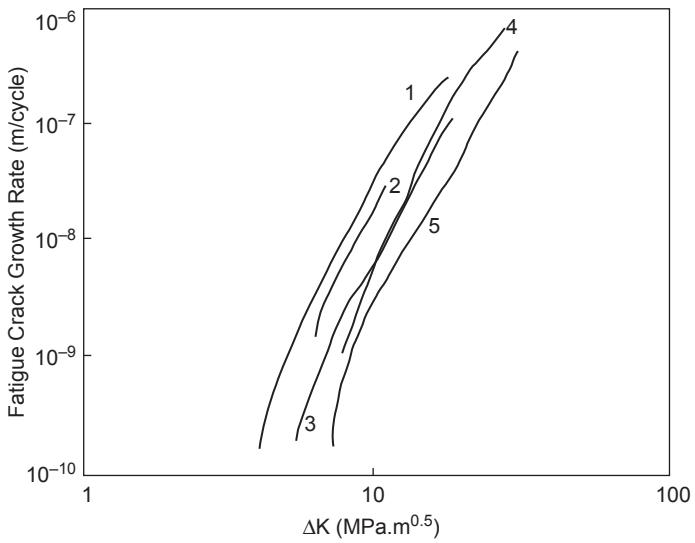


FIGURE 5.45

Fatigue crack growth rates for various microstructures in Ti–6Al–4V (air, R = 0.1) [46].

Adapted and reprinted with permission of ASM International. All rights reserved. www.asminternational.org.

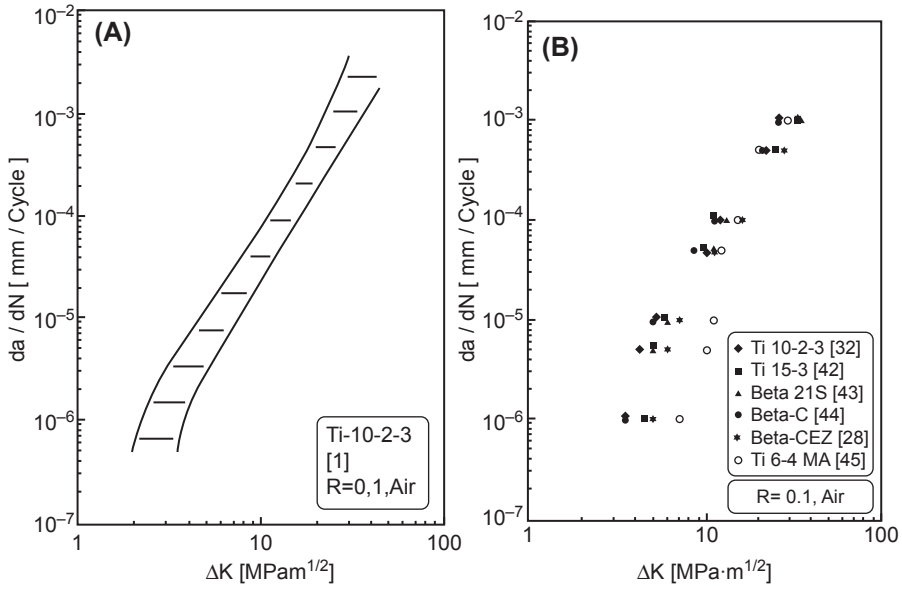


FIGURE 5.46

Fatigue crack growth rates for β alloys. (A) Band for several processing conditions for Ti–10V–2Fe–3Al (B) several β alloys [71].

Table 5.11 Effect of Volume Fraction of Transformed Microstructure on Fracture Toughness for Ti−6Al−4V [80]

Heat Treatment Temperature (°C)[a]	Fraction of Transformed Microstructure (%)	K_{Ic} (MPa.m$^{0.5}$)
1050	100	69
950	70	55
850	20	40
750	10	38

[a] *Heated at temperature for 1 h and air cooled.*

Data used with permission of ASM International. All rights reserved. www.asminternational.org.

Thus, the strength of α/β alloys is highest in a solution heat treated and aged alloy containing a certain amount of α_p, as discussed earlier, whereas the highest toughness is achieved in β annealed alloys with coarse, lamellar microstructures.

The reduction of toughness with decreasing volume fraction of the transformed microstructure (correspondingly increasing α_p volume fraction) is shown for Ti−6Al−4V in Table 5.11 [80]. The increase in toughness at similar strength levels for lamellar microstructures compared with those containing α_p is more pronounced for higher strength α/β alloys such as Ti−6Al−2Sn−4Zr−6Mo, as seen from Table 5.12 [46,88].

The data presented in this table illustrates several microstructure−property relationships discussed already. For a given heat treatment condition, reducing interstitial amounts increases fracture toughness with some loss of strength, the effect being more pronounced in the α + β processed alloy than in the alloy cooled from β, which already possess higher toughness. The recrystallization anneal treatment provides a good balance of strength and toughness, especially for the alloy with lower interstitial levels. For the higher strength alloy, Ti−6Al−2Sn−4Zr−6Mo, fracture toughness increases by a larger percent in the β forged alloy compared with that in the α + β condition. This increase is accompanied by a loss in ductility and a slight loss in strength.

Between the near-β and the metastable β alloys, the former provides the possibilities to tailor the microstructures to achieve a wider range of strength−fracture toughness combinations through thermomechanical processing [80,83,89]. The metastable β alloys, strengthened predominantly by very fine α precipitates are not amenable to extensive manipulation of the microstructure by such processing. For both types of these alloys, different property combinations can be obtained by varying aging treatments. For the near- β alloy, Ti−10V−2Fe−3Al, high toughness is achieved by optimum processing to produce a 10% volume fraction of elongated α_p, which results in crack deviation, compared with globular α_p, as shown in Fig. 5.47 [71,90]. Coarser and elongated intragranular α laths with discontinuous grain boundary α precipitates provide the highest fracture toughness for Ti−5Al−5V−5Mo−3Cr [91]. The effect of β grain size and grain boundary α film will depend on the strength of the aged matrix. The necklaced structure, discussed earlier, with the broken-up grain boundary film increases toughness without reducing ductility.

Table 5.12 Strength–Fracture Toughness Relationships for α/β Ti Alloys

Interstitial Content	Heat Treatment	Tensile Strength, MPa (ksi)	Yield Strength, MPa (ksi)	Elongation (%)	Reduction of Area (%)	K_{Ic} (MPa.m$^{0.5}$)
(a) Ti–6Al–4V With Two Different Levels of Interstitial Content [46]						
ELI	STOA	1000 (145)	895 (130)	12	30	60
	RA	930 (135)	860 (125)	10	25	75
	BA	860 (125)	795 (115)	8	20	99
STD	STOA	1000 (145)	938 (136)			43
	RA	1000 (145)	931 (135)			56
	BA	990 (144)	910 (132)	11	20	95

Condition	Tensile Strength, MPa (ksi)	Yield Strength, MPa (ksi)	Elongation (%)	K_{Ic} (MPa.m$^{0.5}$)
(b) Ti–6Al–2Sn–4Zr–6Mo [88]				
α + β Forged/STA[a] (10% α_p)	1213 (176)	1116 (162)	13	34
A + β Forged/STA[a] (50% α_p)	1240 (180)	1150 (167)	14	26
α + β Forged/Annealed[b] (50% α_p)	1130 (164)	1061 (154)	13	26
β Forged/STA[a]	1199 (174)	1047 (152)	7	57

BA, *beta anneal;* BSTOA, *beta STOA;* ELI, *extra low interstitial content (0.03N, 0.13O);* RA, *recrystallization anneal;* STA, *solution heat treat and age;* STD, *standard interstitial content (0.05N 0.20O);* STOA, *solution heat treat and overage.*

[a] *855°C/1 h/air cool + 595°C/air cool.*

[b] *705°C/air cool.*

Data used with permission of ASM International. All rights reserved. www.asminternational.org.

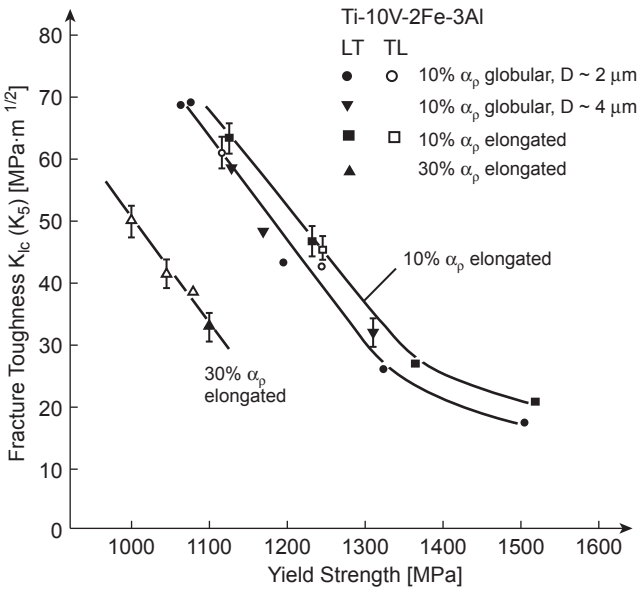


FIGURE 5.47

Variation of fracture toughness of Ti–10V–2Fe–3Al with the morphology and volume fraction of primary α [71].

5.4.4 STRESS CORROSION CRACKING

It was mentioned earlier that corrosion is not an issue for the use of Ti alloys in airframes. However, the stress corrosion cracking (SCC) threshold can be reduced for Ti alloys under certain conditions in which ordering can occur. Analysis of the experimental data for Ti–6Al–4V sheet has shown that the SCC threshold is controlled by ordering, texture and oxygen content [92]. An ordering factor was developed in this study to determine its effects on SCC behavior. Higher ordering factor, promoted by oxygen, lowered the SCC threshold values. A more recent study [93] comparing the behavior of Ti–6Al–4V with standard and extra low interstitial (ELI) content, showed that cooling rate from the annealing temperature affects ordering and SCC threshold for the ELI and not the standard material. Although the ELI material has a lower ordering factor, it shows significant difference in SCC thresholds between air cooling and slow, furnace cooling, which promotes ordering.

5.4.5 HIGH TEMPERATURE PROPERTIES

The dependence on microstructural features of the tensile, durability and damage tolerance properties of Ti alloys generally exhibits similar behavior at room and elevated temperatures. Creep strength is improved by increasing the volume fraction

of the α phase, with its lower solute diffusion rates, as in near-α alloys. The morphology of this phase is also important, since creep resistance decreases with increasing volume fraction of equiaxed α. Optimum combinations of fatigue and creep properties are obtained at an equiaxed, α_p content in the range of 5%–10% [5]. Maintaining such a small volume fraction requires processing close to and below T_β necessitating careful process control (see Fig. 5.11). For both lamellar and bimodal structures, creep resistance is maximum at intermediate cooling rates, which produce the characteristic basket weave morphologies.

High volume fraction of nondeformable α platelets with small interparticle spacing in alloys such as Ti–6Al–2Sn–4Zr–6Mo renders sufficient creep resistance enabling their use up to about 450°C (840°F). Creep resistance of near-α alloys is increased by coherent α_2 particles, which are formed by aging below the solvus. Due to the very low volume fraction of β in creep-resistant alloys, its thickness in the interlamellar region is reduced considerably and becomes zero in many areas of the colony structure. Precipitation of incoherent silicide particles in these areas in Si containing alloys restores the obstacles to deformation.

5.4.6 SUMMARY OF COMPOSITION–PROCESSING–MICROSTRUCTURE–PROPERTIES RELATIONSHIPS

Structural alloys of interest for aerospace applications belong primarily to the α/β class. Higher resistance to creep and higher room temperature strength are achieved in near-α (e.g., Ti–6Al–2Sn–4Zr–2Mo–0.1Si) and near-β alloys (e.g., Ti–10V–2Fe–3Al), respectively. Ti–6Al–4V provides a good balance of these properties and is the most commonly used structural Ti alloy. Although not as creep resistant as near-α alloys, fine, incoherent secondary α particles impart a measure of thermal stability in α/β alloys with higher β stabilization (e.g., Ti–6Al–2Sn–4Zr–6Mo) rendering them suitable for use up to about 450°C. Metastable β alloys do not develop as high a strength as near-β alloys and are used for applications like springs and tubing (e.g., Beta C) and in intermediate temperature areas such as in nozzles (e.g., Timetal 21S). Another important application for Ti alloys, that will not be discussed, is for fasteners for which tensile, shear, and fatigue strength are all important. As discussed in earlier sections, the ability to thermomechanically process and heat treat above or below T_β provides the opportunity to achieve a wider range of microstructures and properties in the α/β alloys. Metastable β alloys are somewhat limited in this regard due to their solution heat treatment only above T_β and reliance for their strength predominantly on precipitation hardening.

Tables 5.4 and 5.5 (based on the detailed descriptions in Ref. [33]) provide a summary of the sequence of processing and its effects on microstructure evolution, respectively, for representative α/β alloys such as Ti–6Al–4V. Tables 5.6 and 5.7 (based on the detailed descriptions in Ref. [59]) provide similar information for the near-β and metastable β alloys. The metallurgical changes occurring during the key processing steps are described in Table 5.8 and the typical size range of the resulting microstructural features are shown in Table 5.9. In the absence of clearly defined temper

designations (unlike Al alloys), the term annealing is used in commercial practice to describe many thermal treatments whose outcome will depend on the temperature and time of exposure and the cooling rate following the treatment. The typical temperature ranges for these treatments is shown in Figs. 5.5 and 5.17 and examples for commercial alloys will be provided in a subsequent section.

The microstructure–property relationships are summarized briefly as follows:

- Fully lamellar, coarse microstructures exhibit the highest fracture toughness and resistance to FCG.
- Fully equiaxed, fine microstructures exhibit the highest ductility and resistance to fatigue crack initiation (fatigue strength).
- Bimodal microstructures provide a balance of all the properties, as determined by the relative proportions and scale of the primary α and the transformed β components.
- Strength is determined by the slip distance, with smaller grain sizes and finer lamellar spacing resulting in higher strength. Desired combinations of strength and other properties can be obtained by varying the solution annealing and aging parameters.

These relationships were illustrated with examples from the properties of commercial alloys and will also be discussed in discussing specific alloys. In this respect, the data sheets in [17] and those from suppliers are excellent sources of information for in depth review and understanding of the composition–processing–microstructure relationships.

5.4.7 MODELING OF COMPOSITION–PROCESSING–MICROSTRUCTURE–PROPERTIES RELATIONSHIPS

Predictive modeling of several aspects of the characteristics and behavior of Ti alloys was discussed in previous sections. Thermodynamic, phenomenological and neural network models that have been used to predict T_β, β approach, optimum processing windows, microstructure and texture, as appropriate, were outlined along with their successes and limitations. This section will discuss the status of the modeling of individual properties of Ti alloys followed by the progress that is being made in their integration into the "Integrated Computational Materials Engineering (ICME)" framework discussed in the first chapter.

Despite the large number of microstructural features that affect the properties of Ti alloys, there is excellent qualitative understanding among their relationships, as evidenced by the successful development and application of Ti alloys and processing approaches for critical applications. It was mentioned earlier that one of the major difficulties in generating experimental data suitable for use in developing quantitative models is the inability to vary one individual microstructural feature, e.g., α lath thickness, whereas keeping all others constant. However, such an approach is possible in virtual experiments, which have been used with some success to develop

neural network models and to identify the relative contributions of the microstructural features to individual properties.

5.4.7.1 Modeling of Strength

Among all the mechanical properties of interest, yield strength is generally the easiest to predict. As described in the previous chapter, the mechanisms of actions of all the factors that contribute to the flow stress of PH Al alloys and their superposition are well understood enabling accurate quantitative predictions of their yield stress values using physics based models. This is not the case for multicomponent Ti alloys because the contributions from each of the microstructural features to the various strengthening mechanisms and how they are superposed are not known. In this regard, considerable progress has been made over the past decade in developing neural network models for tensile properties, principally yield stress, for Ti−6Al−4V [75,94−96]. In one of these earlier investigations [94], Bayesian neural network modeling of results from virtual experiments on α/β-processed Ti−6Al−4V determined that the most significant contribution to strength came from solid solution hardening of the α phase by aluminum and oxygen and, unexpectedly, of the β phase by iron to some extent and by the volume fraction of the equiaxed α particles [23].

More recently, mechanism-based models based upon integration of neural network, genetic algorithms and Monte Carlo simulations have been developed for the yield stress of α + β processed [97] and β processed [98] Ti−6Al−4V. For studying the behavior of the α + β processed condition, nine alloys, each with different chemistries within that nominally specified for Ti−6Al−4V were processed under six different α + β TMP conditions. The microstructural features (size of equiaxed α, volume fraction of equiaxed and total α, and width of α laths in transformed β) and tensile properties of the 54 samples were characterized for use in the development of the neural network models. An example of the scatter in the measured yield stress of the 54 samples as a function of the corresponding mean equiaxed α particle size is shown in Fig. 5.48A. Although each of these samples had varying sizes of other microstructural features, results of the virtual experiment in which all other features were kept constant at their average values and only the equiaxed mean size was varied, is shown in Fig. 5.48B.

The expected strengthening mechanisms were used to postulate an equation for estimating the yield stress of α + β processed Ti−6Al−4V considering the contributions from the intrinsic strength of the alloy, solid solution strengthening of the α and β phases, Hall−Petch effects from the equiaxed and lath α and the effect of the basket weave microstructure [97]. The results showed that solid solution strengthening accounts for nearly 80% of the yield stress followed by 10% from the intrinsic strength of the phases. This is somewhat surprising given that interphase interfaces, through their effects on the scale of the microstructure, are expected to contribute significantly to the yield stress. In this regard, α/β alloys with strength higher than that of Ti−6Al−4V generally contain Zr and Sn, which increase the solid solution hardening of α. Given that α and β are ductile, the only extrinsic resistance to deformation arises from grain boundaries, interphase interfaces and the

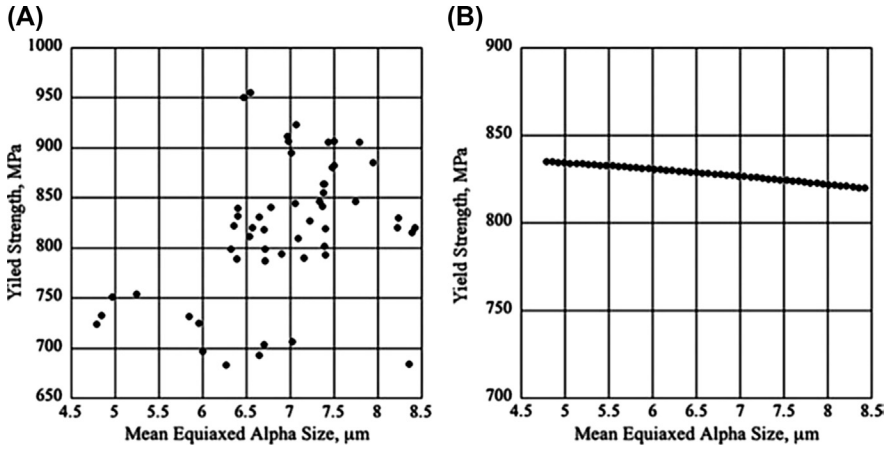


FIGURE 5.48

Variation of yield strength with size of equiaxed α. (A) Experimental data and (B) neural network model prediction at constant values of all other features [97].

morphological arrangements of the phases, which together are shown to have relatively small effects. However, these features will have more pronounced effects on the ductility, durability and damage tolerance. For near-β and metastable β alloys in which the fine, nondeformable and incoherent α particles act as obstacles to dislocation motion, the Orowan mechanism can be expected to contribute substantially to strength.

A linear addition rule was used in this study to estimate the superposition of the strengthening contributions from all the factors. It is likely that other rules exist based upon the relative strengths of various obstacles to plastic deformation. Further, analysis of the large amounts of data available on many alloys and processing conditions can refine the models and improve the predictive capability. These results are only the beginning, but are discussed here to illustrate promising methods to modeling strength.

The advantage of neural network modeling is the ability to vary a single microstructural feature and determine its effects while keeping all the others constant in virtual experiments. However, its application requires large experimental databases, that are often difficult and expensive to generate, to train the model. Crystal plasticity modeling, which does not need extensive databases, has been used to delineate the effects of microstructural features on the monotonic and cyclic behavior of Ti alloys. Deformation of Ti−6Al−4V with a bimodal microstructure was simulated by developing a microstructure-based constitutive model that included the effects of dislocation interactions (slip) with microstructural features and the use of finite element mesh for its calibration to fit with experimental measurements [99]. The agreement between the predicted and measured yield stress as a function of the volume fraction of primary α and the grain size was good, as shown in Fig. 5.49. The

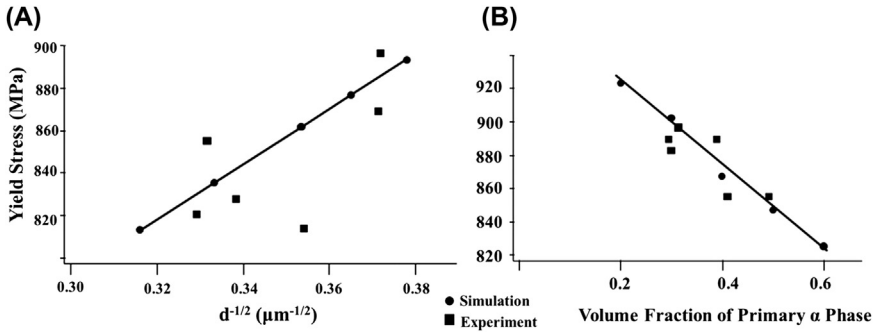


FIGURE 5.49

Yield stress for Ti−6Al−4V with a bimodal microstructure predicted from crystal plasticity modeling and compared with measured values [99].

observed deviations were attributed to the inability to hold all the other features except the one being assessed, constant in actual experiments. A similar study simulating the fatigue behavior of β annealed Ti−6Al−4V and β annealed, slow cooled and aged Ti-18 suggested that reduced colony size, reduced volume fraction of α and transverse textures improve resistance to crack nucleation and early growth of fatigue cracks, which is in accordance with experimental observations [100].

5.4.7.2 Modeling of Fracture Toughness

Efforts to model the fracture toughness of Ti alloys have been sparse. They have generally involved quantifying the relationships between experimentally measured fracture toughness values and those microstructural parameters that are known to affect the fracture process. These relationships are then validated against models for fracture toughness to identify those that provide the best predictive capability. The challenge with these approaches is the identification of the appropriate microstructural parameters and their quantitative measures for use in the models.

For Ti−6Al−4V and Ti−6Al−5Zr−4Mo−1Cu−0.2Si, which were solution heat treated below T_β, air cooled and water quenched, respectively, and aged, voids nucleated at the interface between the α platelets and β in the transformed β microstructure [101]. The K_{Ic} values increased linearly with the size of the α platelets, as expected. From a geometric modeling, based on fractographic observations, of the interactions of the crack tip and the α platelets, the appropriate microstructural parameter for use in the model was determined to be $\left(2\left(\lambda_\alpha + \lambda_\beta\right)\right)^{0.5}$ where λ_α and λ_β are the size of the α platelet and the width of the interplatelet β ribs, respectively. Although a few of the models provided reasonable agreements with the measured fracture toughness, they were not consistent for the entire range of values for both the alloys. For the near-β alloy, Ti−5Al−5Mo−5V−1Cr−1Fe, with a basket weave microstructure, the toughness was modeled to consist of an intrinsic value that is determined by the elastic and monotonic tensile properties of the alloy and an extrinsic value that was determined by the crack path tortuosity [102]. The latter was

expressed as a function of L(ε) and L_o, the actual length of the tortuous crack path and the straight path, respectively. Although the intrinsic values of toughness contributed most to the fracture toughness, the extrinsic values were more sensitive to the microstructures, as to be expected.

As discussed earlier for yield strength, Bayesian neural network modeling has been integrated with an experimental investigation to identify the relative effects of various microstructural features on the fracture toughness of Ti−6Al−4V [103]. The results showed that the size of the equiaxed α particles for certain range of microstructures followed by the colony boundaries were dominant in α + β processed alloys. The preponderance of microcracking in the interphase interface planes parallel to the basal planes of adjacent grains coupled with the observed β enrichment of basal twist boundaries in these planes was suggested to contribute to increasing fracture toughness at lower levels of Fe. Although these types of modeling are in the early stages, with the availability of additional data from critical experiments, they provide a potential to develop predictive modeling capability in the future.

5.4.7.3 Integrated Modeling

Efforts are underway currently to integrate the available predictive models for microstructure and texture evolution during various stages of processing with the property models so that they could be predicted at specific locations in a manufactured component [104]. Such an integrated model provides capabilities to design and process components with targeted properties in the framework of ICME, without having to incur significant cost and time for extensive experimental trials. Although the effort is focused on Ti−6Al−4V for use in engines, it provides a framework for modeling other Ti alloys and applications. The approach is shown schematically in Fig. 5.50.

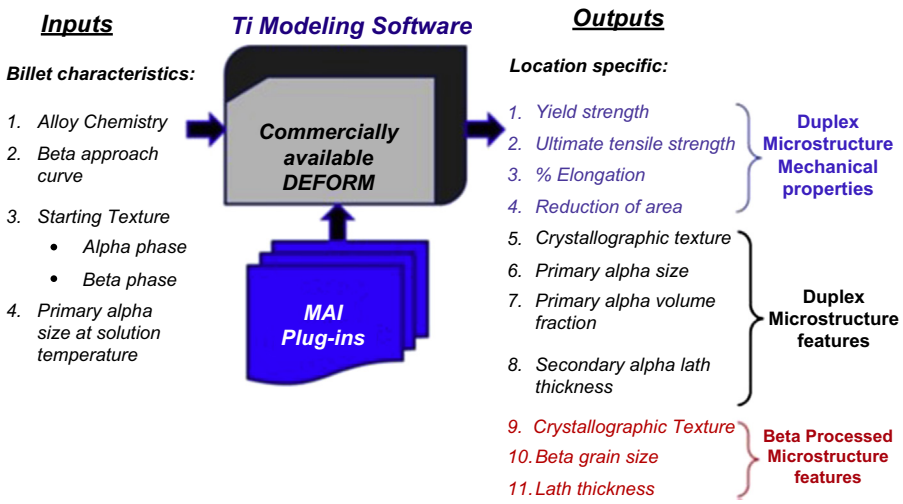


FIGURE 5.50

Overview of the integrated modeling program [104].

Characteristics of the starting billet are used as inputs into the commercially available DEFORM software, which predicts the microstructure (for e.g., size and volume fraction of α_p, size of secondary α laths and texture) and properties (tensile properties) as a function of location in the final product (similar to the prediction of residual stresses at various locations in Al alloy forgings described in the previous chapter). This information can subsequently be used for predicting other properties using appropriate models. Evolution of microtexture, which affects properties deleteriously, has also been modeled for Ti−6Al−4V and Ti−6Al−2Sn−4Zr−2Mo.

Modeling of Ti alloys has evolved from capabilities to predict characteristics such as T_β, texture and yield stress individually using thermodynamic, phenomenological and statistical models to the integrated capability discussed above. This allows optimization of processing, microstructure and properties in complex parts thus eliminating waste, reducing cost and rendering the use of light weight Ti alloys very attractive for all critical applications.

5.5 COMMERCIAL TITANIUM ALLOYS

The number of structural Ti alloys currently in service is quite small. Among these, Ti−6Al−4V accounts for the most usage followed by Ti−6Al−2Sn−4Zr−2Mo for higher temperature service and Ti−10V−2Fe−3Al and Ti−5Al−5Mo−5V−3Cr for higher strength applications. A few other alloys are used for applications such as fasteners or to satisfy unique performance requirements. The wide range of processing windows possible in α/β alloys enable a variety of microstructure−property combinations that satisfy the requirements for most structural applications to be achieved in the limited number of alloys. Accordingly, the number of new structural Ti alloys developed in recent years is very limited, and aimed principally at improving processability and reducing the cost incurred in their use. Most of the new Ti alloys presently under development are stable β alloys for biomedical applications.

Fig. 5.51 lists the wrought structural Ti alloys, whose compositions are listed in Table 5.2, developed for use in airframes and engines that are currently described in US suppliers' documents and other publications. It describes their evolution and attributes relative to Ti−6Al−4V or Ti−13V−11Cr−3Al. The latter, although only in limited use currently for secondary applications, was the first β Ti alloy used extensively in critical airframe structures. Many of the alloys listed in Fig. 5.51 are not used widely, if at all, but are included in the discussion to illustrate the metallurgy underlying their individual compositions, processing, microstructures and properties. Of course, they all follow the general relationships described in detail earlier for the various classes of alloys.

5.5.1 TI−6AL−4V AND TI−6AL−4V ELI

Ti−6Al−4V, being the most widely used structural Ti alloy, perhaps also has been the most thoroughly characterized. Much of the earlier discussion on the effects of

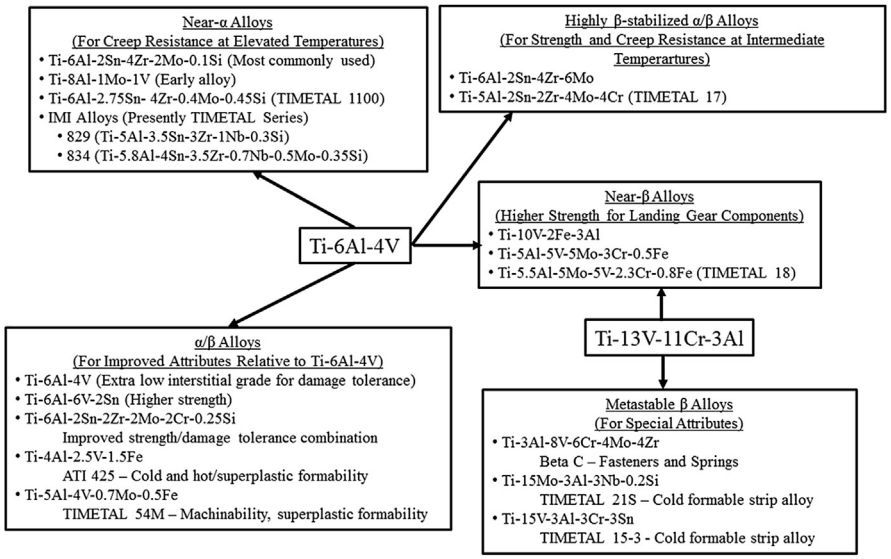


FIGURE 5.51

Evolution and attributes of current structural titanium alloys.

composition and processing on microstructure and properties used data for this alloy as examples. The integrated modeling in the ICME framework also uses Ti−6Al−4 V as the baseline alloy for its development and validation. For most applications, this alloy is used in the mill annealed condition, which provides a good combination of properties, although, as shown in Table 5.13, various heat treatments can be used to maximize selected properties [46]. The information in this table is illustrative of the processing−microstructure−properties relationships discussed earlier. Highest strength is achieved by solution heat treatment (SHT) slightly below T_β, water quenching to maximize the aging response, and aging. Due to the limited hardenability of the alloy, the strength of SHT and aged (STA) material decreases continuously as the section size increases above about 20 mm (0.8 in.). Coarser structures achieved by slower cooling in the various annealing treatments increase damage tolerance. Although beta annealed ELI material exhibits the maximum damage tolerance, a good balance of strength and ductility can be achieved by recrystallization annealing (Table 5.12). Many variations of these treatments are used to achieve desired property combinations.

5.5.2 α/β ALLOYS

Several alloys in the α/β class have been developed to achieve different attributes relative to Ti−6Al−4V such as reduced cost, ease of fabricability or improved properties.

Table 5.13 Heat Treatment Conditions and Effects on Properties for Ti–6Al–4V

Heat Treatment	Procedure	Comments
Stress relief annealing	2–4 h at 595°C/AC	Partial stress relief
Mill annealing	2 h at 735 ± 15°C/AC	Good combination of properties
Recrystallization annealing	4 h at 925°C, cool to 760°C at 55°C/h or slower, cool to 480°C at 370°C/h or faster, AC	Improve damage tolerance
Duplex annealing	10 m at 940°C/AC, 4 h at 675°C/AC	Improve damage tolerance
Beta annealing	10 m at 1035°C/AC, 2 h at 730°C/AC	Maximum damage tolerance with reduced fatigue strength and ductility
Beta STA	30 m at 1035°C/WQ, 4 h at 510–675°C	
Beta STOA	30 m at 1035°C/WQ, 2–4 h at 675–730°C	Improved fatigue strength at the expense of damage tolerance compared to beta annealing
STA	10 m at 940°C/WQ, 2–4 h at 510–540°C	Highest strength at lower ductility and fracture toughness compared with annealed condition
STOA	10 m at 940°C/WQ, 2–4 h at 675°C	Strength between annealed and STA conditions with better damage tolerance compared with STA

AC, *air cool;* WQ, *water quench.*

Data used with permission of ASM International. All rights reserved. www.asminternational.org.

5.5.2.1 TIMETAL 62S

This alloy was developed as a substitute for Ti–6Al–4V to possess equivalent processing characteristics and properties at reduced cost by substituting Fe for V. The amount of Al was retained at 6% and that of Fe and O were selected to provide the required strength without loss of postcreep ductility that occurs at higher levels of these elements [105]. Strength increases by 8.5 MPa (1.2 ksi) for every 0.01% of O and by 40 MPa (5.8 ksi) for every 1% of Fe. The amount of Si was also limited to reduce the cost of alloy formulation.

5.5.2.2 Ti–6Al–6V–2Sn

This alloy can be used in airframe structures requiring a higher strength material than Ti–6Al–4V. The higher β stabilization of this alloy compared with Ti–6Al–4V, promotes higher section hardenability and potential for higher strength. Heat treatability is improved by the presence of 6 wt% V and a total of about 1 wt% Cu and Fe enabling the alloy to develop very high strength in the aged condition compared

with Ti−6Al−4V, as shown in Table 5.14 [14,106]. The alloy can be used at temperatures up to 315°C (600°F). However, its application is limited to secondary structures due to its generally lower damage tolerance. In the STA condition, the typical K_{Ic} is 49 MPa $m^{0.5}$ (45 (ksi.in.$^{0.5}$)) at a yield strength of 1172 MPa (170 ksi), although it can be improved by β STA or duplex annealing at the expense of strength [107].

5.5.2.3 Ti−6Al−2Sn−2Zr−2Mo−2Cr−0.15Si (Ti-6-22-22)

This alloy was developed to provide better combinations of strength and damage tolerance than exhibited by Ti−6Al−4V with initial applications aimed at high performance military aircraft [108]. Its first use was in the F-22 fighter airframe, 42% of which is comprised of six different Ti alloys. Both cast and wrought (standard and ELI grades) Ti−6Al−4V make up most of the titanium usage. Although initially considered for replacement of all the wrought Ti−6Al−4V ELI, Ti-6-22-22 was finally selected for applications for which strength or durability was the principal design driver [109]. Compared with Ti−6Al−4V, the higher alloying content results in increased solid solution strengthening and the presence of Si promotes precipitation hardening by $(Ti,Zr)_5Si_3$. Although long-term aging in the temperature range of 450−550°C (840−1020°F) reduces toughness due to precipitation of α_2 and (Ti,Zr) Cr_2, it is retained on aging at 650°C (1200°F) due to the coarsening of the secondary α platelets [110].

With its superior strength and damage tolerance in section sizes up to 100 mm (4 in.) compared with Ti−6Al−4V, Ti-6-22-22 is a candidate for application in commercial airplane structures and engines. The alloy can be processed to impart various microstructure types, basket weave for high damage tolerance, equiaxed for high strength and ductility and bimodal for optimum strength−fatigue−creep property combinations for engines [111].

A triplex annealing treatment consisting of a β anneal followed by a $\alpha + \beta$ anneal and aging produces a coarse lamellar α structure for damage tolerance and aged transformed β matrix for strength. In the heat treated condition for sheet, the minimum tensile properties of Ti-6-22-22 are 1241 MPa (180 ksi) (tensile strength), 1103 MPa (160 ksi) (yield strength) and 5% (elongation) compared with 1103 MPa (160 ksi), 1000 MPa (145 ksi) and 5%, respectively, for Ti−6Al−4V. Depending on the product thickness, the toughness of β processed Ti-6-22-22 in the STA condition can reach values close to about 100 MPa $m^{0.5}$ [14].

5.5.2.4 α/β Alloys for Improved Formability

In addition to its broad applicability, one of the beneficial aspects of Ti−6Al−4V is its superplastic formability. Being closer to near-α compositions, this alloy possesses low hardenability and is difficult to form. Alloy development to improve these characteristics have resulted in SP-700, TIMETAL 54M and ATI 425 developed by RTI (presently Arconic), Timet and ATI, respectively. These alloys generally have higher β stabilization than Ti−6Al−4V and lower T_β to reduce flow stresses and to develop the required strength by heat treatment. Addition of Fe with high diffusion rates improves formability and alloying elements are chosen to refine the microstructures.

Table 5.14 Guaranteed Minimum Properties for Solution Treated and Aged Ti Alloys

Alloy	Thickness—t, mm (in.)		Yield Strength, MPa (ksi)	Tensile Strength, MPa (ksi)	Elongation (%)		Reduction of Area (%)	
	As Rolled or Forged	As Heat Treated[a]			L	T	L	T
Ti–6Al–4V	≤25.4 (≤1)	12.7 < t ≤ 25.4 (0.5 < t ≤ 1)	1034 (150)	1103 (160)	10	8	25	20
	76.2 < t ≤ 101.6 (3 < t ≤ 4)	50.8 < t ≤ 101.6 (2 < t ≤ 4)	827 (120)	896 (130)	6	4	15	10
Ti–6Al–6V–2Sn	≤25.4 (≤1)		1172 (170)	1241 (180)	8	6	20	15
	76.2 < t ≤ 101.6 (3 < t ≤ 4)		965 (140)	1034 (150)	8	6	20	15

AC, *air cool;* L, *longitudinal;* T, *transverse;* WQ, *water quench.*

[a] *Ti–6Al–4V: 857–913°C (1575–1675°F), 1 h, WQ and 482–593°C (900–1100°F), 4–8 h, AC. Ti–6Al–6V–2Sn: 857–913°C (1575–1675°F), 1 h, WQ and 482–593°C (900–1100°F), 4–8 h, AC.*

SP-700 is the oldest of these alloys, which was developed specifically for superplastic forming at temperatures lower than used for Ti−6Al−4V [112]. Lower temperatures improve life of the dies used for forming and generally reduce production costs. SP-700 can be superplastically formed at 760°C (1400°F), compared with Ti−6Al−4V, which requires temperatures between 900 and 920°C (1650 and 1680°F) [107]. Due to better hardenability, the properties of SP-700 are also less sensitive to quench rates and quench delays in thick sections. This alloy replaced Ti−6Al−4V for the door threshold corners of Boeing 757. The production of SP-700 ended in 2003. Ti−6Al−4V with ∼1 μm grain size, with characteristics similar to SP-700 and capable of superplastic forming and diffusion bonding at 775°C (1425°F) is presently available.

TIMETAL 54M possesses better machinability, particularly at high machining speeds [113] and superplastic formability [114] than Ti−6Al−4V. ATI 425 contains lower Al and V than Ti−6Al−4V, addition of Fe and higher, controlled amounts of O for good combinations of ductility and strength. It is melted using single plasma melt technology, which eliminates inclusions and provides better chemistry control [115]. ATI 425 possesses good cold and hot formability.

5.5.2.5 α/β Alloys for Intermediate Temperature Applications

α/β alloys with higher levels of β stabilizers and $[Mo]_{eq}$ in the range of 5%−10% possess improved formability and forgeability due to the more active number of slip systems in the BCC β phase [13]. These β-rich α/β alloys possess lower T_β, better hardenability, a good heat treatment response and higher strength in the room to intermediate temperature range compared with Ti−6Al−4V. Two such alloys processed as forgings and used in engine components are Ti−6Al−2Sn−4Zr−6Mo and Ti−5Al−2Zr−2Sn−4Mo−4Cr (Ti-17).

Ti−6Al−2Sn−4Zr−6Mo combines the long-term properties of the near-α alloy, Ti−6Al−2Sn−4Zr−2Mo−0.08Si up to intermediate temperatures with the short-term strength of fully hardened α/β alloys [88]. As with other α/β alloys discussed earlier, it can be heat treated and annealed to produce various microstructures and combinations of properties, as listed for example in Table 5.12. Optimum values of strength, ductility and toughness are achieved in alloys processed to contain about 10% by volume of α_p in a coarse, transformed β matrix.

Ti-17 is used in the engine mount fitting for the GE90 engine on the Boeing 777. This alloy is used for forgings up to 150 mm (6 in.) thick requiring combinations of high strength, toughness and creep properties [116]. As expected, toughness of STA alloy increases with increasing SHT temperature due to higher amounts of the transformed β microstructure, particularly in the range from 850 to 875°C (1562−1607°F), whereas the yield strength remains within a narrow range, as shown in Fig. 5.52. For a given yield strength level, the β processed alloy possesses higher fracture toughness than α/β processed alloy, as shown in Table 5.15.

5.5.3 NEAR-α ALLOYS

These alloys are used for applications principally in engine components and to a limited extent in airframe structures in areas experiencing temperatures beyond

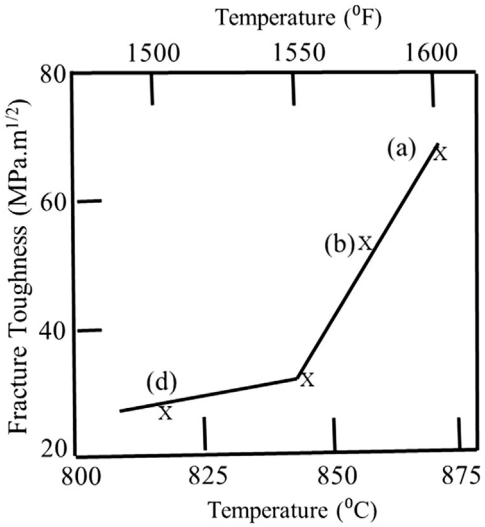


FIGURE 5.52

Strength and fracture toughness of Ti-17.

Adapted and reprinted with permission of ASM International. All rights reserved. www.asminternational.org.

the capability of Ti−6Al−4V and the β-rich α/β alloys. Most of these applications use Ti−6Al−2Sn−4Zr−2Mo−0.08Si up to its service limit of about 540°C (1000°F). This alloy was developed in the 1960s. For higher temperatures, TIMETAL 834 or Ti-1100 can be used up to 600°C (1100°F), the practical upper limit

Table 5.15 Fracture Toughness of Alloy Ti-17 as a Function of Strength Level for Two Processing Conditions [116]

Condition	Yield Strength, MPa (ksi)	K_{Ic} (MPa.m$^{0.5}$)
α/β processed	1172 (170)	33
	1103 (160)	40
	1034 (150)	50
β processed	1172 (170)	48
	1103 (160)	59
	1034 (150)	80

Data used with permission of ASM International. All rights reserved. www.asminternational.org.

for using Ti alloys. Although many of the other near-α alloys have been superseded, it is instructive to review their evolution and the metallurgy underlying their design.

- The earliest of these alloys were Ti−11Sn−5Zr−2.25Al−1Mo−0.2Si (IMI and now TIMETAL 679) developed in the United Kingdom and Ti−8Al−1V−1Mo in the United States, both limited for use up to about 450°C (840°F). They contain higher amounts of solid solution hardening elements for which Sn is more effective than Al as the temperature increases. Higher amounts of Sn could be tolerated without formation of α_2 as in IMI 679, which was not the case with Ti−8Al−1V−1Mo [5]. Both alloys also had small amounts of β stabilizers for amenability to heat treatments. These alloys have been superseded by Ti−6Al−2Sn−4Zr−2Mo−0.08Si with its better combination of properties and capability to operate at higher temperatures.
- IMI 685 with a composition of Ti−6Al−5Zr−0.5Mo−0.25Si and use temperature limit of about 520°C (970°F) was developed subsequently in the United Kingdom. It was designed for forgings and heat treatment in the β field, which enabled increasing the amount of Si. Sn was replaced by higher amounts of Al and the creep resistance was increased by reducing Mo. IMI 829 (Ti−5.5Al−3.5Sn−3Zr−0.3Mo−1Nb−0.3Si) with a useful limit of about 550°C (1020°F) was developed next. Addition of Nb improved resistance to oxidation.
- IMI 829 was followed by IMI 834 (Ti−5.5Al−4Sn−4Zr−0.3Mo−1Nb−0.35Si−0.06C), which can be used up to 600°C (1100°F) by adjustments in the composition. The key difference is the use of C as an alloying element to modify the β approach curve to a shallower slope so that controlled processing very near T_β is practical (see Fig. 5.11). To achieve optimum combinations of properties, the amount of α_p needs to be maintained to within about 10%, for which such precision in processing is necessary.
- Ti-1100 (Ti−6Al−2.75Sn−4Zr−0.4Mo−0.45Si), a derivative of Ti−6Al−2Sn−4Zr−2Mo−0.08Si, was developed in the United States for use up to 600°C (1100°F), hence the name Ti-1100 [117]. In this alloy, Si and Sn are added to the maximum extent possible without deleteriously affecting postcreep ductility, Fe is controlled to a low level and the amount of Zr is increased to obtain a more uniform distribution of the silicides [118]. Although IMI 834 is designed for processing in the α + β field, Ti-1100 is β processed for maximizing creep resistance and damage tolerance.

Up to its maximum use temperature, Ti−6Al−2Sn−4Zr−2Mo−0.08Si is still the most widely used alloy for high temperature applications. It can be processed and heat treated to produce different types of microstructure for tailoring property combinations like representative α/β alloys, as shown in Table 5.16 [119].

Alloys forged in the β field generally exhibit higher toughness and additionally higher strength if followed by heat treatment in the α + β field. Alloys forged in the α + β field exhibit lower toughness if followed by heat treatment in the α + β field. The toughness of the alloys forged in the α + β field followed by heat treatment in the β field decreases with increasing strength. These observations are consistent with

Table 5.16 Mechanical Properties of Ti–6Al–2Sn–4Zr–2Mo–0.08Si Forgings

Forging/Heat Treating Condition	Creep[a] h to 0.2% Strain	K_{Ic} (MPa.m$^{0.5}$)	Room Temperature		480°C (900°F)		Postcreep	
			YS MPa (ksi)	e (%)	YS MPa (ksi)	e (%)	YS MPa (ksi)	e (%)
$(\alpha + \beta)/\beta$	199	81	903 (131)	13	537 (78)	13	889 (129)	10
$(\alpha + \beta)/\beta$	169	71[b]	924 (134)	10	565 (82)	11	–	–
$(\alpha + \beta)/(\alpha + \beta)$	56	49[b]	951 (138)	14	593 (86)	15	–	–
$(\alpha + \beta)/\beta$	19	38[b]	1068 (155)	3	855 (124)	5	–	–
$(\alpha + \beta)/(\alpha + \beta)$	164	55[b]	896 (130)	14	565 (82)	17	–	–
$\beta/(\alpha + \beta)$	185	77[b]	930 (135)	11	579 (84)	17	–	–
$\beta/(\alpha + \beta)$	160	82[b]	937 (136)	10	–	–	–	–
$\beta/(\alpha + \beta)$	116	83	896 (130)	11	565 (82)	15	924 (134)	12
β/β	134	79	841 (122)	7	551 (880)	12	882 (128)	12

[a] *Creep at 565°C (1050°F) and 172 MPa (25 ksi).*
[b] *Estimated values.*
Data used with permission of ASM International. All rights reserved. www.asminternational.org.

the processing–microstructure–properties relationships discussed earlier. To enhance the creep resistance, the near-α alloys are aged below the α_2 solvus for its precipitation during aging.

The high melting point of titanium and the relative shallowness of the β approach curve, up to about 800°C (~1475°F) for the near-α alloys, would ensure stable volume fractions of the phases during service. However, the affinity of Ti for O, and its diffusion and stabilization of the α phase limits the usefulness of these alloys to lower temperatures due to the formation of an "α case" on the surface. In Ti–6Al–2Sn–4Zr–2Mo–0.08Si, the depth of this case increases rapidly above 600°C (~1100°F), reaching about 80 μm at 650°C (~1200°F) from less than 20 μm at 538°C (1000°F) following exposure for 500 h [120]. This α case that forms by the diffusion of O in α and β and in their interfaces during exposure representative of long-term service at these temperatures has been termed "oxygen-rich layer" (ORL) to distinguish it from the, brittle α cases that forms on the surface during casting and high temperature processing close to T_β, where the volume fraction of the β phase is high [121]. ORL is not distinct from the microstructure in the sense that it does not produce a metallurgical discontinuity as seen with the α case. The effect of microstructure on the extent of formation of ORL and the resulting increase in hardness and weight has been characterized experimentally for Ti–6Al–2Sn–4Zr–2Mo–0.08Si following exposure for 420 h at 650°C (1200°F), as shown in Fig. 5.53.

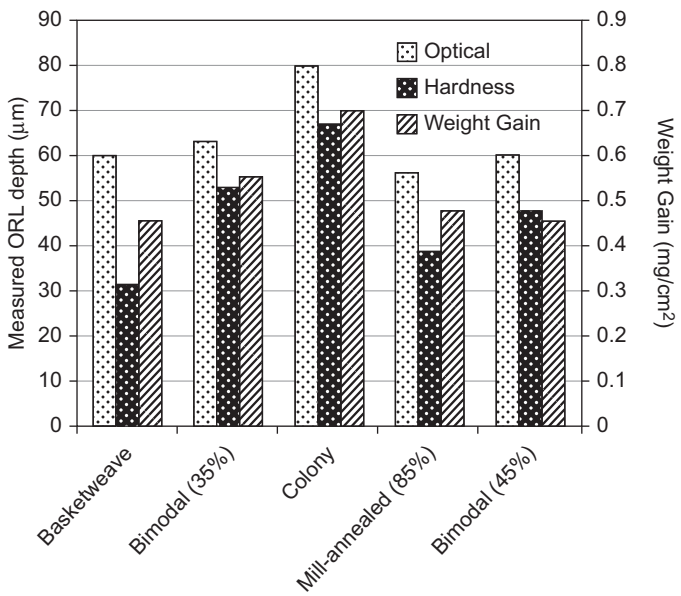


FIGURE 5.53

Effects of microstructure type on characteristics of ORL for Ti–6Al–2Sn–4Zr–2Mo–0.08Si exposed at 650°C (1200°F) for 420 h. The volume fraction of primary α is indicated for the bimodal and mill annealed microstructures [121].

The data were used to calculate the effective diffusion coefficients from which the thickness evolution of the ORL can be predicted. From a modeling of the critical strain for fatigue crack initiation, such data can be used along with crack growth rate information to predict the service lives for various microstructures. This approach is analogous to the deterministic models that predict the fatigue lives of alloys from quantitative corrosion measures in PH Al alloys as discussed in the previous chapter (Fig. 4.40).

5.5.4 NEAR-β AND METASTABLE β ALLOYS

The difference between near-β and metastable β alloys is that the former do not contain sufficient β stabilizers to retain an all β microstructure upon air cooling of thin sections from the single-phase field [122]. The near-β alloys are also solution heat treated below T_β and, therefore, have α_p in their microstructure. Both alloys are fabricated in the SHT condition following which they are aged to precipitate the α phase. The aging parameters, and the amount of α_p in the case of near-β alloys, can be varied to give a range of property combinations. Ti−13V−11Cr−3Al, the first Ti alloy in which β was retained in metastable condition at room temperature, has been replaced by other alloys in recent years. Although many new alloys were developed, only the five alloys not including Ti−13V−11Cr−3Al and TIMETAL 18, shown in Table 5.2, are in production and in commercial use presently [13]. TIMETAL 18 is a more recently developed near-β alloy [123].

5.5.4.1 Near-β Alloys

The combinations of strength and toughness achievable in near-β alloys have resulted in their use to replace ultrahigh strength steel alloys in selected airframe applications. The two alloys, Ti−10V−2Fe−3Al and Ti−5Al−5Mo−5V−3Cr, are both fabricated as forgings.

Following the insertion of Ti−10V−2Fe−3Al in the Boeing 777, which saved 270 kg (595 lbs) per airplane [13], the alloy has been used in Airbus airplanes and in military fighters and transport aircraft. The nominal addition of 2 wt% Fe provides hardenability, whereas 3 wt% Al is sufficient for strengthening by the precipitation of α. The level of O is controlled to provide the required toughness. Ti−10V−2Fe−3 Al requires water quenching to retain sufficient metastable β thereby limiting its useful product thickness to about 75 mm (3 in.). A wide range of strength can be achieved in this alloy by varying the amount of α_p (affected by SHT temperature) and the size of secondary α precipitates (affected by aging conditions), as shown in Table 5.10. Both ductility and toughness are affected by the α_p morphology, which is determined by the TMP parameters. For a given strength level, higher ductility is achieved by increasing amounts of globular α, but at the expense of toughness. In terms of the effects of processing, toughness increases with increasing aspect ratio of the elongated α_p, as shown in Table 5.17 for two different strength levels [83]. The reduction of fracture toughness at higher volume fractions of α_p at constant strength and for constant aging conditions is shown in Table 5.18 [90]. A typical microstructure of Ti−10V−2Fe−3Al for optimum properties is shown in Fig. 5.32.

Table 5.17 Mechanical Properties of Ti−10V−2Fe−3Al Forgings for Various α_p Aspect Ratios

α_p Aspect Ratio	Yield Strength, MPa (ksi)	Tensile Strength, MPa (ksi)	Elongation (%)	Reduction of Area (%)	K_{Ic} (MPa.m$^{0.5}$)
High	1149 (167)	1288 (187)	3	3.3	46.8
Low	1190 (173)	1278 (185)	7	12.8	37.0
High	1002 (145)	1067 (155)	9	24.3	86.1
Low	990(144)	1009 (146)	15	50.7	67.0

Alloy forged above T_β for thickness reduction of 50%−70% followed by $\alpha + \beta$ forging and heat treatment.
Data used with permission of ASM International. All rights reserved. www.asminternational.org.

Table 5.18 Variation of Mechanical Properties of Ti−10V−2Fe−3Al−0.3Fe Forgings with α_p Volume Fraction

α_p Volume %	Yield Strength, MPa (ksi)	K_{Ic} (MPa.m$^{0.5}$)
Constant Yield Stress		
10	1091 (158)	63
30	1096 (159)	39.1
Constant Aging Treatment (400°C for 20 h)		
10	1402 (203)	18.5
30	1096 (159)	39.1

Ti−5Al−5Mo−5V−3Cr−0.3Fe, used in the Boeing 787, is a derivative of the Russian alloy VT22 (nominal composition of Ti−5Al−5Mo−5V−1Cr−1Fe) with higher Cr. Fe is limited to 0.5% to reduce segregation during melting, thereby eliminating the need for homogenization [13]. Air cooling from SHT temperature is sufficient to develop higher strength after aging than can be achieved in VT22 and Ti−10V−2Fe−3Al. Due to its shallower β approach curve, shown in Fig. 5.11 [26] Ti−5Al−5Mo−5V−3Cr−0.3Fe has a wider processing window and is less sensitive to processing variations. As with Ti−10V−2Fe−3Al, properties can be varied by TMP and heat treatments. Following SHT and quenching, the alloy can be aged using the standard treatment (STA) of SHT at a temperature 20−60°C (36−108°F) below T_β for 1 h, air cooling and aging for a minimum of 8 h at 550−650°C (1020−1200°F) to produce a microstructure with 10%−20% globular α_p in a decomposed β matrix consisting of very fine α precipitates. Higher levels of ductility can be achieved by a modified heat treatment consisting of SHT at a temperature 20−60°C (36−108°F) below T_β, furnace cooling and holding at 720−790°C (1325−1450°F) for 1−3 h and aging. A beta annealed, slow cooled, and aged (BASCA) treatment consisting of SHT at a temperature 20−60°C (36−108°F) above T_β, cooling at a controlled rate to

Table 5.19 Minimum Mechanical Properties of Ti–5Al–5Mo–5V–3Cr for Section Sizes up to 150 mm (6 in.)

Heat Treatment	Yield Strength, MPa (ksi)	Tensile Strength, (MPa)	Elongation (%)	Reduction of Area (%)	K_{Ic} ($MPa.m^{0.5}$)
SHT	800 (116)	880 (128)	15	50	–
Standard	1170 (170)	1240 (180)	4	10	33
BASCA	965 (140)	1080 (157)	6	–	65

650–800°C (1200–1470°F), holding for a minimum of 4 h and then aging increases the volume fraction of lamellar α (Fig. 5.54) [13] and provides optimum combination of strength and toughness. Table 5.19 lists the properties of this alloy for the different aging conditions. Although the formation of ω during quenching from above T_β and the mechanisms of subsequent precipitation of α has been investigated [124], the aging of Ti–5Al–5Mo–5V–3Cr–0.3Fe occurs above the ω solvus and is not present in the aged alloy. A European variant of this alloy has the composition of Ti–5Al–5Mo–5V–3Cr–1Zr.

TIMETAL 18 is a recently developed near-β Ti alloy in which the composition relative to Ti–5Al–5Mo–5V–3Cr–0.3Fe has been adjusted by increasing the amounts of Al and O to raise the $[Al]_{eq}$ and maximize strengthening. The amounts of β stabilizers have been adjusted to achieve a nominal $[Mo]_{eq}$ of 14.2 and a β isomorphous to β stabilizers ratio of 1.4 [125]. This alloy exhibits about 55–83 MPa (8–12 ksi) higher strength level than Ti–5Al–5Mo–5V–3Cr–0.3Fe at comparable levels of ductility [123].

5.5.4.2 Metastable β Alloys

Among the three metastable β alloys in commercial production (Table 5.2), Beta C with the highest $[Mo]_{eq}$ was developed as an alternative to Ti–13V–11Cr–3Al by reducing the Cr level to improve meltability and reduce segregation and by adjusting the amounts of other β stabilizers [126–128]. Beta C is used for aircraft fasteners and spring applications providing significant weight savings over competing, representative steel alloys such as 17-4 PH stainless steel. It is also used in many other applications including the water catapult brake in Navy aircraft carriers. Beta C can be hardened in sections up to 150 mm (6 in.) thick. SHT of this alloy is performed above T_β and it can be used in this condition or aged to increase strength. Due to the complex chemistry of the alloy, α, β′, ω, $TiCr_2$, and $(Ti,Zr)_5Si_3$ can precipitate depending on the aging temperature [13]. In practice, aging is performed at a high enough temperature to prevent formation of ω and for a short enough time to prevent $TiCr_2$. Strength as high as about 1450 MPa (210 ksi) can be achieved in relatively smaller section sizes and a minimum tensile strength of about 1240 MPa (180 ksi) in 150 mm (6 in.) sections. The toughness can vary between about 50 and 90 MPa $m^{0.5}$.

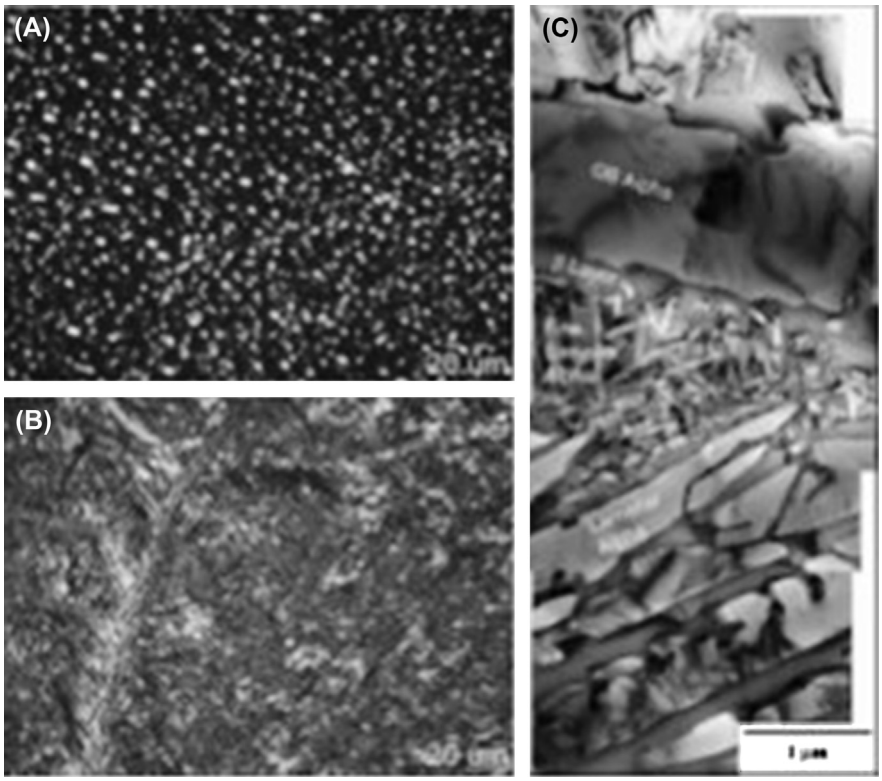


FIGURE 5.54

Microstructure of Ti–5Al–5Mo–5V–3Cr. (A) Standard treatment showing globular α in a decomposed β matrix, (B) beta annealed, slow cooled, and aged (BASCA) treatment showing coarse α platelets, and (C) TEM image of BASCA treated alloy showing coarse and fine lamellar α [13].

TIMETAL 15-3 (Ti–15V–3Cr–3Al–3Sn) and TIMETAL 21S (Ti–15Mo–3 Al–2.7Nb–0.25Si), developed for strip products, are cold formable, age hardened metastable β alloys that have found use in aircraft applications [129]. TIMETAL 15-3 was used on the B-1B bomber nacelle structure and its use as a welded product in the environmental control system of the Boeing 777 replacing CP Ti, saved 63.5 kg (140 lbs) per airplane [13]. The effect of prior cold work on strength of TIMETAL 15-3 after aging is shown in Fig. 5.40. TIMETAL 21S was designed for the ability to cold roll into strip and foil product and for improved oxidation resistance, which ruled out addition of V. The alloy is based on the Ti–Mo system with additions of Al, Nb, Si, and controlled amounts of O. It is used in engine exhaust components replacing Inconel 625 eliminated about 164 kg (362 lbs) on the Boeing 777 [13].

5.6 NEW ALLOY DESIGN

The opportunity space for the development of new Ti alloys is rather limited, as the available alloys in production exhibit adequate property combinations for most applications. This is also consistent with the very few number of alloys that have been commercialized since the publication of the comprehensive information on the metallurgy and properties of all alloys developed in the United States and United Kingdom as of 1994 [17]. As described earlier, of the three such alloys in production, ATI 425 and TIMETAL 54M were developed with attributes to reduce the cost of fabricating components and Ti−5Al−5Mo−5V−3Cr for wider processing window relative to that of the incumbent alloy Ti−10V−2Fe−3Al.

Most of the recent research and development efforts on structural Ti alloys have focused on reducing the cost associated with their primary production, component fabrication and the associated aspects of insertion, which include secondary fabrication, alloy characterization, and property development. Cost reduction using castings or superplastically formed components has been ongoing for many years. The F-22 fighter airplane used many cast Ti−6Al−4V parts [109] and the F-15E used superplastically formed Ti−6Al−4V [43]. Development efforts in powder metallurgy for near net shape consolidation of parts have been ongoing since the 1980s. Recent activities have focused on direct reduction of Ti ore to produce sponge and on various powder metallurgy [51−53] and additive manufacturing [130,131] methods to reduce the cost of raw material, component fabrication, and insertion.

Most of the cost reduction efforts have used Ti−6Al−4V and in a few cases other existing wrought alloy chemistries, as the base to develop and validate the processes. New alloy development with nontraditional compositions has attempted to utilize the beneficial effects of rapid solidification processing to produce a variety of alloys including dispersion strengthened Ti alloys containing rare earth metal (RE) additions and ternary Ti−Al−RE alloys for additional precipitation strengthening [132]. However, these alloys were not scaled up and commercialized due to issues associated with debits in toughness and fatigue properties.

Utilizing traditional empirical approaches, new, wrought and cast Ti alloys in the traditional composition space continue to be developed and reported. One such alloy, TIMETAL 575 with a nominal composition of Ti−5.3Al−7.7V−0.25Fe−0.5Si−0.01C−0.18O−0.01N and an Al/V ratio between 0.65 and 0.8, exhibits higher specific strength than Ti−6Al−4V, maintains ductility and hardenability in thick sections and attains a strength increment of about 100 MPa (∼15 ksi) due to the Si additions [133]. It can also use Ti−6Al−4V chips as raw material. The materials by design approach has been applied to design and develop castable Ti alloys with refined and interlocking α/β microstructure that provide static properties equivalent to wrought Ti−6Al−4V [134,135]. Compared to Ti−6Al−4V, these cast alloys contain less V and have higher tolerance for O and Fe. They can also use significant amounts of Ti−6Al−4V scrap as input stock. Also, compared to Ti−6Al−4V cast equivalently, one of the alloys has been shown to offer about 170 MPa (∼25 ksi) higher tensile strength and 2.5% greater elongation. The goal is to provide improved

performance and/or reduce costs relative to current alloys. A patent application by QuesTek describes alloys with compositions in the range of 3%−6% Al, 0%−1.5% Sn, 2%−4%V, 0.5%−4.5%Mo, 1%−2.5% Cr, 0.2%−0.55% Fe, 0%−0.35%O, 0%−0.007%B, and 0%−0.60% other elements and impurities. It also provides "processing−microstructure−properties" charts and the computational models used for determining the phase relationships and properties [136].

Understanding and optimizing of microstructures have played a major role in Ti alloy and process development since its early stages and have underpinned all the advances, as illustrated in Fig. 5.26 [54]. In addition, it has also enabled improvements in many areas of manufacturing such as in formability as discussed in detail earlier. Another example in this regard is the development of microstructures to improve the machinability of Ti alloys, which contributes a substantial part to the cost of component fabrication [137]. In terms of microstructure, globular and fine lamellar α are reported to improve machinability while transformed β structures degrade it. A microstructure containing 10%−15% globular α_p and maximum volume fraction of secondary α in Ti−5Al−5Mo−5V−3Cr−0.3Fe was obtained by solution heat treatment at 815°C (1500°F) followed by extended annealing (aging) at about 650°C (1200°F) for 24 h. This microstructure minimized strength and maximized modulus and thermal conductivity thereby improving machinability as measured by a 50%−300% increase in tool life.

Although the pace of new alloy development has been limited, significant activity is ongoing for the engineering of new microstructures or those that will facilitate lower cost processing and improve properties, all of which provide directions for new alloy development. Although many of these involve processes such as severe plastic deformation, a few are amenable to development via casting and wrought alloy processing. One such promising example is the use of small additions of B up to about 0.1 wt% to alloys like Ti−6Al−4V, which significantly refines the grain size in the casting thereby facilitating easy ingot breakdown in commercial production. The order of magnitude reduction in the β grain size, from about 2000 to 200 μm in Ti−6Al−4V, and α lath size increases strength although reducing fracture toughness, as expected, although it was still maintained at an adequate level [138,139]. Additions of higher levels of B providing the possibility of developing higher modulus alloys via powder metallurgy processing routes have also been investigated.

The engineering of microstructures like basket weave or bimodal into Ti alloys to achieve desired property combinations has been aided largely by the accumulating knowledge of the effects of composition and processing. Understanding and modeling of the thermodynamics and kinetics of phase transformations that determine the pathways to these microstructures and their applications for alloy design have only begun recently, as for example in the development of castable Ti alloys discussed earlier. Using the graphical thermodynamics method, a recent study has determined the various kinetic pathways for the transformation of β to the α and β phases as a function of composition, rationalizing the experimentally observed microstructures [140]. These pathways include competing spinodal and nucleation/growth

processes, and continuous and discontinuous displacive transformations. An integrated CALPHAD-phase field modeling approach has identified pseudospinodal and precursory spinodal pathways to producing highly refined $\alpha + \beta$ microstructures in binary Ti−Mo alloys, which show promise for application to develop engineering alloys with enhanced properties [141].

5.7 SUMMARY

In summarizing the topics discussed in this chapter, it should become clear that despite the differences in the metallurgy of titanium and aluminum alloys, the underlying complexity and prognosis for new alloy development is somewhat similar for both. The important difference for Ti alloys is the much higher emphasis on cost reduction that drives any new alloy design. In this respect, it will not be surprising if new compositions within the traditional space possessing unique properties are identified, in the manner of the invention of aluminum alloy 7085, described in the previous chapter. The importance of titanium alloys for demanding applications both for commercial and military applications and the need to reduce cost have resulted in significant resources being expended for research in areas ranging from low cost extraction processes for titanium through alloy design, primary processing, component manufacturing, and qualification for service insertion. A large portion of this effort is devoted to the development of integrated computational models in the framework of ICME, utilizing the already developed and maturing models at discrete length scales. With the ability to rapidly characterize microstructures and provide mechanistic understanding of alloy behavior, these efforts bode well for the design and use of affordable, high performance Ti alloys for the future.

REFERENCES

[1] R.R. Boyer, R.D. Briggs, The use of β titanium alloys in the aerospace industry, Journal of Materials Engineering and Performance 14 (6) (2005) 681−685.
[2] R.B. Deo, J.H. Starnes, Jr., R.C. Holzwarth, Low cost composite materials and structures for aircraft applications, Paper Presented at NATO Research and Technology Organization Applied Vehicle Technology, Specialists' Meeting, Loen, Norway, May 7−11, 2001, Published in RTO-MP-069 (II). Available from NASA.
[3] V. Venkatesh, R. Boyer, Conference highlights: advancements in titanium technology, Advanced Materials and Processes 174 (5) (2016) 37−39.
[4] Boeing 787 − from the ground up, Aero Quarterly, A Publication of the Boeing Company, Quarter 4 (2006) 17−23.
[5] I. Polmear, D. St. John, Titanium alloys, in: Light Alloys: From Traditional Alloys to Nanocrystals, Elsevier, 2006, pp. 299−365.
[6] E.W. Collings, Introduction to titanium alloy design, in: J.L. Walter, M.R. Jackson, C.T. Sims (Eds.), Alloying, ASM International, 1988, pp. 257−370.

[7] E.W. Collings, Physical metallurgy of titanium alloys, Section 2. Classification of titanium alloys, in: G. Welsch, R. Boyer, E.W. Collings (Eds.), Materials Properties Handbook: Titanium Alloys, ASM International, 1994, pp. 5−11.
[8] M. Peters, J. Hemptenmacher, J. Kumpfert, C. Leyens, Structure and properties of titanium and titanium alloys, in: C. Leyens, M. Peters (Eds.), Titanium and Titanium Alloys, Wiley, 2003, pp. 1−36.
[9] G.J. Lutjering, J.C. Williams, Fundamental aspects, in: Titanium, Springer, 2007, pp. 15−52.
[10] F.H. Froes, Principles of alloying titanium, in: Titanium − Physical Metallurgy, Processing and Applications, ASM International, 2015, pp. 51−74.
[11] F.H. Froes, Principles of beta transformation and heat treatment of titanium alloys, in: Titanium − Physical Metallurgy, Processing and Applications, ASM International, 2015, pp. 75−94.
[12] H.W. Rosenberg, Titanium alloying in theory and practice, in: R.I. Jaffee, N.E. Promisel (Eds.), The Science, Technology and Application of Titanium, Pergamon Press, 1968, pp. 851−859.
[13] J.D. Cotton, R.D. Briggs, R.R. Boyer, S. Tamirisakandala, P. Russo, N. Shchentikov, J.C. Fanning, State of the art in beta titanium alloys for airframe applications, JOM 67 (6) (2015) 1281−1303.
[14] Titanium Alloy Guide, RMI Titanium Company technical data document.
[15] S. Abkowitz, The emergence of the titanium industry and the development of the Ti-6Al-4V alloy, JOM Monograph, The Minerals, Metals and Materials Society, PA (1999).
[16] C.R. Simcoe, Titanium: a metal for the aerospace age, Advanced Materials and Processes 173 (2015). Part I (March) 30−31; Part II (April) 34−; Part III (May) 28− and response by S. Abkowitz, (September) 46−.
[17] Titanium data sheets, in: G. Welsch, R. Boyer, E.W. Collings (Eds.), Materials Properties Handbook: Titanium Alloys, ASM International, 1994, pp. 125−1007.
[18] G.J. Lutjering, J.C. Williams, High temperature alloys, in: Titanium, Springer, 2007, pp. 259−282.
[19] M. Donachie, Heat treating titanium and its alloys, in: Heat Treating Progress, ASM, June/July 2001, p. 47.
[20] E.W. Collings, H.L. Gegel, A physical basis for solid-solution strengthening and phase stability in alloys of titanium, Scripta Metallurgica 7 (1973) 437−444.
[21] E.W. Collings, H.L. Gegel, J.C. Ho, Solid Solution Strengthening and Fundamental Strengthening of Titanium Alloys, Technical report AFML-TR-72-1, Air Force Materials Laboratory, Wright Patterson Air Force Base, OH, September 1972.
[22] T.K.G. Namboodhiri, On the Ti-Al phase diagram, Materials Science and Engineering 57 (1983) 21−22.
[23] A.A. Radecka, P.A.J. Bagot, T.L. Martin, J. Coakley, V.A. Vorontsov, M.P. Moody, H. Ishii, D. Rugg, D. Dye, The formation of ordered clusters in Ti-7Al and Ti-6Al-4V, Acta Materialia 112 (2016) 141−149.
[24] T. Li, D. Kent, G. Sha, L.T. Stephenson, A.V. Ceguerra, S.P. Ringer, M.S. Dargusch, J.M. Cairney, New insights into the phase transformations to isothermal ω and ω -assisted α in near β-Ti alloys, Acta Materialia 106 (2016) 353−366.
[25] IMI 834 data sheets, in: G. Welsch, R. Boyer, E.W. Collings (Eds.), Materials Properties Handbook: Titanium Alloys, ASM International, 1994.
[26] N.G. Jones, R.J. Dashwood, D. Dye, M. Jackson, Thermomechanical processing of Ti−5Al−5Mo−5V−3Cr, Materials Science and Engineering A 490 (2008) 369−377.

[27] F. Zhang, F.-Y. Xie, S.-L. Chen, Y.A. Chang, D. Furrer, V. Venkatesh, Prediction of titanium alloy properties using thermodynamic modeling tools, Journal of Materials Engineering and Performance 14 (2005) 717−721.
[28] Y. Wang, N. Ma, Q. Chen, F. Zhang, S.-L. Chen, Y.A. Chang, Predicting phase equilibrium, phase transformation, and microstructure evolution in titanium alloys, JOM 57 (9) (2005) 32−39.
[29] W. Sha, S. Malinov, Thermodynamic modeling, in: Titanium Alloys: Modelling of Microstructure, Properties and Applications, CRC Press, 2009, pp. 95−116.
[30] W. Sha, S. Malinov, Neural network models and applications in phase transformation studies, in: Titanium Alloys: Modelling of Microstructure, Properties and Applications, CRC Press, 2009, pp. 331−364.
[31] N.S. Reddy, C.S. Lee, J.H. Kim, S.L. Semiatin, Determination of the beta-approach curve and beta transus temperarture for titanium alloys using sensitivity analysis of a trained neural network, Materials Science and Engineering, A 434 (2006) 218−226.
[32] Y.V.R.K. Prasad, T. Seshacharyulu, S.C. Medeiros, W.G. Frazier, J.T. Morgan, J.C. Malas, Titanium alloy processing, Advanced Materials and Processes 157 (6) (2000) 85−89.
[33] G.J. Lutjering, J.C. Williams, Alpha + beta alloys, in: Titanium, Springer, 2007, pp. 203−258.
[34] L.M. Gammon, R.D. Briggs, J.M. Packard, K.W. Batson, R. Boyer, C.W. Domby, Metallography and microstructures of titanium and its alloys, in: Metallography and Microstructures, ASM Handbook, vol. 9, ASM International, 2004, pp. 899−917.
[35] S. Tamirisakandala, B. Vedam, R.R. Bhat, Recent advances in the deformation processing of titanium alloys, Journal of Engineering Materials and Performance 12 (6) (2003) 661−673.
[36] G.J. Lutjering, J.C. Williams, Technological aspects, in: Titanium, Springer, 2007, pp. 53−173.
[37] S.L. Semiatin, V. Seetharaman, I. Weiss, The thermomechanical processing of alpha/beta alloys, JOM 49 (6) (1997) 33−39.
[38] I. Weiss, S.L. Semiatin, Thermomechanical processing of beta titanium alloys—an overview, Materials Science and Engineering, A 243 (1998) 46−65.
[39] Rolling, technical note, in: G. Welsch, R. Boyer, E.W. Collings (Eds.), Materials Properties Handbook: Titanium Alloys, ASM International, 1994, pp. 1167−1168.
[40] F.H. Froes, Secondary working of bar and billet, in: Titanium − Physical Metallurgy, Processing and Applications, ASM International, 2015, pp. 226−242.
[41] F.H. Froes, Forming of titanium plate, sheet, strip and tubing, in: Titanium − Physical Metallurgy, Processing and Applications, ASM International, 2015, pp. 243−263.
[42] M.W. Mahoney, Superplastic forming: technical note, in: G. Welsch, R. Boyer, E.W. Collings (Eds.), Materials Properties Handbook: Titanium Alloys, ASM International, 1994, pp. 1101−1109.
[43] E.J. Tuegel, M.O. Pruitt, L.D. Hefti, SPF/DB takes off, Advanced Materials and Processes 136 (7) (1989) 36−41.
[44] J.D. Cotton, W.L. Merrick, M.L. Watts, Thermal Processing Method for Improved Machinability of Titanium Alloys, US Patent US8500929 B2, 2013.
[45] E.W. Collings, Physical metallurgy of titanium alloys, Section 5. Equilibrium phases, in: G. Welsch, R. Boyer, E.W. Collings (Eds.), Materials Properties Handbook: Titanium Alloys, ASM International, 1994, pp. 76−80.

[46] Ti-6Al-4V Data Sheets, in: G. Welsch, R. Boyer, E.W. Collings (Eds.), Materials Properties Handbook: Titanium Alloys, ASM International, 1994, pp. 483−636.
[47] M.J. Donachie, Relationship among structure, processing and properties, in: Titanium: A Technical Guide, ASM International, 2000, pp. 95−121.
[48] D. Banerjee, J.C. Williams, Perspectives on titanium science and technology, Acta Materialia 61 (2013) 844−879.
[49] E. Alabort, D. Putman, R.C. Reed, Superplasticity in Ti-6Al-4V: characterisation, modelling and applications, Acta Materialia 95 (2015) 428−442.
[50] J.R. Pickens, Low cost titanium for ships and tanks, Advanced Materials and Processes 162 (5) (2004) 37−39.
[51] F.H. Froes, M.N. Gungor, M.A. Imam, Cost-affordable titanium: the component fabrication perspective, JOM 59 (6) (2007) 28−31.
[52] F.H. Froes, Titanium powder metallurgy: a review − Part 1, Advanced Materials and Processes 170 (9) (2012) 16−22; Part 2, Advanced Materials and Processes 170 (10) (2012) 26−29.
[53] F.H. Froes, Melting, casting and powder metallurgy, in: Titanium − Physical Metallurgy, Processing and Applications, ASM International, 2015, pp. 161−205.
[54] S. Tamirisakandala, P. Russo, 60 years of microstructure development in titanium alloy technology development, in: Proceedings of 13th World Conference on Titanium − 2015, Wiley-TMS, 2016, pp. 713−716.
[55] T. Searles, J. Tiley, A. Tanner, R. Williams, B. Rollins, E. Lee, S. Kar, R. Banerjee, H.L. Fraser, Rapid characterization of titanium microstructural features for specific modeling of mechanical properties, Measurement Science and Technology 16 (2005) 60−69.
[56] P.C. Collins, B. Welk, T. Searles, J. Tiley, J.C. Russ, H.L. Fraser, Development of methods for the quantification of microstructural features in $\alpha+\beta$ processed α/β titanium alloys, Materials Science and Engineering A 508 (2009) 174−182.
[57] D. Banerjee, A. Pilchak, J.C. Williams, Processing, structure, texture and microtexture in titanium alloys, Materials Science Forum, Trans Tech Publications 710 (2012) 66−84.
[58] G. Lutjering, Influence of processing on microstructure and mechanical properties of $(\alpha+\beta)$ titanium alloys, Materials Science and Engineering, A 243 (1998) 32−45.
[59] G.J. Lutjering, J.C. Williams, Beta alloys, in: Titanium, Springer, 2007, pp. 283−326.
[60] S.L. Semiatin, D.U. Furrer, Modeling of microstructure evolution during the thermomechanical processing of titanium alloys, in: Fundamentals of Modeling for Metals Processing, ASM Handbook, vol. 22A, ASM International, 2009, pp. 522−535.
[61] S.L. Semiatin, M.G. Glavicic, S.V. Shevchenko, O.M. Ivasishin, Y.B. Chun, S.K. Hwang, Modeling and simulation of texture evolution during the thermomechanical processing of titanium alloys, in: Fundamentals of Modeling for Metals Processing, ASM Handbook, vol. 22A, ASM International, 2009, pp. 536−552.
[62] S. Zherebtsov, M. Murzinova, G. Salishchev, S.L. Semiatin, Spheroidization of the lamellar microstructure in Ti−6Al−4V alloy during warm deformation and annealing, Acta Materialia 59 (2011) 4138−4150.
[63] N. Stefannson, S.L. Semiatin, D. Eylon, The kinetics of static globularization of Ti-6Al-4V, Metallurgical and Materials Transactions 33A (2002) 3527−3534.
[64] S.L. Semiatin, B.C. Kirby, G.A. Salischev, Coarsening behavior of an alpha-beta titanium alloy, Metallurgical and Materials Transactions 35A (2004) 2809−2819.

[65] M.A. Groeber, M.A. Jackson, DREAM.3D: a digital representation environment for the analysis of microstructure in 3D, Integrating Materials and Manufacturing Innovation 3 (2014), http://dx.doi.org/10.1186/2193-9772-3-5.
[66] W. Sha, S. Malinov, The Johnson−Mehl−Avrami method adapted to continuous cooling, in: Titanium Alloys: Modelling of Microstructure, Properties and Applications, CRC Press, 2009, pp. 165−202.
[67] T.R. Bieler, S.L. Semiatin, The origins of heterogeneous deformation during primary hot working of Ti−6Al−4V, International Journal of Plasticity 18 (2002) 1165−1189.
[68] S. Suwas, R.K. Ray, Texture control in some engineering materials, in: Crystallographic Texture in Materials, Springer, 2014, pp. 225−254.
[69] S. Mandal, S. Balachandran, D. Banerjee, A.D. Rollett, Texture and microstructure modeling in two phase titanium alloys, in: 13th World Conference on Titanium, TMS, San Diego, CA, August 16−20, 2015.
[70] G. Lutjering, J.C. Williams, A. Gysler, Microstructure and mechanical properties of titanium alloys, in: J.C.M. Li (Ed.), Microstructure and Properties of Materials, vol. 2, World Scientific, 2000, pp. 1−77.
[71] G. Terlinde, G. Fisher, Beta titanium alloys, in: C. Leyens, M. Peters (Eds.), Titanium and Titanium Alloys, Wiley, 2003, pp. 37−57.
[72] L. Wagner, J.K. Bigoney, Fatigue of titanium alloys, in: C. Leyens, M. Peters (Eds.), Titanium and Titanium Alloys, Wiley, 2003, pp. 153−185.
[73] R. Wanhill, S. Barter, Fatigue of Beta Processed and Beta Heat-treated Titanium Alloys, Springer, 2012, pp. 1−51.
[74] F.H. Froes, Mechanical properties and testing of titanium alloys, in: Titanium − Physical Metallurgy, Processing and Applications, ASM International, 2015, pp. 113−140.
[75] P.C. Collins, S. Koduri, B. Welk, J. Tailey, H.L. Fraser, Neural networks relating alloy composition, microstructure, and tensile properties of α/β-processed TIMETAL® 6-4, Metallurgical and Materials Transactions 44A (2013) 1441−1453.
[76] A.L. Pilchak, J. Shank, J.C. Tucker, S. Srivatsa, P.N. Fagin, S.L. Semiatin, A dataset for the development of microstructure-sensitive process models for near-alpha titanium alloys, Intergrating Materials and Manufacturing Innovation (2016), http://dx.doi.org/10.1186/s40192-016-0056-1.
[77] S. Ankem, H. Margolin, C.A. Greene, B.W. Neuberger, P.G. Oberson, Mechanical properties of alloys containing two ductile phases, Progress in Materials Science 51 (2006) 632−709.
[78] Metallography, RMI Titanium Company Publication.
[79] Y. Chong, N. Tsuji, T. Bhattacharjee, Investigation on the bi-lamellar microstructure in Ti-6Al-4V, in: Proceedings of the 13th World Conference on Titanium, TMS-Wiley, 2016, pp. 663−667.
[80] Strength and toughening, in: Fatigue and Fracture, ASM Handbook, vol. 19, ASM International, 1996, pp. 829−837.
[81] Properties and Processing of TIMETAL® 6-4, Titanium Metals Corporation Data Sheet.
[82] L. Wagner, Fatigue life behavior, in: Fatigue and Fracture, ASM Handbook, vol. 19, ASM International, 1996, pp. 837−845.
[83] Ti-10V-2Fe-3Al data sheets, in: G. Welsch, R. Boyer, E.W. Collings (Eds.), Materials Properties Handbook: Titanium Alloys, ASM International, 1994, pp. 839−865.
[84] Ti-15V-3Cr-3Al-3Sn data sheets, in: G. Welsch, R. Boyer, E.W. Collings (Eds.), Materials Properties Handbook: Titanium Alloys, ASM International, 1994, pp. 899−929.

[85] M.R. Bache, A review of dwell sensitive fatigue in titanium alloys: the role of microstructure, texture and operating condition, International Journal of Fatigue 25 (2003) 1079−1087.
[86] Z. Zheng, D.S. Balint, F.P.E. Dunne, Dwell fatigue in two Ti alloys: an integrated crystal plasticity and discrete dislocation study, Journal of the Mechanics and Physics of Solids 96 (2016) 411−427.
[87] S.K. Jha, K.S. Ravichandran, High-cycle fatigue resistance in beta-titanium alloys, JOM 52 (3) (2000) 30−35.
[88] Ti-6Al-2Sn-4Zr-6Mo data sheets, in: G. Welsch, R. Boyer, E.W. Collings (Eds.), Materials Properties Handbook: Titanium Alloys, ASM International, 1994, pp. 465−481.
[89] R. Boyer, G.W. Kuhlman, Processing properties relationships of Ti-10V-2Fe-3Al, Metallurgical Transactions 18A (1987) 2095−2103.
[90] G. Terlinde, H.-J. Rathjen, K.-H. Schwalbe, Microstructure and fracture toughness of the aged β-Ti alloy Ti-10V-2Fe-3Al, Metallurgical Transactions 19A (1988) 1037−1049.
[91] A. Ghosh, S. Sivaprasad, A. Bhattacharjee, S.K. Kar, Microstructure−fracture toughness correlation in an aircraft structural component alloy Ti−5Al−5V−5Mo−3Cr, Materials Science and Engineering A 568 (2013) 61−67.
[92] R.R. Boyer, W.F. Spurr, Effect of composition, microstructure and texture on stress-corrosion cracking of Ti-6Al-4V sheet, Metallurgical Transactions 9A (1978) 1443−1448.
[93] R. Briggs, Stress corrosion cracking threshold of Ti-6Al-4V extrusions, Aeromat 2013, ASM International Conference, 2013, Bellevue, WA.
[94] S. Kar, T. Searles, E. Lee, G.B. Viswanathan, J. Tiley, R. Banerjee, H.L. Fraser, Modeling the tensile properties in β-processed α/β Ti alloys, Metallurgical and Materials Transactions 37A (2006) 559−566.
[95] Y. Sun, W. Zeng, Y. Han, Y. Zhao, G. Wang, M.S. Dargusch, P. Guo, Modeling the correlation between microstructure and the properties of the Ti-6Al-4V alloy based on an artificial neural network, Materials Science and Engineering, A 528 (2011) 8757−8764.
[96] Y. Sun, W. Zeng, Y. Han, X. Ma, Y. Zhao, P. Guo, G. Wang, M.S. Dargusch, Determination of the influence of processing parameters on the mechanical properties of the Ti-6Al-4V alloy using an artificial neural network, Computational Materials Science 60 (2012) 239−244.
[97] I. Ghamarian, P. Samimi, V. Dixit, P.C. Collins, A constitutive equation relating composition and microstructure to properties in Ti-6Al-4V: as derived using a novel integrated computational approach, Metallurgical and Materials Transactions 46A (2015) 5021−5037.
[98] I. Ghamarian, B. Hayes, P. Samimi, B.A. Welk, H.L. Fraser, P.C. Collins, Developing a phenomenological equation to predict yield strength from composition and microstructure in β processed Ti-6Al-4V, Materials Science and Engineering, A 660 (2016) 172−180.
[99] M. Zhang, J. Zhang, D.L. McDowell, Microstructure-based crystal plasticity modeling of cyclic deformation of Ti−6Al−4V, International Journal of Plasticity 23 (2007) 1328−1348.
[100] B.D. Smith, D.S. Shih, D.L. McDowell, Fatigue hot spot simulation for two Widmanstätten titanium microstructures, International Journal of Fatigue 92 (2016) 116−129.

[101] N.L. Richards, Quantitative evaluation of fracture toughness-microstructural relationships in alpha-beta titanium alloys, Journal of Materials Engineering Performance 13 (2) (2004) 218–225.
[102] X. Shi, W. Zeng, C. Shi, H. Wang, Z. Jia, The fracture toughness and its prediction model for Ti-5Al-5Mo-5V-1Cr-1Fe titanium alloys with basketweave microstructure, Journal of Alloys and Compounds 632 (2015) 748–755.
[103] Y. Liu, P. Samimi, I. Ghamarian, D.A. Brice, D.E. Huber, Z. Wang, V. Dixit, S. Koduri, H.L. Fraser, P.C. Collins, Discovery via integration of experimentation and modeling: three examples for titanium alloys, JOM 67 (1) (2015) 164–178.
[104] M.G. Glavicic, V. Venkatesh, Integrated computational materials engineering of titanium: current capabilities being developed under the metals affordability initiative, JOM 66 (7) (2014) 1310–1320.
[105] T. O'Connell, TIMETAL® 62S data sheets, in: G. Welsch, R. Boyer, E.W. Collings (Eds.), Materials Properties Handbook: Titanium Alloys, ASM International, 1994, pp. 679–684.
[106] Ti-6Al-6V-2Sn data sheets, in: G. Welsch, R. Boyer, E.W. Collings (Eds.), Materials Properties Handbook: Titanium Alloys, ASM International, 1994, pp. 637–666.
[107] L.D. Hefti, Fine-grain titanium 6Al-4V for superplastic forming and diffusion bonding of aerospace products, JOM 62 (5) (2010) 42–45.
[108] P. Russo, Ti-6-22-22S data sheets, in: G. Welsch, R. Boyer, E.W. Collings (Eds.), Materials Properties Handbook: Titanium Alloys, ASM International, 1994, pp. 713–732.
[109] J.D. Cotton, L.P. Clark, H.R. Phelps, Titanium alloys on the F-22 fighter airframe, Advanced Materials and Processes 160 (May 2002) 25–28.
[110] X.D. Zhang, D.J. Evans, W.A. Baeslack III, H.L. Fraser, Effect of long term aging on the microstructural stability and mechanical properties of Ti-6Al-2Cr-2Mo-2Sn-2Zr alloy, Materials Science and Engineering, A 344 (2003) 300–311.
[111] S. Tamirisa, E. Crist, Advanced titanium alloy Ti-6Al-2Sn-2Zr-2Mo-2Cr (Ti-62222) for commercial aerospace applications, Titanium 2012, International Titanium Association Conference, October 7–10, 2012, Atlanta, GA.
[112] SP-700 data sheets, in: G. Welsch, R. Boyer, E.W. Collings (Eds.), Materials Properties Handbook: Titanium Alloys, ASM International, 1994, pp. 685–692.
[113] M. Armendia, A. Garay, L.-M. Iriarte, P.-J. Arrazola, Comparison of the machinabilities of Ti6Al4V and TIMETAL® 54M using uncoated WC–Co tools, Journal of Materials Processing Technology 210 (2010) 197–203.
[114] P. Gudipati, Y. Kosaka, J. Fanning, Superplastic Formability of TIMETAL® 54M Sheet (Ti-5Al-4V-0.6Mo-0.4Fe), AeroMAT 2009, Dayton, OH, June 07–11, 2009.
[115] V. Venkatesh, R.R. Boyer, Recent advances in titanium technology in the USA, in: Proceedings of the 13th World Conference on Titanium, TMS-Wiley, 2016, pp. 13–18.
[116] Ti-5Al-2Sn-2Zr-4Mo-4Cr data sheets, in: G. Welsch, R. Boyer, E.W. Collings (Eds.), Materials Properties Handbook: Titanium Alloys, ASM International, 1994, pp. 453–463.
[117] P.J. Bania, An advanced alloy for elevated temperatures, JOM 40 (3) (1988) 20–22.
[118] TIMETAL® 1100 data sheets, in: G. Welsch, R. Boyer, E.W. Collings (Eds.), Materials Properties Handbook: Titanium Alloys, ASM International, 1994, pp. 411–414.
[119] Ti-6Al-2Sn-4Zr-2Mo-0.08Si data sheets, in: G. Welsch, R. Boyer, E.W. Collings (Eds.), Materials Properties Handbook: Titanium Alloys, ASM International, 1994, pp. 337–375.

[120] K.S. McReynolds, S. Tamirisakandala, A study on alpha-case depth in Ti-6Al-2Sn-4Zr-2Mo, Metallurgical and Materials Transactions, A 42A (2011) 1732−1736.
[121] D.P. Satko, J.B. Shaffer, J.S. Tiley, S.L. Semiatin, A.L. Pilchak, S.R. Kalidindi, Y. Kosaka, M.G. Glavicic, A.A. Salem, Effect of microstructure on oxygen rich layer evolution and its impact on fatigue life during high-temperature application of α/β titanium, Acta Materialia 107 (2016) 377−389.
[122] S.L. Nyakana, J.C. Fanning, R.R. Boyer, Quick reference guide for β titanium alloys in the 00s, Journal of Materials Engineering and Performance 14 (6) (2005) 799−811.
[123] J. Fanning, Properties of Ti 18 − a new high strength near beta alloy for forged products and fastener stock, in: Proceedings of the 13th World Conference on Titanium, TMS-Wiley, 2016, pp. 859−864.
[124] S. Nag, R. Banerjee, R. Srinivasan, J.Y. Hwang, M. Harper, H.L. Fraser, ω-assisted nucleation and growth of a precipitates in the Ti−5Al−5Mo−5V−3Cr−0.5Fe beta titanium alloy, Acta Materialia 57 (2009) 2136−2147.
[125] J. Fanning, Recent developments in high-strength near-beta titanium alloys, Titanium 2011, International Titanium Association Conference, October 2−5, 2011, San Diego, CA.
[126] Ti-3Al-8V-6Cr-4Mo-4Zr data sheets, in: G. Welsch, R. Boyer, E.W. Collings (Eds.), Materials Properties Handbook: Titanium Alloys, ASM International, 1994, pp. 797−827.
[127] K.O. Yu, E.M. Crist, R. Pesa, N. Cecchini, C.M. Bugle, Single-melt beta C for spring and fastener applications, Journal of Materials Engineering and Performance 14 (6) (2005) 697−702.
[128] S. Tamirisa, P. Russo, Beta-C titanium alloy revisited, ASM Aeromat Conference, May 2015, Long Beach, CA.
[129] J.C. Fanning, S.P. Fox, Recent developments in metastable β strip alloys, Journal of Materials Engineering and Performance 14 (6) (2005) 703−708.
[130] P. Edwards, A. O'Connor, M. Ramulu, Electron beam additive manufacturing of titanium components: properties and performance, Journal of Manufacturing Science and Engineering 135 (2013) 060161−060167.
[131] W.E. Frazier, Metal additive manufacturing: a review, Journal of Materials Engineering and Performance 23 (2014) 1917−1928.
[132] E.W. Collings, Physical metallurgy of titanium alloys, Section 11. "Rapid solidification processing of precipitate- and dispersion-strengthened titanium alloys", in: G. Welsch, R. Boyer, E.W. Collings (Eds.), Materials Properties Handbook: Titanium Alloys, ASM International, 1994, pp. 87−93.
[133] M. Thomas, J. Hewitt, M. Bache, R. Thomas, P. Garratt, Y. Kosaka, TIMETAL® 575: a novel high strength forgeable αβ/titanium alloy, in: Proceedings of the 13th World Conference on Titanium, TMS-Wiley, 2016, pp. 1537−1541.
[134] Sebastian, J. Olson, G. Grabowski, J., Application of integrated computational materials engineering to the design of new high performance titanium alloys, Titanium, 2014. International Titanium Association Conference, September 21−24, 2014, Chicago, IL.
[135] Low-Cost, Castable QuesTalloy™ Ti-6-4 Mod, Questek Innovations LLC Data.
[136] J.A. Wright, J. Sebastian, H.-J. Jou, Titanium Alloys, US Patent Application 2011/0268602 A1, November 3, 2011.

[137] J.D. Cotton, M.L. Watts, Relating Microstructure and Machinability in Titanium Alloy Ti-5553, AEROMAT 2009, Dayton, OH, June 07−11, 2009.
[138] I. Sen, S. Tamirisakandala, D.B. Miracle, U. Ramamurty, Microstructural effects on the mechanical behavior of B-Modified Ti-6Al-4V alloys, Acta Materialia 55 (2007) 4983−4993.
[139] S. Tamirisakandala, D.B. Miracle, R. Srinivasan, J.S. Gunasekera, Titanium alloyed with boron, Advanced Materials and Processes 164 (12) (2006) 41−43.
[140] T.W. Heo, D.S. Shih, L.-Q. Chen, Kinetic pathways of phase transformations in two-phase Ti-alloys, Metallurgical and Materials Transactions, A 45A (2014) 3438−3445.
[141] D. Wang, R. Shi, Y. Zheng, R. Banerjee, H.L. Fraser, Y. Wang, Integrated computational materials engineering (ICME) approach to design of novel microstructures for Ti-alloys, JOM 66 (7) (2014) 1287−1298.

CHAPTER

Ultrahigh Strength Steels

6

CHAPTER OUTLINE

Synopsis **290**
6.1 Ultrahigh Strength Steels for Airframe Structures **290**
6.2 Classification of Ultrahigh Strength Steels **291**
6.3 Physical Metallurgy of Ultrahigh Strength Steels **292**
6.3.1 Alloying of Ultrahigh Strength Steels 294
6.3.1.1 Alloying Elements in Steels 296
6.3.1.2 Alloying of Medium Carbon, Low Alloy Steels 296
6.3.1.3 Alloying of Secondary Hardening, High Alloy Steels 298
6.3.1.4 Alloying of Precipitation Hardening Stainless Steels 299
6.3.2 Phases in Ultrahigh Strength Steels 300
6.3.2.1 Martensite 301
6.3.2.2 Austenite 303
6.3.2.3 Second-Phase Particles 306
6.3.3 Composition—Processing—Microstructure Relationships in Ultrahigh Strength Steels 307
6.3.3.1 Modeling of M_s Temperature 308
6.3.3.2 Hardenability 309
6.3.3.3 Tempering 309
6.4 Properties of Ultrahigh Strength Steels and Their Relationships to Composition, Processing, and Microstructure **312**
6.4.1 Strength 313
6.4.1.1 Medium Carbon, Low Alloy Steels 313
6.4.1.2 Secondary Hardening, High Alloy Steels 314
6.4.1.3 Precipitation Hardening, Stainless Steels 317
6.4.2 Ductility 317
6.4.3 Toughness 319
6.4.3.1 Medium Carbon, Low Alloy Steels 319
6.4.3.2 Secondary Hardening, High Alloy Steels 320
6.4.3.3 Precipitation Hardening Stainless Steels 323
6.4.4 Fatigue Properties 323
6.4.5 Embrittlement 324
6.4.6 Stress Corrosion Cracking Behavior 324
6.4.7 Summary 325

Metallurgy and Design of Alloys with Hierarchical Microstructures. http://dx.doi.org/10.1016/B978-0-12-812068-2.00006-0
Copyright © 2017 Elsevier Inc. All rights reserved.

6.5 Commercial Ultrahigh Strength Steels 327
6.5.1 Medium Carbon, Low Alloy Steels 327
6.5.2 Secondary Hardening, High Alloy Steels 328
6.5.3 Precipitation Hardening Stainless Steels 331
6.6 New Alloy Design 333
6.7 Summary 339
References 339

SYNOPSIS

This chapter describes the metallurgy of ultrahigh strength (UHS) steels used in airframe structures, particularly for landing gear components, for which medium carbon, low alloy steels have been the dominant materials. High alloy steels exhibiting better toughness and corrosion resistance are used for structures operating under more demanding loading conditions and environments such as in aircraft carriers. Steels are unique from the perspective of being in use significantly longer than any other metallic structural material and yet, being the first family of airframe alloys to be successfully designed computationally and commercialized, still provide significant opportunities for property enhancement. In the framework of the composition—microstructure—processing—properties relationships, the discussion in this chapter is limited to how UHS steels used in airframe structures have evolved historically, the metallurgy and mechanisms underlying their behavior and how this knowledge has been applied to new alloy design.

6.1 ULTRAHIGH STRENGTH STEELS FOR AIRFRAME STRUCTURES

The performance requirements for components such as gears in helicopter transmissions, engine bearings, and airplane landing gear cylinders can generally be satisfied in a structurally efficient and cost-effective way only by ultrahigh strength (UHS) steels. These materials are also used in aircraft for flap tracks, actuating components, fasteners, and high-pressure hydraulic tubing. These critical applications require very high strength materials for structures often designed with severe space constraints. Landing gear structures need materials with high static and fatigue strength, high stiffness, good toughness, and resistance to environment and wear while also meeting the need for low cost and weight [1]. Components requiring materials with the highest strength generally use the medium carbon, low alloy steels 4340 and 300M, which can be heat treated to tensile strength levels approaching 2000 MPa (~300 ksi), although they are typically used at lower strength levels and higher toughness.

The use of steels in commercial airplanes is primarily for landing gear components and shows a small decrease for the 777 and 787 compared with earlier planes and a larger decrease for the Airbus A350 (see Table 4.1). As discussed in the

previous chapter, near-β titanium alloys have begun to replace UHS steels in many landing gear parts beginning with the Boeing 777. Ti−10V−2Fe−3Al with a minimum tensile strength of 1193 MPa (173 ksi) replaced several parts using 4340M with a strength of about 1930 MPa (280 ksi), thereby saving 580 kg (1279 lbs) per plane in addition to providing superior corrosion resistance and lower maintenance costs [2]. The cost of substitution arising from the higher cost of titanium alloys needs to be justified for the weight saving benefits. The 787 uses Ti−5Al−5V−5Mo−3Cr due to its slightly higher strength and processing advantages.

Steels with tensile strength levels greater than about 1400 MPa (∼200 ksi) are considered the UHS type, with many having tensile strength as high as about 2400 MPa (350 ksi). As seen by their replacement with titanium alloys, many landing gear parts do not require materials with such high strength and for which steels such as Hy-Tuf with strengths lower than 1400 MPa (200 ksi) can be used. UHS steels can reduce component profile and space requirements and when used in flap tracks, carriages, and actuating components can contribute to optimizing wing shape and improving airplane performance [3]. For demanding applications in landing gear components, for example, in naval aircraft operating in a carrier environment, the medium carbon, low alloy steels (MC-LA) do not possess adequate toughness and resistance to environment, and high alloy steels like Aermet 100 with better properties are used. However, these high alloy steels are not the stainless type and require corrosion protection coatings like the MC-LA steels. The in-service performance of these steels is improved by surface treatments and cold working, which are often tailored for individual components and are not discussed in this chapter. The focus of this chapter is on the metallurgy of alloys in current use in airframes and those being developed with better properties, particularly by computational design.

6.2 CLASSIFICATION OF ULTRAHIGH STRENGTH STEELS

Among structural alloys, steels have had the longest history of development and can be designed and processed to possess the most variations in property combinations for the largest diversity of applications. Their classifications and characteristics are covered extensively in many widely available publications like the *ASM Handbook* volumes. Briefly, steels are Fe-based alloys with up to 2 wt% C and are classified as plain carbon or alloy steels. Plain carbon steels are those for which no minimum is specified for alloying elements like Ni, Cr, Mo, etc. that are added for specific effects and the levels of Mn, Cu, and Si are specified to be 1.65, 0.60, and 0.60 wt%, or less, respectively. Steels with C content less than 0.30, 0.30−0.60, 0.60−1.00, and 1.00−2.00 wt% are further classified as low, medium, high, or ultrahigh carbon steels, respectively.

Alloy steels contain Mn, Cu, or Si in amounts higher than specified for plain carbon steels or other alloying elements added in specified amounts. These are classified as low alloy steels if they contain less than 5 wt% of alloying elements and high

alloy steels otherwise. In addition to the classifications based upon composition and strength levels, steels are also categorized in other ways based on their characteristics, e.g., stainless or tool steels. Steels are designated by American Iron and Steel Institute/Society of Automotive Engineers, e.g., 4340 in which the first two digits indicate the alloying elements and the last two, the C content or by the unified numbering system, e.g., G43400 for the 4340 steel. Steels may also be identified by their own commonly known trade names like 300M, an MC-LA steel, or Custom 455, a precipitation-hardened stainless steel.

The distinction between low alloy and high alloy steels stated earlier is arbitrary. High alloy steels used for airframe structures typically contain more than 10 wt% of alloying additions. These steels are of two types, those strengthened by alloy carbides (secondary hardening steels containing carbon) or by intermetallic compounds [maraging steels and precipitation hardening stainless steels (PH-SSs), which both have very low levels of carbon]. MC-LA steels and the secondary hardening, high alloy (SH-HA) steels find the most applications in landing gear components. PH-SS are also used in many areas of the airframes, e.g., engine attachment fittings, fasteners, and cargo handling equipment [4]. All these types of steels are more commonly used in airframes than the maraging steels and will be discussed in this chapter.

High alloy steels developed for combinations of higher strength and toughness are Fe−Ni alloys with low to medium amounts of C, combinations of elements like Cr and Mo for secondary hardening, and Co for solid solution strengthening and for enhancing the kinetics of carbide formation. The PH-SS alloys contain higher amounts of Cr and combinations of various alloying elements for precipitation of intermetallic compounds. The compositions of representative UHS steels used in airframe structures are shown in Table 6.1 [4,5].

6.3 PHYSICAL METALLURGY OF ULTRAHIGH STRENGTH STEELS

UHS steels are multicomponent alloys containing several alloying elements for desirable processing attributes, microstructures, and properties. The similarities and differences between UHS steels and the light alloys can be illustrated by comparing their microstructure−properties relationships. As with structural aluminum and titanium alloys, the highest strength is achieved in steels by precipitation hardening, for which C and/or selected alloying elements are added to form carbides or intermetallic compounds. Alloying elements are also added to control the matrix microstructure, increase hardenability, and influence precipitation kinetics. Like precipitation hardened aluminum alloys, control of impurities and inclusions is critical for UHS steels, because of their deleterious effects on fracture toughness and environmental sensitivity, which is not a concern for titanium alloys. For all these alloys, property combinations, for example, strength and toughness, can be varied by heat treatments.

Table 6.1 Nominal Compositions of Ultrahigh Strength Steels (wt%)

Steel Type		Alloy	C	Ni	Co	Cr	Mo	Mn	Cu	V	Si	Al	Ti	Nb
MC-LA		4340	0.40	1.8	–	0.85	0.25	0.7	–	–	0.2	–	–	–
		300M	0.40	1.8	–	0.85	0.4	0.7	–	0.1	1.6	–	–	–
		D6AC[a]	0.46	0.6	–	1.1	1	0.75		0.1	0.25			
SH-HA		HY 180	0.10	10	8	2	1	0.15	–	–	–	–	–	–
		HP-9-4-30	0.30	9	4	0.8	1	0.2	0.08	0.1 max	–	–	–	–
		AF1410	0.16	10	14	2	1	–	–	–	–	–	–	–
		Aermet 100	0.23	11.1	13.4	3.1	1.2	–	–	–	–	–	–	–
PH-SS	M	17-4 PH	0.04	4.7	–	15–17.5	–	0.65	3.5	–	0.35	–	–	0.3
		15-5 PH	0.04	4.6	–	14–15.5	–	0.25	3.3	–	0.4	–	–	–
		PH 13-8 Mo	0.04	8	–	12.25 –13.25	2.2	–	–	–	–	1.1	–	–
		Custom 455	0.05	8.5	–	11.7	0.5	0.5	2	–	0.5	–	1.1	–
		Custom 465	0.02	11	–	11.7	1	–	–	–	–	–	1.65	–
		Custom 475	0.01 max	8	8.5	11	5	0.5 max	–	–	0.5 max	1.25	–	–
	SA	17-7 PH	0.09	7	–	16–18	–	1 max			1 max	1.25	–	–
	A	A286	0.05	26	–	15	1.25	1.5	–	0.3	0.75	0.2	2.2	–

A, *austenitic;* M, *martensitic;* MC-LA, *medium carbon-low alloy;* PH-SS, *precipitation hardening, stainless steel;* SA, *semiaustenitic;* SH-HA, *secondary hardening, high alloy.*

[a] *D6AC denotes vacuum melted steel. Air melted steel would be denoted as D6A.*

A brief description of the melting, thermomechanical processing (TMP), and heat treatment practices for UHS steels, schematically shown in Fig. 6.1, will be helpful for the subsequent discussion of their physical metallurgy.

UHS steels need to possess good fracture toughness and fatigue properties for use in critical applications, for which a high degree of cleanliness and homogeneity is required in the material. Vacuum induction melting (VIM) followed by additional refinement, such as by electroslag remelting and/or vacuum arc remelting (VAR), minimizes segregation, impurity elements, and nonmetallic inclusions [6]. MC-LA steels (4340 and 300M) are available in various qualities depending on the melting practice, but the trend has been to use the VIM/VAR double vacuum melting approach, which is also generally required if these steels are used at strength levels above about 1400 MPa (200 ksi). High alloy steels are always melted using the VIM/VAR or other sequences of vacuum melting processes [7].

TMP of UHS steel ingots is typically conducted by forging within selected temperature ranges and cooling at specified rates for each alloy. Forging must be carefully controlled, as the hot working conditions affect the properties of the alloys after heat treatment. Alloy 4340 is forged in the range of 1065−1230°C (1950−2250°F) followed by air or furnace cooling. 300M is forged in the range of 1065−1095°C (1950−2000°F) and furnace cooled. Primary breakdown of Aermet 100 is performed at a maximum temperature of about 1230°C (2250°F) and the finish forging by starting at about 980°C (1800°F) and ending below about 900°C (1650°F) followed by air cooling [8]. Custom 465 PH stainless steel is forged in the range of 1010−1093°C (1850−2000°F) and air cooled [9]. The final step in the processing of UHS steels is heat treatment, which involves a high temperature soak (austenitizing or solution heat treatment), quenching at different rates, and tempering or precipitation hardening. The quenching rates will depend on the hardenability and section sizes of the alloys.

6.3.1 ALLOYING OF ULTRAHIGH STRENGTH STEELS

As with titanium, the occurrence of Fe in various allotropic forms and the effects of alloying elements on their stabilities provide the opportunity for phase transformations to manipulate microstructures and enhance the properties. However, the details vary significantly between titanium alloys and UHS steels. Fe occurs in three allotropic forms: the low temperature phase, body centered cubic (BCC) α-iron or α-ferrite up to 912°C (1674°F), face centered cubic (FCC) γ-iron or austenite

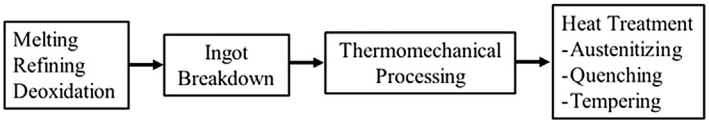


FIGURE 6.1

Schematic of the sequence of processing steps for Ultrahigh Strength steels.

from 912 to 1394°C (1674−2541°F), and BCC δ-iron or δ-ferrite from 1394°C (2541°F) to 1538°C (2800°F) (melting point) [10]. δ-Ferrite is of no significance in the heat treatment of most steels but can be present in certain stainless steels deleteriously affecting the properties. Unless referred to otherwise, ferrite will always denote the α-iron variant.

Alloying elements can stabilize the γ phase (austenite stabilizers) or α (δ) phase (ferrite stabilizers) as shown in Fig. 6.2 [11]. The former is of two types. The elements Mn, Ni, and Co (Type 1) extend the stability of γ toward room temperature. C, N, Cu, and Zn (Type 2) are among those elements for which extension of the γ field to lower temperatures is limited by the formation Fe-rich compounds. Ferrite stabilizers restrict the range of austenite stability by closing the γ field resulting in a continuous, wider δ and α phase fields (Type 3—Si, Al, Be, Cr, Ti, V, Mo, and W) or by contracting the γ field in which case ferrite and austenite are in equilibrium with an intermetallic compound or occur as solid solutions (Type 4—B, Ta, Zr, and Nb).

Steels are classified as austenitic or ferritic depending on which phase is dominant at room temperature. Most of the ferrite stabilizers, Mo, Cr, Ti, etc., are also strong carbide formers and contribute to hardening in SH-HA steels. MC-LA and SH-HA steels are strengthened by iron carbides and alloy carbides, respectively, which form during the tempering of martensite that is obtained by quenching the

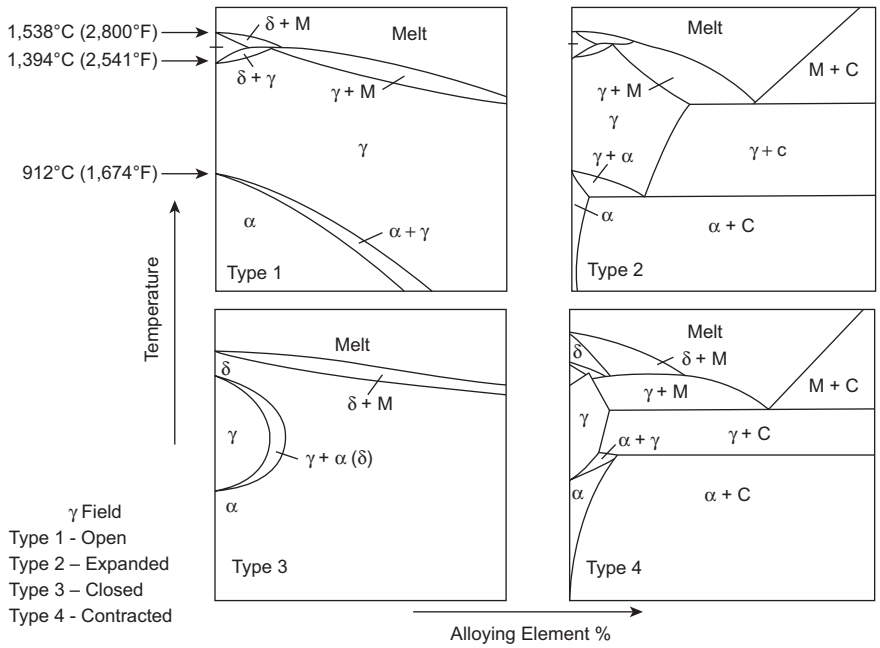


FIGURE 6.2

Effects of alloying elements on phase relationships in steels [11].

alloys from the austenite state. Martensite tempering in these steels occurs in four stages, each of which is associated with certain microstructural changes, as shown in Table 6.2 [12]. Sometimes, the coarsening of Fe_3C is considered a separate stage occurring in the fourth stage [13]. Precipitation of alloy carbides and secondary hardening then occur in the fifth stage. PH-SSs are strengthened by intermetallic compounds that precipitate during the aging of the supersaturated solid solution obtained by quenching.

6.3.1.1 Alloying Elements in Steels

Plain carbon steels, which are the most widely used, do not possess adequate combinations of strength and toughness for airframe applications. Alloying elements are added to improve their mechanical properties, corrosion resistance, and hardenability. The carbide forming alloying elements retard softening during tempering, thereby enabling similar hardness levels to be achieved by aging at higher temperatures with lower levels of C, resulting in generally higher strength–toughness combinations. The impurity elements P and S are found in steels in small quantities and have important effects on their properties. Depending on the processing conditions, segregation of P to grain boundaries causes embrittlement of the steels. Alloying elements are also added to control the formation of sulfides and mitigate their effects on hot formability and toughness. These aspects will be discussed, as applicable, for each of the UHS steel types.

6.3.1.2 Alloying of Medium Carbon, Low Alloy Steels

MC-LA steels used in airframe structures typically contain about 0.4 wt% C and selected combination of Mn, Ni, Cr, Mo, Si, and V. Alloy 4340 provides a balanced combination of strength and hardenability with adequate ductility and toughness for many applications. This alloy is also used as the benchmark for comparison of alloys with improved properties. Highest strength is achieved in 4340 by tempering at ~200°C (~400°F), which is in the range of the first stage. Increasing the tempering temperature progressively decreases the strength and increases the ductility. The extent of these changes upon tempering at 1200°F (650°C) compared with tempering at 400°F (200°C) is shown in Fig. 6.3 [12].

Table 6.2 Tempering Stages in Carbide Forming Steels

Stage	Temperature Range and Microstructural Changes
I	<250°C (<482°F). Decomposition of supersaturated martensite into transition carbides—ε ($Fe_{2.4}C$) and η (Fe_2C), and low-C (about 0.25 wt%) martensite (α'').
II	200–300°C (392–572°F). Decomposition of retained austenite to ferrite and cementite (Fe_3C).
III	250–350°C (482–662°F). Transformation of low-C martensite and ε carbide to ferrite and Fe_3C.
IV	450–650°C (842–1202°F). Formation of alloy carbides (secondary hardening).

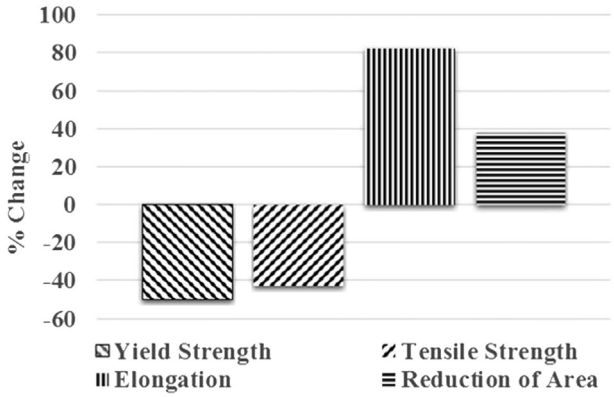


FIGURE 6.3

Change in the tensile properties of 4340, oil quenched from 1475°C (802°F) and tempered for 1 h at 1200°F (650°C) compared with the properties after tempering for 1 h at 400°F (200°C).

Data from G. Krauss, Tempering, In: Steels: Processing, Structure, and Performance, 2015, ASM International, 373–403.

Required strength is achieved in MC-LA UHS steels with carbon additions of about 0.4 wt%. Lower C levels reduce strength and hardenability while higher C levels decrease toughness. Ni and Cr provide solid solution hardening, and improve toughness, fatigue resistance, and hardenability [14]. Mo increases hardenability while reducing susceptibility to temper embrittlement (TE). However, as shown in Fig. 6.4 for 4340 [15], these alloys suffer a reduction in toughness, despite decreasing strength and increasing ductility, when tempered in the range of 200−400°C (400−675°F). This "tempered martensite embrittlement" phenomenon is caused by the formation of cementite (Fe_3C) in the second and third stages of tempering. The impurity element P reduces toughness of alloys tempered at all temperatures. The various embrittlement phenomena and how they are affected by impurity elements and processing will be discussed subsequently.

Tempering of 4340 at 400°C (675°F) or higher for improved toughness results in a significant loss of strength. Si additions to 4340 retard the formation of cementite allowing tempering at higher temperatures without loss of strength and toughness. Si also causes solid solution strengthening and provides deeper hardenability [4,14]. Alloy 300M is essentially 4340 modified by increasing the amount of Si to 1.6 wt %, Mo slightly, and adding a small amount of V for grain refinement to increase toughness and transverse ductility. 300M possesses better strength and toughness when compared with 4340, without suffering from the reduction in toughness until higher tempering temperatures, as shown in Fig. 6.5 [16]. Alloys in this family of steels with slightly lower or higher levels of C that are used in airframes will be discussed in the section on commercial alloys.

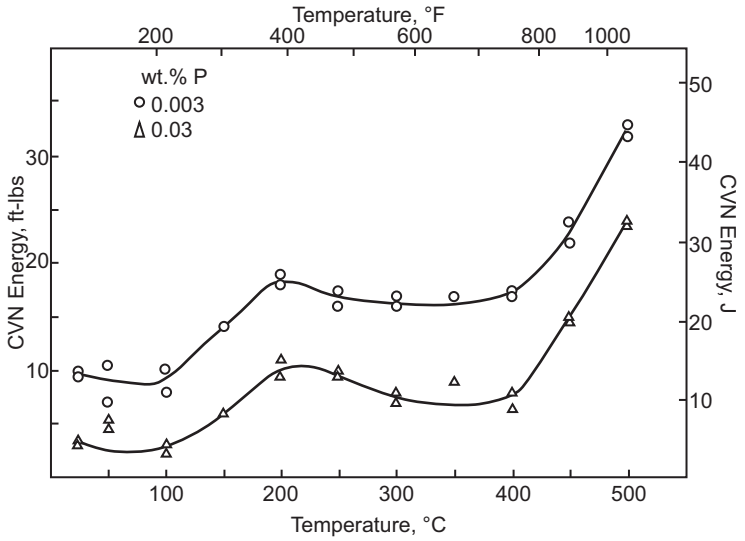


FIGURE 6.4

Effects of tempering temperature on toughness of 4340 with two levels of P, oil quenched from 870°C (1600°F), and tempered for 1 h at the indicated temperature [15].

6.3.1.3 Alloying of Secondary Hardening, High Alloy Steels

The need to increase the toughness and stress corrosion cracking resistance beyond that exhibited by 300M without sacrificing strength resulted in the development of SH-HA steels. These alloys are strengthened by the formation of alloy carbides during the fourth stage of tempering. Desired improvements are made possible in these steels compared with MC-LA steels by the addition of Co and by increasing the amount of Ni and adjusting the levels of Cr and Mo. All these alloying elements increase the hardenability and, except for Co, depress the temperature at which martensite transformation (M_s) begins. In addition, Ni lowers the ductile brittle transition temperature (DBTT), increases toughness, and provides solid solution strengthening. The alloying elements, particularly Ni and Co, should be balanced to ensure that the M_s temperature is sufficiently high to result in lath martensite upon quenching, but low enough to prevent auto tempering during quenching. The amount of C is lower than in medium C steels but is sufficient to precipitate the desired volume fraction of $(Mo,Cr)_2C$. Co retards the recovery of dislocations in the lath martensitic matrix and promotes a finer dispersion of alloy carbides by heterogeneous nucleation.

A detailed study of the effects of varying amounts of C, Co, Mo, and Cr on the properties of quenched and tempered Fe−10Ni alloy has elucidated the effects of these alloying elements in SH-HA steels [17]. Commercial alloys of this family include the HP-9-4-X (X = 0.2, 0.25, 0.3 or 0.45 wt% C) series, HY180, and AF1410 (Table 6.1). The HP-9-4 alloy with 0.3 C is the only one produced in large

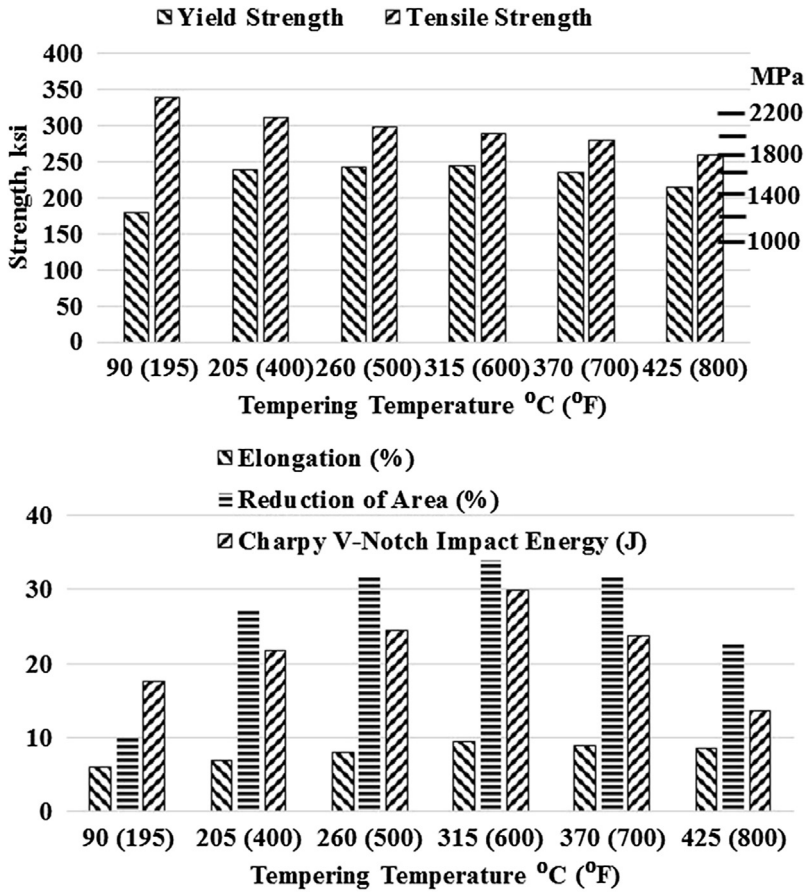


FIGURE 6.5

Effect of tempering temperature on typical properties of 300M steel [16].

quantities for commercial use [16]. These alloys possess significantly higher toughness than 300M, but at somewhat lower strength levels. Increasing C to 0.23 wt%, increasing the Cr to Mo ratio, and minor adjustments to the levels of Ni and Co resulted in Aermet 100, which possessed the required strength and toughness and was selected for landing gear applications for the F/A-18 E/F, replacing the 300M alloy used in the earlier models of this aircraft [5]. Some of these alloys have varying additions of rare earth elements to tie up the nonmetallic impurities and mitigate the deleterious effects of sulfide inclusions on fracture toughness.

6.3.1.4 Alloying of Precipitation Hardening Stainless Steels

The SH-HA steels are not "corrosion-resistant" stainless steels. Although more resistant to pitting and stress corrosion cracking than MC-LA steels, they still

need coatings for protection from the effects of environment. Stainless steels strengthened by precipitation hardening have been developed to achieve UHS levels with adequate fracture toughness and can be used without the need for corrosion protection coatings. These PH-SS alloys are Fe−Ni−Cr alloys containing varying levels of Ni, minimum of 10.5 wt% Cr, as in conventional stainless steels, and one or more of the elements Al, Ti, Cu, Nb, etc., that form intermetallic compounds and provide precipitation hardening. These alloys are classified as austenitic, semiaustenitic, or martensitic type. The amount of Ni is sufficiently high in the austenitic type of PH-SS to stabilize austenite to room temperature. In martensitic stainless steels, martensite forms upon quenching from the austenitizing temperature. The semiaustenitic steels are composed predominantly of austenite upon quenching and are further heart treated by special conditioning treatments to form martensite. All these alloys are precipitation hardened by aging following quenching from the solution heat treatment temperature. Toughness of PH-SS alloys generally increases with increasing Ni content. The amount of C is kept very low to maintain an adequate level of toughness. The very recent, computationally designed, and developed corrosion resistant steel Ferrium S53, strengthened by the precipitation of carbides will be discussed in Section 6.6.

In the three classes of alloys discussed earlier, varying combinations of strength, toughness, and corrosion resistance are achieved for a wide range of requirements by using a relatively small number of alloying elements, as was also the case for structural aluminum and titanium alloys. In UHS steels, these elements are selected for either the formation of strengthening phases (C or intermetallic compound formers) or imparting specific characteristics to the matrix, for example, hardenability. Despite the higher cost of the high alloy, secondary hardening, and stainless steels compared with the medium carbon steels due to the use of alloying elements like Co, their excellent property attributes render many possible applications for which no alternative, practical materials are yet available.

6.3.2 PHASES IN ULTRAHIGH STRENGTH STEELS

The properties of most UHS steels are determined by the microstructures resulting from the transformation of austenite to martensite and its subsequent tempering. As with aluminum alloys, impurities and inclusions also have a significant effect on the fracture toughness and fatigue properties. The formation and tempering of martensite in steels have been covered in detail in many publications. This section will describe the phases that constitute the microstructure and affect the behavior of UHS steels used in airframe structures.

The microstructure of these steels consists of the tempered martensite matrix and second-phase particles. Austenitic PH-SSs do not undergo martensitic transformation and the austenite phase in these steels is just solution treated and aged. Other phases that can be present in these alloys are austenite that is retained due to its incomplete transformation to martensite, reverted austenite that forms due to

compositional changes in the matrix phase during tempering, and δ-ferrite in certain PH-SS alloys.

The similarities and differences between the way the phases that make up the microstructure of aluminum, titanium, and steel alloys evolve are shown in Table 6.3. This table provides only a general overview and many aspects unique to each alloy type and the different families within them are not shown.

6.3.2.1 Martensite

The martensitic transformation has been used in practice to develop useful materials for centuries but its mechanisms have begun to be elucidated rather only recently

Table 6.3 Microstructure Evolution in Aluminum, Titanium, and Steel Alloys

	Alloy Type		
Processing	**Aluminum**	**Titanium**	**Ultrahigh Strength Steels**
Melting and solidification	• Segregation of alloying elements • Formation of constituent particles (intermetallics)	• Segregation of alloying elements • As cast, α/β lamellar microstructure	• Segregation of alloying elements • Formation of inclusions (oxides and sulfides)
Ingot breakdown and homogenization	• Elimination of segregation • Precipitation of dispersoids	• Elimination of segregation • Recrystallization and grain refinement	• Elimination of segregation • Recrystallization and grain refinement
Thermomechanical processing	• Distribution of constituents • Dynamic recovery/ recrystallization • Substructure formation • Texture development	• α-Globularization • α, β-Recrystallization • Texture development	• Distribution of inclusions • Substructure formation • Texture development
Heat treatment	• Static recrystallization • Precipitation of strengthening phases	• Solute element partitioning • Secondary α precipitation	• Impurity segregation to grain boundaries • Tempered martensite • Formation of strengthening phases • Formation of reverted austenite

with the development of electron microscopy and other advanced characterization techniques. It is also among the most widely investigated. This athermal, diffusionless transformation occurs by the cooperative movement of atoms over distances less than an atomic diameter. The composition of martensite is identical to that of the parent austenite (γ) phase. The transformation is accompanied by a change in crystal structure, a large shape change, and a relatively small volume change [18].

The α' martensite with a body centered tetragonal crystal structure is the most common type that occurs in ferrous alloys. It exhibits an orientation relationship with the austenite and an internal substructure, which affects the microstructural changes that occur during tempering. Martensite crystals form and grow on preferred planes, termed the habit planes, of the austenite phase. The habit planes and the orientation relationships depend on the composition of the alloys with the two well known being [19]:

$\{111\}_\gamma \| \{101\}_{\alpha'}$, $<110>_\gamma \| <111>_{\alpha'}$ with $\{225\}_\gamma$ habit planes (Kurdjumov–Sachs relationship) and $\{111\}_\gamma \| \{011\}_{\alpha'}$, $<112>_\gamma \| <011>_{\alpha'}$ with $\{259\}_\gamma$ habit planes (Greninger–Troiano relationship).

Depending on the austenite composition, martensite can occur in two principal morphologies: lath and plate. The hierarchical substructure of lath martensite is characterized by the subdivision of the austenite grain into packets made up of laths of common habit planes, where the packets are further subdivided into blocks that are made up of parallel laths with the same variant of the orientation relationship [19]. Fig. 6.6 shows micrographs of lath martensite in a plain carbon steel and Fig. 6.7 schematically shows the hierarchy of the martensitic substructure. The formation of thin laths minimizes the strain energy resulting from the high shear strains caused by the carbon supersaturation in the martensite. The process results in very high dislocation densities in lath martensite, of the order of 10^{14} m^{-2}, from the carbon supersaturation. In contrast to the laths that are parallel, the plates in martensites with the plate morphology are nonparallel. The impingement of plates with different variants of the orientation relationship results in microcracks, particularly in the larger plates [20].

The very high dislocation density of lath martensite is a result of the plastic deformation by slip, which occurs at higher temperatures in contrast with that by

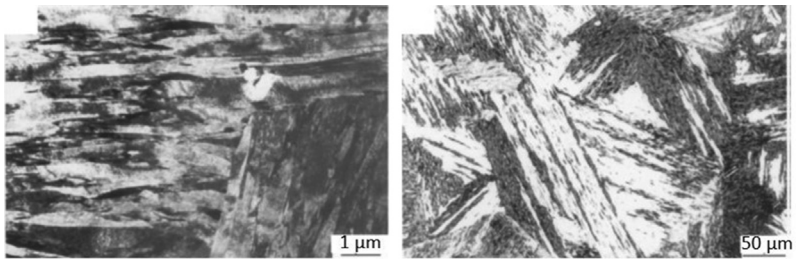


FIGURE 6.6

Micrographs showing lath martensite [19].

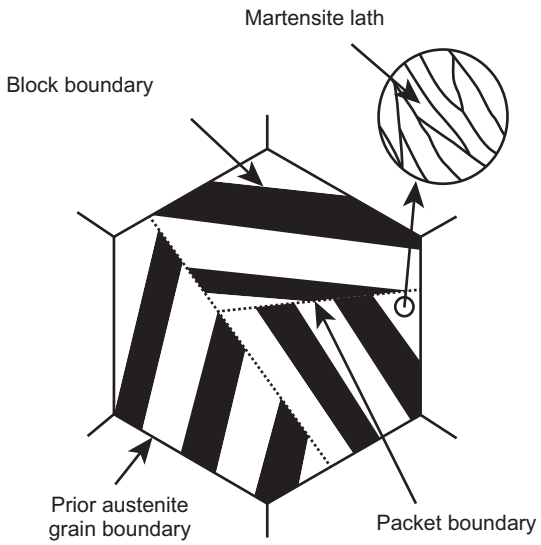


FIGURE 6.7

Schematic of lath martensite morphology [19].

twins that occurs at lower temperatures and constitutes the substructure of plate martensite. Thus higher M_s temperatures promote the formation of lath martensite. Commercial, UHS steels are generally designed to form lath martensite, which provides higher toughness compared with microstructures containing plate martensite.

6.3.2.2 Austenite

The FCC austenite (γ) phase plays a critical role in determining the property combinations of UHS steels. As the higher temperature phase with a larger solubility of alloying elements than the lower temperature ferrite, it offers the opportunity for solution heat treatment (austenitizing), quenching (for formation of martensite), and aging (tempering) to produce desirable microstructures. This approach for property development is like the process of precipitation hardening of aluminum alloys but occurs with a change in crystal structure of the lower temperature phase.

In the thermomechanically processed condition, steels contain undissolved carbides in MC-LA and SH-HA steels, intermetallic particles in PH-SS alloys and inclusions. The carbides are generally of the M_3C, $M_{23}C_6$, and M_7C_3 type, which need to be completely dissolved and reprecipitated as M_2C carbide particles with the required size distribution and spacing to provide optimum combinations of strength and toughness. The austenitization temperature should be high enough to dissolve all the primary carbides and intermetallic particles but not too high to promote excessive growth of the austenite grains. As will be discussed later, prior austenite grain size determines the packet and block sizes of the lath martensite, which affect the properties of the tempered steel [21].

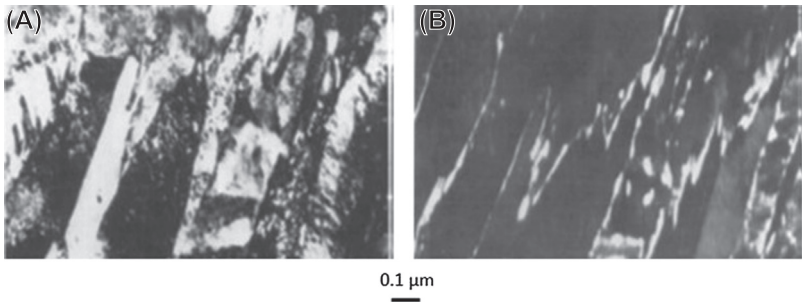


FIGURE 6.8

Transmission electron microscopy images of 300M, direct oil-quenched from 870°C (1600°F) showing retained austenite films surrounding martensite laths: (A) bright field image; (B) dark-field image of austenite reflection, showing contrast reversal [22].

Austenite can be retained in the quenched steel if the martensite transformation does not go to completion, with the amount depending on the M_s temperature and the quenching rate. The retained austenite volume fraction is less than about 0.04 in 300M steel quenched in oil from an austenitizing temperature of 870°C (1600°F) (corresponding to commercial practice) and is distributed as fine interlath films, as shown in Fig. 6.8 [22]. This amount increases to about 0.25 in the alloy slow cooled in air. The volume fraction of retained austenite in oil-quenched Aermet 100 is about 0.018, which transforms completely to martensite upon refrigeration, as practiced commercially [23]. Fig. 6.9A shows the microstructure of this steel consisting of martensite plates (the term "plate" rather than "lath" was used in this investigation because of their separation by high-angle boundaries) and twins with the absence of retained austenite due to the refrigeration. The martensite in

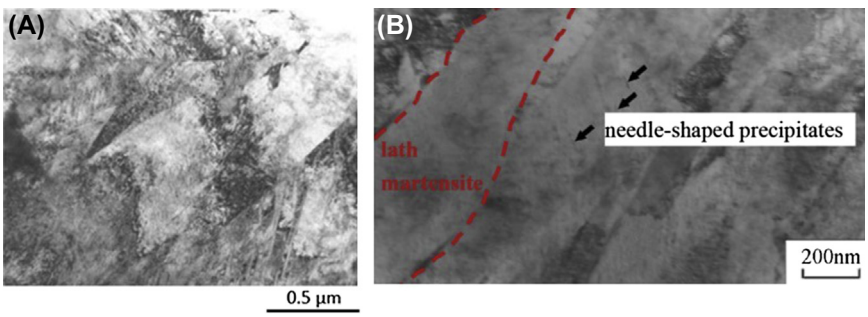


FIGURE 6.9

Transmission electron microscopy images of Aermet 100 (A) as oil-quenched and cryogenically treated [23] and (B) after tempering at 477°C (890°F) 6.5 h [24].

Aermet 100 with its low C content is, however, considered to be lath type, as shown in Fig. 6.9B.

In contrast to its retention upon quenching, austenite can also form in highly alloyed steels during tempering in a certain temperature range. Fig. 6.10 shows this "reverted" austenite that formed along martensite plate boundaries in Aermet 100 [23]. The defocused, bright field image (Fig. 6.10B) and the corresponding dark field image (Fig. 6.10C) show the reverted austenite very clearly. Formation of this phase has been shown to be accompanied by its enrichment with Ni and Cr and depletion of Co in an alloy with a composition close to Aermet 100 [25].

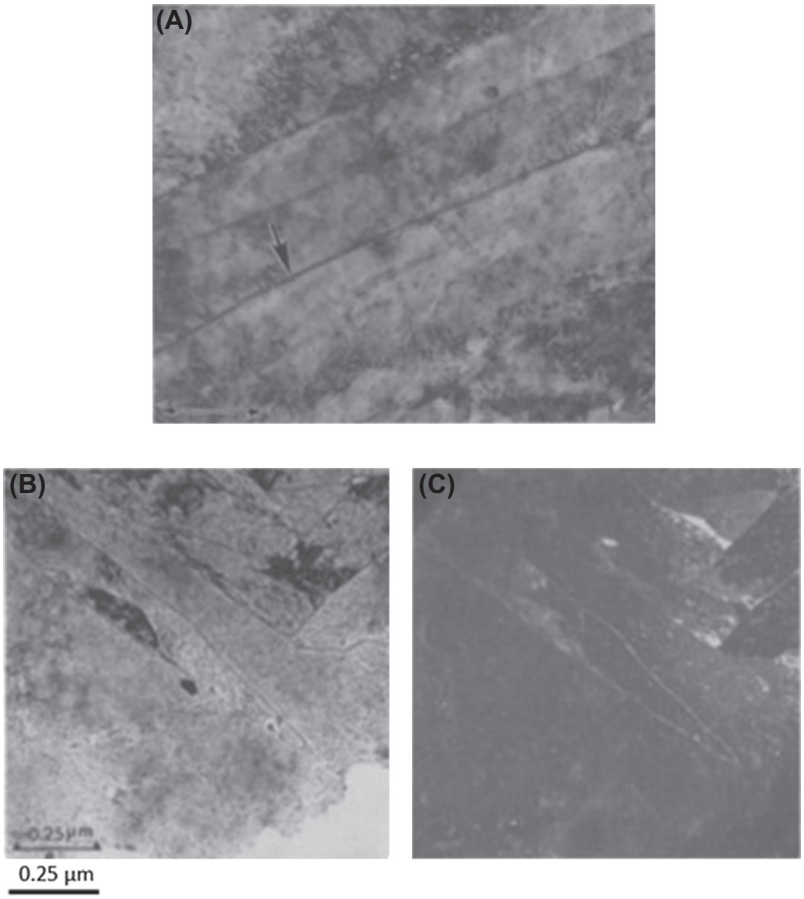


FIGURE 6.10

Reverted austenite formation during tempering at 482°C (900°F): (A) bright-field image showing austenite (*arrow*), (B) defocused bright-field image, and (C) corresponding dark-field image showing reversal of contrast of austenite [23].

6.3.2.3 Second-Phase Particles

The second-phase particles in UHS steels include (1) nonmetallic inclusions arising from melting whose morphologies and distribution are determined by subsequent TMP, (2) carbides and intermetallics remaining undissolved during austenitizing (solution heat treatment), and (3) carbides and intermetallic particles that precipitate during aging and tempering. Examples of some of the second-phase particles occurring in UHS steels and their characteristics are listed in Table 6.4.

Oxides arising from melt processing and sulfides formed by the addition of various elements to prevent the formation of FeS, which reduces the hot workability, are the principal nonmetallic inclusions in steels [26]. As with commercial aluminum alloys, these inclusions have deleterious effects on the transverse properties, fracture toughness, and fatigue behavior. Although fracture in both aluminum alloys and UHS steels is caused by flow localization, void nucleation, growth, and coalescence, the only way to improve the toughness of aluminum alloys (for a given microstructure) is by increasing its purity by lowering Fe and Si, thereby reducing the volume fraction of the constituents, which once formed cannot be dissolved. Use of vacuum melting, deoxidation, and desulfurization treatments has significantly reduced the presence of these inclusions in UHS steels. The volume fraction of carbide inclusions can be reduced to some extent by raising the temperature of austenitization. This is similar to the dissolution of soluble constituents by increasing the solution heat treatment temperature of Al alloys.

Precipitation can also occur during quenching (auto tempering) in steels with sufficiently high M_s. Phases that precipitate and harden the carbide-strengthened steels are the ε carbides in low-alloy and M_2C type carbides in high-alloy steels. The identity of the intermetallic particles that precipitate and strengthen PH-SS alloys depends on their composition, e.g., NiAl in PH 13-8 Mo and a Cu-rich phase in 15-5 PH steels.

Table 6.4 Second Phase Particles in Ultrahigh Strength Steels

Alloy	Particle Type	Size	Volume Fraction (%)
4340	MnS inclusion (stringer)	~10–50 μm long ~2 μm wide	~0.2
4340 (desulfurized)	MnS inclusion (stringer)	~5 μm long ~2 μm wide	~0.04
AF 1410	CrS inclusion	~0.2 μm	~0.03
AF 1410 (La modified)	La_2O_2S inclusion	~0.6 μm	~0.04
4340, 300M	ε carbide precipitate	~2–10 nm	~1
AF 1410	M_2C precipitate	~2–10 nm	~1
PH 13-8 Mo	NiAl, Ni_3Mo precipitate	~2–10 nm	~1

6.3.3 COMPOSITION–PROCESSING–MICROSTRUCTURE RELATIONSHIPS IN ULTRAHIGH STRENGTH STEELS

The phases and microstructural features that affect the properties of UHS steels evolve through all stages of their processing, as discussed earlier (Table 6.3). Table 6.5 shows the processing–microstructure relationships for the MC-LA steels, which will be described first and then used as a basis to discuss the improvements in SH-HA and PH-SS alloys.

MC-LA steels with much better cleanliness and lower impurity content are produced by vacuum induction melting along with secondary refining methods such as vacuum arc remelting and electroslag refining, resulting in improved properties. However, the sulfide and oxide inclusions and impurities will not be eliminated completely and will affect the microstructure and properties. The distribution and alignment of the inclusions along the working direction of the ingot will reduce ductility in the transverse direction, analogous to the effects of inclusions on the anisotropy of the mechanical properties of aluminum alloys.

Austenitization temperature and time determine the austenite grain size, which affects the M_s temperature, the martensite morphology, and eventually the properties of the tempered alloy. They also determine the extent of dissolution of the primary carbides with an indirect effect on M_s as determined by the amount of C in solution during quenching. The impurity element P segregates to the austenite grain boundary and causes embrittlement in conjunction with the formation of cementite at the prior austenite grain boundaries during tempering (Fig. 6.4). At sufficiently high values of M_s, carbides can precipitate during the quench (auto tempering). M_s also affects the amount of retained austenite in the quenched alloy. Tempering conditions determine the nature and distribution of carbides that form and affect properties.

Significant advances have been made in the ability to predictively model the phase evolution and relationships in Ultrahigh Strength steels [27,28].

Table 6.5 Evolution of Microstructural Features in MC-LA Ultrahigh Strength Steels

Processing Step	Phases and Microstructural Features
Melting (refining/deoxidation) and solidification	Inclusions Microsegregation of alloying elements
Thermomechanical processing	Morphology and distribution of inclusions
Austenitizing	Austenite grain size Undissolved carbides Segregation of impurities to grain boundaries
Quenching	Carbides formed during quench (auto tempering) Martensite and its morphology
Tempering	Carbides (type depending on tempering temperature)

Thermodynamic/kinetic modeling can simulate microsegregation and enable the design of homogenization treatment for ingots, as has been demonstrated successfully for the SH-HA, Aermet 100 steel using the ThermoCalc and Dictra software [29]. Similarly, using thermodynamic databases for carbides, the austenitization time and temperature required to achieve the complete dissolution of carbides can be estimated. Some of the important alloy characteristics and metallurgy are discussed in the following.

6.3.3.1 Modeling of M_s Temperature

M_s affects the martensite morphology, with the desirable lath type favored by higher temperatures. Thus the capability for predicting M_s is important for alloy design. Alloying elements, except Co and Al, depress M_s. Many empirical models have been developed for estimating M_s as a function of composition, one of the most recent being (for an alloy with C, Mn, Si, Cr, Ni, Mo, V, Co, Al, Cu, Nb, Ti, and B in wt%) [30]:

$$\begin{aligned}\mathrm{M_s}\ (^\circ\mathrm{C}) = {} & 545 - 601.2(1 - \mathrm{e}^{-0.868\mathrm{C}}) - 34.4\mathrm{Mn} \\ & - 13.7\mathrm{Si} - 9.2\mathrm{Cr} - 17.3\mathrm{Ni} - 15.4\mathrm{M}\% + 10.8\% \\ & + 4.7\mathrm{Co} - 1.4\mathrm{Al} - 16.3\mathrm{Cu}\% - 361\mathrm{Nb} - 2.44\mathrm{Ti} - 3448\mathrm{B}.\end{aligned}$$

This relationship has been obtained empirically from a database of M_s temperatures for 1000 different compositions. M_s for a given alloy will decrease with decreasing austenite grain size and the following equation has been developed to relate these [31]:

$$M_S^\circ - T = \left(\frac{1}{b}\right)\ln\left[\left(\frac{1}{(aV_\gamma)}\right)\left\{\exp\left(-\frac{\ln[(1-f)]}{m}\right) - 1\right\} + 1\right]$$

where M_S° is the highest temperature at which martensite can form, V_γ is the average austenite grain volume (measure of grain size), m is the aspect ratio of martensite plates, f is volume fraction of martensite, and a and b are empirical fitting constants. In this relationship, T becomes M_s when f becomes the first detectable martensite volume fraction and $M_s \rightarrow M_S^\circ$ when $V_\gamma \rightarrow \infty$. This equation has been used to develop the following relationship for M_s as a function of both austenite grain size and composition for an alloy with C, Mn, Si, Ni, Cr, Mo, and Cu, in wt% [32]:

$$\begin{aligned}\mathrm{M_s}\ (^\circ\mathrm{C}) = {} & 475.9 - 335.1\mathrm{C} - 34.5\mathrm{Mn} - 1.3\mathrm{Si} - 13.1\mathrm{Cr} \\ & - 15.5\mathrm{Ni} - 10.7\mathrm{Mo} - 9.6\mathrm{Cu} + 11.67\ \ln(\mathrm{d}_\gamma),\end{aligned}$$

where d_γ is the average austenite grain diameter.

Given the varieties of steels in commercial use, many empirical models, such as described above, have been developed for the prediction of M_s. However, these models have limited applicability and are generally valid only for alloys in the range of compositions corresponding to the data used in their formulation [33]. Artificial neural network models with the ability to delineate the effects of individual or a combination of alloying elements on the M_s have also been developed [34].

Models for M_s that are based on thermodynamics balance the barrier and the available driving force for the martensitic transformation, which depend on its mechanisms and the difference in the Gibbs free energy between the austenite and martensite phases, respectively [35]. The driving force is a function of temperature for a given composition of steel and the transformation cannot occur until it overcomes the barrier. In one such model, the barrier to the nucleation and growth of martensite is calculated as the lattice friction in the solid solution strengthened matrix that must be overcome by the interfacial dislocations nucleating the martensite embryo [36]. Using a multicomponent thermodynamic database to calculate the Gibbs free energy difference between the austenite and martensite phases, this model has demonstrated the ability to predict the M_s temperature with an accuracy of $\pm 40^{\circ}$C ($\pm 72^{\circ}$F). More recently, using data from rapid cooling experiments, barriers for the formation of lath and plate martensite have been estimated for binary alloys [35]. In conjunction with thermodynamic calculations of the driving force, M_s temperatures for commercial steels have been predicted with an accuracy at least as good as that for the experimental measurements. The evaluation of neural network and thermodynamic models using experimentally determined M_s available for many steels has demonstrated the advantages of combining the two into a hybrid model [37].

6.3.3.2 Hardenability

As with aluminum and titanium alloys discussed in previous chapters, hardenability is an important attribute for steels in terms of achieving complete martensitic transformation through the thickness of the quenched part. In practice, there will always be some, however small, amount of austenite retained after the quench. Hardenability is then defined as the "capacity to transform partially or completely to some percentage of martensite at a given depth when cooled under some given conditions" [38]. Increased hardenability allows slower quench rates to be used thereby reducing the possibility of cracking of the product. Hardenability of a given steel also depends upon the condition of austenitization through its effect on M_s, which determines the solute content in the austenite and its grain size, as discussed earlier. Many commercial software packages are available for estimating the hardenability of steels. All the alloying elements used in UHS steels increase hardenability to varying degrees by shifting the time−temperature−transformation diagrams to the right. These steels have deep hardenability and landing gear parts are typically quenched in oil or by high pressure gas [39]. In practice, depending on the part thickness, some steels are hardened by quenching in air.

6.3.3.3 Tempering

Tempering is the final step in the heat treatment of steels during which a wide range of microstructures (Table 6.2) and combinations of strength and toughness can be achieved, as shown for 4340 in Figs. 6.3 and 6.4 and for 300M in Fig. 6.5. Although 4340 can be tempered in the range of 200−650°C (400−1200°F) (with consideration given to occurrence of tempered martensite embrittlement), 300M is typically

tempered in the range of 260–315°C (500–600°F) to achieve the best combination of properties. Because of the retardation of cementite precipitation due to the Si additions, this alloy develops high strength from the precipitation of ε carbide.

Secondary hardening steels are strengthened by the precipitation of nanometer-sized M_2C carbides, as shown for Aermet 100 steel in Fig. 6.11 [40]. Aging in the temperature range of 454–482°C (850–900°F) results in peak strength with overaging occurring upon aging at 510°C (950°F) and higher. The carbides are needle shaped and about 5 nm long in the peak aged condition, which grow to between 13 and 20 mm in length upon overaging.

Fig. 6.12 shows the evolution of the characteristics of the M_2C carbides in AF 1410 steel, quantified by several advanced techniques, during tempering at the standard temperature of 510°C (950°F) to achieve the desired combination of strength and toughness [27]. The hardness begins to decrease and overaging begins at a particle size of about 5 nm and the precipitates become incoherent at a size of about 10 nm. Carbides in SH-HA steels contain multiple alloying elements and provide only a narrow range of time and temperature in the fourth stage of tempering to achieve the optimum levels of strength and toughness. Accordingly, significant effort has been undertaken to characterize and model the precipitation and coarsening behavior of these carbide phases in secondary hardening steels. Such an

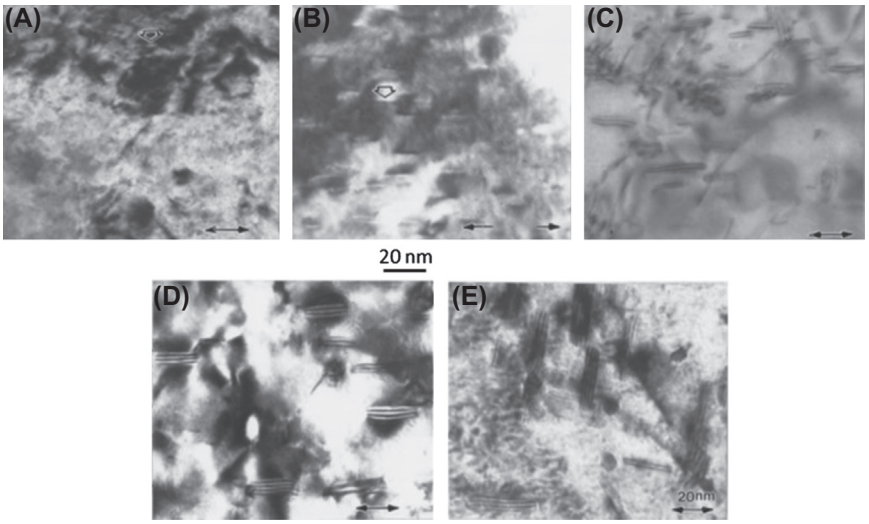


FIGURE 6.11

Bright-field images taken near $[001]_\alpha$ orientation for samples aged at (A) 454°C (850°F) (B) 482°C (900°F), (C) 510°C (950°F), (D) 538°C (1000°F), and (E) 565°C (1050°F). The $[100]_\alpha$ direction for all the images is along the horizontal axis. (A) and (B) show strain contrast from the needles (*arrows*), whereas fringes are seen in (C) through (E) [40].

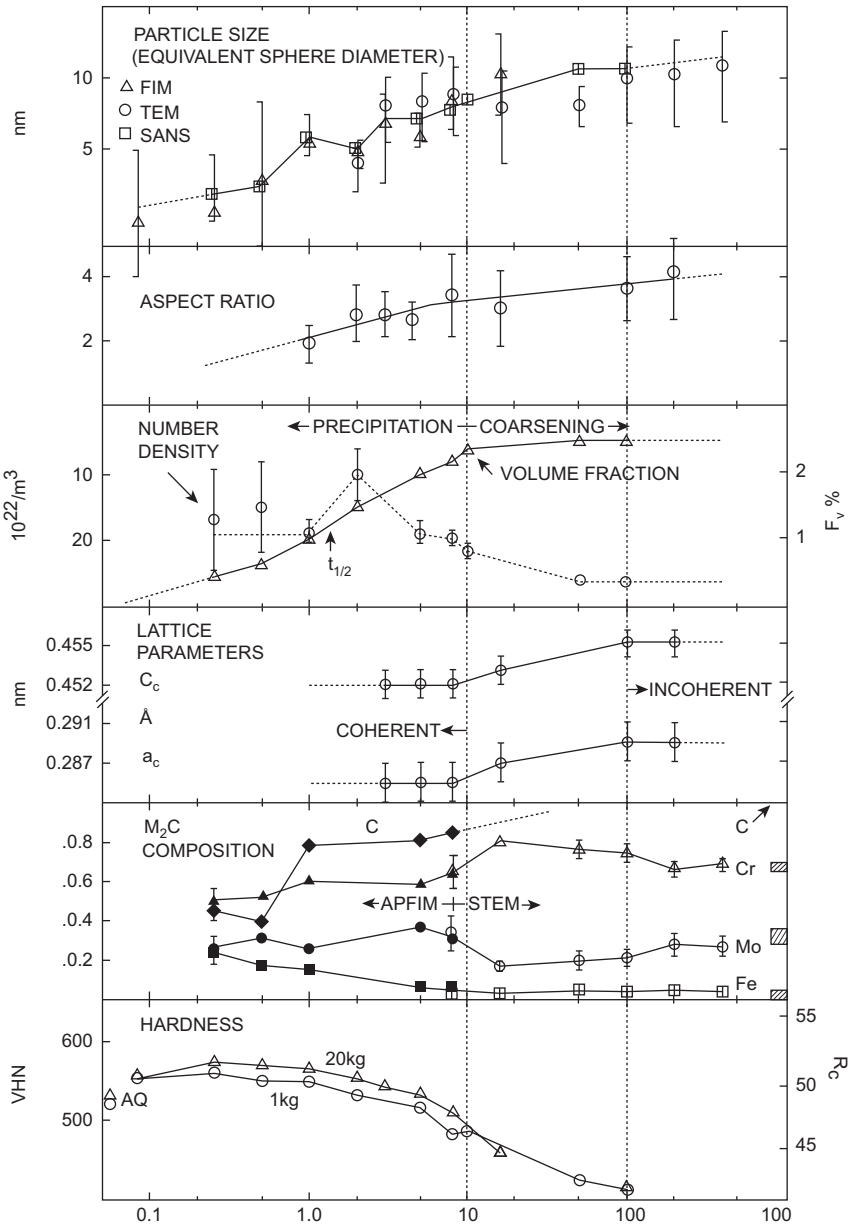


FIGURE 6.12

Characteristics of M_2C carbides in AF 1410 steel as a function of time for tempering at 510°C (950°F) [27].

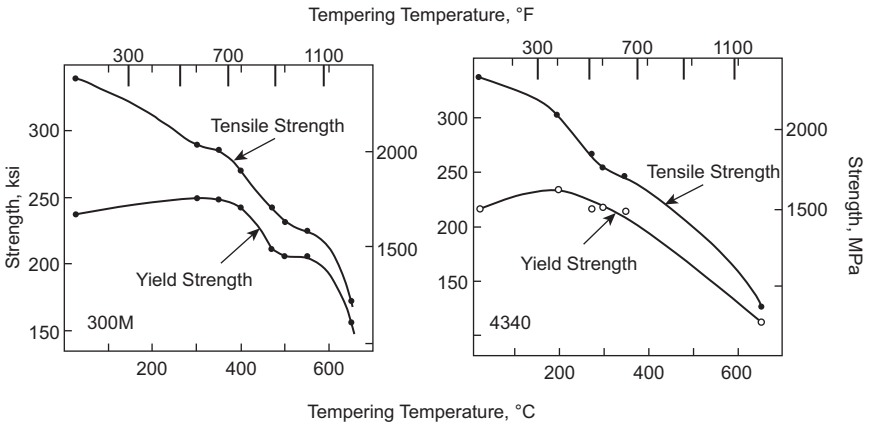


FIGURE 6.13

Tensile properties of 4340 and 300M alloys, austenitized at 870°C (1600°F) for 1 h, quenched in oil, and tempered for 1 h at various temperatures [22].

approach has determined the optimum carbide size to be 3 nm in diameter and has enabled a strength increase of 50% compared with earlier secondary hardening steels with similar levels of C.

The martensitic, semiaustenitic, and austenitic PH-SSs are all solution treated, quenched, and aged at temperatures and for times depending on the alloy to precipitate the strengthening intermetallic phases. The processing, microstructure, and properties of these alloys will be discussed in detail with reference to specific alloy compositions. Additional considerations regarding tempering include the need to prevent the occurrence of both temper and tempered martensite embrittlement and the effects of the precipitation of "reverted" austenite and any further transformation of the retained austenite.

6.4 PROPERTIES OF ULTRAHIGH STRENGTH STEELS AND THEIR RELATIONSHIPS TO COMPOSITION, PROCESSING, AND MICROSTRUCTURE

This section discusses the important properties for UHS steels, their dependence on microstructure, and the extent to which they can be modeled. These steels are selected primarily for the very high strength levels along with the required toughness and resistance to degradation in service environments that they exhibit. Steels have been in use longer than any other metallic structural material and thus a large amount of information on their microstructure and properties is available. This has enabled the development and application of many empirical models, which have also been

very helpful for the mechanistic understanding of the microstructure–properties relationships and for the computational design of new alloys.

6.4.1 STRENGTH

Relationships have been developed for predicting the hardness of tempered, low alloy steels containing one or more of C, Mn, P, Si, Ni, Cr, Mo, and V, from an experimentally determined database of the tempering behavior of binary Fe–C, ternary Fe–C–Mn, and quaternary, Fe–C–Mn–X (X being one of the other elements) alloys [41]. Hardness of any alloy with selected alloying elements and compositions in the range investigated can be calculated from this database. The relationship has been validated by the very close agreement between the calculated and measured hardness of 4340 under identical tempering conditions [42]. These empirical relationships are useful for quality control, e.g., for determining slack quench, but do not provide any insight into the mechanisms of strengthening.

6.4.1.1 Medium Carbon, Low Alloy Steels

The strength of quenched and tempered martensitic steels results from the superposition of the contributions from lattice friction, dislocation density, size effects of the hierarchical features of the martensite substructure, solid solution hardening, and precipitation hardening. All these factors except precipitation hardening contribute to the strength of the as-quenched steels. The size of the packets and blocks, which are separated by high angle boundaries, in the martensite substructure is affected by the prior austenite grain size. In MC-LA and SH-HA steels, recovery of the substructure and precipitation of carbides proceed through the tempering stages and the yield strength of martensite can be predicted from the strengthening arising from block boundaries, dislocation density, and the carbides [21].

As tempering proceeds, strengthening from carbide precipitation is offset by the matrix recovery and the reduction of both dislocation density and solid solution contribution. For 4340 and 300M steels, peak strength occurs upon tempering at about 200°C (~400°F) and 300°C (~575°F), respectively, as shown in Fig. 6.13 [22]. These steels are strengthened by the transition, ε carbide. Precipitation of cementite and recovery of the substructure, both lead to rapid loss of strength. The peak strength for 300M occurs at the higher temperature due to the retardation of cementite precipitation by the addition of Si, as discussed already. For both steels, strength continues to decrease with increasing tempering temperature due to the coarsening of cementite and continued reduction in the dislocation density.

Early studies of medium and high C, low alloy martensitic steels have shown that all the C has precipitated as carbides upon tempering at 250°C (~480°C) for 1 h and that the lath structure is retained up to about 450°C (~840°C) and replaced by a dislocation substructure at higher temperatures [43]. Dislocation density in the lath structure decreases with increasing temperature, although it has been estimated to contribute to about a third of the yield strength for tempering up to about 450°C (~840°F). The carbides coarsen progressively starting at 250°C (~480°F) and

spheroidize beyond about 550°C (1020°F). This study developed the following expression for the yield stress of tempered Fe−0.42C−0.11Mn−0.22Si−0.13 Mo−0.07S−0.011P alloy:

$$\sigma_y = \sigma_o + 2\alpha G b \rho^{\frac{1}{2}} + \left(\frac{Gb}{2\pi\lambda}\right)\left(1 + \frac{1}{1-\nu}\right)\ln\left(\frac{\lambda}{2b}\right)$$

where σ_y is the yield stress, σ_o is the friction stress (~343 MPa, 50 ksi), α is a coefficient (~0.4), G is the shear modulus, b is the Burgers vector, ρ is the dislocation density, ν is the Poisson's ratio, and λ is the spacing of the carbide particles.

Strengthening contributions from the carbides and the dislocation substructure have been considered mutually dependent because they change simultaneously with increasing tempering temperature and together contribute to more than 70% of the strength. Considering these factors, the following expression has been derived for the yield stress of 4340 [13]:

$$\sigma_y = \sigma_o + 126\, M^{-1} + 68\lambda^{-1}$$

where σ_o (~572 MPa, 83 ksi) includes solid solution hardening, M is the average cell width, λ is the average particle spacing, and the other factors are as described earlier.

Many expressions have been proposed for predicting the strength of MC-LA steels showing that the effects of microstructural features that contribute to the strength of tempered martensite are amenable to mechanistic modeling. The challenges are to delineate the contributions from the various features and how they superpose to determine the flow stress, and the difficulty in experimentally characterizing them for model validation.

6.4.1.2 Secondary Hardening, High Alloy Steels

Tempering conditions that produce high levels of toughness in MC-LA steels also reduce strength significantly. SH-HA steels develop better combinations of strength and toughness by the precipitation of alloy carbides during the fourth stage of tempering. Mo and Cr are the carbide forming elements used in the secondary hardening steels (Table 6.1). The approach to the selection of alloying elements for these steels was discussed earlier. The effects of tempering on the hardness and strength of an Fe−10Ni−8Co−2Cr−1Mo steel with various levels of C are shown in Fig. 6.14 [17].

During tempering at temperatures below 425°C (800°F), strength decreases due to the precipitation of $(Fe,Mo,Cr)_3C$. Strength increases up to the peak in the secondary hardening range (425−540°C, 800−1000°F) is due to the dissolution of M_3C and the precipitation of $(Mo,Cr)_2C$. The decrease in strength beyond the peak (540−650°C, 1000−1200°F) is caused by coarsening of the alloy carbide, annealing of the substructure, and the formation of austenite that is stable upon cooling to room temperature. Hardness increases upon tempering at temperatures higher than 650°C (1200°F) is caused by the transformation of the low alloy content austenite that formed during tempering to martensite upon cooling. The contributions to yield

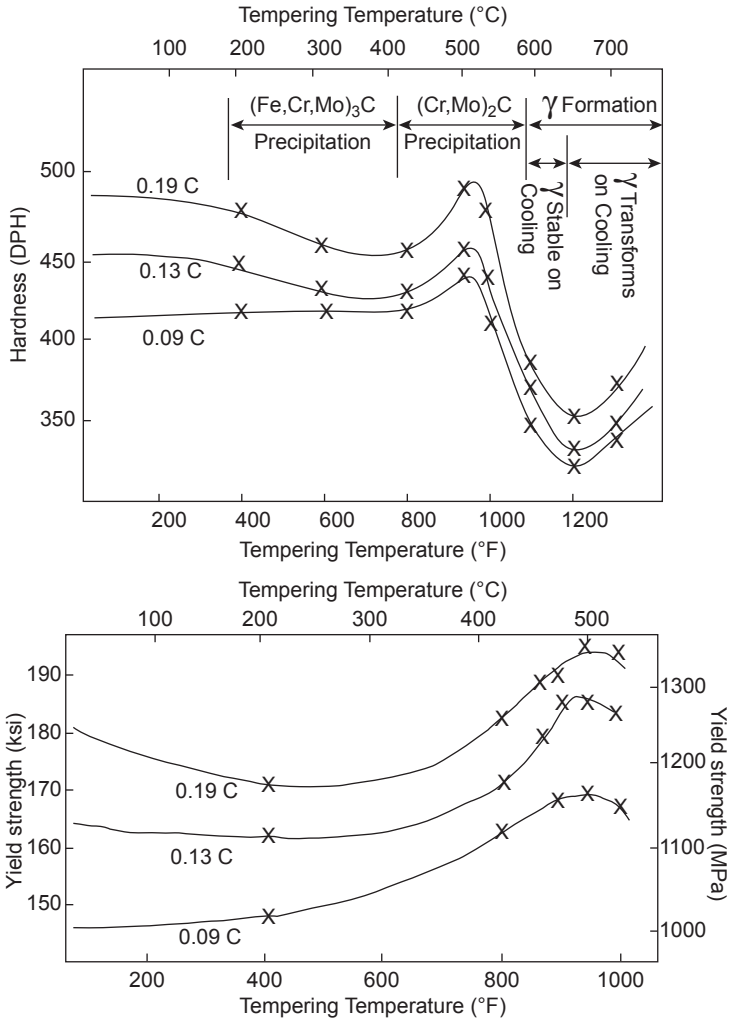


FIGURE 6.14

Effect of tempering for 1 h at various temperatures on the mechanical properties of Fe—10Ni—8Co—2Cr—1Mo steel with various C levels.

Adapted from G.R. Speich, D.S. Dabkowski, L.F. Porter, Strength and toughness of Fe-10Ni alloys containing C, Cr, Mo, and Co, Metallurgical Transactions 4 (1973) 303–315.

strength from the microstructural features for these steels have been represented as [17]:

$$\sigma_y = \sigma_o + 5.9\, GbdD^{-1} + 0.5\, Gb\lambda^{-1} + \sigma_{ss}$$

where, σ_y, σ_o, σ_{ss} are the yield stress of the alloy, lattice friction stress, and contribution from solid solution strengthening, respectively, G is the shear modulus, b is the Burgers vector, D is the dislocation cell size, and λ is the spacing of the carbide particles. This equation is similar to that for MC-LA steels earlier, except for the addition of the term for solid solution hardening. The carbide particles nucleate at dislocations and λ is at least two orders of magnitude smaller than the dislocation cell size. Thus the strengthening of these steels comes predominantly from the contributions by carbide particles. In addition, the range of time and temperature for achieving peak strength in these types of steels is very narrow, as seen from Figs. 6.12 and 6.14. The temperature should be sufficiently high for $(Mo,Cr)_2C$ formation (fourth stage of tempering) but not too high to anneal the dislocation substructure. Th carbides coarsen very rapidly and cause overaging within very short aging times beyond the peak aging condition.

All the SH-HA steels contain Co, which retards recovery and accelerates the heterogeneous nucleation of alloy carbides during secondary hardening and Ni, which promotes toughness and increases hardenability. Considerable effort has been undertaken to optimize the size, distribution, and volume fraction of the carbides to achieve maximum strength in conjunction with the required toughness and environmental resistance in these alloys, as will be discussed in the sections describing alloys designed conventionally and by computational methods.

C has a significant effect in contributing to the strength of SH-HA steels, as shown in Fig. 6.15 [44], which compares the strength properties of several UHS steels heat treated under conditions typically used in practice. The nominal C level

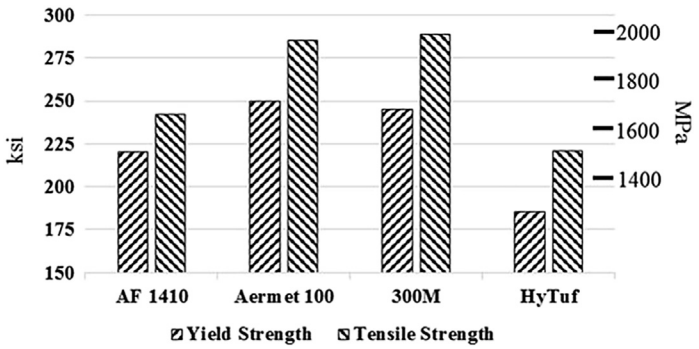


FIGURE 6.15

Typical strength of ultrahigh strength steels.

Adapted from P.M. Novotny, T.J. McCaffrey, An Advanced Alloy for Landing Gear and Aircraft Structural Applications—Aermet® 100 Alloy, SAE Technical Paper Series 922040, AeroTech '92, Anaheim, CA, 1992.

of Aermet 100 and AF 1410 are 0.23 and 0.16 wt%, respectively, and the strength of Aermet 100 is much higher. Alloy carbides along with the presence of Ni and Co also provide equivalent strength at lower C content, as seen by comparing the strength of Aermet 100 with that of 300M. The strength of 300M (0.4 wt% C) is higher than that of HyTuf (0.25 wt% C).

6.4.1.3 Precipitation Hardening, Stainless Steels

The PH-SS alloys used in airframes are principally the martensitic type (Table 6.1). All these alloys are precipitation hardened by various intermetallic compounds determined by the alloying additions. A range of strength and toughness combinations can be obtained by quenching to form lath martensite followed by aging under various conditions. For e.g., alloy 17-4 PH attains peak strength upon aging at 482°C (900°F). Due to the extremely fine nature of the strengthening precipitates, the microstructural changes occurring upon aging these steels are only beginning to be characterized. 17-4 PH and 15-5 PH are strengthened by Cu-enriched precipitates and PH 13-8 Mo by the NiAl phase [45]. Strength of these alloys can also be increased by introducing cold work following solution treatment (austenitizing) and prior to aging.

Precipitation hardening mechanisms in PH-SS alloys are like those observed in aluminum alloys discussed in an earlier chapter and are thus amenable to modeling of their flow stress. The increase in flow stress for PH 13-8 alloy calculated from a superposition of contributions from the coherency, modulus, and order of NiAl precipitates was found to be lower than the experimentally measured values [46]. Formation of austenite particles during aging that remained stable upon cooling contributed to the flow stress explaining the underestimation of the calculated values.

6.4.2 DUCTILITY

The strength—ductility relationships for UHS steels generally follow the trends expected for structural materials, with the absolute values of ductility adequate for structural applications. Inclusions play a significant role in affecting ductility, particularly in the transverse direction. This is illustrated by comparing the properties of air melted and vacuum arc melted 4340 and 300M steels, as shown in Fig. 6.16 [16].

The cleaner microstructure produced by vacuum arc remelting results in better transverse ductility, particularly the reduction of area, for all tempering temperatures, although strength is affected very little. All Mn containing alloys have MnS inclusions, which tend to be drawn in the direction of working. The ductility of vacuum remelted steels can be increased further by decreasing the volume fraction of the lenticular MnS particles as well as by changing the type and morphology of inclusions to spherical, rare earth sulfides by adding Ce and La. Both the long transverse and short transverse (through-thickness direction) ductility of vacuum melted 4340 steel have been improved this way [47]. The beneficial effect on ductility is much higher for the short transverse direction compared with the other orientations.

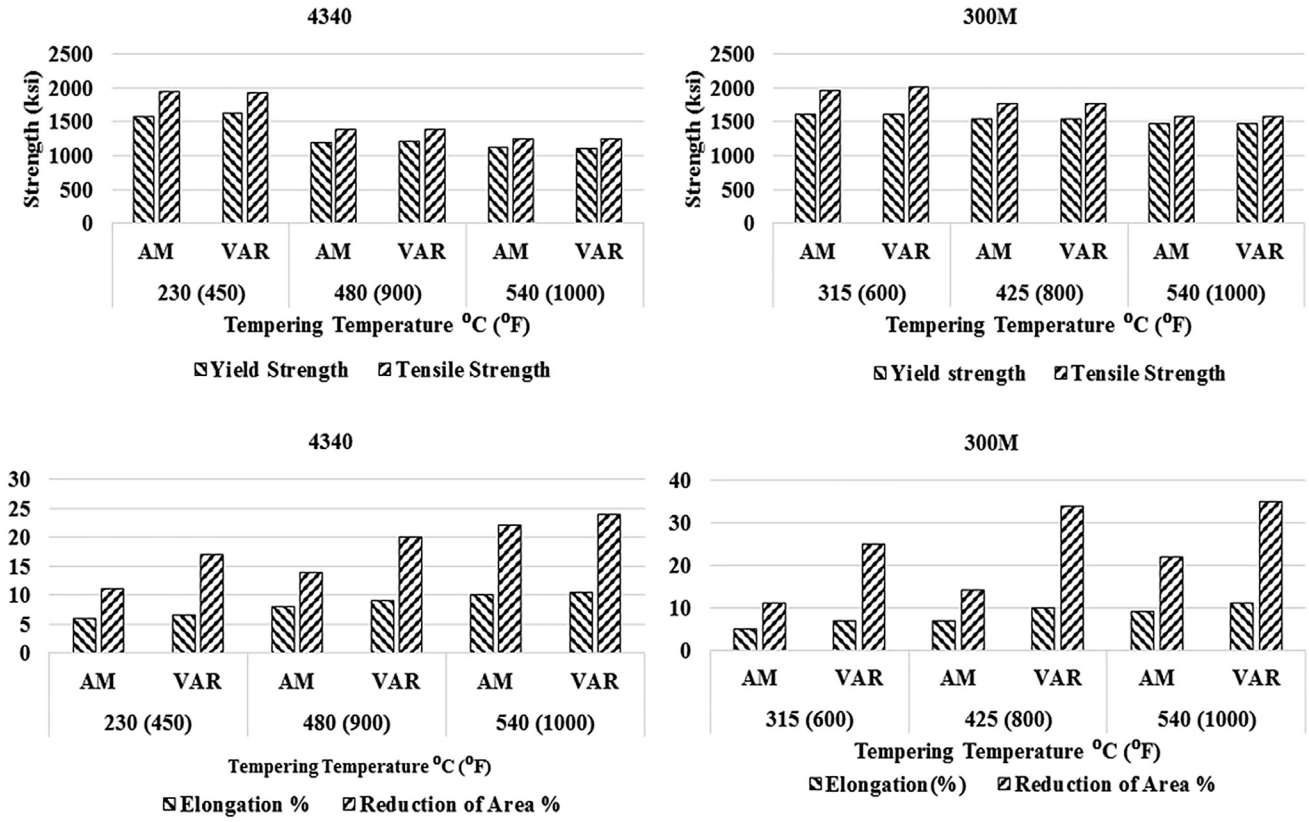


FIGURE 6.16

Effect of melting practice on transverse tensile properties of ultrahigh strength steels. *AM*, air melted; *VAR*, vacuum arc remelted [16].

6.4.3 TOUGHNESS

UHS steels with combinations of strength and toughness superior to those of alloys 4340 and 300M are Ni−Co steels containing sufficient C additions and the carbide forming elements Cr and Mo for secondary hardening. Two such families of steels introduced in the 1960s and 1970s were the HP-9-4-X (9Ni−4Co) series and alloys with additions of 10 wt% Ni and higher amounts of Co (HY-180 and AF 1410). Although these alloys were being developed, significant activity was already underway to understand the fracture behavior of MC-LA steels and to improve their toughness through ancillary alloying additions and control of melting, which will be discussed first and followed by the fracture behavior of the high alloy steels.

6.4.3.1 Medium Carbon, Low Alloy Steels

Microstructural features that affect the toughness of MC-LA steels are the prior austenite grain boundaries, which sometimes contain segregated impurity atoms and carbide allotriomorphs, inclusions, carbides undissolved during austenitizing, retained austenite, precipitated transition carbides and the martensite substructure [48]. The extent of tempering performed to achieve the desired strength level determines the martensite substructure and the size and volume fraction of the strengthening transition carbides. The effects of these features generally follow the strength−toughness relationships typical of precipitation hardened alloys, such as aluminum alloys, except for the effects of tempered martensite embrittlement, discussed later.

Steels for use in critical airframe structures are always melted in vacuum, which along with follow up vacuum arc remelting or electroslag refining, provides cleaner materials with lower inclusion content. These primary inclusions, typically greater than about 1 μm in size, initiate cracks by nucleating voids during loading, and reducing their volume fraction increases fracture toughness. This behavior is similar to the observed increase in the toughness of aluminum alloys with decreasing volume fraction of constituent particles achieved by reducing the amounts of Fe and Si impurities, as discussed in Chapter 4. The primary inclusions in steels are MnS, whose volume fraction is reduced by lowering the S content of steel, as shown by the study in which the volume decreased from 0.168% to 0.038% with decrease of S from 0.016 to 0.002 wt% in 4340 steel of otherwise equivalent composition [49]. This study also showed that changing the MnS morphology and distribution from stringers to elliptical shape with aspect ratios of 17.5 and 3.8, respectively, increased K_{Ic} of 4340 in both the rolling and transverse directions. In addition, altering the type and morphologies of sulfides by using rear earth element additions also has a beneficial effect on toughness.

In quenched and tempered steels like 4340, the growth of voids nucleating from the primary inclusion is interrupted by void sheets composed of smaller voids nucleating at secondary particles (<1 μm) such as the cementite precipitates (Fig. 6.17) [50].

This process is again like the link up of voids nucleated at the constituent particles by the smaller voids nucleated by the dispersoids in aluminum alloys. Although

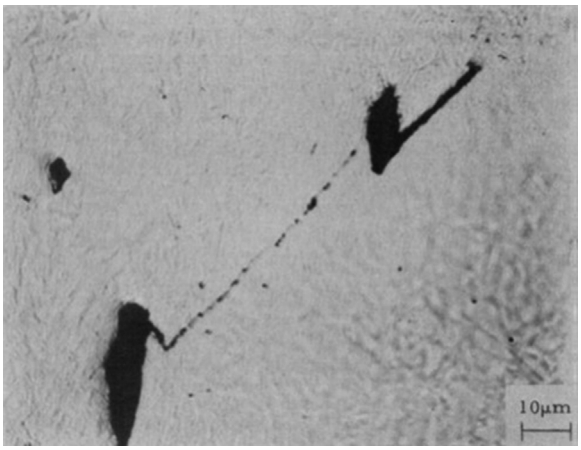


FIGURE 6.17

Void coalescence by void sheet formation in 4340 steel [50].

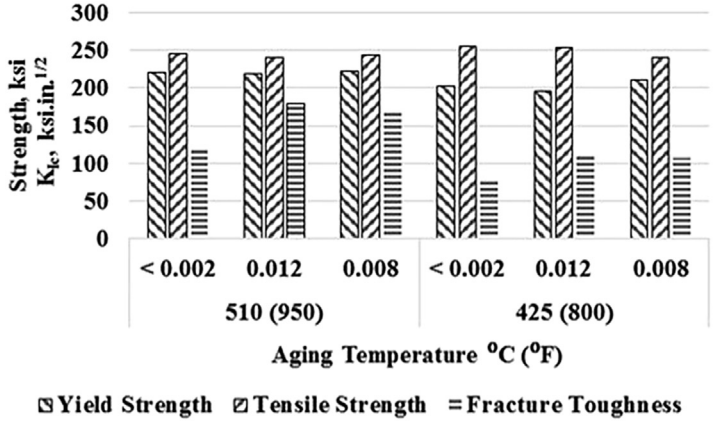
dispersoid forming elements are added to aluminum alloys specifically to control the degree of recrystallization and grain growth, many types of secondary particles occur in steels, which are not always present by design. Secondary particles also have an effect in controlling the grain size during austenitization, thereby having an indirect effect on toughness. The effects of the type, volume fraction, spacing, and distribution of both primary inclusions and secondary particles have been studied in detail for secondary hardening, high alloy steels, as will be discussed next.

6.4.3.2 Secondary Hardening, High Alloy Steels

The goal of developing these steels is to achieve toughness levels higher than those of low alloy steels, preferably at similar or without much of a sacrifice in strength. Accordingly, the effects of processing and microstructure of the secondary hardening steels have received significant attention. The factors that affect the toughness of these steels are generally the same as those for low alloy steels with the addition of the contribution from the alloy carbides that form during secondary hardening.

The fracture process in secondary hardening steels begins with the nucleation of voids at the primary inclusions and proceeds by their growth and coalescence facilitated by the smaller voids that nucleate from the secondary particles. Both the volume fraction and the spacing of the primary particles influence toughness. The secondary hardening steels either have no Mn additions (AF 1410, Aermet 100) or much lower levels (HY-180, HP-9-4-X) than in the low alloy steels (4340 and 300M). The primary inclusions in AF1410 and Aermet 100 would be CrS and not MnS.

The effect of varying inclusion spacing on the fracture toughness of AF 1410 was determined by studying the alloy with and without La [4]. The La content, inclusion characteristics and properties of these alloys, is shown in Fig. 6.18.



La Content (wt.%)	Inclusions			
	Primary Type	Volume Fraction	Average Radius (μm)	Average Spacing (μm)
< 0.002	CrS	0.00034	0.18	2.3
0.012	La_2O_2S	0.00042	0.64	7.6
0.008	La_2O_2S	0.00036	1.24	15.4

La Content (wt.%)	Aging Temperature °C (°F)	Strain to Fracture	δ_{fc} (μm)
< 0.002	510 (950)	1.16	28
	425 (800)	0.94	12
0.012	510 (950)	1.16	67
	425 (800)	0.96	23
0.008	510 (950)	1.31	59
	425 (800)	0.98	23

FIGURE 6.18

Effect of inclusion characteristics on the mechanical properties of AF 1410 steel.

Adapted from W.M. Garrison Jr., Ultrahigh-strength steels for aerospace applications, JOM 42 (5) (1990) 20–24.

Although the volume fraction of primary inclusions was nearly the same in all alloys, their spacing in the alloys with La was higher due to the higher average particle radius. For each aging condition, the toughness as measured by K_{Ic} and δ_{Ic} (crack opening displacement) were both higher for the alloys with La than for that with Cr. The similar toughness for both alloys with La additions was attributed to a critical value beyond which inclusion spacing has no effect. The higher toughness of alloys aged at 510°C (950°F) compared with those aged at 425°C (800°F) can be attributed to the very low secondary void nucleation from the precipitated particles in the alloys aged at 510°C (950°F) [51]. Although voids nucleated from the secondary particles inherited from the austenitization treatment in alloys aged at both temperatures, the extent of nucleation from the particles that precipitated during aging was much smaller for the alloys aged at 510°C (950°F). La additions must be optimized to ensure that there is no excess beyond that needed to tie up the S. Otherwise formation of large lanthanum oxide inclusions will significantly reduce toughness [52].

The nature, morphology, and distribution of the primary inclusions can be controlled by optimizing alloying additions, melting practice and TMP for improving toughness. Varying the austenitization (solution treatment) temperature is the only way to minimize secondary inclusions (other than those that form during tempering), as observed in AF 1410 by the dissolution of most of these particles at the higher temperature [53]. Various carbides ranging in size from 5 to 125 nm and $(Ti,Mo)_xC,N$ from 10 to 180 nm were present following solution heat treatment at 1525°F (830°C), but only the latter was present in a size range from 20 to 35 nm after treatment at 1625°F (885°C). Coupled with a lower temperature postage heat treatment, solution treatment at the higher temperature increased Charpy toughness by 40%, while maintaining strength at the normal level. This approach provides the opportunity to optimize the secondary dispersions for maintaining a sufficiently fine grain size and achieving the desired combinations of strength and toughness.

As shown in Fig. 6.14, secondary hardening steels achieve peak strength upon aging at temperatures in the range where alloy carbides precipitate. A simultaneous increase in toughness also occurs due to the absence of cementite and any secondary void nucleation from the nanometer-sized alloy carbides. The formation of a thin film of reverted austenite at the martensite plate boundaries in this temperature range enhances toughness, as observed for Aermet 100 steel [23]. The peak in toughness occurs at a temperature slightly higher than that at which peak strength is observed. The aging conditions for these steels are selected to achieve the microstructural conditions balancing strength and toughness. Retained austenite does not play a role in these steels in commercial practice. The small amount of retained austenite that may be present upon quenching is converted to martensite by a refrigeration treatment prior to aging the alloy. Fig. 6.19 compares the fracture toughness of secondary hardness steels with those of low alloy steels [44].

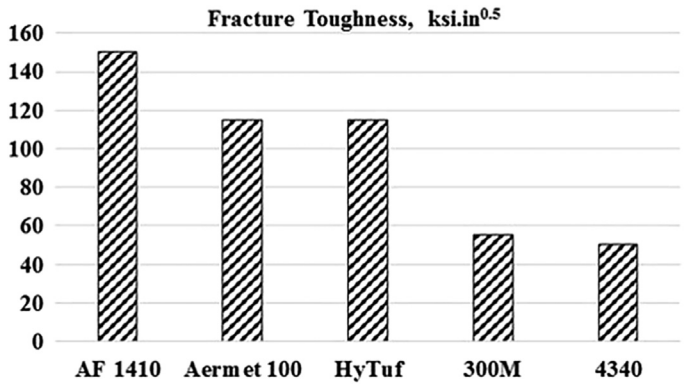


FIGURE 6.19

Typical fracture toughness of ultrahigh strength steels.

Adapted from P.M. Novotny, T.J. McCaffrey, An Advanced Alloy for Landing Gear and Aircraft Structural Applications – Aermet® 100 Alloy, SAE Technical Paper Series 922040, AeroTech '92, Anaheim, CA, 1992.

6.4.3.3 Precipitation Hardening Stainless Steels

The fracture toughness of these steels generally increases with increasing aging temperature corresponding with decreasing strength due to overaging. These alloys contain Cr, a ferrite stabilizer, Ni, an austenite stabilizer, and other elements with varying effects on phase stabilization. The alloys are thus prone to the formation of δ ferrite during processing and to the presence of this phase as stringers in the microstructure with deleterious effects on transverse properties. This phase can be eliminated by the proper balancing of alloy chemistry, as has been accomplished in more recently developed alloys.

6.4.4 FATIGUE PROPERTIES

Properties of importance for the selection of UHS steels for airframe applications are strength and toughness. Accordingly, significantly larger amounts of data are available for these properties than for those characterizing the fatigue behavior. Although the fatigue crack initiation resistance characterized by fatigue strength and stress–life curves generally scale with strength, as shown by a comparison between Aermet 100 and AF 1410, these properties are higher for the secondary hardening steels compared with that for the low alloy steels [44]. The typical maximum stress amplitude for a fatigue life 10^7 increases from about 100 ksi (690 MPa) for 4340 to 120 ksi (827 MPa) for 300M to 140 ksi (965 MPa) for AF 1410 to 160 ksi (1103 MPa) for Aermet 100. The crack growth resistance of Aermet 100 is higher than that of the low alloy steels 4340 and 300M [54]. For a given UHS steel, microstructure generally has very little effect on the crack growth rates in region 2, but a substantial effect in the threshold region [55].

6.4.5 EMBRITTLEMENT

UHS steels are susceptible to various types of embrittlement depending upon their composition, processing, and microstructure. Tempered martensite embrittlement occurring, for example, in alloy 4340 was discussed earlier (Fig. 6.4). It is caused by the combined actions of P segregation to grain boundaries and the precipitation of cementite during tempering. TE occurs in alloy steels upon isothermally aging for long times or slowly cooling through the temperature range of 370−575°C (700−1065°F) and manifests by an increase in the DBTT [56]. It can be eliminated by heating for a short time above 575°C (1065°F). TE is caused by the cosegregation of impurity elements such as P with the alloying elements at grain boundaries. The susceptibility to TE is increased by Si and Mn and decreased by Mo. It should be noted that Si and Mn are not added to the high toughness secondary hardening steels, AF 1410, and Aermet 100.

UHS steels are also susceptible to hydrogen embrittlement (HE) caused by the introduction of even very low levels of hydrogen in the steel and its diffusion to areas of stress concentrations [57]. Hydrogen can be introduced during surface treatment such as electroplating, which can be diffused out by baking at about 150°C (300°F). Failure by HE is characterized by a delay, which is necessitated by the time needed for the diffusion of hydrogen to areas of high stress [56]. The microstructural features of quenched and tempered steels provide many types of traps for hydrogen in the material. Reversible traps such as solute atoms and dislocations act as sources for hydrogen while irreversible traps such as inclusions act as sinks. MnS is an effective trap for hydrogen, but it is deleterious to the properties of steels in other ways. The reverted austenite that forms around martensite laths during heat treatment of Aermet 100 renders this alloy more resistant to HE compared with 300M at comparable strength levels [58]. The solubility of hydrogen is higher in austenite, which acts as a sink, reduces its diffusivity and prevents its absorption by the martensite. Other strong, irreversible hydrogen traps for Aermet 100 are the undissolved carbides and highly misoriented grain boundaries, while the M_2C carbides are reversible traps [59].

6.4.6 STRESS CORROSION CRACKING BEHAVIOR

The MC-LA steels possess very low resistance to stress corrosion cracking in aqueous environments. Alloy Aermet 100 was designed to possess combinations of strength, toughness, and resistance to stress corrosion cracking better than that of the low alloy steels at equivalent strength levels. Fig. 6.20 shows K_{Iscc} data for alloy 4340 as a function of yield stress in a 3.5% NaCl environment [60]. The threshold decreases with increasing yield stress, as is generally observed, and is quite low ($\sim$15 MPa $m^{0.5}$) at strength levels above about 1500 MPa ($\sim$220 ksi). K_{Iscc} of alloys improves with increasing toughness, as shown in Fig. 6.21 [44].

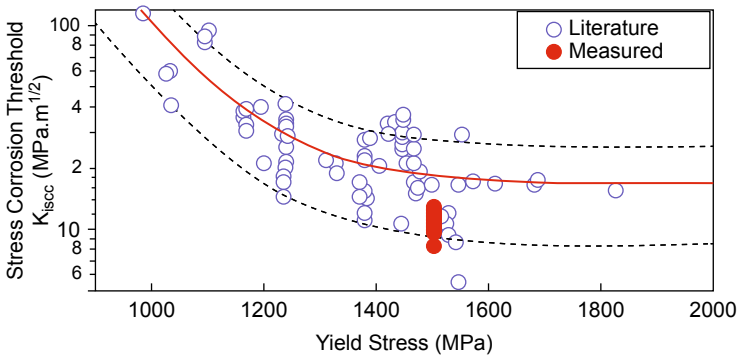


FIGURE 6.20

K_{Iscc} for alloy 4340 as a function of yield strength [60].

6.4.7 SUMMARY

UHS steels used for airframe applications are hardened by the precipitation of carbides or intermetallic compounds. Strength levels greater than 1400 MPa (~200 ksi) can be achieved by C additions of about 0.4 and 0.2 wt%, respectively, to low alloy steels strengthened by metastable ε iron carbides and secondary hardening steel by alloy carbides. Si addition retards the precipitation of cementite in low alloy steels, which enables tempering at higher temperatures for improving toughness, as for example in 300M, commonly used for landing gear structures, at strength levels equivalent to that of the representative UHS low alloy, carbon steel, 4340.

Increases in toughness and stress corrosion resistance at strength levels beyond that of the low alloy steels 4340 and 300M can be achieved only in secondary hardening steels. The strength of these steels can be adjusted by maintaining adequate

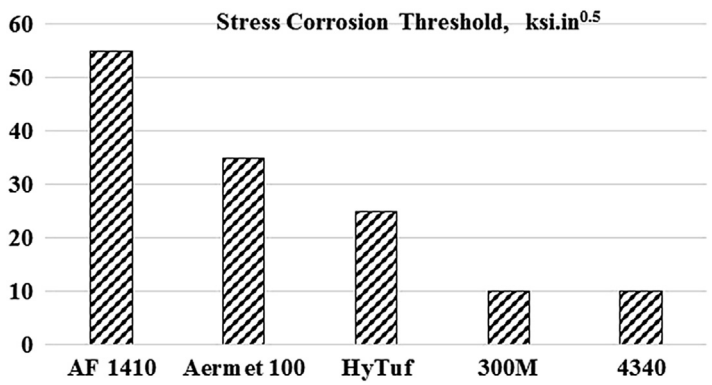


FIGURE 6.21

K_{Iscc} for ultrahigh strength steels [44].

levels of C in the range used for low C steels in conjunction with sufficient stoichiometric amounts of carbide forming elements, the most commonly used being Cr and Mo. Aging at temperatures in the range for the precipitation of M_2C, which is above that for the dissolution of cementite, provides both high strength and toughness. High strength is achieved by the formation of nm sized, coherent M_2C precipitates and high toughness by the absence of precipitated particles that can nucleate secondary voids. The threshold for stress corrosion cracking increases with increasing fracture toughness.

The strength of wrought stainless steels is increased by precipitation of intermetallics. The C levels in these steels are very low and just sufficient to provide hardenability. Most of these types of steels used in airframes are the martensitic type and the alloy chemistry is balanced to avoid the formation δ ferrite. The strength of these steels is somewhat lower than that of the maximum strength achievable in the carbide strengthened steels.

Primary inclusions greater than about 1 μm reduce the toughness of UHS steels by cracking and void nucleation, like the effects of constituent particles in aluminum alloys. All the UHS steels used in aerospace structures use vacuum melting and refining technologies that have made significant improvements in reducing the inclusion content, refining their sizes and reducing impurity levels, with beneficial effect on toughness. Secondary voids nucleate at smaller particles such as those that remain undissolved during solution treatment (austenitizing) and at precipitated particles. The volume fraction of the undissolved particles can be reduced by solution treating at higher temperatures, which would increase the austenite grain size with its own possible deleterious effects on properties.

Despite the long history of ferrous alloys, the development of UHS steels, particularly the secondary hardening and the PH-SSs, is rather recent. Further, the martensite transformation and the microstructural features that determine the properties occur at ultrafine length scales and their mechanisms are only beginning to be understood with the advent of sophisticated characterization techniques. The continuing need for high performance steels, the diversity of their hierarchical microstructures, and the challenges in their elucidation, and the rapid development of modeling and simulation methods, have all spurred and enabled the successful computational design and insertion of these steels for demanding applications, as illustrated by the recent flight of qualification of "cybersteels" [27,28].

Fig. 6.22 summarizes the processing−microstructure−properties relationships for the carbide strengthened UHS steels that are used in airframe applications and discussed in this chapter. It extends the processing−microstructure relationships shown in Table 6.5 to include their effects on properties. Similar relationships apply for the PH-SSs, except that they are strengthened by intermetallic phases. These will be illustrated further while describing specific commercial alloys and approaches to new alloy design.

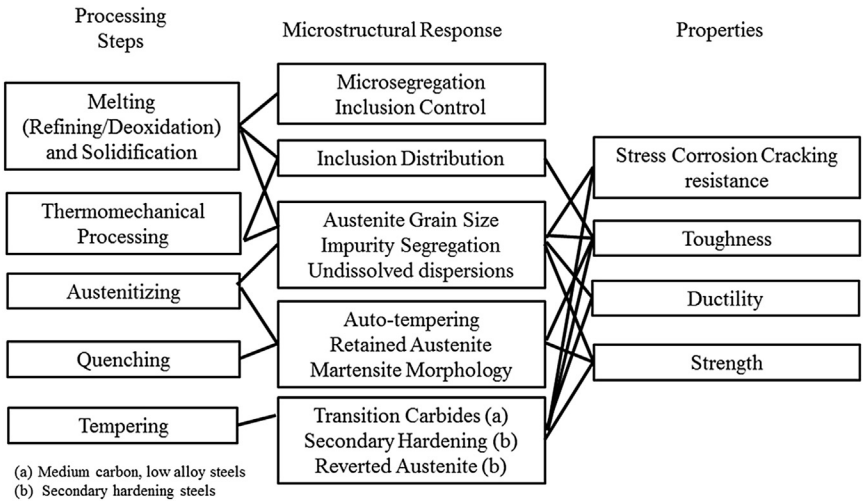


FIGURE 6.22

Schematic of processing—microstructure—property relationships for carbide strengthened steels.

6.5 COMMERCIAL ULTRAHIGH STRENGTH STEELS

The total number of UHS steels currently in service in airframe structural applications is quite small. Most of the components in landing gear assemblies that require high strength materials use 4340 and 300M, with Aermet 100 being used in applications additionally requiring higher toughness and resistance to stress corrosion. AF 1410 is presently a restricted alloy that is not commercially available, although it was the earliest alloy that possessed yield strength near 1500 MPa (~220 ksi) and fracture toughness near 200 MPa $m^{0.5}$. All these alloys need protective coatings for use in service. The PH-SSs are used in a variety of applications requiring combinations of high strength and corrosion resistance and good fracture toughness. Over the past decade, several computationally designed steels have been developed by QuesTek. Designated the Ferrium series, these alloys possess attractive property combinations and are currently being commercialized for targeted improvements over incumbent alloys.

6.5.1 MEDIUM CARBON, LOW ALLOY STEELS

The three commonly used steels of this type are 4340, 300M, and D6AC whose compositions are shown in Table 6.1. The effects of processing and microstructure on the properties of 4340 and 300M were discussed in some detail in earlier sections to illustrate their metallurgy. All these alloys are medium carbon, Ni—Cr—Mo steels. Compared with 4340, 300M has higher Si and D6AC has slightly higher C, Cr,

and Mo and uses V as a grain refiner. Although the medium C, 41XX series Cr−Mo steels (e.g., 4130 and 4140) also develop UHS, the presence of Ni in the 43XX series imparts additional hardenability and solid solution strengthening. Thin sections of 4340 can be hardened by quenching in air while sections up to 75 mm (3 in.) thick can be hardened by oil quenching. Both 300M and D6AC exhibit deeper hardenability than 4340. The MC-LA steels need to be tempered in specified, recommended ranges of temperature to avoid the problems of embrittlement. The alloys are generally tempered to provide the best combinations of strength, toughness, and resistance to stress corrosion. For example, 300M is restricted to tempering in the range of 260−315°C (500−600°F), as tempering outside this range results in severe reduction in property combinations. However, this is in the temperature range in which 4340 suffers tempered martensite embrittlement (Fig. 6.4).

Properties of MC-LA steels have been improved primarily by adapting vacuum melting practices, reducing inclusion content and increasing purity, as shown, for example, in Fig. 6.16, and very limited number of new alloys have been developed. One example is the alloy NC310YW (Fe−0.4C−2.7Si−1.75Ni−0.85Cr−0.4 Mo−0.2V) developed in France that exhibits a toughness of 52 MPa $m^{0.5}$ at yield and tensile strength levels of 2150 and 1790 MPa (310 and 260 ksi), respectively [61]. The effects of alloy cleanliness in improving the fracture toughness and fatigue properties were already discussed. Components fabricated from these alloys are generally protected from corrosion by Cd plating, following which they need to be processed carefully to eliminate the possibility of HE.

Steels with lower C levels but with compositions otherwise similar to MC-LA steels, develop sufficient strength but at much higher levels of fracture toughness, rendering them attractive for many airframe applications. An example is alloy Hy-Tuf (Fe−0.25C−1.35Mn−0.3Cr−1.8Ni−0.4 Mo) that exhibits tensile strength in the 1500−1655 MPa (∼220−240 ksi) range with good ductility, fracture toughness, and impact strength [62]. After tempering at 288°C (550°F) for 2 h, this steel develops a fracture toughness of 110 MPa $m^{0.5}$ at yield and tensile strength levels of about 1450 and 1600 MPa (210 and 230 ksi), respectively. The alloy has found applications in many airframe structural components and is an attractive, lower cost substitute for the highly alloyed, secondary hardening steels.

6.5.2 SECONDARY HARDENING, HIGH ALLOY STEELS

The secondary hardening steels strengthened by alloy carbides that are in current use all contain Co. Their commercialization began with the development of HP 9Ni−4 Co−xC (x = 0.2, 0.25, 0.3 or 0.45) steels with small amounts of Cr, Mo, and V and the 10Ni−8Co−Cr−Mo steels with 0.1−0.2 C. Of the four HP steels, only HP 9Ni−4Co−0.3C has been produced in significant amounts. It has deep hardenability and develops a toughness of about 100 MPa $m^{0.5}$ at tensile strength levels in the range of 1520−1650 MPa (220−240 ksi) [16].

Higher combinations of strength and toughness are achieved in alloy AF1410, which is essentially alloy HY180, except for higher additions of Co and C

(Table 6.1). The effects of the alloying elements were discussed in earlier sections. High levels of Ni lower the M_s temperature thus increasing the amount of retained austenite, which is countered by the addition of Co. Ni also lowers the DBTT and results in high toughness. The strengthening contribution from each of the alloying elements in Fe−0.12C−10Ni−8Co−2Cr−1Mo steel to a baseline Fe−10Ni steel is shown in Fig. 6.23 [17]. The predominant contribution to strength from the alloy carbides is evident. The alloy with 2% Cr and 1% Mo was determined to provide the optimum strength by secondary hardening.

Alloy AF1410 exhibits the highest toughness of all the UHS steels hardened to peak strength (Fig. 6.19). The evolution of M_2C carbides that strengthen these alloys during secondary hardening has been characterized thoroughly (Fig. 6.12) and used in the computational design of alloys, as will be discussed later. Quenching of AF1410 produces highly dislocated lath martensite. The precipitation sequence during tempering is Fe_3C at 425°C (800°F), $(Fe,Cr,Mo)_2C$ at 455°C (850°F), and $(Cr,Mo)_2C$ at 480°C (900°F). $(Cr,Mo)_2C$ begins to coarsen at 510°C (950°F) and is replaced by M_6C at 540°C (1000°F) [16]. Peak strength and maximum impact energy occur upon tempering at 480 and 508°C (900 and 950°F), respectively. AF 1410 is not commercially available. It has been used as the basis to develop alloys with strength levels comparable to 300M with some sacrifice in toughness.

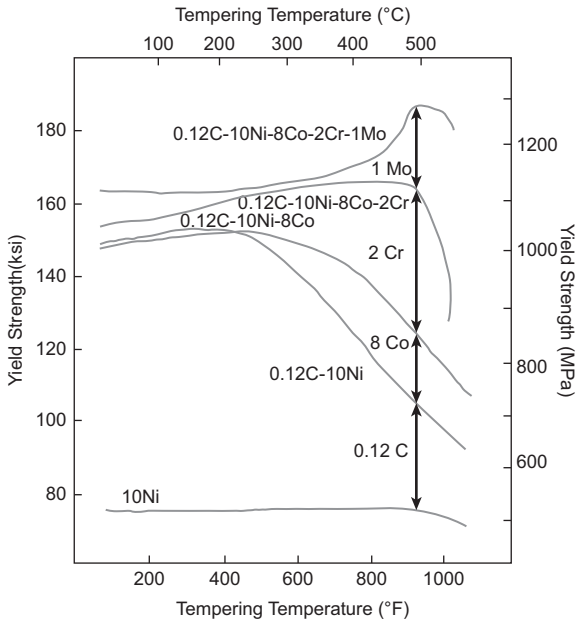


FIGURE 6.23

Effects of alloying elements in Fe−10Ni steel [austenitized at 845°C (1550°F), water quenched and tempered for 1 h] [17].

The development and insertion of Aermet 100 in service has already been described. This alloy forms plate martensite on quenching and is strengthened by M_2C precipitates. As mentioned earlier, the term plate has been used to describe the morphology of martensite due to the high angle nature of its boundaries. Aermet 100 is aged at 482°C (900°F) in standard practice to achieve the highest level of toughness. Aging at 468°C (850°F) results in peak strength and lower toughness. In this condition, the microstructure consists of needle-shaped zones rich in Cr and Mo. Aging at 482°C (900°F) results in the formation M_2C carbides and reverted austenite at the martensite plate boundaries. The microstructural evolution during tempering of Aermet 100 is shown in Figs. 6.10 and 6.11 [23].

Increasing the level of C with corresponding adjustments in the amounts of the other alloying resulted in Aermet 310 (Fe−0.25C−11Ni−2.4Cr−1.4Mo−15Co) and Aermet 340 (Fe−0.33C−12Ni−2.25Cr−1.85Mo−15.6Co) [63]. The properties of these alloys are shown in Fig. 6.24 [64]. In this figure, the alloys are also

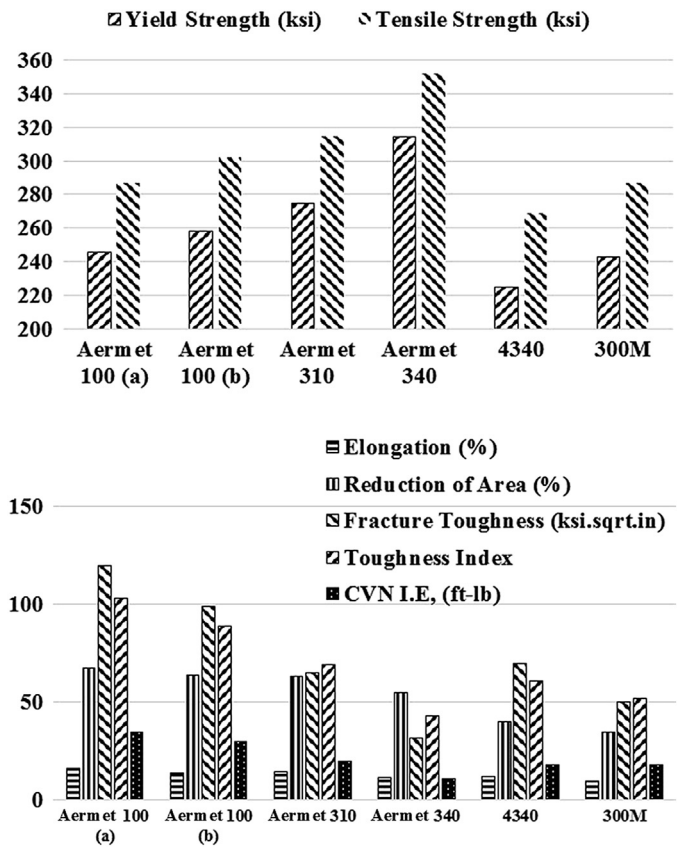


FIGURE 6.24

Mechanical properties of ultrahigh strength Aermet series steels [64].

compared based on a "toughness index," which is calculated as the geometric mean of the normalized values of different measures of toughness. This comparison uses three measures of toughness: the area under the stress–strain curve, K_{Ic}, and the impact energy from Charpy V-notch tests. Data from tests on Aermet 100 were analyzed and used to determine the normalization factors and the toughness index as follows:

$$\text{Toughness Index} = \left[\left(\frac{A}{50}\right) \times (\text{CVN} \times 3) \times K_{Ic}\right]^{\frac{1}{3}}$$

where, CVN is the impact energy and A, the area under the stress strain curve, is

$$A = (\%\ \text{elongation}) \times \left(\frac{\text{Yield Strength} + \text{Tensile Strength}}{2}\right)$$

6.5.3 PRECIPITATION HARDENING STAINLESS STEELS

These steels are Fe–Cr–Ni alloys with sufficient Cr to render them stainless type. The amounts of Cr and Ni determines whether the steel will be martensitic, semiaustenitic, or the austenitic type. Compared to the quenched and tempered, martensitic, Fe–Cr–C stainless steels, the PH-SS alloys have very limited amounts of C and are strengthened by the precipitation of intermetallic compounds. The austenitic PH-SS alloys have very high amounts of alloying elements that their M_s is well below the room temperature. They are also aged at high temperatures, and without any possibility of phase transformations they are used for heat resistant applications. The semiaustenitic PH-SSs contain δ ferrite in equilibrium at the austenitization temperature and are given a conditioning treatment for the martensitic transformation to occur. Most of the PH-SS alloys used in airframes are the martensitic type and are discussed in this section.

Martensitic PH-SSs contain between about 11 and 17 wt% Cr with the amount of Ni balanced to achieve adequate corrosion resistance, an M_s above room temperature and a fully martensitic structure while also preventing δ ferrite formation during austenitization and its retention upon quenching [65]. The composition of several of these steels is shown in Table 6.1. Other elements are added to form intermetallic compounds during aging for precipitation hardening.

One of the earliest of the martensitic PH-SS alloys is 17-4 PH, developed in the 1940s. In the solution treated and quenched condition, its microstructure consists of lath martensite, δ ferrite stringers drawn out in the working direction, large silicide stringers, and carbide particles, as shown in Fig. 6.25 [66].

Precipitation hardening begins with the formation of coherent Cu-rich clusters that transform to incoherent ε-Cu precipitates with continued aging. The amount of δ ferrite in this alloy has been measured to be about five volume % [67]. Peak strength and the minimum in fracture toughness occur upon aging at 482°C (900°F). Fractographic evaluations suggest void nucleation from δ ferrite–matrix

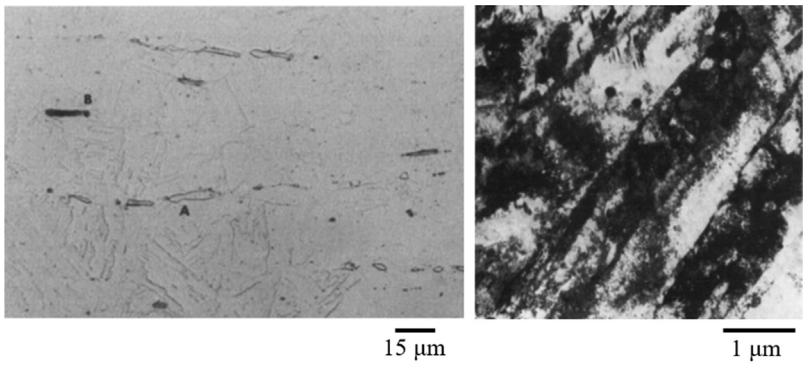


FIGURE 6.25

Microstructure of unaged 17-4 PH [66].

interfaces with deleterious effects on toughness, particularly in the direction normal to the stringers.

Martensitic PH-SS alloys developed subsequently have better toughness made possible through alloy design to eliminate δ ferrite and retained austenite. In the first of these, 15-5 PH, the amounts of Cr and Ni are adjusted relative to 17-4 PH to eliminate the formation of δ ferrite. Later alloys all have lower Cr, higher Ni, Mo additions, and other compositional changes (Table 6.1). Decreasing Cr and increasing Ni suppress δ ferrite, Co raises M_s, Mo offsets the decrease of corrosion resistance caused by lowering of Cr, and Al, Ti, and other elements form strengthening intermetallics [68]. The alloys are solution treated in the range of 980−1065°C (1800−1950°F), quenched, and aged in the range of about 482−600°C (900−1100°F) to obtain various combinations of strength and toughness, as shown in Fig. 6.26 [5]. The alloys possess the good corrosion resistance typical of the stain steel family of alloys. Applications for Custom 465 include flap tracks, slat tracks, actuators, and landing gear components. Custom 475, achieves a tensile strength of about 2000 MPa (290 ksi) with good ductility, toughness, and corrosion resistance in the H975 condition (alloy aged at 975°F, 525°C) [69]. Cold work prior to aging increases strength.

The range of aging temperatures for martensitic PH-SS alloys is sufficiently high that martensite may transform to austenite. In PH 13-8 Mo steel, the "reverted" austenite starts forming on aging at temperatures above 525°C (975°F) [46] with its volume fraction increasing to about 30% upon prolonged aging at 575°C (1065°F), as shown in Fig. 6.27 [70]. Precipitation of NiAl and formation of austenite occur simultaneously during the early stages of aging. With continued aging, the increase in the volume fraction of austenite is accompanied by dissolution of NiAl. The microstructure of PH 13-8 Mo aged for 100 h at 575°C (1065°F) is shown in Fig. 6.28 [70]. The austenite is enriched in Ni and remains stable upon cooling to room temperature contributing to strength in peak aged alloys and to toughness in alloys aged past this condition.

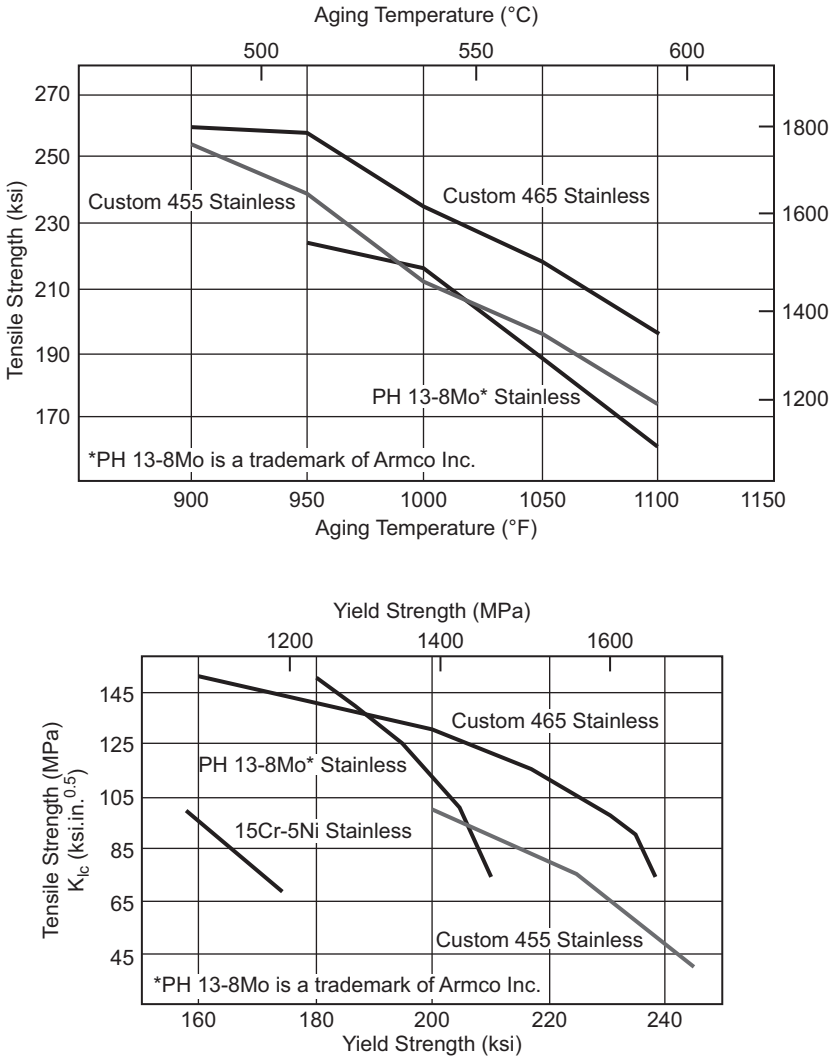


FIGURE 6.26

Variation of tensile strength with aging temperature and the yield strength—fracture toughness relationships for precipitation hardening stainless steels [5].

Reprinted with permission of ASM International. All rights reserved. www.asminternational.org.

6.6 NEW ALLOY DESIGN

New UHS steels designed for critical structural applications need to combine high toughness and corrosion resistance without sacrificing strength. Cost is a major consideration, as many of the present secondary hardening and precipitation

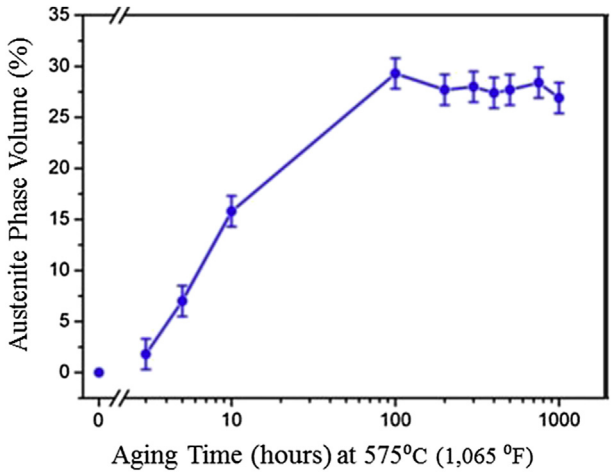


FIGURE 6.27

Volume fraction of austenite in PH 13-8 Mo on aging at 575°C (1065°F) [70].

hardening stainless UHS steels use high amounts of Ni and Co. All steels, other than the stainless type, need to be protected from corrosion damage by coatings, typically achieved by Cd plating. Many landing gear components also need wear resistance, which is accomplished by hard chromium plating. With the drive to eliminate these hazardous coating materials, which are otherwise very effective, the additional challenge is to develop steels with the required properties and attributes, but without the need for surface protection. Although new conventional alloys with incremental improvements in properties are being designed and commercialized, a family of computationally designed UHS steels, designated the Ferrium series, addressing

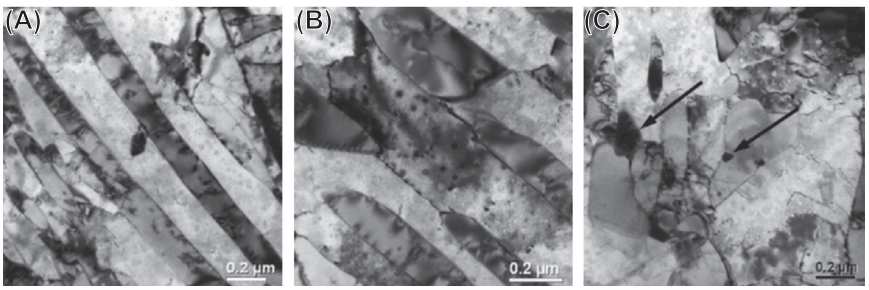


FIGURE 6.28

Microstructure of PH 13-8 Mo aged at 575°C (1065°F) for 100 h [70]: (A) lath-like austenite is seen, (B) NiAl precipitates in the martensite lath, and (C) Mo-rich particles within and next to austenite.

these challenging requirements has recently been commercialized and inserted in service. These steels have been designed and developed by QuesTek using Materials by Design (Systems Approach) that was discussed in the introductory chapters.

There are several advantages to using computational methods for alloy design. First is the ability to tailor compositions and processing to satisfy the performance goals and overcome the shortcomings of incumbent materials for specific applications. Although the new alloys need not necessarily be designed entirely from first principles, there is also no restriction that the compositions need to be within the prescribed limits for the various classes of alloys that they are intended to replace. The ability to model the underlying physical phenomena in materials behavior enables design of alloys that combine the desirable attributes from several alloy classes. Finally, the ability to qualify and commercialize alloys with reduced time and expense is a major benefit, particularly considering the schedule constraints in new airplane design discussed in the first chapter. Although opportunities for new materials insertion are few and far between, should the need for a new material arise, it needs to be qualified, ready and available, because the window for its selection is rather short.

Table 6.6 lists the compositions of three commercialized Ferrium alloys and the typical properties of two of these alloys [71]. It is instructive to compare their compositions with those of conventional UHS steels. All the Ferrium alloys rely on strengthening by carbide precipitation, as do the secondary hardening steels. The carbide forming tendency of alloying elements in steels increases in the order of Cr, W, Mo, V, Ti, Nb, Ta, and Zr [11]. Of these elements, Cr and Mo are exclusively used in the secondary hardening, high toughness steels discussed thus far. Although W is used primarily in high hardness tool steels, the Ferrium steels also have this element as an alloying addition. Compared with Aermet 100, Ferrium S53 has similar amounts of C and Co, and higher Cr, but in amounts slightly less than in Custom 475, which itself is near the very low end of the amounts added to stainless steels. Ferrium M54 has slightly higher C and lower Co than Aermet 100. Ferrium C64 is a carburizable steel that can develop very high surface and core hardness for use as alternatives to gear steels, which have not been discussed in this chapter.

With its high level of Cr, S53 has been designed for superior corrosion resistance and for use without the Cd coatings that the incumbent alloys 4340 and 300M require. The metallurgy underlying its design and some of the microstructural features responsible for its properties are briefly as follows [72–74];

- Passive film formation to impart corrosion resistance and eliminate the need for Cd plating requires Cr in amounts typically added to stainless steels. Due to its effects on lowering M_s, Cr restricts the amounts of other elements that are needed. Furthermore, it results in microsegregation during solidification and lowers the solubility of C, which is required for carbide precipitation and strengthening.

Table 6.6 Nominal Compositions (wt%) and Properties of Ferrium Steels

Alloy	C	Cr	Ni	Mo	W	Co	V
Ferrium S 53	0.2	10	5.5	2	1	14	0.3
Ferrium M 54	0.3	1	10	2	1.3	7	0.1
Ferrium C 64	0.11	3.5	7.5	1.75	0.2	16.3	0.02
Aermet 100	0.23	3.1	11.1	1.2		13.4	
300M	0.4	0.85	1.8	0.4			
Custom 475	0.02	11	8.5	5		8	

Alloy	Yield Strength MPa (ksi)	Tensile Strength MPa (ksi)	Elongation (%)	Reduction of Area (%)	K_{Ic} (MPa $m^{0.5}$)	K_{Iscc} (MPa $m^{0.5}$)
S53 AMS 5922	1551 (225)	1986 (288)	15	57	72	20–44
300M (BS S155) AMS 6419	1669 (242)	1979 (287)	11	37	55	15
4340 AMS 6414	1531 (222)	1903 (276)	11	35	55	10

BS S 155 is a British standard.
Properties are for S53 tempered at 482°C (900°F), 300M at 300°C (572°F), and 4340 at 205°C (400°F).
Corrosion resistance of S53 is high compared with the low resistance for 300M and 4340.

Alloy	Yield Strength MPa (ksi)	Tensile Strength MPa (ksi)	Elongation (%)	Reduction of Area (%)	K_{Ic} (MPa $m^{0.5}$)	K_{Iscc} (MPa $m^{0.5}$)
M54 AMS 6516	1731 (251)	2020 (293)	15	61	127	110
Hy Tuf AMS 6425	1.379 (200)	1634 (237)	12	45	127	30
Aermet 100 AMS 6532	1724 (250)	1965 (285)	13	65	127	22

Properties are for M54 tempered at 515°C (960°F), HyTuf at 260°C (500°F), and Aermet 100 at 482°C (900°F).

- C is limited to just the amount needed to achieve the required strength by optimizing the size (~3 nm) and volume fraction of the M_2C carbides (see Fig. 6.12 that shows the effects of carbide size and volume fraction on the hardness of AF 1410) and to eliminate the formation of Cr carbides in the grain boundaries.
- The role of Co, which raises the M_s, is to retard dislocation recovery and promote the heterogeneous nucleation of M_2C carbides, while interacting with Cr to enhance its partitioning to the passive film. The size of the strengthening carbides is also in the range of that of the passive film facilitating this partitioning. The resulting corrosion resistance would be equivalent to that in steels with higher levels of Cr.
- Melting practice is optimized to form Ti-rich MC carbides that pin the grain boundaries and refine the grain size during solution treatment. Formation of oxides and oxysulfides that nucleate primary voids is also minimized to improve fracture toughness.

Ferrium M54, a nonstainless steel, is designed as a lower cost alternative for Aermet 100 and besides exhibiting high toughness it also possesses very high resistance to stress corrosion cracking. At the higher tempering temperatures made possible by the addition of W, the formation of austenite promotes transformation-induced plasticity resulting in high values of toughness [75].

The computational design of Ferrium S53 (and other such steels) can be illustrated by using the processing−microstructure−properties relationships scheme to achieve desired performance goals, as shown in Fig. 6.29 [27]. This approach was

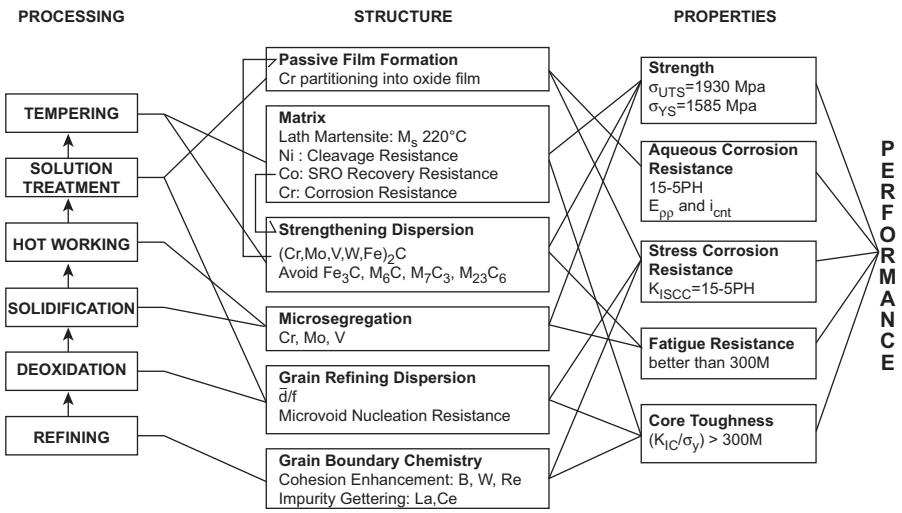


FIGURE 6.29

Systems diagram for ultrahigh strength steels showing the property objectives, microstructural subsystems, and the required processing sequence [27].

discussed briefly in the introductory chapters and the microstructural changes accompanying some of the processing steps and their effects on properties were described earlier. The predictive science capability required for such endeavors for designing UHS steels with hierarchical microstructures had its beginning about three decades ago [53]. Ferrium S53 was designed in 3 years with only five iterations. Following qualification in conjunction with the US Government funded "Accelerated Insertion of Materials" program, it was flight tested in a landing gear in 2010 [27]. For alloy M54, the time between identifying design goals and full-scale ingot production was less than 2 years [76]. The first flight of this alloy in a US Navy tail hook shank took place in 2014.

As shown in Fig. 6.29, the property targets for Ferrium S53 included achieving corrosion and stress corrosion resistance equivalent to that of 15-5 stainless steel (15 wt% Cr), with toughness and fatigue properties greater than that of 300M at comparable strength levels. Among the activities involved in the computational design of this and other alloys were the early quantification of M_2C precipitation in AF 1410 (Fig. 6.12) using a variety of characterization techniques, simulation of microsegregation during solidification and its effects on subsequent processing, optimization of dispersions for grain refinement, and determining the embrittling potency of alloying elements to mitigate their effects. The individual property targets are treated as subsystems, e.g., strength, toughness, and embrittlement resistance [77], for multiobjective optimization. A hierarchy of modeling and complementary characterization tools are then used across the length scale of the "microstructure" that affect the subsystems, to predict and determine that which would meet the property targets, as listed in a summary of key aspects in Table 6.7.

Table 6.7 Examples of Modeling and Characterization in Support of the "Systems Approach" for Alloy Design

Property Goal	Microstructure Evolution and Length Scale	Hierarchy of Modeling and Characterization Tools
Strength	• Martensitic transformation (μm) • Carbide precipitation (nm)	• Thermodynamics and kinetics models for transformation (ThermoCalc, DICTRA), ABAQUS for calculating precipitate properties (elastic and interfacial energies) • Transmission electron microscopy (TEM), atom probe tomography, small angle neutron scattering
Toughness	• Grain refining particles (0.1 μm)	• Models for fracture processes, ABAQUS • TEM, fracture mechanics testing
Embrittlement resistance	• Quantum level	• Models for gain boundary cohesion • Scanning Auger microscopy

6.7 SUMMARY

Steels have been used for a long time, but the development of UHS steels for airframes is relatively recent, as shown in Table 6.8.

Table 6.8 Evolution of Ultrahigh Strength Steels for Use in Airframes

Alloy Type	Pre-1960s	1960s	1970s 1980s	1990s	2000s	2010s
Medium C, low alloy	4340 300M Hy Tuf	Vacuum melting technologies for improved quality				
Secondary hardening		HY 180 HP 9-4-X	AF 1410	Aermet 100	Aermet 310 Aermet 340	Ferrium S53 Ferrium M54 (stainless)
Precipitation hardening stainless (martensitic)	17–4 15–5 (δ ferrite free)	13-8 Mo Custom 455		Custom 465	Custom 475	

Although constituting only a small fraction of the total usage of steels, the UHS steels are used in very critical structural applications. The composition and processing space for these steels discussed in this chapter still provides opportunities for property improvements. In this respect, the successful demonstration of computational alloy design can be expected to accelerate the development and insertion of improved alloys in both traditional compositions or otherwise.

REFERENCES

[1] D.P. Davies, Structural steels, in: H.M. Fowler (Ed.), High Performance Materials in Aerospace, Springer Science, 1995, pp. 154–181.

[2] R.R. Boyer, Attributes, characteristics, and applications of titanium and its alloys, JOM 62 (5) (2010) 21–24.

[3] R.M. Garber, C. Dickerson, Maintenance of high-strength alloy steel components, Aero, Boeing Publication, April 2Q, 2003, pp. 22–35. http://www.boeing.com/commercial/aeromagazine/aero_22/.

[4] W.M. Garrison Jr., Ultrahigh-strength steels for aerospace applications, JOM 42 (5) (1990) 20–24.

[5] J.M. Dahl, Ferrous-base aerospace alloys, Advanced Materials and Processes 157 (5) (2000) 33–36.

[6] D. Wegman, Carpenter technology outlines how high-tech melting creates high-performance metal alloy, Machine Design (September 25, 2009). http://machinedesign.com/archive/carpenter-technology-outlines-how-high-tech-melting-creates-high-performance-metal-alloys.
[7] T. Philip, T. McCaffrey, Ultrahigh strength steels, in: G.T. Murray (Ed.), Handbook of Materials Selection for Engineering, Marcel Decker, 1997, pp. 148–161.
[8] CarTech® Aermet® 100 Technical Data Sheet, Carpenter Technology Corporation, 2016.
[9] CarTech® Custom 465® Stainless Technical Data Sheet, Carpenter Technology Corporation, 2016.
[10] G. Krauss, Phases and structures, in: Steels: Processing, Structure, and Performance, ASM International, 2015, pp. 17–38.
[11] A.K. Sinha, Iron-carbon alloys, in: Ferrous Physical Metallurgy, Butterworths, 1989, pp. 1–42.
[12] G. Krauss, Tempering, in: Steels: Processing, Structure, and Performance, ASM International, 2015, pp. 373–403.
[13] A.K. Sinha, Tempering, in: Ferrous Physical Metallurgy, Butterworths, 1989, pp. 523–608.
[14] F.C. Campbell, Alloy steels, in: Elements of Metallurgy and Engineering Alloys, ASM International, 2008, pp. 371–393.
[15] J.P. Materkowski, G. Krauss, Tempered martensite embrittlement in SAE 4340 steel, Metallurgical Transactions A 10A (1979) 1643–1651.
[16] T.V. Philip, T.J. McCaffrey, Ultrahigh-strength steels, in: Properties and Selection: Irons, Steels, and High-Performance Alloys, ASM Handbook, vol. 1, ASM International, 1990, pp. 430–448.
[17] G.R. Speich, D.S. Dabkowski, L.F. Porter, Strength and toughness of Fe-10Ni alloys containing C, Cr, Mo, and Co, Metallurgical Transactions 4 (1973) 303–315.
[18] P.M. Kelly, Crystallography of martensite transformation in steels, in: Phase Transformations in Steels, Diffusionless Transformations, High Strength Steels, Modelling and Advanced Analytical Techniques, vol. 2, Woodhead Publishing, 2012, pp. 3–33.
[19] T. Maki, Morphology and substructure of martensite in steels, in: Phase Transformations in Steels, Diffusionless Transformations, High Strength Steels, Modelling and Advanced Analytical Techniques, vol. 2, Woodhead Publishing, 2012, pp. 34–58.
[20] G. Krauss, Martensite, in: Steels: Processing, Structure, and Performance, ASM International, 2015, pp. 63–97.
[21] E.I. Galindo-Nava, P.E.J. Rivera-Díaz-del-Castillo, A model for the microstructure behaviour and strength evolution in lath martensite, Acta Materialia 98 (2015) 81–93.
[22] R.M. Horn, R.O. Ritchie, Mechanisms of tempered martensite embrittlement in low alloy steels, Metallurgical Transactions 9A (1978) 1040–1053.
[23] R. Ayer, P.M. Machmeier, Transmission electron microscopy of hardening and toughening phenomena in Aermet 100 steel, Metallurgical Transactions 24A (1993) 1943–1955.
[24] X. Shi, W. Zeng, Q. Zhao, W. Peng, C. Kang, Study on the microstructure and mechanical properties of Aermet 100 steel at the tempering temperature around 482°C (900°C), Journal of Alloys and Compounds 679 (2016) 184–190.
[25] M. Gruber, G. Ressel, F.M. Martin, S. Ploberger, S. Marsoner, R. Ebner, Formation and growth kinetics of reverted austenite during tempering of a high Co-Ni steel, Metallurgical and Materials Transactions 47A (2016) 5932–5941.

[26] G. Krauss, Primary processing effects on steel microstructure and properties, in: Steels: Processing, Structure, and Performance, ASM International, 2015, pp. 163−196.
[27] G.B. Olson, Genomic materials design: the ferrous frontier, Acta Materialia 61 (2015) 771−781.
[28] G.B. Olson, C.J. Kuehmann, Materials genomics: from CALPHAD to flight, Scripta Materialia 70 (2014) 25−30.
[29] H.E. Lippard, C.E. Campbell, T. Bjorklind, U. Borggren, P. Kellgren, V.P. Dravid, G.B. Olson, Microsegregation behavior during solidification and homogenization of Aermet 100 steel, Metallurgical Transactions B 29B (1998) 205−216.
[30] D. Barbier, Expansion of the martensite transformation temperature relation to larger alloying elements and contents, Advanced Engineering Materials 16 (1) (2014) 122−127.
[31] H.-S. Wang, H.K.D.H. Bhadeshia, Austenite grain size and then martensite start temperature, Scripta Materialia 60 (2009) 493−495.
[32] S.-J. Lee, K.-S. Park, Prediction of martensite start temperature in alloy steels with different grain sizes, Metallurgical Transactions A 44A (2013) 3423−3427.
[33] T. Sourmail, C. Garcia-Mateo, Critical assessment of models for predicting the M_s temperature of steels, Computational Materials Science 34 (2005) 323−334.
[34] C. Capdevila, Neural network modeling of phase transformations in steels, in: Phase Transformations in Steels, Diffusionless Transformations, High Strength Steels, Modelling and Advanced Analytical Techniques, vol. 2, Woodhead Publishing, 2012, pp. 464−503.
[35] A. Stormvinter, A. Borgenstam, J. Agren, Thermodynamically based prediction of the martensite start temperature for commercial steels, Metallurgical and Materials Transactions A 43A (2012) 3870−3879.
[36] G. Ghosh, G.B. Olson, Computational thermodynamics and the kinetics of martensitic transformation, Journal of Phase Equilibria 22 (3) (2001) 199−207.
[37] M. Peet, Prediction of martensite start temperature, Materials Science and Technology 31 (2015) 1370−1375.
[38] G. Krauss, Hardness and hardenability, in: Steels: Processing, Structure, and Performance, ASM International, 2015, pp. 335−372.
[39] D.S. MacKenzie, Heat treatment of landing gear parts, Heat Treating Progress (May/June 2008) 23−26.
[40] R. Ayer, P. Machmeier, On the characteristics of M_2C carbides in the peak hardening regime of Aermet 100 steel, Metallurgical and Materials Transactions 29A (1998) 903−905.
[41] R.A. Grange, C.R. Hribal, L.F. Porter, Hardness of tempered martensite in C and low alloy steels, Metallurgical Transactions 8A (1977) 1775−1785.
[42] B.L. Bramfitt, Structure/property relationships in irons and steels, in: J.R. Davis (Ed.), Metals Handbook Desk Edition, second ed., ASM International, 1998, pp. 153−173.
[43] L. Malik, J.A. Lund, A study of strengthening mechanisms in tempered martensite from a medium carbon steel, Metallurgical Transactions 3 (1972) 1403−1406.
[44] P.M. Novotny, T.J. McCaffrey, An Advanced Alloy for Landing Gear and Aircraft Structural Applications − Aermet® 100 Alloy, SAE Technical Paper Series 922040, AeroTech '92, Anaheim, CA, 1992.
[45] K.H. Lo, C.H. Shek, J.K.L. Lai, Recent developments in stainless steels, Materials Science and Engineering R 65 (2009) 39−104.

[46] V. Seetharaman, M. Sundararaman, R. Krishnan, Precipitation hardening in a PH 13-8 Mo stainless steel, Materials Science and Engineering 47 (1981) 1−11.
[47] G.R. Speich, W.A. Spitzig, Effect of volume fraction and shape of sulfide inclusions on through-thickness ductility and impact energy of high-strength 4340-plate steels, Metallurgical Transactions 13A (1982) 2239−2258.
[48] G. Krauss, Shear fracture of ultrahigh strength low alloy steels, in: G.B. Olson, M. Azrin, E.S. Wright (Eds.), Innovations in Ultrahigh Strength Steel Technology, Proceedings of Sagamore Army Material Research Conference, Lake George, NY, 1987, pp. 263−285.
[49] Y. Tomita, Improved fracture toughness of ultrahigh strength steels through control of non-metallic inclusions, Journal of Materials Science 28 (1993) 853−859.
[50] T.B. Cox, J.R. Low, An investigation of the plastic fracture of AISI 4340 and 18 Nickel-200 Grade maraging steels, Metallurgical Transactions 5 (1974) 1457−1470.
[51] K.J. Handerhan, W.M. Garrison, N.R. Moody, A comparison of the fracture behavior of two heats of the secondary hardening steel AF 1410, Metallurgical Transactions 20A (1989) 105−123.
[52] W.M. Garrison, J.L. Maloney, Lanthanum additions and the toughness of ultra-high strength steels and the determination of appropriate lanthanum additions, Materials Science and Engineering A 403 (2005) 299−310.
[53] G.B. Olson, Overview: science of steel, in: G.B. Olson, M. Azrin, E.S. Wright (Eds.), Innovations in Ultrahigh Strength Steel Technology, Proceedings of Sagamore Army Material Research Conference, Lake George, NY, 1987, pp. 3−66.
[54] E. Lee, A.K. Vasudevan, Environmentally influenced fatigue in high strength steels, Journal of ASTM International 2 (3) (2005) 1−13.
[55] Fracture mechanics properties of carbon and alloy steels, in: Fatigue and Fracture, ASM Handbook, vol. 19, ASM International, 1996, pp. 614−654.
[56] G. Krauss, Low toughness embrittlement phenomena in steels, in: Steels: Processing, Structure, and Performance, ASM International, 2015, pp. 439−485.
[57] H.K.D.H. Bhadeshia, Prevention of hydrogen embrittlement in steels, ISIJ International 56 (2016) 24−36.
[58] D. Figueroa, M.J. Robinson, Hydrogen transport and embrittlement of 300M and Aermet 100 ultrahigh strength steels, Corrosion Science 52 (2010) 1593−1602.
[59] D. Li, R.P. Gangloff, J.R. Scully, Hydrogen trap states in ultrahigh strength Aermet 100 steel, Metallurgical and Materials Transactions A 35A (2004) 849−864.
[60] S. Kalnaus, J. Zhang, Y. Jiang, Stress-corrosion cracking of AISI 4340 steel in aqueous environments, Metallurgical and Materials Transactions A 42A (2011) 434−447.
[61] NC310YW Steel, Data Sheet, Aubert & Duval.
[62] LESCALLOY®, HY-TUF VAC-ARC®, Alloy Digest, ASM Alloy Digest, Filing Code SA-499, 1999.
[63] P.M. Novotny, G.E. Maurer, Ultra-high strength steels vs. titanium alloys, Advanced Materials and Processes 165 (11) (2007) 37−40.
[64] P.M. Novotny, Toughness index for alloy comparisons, Advanced Materials and Processes 165 (11) (2007) 29−31.
[65] A. Magnee, J.M. Draper, J. Dumont, D. Coutsouradis, L. Habraken, Stainless maraging steels − physical metallurgy, in: Cobalt-Containing High Strength Steels, Cobalt Information Center, 1974, pp. 81−101.
[66] H.J. Rack, D. Kalish, The strength, fracture toughness and low cycle fatigue behavior of 17-4 PH stainless steel, Metallurgical Transactions 5 (1974) 1595−1605.

[67] U.K. Viswanathan, S. Banerjee, R. Krishnan, Effects of aging on the microstructure of 17-4 PH stainless steel, Materials Science and Engineering A 104 (1988) 181−189.
[68] L. Ling, Heat treating of precipitation-hardenable (PH) stainless steels and iron base superalloys, in: Heat Treating of Iron and Steels, ASM Handbook, vol. 4D, ASM International, 2014, pp. 397−417.
[69] CARPENTER CUSTOM 475™ (High Strength Martensitic Precipitation Hardening Stainless Steel), Alloy Digest Filing Code SS-974, 2006.
[70] R. Schnitzer, R. Radis, M. Nöhrer, M. Schober, R. Hochfellner, S. Zinner, E. Povoden-Karadeniz, E. Kozeschnik, H. Leitner, Reverted austenite in PH 13-8 maraging steels, Materials Chemistry and Physics 122 (2010) 138−145.
[71] QuesTek and Carpenter Technology Data Sheets on Ferrium® Steels.
[72] C.J. Kuehmann, G.B. Olson, H.-J. Jou, Nanocarbide Precipitation Strengthened Ultrahigh Strength, Corrosion Resistant, Structural Steels, US Patent 7160399 B2, January 9, 2007.
[73] C.J. Kuehmann, G.B. Olson, H.-J. Jou, Nanocarbide Precipitation Strengthened Ultrahigh Strength, Corrosion Resistant, Structural Steels and Method of Making Said Steels, US Patent 7235213 B2, June 26, 2007.
[74] C.J. Kuehmann, G.B. Olson, H.-J. Jou, Nanocarbide Precipitation Strengthened Ultrahigh Strength, Corrosion Resistant, Structural Steels, US Patent 7967927 B2, June 28, 2011.
[75] H.-J. Jou, Lower-cost, Ultrahigh Strength, High Toughness Steel, US Patent 9051535 B2, June 9, 2015.
[76] J. Grabowski, C. Kuehmann, J. Sebastian, H.-J. Jou, R. Kooy, C. Kern, Ferrium® M54™: a new fatigue-resistant, lower cost, ultra-high strength steel for landing gear and arrestment applications, in: Aircraft Airworthiness & Sustainment Conference, April 3, 2012, Baltimore, MD.
[77] G.B. Olson, Computational design of hierarchically structured materials, Science 277 (1237) (1997) 1237−1242.

CHAPTER

Magnesium Alloys 7

CHAPTER OUTLINE

Synopsis **345**
7.1 The Promise and Timing of Magnesium Alloys **346**
7.2 Key Challenges for Magnesium Alloys **346**
7.3 Classifications of Magnesium Alloys **347**
7.4 Physical Metallurgy of Magnesium Alloys **348**
7.4.1 Concepts of Microstructural Efficiency and Alloying Efficiency 351
7.4.2 Effect of Alloying Addition on Texture 356
7.4.3 Precipitation in Commercial Magnesium Alloys 356
7.4.4 Effect of Microalloying on Precipitation 361
7.5 Processing–Microstructure–Properties of Magnesium Alloys **363**
7.5.1 Microstructural Evolution During Thermomechanical Processing 364
7.5.2 Strength–Ductility Response 365
7.5.2.1 Low Formability: Effect of Composition 367
7.5.2.2 Tension–Compression Yield Asymmetry 370
7.5.2.3 Role of Second-Phase Particles 371
7.5.2.4 Influence of Grain Size on Twinning and Strengthening 371
7.5.2.5 Ductility of Magnesium Alloys 373
7.5.2.6 Superposition of Various Strengthening Mechanisms and Microstructural Efficiency 374
7.5.3 Toughness Response 376
7.5.4 Fatigue Response 376
7.6 Summary **378**
References **379**

SYNOPSIS

Magnesium is the lightest element among the candidates for structural applications. Compared to the mainstream aluminum, titanium, and iron alloys covered in Chapters 4–6, whereas magnesium alloys have the potential to transition into airframe applications because of their weight advantage, they suffer from some limiting attributes that are the focus of ongoing research. The primary argument for considering magnesium alloys is built on specific properties. However, to

Metallurgy and Design of Alloys with Hierarchical Microstructures. http://dx.doi.org/10.1016/B978-0-12-812068-2.00007-2
Copyright © 2017 Elsevier Inc. All rights reserved.

have real opportunities for insertion, it is important that the combination of properties becomes competitive with aluminum alloys, as highlighted in this chapter through some examples. Concepts of microstructural efficiency and alloying efficiency are introduced. These concepts allow discussion of pathways for development of hierarchical microstructure in cost-effective magnesium alloys. Appropriate selection of alloying elements can promote synergy between microstructural and alloying efficiency.

7.1 THE PROMISE AND TIMING OF MAGNESIUM ALLOYS

Magnesium alloys have an interesting history of use in airframe structures. Very early on, magnesium alloys were used for aircraft structures. For example, Mathaudhu [1] has highlighted that the B-36 "Peacemaker" aircraft incorporated 8620 kg (19,000 lbs) of magnesium alloys, consisting of 5555 kg (12,200 lbs) of sheet, which covered 25% of the exterior, 700 kg (1500 lbs) of magnesium forgings, and 300 kg (660 lbs) of magnesium castings. The B-36 was built in 1946. Mathaudhu [1] also included the example of the H-19 "Chickasaw" built in 1951. The H-19 was the US Army's first true transport helicopter and had the highest percentage (by weight) of magnesium castings and sheet of any aircraft then in service (17%). These numbers are very significant and demonstrative of the position magnesium alloys enjoyed during the initial period of aircraft development. Applications for magnesium alloys in current Boeing planes like 737 and 747 are limited to a few components like small wing components and parts of the doors. There are more applications in helicopters, and components like cast transmission housing are sizable. With the considerations and approvals from the Federal Aviation Administration (FAA), the trends for applications are likely to be positive for magnesium alloys.

Magnesium alloys have been the subject of a number of recent initiatives. The extent of interest and timing can be gauged by the initiatives of various federal agencies. The US National Science Foundation (NSF) workshop on "Mg Science and Technology" was held in May 2011 [2]. The US Army Research Laboratory had organized a Sagamore Conference on Lightweight Materials in 2010. The US Department of Energy supported a 3-year "Mg front-end" program under United States Automotive Materials Partnership from 2008. There are similar activities on magnesium alloys in Europe, China, and Japan and in most cases the magnitude of effort, as evident by the volume of publications, is much larger.

7.2 KEY CHALLENGES FOR MAGNESIUM ALLOYS

Magnesium alloys suffer from a combination of "real" and "perceived" challenges. In this chapter, the inferior properties as compared to aluminum and titanium alloys are treated as real. On the other hand, the issue of flammability has been a perceived challenge. This originated from the fact that conventional fire fighting methods are not effective against magnesium fire. Once the reputation was set that magnesium alloys undergo sustained burning in the event of fire, the development of new rare

earth (RE) and calcium bearing alloys were not evaluated effectively until the last decade. Based on a series of studies and evaluations [3], the Society of Automotive Engineers (SAE), which develops standards for aviation, published SAE AS8049 Revision C, in which a key paragraph has been changed from reading that "magnesium alloys shall not be used" to the new wording:

> *"Magnesium alloys may be used in aircraft seat construction provided they are tested to and meet the flammability performance requirements in the FAA Fire Safety Branch document: Aircraft Materials Fire Test Handbook—DOT/FAA/AR-00/12, Chapter 25, Oil Burner Flammability Test for Magnesium Alloy Seat Structure."*

With this approval from the FAA, it is likely that the use of magnesium alloys in the interior of planes will start. That brings the other limitations or challenges in focus as compared to the mainstream alloys. In no particular order of importance, these are

- Limited formability
- Anisotropy in flow strength
- Lack of crack resistance, low fracture toughness, low impact toughness
- Low strength, particularly for non-RE element containing alloys
- Poor corrosion resistance
- Higher cost, particularly for RE element containing alloys

The first four aspects in the list above are related to plasticity in magnesium alloys and these aspects are presented in subsequent sections with microstructural approaches that are effective. The poor corrosion resistance is intrinsic with the position of magnesium in the galvanic series. Although alloying approaches and microstructural refinement improve the corrosion resistance, the improvement is marginal compared to the corrosion resistance of other engineering alloys. The consideration of cost is an important factor for widespread commercial use. Although most of the mechanical behavior related factors listed above can be influenced by alloying with RE elements, it comes at high cost. In a comprehensive review of precipitation-strengthened magnesium alloys, Nie [4] compared the pace of development in aluminum alloys with magnesium alloys (Fig. 7.1). The NSF workshop report on magnesium alloys [2] includes a quote "Al alloys of incredible strength were developed by Edisonian trial and error, over the course of 80 years. The science and engineering community will only permit us 5−10 years to make similar improvements to Mg alloys."—J.F. Nie. This quote is also reflective of the shift in alloy design approach and the central theme of this book.

7.3 CLASSIFICATIONS OF MAGNESIUM ALLOYS

Table 7.1 summarizes the different alloys and temper designations as outlined in ASTM standard B296 [5,6]. The classification of Mg alloys by ASTM standard is applicable to both cast and wrought alloys.

Magnesium alloys can also be grouped together based on their preferred processing route for manufacturing a semifinished or finished product form (Fig. 7.2). An

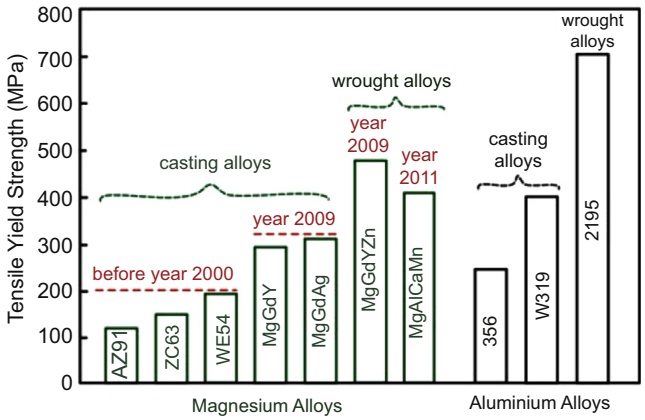


FIGURE 7.1

A plot created by Nie [4] showing the development of precipitation-hardenable casting and wrought magnesium alloys. Representative precipitation-hardenable aluminum casting (356 and W319) and wrought (2195) alloys are also provided for the purpose of a comparison of tensile yield strength.

alloy containing same principal alloying elements can be processed using more than one manufacturing route depending on the exact composition of the alloy and the design requirement for the alloy. For example, the investment casting route can be adopted instead of sand casting if the design requirement demands high-dimensional tolerances or very good surface finish. Similarly, AM50A and AM60A are suited for die casting applications, whereas AM100A is more amenable for sand and permanent casting techniques.

The composition-based classification can be based on whether aluminum is present. Mordike and Ebert [7] have mapped the direction of alloy development (Fig. 7.3) that is useful to list the main classes of Mg alloys (RE element):

- Al containing alloys—Mg−Al−Mn, Mg−Al−Zn (a very popular class with AZ31, AZ61, and AZ91 alloys), Mg−Al−Ca−RE alloys, Mg−Al−RE, Mg−Al−Si, Mg−Al−Ca−Mn
- Non-Al alloys—Mg−Y−RE−Zr (WE43 and WE54 are very popular casting alloys used for helicopter turbine housings), Mg−Zn−Cu, Mg−Zn−Zr, Mg−RE−Zn−Zr, Mg−Sc−X−M, Mg−Si, Mg−Li−X, Mg−Ag−RE−Zr

7.4 PHYSICAL METALLURGY OF MAGNESIUM ALLOYS

As discussed in the section listing key challenges, a number of these relate to how deformation proceeds in magnesium alloys. Much of the discussion in this chapter uses aluminum alloys for comparison. The standard microstructural features observed in aluminum alloys also apply to magnesium alloys, namely, solid solution,

Table 7.1 The Alloy and Temper Designation as per ASTM Standard

Part I: Two Letter Designation of Two Major Alloying Elements	Part II: Two Numbers Indicating Amounts of Two Major Alloying Elements in the Same Order	Part III: Order of the Modification of the Alloy Consisting of the Same Amount of Two Major Alloying Elements	Part IV: Thermo-Mechanical Processing History of the Alloy in Order to Introduce or Control Certain Property (-ies)
Aluminum (A), bismuth (B), copper (C), cadmium (D), rare earth (E), iron (F), magnesium (G), thorium (H), zirconium (K), lithium (L), manganese (M), nickel (N), lead (P), silver (Q), chromium (R), silicon (S), tin (T), yttrium (W), antimony (Y), zinc (Z)	The two numbers indicating composition of two major alloying elements are rounded off to their nearest integer.	First compositions, registered ASTM: A Second compositions, registered ASTM: B Third compositions: C High purity, registered ASTM: D High corrosion resistant, registered ASTM: E Not registered with ASTM: X1	As fabricated: F Annealed: O Strain hardened (applicable to wrought products only): H (subdivisions H1, H2, and H3 which are followed by one or more digits) Solution heat-treated: W (unstable temper) Thermally treated to produce stable temper other than F, O, or H: T (subdivisions T1, T3,…,T10 which may be followed by one or more digits)

Adapted from M. Avedesian, H. Baker (Eds.), ASM Specialty Handbook: Magnesium and Magnesium Alloys, ASM International, 1999, ISBN:978-0-87170-657-7. Adapted and reproduced from R.S. Mishra, P.S. De, N. Kumar, Friction Stir Welding and Processing: Science and Engineering, Springer, 2014, pp. 149–187, ISBN:978-3-319-07043-8.

precipitates, dispersoids, and texture. However, the impact of these microstructural features on plasticity is different from the face centered cubic (FCC) aluminum alloys because of the different crystal structure and slip and twinning systems in the hexagonal closed packed (HCP) magnesium alloys. Fig. 7.4 shows the slip and twinning systems for magnesium alloys. The most important thing to note is the difference in critical resolved shear stress (CRSS) for various slip systems (Table 7.2 [8]). The ratio of CRSS for basal and nonbasal slip system influences the manner in which deformation starts and the nature of the stress–strain curve. Hutchinson and Barnett [8] have also evaluated the role of dislocation density on the shift in the ratio of CRSS for basal and nonbasal slip system. High stored dislocation density activates nonbasal slip.

The most common alloying elements are aluminum (A), RE (E), lithium (L), manganese (M), silver (Q), yttrium (W), and zinc (Z). Nie [4] has comprehensively

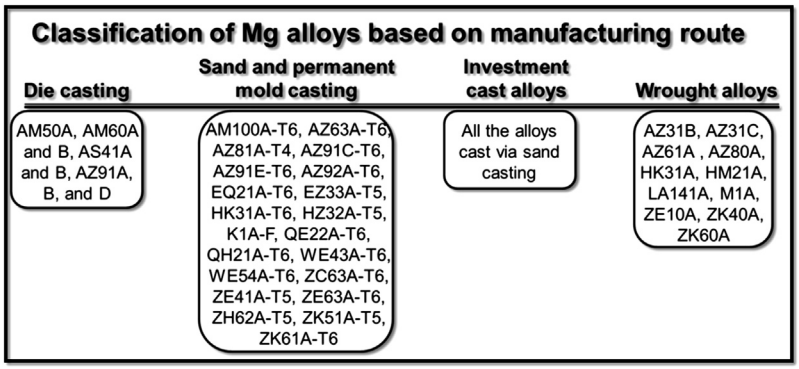


FIGURE 7.2

Grouping of commercially available cast and wrought Mg alloys based on their suitable manufacturing routes.

Data collected from M. Avedesian, H. Baker (Eds.), ASM Speciality Handbook—Magnesium and Magnesium Alloys, ASM International, 1999, ISBN:978-0-87170-657-7. Data taken from R.S. Mishra, P.S. De, N. Kumar, Friction Stir Welding and Processing: Science and Engineering, Springer, 2014, pp. 149–187, ISBN:978-3-319-07043-8.

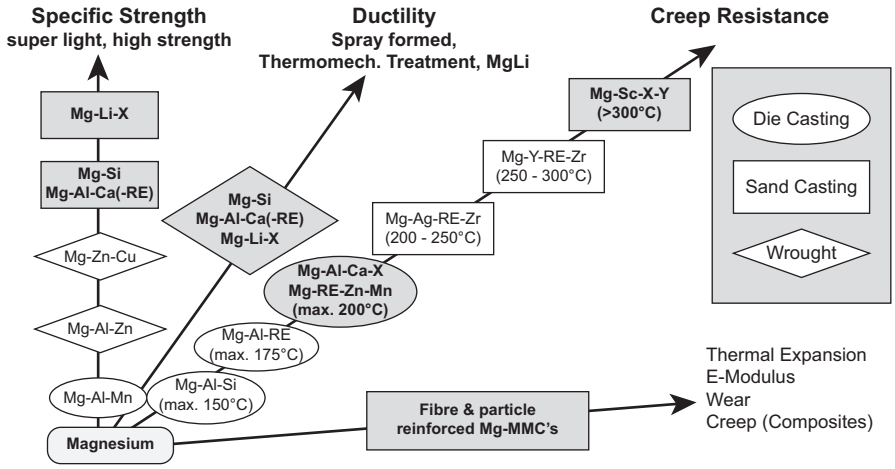


FIGURE 7.3

A map depicting the direction of Mg alloy development [7], which also gives a classification of alloys.

reviewed the precipitation sequence in magnesium alloys (Table 7.3). The popular alloys in the AZ and WE series have different levels of complexity. The precipitates in WE alloys go through a more complex set of transformations. As with aluminum alloys, the size, shape, and orientation are all critical for the effectiveness of these

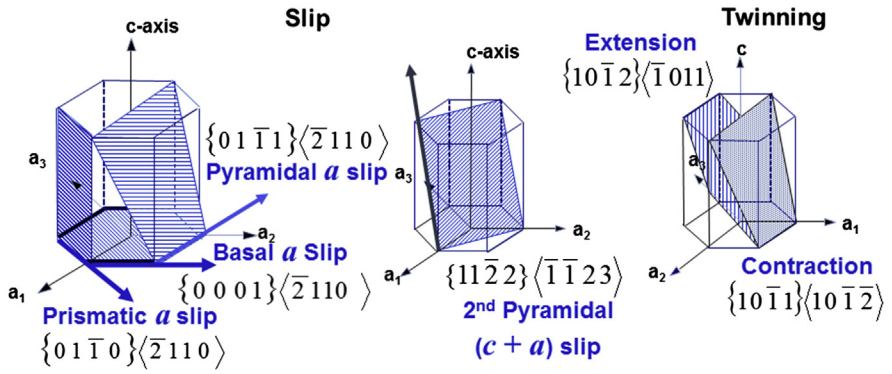


FIGURE 7.4

Slip and twinning systems in Mg alloys.

precipitates. Common precipitate shapes are spherical, rod, and disk. Combining these shapes with slip system results in the following illustrative possibilities:

- Spherical precipitates are effective in blocking dislocations gliding on basal, prismatic, and pyramidal planes,
- Disk-shaped precipitates on the basal plane are not very effective in blocking basal slip,
- Disk-shaped precipitates on the prismatic plane are very effective in blocking basal slip,
- Rod-shaped precipitates along the *c*-axis are very effective, whereas the same shape along *a*-direction is not so effective.

Nie [4,9] has discussed these and Fig. 7.5 illustrates the disc-shaped precipitates on basal and prismatic planes. The desired microstructural features are summarized in Table 7.4. The difference between the ideal and real microstructure is very important to acknowledge. It highlights the particular nature of the alloy system and the intricacies associated with different parent elements. This concept is developed further in a short section on "microstructural efficiency" and "alloying efficiency."

7.4.1 CONCEPTS OF MICROSTRUCTURAL EFFICIENCY AND ALLOYING EFFICIENCY

As highlighted in Fig. 7.1, precipitation-strengthened magnesium alloys have not been developed to the extent that precipitation-strengthened aluminum alloys have been. Some of this is intrinsic to magnesium as a host element. The change in crystal structure from FCC for aluminum to HCP for magnesium impacts the slip systems as well as second-phase precipitation. A simple way to define *microstructural efficiency* is,

$$\text{Microstructural efficiency} = \frac{\text{Experimental property}}{\text{theoretically calculated property}}$$

Table 7.2 Compilation of Single-Crystal and Polycrystal Critical Resolved Shear Stress Values by Hutchinson and Barnett [8] for Some Important HCP (Hexagonal Closed Packed) Metals Obtained From Single-Crystal Experiments and Estimated for Polycrystalline Materials (MPa)

Material/method	Basal $\langle a \rangle$	Prism $\langle a \rangle$	Pyramidal $\langle c+a \rangle^*$	Ratio hard/soft
Mg single crystal	0.81			
Mg single crystal	0.76			
Mg single crystal	0.52			
Mg single crystal		39		
Mg single crystal		50		
Mg single crystal (range)				48–96
Mg—0.1% Al single crystal	1	45		45
Mg—0.25% Zn single crystal	1.2	45		38
Mg AZ31 polycrystal VPSC model	45	110		2.4
Mg AZ31 polycrystal EPSC model	10	55		5.5
Mg AZ31 polycrystal EPSC model	20	90		4.5
Mg AZ31 polycrystal EPSC model	30	90		3.0
Mg AZ31 Sachs model	50	100		2.0
Mg ZM20 small grain EPSC model	12	53		4.4
Mg ZM30 large grain EPSC model	2	27		13.5
Ti—6% Al single crystal	190	200	770	4.1
Ti—6/4 polycrystal Sachs model	444	380	631	1.7

EPSC, *elastic plastic self-consistent;* VPSC, *viscoplastic self-consistent*

For example, to block the basal dislocations, fine needle-shaped precipitates on the prismatic orientation or very fine spherical precipitates would be the most effective. The overall strengthening originates from the following:

- *Peierls stress or lattice friction stress*: This is directly tied with the basic crystal structure of the host element. It does not impact the microstructural efficiency or alloying efficiency.
- *Solid solution strengthening*: This depends on the atomic size difference of solute, shear modulus value difference of solute, and the amount of solute in solid solution. The ability of host element to retain high amount of alloying element in the solution dictates the overall effectiveness of this mechanism.

Table 7.3 A Very Comprehensive Listing of Precipitation Sequence in Magnesium Alloys Compiled by Nie [4]

Mg-Al	SSSS → β ($Mg_{17}Al_{12}$) bcc ($I\bar{4}3m$, a = 1.06 nm); $(0001)_\alpha$ plate/lath					
Mg-Al -Ca	SSSS → ordered G.P. zones hcp a = 0.556 nm monolayer $(0001)_\alpha$ disc	→ C15 (Al_2Ca) fcc, $Fd\bar{3}m$ a = 0.802 nm $(0001)_\alpha$ plate				
Mg-Zn	SSSS → G.P. zones	→ β_1' (Mg_4Zn_7) monoclinic, B/2m a = 2.60 nm b = 1.43 nm c = 0.52 nm γ = 102.5° $[0001]_\alpha$ rod	→ β_2' ($MgZn_2$) hcp, $P6_3/mmc$ a = 0.52 nm c = 0.86 nm $(0001)_\alpha$ plate	→ β ($MgZn$) monoclinic a = 1.61 nm b = 2.58 nm c = 0.88 nm β = 112.4°		
Mg-Zn-Al[a]	SSSS → G.P. zones	→ i icosahedral or approximant diamond shape	→ Φ and/or T Φ: orthorhombic, Pbcn a = 0.90 nm b = 1.70 nm c = 1.97 nm $(0001)_\alpha$ lath	T : bcc, $Im\bar{3}$ a = 1.40 nm		
Mg-Sn(-Zn)	SSSS → β (Mg_2Sn) fcc ($Fm\bar{3}m$, a = 0.68 nm), $(0001)_\alpha$ and $\{11\bar{2}2\}_\alpha$ plate/lath, $[0001]_\alpha$ rod and polygon					
Mg-Ca-Zn	SSSS → ordered G.P. zones hcp a = 0.556 nm monolayer $(0001)_\alpha$ disc	→ η′ (MgCaZn) hcp, $P6_3/mmc$ a = 0.56 nm c = 1.04 nm $(0001)_\alpha$ plate	→ η ($Mg_2(Ca,Zn)$) hcp, $P6_3/mmc$ a = 0.62 nm c = 1.01 nm $(0001)_\alpha$ plate			
Mg-Nd	SSSS → ordered G.P. zones zig-zag shape d = 0.37 nm[b]	→ β″ (Mg_3Nd) hcp, $D0_{19}$ a = 0.64 nm c = 0.52 nm hexagonal prism	→ β′ (Mg_7Nd) orthorhombic a = 0.64 nm b = 1.14 nm c = 0.52 nm lenticular shape	→ β_1 (Mg_3Nd) fcc, $Fm\bar{3}m$ a = 0.74 nm $\{10\bar{1}0\}_\alpha$ plate	→ β ($Mg_{12}Nd$) tetragonal, I4/mmm a = 1.03 nm c = 0.59 nm $[0001]_\alpha$ rod	
Mg-Nd-Zn	SSSS → ordered G.P. zones hcp a = 0.556 nm monolayer $(0001)_\alpha$ disc	→ γ″ ($Mg_5(Nd,Zn)$) hcp, $P\bar{6}2m$ a = 0.55 nm c = 0.52 nm $(0001)_\alpha$ plate	→ γ (possibly $Mg_3(Nd,Zn)$) fcc, possibly $Fm\bar{3}m$ a = 0.70 nm plate on irrational plane		↓ β_c ($Mg_{41}Nd_5$) tetragonal, I4/m a = 1.47 nm c = 1.04 nm	
Mg-Gd(-Y)	SSSS → ordered G.P. zones zig-zag shape d = 0.37 nm[b]	→ β″ (Mg_3Gd) hcp, $D0_{19}$ a = 0.64 nm c = 0.52 nm hexagonal prism	→ β′ (Mg_7Gd) orthorhombic a = 0.65 nm b = 2.27 nm c = 0.52 nm lenticular shape	→ β_1 (Mg_3Gd) fcc, $Fm\bar{3}m$ a = 0.73 nm $\{10\bar{1}0\}_\alpha$ plate	→ β (Mg_5Gd) fcc, $Fm\bar{3}m$ a = 2.23 nm $\{10\bar{1}0\}_\alpha$ plate	
Mg-Y	SSSS → β′ (Mg_7Y) orthorhombic a = 0.65 nm b = 2.27 nm c = 0.52 nm globular shape	→ β ($Mg_{24}Y_5$) bcc, $I\bar{4}3m$ a = 1.13 nm $\{10\bar{1}0\}_\alpha$ or $\{31\bar{4}0\}_\alpha$ plate				
Mg-Y-Nd	SSSS → ordered G.P. zones zig-zag shape d = 0.37 nm[b]	→ β″ (Mg_3Nd) hcp, $D0_{19}$ a = 0.64 nm c = 0.52 nm hexagonal prism	→ β′ ($Mg_{12}YNd$) orthorhombic a = 0.64 nm b = 2.24 nm c = 0.52 nm globular shape	→ β_1 ($Mg_3(Nd,Y)$) fcc, $Fm\bar{3}m$ a = 0.74 nm $\{10\bar{1}0\}_\alpha$ plate	→ β ($Mg_{14}Nd_2Y$) fcc, $Fm\bar{3}m$ a = 2.20 nm $\{10\bar{1}0\}_\alpha$ plate	
Mg-Gd-Zn[c]	SSSS → γ″ ($Mg_{70}Gd_{15}Zn_{15}$) ordered hcp, $P\bar{6}2m$ a = 0.56 nm c = 0.44 nm $(0001)_\alpha$ plate	→ γ′ (MgGdZn) hcp, $P\bar{3}m1$ a = 0.32 nm b = 0.78 nm $(0001)_\alpha$ plate	→ γ ($Mg_{12}GdZn$) ordered hcp, 14H a = 1.11 nm c = 3.65 nm $(0001)_\alpha$ plate			
Mg-Y-Zn	SSSS → I_2 stacking fault $(0001)_\alpha$ plane	→ γ′ (MgYZn) hcp, $P\bar{3}m1$ a = 0.32 nm c = 0.78 nm $(0001)_\alpha$ plate	→ γ ($Mg_{12}YZn$) ordered hcp, 14H a = 1.11 nm c = 3.65 nm $(0001)_\alpha$ plate			
Mg-Y-Ag-Zn	SSSS → G.P. zones monolayer $(0001)_\alpha$ disc	→ γ″ ordered hcp, $P\bar{6}2m$ a = 0.56 nm c = 0.45 nm $(0001)_\alpha$ plate	→ γ′ hcp, $P\bar{3}m1$ a = 0.32 nm c = 0.78 nm $(0001)_\alpha$ plate	→ γ+δ γ: ordered hcp, 14H a = 1.11 nm c = 3.65 nm $(0001)_\alpha$ plate	δ: fcc, $Fd\bar{3}m$ a = 1.59 nm	

[§]Precipitation process is not well studied; *d is separation distance of columns of RE atoms; [#]low Gd:Zn weight ratio and low Gd content.

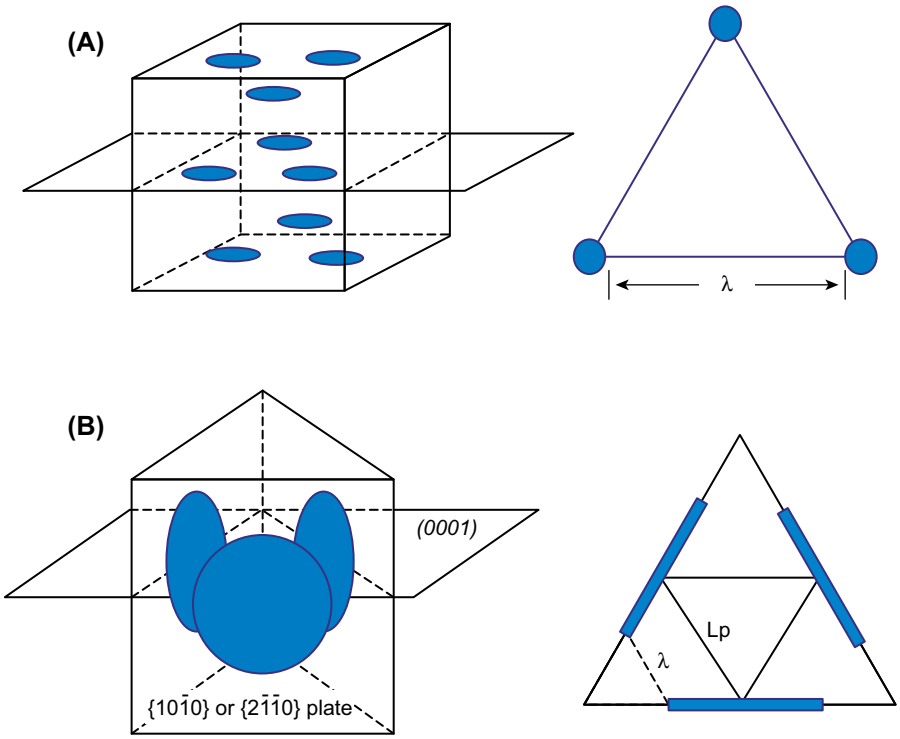


FIGURE 7.5

Schematic diagrams showing the effects of the orientation of precipitate plates on interparticle spacing for the dislocation slip on basal plane of the magnesium matrix phase [4].

Table 7.4 A Comparison of Desired Microstructural Features With Usually Observed Ones

Desired Microstructure	Microstructure Typically Obtained in Practice	Reason
Effective size, morphology, and distribution of precipitates	Highly elongated with low density	Low nucleation density and anisotropic growth along preferred growth direction
Fine grain size	Coarse or mixed distribution	Grain boundaries are nucleation site for grains
Random texture	Highly textured	Dominance of certain slip systems during deformation

Again, this mechanism does not impact the microstructural efficiency or alloying efficiency.

- *Grain boundary strengthening*: At the first glance, grain boundary strengthening is directly related to the grain size. However, for magnesium alloys, twinning as well as texture impacts the Hall−Petch (HP) relationship and this is covered in a later section. The impact of boundary strengthening on microstructural efficiency or alloying efficiency is secondary.
- *Texture strengthening*: The combination of grain size and final texture after thermomechanical processing impacts a number of different mechanical properties. A quantitative relationship is not available for texture strengthening. The most obvious impact of texture is on the anisotropy of mechanical properties. Again, the impact of texture strengthening on microstructural efficiency or alloying efficiency is secondary.
- *Composite strengthening*: The composite strengthening depends on the stiffness of second phase. Although the primary impact is obvious, the secondary impact can be very significant depending on the property. Rosler and Baker [10] have proposed a theoretical concept to obtain a synergetic effect through dual-scale particle strengthening by the interaction of small dispersoids (in nanometer size range) and larger reinforcement particles (in micrometer to millimeter range); a clear example of hierarchical microstructure. This can be a very significant concept for mechanical properties that are nonlinear. For example, dislocation creep behavior is expressed as a power law. A slight change in the stress value changes the creep rates quite significantly. Because of elastic deformation mismatch, load transfer to the reinforcement phase lowers the load on the matrix phase. The lower load in the matrix phase reduces the creep rate. Dutt et al. [11] have shown the applicability of this concept for Ni−Cr−Al_2O_3−Y_2O_3 system. Several magnesium alloys and composites have hierarchical microstructure with nano- and microlength scales. The synergistic approach is likely to enhance the microstructural efficiency for creep and fatigue-related properties.
- *Precipitation strengthening*: This is the most important aspect for magnesium alloys. From Chapter 4, the effectiveness of precipitation strengthening in 2XXX and 7XXX series of alloys series is quite clear. AA2195 alloy has been highlighted in Fig. 7.1 because of its exceptional combination of mechanical properties, compared with the conventional magnesium alloys. The most popular AZ series of magnesium alloys has three widely used compositions of AZ31, AZ61, and AZ91. Fig. 7.6 shows the change in volume % of second phase particles as a function of atomic % of total alloying elements. The concept of *alloying efficiency* can be developed in two steps. The first consideration involves the type of second phase particles that forms. If the alloying element X results in a phase Mg_3X and the alloying element Y results in Mg_2Y, then X has a higher alloying efficiency, as it results in higher volume fraction of precipitate per atom% of addition. The second consideration is regarding the efficacy of second-phase particles to alter the desired property. For example, how efficient is the contribution of the strengthening precipitates? Specifically, in the WE43 alloy, excess Y is tied up in constituent particles [12]. The tying up of alloying elements in a form or in a location that is noneffective leads to loss of alloying

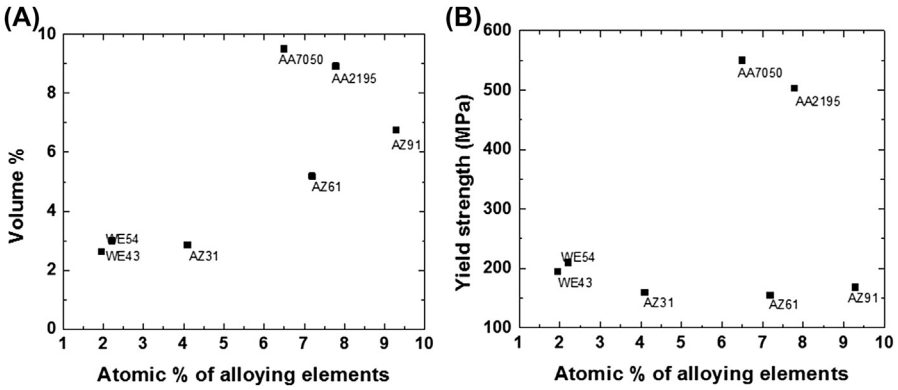


FIGURE 7.6

A plot of (A) volume fraction of second phase with atomic % of alloying element in a few magnesium alloys and (B) corresponding yield strength variation. For comparison two aluminum alloys have been included. The strength values are taken from the Cambridge Engineering Selector (CES) software database.

efficiency. Thus, the alloying efficiency is defined by the volume fraction of functional phase per at. % combined with its effective distribution. The fact that the increase in second-phase volume fraction in AZ alloys from AZ31 to AZ91 does not proportionately impact the strength is clear from Fig. 7.6B. Note the comparative strength-alloying level correlation in aluminum alloys.

7.4.2 EFFECT OF ALLOYING ADDITION ON TEXTURE

Texture in thermo-mechanically processed magnesium is usually dominated by basal texture. The AZ31 sheets have a pronounced basal texture. Significant body of research has established that alloying with RE elements leads to reduction or elimination of texture. Fig. 7.7 shows the variation of grain size and intensity of basal texture as a function of minor levels of RE alloying addition [13]. It shows that the nature of recrystallization and grain growth changes with RE alloying addition. The alloying approach that promotes nonbasal slip is likely to impact the reduction in texture. The anisotropy in the subsequent flow behavior is directly related to this. An example of elimination of anisotropy is included in the next section.

7.4.3 PRECIPITATION IN COMMERCIAL MAGNESIUM ALLOYS

As highlighted in Fig. 7.5 and Table 7.4, the size, morphology, and orientation of precipitates are important. Fig. 7.6 suggests that the precipitation in commercial magnesium alloys is not as effective as in aluminum alloys. The nucleation and growth of precipitates need to be treated differently. High nucleation density is critical for obtaining effective dispersion strengthening. The physical metallurgy of magnesium alloys differs from that of aluminum alloys because of the crystal

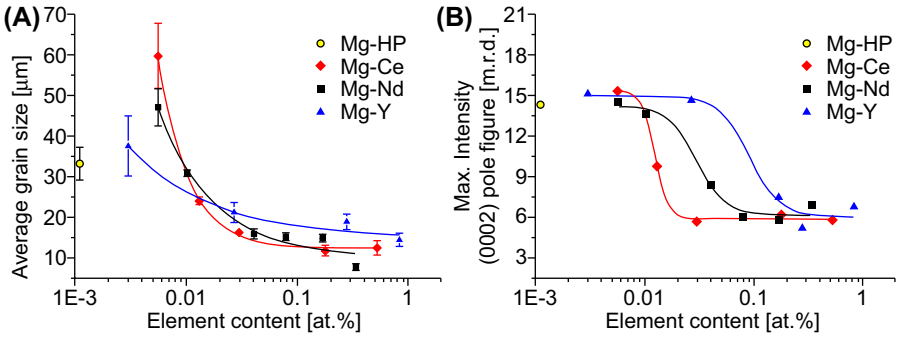


FIGURE 7.7

Variation of (A) average grain size after annealing and (B) maximum (0002)-pole figure intensity in as-rolled condition as a function of the rare earth alloying elements [13].

structure difference and its impact on nucleation and growth of precipitates. Enhancement of nucleation density can be achieved either by alloying, treated in the next section on microalloying, or by introducing defects like dislocations, which can serve as nucleating sites. For example, the T3 and T8 tempers rely on cold work induced dislocations to enhance precipitate density. Nie [9] has covered precipitation in great detail, and the discussion here is limited to AZ91 and WE43 to highlight two classes of magnesium alloys.

The AZ91 alloy has one of the highest volume fraction of precipitates among magnesium alloys. The β-$Mg_{17}(Al,Zn)_{12}$ particles nucleate in α-Mg matrix and the process can be continuous or discontinuous. Continuous precipitation is precipitation within the grain. In contrast, the discontinuation precipitation starts from grain boundaries and the lamellar morphology emerges. Note that the refinement in grain size would impact the balance of continuous and discontinuous precipitation. Figs. 7.8 and 7.9 show scanning and transmission electron micrographs, respectively, to highlight the overall nature of the distribution and size of phases [14]. Two noteworthy microstructural features emerge. As the aim of understanding physical metallurgy of precipitates is to relate microstructural features with mechanical properties, the scale of precipitates becomes important. Note that the scale is relatively coarser for the discontinuously nucleated precipitates compared to continuously nucleated precipitates.

The WE 43 alloy is very popular as a casting alloy, which in the last 15 years, has been produced as wrought products by Magnesium Elektron. The wrought alloy provides a variety of microstructural paths to create various precipitate morphologies. Figs. 7.10–7.12 show a few examples of precipitates in WE43 alloy from the work of Kumar et al. [15]. Note that very wide-ranging possibilities exist in an alloy like WE43 because prior history influences the level of supersaturation. Palanivel

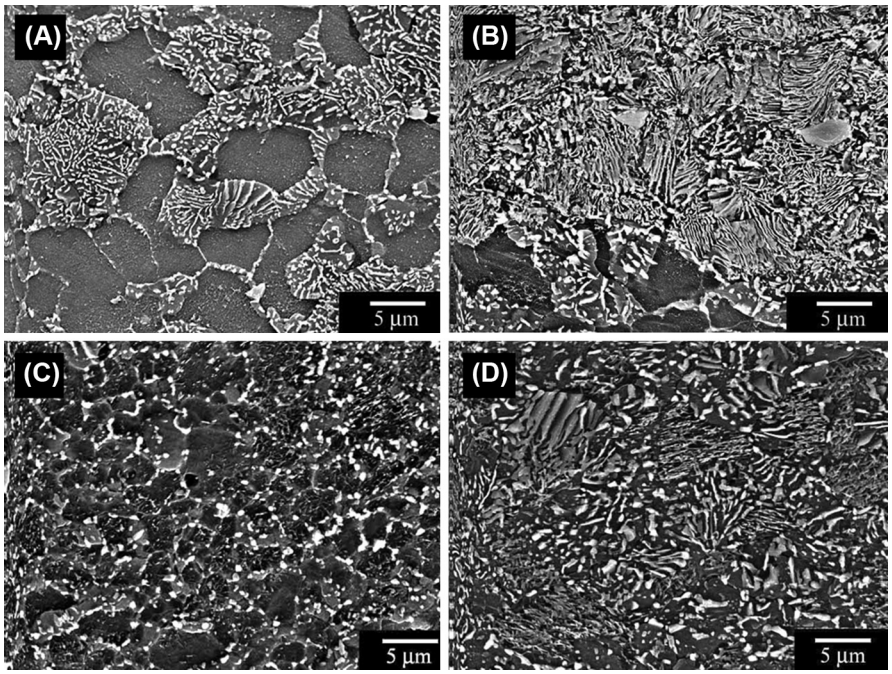


FIGURE 7.8

Scanning electron microscope (SEM) micrographs of friction stir processed (FSP)+aged alloy after aging at, (A) 150°C for 24 h, (B) 150°C for 48 h, (C) 200°C for 12 h, and (D) 200°C for 48 h. The micrographs show discontinuous and continuous precipitates under different aging conditions [14].

et al. [12] have highlighted the fact that there is excess Y in this alloy and even after solution heat treatment, Mg_2Y constituent particles are present. These figures capture two thermomechanical paths, (1) a conventional pathway of rolling where WE43 is hot rolled and subsequently aged and (2) a nonconventional friction stir processing path that involves imparting very high plastic strain and high strain rate at high temperature.

The details of precipitation in thermomechanically processed alloys change because of the microstructural details. Nie [9] has summarized precipitation in the Mg−Nd−Y system and the metastable phases go through morphological changes—β'' (hexagonal prism) → β' (lenticular shape) → β_1 (plate) → β (rod). Fig. 7.10 shows the precipitates after hot rolling and aging [15]. Note that the dislocation substructure helps in creating an inhomogeneous distribution of precipitates. In select regions, high density of honeycomb network was observed. Such networks on prismatic planes are ideal to block basal slip. Note also that hexagonal network

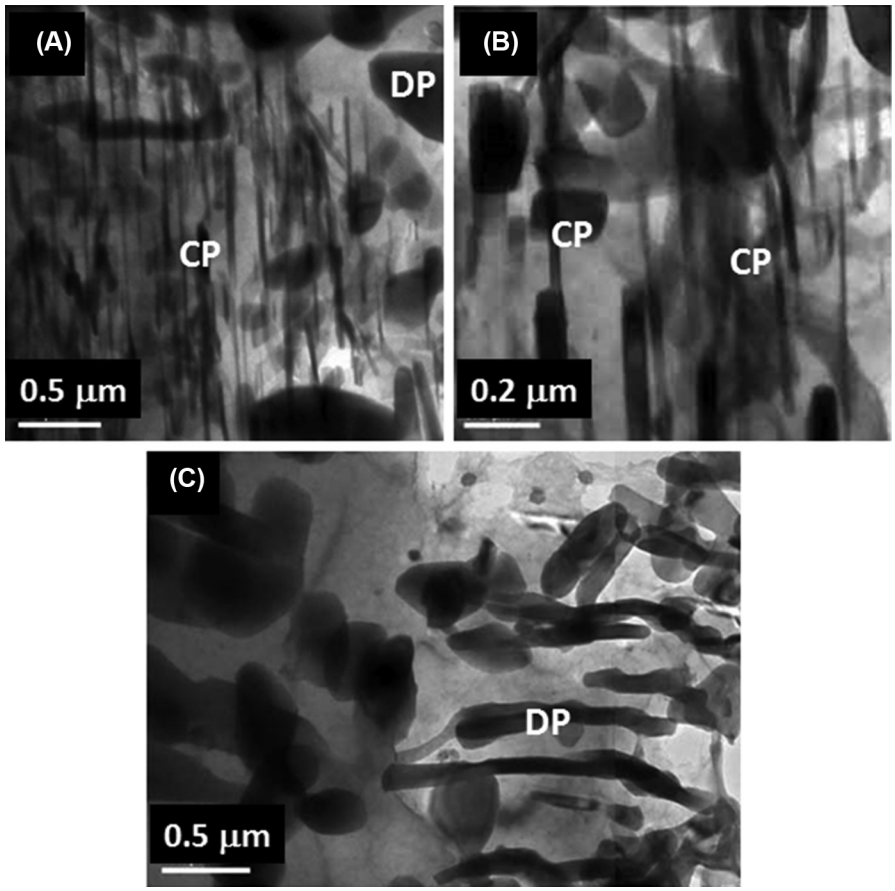


FIGURE 7.9

Transmission electron microscopy (TEM) micrographs of friction stir processed (FSP) + aged (at 200°C for 48 h) alloy showing (A) continuous precipitates of lath morphology, (B) continuous precipitates of different morphologies (laths and rods), and (C) discontinuous precipitates having lamellar and globular morphologies [14].

is built with β' and β_1 segments. Embury et al. [16] have discussed the interaction of plasticity and diffusion controlled precipitation reactions. For the current discussion, dislocation-mediated precipitation is important. Fig. 7.11 highlights this effect further [15]. The microstructures shown in Fig. 7.11 are after friction stir processing. Note the three different features. First, the retained dislocations are decorated by very fine precipitates along the core. These have been identified as β', about 2 nm wide [15]. The grain boundaries precipitates in this condition have two separate

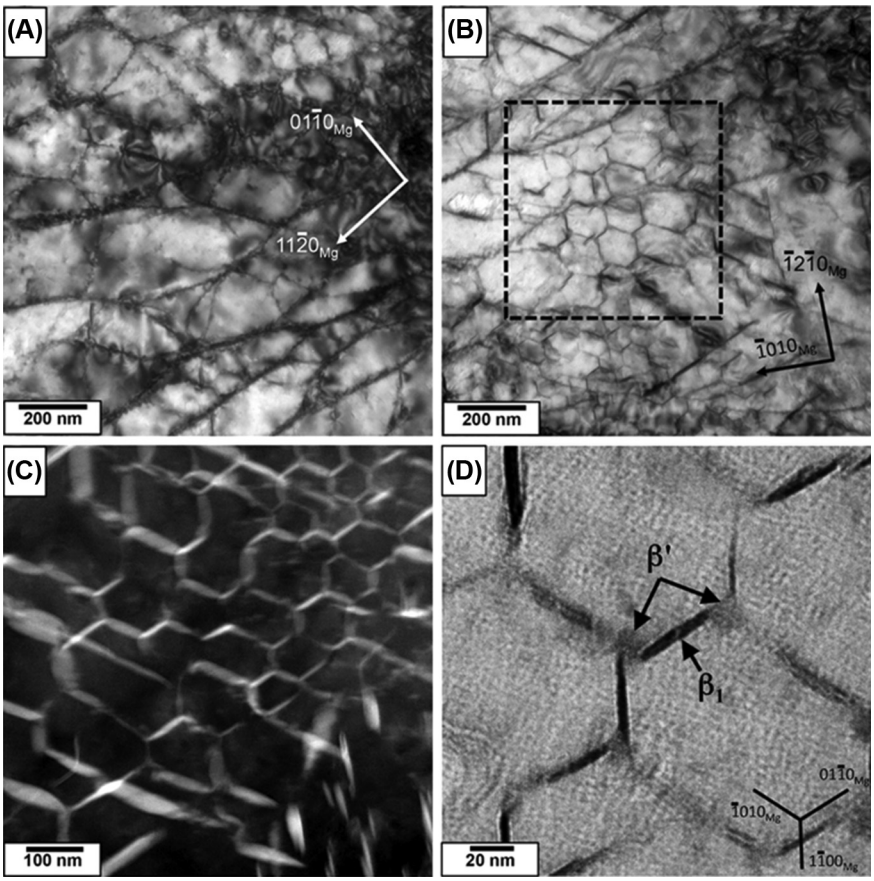


FIGURE 7.10

Bright field (BF) transmission electron microscopy (TEM) image showing precipitates in (A) vein-like and (B) partial honeycomb networked arrangement. (C) High angle annular dark field scanning transmission electron microscopy (HAADF-STEM) image of an extensive honeycomb network. (D) BF TEM image showing β′ precipitate at the nodes of β_1 plates. All BF TEM images were obtained with beam approximately close to $[0001]_{Mg}$ zone axis [15].

length scales. This is highlighted in the inset of Fig. 7.11D. Subsequent aging of friction stir processed (FSP) WE43 alloy leads to coarsening of intragranular and grain boundary precipitates (Fig. 7.12) [15]. The intragranular precipitates transform to β_1 phase with plate or disc shape. The size of β_1 precipitates is not ideal for very high strengthening and this is a major reason behind the observed lower microstructural efficiency discussed earlier.

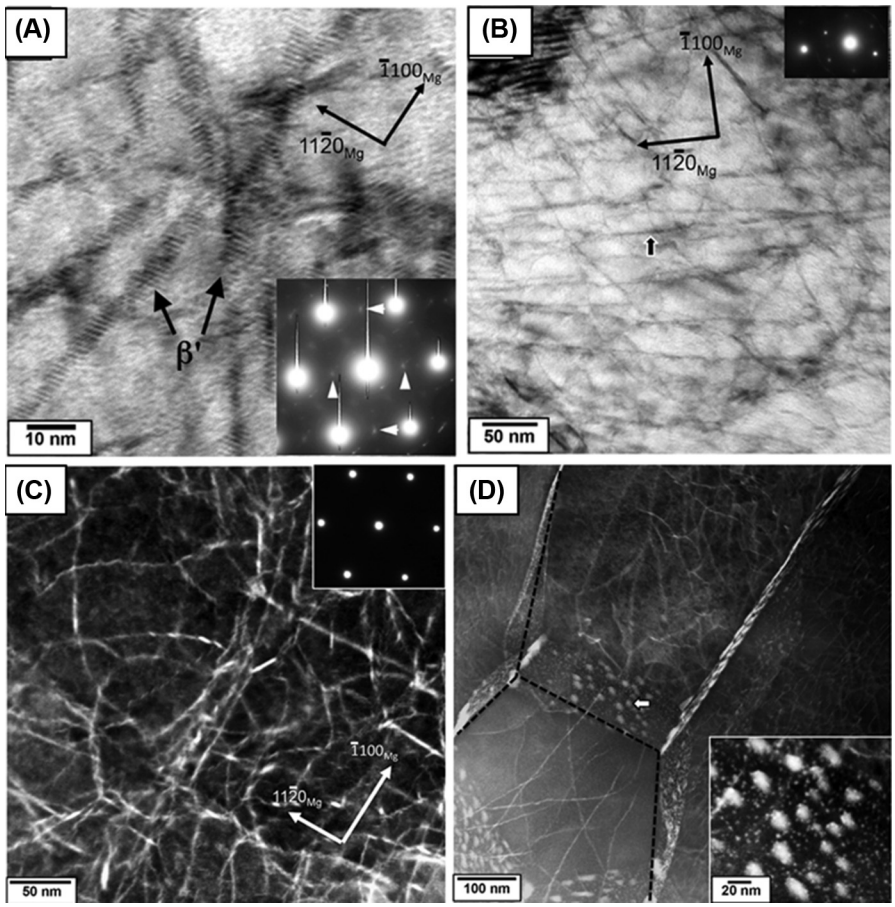


FIGURE 7.11

Transmission electron microscopy (TEM) images of post-friction stir processed (FSP) microstructure: (A) bright field (BF) TEM image showing β′ precipitates, whereas the inset shows $[0001]_{Mg}$ selected area diffraction pattern (SADP) from the same region and (B) BF TEM image under two-beam condition depicting fine-scale linear precipitates. High-angle annular dark field scanning transmission electron microscopy (HAADF-STEM) images of post-FSP microstructure. (C) Image recorded along $[0001]_{Mg}$ zone axis (inset) showing precipitate distribution within a grain, and (D) lower magnification HAADF-STEM indicating globular grain boundary precipitate along with intragranular precipitation [15].

7.4.4 EFFECT OF MICROALLOYING ON PRECIPITATION

A key physical metallurgy aspect as emphasized earlier is related to the nucleation density of precipitates. Significant research has been done to look at this aspect in

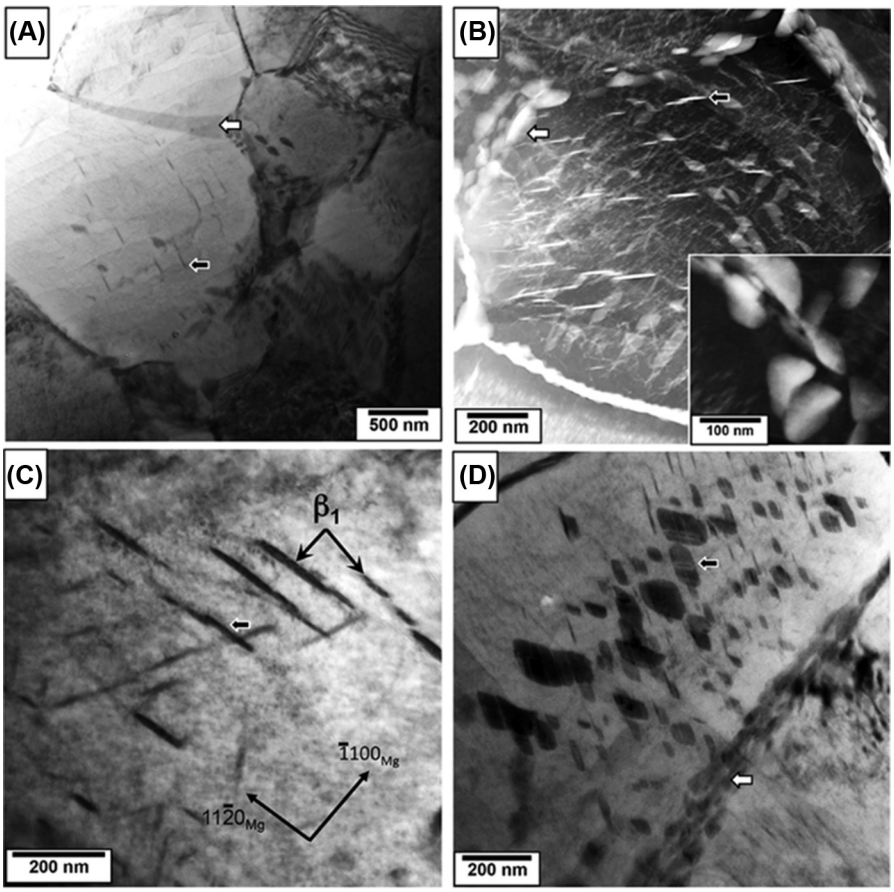


FIGURE 7.12

Transmission electron microscopy (TEM) images of the aged friction stir processed (FSP) microstructure. (A) Low-magnification bright field (BF) TEM image showing intragranular and grain boundary precipitation along with refine α-Mg grains. (B) High-angle annular dark field scanning transmission electron microscopy (HAADF-STEM) image showing coarse intragranular and grain boundary (inset) precipitates. (C) BF TEM image showing orientation of a particular variant of β_1 precipitates within α-Mg. (D) BF TEM image showing broad faces of β_1 precipitates [15].

relatively dilute alloys. Mendis et al. [17] have put forth a set of thermodynamics and kinetic conditions that would enhance nucleation using microalloying based on the following (text below reproduced from [17]):

> *"(1)* A driving force for heterogeneity formation (i.e. a clustering or coclustering tendency of the microalloying elements upon cooling from the solution treatment temperature) must exist.

(2) There should not be any repulsive tendencies between the solute forming the strengthening precipitates and the microalloying additions forming the cluster or precipitate at which nucleation is desired, otherwise the heterogeneity would not be expected to be effective at catalyzing nucleation.

(3) The natural length (λ*) and time (t*) scales for cluster or precipitate formation must be finer and faster than the length (λ) and time (t) scales associated with precipitation of the strengthening precipitate in the equivalent alloy without microalloying additions."

Mendis et al. [17] showed the effectiveness of this approach in a model Mg—Sn system. Fig. 7.13 shows the impact of microalloying on aging response of Mg—Zn and Mg—Sn alloys [18]. Note the increase in effective hardness and shorter time for peak hardness.

7.5 PROCESSING—MICROSTRUCTURE—PROPERTIES OF MAGNESIUM ALLOYS

Unlike the alloy systems covered in Chapters 4—6, magnesium alloys are influenced significantly by texture, which evolves during processing. In this section, the linkages among processing, microstructure, and properties are highlighted with a few examples, without any attempt to comprehensively cover the large body of literature, as these alloys have yet to make a full impact in terms of use in aircraft structures. Nevertheless, the information presented is adequate to capture the important aspects, which are as follows:

- Impact of processing on grain size,
- Influence of grain size on deformation by slip or twinning,
- Tension-compression asymmetry in flow behavior, and
- Effectiveness of strengthening mechanisms.

Hardness measurement gives a very quick indication of the level of strength of an alloy and it is also easy and adequate for comparative assessment of alloys. The three light elements used as base for structural applications are magnesium, aluminum, and titanium. It is instructive to compare the range of hardness values in alloys based on these elements. The magnesium alloys have hardness values in the range of 50—120 HV. Note that the peak hardness values in Fig. 7.13 is around 100 HV. WE43 alloy has maximum hardness of ~120 HV. Compare this to precipitation-strengthened aluminum alloys that have hardness values in the range of 60—180 HV. AA2XXX and AA7XXX alloys have typical hardness values in the range of 120—180 HV for various tempers. For the α/β titanium alloys, the hardness values are in the range of 300—350 HV. Given that the starting point for consideration of magnesium alloys is for the replacement of aluminum alloys, it is important to compare the magnesium alloy hardness value range of 60—120 HV with 120—180 HV for aluminum alloys. Of course, the density of magnesium alloys is typically two-thirds of that of aluminum alloys and that normalization indicates

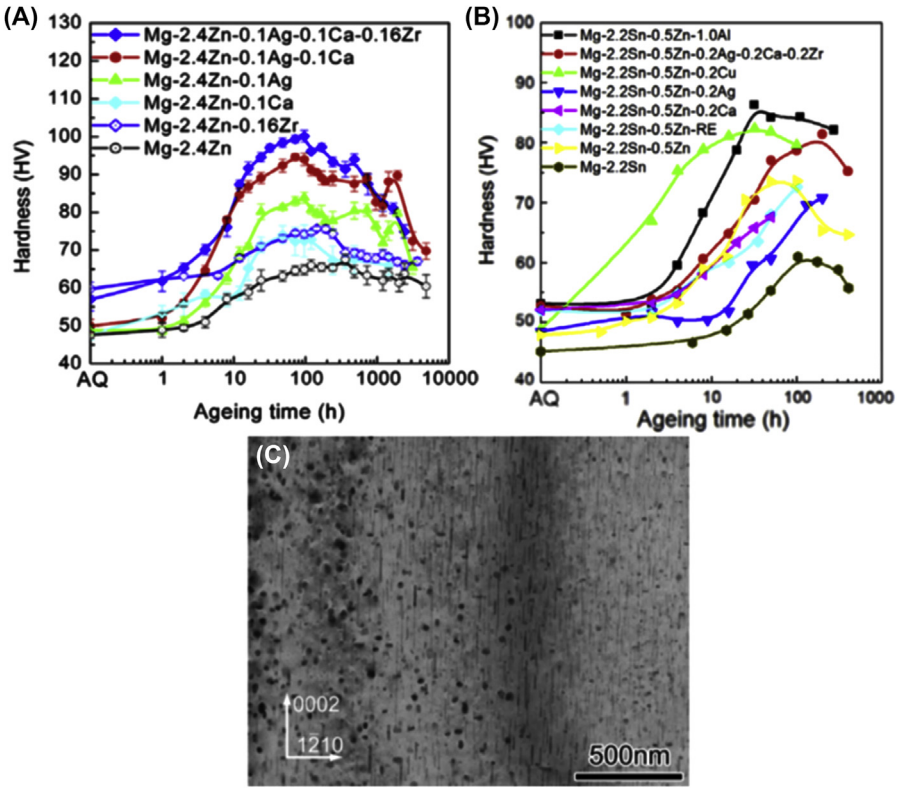


FIGURE 7.13

The age-hardening response for (A) Mg–2.4Zn–0.1Ag–0.1Ca–0.16Zr alloys at 160°C [18] and (B) Mg–2.2Sn–0.5Zn alloy with various microalloying elements at 200°C [19]. (C) Transmission electron microscopy (TEM) micrographs showing peak-aged Mg–2.4Zn–0.1Ag–0.1Ca–0.16Zr alloy [19].

that if the hardness of magnesium alloys exceeds 100 HV while providing a balance of other properties, their insertion becomes more viable.

7.5.1 MICROSTRUCTURAL EVOLUTION DURING THERMOMECHANICAL PROCESSING

Conventional thermomechanical processing of magnesium alloys is impacted by the details of operative slip systems and twinning. Among the nontraditional severe plastic deformation techniques, equal channel angular extrusion (ECAE) and

friction stir processing are quite popular for exploring grain refinement. There are significant differences in each approach because of the strain path and process temperature. Consider four specific processes: (1) rolling, (2) extrusion, (3) ECAE, and (4) FSP. In rolling, the process temperature and strain path are independently controlled. Typically, multiple passes are used to achieve the desired total reduction by rolling. Dynamic recrystallization depends on the overall strain and microstructural level details. Because of multiple passes, recovery can be important. During conventional forward extrusion, the overall strain is achieved in one pass and die angle/profile determines the severity of strain accumulation. On the other hand, ECAE involves multiple passes and the microstructural refinement is progressive. Compared to these techniques, friction stir processing is very different. It involves very large strain and strain rate at relatively high temperatures. The dynamic recrystallization is extensive in such a case.

Prasad and Rao [20] have established processing maps for AZ31 alloy and have defined various dynamic recrystallization domains. This study clearly shows the effect of texture on grain refinement. The Zener—Hollomon parameter, Z, defined as [21],

$$Z = \dot{\varepsilon} \exp\left(\frac{Q}{RT}\right)$$

where $\dot{\varepsilon}$ is the strain rate, T is the deformation temperature, Q is the activation energy, and R is the gas constant and they can be used to correlate evolution of grain size during high-temperature deformation. In addition to the regular strain inhomogeneity caused by grains and particles in aluminum alloys, magnesium alloys exhibit further complexity in recrystallization because of twins. As an example, Fig. 7.14 shows the impact of twins on recrystallization in AZ31 reported by Al-Samman and Gottstein [22]. Note the associated orientation change because of twinning. Fig. 7.14B shows the correlation between the steady-state flow stress and the recrystallized grain size. Similar expression has also been reported by del Valle and Ruano [23] who have explained the rotation of recrystallized grains that would result in preferred orientation after processing. The correlation between flow stress and recrystallized grain size is an alternate expression of Zener—Hollomon parameter and both emphasize the importance of low-temperature processing for obtaining fine-grained material. This is even more critical for magnesium alloys, which show transition in a few mechanical response below a critical grain size, as explained in the following subsections. The apparent activation energy estimated for the Zener—Hollomon relationship for AZ31 is close to that for lattice self-diffusion in magnesium (135 kJ/mol) [20]. Similar activation energy value has been reported by Kubota et al. [24] for AZ91, which indicates a wider applicability of the relationships that have been established.

7.5.2 STRENGTH—DUCTILITY RESPONSE

Fig. 7.15 shows a comparison of the best reported values of tensile yield strength versus ductility for high-strength Mg alloys processed by various methods. Clearly,

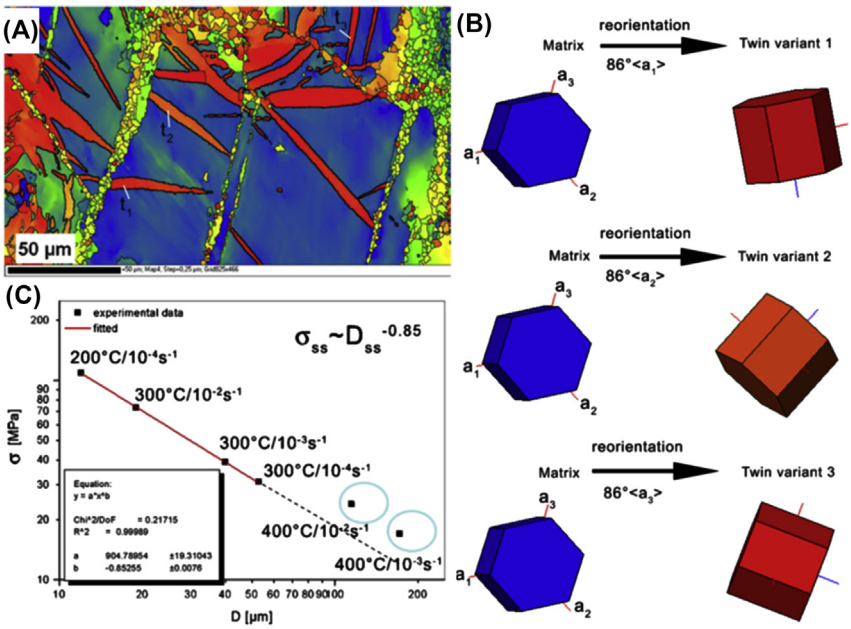


FIGURE 7.14

(A) Electron backscatter diffraction (EBSD) map showing recrystallization of grains in former twins and (B) associated rotation of orientation. (C) A correlation between steady-state flow stress and recrystallized grain size [22].

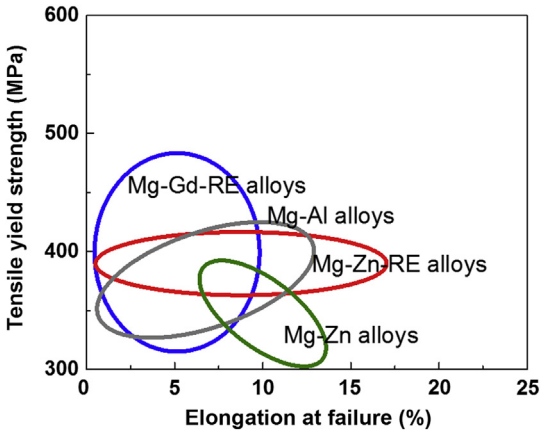


FIGURE 7.15

A comparison of tensile yield strength versus ductility of reported high strength Mg alloys processed by various methods.

a combination of 400 MPa strength and 10% elongation in magnesium alloys produced at a commercial scale will render them very competitive. Majority of data considered for this figure were produced by severe plastic deformation processes or powder metallurgy techniques. The commercial alloys generally lack this level of performance. Nie [4] has compiled the data for a large number of cast and wrought alloys, which is reproduced in Table 7.5. A key to enhancing ductility in magnesium alloys is to promote nonbasal slip activity as highlighted by Koike et al. [25].

7.5.2.1 Low Formability: Effect of Composition

In general, overcoming the very low room temperature ductility, and hence the very low formability, has been the biggest challenge for successful insertion of Mg alloys in structural applications. For these alloys to compete with structural ferrous and nonferrous (primarily aluminum alloys), the ductility and formability have to be enhanced. Among the many factors affecting ductility of this material, the effect of composition is critical. The effect of different alloying additions on the ductility of Mg alloys is manifested through the change in texture. Elements such as Ce, La, Y, Zr, Nd, etc., have been added to Mg to modify texture development during extrusion or rolling [26–34]. It can be noted that maximum texture intensity appears near $[10\bar{1}0]$. Tensile testing of such materials with tensile axis parallel to the extrusion axis results in very low ductility due to the orientation of the *c*-axis within 20° (95% of the *c*-axis) of the transverse direction, which makes basal slip very difficult. Plastic deformation in Mg alloys is primarily due to slip on the basal plane and twinning. After the addition of 0.4 wt% RE elements, Stanford et al. [29] have shown the appearance of a second peak at $[11\bar{2}1]$ parallel to the extrusion direction. Stanford [31] also studied the effect of varying concentration of Y, Ce, Gd, and La on the development of $[11\bar{2}1]$ texture parallel to the extrusion axis and concluded that a minimum of 0.04 at% Ce, 0.03 at% La, and 0.06 wt% Gd were necessary to bring such a change in the texture. No effect on texture modification was observed by the addition of Y at a varying concentration.

The effect of such microstructural modification manifests itself in the stress–strain curve. For example, the tensile stress–strain curves of Mg-1.5 wt% Mn (M1), AZ31, and Mg-1 wt% Mn-0.4 wt% RE (ME10) alloys are shown in Fig. 7.16 along with the corresponding extrusion textures [30]. Clearly, $[11\bar{2}1]$ texture caused not only a very high value of elongation-to-failure but also resulted in higher uniform elongation.

A number of theories have been put forth to explain this change in texture due to the addition of alloying elements, in particular REs. Deformation heterogeneities (e.g., shear band), particle pinning, solute drag, particle-stimulated nucleation of recrystallization, and abnormal grain growth have been attributed to be the cause of weakening of fiber texture by the addition of different alloying elements [26,31,32,35,36]. The role of alloying on manipulating the *c*/*a* ratio has also been considered and it is postulated that enhanced ductility is the result of the modification of *c*/*a* ratio and a reduction in the CRSS for nonbasal slip [25,37–40].

Table 7.5 Tensile Properties at Room Temperature of Magnesium Casting and Wrought Alloys

Alloy	Composition (wt pct)	Testing Condition	Tensile Properties		
			UTS (MPa)	YS (MPa)	E (pct)
Casting Alloys					
AZ91	Mg–8.7Al–0.7Zn–0.1Mn	T6	200	120	2
ZK61	Mg–6Zn–0.7Zr	T6	310	195	10
ZC63	Mg–6Zn–2.7Cu–0.3Mn	T6	210	125	4
ZA85	Mg–7.7Zn–4.9Al–0.3Mn	T6	195	138	2
QE22	Mg–2.5Ag–2.1Di–0.7Zr	T6	260	195	3
WE54	Mg–5.2Y–3RE–0.7Zr	T6	280	205	4
WE43	Mg–4Y–3.4RE–0.7Zr	T6	250	180	7
MRI201S		T6	260	170	6
MEZ	Mg–2.5RE–0.5Zn	T6	108	76	2
NEZ	Mg–3Nd–0.5Zn	T6	165	114	2
EV31	Mg–3Nd–2Gd–0.6Zn –0.5Zr	T6	292	178	7
VZ61	Mg–6Gd–1Zn–0.6Zr	T6	220	127	12
XZE111	Mg–1Ca–1Zn–1Nd–0.6Zr	T6	227	153	7
VW114	Mg–11.3Gd–3.8Y–0.7Zr	T6	330	300	2
VWZ1142	Mg–11.1Gd–4.1Y–1.7Zn –0.5Zr	T6	361	231	4
VE112	Mg–11Gd–2Nd–0.5Zr	T6	350	230	2
VQ182	Mg–18.2Gd–1.9Ag–0.3Zr	T6	414	293	2
VW102	Mg–10Gd–2Y–0.5Zr	T6	362	239	5
Extrusion Alloys					
AX43	Mg–3.5Al–3.3Ca–0.4Mn	F	420	410	6
ZK60	Mg–6Zn–0.6Zr	F	310	250	3
ZX51	Mg–4.7Zn–0.5Ca	F	329	291	16
ZXK601	Mg–5.7Zn–0.2Ca–0.8Zr	F	357	310	18
ZQX6	Mg–6Zn–0.4Ag–0.2Ca –0.6Zr	F	351	289	17
		T6	355	325	14
XZ11	Mg–1Ca–1Zn–0.6Zr	F	314	306	17
WE43	Mg–4Y–3Nd–0.5Zr	T6	245	160	6
WE54	Mg–5.3Y–3.5Nd–0.5Zr	T5	300	200	10
Elektron 675	Mg–6Y–7Gd–0.5Zr	T6	275	190	10
		T5	410	310	9
VK14	Mg–14Gd–0.5Zr	F	295	190	20

Table 7.5 Tensile Properties at Room Temperature of Magnesium Casting and Wrought Alloys—cont'd

Alloy	Composition (wt pct)	Testing Condition	Tensile Properties		
			UTS (MPa)	YS (MPa)	E (pct)
		T6	446	305	7
		T8	482	445	2
VZ142	Mg—14Gd—2.3Zn	F	380	345	—
WZ75	Mg—6.7Y—4.9Zn	F	425	390	5
VWZ1062	Mg—10Gd—5.7Y—1.6Zn —0.7Zr	F	461	419	4
		T5	542	473	8
ZW51	Mg—5Zn—0.9Y—0.2Zr	F	363	317	—
Sheet/ Plate Alloys					
ZM61	Mg—6Zn—1Mn	T6	310	256	16
ZAM631	Mg—6Zn—3Al—1Mn	T6	360	319	6
ZQX610	Mg—6.3Zn—0.5Ag—0.2Ca —0.1Zr	T6	342	316	17
VWZ1142	Mg—11Gd—4Y—1.7Zn —0.5Zr	T6	455	375	10

E, *elongation;* UTS, *ultimate tensile strength;* YS, *yield strength.*
From J.F. Nie, Precipitation and hardening in magnesium alloys, Metallurgical and Materials Transactions A 43 (2012) 3891–3939.

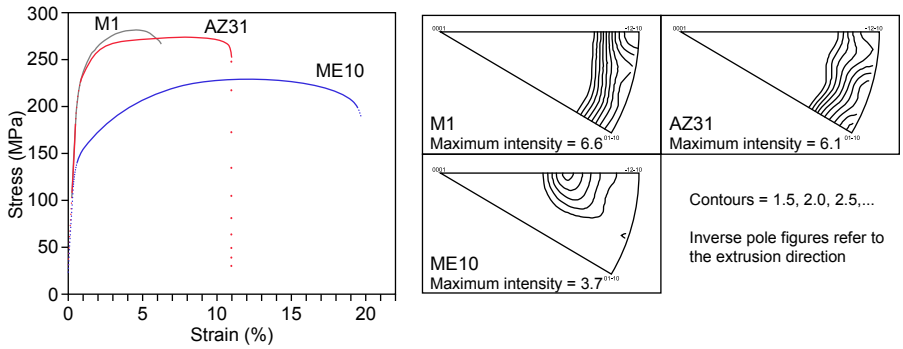


FIGURE 7.16

Stress—strain curves of three different Mg alloys and their corresponding extrusion texture before the start of the test [30].

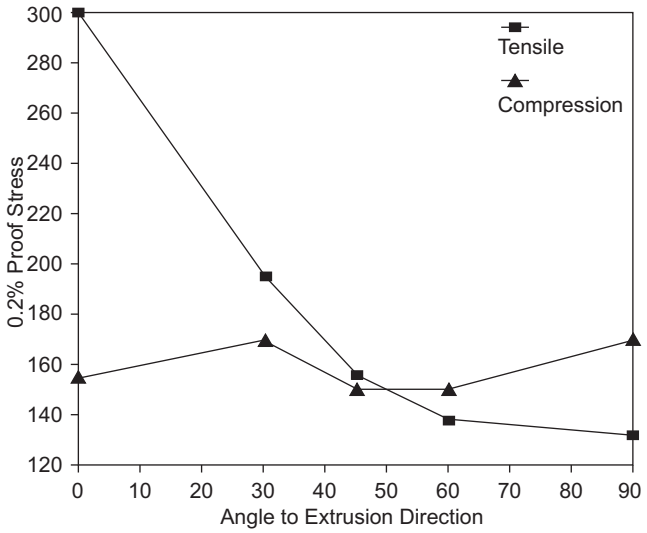


FIGURE 7.17

Effect of test sample orientation to extrusion direction on yield stress in tension and compression [36].

7.5.2.2 Tension–Compression Yield Asymmetry

Another impediment for the successful commercialization of Mg alloys has been the presence of tension–compression yield asymmetry. This aspect has been well documented in many alloys [36]. Fig. 7.17 shows the effect of tensile or compressive axis orientation relative to the extrusion direction on the yield asymmetry. It should be noted that yield asymmetry was lower in the transverse direction. Second, the tensile yield strength has a very high dependence on orientation relative to extrusion direction, but not the compressive yield strength.

The reason for such anisotropy has been attributed to twinning of Mg alloys under tension and compression. Because five independent slip systems are required to accommodate a general deformation of the crystals in a polycrystalline materials and Mg provides only two basal slip systems, deformation twinning is very prominent in Mg alloys [41,42]. The basal slip occurs easily due to very small CRSS compared to that for nonbasal slip planes, such as prismatic or pyramidal planes or even for twinning. There are two types of twinning deformation modes—tension twin $\{10\bar{1}2\}\langle 10\bar{1}2\rangle$ and compression twin $\{10\bar{1}1\}\langle 10\bar{1}2\rangle$. The CRSS for tension and compression twins are 2 MPa and 76–153 MPa, respectively. Hence, tension twins are predominantly observed during the deformation of Mg alloys [39,43–46]. Tension twins can be active only when the tensile axis is parallel to *c*-axis or compression axis is parallel to basal plane (or perpendicular to *c*-axis).

The texture developed during extrusion or rolling of Mg alloys is such that when these alloys are tested along the extrusion or rolling directions, the slip plane normal or *c*-axis are perpendicular to these directions. Consequently, slip or twinning becomes very difficult and these alloys show very high yield strength when tested in tension. However, when tested in compression, the basal plane and *c*-axis are

favorably oriented for slip and twinning, respectively. Hence, this leads to the observed tension—compression asymmetry.

Removal of this anisotropy would require the activation of nonbasal slip systems and twinning in tension, or inhibition of twinning during compression. It can be achieved by carefully selecting a suitable processing—microstructure—property path. In order to reduce tension—compression anisotropy, Wang and Huang [45] studied the role of twinning and untwinning on the yielding behavior. It was shown that when a tensile Mg—Al—Zn sample was predeformed in compression, it showed the same level of yield strength as exhibited in compression.

7.5.2.3 Role of Second-Phase Particles

The role of precipitates has also been investigated by many researchers [18,47—57]. Due to very limited work on the interaction of precipitates and twins in Mg alloys, the understanding of the role of precipitates on twinning has not matured sufficiently. However, the initial observation has shown the difficulty of twin boundary propagation through the distribution of precipitates [57], which helps to reduce tension—compression yield anisotropy. Initial studies on precipitates—twin interaction have produced contradicting observations. The work of Clark [55,56] showed a rotation of $\sim 10^{\circ}$ about $<11\bar{2}0>$ after twinning and suggested the shearing of precipitates by twins and suppression of $<11\bar{2}0>$ twins due to precipitates. However, Gharghouri et al. [57] showed no rotation of particles after the twinning of the matrix and showed that precipitates can change their habit plane in order to avoid its intersection with twins. Stanford and Barnett [47] studied age-hardenable Mg—5 wt% Zn and concluded that precipitates resulted in both an increase in the number of twins and a reduction in the size and total volume fraction of twins. Recently, Robson et al. [48] noted that the presence of precipitates promoted nucleation of $\{10\bar{1}2\}$ twins in Mg—5 wt% Zn alloy. However, the growth of the twins was hindered by the precipitates, which is in accordance with the earlier observation [47]. The research conducted by Jain et al. [49] on Mg—8Al—0.5Zn revealed that aging treatment resulted in the reduction of asymmetry ratio to 0.87 in aged condition from 0.59 in solution treated samples. Similar observations of reduction in tension—compression yield anisotropy have been reported by Ma et al. [50], Xin et al. [52], and Lv et al. [53]. In a proposed model elucidating the precipitate shape effect, Robson et al. [51] have pointed out that depending upon the plate shape and habit, and their relative orientation from basal plane or c-axis, yield asymmetry can either increase or decrease. However, due to the availability of limited data, any effect of plate shape and orientation on the yield asymmetry cannot be confirmed.

7.5.2.4 Influence of Grain Size on Twinning and Strengthening

The role of decreasing grain size on the tensile—compressive yield asymmetry has also been studied and a reduction in asymmetry has been observed with a decrease in the grain size [58,59]. It has been reported that the stress required to cause twinning also shows a similar dependence as to HP relationship and it can be represented as,

$$\sigma_T = \sigma_{T0} + k_T d^{-1/2} \tag{7.1}$$

Here, k_T is a constant similar to HP slope but higher in value. The HP equation for slip is,

$$\sigma_y = \sigma_{y0} + k_s d^{-1/2} \tag{7.2}$$

Eq. (7.1) predicts that with decrease in grain size, stress required for twinning becomes higher. Consequently, slip should become easier than twinning above a certain threshold. Theoretically, the grain size at which this transition would occur can be calculated by equating Eqs. (7.1) and (7.2) and the grain size is given as,

$$d_{twin \rightarrow slip} = \left(\frac{k_s - k_T}{\sigma_{T0} - \sigma_{y0}} \right)^2 \tag{7.3}$$

The work of Wang et al. [58] on Mg−3Al−1Zn reveals the existence of a critical grain size at 4 μm for such a transition. The data compiled by Panigrahi et al. [60] for tension−compression yield asymmetry are shown in Fig. 7.18A revealing a ∼1 μm critical grain size for this transition to occur. As stated earlier, researchers have

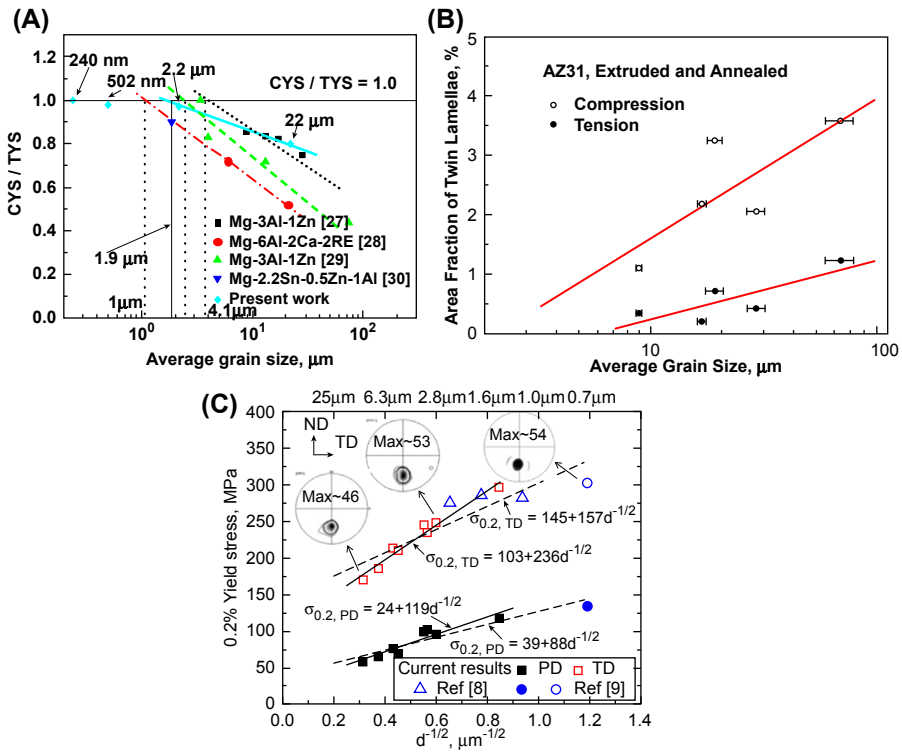


FIGURE 7.18

(A) Plot showing variation of tension−compression asymmetry as a function of average grain size [60]. (B) Plot showing propensity of twinning as a function of grain size [58]. (C) Hall−Petch relationship for AZ31 alloy showing the effect of texture on grain boundary strengthening [61].

attributed this to the difficulty in twinning with decrease in grain size [58,59,62–64]. As can be seen in Fig. 7.18B, the propensity of twinning dwindles with decrease in grain size [58]. There is no conclusive study illustrating the exact mechanism through which smaller grain size makes twinning difficult and facilitates the slip process.

Yuan et al. [61] have shown that texture plays a pivotal role in HP strengthening of Mg alloys. The effect of texture on HP slope is shown in Fig. 7.18C. As can be seen, easy orientation of basal slip results in a smaller HP slope (88–119 MPa-$\mu m^{1/2}$), and hence lower contribution of grain boundary strengthening than the case where basal planes are unfavorably oriented for the slip to take place. In the latter case, the HP slope is 157–236 MPa-$\mu m^{1/2}$.

7.5.2.5 Ductility of Magnesium Alloys

Due to very limited room temperature ductility and workability, significant research has been performed to understand the effect of various parameters on the ductility of Mg alloys. Mukai et al. [65] obtained a total elongation-to-failure of ~50% for AZ31 alloy that was annealed following extrusion. The elongation-to-failure was ~25% in the as-extruded condition. In this condition, the texture was predominantly fiber type, whereas it changed to equal distribution of basal plane relative to extrusion and transverse direction. It should be noted that in both cases, grain size was ~15 μm. Similar results were obtained by Agnew et al. [66] on AZ31B tested in as-extruded and ECA (equal channel angular) + annealed condition. The textures of the alloy in these conditions are shown in Fig. 7.19. The enhanced ductility in ECA + annealed condition (Fig. 7.19D) was attributed to favorable orientation of basal plane for the slip relative to the extrusion direction.

The explanation of such a large elongation has been questioned by Koike et al. [25] based on their argument that basal plane mediated dislocation slip plasticity alone cannot give rise to this level of elongation. Based on the observation of a limited number of grains under TEM, the fraction of nonbasal dislocations or basal dislocations was calculated. They noted that a yield anisotropy factor of little more

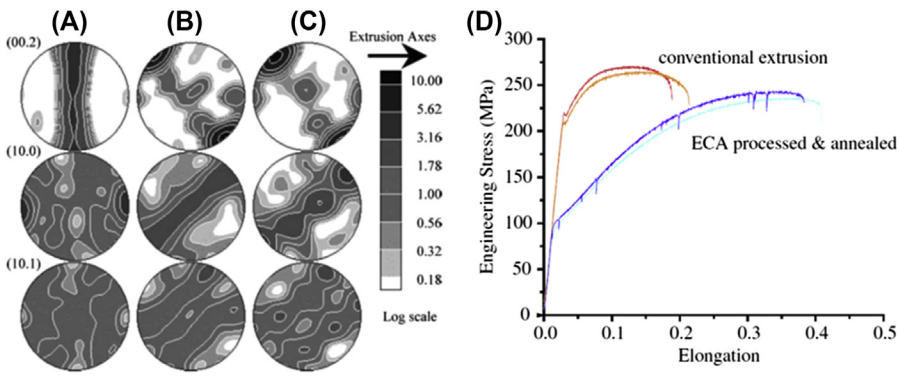


FIGURE 7.19

Texture in (A) as-extruded, (B) ECA processed, (C) ECA + annealed condition for AZ31B [66]. (D) Tensile stress–strain curves showing effect of texture [66].

than one is required to activate nonbasal glide. This is an interesting finding given that the yield anisotropy for nonbasal dislocation activity is ~50−100 for single crystals. It should be noted that the grain size in this study was ~6.5 μm and some twinning was observed only after 16% of plastic deformation. The activation of nonbasal slip system at room temperature deformation was explained on the basis of incompatibility stresses. Elastic incompatibility is not significant in Mg alloys. Plastic heterogeneity is large in Mg alloys and may give rise to plastic compatibility stress. The activation of nonbasal slip system based on compatibility stresses can be key to the onset of nonbasal slip activity. The nonbasal slip activity should lead to higher work hardening. Kumar et al. [15] have related the rate of change in work hardening with uniform ductility, which is shown in Fig. 7.20. Note that uniform ductility relates well with formability as it represents resistance to necking and/or cavity formation. Lower values of rate of change in work hardening are preferable, which means that sustained work hardening is important for enhanced uniform ductility. This discussion lends to microstructural design opportunity and if deformation features are triggered at various levels of stress or plastic strain, it would lead to sustained work hardening.

7.5.2.6 Superposition of Various Strengthening Mechanisms and Microstructural Efficiency

Precipitation-strengthened alloys benefit from multiple strengthening mechanisms and understanding of how the various contributions applied would help in designing

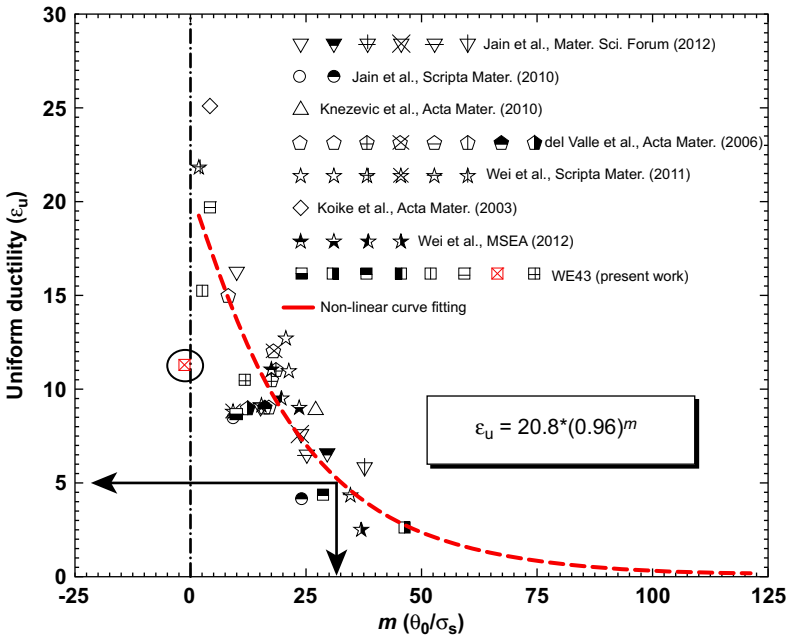


FIGURE 7.20

Variation of uniform ductility as a function of rate of change in work hardening rate (m).

alloys to maximize microstructural efficiency and alloying efficiency. The contributors are

- Lattice friction or Peierls stress
- Solid solution strengthening
- Dislocation density strengthening
- Grain/twin boundary strengthening
- Precipitate/particle strengthening
- Composite effect (load transfer to stiffer phase)

Among these, intragranular obstacles (solutes, dislocations, and particles) interact with mobile dislocations during their movement across the grain. Although several key articles have addressed specific aspects of these contributions [67—71], the general discussion of their effectiveness and normalization with maximum potential has been missing because of a lack of framework. The appendices at the end of this book discuss the general approach. The development of most effective hierarchical microstructure depends on linking the property objectives with the best micromechanisms associated with those properties. The Peierls stress is somewhat fixed with the element and crystal structure. For a given grain size, the thermomechanical processing and heat treatment change the other contributions. An example of this is shown in Fig. 7.21 for AZ91 alloy [69]. Note that the contribution of strengthening from the precipitates is the highest. Theoretically, this can be maximized by having precipitates in prismatic or pyramidal orientation with just enough thickness to avoid shearing. This level of strengthening then represents the maximum potential for a given composition and volume fraction of second phase

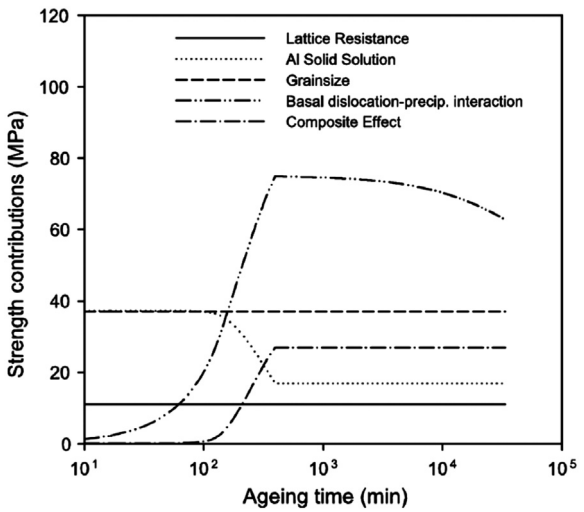


FIGURE 7.21

Individual contributions to the overall calculated the yield strength of AZ91 alloy [69].

particles. Dividing the experimental value with this number will give the microstructural efficiency. Similar consideration can be given to grain size refinement. For grain refinement, one can calculate the required strain for recrystallization and this represents processing cost for refined microstructure. Combining the microstructural efficiency with cost creates the overall framework for maximizing cost-effective performance of lightweight alloys.

7.5.3 TOUGHNESS RESPONSE

Along with strength and ductility, toughness is a key property for damage tolerant design of aircraft structural components. Although the typical toughness values of magnesium alloys are low, they can be improved by grain refinement as well as by optimization of precipitate characteristics. Low fracture toughness and strain localization also impact the way magnesium alloys fracture during dynamic loading. Fig. 7.22 shows an overview of fracture toughness as a function of specific strength along with the highest value obtained in magnesium alloys [72]. Somekawa et al. [72] demonstrated the synergistic effect of fine grain size and quasicrystalline phase. Results of Liao et al. [73] on the impact toughness of AZ31 also establish the critical grain size of $\sim 3\ \mu m$. This is consistent with the earlier discussion on the activation of nonbasal deformation mechanism below a critical grain size. The microstructural evidence showed that twinning behavior is suppressed below this critical grain size.

7.5.4 FATIGUE RESPONSE

The fatigue response is important for components under cyclic loading. This is particularly important for airframe structures. The fatigue limit or endurance limit can be defined as the stress level for life of 10^7 cycles. Aluminum alloys do not exhibit true endurance limit and in contrast steels have a well-defined endurance limit. Fig. 7.23 shows a compilation of some S−N data for AZ31, AZ91, and ZK60 alloys [74−80]. It includes data for cast as well as thermomechanically processed conditions. Although both equal channel angular pressed and FSP alloys have finer grain size, the friction stir processing results in much higher fatigue enhancement. Yin et al. [81] have correlated the role of twinning and slip on crack initiation and growth. Given the suppression of twinning below a critical grain size, it is interesting to speculate that fatigue endurance limit can be increased by refining the grain size and developing a hierarchical microstructure that suppresses twinning and blocks slip. A correlation exists between ultimate tensile strength (UTS) and fatigue limit. For some of the alloys shown in Fig. 7.23, the fatigue limit is as low as 0.2−0.25 of UTS. This is particularly the case for cast alloys which are prone to the presence of casting defects like pores. Li et al. [82] have shown that for a high-strength defect-free NZK alloy, the ratio can be as high as 0.35−0.44 (Fig. 7.24). For comparison, as noted in Chapter 4, the ratio of fatigue limit to UTS is ~ 0.35 for precipitation strengthened aluminum alloys.

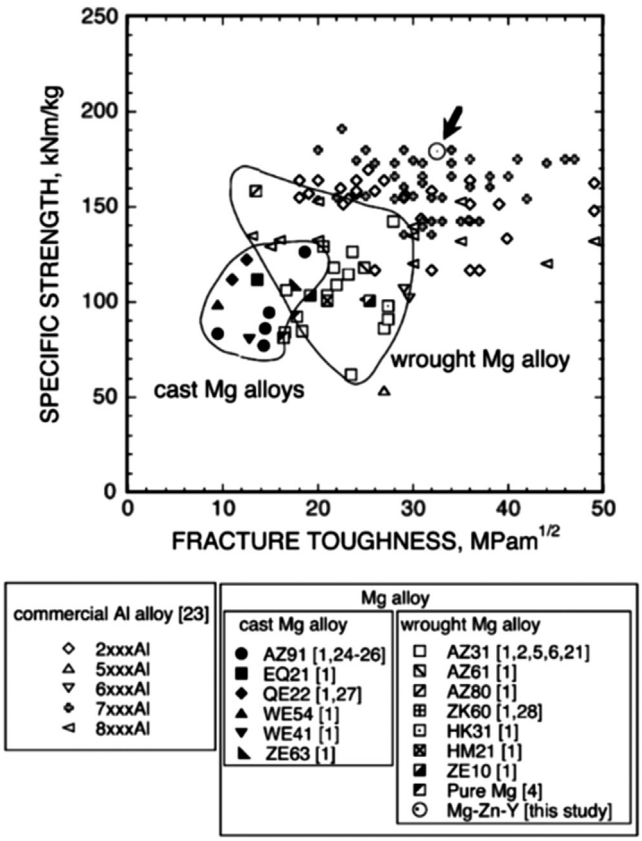


FIGURE 7.22

The relationship between specific strength and fracture toughness of aluminum alloys and magnesium alloys [72].

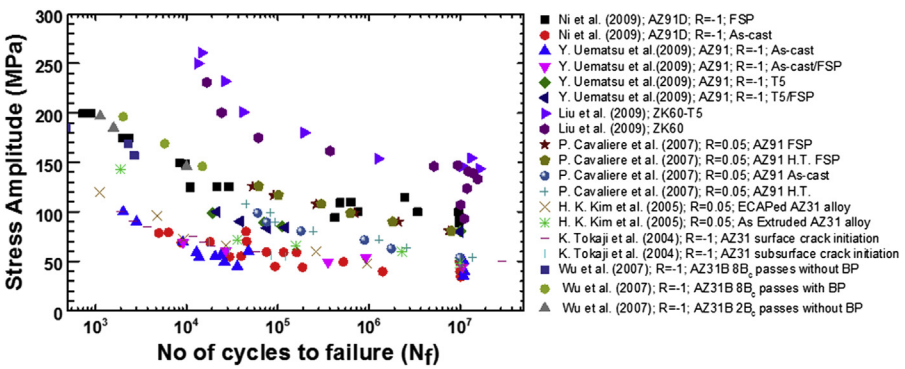


FIGURE 7.23

Variation of fatigue life with stress amplitude for a few magnesium alloys. Note the general trend of enhanced fatigue limit in alloys with refined microstructure.

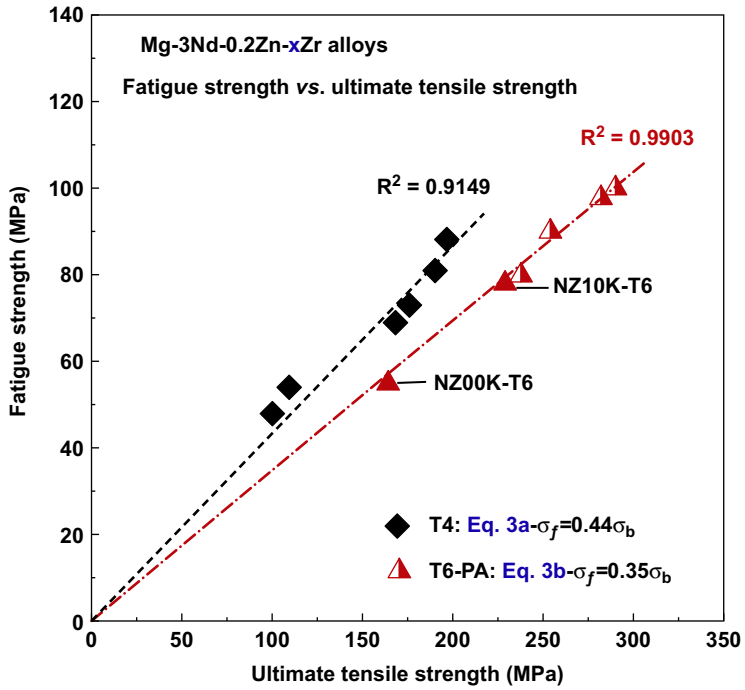


FIGURE 7.24

Relationship between the ultimate tensile strength (σ_b) and the fatigue strength (σ_f) of the Mg—3Nd—0.2Zn—xZr alloys (both T4- and T6-PA-treated conditions) [82].

7.6 SUMMARY

Magnesium alloys have reached a level of maturity where a combination of enhanced strength—ductility—toughness can be obtained through microstructural optimization. Therefore, the focus of the discussion has principally been on the microstructural improvements that will lead to a better combination of properties. Much of the emphasis has been on improving strength and ductility. The critical grain size is in the range of 1—3 μm for transition from twinning to nonbasal dislocation activities. Significant understanding has been established in promoting high precipitation density through microalloying as well as control of orientation of precipitates. The effectiveness of the precipitates is higher for precipitates aligned along the prismatic or pyramidal planes. It is also important to control the size of precipitates, and higher aging temperature is generally not ideal. Microalloying also helps to control the texture. Translating the fundamental understanding to bulk processing of magnesium alloys with the same level of microstructural control is needed to make initial breakthrough for high-volume applications. Corrosion is a perceived concern but has not been an issue in current applications (in helicopters

and subsystems) due to excellent corrosion protection schemes. The intrinsic corrosion resistance of magnesium alloys is likely to remain relatively poor and robust protection scheme is likely to be the best path.

REFERENCES

[1] S.N. Mathaudhu, DoD perspectives on Mg science and technology: the quest for lightweight structure and armor opportunities in protection materials science and technology, in: Mg Science & Technology Workshop – Fundamental Research Issues, Arlington, VA, 2011.

[2] S. Agnew, E. Nyberg, T. Pollock, R. Wagoner, B. Powell, R. Decker, D. Shih, in: "Mg Science & Technology Workshop - Fundamental Research Issues," Arlington, VA, 2011. Available at: http://www.virginia.edu/ms/research/agnew/resources.php.

[3] T. Marker, Evaluating the Flammability of Various Magnesium Alloys during Laboratory- and Full-Scale Aircraft Fire Test, DOT/FAA/AR-11/3, U.S. Dept. of Transportation, Federal Aviation Administration, Atlantic City, N.J., 2013.

[4] J.F. Nie, Precipitation and hardening in magnesium alloys, Metallurgical and Materials Transactions A 43 (2012) 3891–3939.

[5] R.S. Mishra, P.S. De, N. Kumar, Friction Stir Welding and Processing: Science and Engineering, Springer, 2014, ISBN 978-3-319-07043-8, pp. 149–187.

[6] M. Avedesian, H. Baker (Eds.), ASM Specialty Handbook: Magnesium and Magnesium Alloys, ASM International, 1999, ISBN 978-0-87170-657-7.

[7] B.L. Mordike, T. Ebert, Magnesium properties — applications — potential, Materials Science and Engineering, A 302 (2001) 37–45.

[8] W.B. Hutchinson, M.R. Barnett, Effective values of critical resolved shear stress for slip in polycrystalline magnesium and other hcp metals, Scripta Materialia 63 (2010) 737–740.

[9] J.F. Nie, Effects of precipitate shape and orientation on dispersion strengthening in magnesium alloys, Scripta Materialia 48 (2003) 1009–1015.

[10] J. Rösler, M. Bäker, A theoretical concept for the design of high-temperature materials by dual-scale particle strengthening, Acta Materialia 48 (2000) 3553–3567.

[11] A.K. Dutt, S. Pasebani, I. Charit, R.S. Mishra, On the creep behavior of dual-scale particle strengthened nickel based alloy, Materials Science and Engineering, A 676 (2016) 406–410.

[12] S. Palanivel, A. Arora, K.J. Doherty, R.S. Mishra, A framework for shear driven dissolution of thermally stable particles during friction stir welding and processing, Materials Science and Engineering, A 678 (2016) 308–314.

[13] K. Hantzsche, J. Bohlen, J. Wendt, K.U. Kainer, S.B. Yi, D. Letzig, Effect of rare earth additions on microstructure and texture development of magnesium alloy sheets, Scripta Materialia 63 (2010) 725–730.

[14] V. Jain, R.S. Mishra, A.K. Gupta, Gouthama, Study of β-precipitates and their effect on the directional yield asymmetry of friction stir processed and aged AZ91C alloy, Materials Science and Engineering, A 560 (2013) 500–509.

[15] N. Kumar, D. Choudhuri, R. Banerjee, R.S. Mishra, Strength and ductility optimization of Mg-Y-Nd-Zr alloy by microstructural design, International Journal of Plasticity 68 (2015) 77–97.

[16] J.D. Embury, A. Deschamps, Y. Brechet, The interaction of plasticity and diffusion controlled precipitation reactions, Scripta Materialia 49 (2003) 927–932.
[17] C.L. Mendis, C.J. Bettles, M.A. Gibson, S. Gorsse, C.R. Hutchinson, Refinement of precipitate distributions in an age-hardenable Mg–Sn alloy through microalloying, Philosophical Magazine Letters 86 (No. 7) (July 2006) 443–456.
[18] C.L. Mendis, K. Oh-ishi, Y. Kawamura, T. Honma, S. Kamado, K. Hono, Precipitation-hardenable Mg–2.4Zn–0.1Ag–0.1Ca–0.16Zr (at.%) wrought magnesium alloy, Acta Materialia 57 (2009) 749–760.
[19] K. Hono, C.L. Mendis, T.T. Sasaki, K. Oh-ishi, Towards the development of heat-treatable high-strength wrought Mg alloys, Scripta Materialia 63 (2010) 710–715.
[20] Y.V.R.K. Prasad, K.P. Rao, Processing maps for hot deformation of rolled AZ31 magnesium alloy plate: anisotropy of hot workability, Materials Science and Engineering, A 487 (2008) 316–327.
[21] J.J. Jonas, C.M. Sellars, W.J.M.G. Tegart, Strength and structure under hot-working conditions, Metallurgical Reviews 14 (1969) 1–24.
[22] T. Al-Samman, G. Gottstein, Dynamic recrystallization during high temperature deformation of magnesium, Materials Science and Engineering, A 490 (2008) 411–420.
[23] J.A. del Valle, O.A. Ruano, Influence of texture on dynamic recrystallization and deformation mechanisms in rolled or ECAPed AZ31 magnesium alloy, Materials Science and Engineering, A 487 (2008) 473–480.
[24] K. Kubota, M. Mabuchi, K. Higashi, Processing and mechanical properties of fine-grained magnesium alloys, Journal of Materials Science 34 (1999) 2255–2262.
[25] J. Koike, T. Kobayashi, T. Mukai, H. Watanabe, M. Suzuki, K. Maruyama, K. Higashi, The activity of non-basal slip systems and dynamic recovery at room temperature in fine-grained AZ31B magnesium alloys, Acta Materialia 51 (2003) 2055–2065.
[26] J. Bohlen, M.R. Nürnberg, J.W. Senn, D. Letzig, S.R. Agnew, The texture and anisotropy of magnesium-zinc-rare earth alloy sheets, Acta Materialia 55 (2007) 2101–2112.
[27] S.H. Safi-Naqvi, W.B. Hutchinson, M.R. Barnett, Texture and mechanical anisotropy in three extruded magnesium alloys, Materials Science and Technology 24 (2008) 1283–1292.
[28] R.K. Mishra, A.K. Gupta, P.R. Rao, A.K. Sachdev, A.M. Kumar, A.A. Luo, Influence of cerium on the texture and ductility of magnesium extrusions, Scripta Materialia 59 (2008) 562–565.
[29] N. Stanford, D. Atwell, A. Beer, C. Davies, M.R. Barnett, Effect of microalloying with rare-earth elements on the texture of extruded magnesium-based alloys, Scripta Materialia 59 (2008) 772–775.
[30] N. Stanford, M. Barnett, Effect of composition on the texture and deformation behaviour of wrought Mg alloys, Scripta Materialia 58 (2008) 179–182.
[31] N. Stanford, M.R. Barnett, The origin of "rare earth" texture development in extruded Mg-based alloys and its effect on tensile ductility, Materials Science and Engineering, A 496 (2008) 399–408.
[32] L.W.F. Mackenzie, M.O. Pekguleryuz, The recrystallization and texture of magnesium-zinc-cerium alloys, Scripta Materialia 59 (2008) 665–668.
[33] K. Hantzsche, J. Wendt, K.U. Kainer, J. Bohlen, D. Letzig, Mg sheet: the effect of process parameters and alloy composition on texture and mechanical properties, JOM 61 (2009) 38–42.
[34] N. Stanford, Micro-alloying Mg with Y, Ce, Gd and La for texture modification-a comparative study, Materials Science and Engineering, A 527 (2010) 2669–2677.

[35] L.W.F. Mackenzie, B. Davis, F.J. Humphreys, G.W. Lorimer, The deformation, recrystallisation and texture of three magnesium alloy extrusions, Materials Science and Technology 23 (2007) 1173−1180.
[36] E.A. Ball, P.B. Prangnell, Tensile-compressive yield asymmetries in high strength wrought magnesium alloys, Scripta Metallurgica et Materialia 31 (1994) 111−116.
[37] R.S. Busk, Lattice parameters of magnesium alloys, Transactions of the AIME 188 (1950) 1460−1464.
[38] J.C. McDonald, Anomalous behavior during cold working and subsequent heating of certain magnesium base alloys, Transactions of the AIME 212 (1958) 45−46.
[39] R.E. Reed-Hill, W.D. Robertson, The crystallographic characteristics of fracture in magnesium single crystals, Acta Metallurgica 5 (1957) 728−737.
[40] F. Hehmann, F. Sommer, B. Predel, Extension of solid solubility in magnesium by rapid solidification, Materials Science and Engineering, A 125 (1990) 249−265.
[41] E.C. Burke, W.R. Hibbard, Plastic deformation of magnesium single crystals, Transactions of the AIME (1952) 295−303.
[42] E.W. Kelley, W.F. Hosford Jr., Plane-strain compression of magnesium and magnesium alloy crystals, Transactions of the AIME 242 (1968) 5−13.
[43] H. Yoshinaga, R. Horiuchi, Transactions of the JIM 4 (1963) 1−8.
[44] B.C. Wonsiewicz, W.A. Backofen, Transactions of the AIME 239 (1967) 1422−1431.
[45] Y.N. Wang, J.C. Huang, The role of twinning and untwinning in yielding behavior in hot-extruded Mg−Al−Zn alloy, Acta Materialia 55 (2007) 897−905.
[46] Y. Chino, K. Kimura, M. Hakamada, M. Mabuchi, Mechanical anisotropy due to twinning in an extruded AZ31 Mg alloy, Materials Science and Engineering, A 485 (2008) 311−317.
[47] N. Stanford, M.R. Barnett, Effect of particles on the formation of deformation twins in a magnesium-based alloy, Materials Science and Engineering, A 516 (2009) 226−234.
[48] J.D. Robson, N. Stanford, M.R. Barnett, Effect of particles in promoting twin nucleation in a Mg−5 wt.% Zn alloy, Scripta Materialia 63 (2010) 823−826.
[49] J. Jain, W.J. Poole, C.W. Sinclair, M.A. Gharghouri, Reducing the tension-compression yield asymmetry in a Mg-8Al-0.5Zn alloy via precipitation, Scripta Materialia 62 (2010) 301−304.
[50] L. Ma, R.K. Mishra, L. Peng, A.A. Luo, W. Ding, A.K. Sachdev, Texture and mechanical behavior evolution of age-hardenable Mg−Nd−Zn extrusions during aging treatment, Materials Science and Engineering, A 529 (2011) 151−155.
[51] J.D. Robson, N. Stanford, M.R. Barnett, Effect of precipitate shape on slip and twinning in magnesium alloys, Acta Materialia 59 (2011) 1945−1956.
[52] R. Xin, B. Song, K. Zeng, G. Huang, Q. Liu, Effect of aging precipitation on mechanical anisotropy of an extruded Mg−Y−Nd alloy, Materials & Design 34 (2012) 384−388.
[53] C. Lv, T. Liu, D. Liu, S. Jiang, W. Zeng, Effect of heat treatment on tension−compression yield asymmetry of AZ80 magnesium alloy, Materials & Design 33 (2012) 529−533.
[54] N. Stanford, J. Geng, Y.B. Chun, C.H.J. Davies, J.F. Nie, M.R. Barnett, Effect of plate-shaped particle distributions on the deformation behaviour of magnesium alloy AZ91 in tension and compression, Acta Materialia 60 (2012) 218−228.
[55] J.B. Clark, Transmission electron microscopy study of age hardening in a Mg-5 wt.% Zn alloy, Acta Metallurgica 13 (1965) 1281−1289.
[56] J.B. Clark, Age hardening in a Mg-9 wt.% Al alloy, Acta Metallurgica 16 (1968) 141−152.

[57] M.A. Gharghouri, G.C. Weatherly, J.D. Embury, The interaction of twins and precipitates in a Mg-7.7 at.% Al alloy, Philosophical Magazine A 78 (1998) 1137−1149.
[58] J.T. Wang, D.L. Yin, J.Q. Liu, J. Tao, Y.L. Su, X. Zhao, Effect of grain size on mechanical property of Mg−3Al−1Zn alloy, Scripta Materialia 59 (2008) 63−66.
[59] S.M. Yin, C.H. Wang, Y.D. Diao, S.D. Wu, S.X. Li, Influence of grain size and texture on the yield asymmetry of Mg-3Al-1Zn alloy, Journal of Materials Science & Technology 27 (2011) 29−34.
[60] S.K. Panigrahi, K. Kumar, N. Kumar, W. Yuan, R.S. Mishra, R. DeLorme, B. Davis, R.A. Howell, K. Cho, Transition of deformation behavior in an ultrafine grained magnesium alloy, Materials Science and Engineering, A 549 (2012) 123−127.
[61] W. Yuan, S.K. Panigrahi, J.-Q. Su, R.S. Mishra, Influence of grain size and texture on Hall-Petch relationship for a magnesium alloy, Scripta Materialia 65 (11) (2011) 994−997.
[62] M.A. Meyers, O. Vöhringer, V.A. Lubarda, The onset of twinning in metals: a constitutive description, Acta Materialia 49 (2001) 4025−4039.
[63] M.R. Barnett, Z. Keshavarz, A.G. Beer, D. Atwell, Influence of grain size on the compressive deformation of wrought Mg−3Al−1Zn, Acta Materialia 52 (2004) 5093−5103.
[64] L.L. Chang, Y.N. Wang, X. Zhao, M. Qi, Grain size and texture effect on compression behavior of hot-extruded Mg−3Al−1Zn alloys at room temperature, Materials Characterization 60 (2009) 991−994.
[65] T. Mukai, M. Yamanoi, H. Watanabe, K. Higashi, Ductility enhancement in AZ31 magnesium alloy by controlling its grain structure, Scripta Materialia 45 (2001) 89−94.
[66] S.R. Agnew, J.A. Horton, T.M. Lillo, D.W. Brown, Enhanced ductility in strongly textured magnesium produced by equal channel angular processing, Scripta Materialia 50 (2004) 377−381.
[67] C.H. Caceres, D.M. Rovera, Solid solution strengthening in concentrated Mg−Al alloys, Journal of Light Metals 1 (3) (2001) 151−156.
[68] C.H. Cáceres, W.J. Poole, A.L. Bowles, C.J. Davidson, Section thickness, macrohardness and yield strength in high-pressure diecast magnesium alloy AZ91, Materials Science and Engineering, A 402 (1) (2005) 269−277.
[69] C.R. Hutchinson, J.F. Nie, S. Gorsse, Modeling the precipitation processes and strengthening mechanisms in a Mg-Al-(Zn) AZ91 alloy, Metallurgical and Materials Transactions A 36A (2005) 2093−2105.
[70] W.J. Kim, H.G. Jeong, H.T. Jeong, Achieving high strength and high ductility in magnesium alloys using severe plastic deformation combined with low-temperature aging, Scripta Materialia 61 (2009) 1040−1043.
[71] D. Qiu, M.-X. Zhang, Strengthening mechanisms and their superposition law in an age-hardenable Mg-10 wt pct Y Alloy, Metallurgical and Materials Transactions A 43A (2012) 3314−3324.
[72] H. Somekawa, A. Singh, T. Mukai, High fracture toughness of extruded Mg−Zn−Y alloy by the synergistic effect of grain refinement and dispersion of quasicrystalline phase, Scripta Materialia 56 (2007) 1091−1094.
[73] J. Liao, M. Hotta, K. Kaneko, K. Kondoh, Enhanced impact toughness of magnesium alloy by grain refinement, Scripta Materialia 61 (2009) 208−211.
[74] K. Tokaji, M. Kamakura, Y. Ishiizumi, N. Hasegawa, Fatigue behaviour and fracture mechanism of a rolled AZ31 magnesium alloy, International Journal of Fatigue 26 (2004) 1217−1224.

[75] H.-K. Kim, Y.-I. Lee, C.-S. Chung, Fatigue properties of a fine-grained magnesium alloy produced by equal channel angular pressing, Scripta Materialia 52 (2005) 473−477.
[76] P. Cavaliere, P.P. De Marco, Fatigue behaviour of friction stir processed AZ91 magnesium alloy produced by high pressure die casting, Materials Characterization 58 (2007) 226−232.
[77] L. Wu, G.M. Stoica, H.-H. Liao, S.R. Agnew, E.A. Payzant, G. Wang, D.E. Fielden, L. Chen, P.K. Liaw, Fatigue-property enhancement of magnesium alloy, AZ31B, through equal-channel-angular pressing, Metallurgical and Materials Transactions A 38A (2007) 2283−2289.
[78] D.R. Ni, D. Wang, A.H. Feng, G. Yao, Z.Y. Ma, Enhancing the high-cycle fatigue strength of Mg−9Al−1Zn casting by friction stir processing, Scripta Materialia 61 (2009) 568−571.
[79] Y. Uematsu, K. Tokaji, K. Fujiwara, Y. Tozaki, H. Shibata, Fatigue behaviour of cast magnesium alloy AZ91 microstructurally modified by friction stir processing, Fatigue Fracture of Engineering Materials & Structures 32 (2009) 541−551.
[80] W.C. Liu, J. Dong, P. Zhang, Z.Y. Yao, C.Q. Zhai, W.J. Ding, High cycle fatigue behavior of as-extruded ZK60 magnesium alloy, Journal of Materials Science 44 (2009) 2916−2924.
[81] S.M. Yin, F. Yang, X.M. Yang, S.D. Wu, S.X. Li, G.Y. Li, The role of twinning−detwinning on fatigue fracture morphology of Mg−3%Al−1%Zn alloy, Materials Science and Engineering, A 494 (2008) 397−400.
[82] Z. Li, Q. Wang, A.A. Luo, P. Fu, L. Peng, Fatigue strength dependence on the ultimate tensile strength and hardness in magnesium alloys, International Journal of Fatigue 80 (2015) 468−476.

CHAPTER

Complex Concentrated Alloys Including High Entropy Alloys

8

CHAPTER OUTLINE

Synopsis **385**
8.1 Potential and Challenges for CCAs for Airframe Structural Applications **386**
8.2 Foundational Information on HEAs **386**
8.2.1 Four Core Effects 387
8.2.1.1 The High Entropy Effect 388
8.2.1.2 The Lattice Distortion Effect 388
8.2.1.3 The Sluggish Diffusion Effect 389
8.2.1.4 The "Cocktail" Effect 390
8.3 Classifications of CCAs **390**
8.3.1 Constituent Element-Based Classification 391
8.3.2 Traditional Crystal Structure-Based Classification 392
8.3.3 Microstructure-Based Classification 392
8.3.4 Density-Based Classification 393
8.4 Physical Metallurgy of CCAs **394**
8.5 Processing–Microstructure–Properties of CCAs **394**
8.5.1 Linking CCA Core Effects to Deformation Micromechanisms 395
8.5.2 Strength–Ductility Response 396
8.5.3 Toughness Response 398
8.5.4 Fatigue Response 400
8.6 New Alloy Design **401**
8.7 Summary **403**
References **403**

SYNOPSIS

This chapter describes complex concentrated alloys (CCAs), which is a recent nomenclature for a broader set of alloys based on high entropy alloys (HEAs) reported a little more than a decade ago [1,2]. CCAs represent a remarkable shift in alloying strategies and challenge some of the well-established alloying principles. This field is growing rapidly and although no current aircraft application exists for these new alloys, this topic is included in this book based on the current potential and high level of scientific

Metallurgy and Design of Alloys with Hierarchical Microstructures. http://dx.doi.org/10.1016/B978-0-12-812068-2.00008-4

Copyright © 2017 Elsevier Inc. All rights reserved.

interest, particularly considering their unique microstructural features, relationships to properties, and amenability for modeling. Chapters 4–6 discussed the traditional airframe alloys based on aluminum, titanium, and iron. In this chapter, the traditional alloys will be used as benchmarks to comparatively assess the early results on CCAs to point out the possibilities for their design and development.

8.1 POTENTIAL AND CHALLENGES FOR CCAs FOR AIRFRAME STRUCTURAL APPLICATIONS

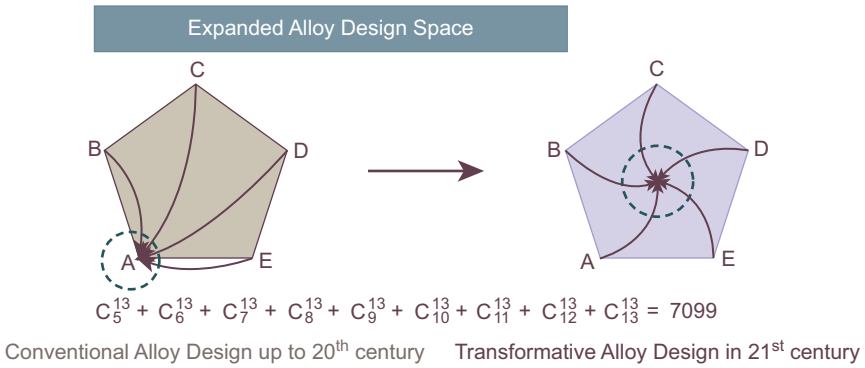
Given the nascent nature of CCAs, it is instructive at the start to establish some benchmarks against which to evaluate their current status and discuss future potential. Using Ashby's materials selection approach [3], there are five major design goals for structures:

- Stiffness-limited design
- Strength-limited design
- Fatigue-limited design
- Toughness-limited design
- Creep-limited design

The property requirements for materials used in various components of aircraft were discussed in the first chapter (see Fig. 1.2). These properties include stiffness, strength, fatigue, and toughness. Corrosion behavior is important and considered in materials selection, but not used for structural design. Creep is important for the propulsion system, which has not been discussed in this book. Therefore, this aspect is not considered further. In addition, the stiffness of material is dependent on chemistry and is insensitive to the microstructure. Therefore, this property is also excluded from further discussion. So, that leaves strength, fatigue, and toughness as major properties that should be considered for discussion of potential use of CCAs in airframe structures. Beyond the intriguing scientific curiosity, do the CCAs have the potential to exceed the performance envelope provided by current engineering alloys?

8.2 FOUNDATIONAL INFORMATION ON HEAs

The first few publications on HEAs appeared in 2004 [1,2,4] and these materials derived their names from the focus on the configurational entropy [5]. The paradigm shift, which is graphically captured in Fig. 8.1, involved the approach of adding elements in equiatomic proportion to create solid-solution face centered cubic (FCC) alloys. This method changed the old approach of adding elements to a "parent" element to create alloys. There is no single dominant matrix element in HEAs. These alloys are also referred as "multiprincipal element alloys" (MPEAs) to capture this fact. This approach opens up the middle space in multicomponent compositional space [6]. The complexity of the search space is captured with the



"...Thus, the effort of experimental determination of a seven component system will be 10^5 times that of a binary diagram and will alone need as much effort as has been spent over the last 100 years in establishing ~4,000 binary and ~8,000 ternary diagrams..."

B.S. Murty, J. W. Yeh, and S. Ranganathan in High-Entropy Alloy published by Butterworth-Heinemann

FIGURE 8.1

An illustration of the alloy design paradigm shift associated with the high entropy alloy approach and the increase in the complex composition search space.

increase in the number of elements [6]. The complexity increases even further with the shifting focus on nonequiatomic approach and move from HEAs to CCAs. Conceptually, this expands the search space from middle of the compositional space to the entire region, where some elements will be major elements and some will be minor elements [7]. But to begin with, it is important to establish the origin of the single-phase solid solution approach. What is the novelty of HEAs? If one adds multiple principal elements and obtains an alloy with a large number of intermetallic phases following the framework of Gibbs phase rule, there is nothing unique as that has been the traditional path for alloy exploration. There is significant difference in opinion on the nomenclature of HEAs and whether the claim of extended solid solution through high entropy is central to this theme. Miracle and Senkov [8] have recently addressed this in depth in a critical review.

8.2.1 FOUR CORE EFFECTS

Yeh [9] set the initial framework for HEAs with the description of four core effects: (1) the high entropy effect, (2) the lattice distortion effect, (3) sluggish diffusion, and (4) the "cocktail" effect. It is important to capture these briefly to facilitate the continued discussion and to build the potential future path for alloy design. Also,

although not all the effects are proven, these are the basis for treating HEAs differently from traditional alloys.

8.2.1.1 The High Entropy Effect

This has been the main driver behind the name HEA. It is argued that an alloy with five or more elements in equiatomic proportions has high configurational entropy, which stabilizes solid solution over the formation of intermetallic compounds. For the discussion focused on strength–ductility–toughness–fatigue combinations for airframe structure, this theme will be used repetitively in this chapter as a means to develop contextual argument for each concept. Note that a high strength stainless steel, A286, used in sheet form for limited aircraft engine structure has almost 48% alloying element content. It is an austenitic precipitation hardening stainless steel discussed in Chapter 6. The FCC austenite phase is stabilized by the addition of Ni. In examining the popular HEA system based on CoCrFeMnNi, an obvious question would be about its performance compared to stainless steels. Ti is added to A286 for the formation of Ni_3Ti precipitates, which is a major strengthener. So, for the development of CCAs with additional strengthening mechanisms, like precipitation strengthening, what happens to the core concept of high entropy? If we go from single-phase microstructure to multiphase microstructure, does this concept lose its validity? Raabe and coworkers [10,11] are pursuing development of steels based on nonequiatomic compositional approach. This is discussed further in a later section.

8.2.1.2 The Lattice Distortion Effect

This effect is based on the fact that atomic radii of constitutive elements of HEAs have different sizes. As shown in Fig. 8.2, a consequence of the increase in the compositional complexity, from pure element (Ni) to ternary, quaternary, and to

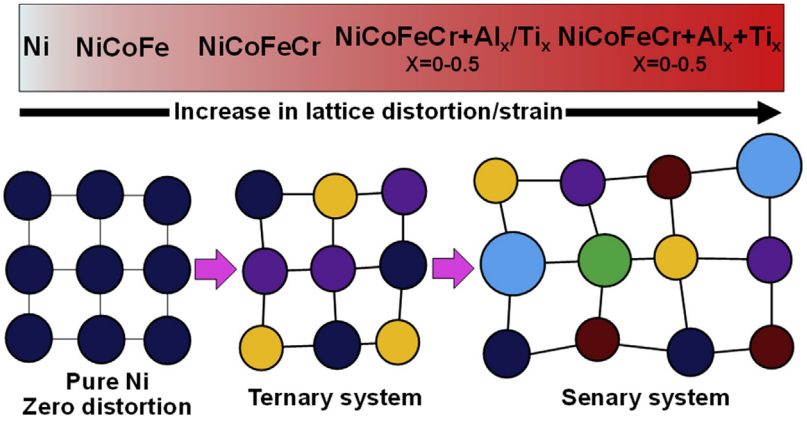


FIGURE 8.2

Schematic of increase in lattice distortion with the number of elements as well as selection of elements with the specific atomic size difference.

senary CCAs, is the continuous increase in the lattice distortion. If the solid solution is truly random, this lattice distortion will be probabilistic in nature. This concept is very important for the strength–ductility–toughness–fatigue combination, which depends on the micromechanisms of plasticity. What is the impact of lattice distortion on dislocation and twinning? Mishra et al. [7] proposed that the lattice distortion leads to lattice strain, which in turn impacts the energetics and kinetics for dislocations and twins. The argument for twinning can be linked with the stacking fault energy of HEAs. Komarasamy et al. [12] have discussed the impact of lattice distortion on the dislocation line energy variation (Fig. 8.3). Additionally, the dislocation line energy depends on the shear modulus of matrix elements. In HEAs, all the elements have different shear modulus values and conceptually that is likely to impact the line energy variation as well. This aspect needs quantification and is likely to be the key concept toward development of high performance CCAs.

8.2.1.3 The Sluggish Diffusion Effect

Diffusion in HEAs is claimed to be slow. It is argued that the activation energy for substitutional diffusion is high and there are point energy traps that can lower the frequency term as well. Similar to the dislocation core energy variation, one can envision a configuration that leads to energy wells. Yeh and coworkers [1,9] had shown through the early work that microstructural coarsening kinetics is slower in

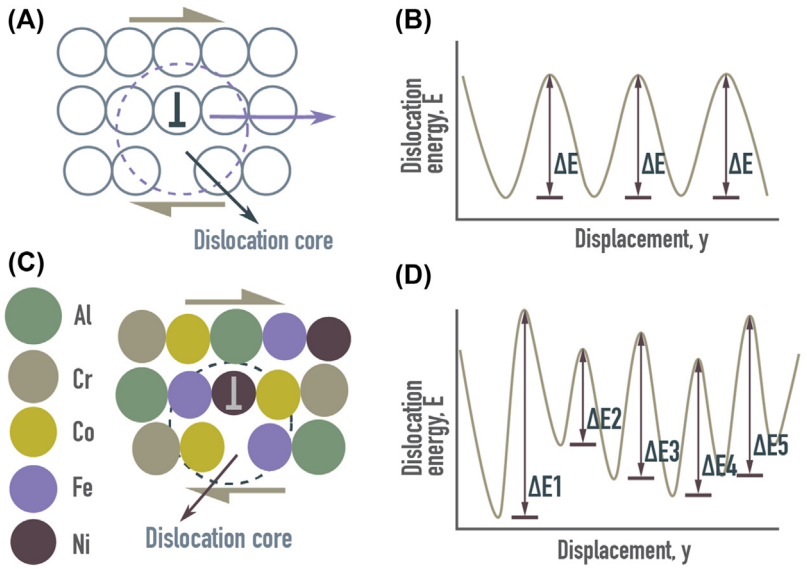


FIGURE 8.3

Schematic of (A) atomic arrangement around dislocation core in pure metals and the corresponding dislocation energy with movement in (B), (C) atomic arrangement around dislocation core in high entropy alloy, and (D) the corresponding energy with displacement [12].

HEAs. This observation continues to establish itself, although the fundamental diffusion activation energy claim has been questioned by Miracle and Senkov [8] through a broader analysis. The microstructural stability depends on the diffusional coefficient as well as the pinning effects. There are key fundamental questions that have not been addressed, but phenomenological observations suggest slower kinetics for grain growth; both during static annealing of cold worked HEAs as well as during a dynamic thermomechanical process like friction stir processing.

8.2.1.4 The "Cocktail" Effect

This is an intriguing concept. The keyword "cocktail" originated from Ranganathan [13], whose paper was titled "Alloyed pleasures: multimetallic cocktails". The implication of this effect is that combination of unusual properties can result in highly alloyed metallic materials. As highlighted in previous chapters, with the focus on strength−ductility−toughness−fatigue−ductility property combinations, can HEAs achieve unpredictable set of properties? Ranganathan [13] highlighted results on so-called "gum metal" [14] and bulk metallic glasses and extended it to the work of Yeh's group, which were not formally published at that time. Gum metal is so named because it shows high strength, low modulus, no/little work hardening, and large ductility. In conventional metallic alloys, the work hardening rate is proportional to the uniform elongation and by extension to the overall ductility. So, if a material does not exhibit any work hardening, the expectation would be that failure processes will onset early. Therefore, Saito et al. [14] claimed superelasticity and superplasticity. Moreover, they discussed dislocation-free plastic deformation, which may not be entirely defendable. Nevertheless, as will be discussed later, early results do show trends that establish exceptional properties in singular mode, meaning that one of the strength−ductility−toughness−fatigue properties is high in a particular alloy. For example, exceptional toughness has been reported in an alloy that has relatively low strength. What approaches can be taken for concurrent maximization of all the properties?

8.3 CLASSIFICATIONS OF CCAs

As in the conventional alloys, a number of different strategies can be taken to classify HEAs and then link them to CCAs. This short section is based on four reviews [5,6,8,15]. The purpose is to provide some context with the focus on aircraft materials. Fig. 8.4 shows a very comprehensive compilation of elements used in all alloys referred as MPEAs. For the current purposes the name CCAs will be used synonymously with MPEAs. As mentioned at the outset, unlike conventional alloys, HEAs do not have any host element. So, early on many researchers referred to these as multiprincipal element alloys to imply the lack of a host or dominant element. There is a trend to follow all the classes of engineered materials with a prefix of "high entropy" and some of it can get confusing and begin to lose focus. For example, in simple terms metals and alloys are disordered crystalline materials; intermetallics are ordered crystalline materials; and ceramics are ordered crystalline materials with

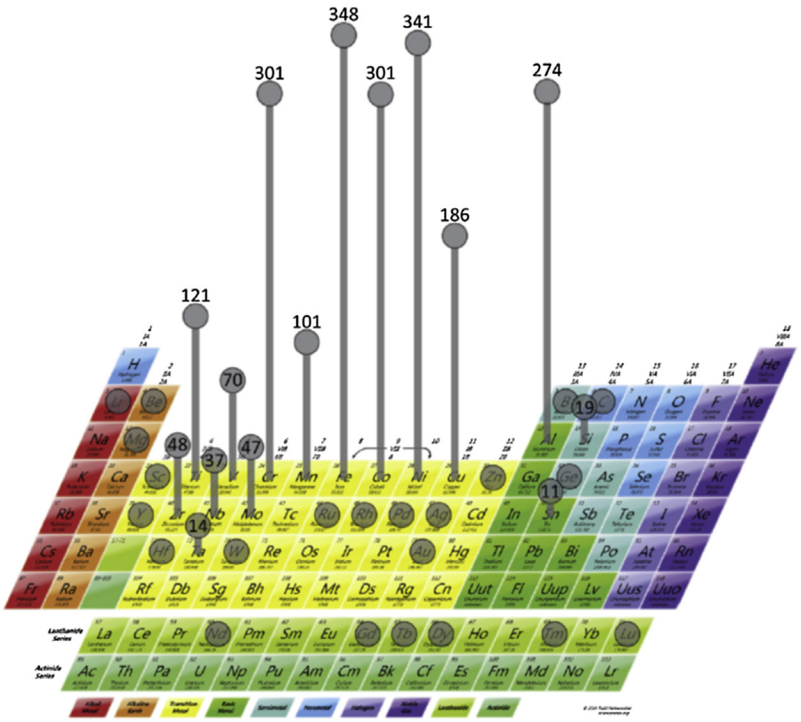


FIGURE 8.4

A plot created by Miracle and Senkov [8] to show the frequency with which elements are used in the 408 multiprincipal element alloys. The *vertical lines* are proportional to the number of alloys that use the indicated element, which is also shown by the associated numbers. No number is given when an element is used in fewer than 10 alloys. Al, Co, Cr, Cu, Fe, Mn, Ni, and Ti are by far the most commonly used elements.

more complex bonding. The broader community has used terms like high entropy intermetallics to represent ordered alloys that have solid solution substitutional elements. For plastic deformation of materials, movement of vacancies and dislocations are required. Focusing just on dislocations as the primary means of accomplishing meaningful plasticity, the distinction between solid solution intermetallic and binary intermetallic is secondary to the configuration of dislocations that result from the ordered crystal structure. For airframe structures, only metallic materials that belong to disordered crystalline materials are important.

8.3.1 CONSTITUENT ELEMENT-BASED CLASSIFICATION

In a detailed compilation, Miracle and Senkov [8] have noted that 3d transition elements have so far dominated the efforts. Based on this, the classification scheme

is written as (1) 3d transition elements based CCAs and (2) refractory metal CCAs. An important consideration for aircraft structural application is the density of materials. So, refractory metal CCAs, with their high density, are not considered further. The main advantage they provide is the high temperature capability, which is not the focus for airframes.

8.3.2 TRADITIONAL CRYSTAL STRUCTURE-BASED CLASSIFICATION

This approach is rather simple and the classification scheme is written as (1) FCC, (2) body centered cubic (BCC), and (3) hexagonal close packed (HCP). Note that a vast majority of 3d transition element-based CCAs are FCC. There is only one report of HCP CCA. But as emphasized in the next microstructure-based classification, there is a significant opportunity in the FCC- and BCC-based approaches for CCAs.

8.3.3 MICROSTRUCTURE-BASED CLASSIFICATION

This approach is the most appropriate for CCAs, as it allows to build complex microstructures based on simple structure matrix. In fact, this was the basis for the discussion of hierarchical microstructures as a means to achieve desirable property combinations in traditional alloys discussed in the earlier chapters. Aluminum and magnesium do not undergo allotropic transformation, so the alloy matrix remains a simple solid solution. High strength Al and Mg alloys use precipitation strengthening along with grain boundary and solid solution strengthening. On the other hand, steels and titanium alloys go through solid state phase transformation and the matrix grains can have higher level of morphological and chemical complexity. In titanium alloys, the main classification was based on alpha and beta phases, i.e., α, α/β, and β alloys. The α phase has HCP structure and the β phase is BCC. Similar approach is well suited for the CCAs. Fig. 8.5 shows the transition in phase as a function of Al in an $Al_xCoCrFeNi$ system [16]. The actual microstructures are a lot more complex than the simple FCC to BCC transition. For example, the $Al_{0.7}CoCrFeNi$ composition has FCC + BCC + B2 phases.

So, the classification under this category can be

- Single-phase solid solution alloys
- Precipitation strengthened alloys
- Dual-phase alloys
- Precipitation strengthened dual-phase alloys including interstitial alloys
- Dispersion strengthened alloys

Of course, many more combinations are possible, but these capture the type of alloys that can have properties attractive for structural applications. Recently, Li et al. [11] have published metastable dual-phase HEAs, which are also examples of nonequiatomic compositional approach. This will be discussed further in the subsequent sections.

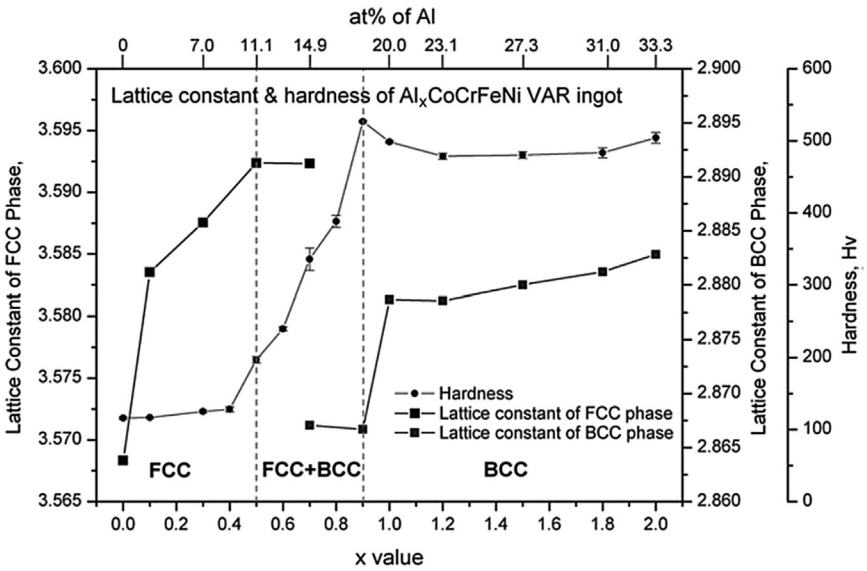


FIGURE 8.5

Variation of lattice constant and hardness of the $Al_xCoCrFeNi$ alloys as functions of Al content. Note the phase change with increasing Al content [16].

8.3.4 DENSITY-BASED CLASSIFICATION

The density-based classification is quite meaningful for aircraft structures. The material selection for such applications is governed by normalizing properties by density, referred to as specific properties (property/density). High structural performance depends on maximizing the specific properties. Following the density-based approach, the classification can be simply

- Light-weight CCAs—a somewhat subjective value in the range of ~5–5.5 g/cc can be used as a cutoff. This is based on classification of Ti, Al, and Mg alloys as lightweight alloys. Only a few alloys have been reported in this category and all of them have been processed by powder metallurgy route.
- Medium-weight CCAs—the upper limit of this can be set around 8.5 g/cc. The 3d elements fall in this category and the CCAs based on CoCrFeNi can be treated as medium-weight CCAs. Most of the research literature so far belong to this category and conventional casting + thermomechanical processing route works well for these alloys. This is important because a wide range of product forms are possible because of this flexibility.
- Heavy-weight CCAs—the refractory element containing CCAs fall in this category. These alloys are not suitable for aircraft structures. The density penalty is too high to be compensated by property enhancement.

8.4 PHYSICAL METALLURGY OF CCAs

A major factor right from the beginning of HEAs has been the deviation from well-established Hume–Rothery rules for solid solution formation that are based on atomic radii, crystal structure, valency, and electronegativity. Guo et al. [17] have developed a parametric approach using topology (atomic size differences) and chemistry (the mixing enthalpy) to determine the formation of solid solutions. They used a δ parameter to represent the atomic size differences among the constituent elements, which is defined as

$$\delta = \sqrt{\sum_{i=1}^{n} c_i(1 - r_i/\overline{r})^2},$$

where $\overline{r} = \sum_{i=1}^{n} c_i r_i$, c_i, and r_i are the atomic percentage and atomic radius of the ith element, respectively, and n is the number of alloying elements. For the chemical factor including electronegativity, they used a weighted average of mixing enthalpies of different pairs of alloying elements to represent the mixing enthalpy, ΔH_{mix}, of the alloys, which is defined as

$$\Delta H_{\text{mix}} = \sum_{i=1,\ i\neq j}^{n} c_i c_j \Omega_{ij}$$

where $\Omega_{ij} = 4\Delta_{\text{mix}}^{\text{AB}}$ and $\Delta_{\text{mix}}^{\text{AB}}$ is the mixing enthalpy of binary liquid equiatomic AB alloys. Fig. 8.6 shows the success of this approach and establishes (1) a critical atomic size polydispersity $\sim$0.065 determines the phase selection and (2) a more negative ΔH_{mix} (<-12 kJ/mol) favors the amorphous phase formation. The rule becomes sufficient only when intermetallic compounds are not formed.

8.5 PROCESSING–MICROSTRUCTURE–PROPERTIES OF CCAs

The goal of any new structural alloy is to possess a combination of mechanical properties that exceed the currently available alloy capabilities while maintaining economic viability. This is the focus of this section and only a few examples have been taken to highlight the strength, ductility, toughness, and fatigue results. Given the vast number of papers containing mechanical properties, it is important to note that most of the information is for cast microstructure often reporting only hardness values. Although there is a direct relationship between hardness and strength of materials, the hardness values give no indication of the nature of the stress–strain curve and ductility. The focus in this section is on the tensile behavior.

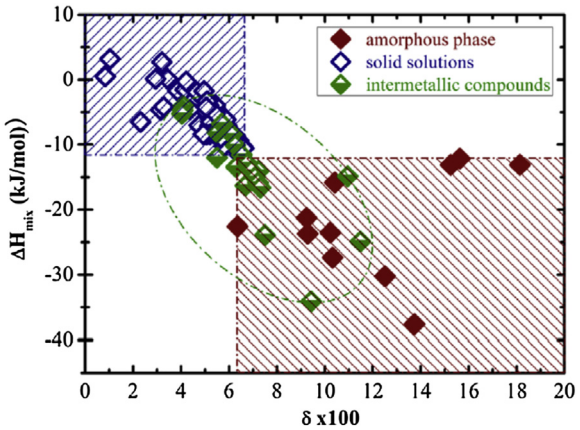


FIGURE 8.6

A δ-ΔH_{mix} plot delineating the phase selection in high entropy alloys. The *dash—dotted* regions highlight the individual region to form solid solutions, intermetallic compounds, and the amorphous phase [17].

8.5.1 LINKING CCA CORE EFFECTS TO DEFORMATION MICROMECHANISMS

Four core effects, namely, the high entropy effect, the lattice distortion effect, sluggish diffusion, and the "cocktail" effect were described earlier. The keywords that are important in discussing the plasticity of metallic materials are

- Vacancies
- Dislocations
- Stacking fault
- Twinning

As mentioned before, the key question is whether these features are influenced by the core effects to make them distinctly different from the conventional alloys. Vacancies can be affected by local energy trap in HEAs and this possibility has been discussed in the context of sluggish diffusion. However, for low temperature airframe structural applications, diffusivity is not important. So, the role of vacancies can be ignored for the ambient temperature mechanical properties.

The role of dislocations, stacking fault energy, and twinning during ambient temperature deformation are intertwined. The stacking fault energy dictates the separation between the dislocation partials, which in turn impacts the dislocation/dislocation interaction and recovery rate during the deformation. The configurational entropy of alloy and lattice distortion depends on the mixing of high number of elements. At the first level, as depicted in Fig. 8.3, the dislocation line energy is

likely to fluctuate with the lattice distortion. Also, the solid solution leads to lower stacking fault energy, which leads to more twinning. Mishra et al. [7] have postulated that the lattice distortion or strain can lead to higher twinning. This shows the linkage between the core effects and dislocation plasticity in CCAs. It is also likely to impact the lattice friction or Peierls stress.

8.5.2 STRENGTH–DUCTILITY RESPONSE

As indicated earlier, majority of tensile deformation data has been generated on the single-phase FCC alloys. At the first glance the stress–strain behavior of single-phase FCC HEAs looks similar to single-phase austenitic stainless steels. The stress–strain curve shows low yield strength, high work hardening, and large ductility. Low yield strength is mainly due to lack of strengthening mechanisms in such materials. Only solid solution and grain boundary strengthening are operative in as-cast and annealed alloys. As noted in Chapters 4–6, the contribution of solid solution strengthening is quite low in traditional alloys. The effectiveness of grain boundary strengthening depends on the level of thermomechanical processing. Fig. 8.7 shows a set of stress–strain curves for $Al_{0.1}CoCrFeNi$ alloy with various grain sizes. The noteworthy features are (1) large regions of strain hardening, (2) an expected increase in the yield strength with refinement of grain size, and (3) change in the nature of work hardening as a function of grain size. It should be noted that the FCC HEAs exhibit distinctly different stress–strain behavior than the BCC HEAs. The stacking-fault energy (SFE) is a fundamental property that governs the configuration of dislocations and twins in a chosen alloy system or element. SFE is crucial in the plastic deformation of conventional FCC metals and alloys, as it determines the separation distance between partials and also the probability of twinning, which is directly related to SFE. SFEs of various conventional FCC metals and alloys along with few FCC HEAs are given in Table 8.1. In the case of Cu, the SFE reduces with the solute additions and the reduction is very significant in the case of the Al-alloying addition. In general, HEAs possess low SFE, and the lowest value can be noted for the conventional solid solution alloy Cu–8 wt% Al and in a nonequiatomic HEA $Fe_{20}Cr_{26}Ni_{14}Co_{20}Mn_{20}$. The nonequiatomic approach can be the basis for developing matrix for CCAs with additional strengthening mechanisms. Furthermore, under high strain rate compression testing conditions, secondary deformation nanotwins were observed in the $Al_{0.1}CoCrFeNi$ HEA [18], as shown in Fig. 8.8. This opens up microstructural tailoring opportunities.

Recently, Li et al. [11] reported a new approach toward development of transformation-induced plasticity-assisted, dual-phase HEA (TRIP-DP-HEA) with exceptional strength–ductility combination, although still short of the level of properties that would trigger consideration for structural applications in airframes. Nevertheless, this is a foundational article to keep moving HEAs toward CCAs. Fig. 8.9 shows stress–strain curves for TRIP-DP-HEA with two different grain sizes. Note the simultaneous increase in strength and ductility with refinement of grain size in the TRIP-DP-HEA. These are early results and create the basis to further design

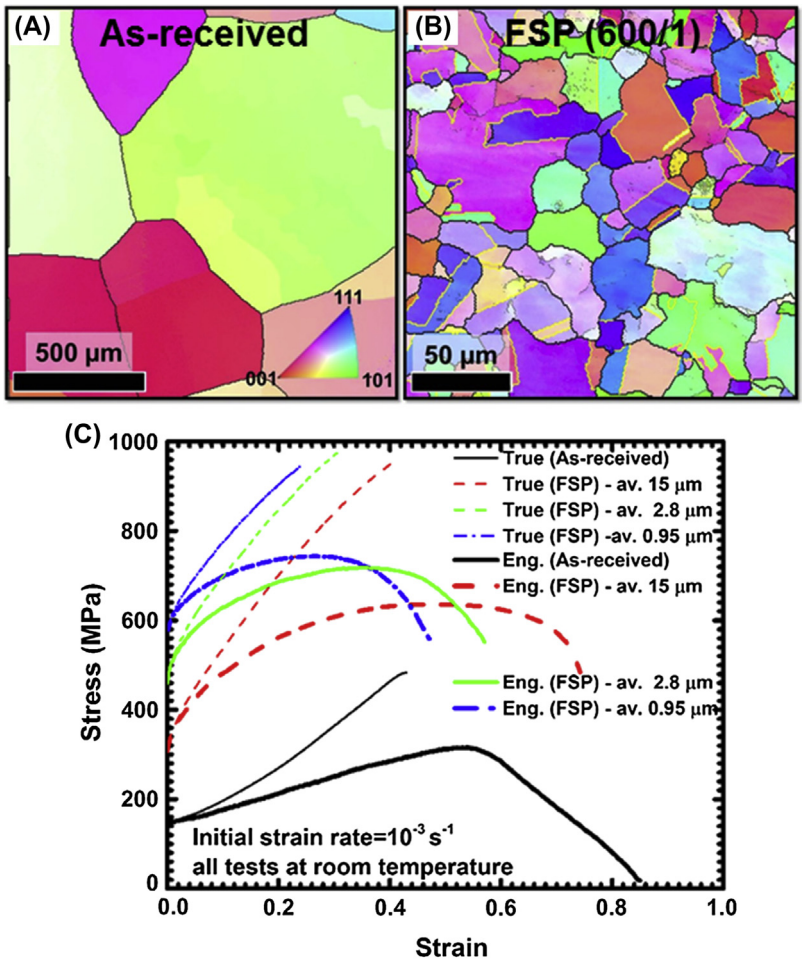


FIGURE 8.7

Electron backscattered diffraction map of $Al_{0.1}CrCoFeNi$ high entropy alloy (HEA) in (A) as-received and (B) friction stir processed samples. The color associated with each grain represents a particular crystallographic axis perpendicular to the plane of the paper, and its index can be assessed from the inverse pole figure triangle embedded in (A). (C) Stress–strain curves for $Al_{0.1}CrCoFeNi$ HEA showing grain size dependence of yield stress and extensive work hardening. Note very high uniform elongation in all conditions.

Adapted from N. Kumar, M. Komarasamy, P. Nelaturu, Z. Tang, P.K. Liaw, R.S. Mishra, Friction stir processing of a high entropy alloy $Al_{0.1}CoCrFeNi$, JOM 67 (2015) 1007–1013.

alloys to enhance the yield strength. The current level of ductility is exceptionally high at >70%. Typically, ductility of 5% or 10% is considered adequate for most applications. As an example, the 4.5 μm grain size TRIP-DP-HEA has multiple microstructural pathways available to enhance strength further either through a forming operation or further thermomechanical processing.

Table 8.1 List of the Stacking-Fault Energy (SFE) of a Few Conventional Face Centered Cubic Metals and Alloys Along With High-Entropy Alloys (HEAs)

Material	SFE (mJ/m^2)	Material	SFE (mJ/m^2)	Material HEA	SFE (mJ/m^2)
Al [19]	166	Cu–2wt% Al [20]	35	FeCrNiCo [21]	17–32
Ni [19]	120–130	Cu–4.5wt% Al [20]	7	FeCrNiCoMn [21]	18.3–27.3
Cu [22]	78	Cu–8wt% Al [20]	2.5	$Fe_{20}Cr_{26}Ni_{14}Co_{20}Mn_{20}$ [21]	3.5
Au [19]	32–50	Ni–60wt% Co [23]	32	$Fe_{20}Cr_{14}Ni_{26}Co_{20}Mn_{20}$ [21]	57.7
Ag [19]	16–22	304SS [22]	25	FeCrNiCoMn at 300K [24]	21
Cu–10wt % Zn [20]	35	Fe–21wt% Cr–14wt% Ni [22]	20	FeCrNiCoMn at 0K [24]	3.4
Cu–30wt % Zn [20]	14	Fe–26wt% Cr–22wt% Ni [22]	37	$Al_{0.3}CoCrFeNi$ [24]	51

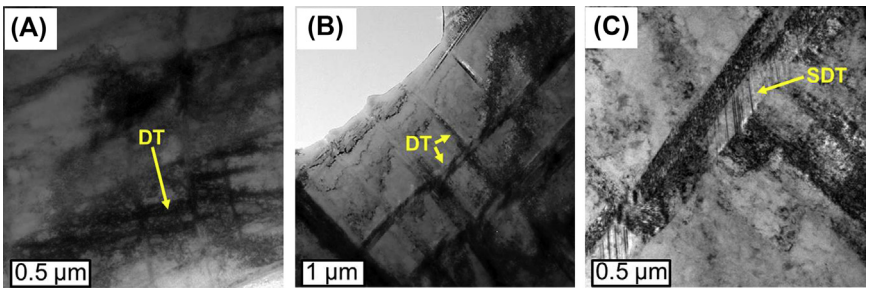


FIGURE 8.8

Postdeformation transmission electron microscope characterization of (A) $10^{-3}\ s^{-1}$ strain rate, (B and C) high strain rate ($2600\ s^{-1}$), and note the secondary deformation twins (SDT) in high strain rate conditions shown in (C) [18].

8.5.3 TOUGHNESS RESPONSE

As discussed in Chapter 6, high toughness steels are used for structural components where fracture toughness is a key design criterion. The results related to fracture toughness of HEAs are very limited. This is mainly due to the complexity of fracture toughness testing and the lack of maturity of HEA field.

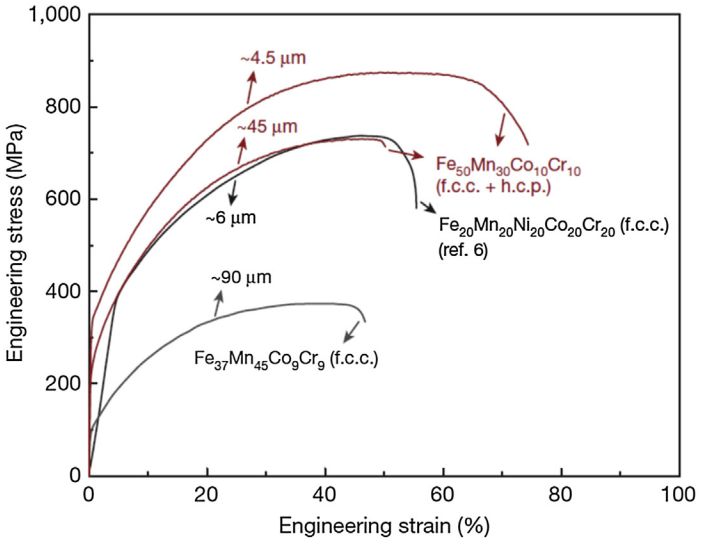


FIGURE 8.9

Stress—strain behavior of the transformation induced plasticity-assisted, dual-phase high entropy alloy (TRIP-DP-HEAs) compared to single-phase HEAs. Grain sizes are shown in micrometers. Note the simultaneous increase in strength and ductility in the TRIP-DP-HEA with refinement of grain size.

Adapted from Z. Li, K.G. Pradeep, Y. Deng, D. Raabe, C.C. Tasan, Metastable high-entropy dual-phase alloys overcome the strength—ductility trade-off, Nature 534 (2016) 227—230.

All the papers so far have been from Ritchie and coworkers [26—28]. Two interesting observations have been made in these studies. First, they reported that a five-element HEA, CrMnFeCoNi, which forms a single-phase FCC solid solution, has exceptional damage tolerance with tensile strengths above 1 GPa and fracture toughness values exceeding 200 MPa $m^{1/2}$ [18]. Although these numbers are impressive, recently they reported that an equiatomic medium-entropy alloy containing only three elements, CrCoNi, as a single-phase FCC solid solution, which displays strength-toughness properties that exceed those of all high-entropy alloys and most multiphase alloys. At room temperature, the CrCoNi alloy showed tensile strengths of almost 1 GPa, failure strains of $\sim$70%, and K_{JIc} fracture-toughness values above 200 MPa $m^{1/2}$ [20]. These results are shown in Fig. 8.10. Note that a toughness-limiting design approach uses the relationship among crack size, strength, and toughness, which for tensile opening of a preexisting crack is expressed as $K_{Ic} = \sigma\sqrt{\pi\, a}$ where K_{Ic} is the critical stress intensity factor referred the fracture toughness of the material, σ is the strength of material, and "$2a$" is the length of the preexisting flaw. The material selection lines in Fig. 8.10 are based on this relationship. Clearly the HEAs look attractive and the underlying mechanism of this enhanced strength—toughness combination is of great importance. A key new microstructural finding relates to nanotwin

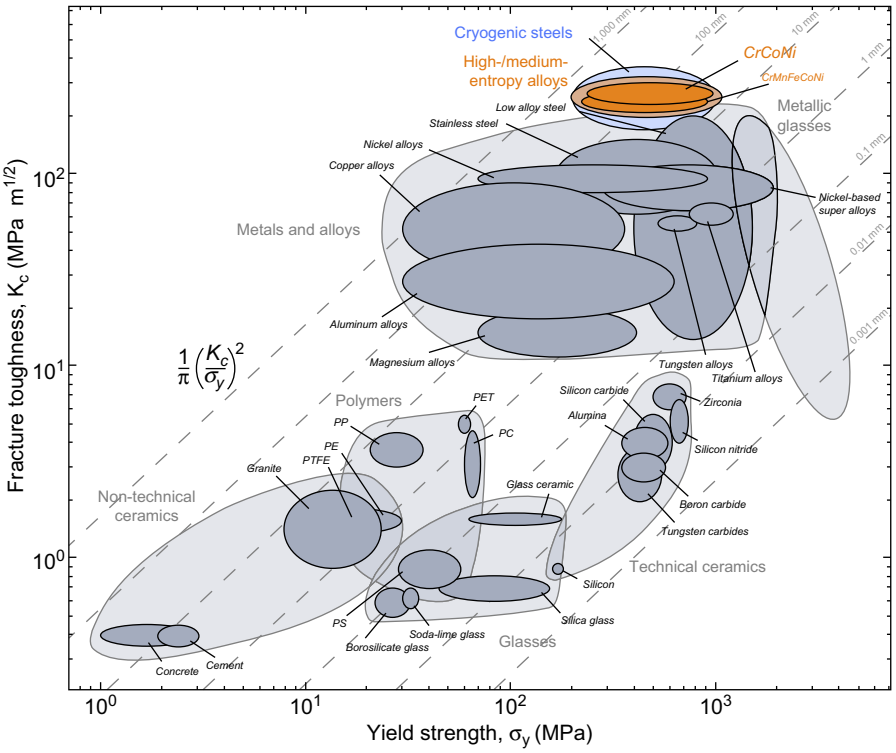


FIGURE 8.10

Ashby map of fracture toughness versus yield strength for various classes of materials showing the combination reported for medium-entropy CrCoNi alloy and high entropy CoCrFeMnNi alloy [28].

bridging of cracks during in situ TEM crack growth study in a thin foil [19]. Fig. 8.11 shows the nanotwin bridging in thin foil. Even though the scaling of the results has some level of uncertainty, they are important because of the strain rate dependent twinning observed in these alloys. Again, the fundamental question is whether the plasticity in HEAs is different from that in conventional alloys and can it lead to CCAs with property combinations that push the limits on the Ashby type materials selection chart. The initial results point to that possibility. Note the similarity of nanotwins in Figs. 8.8 and 8.11.

8.5.4 FATIGUE RESPONSE

Aircraft structures experience cyclic loading and most of the time it is a primary design consideration. Usually, a rule of thumb is that the ratio of fatigue endurance limit (EL) to ultimate tensile strength (UTS) for most engineering alloys lie between

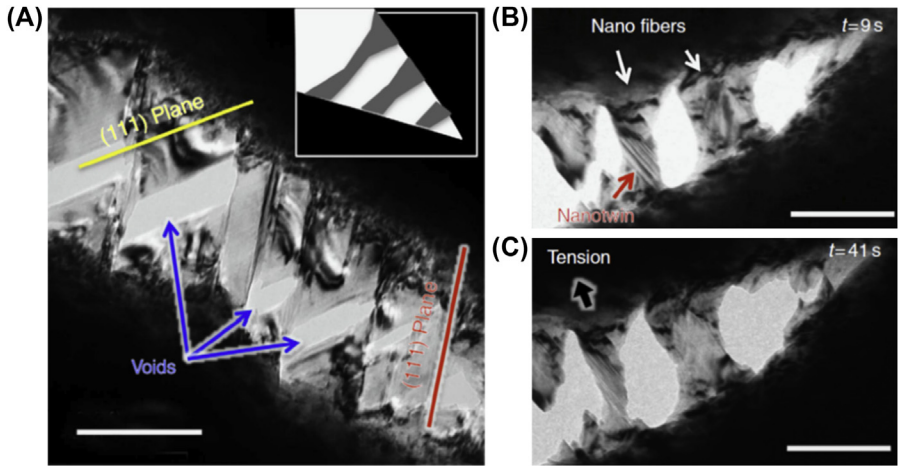


FIGURE 8.11

Crack bridging via near-tip twinned nanobridges. (A) Bright-field transmission electron microscopy (TEM) image of a growing crack during in situ straining of the CrMnFeCoNi high-entropy alloy, showing the formation of nano/submicron voids at the intersection of two slip systems, which then grow along two {111} slip bands (scale bar, 200 nm). The crack tip is located ~500 nm away from the right-lower corner of this image. The inset in a is a schematic of the structure at the crack tip. (B) Two TEM images captured from the in situ TEM movie that show the nanoscale tensile loading of "nanofibers" that bridge the crack in the near-tip region (scale bar, 200 nm). Nanotwins can be seen to form in some of the fibers, enhancing their ductility, and resulting in their significant elongation. (C) High-resolution TEM image of deformation twinning taken during in situ TEM tensile test (scale bar, 5 nm) [27].

0.35 and 0.5. Fig. 8.12 shows a comparison of results from $Al_{0.5}CoCrCuFeNi$ two-phase HEA with different engineering alloys [29]. Tang et al. [30] have investigated the mechanism of deformation and again the role of twinning has been highlighted. However, the variability in these early results is very high to make significant prediction. If one considers the highest endurance values observed so far, then it appears that the right microstructural approach has the potential to surpass the fatigue properties of conventional alloys.

8.6 NEW ALLOY DESIGN

This realm of new alloy design is an exciting phase and initial results so far hint at these possibilities. The key opportunity relates to fundamental stacking fault energy driven approach to (1) extend nonequiatomic HEAs, (2) develop multiphase microstructure to increase the number of strengthening mechanisms, and (3) create twinned microstructures by controlled thermomechanical processing. Combined

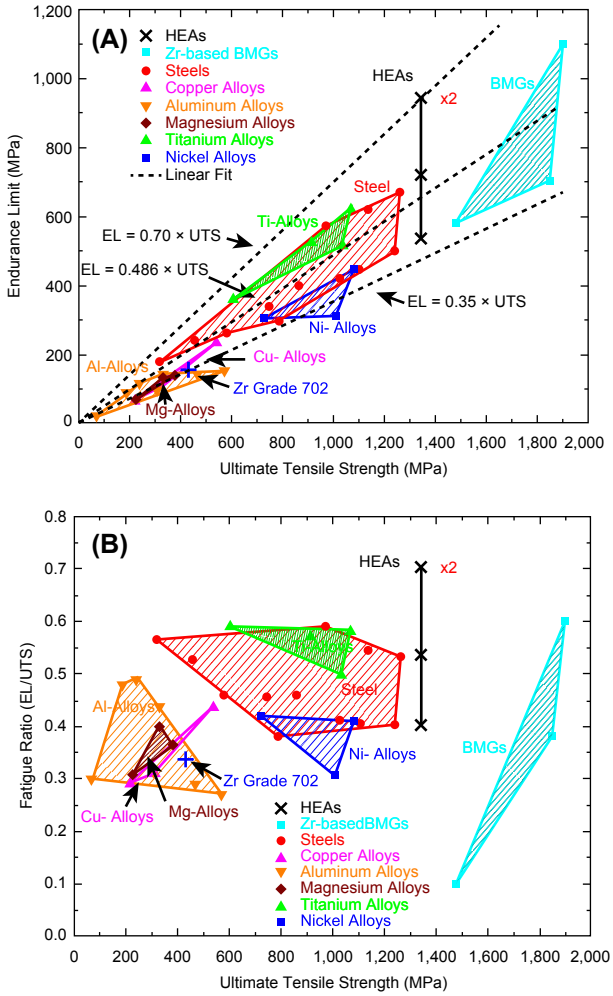


FIGURE 8.12

Plots comparing (A) the endurance limits and (B) the fatigue ratios of the $Al_{0.5}CoCrCuFeNi$ high entropy alloy as a function of the ultimate tensile strength (UTS) of other structural materials and bulk metallic glasses (BMGs) [29].

together, this creates a domain for CCAs where the plasticity changes from the conventional alloys. Combining the high entropy effect that can alter the stacking fault energy with the lattice distortion effect that impacts the dislocation core configuration and twinning, the field has rich possibilities. Mishra et al. [7] have suggested multi-minor element alloying approach to enhance the lattice distortion, which in turn affects the stacking fault energy. High throughput computational and

experimental approaches are needed to accelerate progress in design and discovery of new alloys. Several efforts are underway with calculation of phase diagrams approach [31,32], and along with the phase prediction, steps need to be incorporated to include effects of thermomechanical processing on microstructure properties for CCAs with combination of properties that exceeds the conventional alloys.

8.7 SUMMARY

The field of CCAs is very new and currently no engineering application has been reported. Some of the fundamentals for HEAs that form the basis for CCAs are different from conventional alloys. The core effects of HEAs provide opportunities to tailor the micromechanisms through major and minor element selection. The CCAs in some cases will mimic conventional engineering alloy microstructural paradigm, yet have the potential to expand the property space through the cocktail effect.

REFERENCES

[1] J.W. Yeh, S.K. Chen, S.J. Lin, J.Y. Gan, T.S. Chin, T.T. Shun, Nanostructured high-entropy alloys with multiple principal elements: novel alloy design concepts and outcomes, Advanced Engineering Materials 6 (2004) 299−303.
[2] B. Cantor, I.T.H. Chang, P. Knight, A.J.B. Vincent, Microstructural development in equiatomic multicomponent alloys, Materials Science and Engineering: A 375−377 (2004) 213−218.
[3] M.F. Ashby, Materials Selection in Mechanical Design, fifth ed., Butterworth-Heinemann, December 16, 2016.
[4] T.K. Chen, T.T. Shun, J.W. Yeh, M.S. Wong, Nanostructured nitride films of multielement high-entropy alloys by reactive DC sputtering, Surface and Coatings Technology 188−189 (2004) 193−200.
[5] Y. Zhang, T.T. Zuo, Z. Tang, M.C. Gao, K.A. Dahmen, P.K. Liaw, Z.P. Lu, Microstructures and properties of high-entropy alloys, Progress in Materials Science 61 (2014) 1−93.
[6] B.S. Murty, J.-W. Yeh, S. Ranganathan, High Entropy Alloy, first ed., Butterworth-Heinmann, London, UK, 2014.
[7] R.S. Mishra, N. Kumar, M. Komarasamy, Lattice strain framework for plastic deformation in complex concentrated alloys including high entropy alloys, Materials Science and Technology 31 (10) (2015) 1259−1263.
[8] D.B. Miracle, O.N. Senkov, A critical review of high entropy alloys and related concepts, Acta Materialia 122 (2017) 448−511.
[9] J.-W. Yeh, Recent progress in high entropy alloys, Annales de Chimie Science des Matériaux 31 (2006) 633−648.
[10] D. Raabe, C.C. Tasan, H. Springer, M. Bausch, From high-entropy alloys to high-entropy steels, Steel Research International 86 (10) (2015) 1127−1138.
[11] Z. Li, K.G. Pradeep, Y. Deng, D. Raabe, C.C. Tasan, Metastable high-entropy dual-phase alloys overcome the strength−ductility trade-off, Nature 534 (2016) 227−230.

[12] M. Komarasamy, N. Kumar, R.S. Mishra, P.K. Liaw, Anomalies in the deformation mechanism and kinetics of coarse-grained high entropy alloy, Materials Science and Engineering: A 654 (2016) 256−263.
[13] S. Ranganathan, Alloyed pleasures: multimetallic cocktails, Current Science 85 (2003) 1404−1406.
[14] T. Saito, T. Furuta, J.-H. Hwang, S. Kuramoto, K. Nishino, N. Suzuki, R. Chen, A. Yamada, K. Ito, Y. Seno, T. Nonaka, H. Ikehata, N. Nagasako, C. Iwamoto, Y. Ikuhara, T. Sakamura, Multifunctional alloys obtained via a dislocation-free plastic deformation mechanism, Science 300 (2003) 464−467.
[15] M.H. Tsai, J.W. Yeh, High-entropy alloys: a critical review, Materials Research Letters 2 (2014) 107−123.
[16] W.-R. Wang, W.-L. Wang, S.-C. Wang, Y.-C. Tsai, C.-H. Lai, J.-W. Yeh, Effects of Al addition on the microstructure and mechanical property of Al_xCoCrFeNi high-entropy alloys, Intermetallics 26 (2012) 44−51.
[17] S. Guo, Q. Hu, C. Ng, C.T. Liu, More than entropy in high-entropy alloys: forming solid solutions or amorphous phase, Intermetallics 41 (2013) 96−103.
[18] N. Kumar, Q. Ying, X. Nie, R.S. Mishra, Z. Tang, P.K. Liaw, R.E. Brennan, K.J. Doherty, K.C. Cho, High strain-rate compressive deformation behavior of the $Al_{0.1}$CrFeCoNi high entropy alloy, Materials & Design 86 (2015) 598−602.
[19] N.M. Rosengaard, H.L. Skriver, Calculated stacking-fault energies of elemental metals, Physical Review B 47 (1993) 12865−12873.
[20] O. Johari, G. Thomas, Substructures in explosively formed Cu and Cu-Al alloys, Acta Metallurgica 12 (1964) 1153−1159.
[21] A.J. Zaddach, C. Niu, C.C. Koch, D.L. Irving, Mechanical properties and stacking fault energies of NiFeCrCoMn high-entropy alloy, Journal of Materials Science 65 (2013) 1780−1789.
[22] Y.H. Zhao, Z. Horita, T.G. Langdon, Y.T. Zhu, Evolution of defect structures during cold rolling of ultrafine-grained Cu and Cu−Zn alloys: influence of stacking fault energy, Materials Science and Engineering A 474 (2008) 342−347.
[23] A. Rohatgi, K.S. Vecchio, G.T. Gray III, The influence of stacking fault energy on the mechanical behavior of Cu and Cu-Al alloys: deformation twinning, work hardening, and dynamic recovery, Metallurgical and Materials Transactions 32A (2001) 135−144.
[24] S. Huang, W. Li, S. Lu, F. Tian, J. Shen, E. Holmström, L. Vitos, Temperature dependent stacking fault energy of FeCrCoNiMn high entropy alloy, Scripta Materialia 108 (2015) 44−47.
[25] N. Kumar, M. Komarasamy, P. Nelaturu, Z. Tang, P.K. Liaw, R.S. Mishra, Friction stir processing of a high entropy alloy $Al_{0.1}$CoCrFeNi, JOM 67 (2015) 1007−1013.
[26] B. Gludovatz, A. Hohenwarter, D. Catoor, E.H. Chang, E.P. George, R.O. Ritchie, A fracture-resistant high-entropy alloy for cryogenic applications, Science 345 (2014) 1153.
[27] Z.J. Zhang, M.M. Mao, J. Wang, B. Gludovatz, Z. Zhang, S.X. Mao, E.P. George, Q. Yu, R.O. Ritchie, Nanoscale origins of the damage tolerance of the high-entropy alloy CrMnFeCoNi, Nature Communications 6 (2015) 10143, http://dx.doi.org/10.1038/ncomms10143.
[28] B. Gludovatz, A. Hohenwarter, K.V.S. Thurston, H. Bei, Z. Wu, E.P. George, R.O. Ritchie, Exceptional damage-tolerance of a medium entropy alloy CrCoNi at cryogenic temperatures, Nature Communications 7 (2016) 10602, http://dx.doi.org/10.1038/ncomms10602.

[29] M.A. Hemphill, T. Yuan, G.Y. Wang, J.W. Yeh, C.W. Tsai, A. Chuang, P.K. Liaw, Fatigue behavior of $Al_{0.5}$CoCrCuFeNi high entropy alloys, Acta Materialia 60 (2012) 5723−5734.

[30] Z. Tang, T. Yuan, C.-W. Tsai, J.-W. Yeh, C.D. Lundin, P.K. Liaw, Fatigue behavior of a wrought $Al_{0.5}$CoCrCuFeNi two-phase high-entropy alloy, Acta Materialia 99 (2015) 247−258.

[31] http://www.questek.com/filebase/src/Presentations/QTHEAs.pdf.

[32] C. Zhang, M.C. Gao, CALPHAD modeling of high-entropy alloys, in: M.C. Gao, J.-W. Yeh, P.K. Liaw, Y. Zhang (Eds.), High-Entropy Alloys: Fundamentals and Applications, Springer International Publishing, Switzerland, 2016, pp. 399−444, http://dx.doi.org/10.1007/978-3-319-27013-5.

CHAPTER

Alloy Design for Advanced Manufacturing Processes

9

CHAPTER OUTLINE

Synopsis **407**
9.1 Superplastic Forming **408**
9.1.1 Microstructural Requirement for Superplasticity 409
9.1.2 Design of Alloys for SPF 410
9.1.2.1 Microstructural Design of Aluminum Alloys for Superplasticity ... 410
9.1.2.2 Microstructural Design of Titanium Alloys for Superplasticity 414
9.2 Friction Stir Welding **418**
9.2.1 Overview of Joint Efficiency in Al Alloys Achieved by FSW 419
9.2.2 Correlating Thermal Cycle to the Physical Mechanisms During FSW 420
9.2.2.1 Compositional Dependence of Joint Efficiency 422
9.2.3 Framework for Design of Aluminum Alloys for FSW 425
9.2.3.1 Theoretical Approach: Design of HAZ Free Al Alloys for FSW 425
9.3 Additive Manufacturing **431**
9.3.1 Current Alloys Used for Powder-Bed AM Processes 433
9.3.2 Design of Aluminum and Titanium Alloys for Higher Performance in Additively Manufactured Components 436
9.3.2.1 Build Variability and Inconsistency: Probabilistic Aspect 436
9.3.2.2 Framework for ICME Alloy Design for Powder-Based AM 437
9.4 Summary **444**
References **444**

SYNOPSIS

This chapter focuses on alloy design for specific manufacturing processes. The previous chapters were limited to describing and achieving optimum microstructures in alloys for targeted combination of properties in mill products, which are generally not amenable to fabrication of components using promising manufacturing processes. The illustrative example approach in this chapter considers three such distinct manufacturing processes: (1) superplastic forming (SPF), (2) friction stir welding (FSW), and (3) additive manufacturing (AM). The principles of microstructural design for SPF, FSW, and AM are based on the same metallurgy and mechanisms as for alloy design discussed in earlier chapters in detail. SPF is a

Metallurgy and Design of Alloys with Hierarchical Microstructures. http://dx.doi.org/10.1016/B978-0-12-812068-2.00009-6
Copyright © 2017 Elsevier Inc. All rights reserved.

well-established solid-state manufacturing technology for unitized structures. The forming temperature is kept constant during the operation and gas pressure is adjusted to complete the forming cycle. The alloy design approach for SPF primarily focuses on fine grain size and thermal stability of microstructure. FSW started in 1995 but is still considered a relatively new joining technique because of the long history of other welding techniques. It has developed as a breakthrough joining technique for nonweldable high strength aluminum alloys. Currently, it is applied to existing aluminum alloys for a wide range of applications. The discussion on FSW in this chapter is focused on a few examples of the joint efficiency and its linkage to the physical metallurgy of the alloys. This discussion becomes the basis for suggesting future directions of alloy design to capitalize on the fundamental attributes of this process. The last process considered in this chapter is AM. Although AM of metallic parts is the current rage in manufacturing community for printing components with complex design, the processes themselves have been in existence from 1980s in the name of rapid prototyping. The focus in this chapter is limited to laser-based powder-bed technologies (LBPBT). The context of alloy selection is discussed with the potential pathways for applying design of alloys with hierarchical microstructure for LBPBT. A key message is that the best potential for high-performance engineering application lies in an integrated approach of alloy and process design for each manufacturing process. Of course, the challenges of qualifying a combination of new process and new alloy increase multifold, but this has to be accepted for accelerated progress.

9.1 SUPERPLASTIC FORMING

SPF is used to produce complex-shaped components and unitized structures. It is an attractive, cost-effective near-net shape forming process successfully applied in a commercial environment. The superplastic deformation and forming of materials have come of age in more than four decades of research and technological development. Based on its potential impact in the manufacturing sector, a number of national reports have identified SPF as a critical research area [1–3]. At present, SPF is used for a number of applications. In fact, it is an enabling technology for unitized structures [4]. For example, the F-15E design implemented a superplastically formed and diffusion-bonded Ti–6Al–4V airframe structure as a replacement for built-up assemblies used in earlier models. This resulted in a dramatic part count reduction and demonstrated the successful use of unitized construction in service (elimination of 726 part details and 10,000 fasteners).

The early success stories of SPF of aerospace components were despite the slow forming rates and high cost of starting material with the microstructure required for superplasticity. From the 1980s, there has been a push toward the development of high strain rate superplasticity. The understanding from more than three decades of research has established the relationship between grain size, superplastic strain rate, and superplastic temperatures. For example, mechanically alloyed aluminum

alloys (typical grain size 0.5 μm) exhibit superplasticity at strain rates $>1\ s^{-1}$, comparable to conventional hot forming rates, whereas, for comparison, the usual (typical grain size 15 μm) superplastic strain rates are 10^{-4}–$10^{-3}\ s^{-1}$ [5].

9.1.1 MICROSTRUCTURAL REQUIREMENT FOR SUPERPLASTICITY

Superplasticity is generally defined as an ability of a material to exhibit 200% tensile elongation. This definition is suitable for this book as the entire presentation is limited to metallic materials. The tensile deformation part is important as failure mechanisms like necking and cavitation do not operate under compression. The resistance to necking and cavitation are important for various reasons. The resistance to necking is important as it is associated with thinning during SPF. Obviously, it is desirable to have as uniform a thickness as possible in the final formed part. Although necking represents external loss of cross-section area, cavitation represents its internal loss. Any level of cavitation during SPF will result in a reduction in post-SPF properties. Note that this simple definition of superplasticity does not mention any particular mechanism of deformation. In a very broad classification, superplasticity is divided into two classes: (1) structural superplasticity, which originates from fine grain size, and (2) transformational superplasticity, which originates from phase transformation and is applicable to titanium alloys and steels that exhibit allotropic transformation. Transformational superplasticity is obtained by cycling the forming temperature across the phase transformation temperature and does not have too many practical applications. Therefore, this is not mentioned further. The structural superplasticity will be referred to as just superplasticity for the rest of the chapter, and that is the general convention. Resistance to neck growth during high-temperature deformation was recognized by Woodford [6], who plotted the overall elongation versus strain rate sensitivity (m). For metallic materials, the value of m can vary from 0 to 1, 1 being Newtonian viscous flow where extreme stability of flow is expected (meaning very large elongations). From Woodford's plot and empirical correlation [6], it can be noted that elongation values above 200% are achieved for $m > 0.25$.

The most general constitutive relationship for high-temperature deformation is expressed in the following form,

$$\dot{\varepsilon} = \frac{AD_oEb}{kT}\left(\frac{\sigma}{E}\right)^n\left(\frac{b}{d}\right)^p \exp\left(\frac{-Q}{RT}\right) \tag{9.1}$$

where $\dot{\varepsilon}$ is the strain rate, σ is the flow stress, A is the dimensionless constant, Q is the appropriate activation energy for the rate-limiting process, n is the stress exponent (reciprocal of m), p is the grain size exponent, D_o is the preexponential factor of diffusivity, T is the temperature, E is the Young's modulus, b is the Burgers vector, k is Boltzmann's constant, and R is the universal gas constant. Most physically based superplasticity models predict an m value of 0.5 (i.e., $n = 2$) and p of 2 [7]. The relationship between grain size and optimum strain rate for aluminum alloys is shown in Fig. 9.1A. Also, the superplastic temperature can change with grain size (Fig. 9.1B).

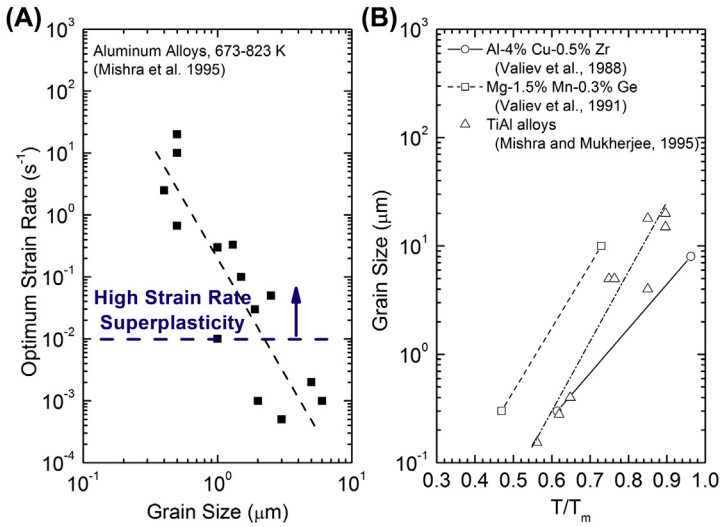


FIGURE 9.1

The influence of grain size on (A) optimum strain rate of aluminum alloys and (B) the superplastic temperature.

Therefore, it is clear that by manipulating the grain size it is possible to (1) increase the superplastic strain rate and (2) decrease the superplastic temperature. Both aspects happen to have attractive technological significance. Note that the correlations for aluminum alloys show that grain size below 1 μm (ultrafine grain size) will lead to high strain rate superplasticity and temperature range would be $\sim 0.55-0.75\ T_m$. The ultrafine grained alloys, however, would experience grain growth in this temperature range unless sufficient amount of second-phase particles are present to pin the grain boundaries. In a very simple way, this becomes the microstructural design guideline for aluminum alloys for exceptional superplastic properties.

9.1.2 DESIGN OF ALLOYS FOR SPF

This section is a brief highlight of a few examples that demonstrate the effectiveness of microstructural design. It is also important to note that these are merely illustrative and many exceptions exist, particularly when details are considered. For example, for a given average grain size, the grain boundary character distribution can be different. The influence of processing technique becomes important at this level of detail.

9.1.2.1 Microstructural Design of Aluminum Alloys for Superplasticity

Fig. 9.2 shows the historical progression of the demonstration of superplasticity in aluminum alloys. Al7475 alloy is a conventional alloy with a grain size of 15 μm (when specially processed for SPF), and this grain size is considered as the upper

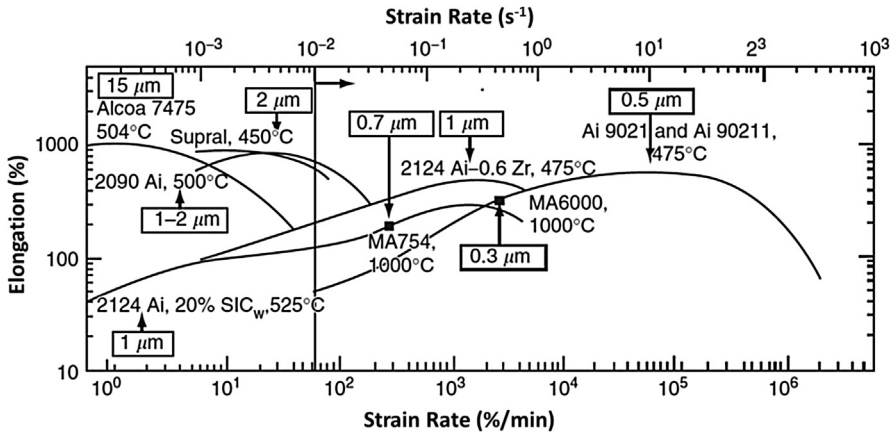


FIGURE 9.2

The effect of grain refinement on the optimum superplastic strain rate [7].

limit for structural superplasticity. Conventional aluminum alloy sheets are produced by thermomechanical processing steps involving rolling. The as-processed microstructure contains significant fraction of low-angle boundaries, which are not conducive for grain boundary sliding, the principal deformation mechanism for superplasticity. So, the microstructural design includes its ability to respond to processing steps. The primary microstructural features and their roles are

- Grain size and grain boundary misorientation distribution—Grain size is the primary microstructural descriptor in Eq. (9.1). As emphasized earlier, finer grain size leads to higher optimum superplastic strain rates and lower superplastic temperatures. However, this is not an entirely adequate descriptor as it does not include grain boundary misorientation information. This aspect was highlighted by Mishra and coworkers in a series of papers using friction stir processing, which typically produced equiaxed grain size with >94% high angle grain boundaries [8–16]. These publications not only establish the shift of optimal superplasticity to high strain rates and to lower temperatures, they show that the kinetics of superplastic deformation is faster than for the conventionally processed aluminum alloys. Fig. 9.3 captures this for a commercial Al2024 alloy. Included in this figure is the space for powder metallurgical processed Al2024 alloy. A key aspect to note is that the strain rate and temperature shift have to be determined experimentally for each condition. Presently, independent control of tailoring microstructure for a desired strain rate and temperature has not been demonstrated. Also, the dimensionless constant "*A*" in Eq. (9.1) depends on the fraction of high angle grain boundaries and represents the overall kinetics. At this stage, a quantitative description of this dependence is not available.

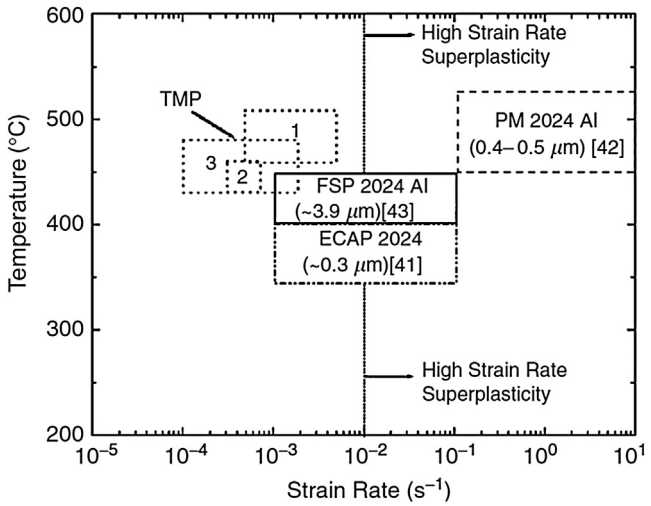


FIGURE 9.3

A temperature–strain rate map depicting the superplastic domains for 2024 Al alloys processed by different routes. For superplasticity of TMP 2024 Al alloys, region 1: grain size 2.5 μm, region 2: grain size 9.2 μm, and region 3: grain size 5–8 μm. (See Ref. [10] for details of data for various regions.)

- Particle size and volume fraction—Conventional aluminum alloys contain Mn, Cr, or Zr as the dispersoid forming element. Dispersoids are stable at high temperature and provide grain boundary pinning during thermomechanical processing. Mechanical alloying introduces higher volume fraction of very fine particles. Apart from grain size stability, the presence of second phase particles at the grain boundaries introduces a threshold term (σ_0) in the constitutive relationship for high strain rate superplasticity [5],

$$\dot{\varepsilon} = 40\frac{D_0 Eb}{kT}\exp\left(\frac{-84,000}{RT}\right)\left(\frac{b}{d}\right)^2\left(\frac{\sigma-\sigma_0}{E}\right)^2 \tag{9.2}$$

The aluminum matrix composites differ from previously mentioned alloys as these contain much coarser second phases. Mishra et al. [17] further modified the constitutive relationship to include a particle size term (d_p),

$$\dot{\varepsilon} = 3.6\times 10^{18}\frac{D_i Eb}{kT}\left(\frac{b}{d_g d_p}\right)^2\left(\frac{\sigma-\sigma_0}{E}\right)^2 \tag{9.3}$$

where D_i is the interfacial diffusion coefficient and d_g is the grain size. Fig. 9.4 shows the transition in superplastic mechanism because of the particle size.

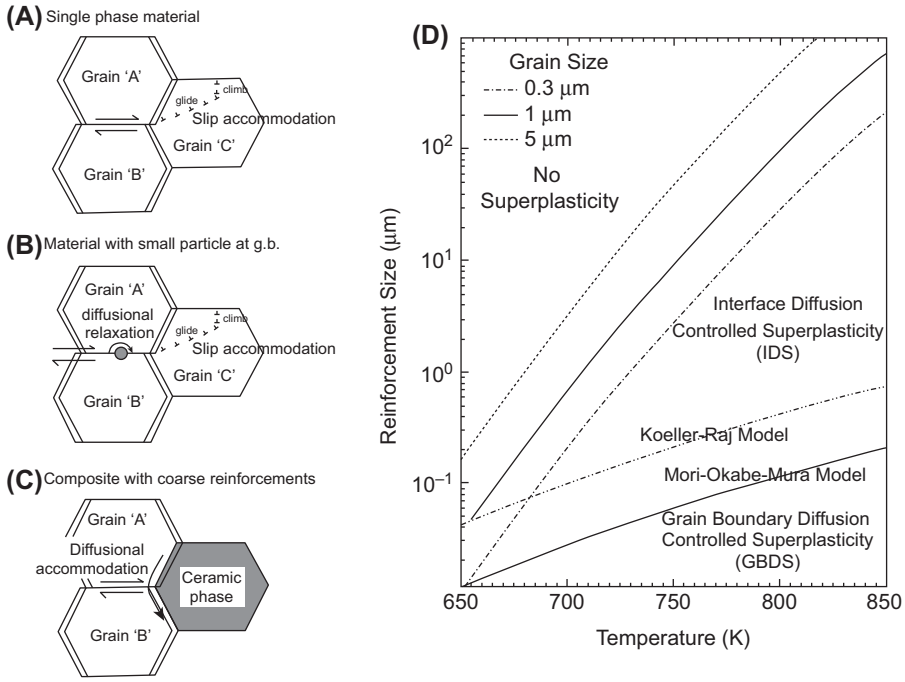


FIGURE 9.4

The effect of second phase particles on the slip accommodation during grain boundary sliding. Note that the ceramic phase in (C) would not allow slip accommodation. (A) Single phase material. (B) Material with small particle at g.b. (C) Composite with coarse reinforcements. (D) A superplastic mechanism map for composites [17].

Based on the fundamentals of microstructure behind superplasticity, Grimes et al. [18] developed a very simple Al-4 wt% Mg-1 wt% Zr alloy that exhibited high strain rate superplasticity in conventionally processed condition. This alloy derived solid solution strengthening from Mg and had a large volume fraction of Al_3Zr particles to create a stable grain structure. Ma et al. [11,13,16] friction stir processed this alloy to evaluate whether the superplastic properties can be enhanced even further. Fig. 9.5 captures the overall enhancement and transition in superplastic mechanisms. Note that the as-rolled alloy exhibits high strain rate superplasticity at 450°C, but the overall elongation is slightly less than 400%. However, after friction stir processing, the elongation at the same strain rate is over 1300%. For SPF of actual components, one does not need this level of plastic deformation. However, at such high levels of elongation, sheet thinning will be uniform and cavitation will be minimal. Fig. 9.6 shows the progression of cavities with strain and enhancement of critical strain with friction stir processing in Al7075 alloy [19]. The critical strain to cavitation information can be used for determining the SPF cycle to avoid any cavitation in the formed part.

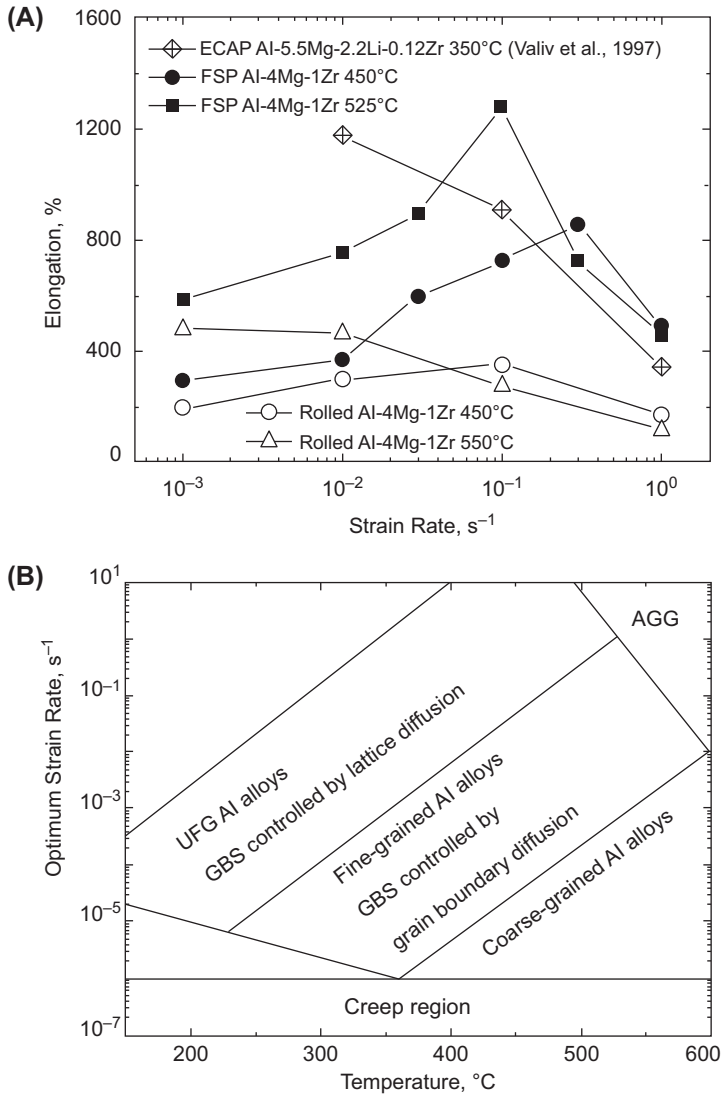


FIGURE 9.5

(A) Variation of elongation with initial strain rate for FSP Al—4Mg—1Zr [11]. (B) A superplastic mechanism map for friction stir processing aluminum alloys [16].

9.1.2.2 Microstructural Design of Titanium Alloys for Superplasticity

The microstructural origin of superplasticity in titanium alloys is very different from that for aluminum alloys. The book on superplasticity by Nieh et al. [20] is an excellent resource for a detailed comparison of various alloy systems. Charit and Mishra [21] have also reviewed superplasticity in various metallic systems and

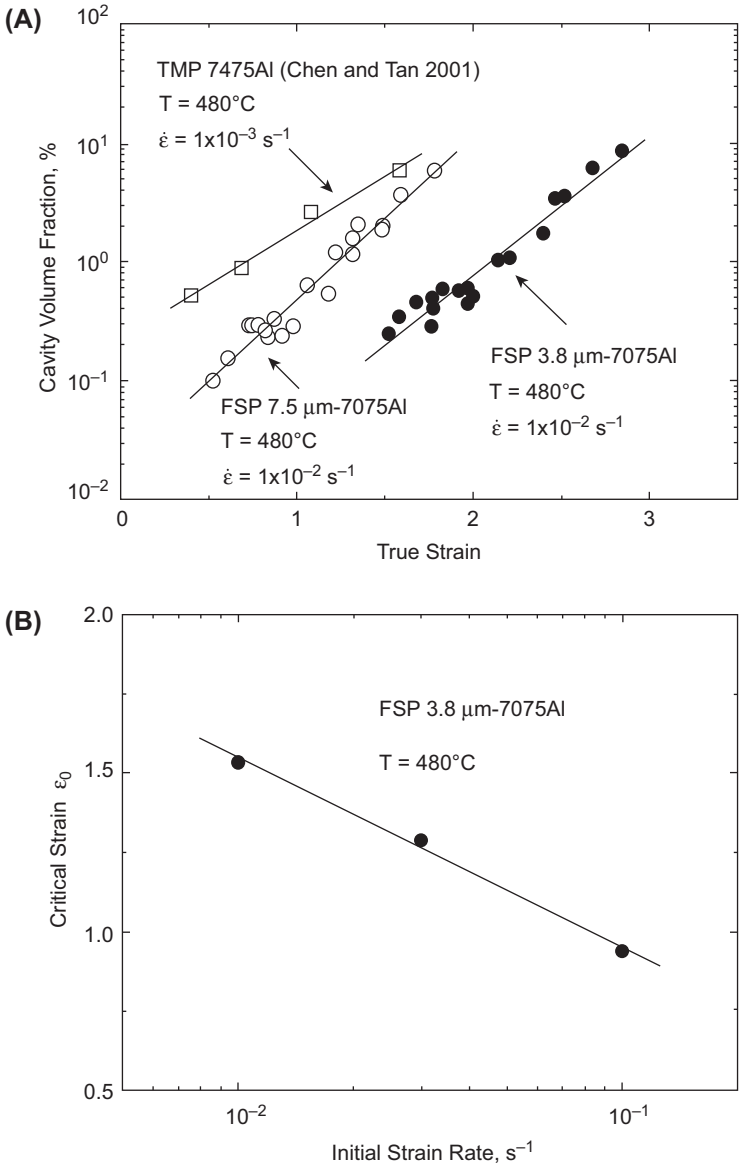


FIGURE 9.6

(A) Variation of cavity volume fraction with true strain for 7.5 and 3.8 μm 7075Al alloys deformed at 480°C and an initial strain rate of $1 \times 10^{-2}\,s^{-1}$ [19]. (B) Variation of critical strain, ε_o, with the initial strain rate for 3.8 μm 7075Al alloy deformed at 480°C [19].

the features important for titanium are very briefly captured below to provide a recommendation for microstructural design. As mentioned in Chapter 5, titanium has a hexagonal closed packed structure (α-phase) at lower temperatures and transforms to β-phase with a body-centered cubic (BCC) structure at temperature of 882°C. Alloying additions stabilize either α or β or a combination of both, depending on the alloy compositions and specific processing treatments. The diffusivity in the β-phase is almost two orders of magnitude faster than that in the α-phase. Most superplastic titanium alloys are dual-phase (α/β) alloys. This two-phase microstructure is critical for microstructural stability at superplastic temperatures. Also, the ratio of phase volume fractions and grain size distributions become important for these dual phase alloys. In general, an alloy with 40–60 vol % of α-phase is expected to have good superplasticity. Issues of dynamic grain growth and phase ratio change with temperature are also important. Take the example of superplastic Ti–6Al–4V alloy (which is an α/β alloy). For Ti–6Al–4 V alloy, the optimum SPF temperatures are in the range of 800–1000°C and the corresponding strain rates vary from 10^{-4} to 10^{-2} s^{-1}. The strain rate sensitivity values have been observed to vary from as high as ~0.85 to ~0.3. Elongations ranging from 450% to 1700% are achieved easily. Fig. 9.7 shows the variation of superplasticity parameters from microcrystalline to nanocrystalline alloys [22]. Note that although the data for the microcrystalline Ti–6Al–4V alloy agree with the grain boundary sliding model, that for submicron and nanocrystalline alloys do not. This has been explained by Mishra et al. [22] on the basis of the difficulty in accommodating grain boundary sliding when the grain size is too fine.

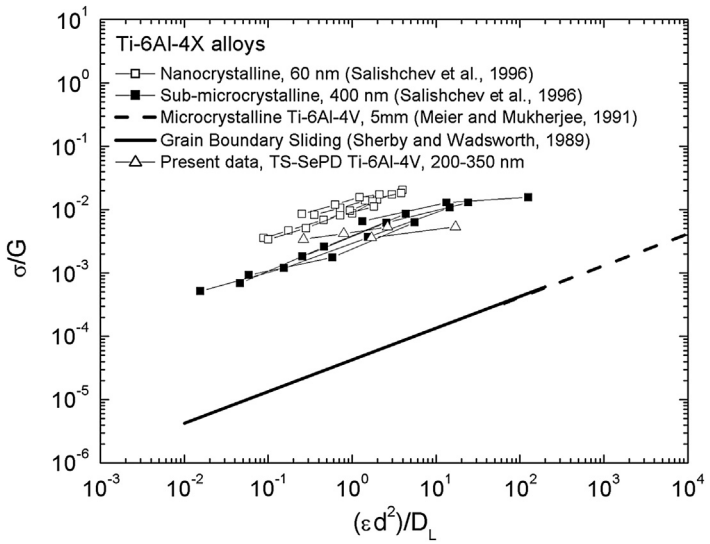


FIGURE 9.7

The variation of normalized stress with grain size and diffusivity compensated strain rate for alloys across microcrystalline to nanocrystalline Ti–6Al–4X alloys (X stands for Mo or V depending on the particular material) [22].

SPF is carried out using gas pressure, typically below 25 MPa. So, higher flow stresses are undesirable from the manufacturing setup point of view even if the kinetics is faster.

A key advantage of SPF of titanium alloy is the ability to use it in conjunction with diffusion bonding to create multisheet stiffened structures. Fig. 9.8A shows simulation results [23] for three-sheet Ti−6Al−4V alloy component formed in the temperature range of 800−900°C. A number of α/β titanium alloys exhibit superplasticity. Alloy Ti−4.5Al−3V−2Mo−2Fe (SP-700) has been specifically developed to lower the superplastic temperature and enhance the forming rates. This alloy exhibits superplasticity at 750°C [24], although as described in Chapter 5, it

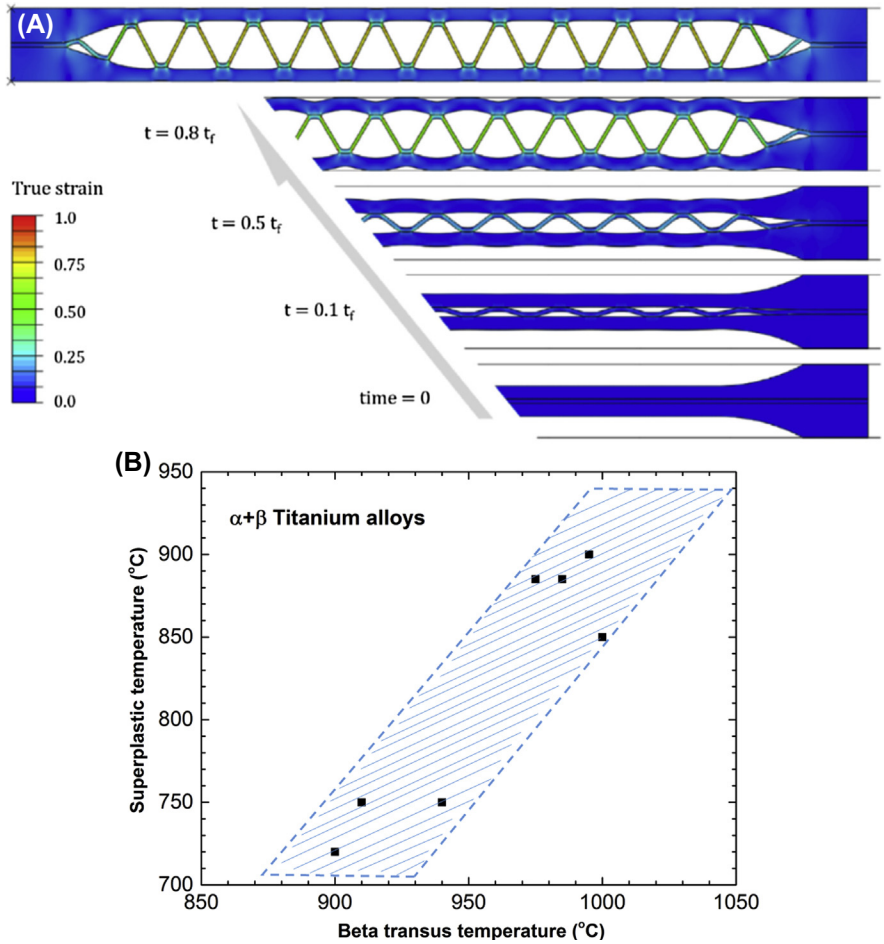


FIGURE 9.8

(A) Simulations of superplastic forming of diffusion-bonded multisheet part [23]. (B) Variation of superplastic temperature with T_β of several titanium alloys.

is no longer in production as fine grained Ti−6Al−4V is available. A general correlation between T_β (beta transus) and superplastic temperature is shown in Fig. 9.8B. T_β is important to define the temperature range where the volume fraction of α and β phases will be in the 40%−60% range. The prior processing to control the grain size and morphology is also important. Because of the presence of two phases, the interfaces can be α/α or α/β or β/β. Each of these will have different kinetics and different requirements for accommodation of strain mismatch. Maximizing the α/β interfaces and minimizing the grain size to near 1 μm will result in the best kinetics and lower SPF forces based on the observations of Mishra et al. [22].

9.2 FRICTION STIR WELDING

From the discussion in Chapters 4, 5, and 7, the need for stronger but lighter metallic materials will continue to be an integral part of the air transportation sector in the future [7]. The specific strength of advanced 7XXX aluminum alloys is comparable to that of Ti−6Al−4V alloy. Cost is as important as the performance, and here too aluminum alloys have significant advantage over titanium alloys. As covered in Chapter 4, at present aerospace industry is the largest consumer of high-strength (>400 MPa) aluminum alloys. Majority of the aluminum alloys used in aerospace industry (2XXX and 7XXX alloys) are joined using riveting (a mechanical fastening technique) because they are nonweldable using conventional welding techniques [25].

In this context, the development of FSW has been truly remarkable as it enables welding of all aluminum alloys including dissimilar alloy combination. FSW is a solid-state welding technique, which was developed at the Welding Institute in 1991 [26]. It is considered to be the most significant development in metal joining in decades. Fig. 9.9 provides a schematic illustration of the process. It shows two work pieces stacked together in butt configuration. A tool, harder/stronger than the work piece material, is first rotated at a predefined rate and made to plunge to a depth necessary for obtaining a defect-free weld. The friction between tool and work piece results in generation of frictional heat and plastic deformation of the

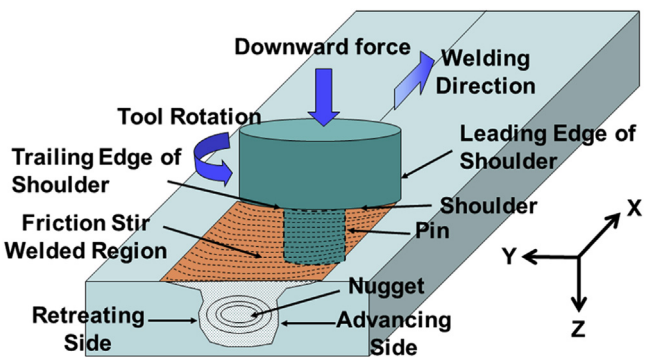


FIGURE 9.9

A schematic drawing of friction stir welding in a butt joint configuration [27].

work piece results in adiabatic heat generation. The rotating and traversing tool moves the softened material from the front of the tool to the back of the tool, which leads to the formation of a joint between both work pieces.

FSW has several advantages over conventional fusion welding technologies. The benefits of FSW range from lower energy consumption to higher joint strength and negligible greenhouse gas emissions. In a recent study, Shrivastava et al. [28] have shown that FSW required overall 40% less energy than that for Gas Metal Arc Welding process. It was also reported by these authors that greenhouse gas emission was 31% lower in FSW.

9.2.1 OVERVIEW OF JOINT EFFICIENCY IN AL ALLOYS ACHIEVED BY FSW

The joint efficiency is defined as the ratio of weld/joint strength to the parent material strength. This comparison can be based on yield strength or the ultimate tensile strength. In general, nonheat-treatable 5XXX Al alloys achieve a joint efficiency greater than 90%, depending on the base metal temper [27]. 5024 Al in H116 temper showed better weld properties compared to the base metal and resulted in 100% joint efficiency with no heat affected zone (HAZ). The main reason for the impressive joint performance was the presence of thermally stable Al_3Sc precipitates, which upon thermal exposure were unaffected and retained their nanometer size and volume fraction. As can be noted from Fig. 9.10, joint efficiency is mostly less than 80% for heat-treatable high-strength Al alloys (data from Refs. [29–42]). The degradation of weld properties in precipitation hardened Al alloys is mainly due to the instability of the strengthening phases in the HAZ upon thermal exposure of ~350°C. For application in airframe structures, it is imperative to maintain the same strength in all zones after welding. The microstructural evolution in various

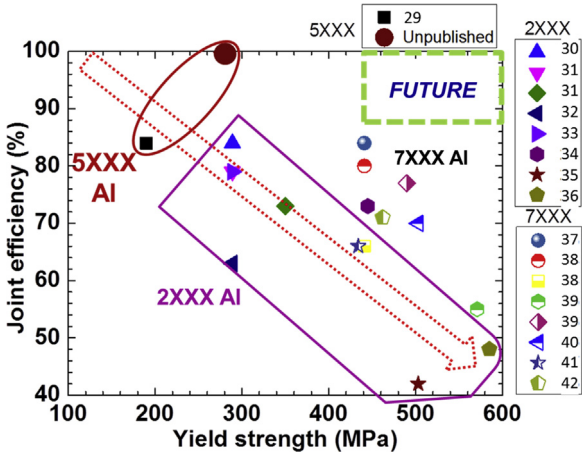


FIGURE 9.10

Joint efficiency versus yield strength for various heat treatable and nonheat treatable Al alloys.

Data from [29–42].

weld zones of high-strength Al alloys has been the subject of detailed study in numerous investigations. Fig. 9.10 clearly shows that as the yield strength of the alloy increases, the joint efficiency decreases. Therefore, the important question is how can near 100% joint efficiency be achieved in high-strength Al alloys without compromising other critical properties like corrosion, damage tolerance, fatigue, etc.? Part of the answer lies in designing alloys that are more suitable for the thermal cycle associated with this process. Additionally, controlling the thermal cycle and developing alternative postweld treatment can also lead to higher joint efficiencies.

9.2.2 CORRELATING THERMAL CYCLE TO THE PHYSICAL MECHANISMS DURING FSW

The primary reason for low joint efficiency in high-strength Al alloy welded structures is the knockdown of strength in the HAZ. Fig. 9.11A shows a schematic of hardness distribution in the transverse cross-section of a friction stir welded plate. It shows a W-shaped profile typically observed in friction stir welded 2XXX and 7XXX aluminum alloys (see Fig. 1.11). Note that although the HAZ is the weakest zone in the welded structure, the hardness of the nugget and thermo-mechanically affected zone (TMAZ) is also lower than that of the base material. A lower hardness

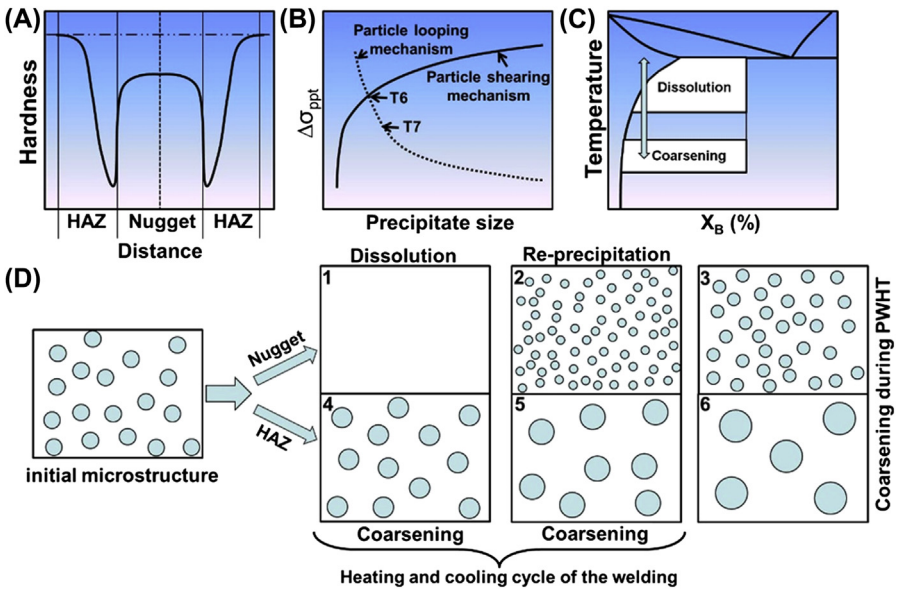


FIGURE 9.11

(A) A schematic hardness profile on the transverse cross-section across various zones of the friction stir welded structure, (B) variation of strength and strengthening mechanisms as a function of the size of the precipitates, (C) a schematic of binary phase diagram to illustrate precipitate coarsening and dissolution during the welding process, and (D) precipitate evolution during heating cycle, cooling cycle, and postweld heat treatment (PWHT) of the alloy in the nugget and heat affected zone (HAZ) of the weld.

in the nugget is generally not a concern, as it is possible to increase the strength of the nugget by proper choice of welding parameters coupled with postweld heat treatment. But, the HAZ has proven to be the Achilles' heel and efforts to maximize the minimum in HAZ have not been satisfactory.

Fig. 9.11B has been included to provide a physical reason behind such a reduction in strength. As discussed in detail in Chapter 4, both 2XXX and 7XXX aluminum alloys derive most of their strength from precipitation strengthening mechanism. Fig. 9.11B shows that for a given volume fraction of precipitates, the contribution from precipitation strengthening is dependent on their size. When precipitates are very small, dislocations shear through the precipitates. But as they grow, a transition point arrives beyond which dislocations glide past precipitates by looping around them. In applications where stress corrosion cracking (SCC) is not an issue, 2XXX and 7XXX alloys are used in T6 temper; Li containing 2XXX alloys in the T8 temper. However, for those applications where SCC is a concern, the T7 temper is used. The alloys in T7 temper have lower strength than T6 temper. Strength–precipitate size combinations for T6 and T7 tempers are labeled in Fig. 9.11B.

Fig. 9.11C shows a schematic binary phase diagram. It highlights the zone of coarsening and dissolution of precipitates during heat treatment. During FSW, a thermal gradient is established along thickness and lateral directions. In certain cases, this gradient may be so steep that it might lead to significant differences in microstructure in different zones of the weld. To illustrate this further, a marker with double arrow has been superimposed on the binary phase diagram in Fig. 9.11C. The nugget of the weld experiences highest temperature and away from it, the peak temperature decreases gradually. It indicates that in certain cases the temperature in the nugget might exceed the solution heat treatment temperature of the alloy and in other zones, for example, in HAZ, it might remain so low that only coarsening of the precipitates takes place. The result of such thermal gradient is a gradient in microstructure from nugget to HAZ. To keep the discussion simple, the effect of plastic strain is ignored (which is important for nugget and TMAZ).

The microstructure of a two-phase aluminum alloy assumed to be in T6 condition is shown schematically in Fig. 9.11D. For the sake of discussion, an idealistic scenario with spherical strengthening precipitates in the aluminum matrix is shown. In reality, the strengthening precipitates typically have a plate shape as seen in the micrographs in Chapter 4. As shown in Fig. 9.11C, in the nugget, temperature might be such that it leads to the complete dissolution of the precipitates. Once temperature falls below the solution heat treatment temperature during cooling cycle, reprecipitation of the strengthening precipitates will take place in the nugget (Fig. 9.11D(2)). If size of the reprecipitated precipitates is such that they are sheared by dislocations, their coarsening during postweld heat treatment (PWHT) (Fig. 9.11D(3)) will result in an increase in the strength of nugget. However, HAZ presents a unique set of challenge. If temperature in HAZ is such that it allows coarsening of the initial microstructure, during heating and cooling cycle of the welding the precipitates will monotonically grow in size (Fig. 9.11D(4,5)). PWHT might cause further coarsening of such precipitates. Fig. 9.11B suggests that there will be a decrease in precipitation strengthening contribution due to coarsening of precipitates in HAZ. Note that bimodal or complex distribution of precipitates has been ignored in this simple

discussion. Again, the real microstructure in various zones can have bimodal or more complex distribution of precipitates. Further complexity comes from grain boundaries and possibility of precipitate free zone (PFZ).

Given the very low coarsening resistance of strengthening precipitates in the commercially available high strength aluminum alloys, the reduction in strength of HAZ is inevitable. For example, Guinier–Preston (GP) zones in 7XXX aluminum dissolve in the range of 160–200°C. GP zones give way to the formation of η' precipitates in this temperature range, which dissolve in the range of 225–250°C. η' precipitates are the main strengthening phase in these alloys (T' phase in high Mg:Zn ratio 7XXX alloys). During FSW, a temperature higher than 250°C is very easily reached causing the transformation of η' into η precipitates, which reduces strengthening contribution. Su et al. [43] have investigated in detail the precipitate evolution in the FS welds of 7050-T651. The base material contained mostly η' $Mg(Zn, Cu, Al)_2$ with small fraction of η, and grain and subgrain boundary precipitates of η $MgZn_2$ and/or $Mg_3Zn_3Al_2$. The PFZ width was around 25 nm. The precipitate evolution observed in different zones is shown in Fig. 9.12. In the nugget region, there was a complete dissolution of the precipitates (nugget temperature >450°C) and the reprecipitation occurred on the dislocations. Grains with high- and low-dislocation density resulted in a high- and low-volume fraction of precipitates, respectively. In TMAZ, the precipitate distribution is heterogeneous with bimodal size distribution consisting of coarse and fine precipitates of 100 and 10 nm size, respectively. There is a clear observation of severe coarsening and dissolution in the TMAZ region due to the exposure to the high temperature (350–400°C). Moreover, the dislocation density is also high. Therefore, the solutes will easily precipitate along the dislocations and subgrain boundaries during the cooling cycle (Fig. 9.12). Both GP zones and η phases were observed in TMAZ and nugget or dynamically recrystallized zone regions. In HAZ, the precipitates, mostly η with some η', were distributed homogeneously in the matrix, coarsened relative to the base material strengthening precipitates. The PFZ width has also increased by a factor of 5. A brief summary of the precipitate evolution is given in Fig. 9.13 [44]. Mishra and Komarasamy [44] reported that irrespective of the base material temper, the precipitate size distribution is generally the same in different weld zones and tempers. Hence, for replacing riveted structures with friction stir welded structures to improve airframe performance, *a new generation of aluminum alloys, which are free from HAZ, needs to be developed*.

9.2.2.1 Compositional Dependence of Joint Efficiency

Two recent short books on FSW of high-strength 7XXX alloys [44] and 2XXX alloys [45] present the overall data and details of microstructural changes. Mishra and Sidhar [45] have highlighted various aspects of Al–Li alloys and dependence of joint efficiency on the alloy chemistry and type of precipitates. The contrast between Al–Mg–Li and Al–Cu–Li alloys is remarkable. In a study of FSW of Al1424 (Al–Mg–Li–Sc) alloy, Sidhar et al. [46] used thermal management with a water-drenched paint roller traversing behind the welding tool and a copper backing plate to facilitate higher cooling rate and lower peak temperature. PWHT of this alloy resulted in 100% joint efficiency. The transmission electron micrographs had established a dense precipitation of fine δ' during PWHT [46]. The presence of Zr in Li

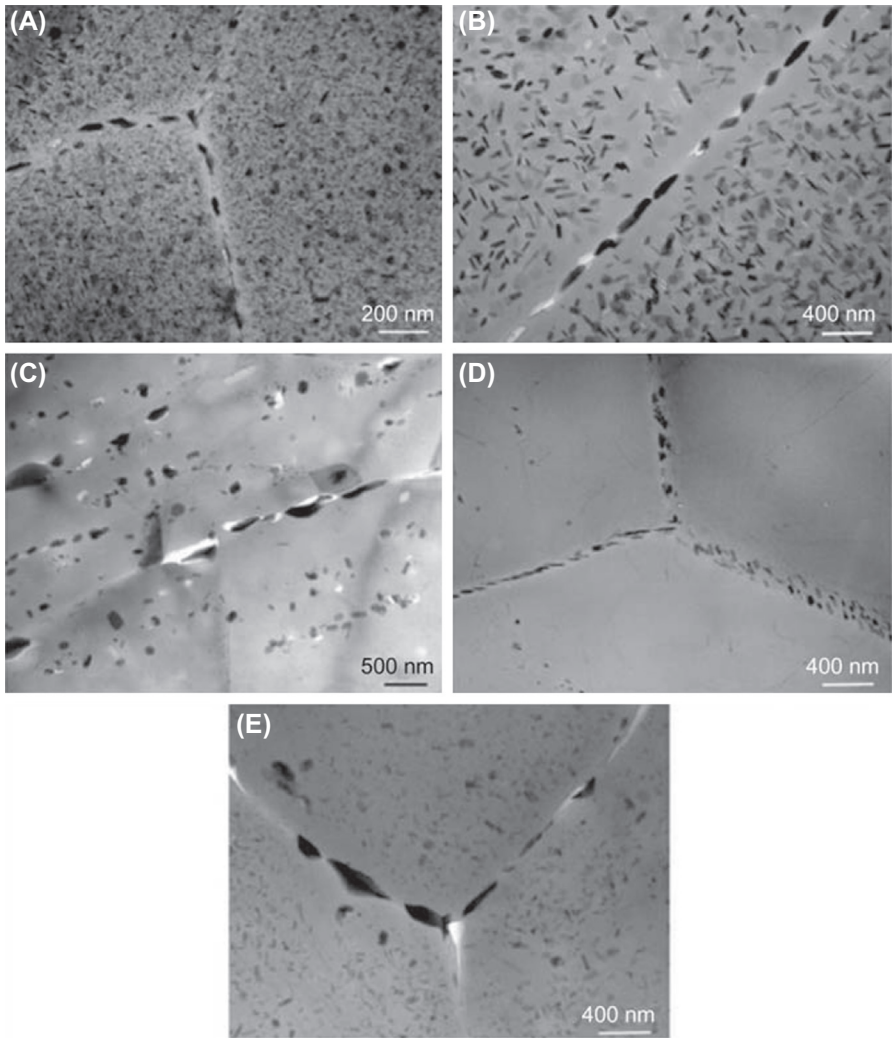


FIGURE 9.12

Precipitate structure in (A) base material, (B) heat affected zone, (C) thermo-mechanically affected zone (TMAZ) I, (D) TMAZ II, and (E) dynamically recrystallized zone [43].

containing alloys can result in hierarchical $L1_2$ precipitates. This is an important concept to utilize in the design of alloys for high-joint efficiency.

Another interesting study with implication for future alloy design involves determining the role of microalloying. Sidhar and Mishra [47] conducted a comparative study on aging kinetics in welds of alloys Al2199 and Al2195 during PWHT using various experimental techniques such as hardness measurements, differential scanning calorimetry, and transmission electron microscopy (TEM). These two alloys

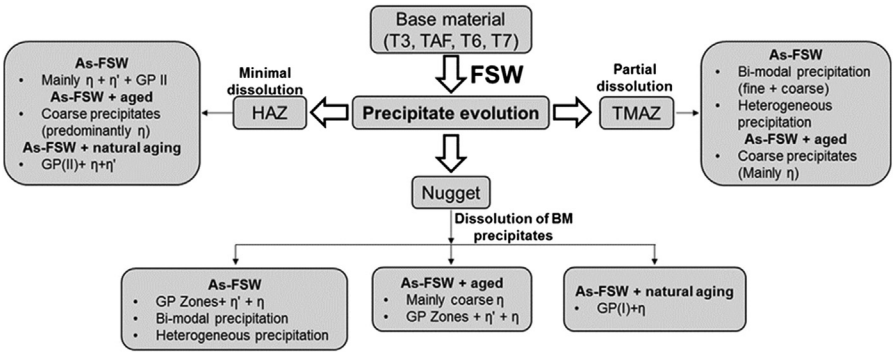


FIGURE 9.13

Overall summary of the precipitate evolution in different zones under various conditions [44].

are considered third generation Al−Cu−Li alloys (discussed in Chapter 4). The hardness profiles for all the samples from welds of alloys Al2195 and Al2199 are shown in Fig. 9.14. Overall, it is clear from the hardness plots that the aging kinetics in weld nugget (WN) and HAZ of Ag-free Al2199 alloy were sluggish compared to that of Ag-containing Al2195 alloy. In WN in the as-welded condition, both the alloys showed a solutionized microstructure in TEM examination. WN of Al2195 alloy, in which T_1 precipitate is the predominant strengthening phase, showed limited strength improvement after aging at 160°C for 16 h. In comparison, WN of Al2199 showed nearly no response to first aging treatment at 160°C for 16 h. Sidhar and Mishra [47] concluded that the absence of Ag and low dislocation density in WN, both of which promote nucleation of T_1 precipitates, were responsible for extremely slow aging response in Al2199 alloy. Whereas, in the case of Al2195

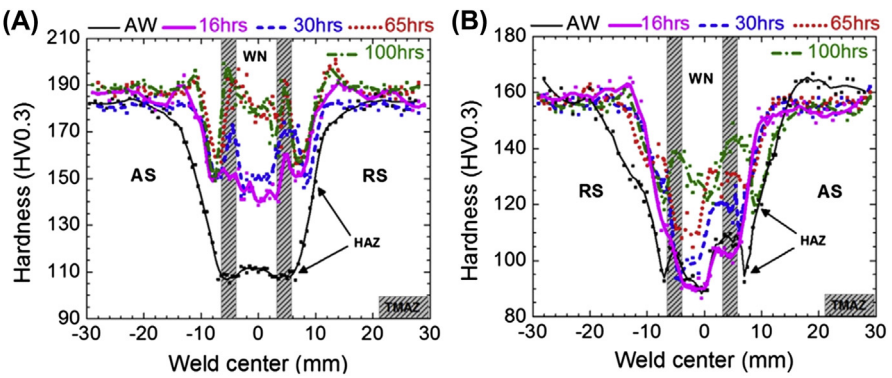


FIGURE 9.14

Hardness plot of welds of (A) Al2195 alloy, (B) Al2199 alloy subjected to various postweld heat treatment [47].

alloy, even though the dislocation density in WN was low, presence of Ag resulted in enhanced aging response compared to Al2199 alloy. Another significant effect of alloy chemistry can be noted by comparing the HAZ of both the alloys. In the TEM analysis, HAZ of both the alloys also showed partial dissolution of T_1 precipitates. However, Al2199 alloy contains a significant volume fraction of low thermal stability δ' precipitates and showed a nearly full dissolution of δ' phase and lesser dissolution of T_1 phase. Such results can be helpful in the selection of microalloying elements that can add to the hierarchical microstructure generation in different zones of welded alloys.

9.2.3 FRAMEWORK FOR DESIGN OF ALUMINUM ALLOYS FOR FSW

To design and develop HAZ free high-strength Al alloys, existing fundamental knowledge applicable to conventional alloy development can be coupled with the process specifics of FSW and seamlessly blended into the computational and experimental tools. Fig. 9.15 shows the steps for achieving the goal of "architecting HAZ free high strength Al alloys for FSW." As displayed in Fig. 9.15, three different steps are needed for such an effort:

1. *Theoretical prediction*: In this approach, existing knowledge from the literature can be compiled in a meaningful manner to select potential microalloying elements for Al 2XXX (including Li containing alloys) and 7XXX alloys that will lead to the absence of HAZ after FSW. The individual principles on the basis of which microalloying additions can be chosen are briefly outlined in Section 9.2.3.1.
2. *Computational prediction*: After the theoretical prediction of promising microalloying additions, the effect of these microalloying elements on the evolution of precipitates in the HAZ of Al 2XXX and 7XXX alloys can be simulated using thermodynamic and kinetic modeling.
3. *Experimental validation*: The final step, of course, in any such alloy design is experimental validation. Overall, such an effort constitutes the Integrated Computational Materials Engineering (ICME) approach, particularly when the required property combinations are coupled with the product performance requirements.

Harnessing the potential of these individual steps holds the key to accelerated development of efficient high-performance Al structures with 100% joint efficiency. Sections 9.2.3.1—9.2.3.1.4 outline the fundamental principles that can guide the overall effort.

9.2.3.1 Theoretical Approach: Design of HAZ Free Al Alloys for FSW

Hierarchical structuring, which is shown in Fig. 9.15, is flexible and strictly applies for single microalloying additions. For single additions, a first level screening of the potential microalloying elements can be done by assessing and exploring across the breadth of the periodic table. In this step, the aim is to filter and arrive at a few

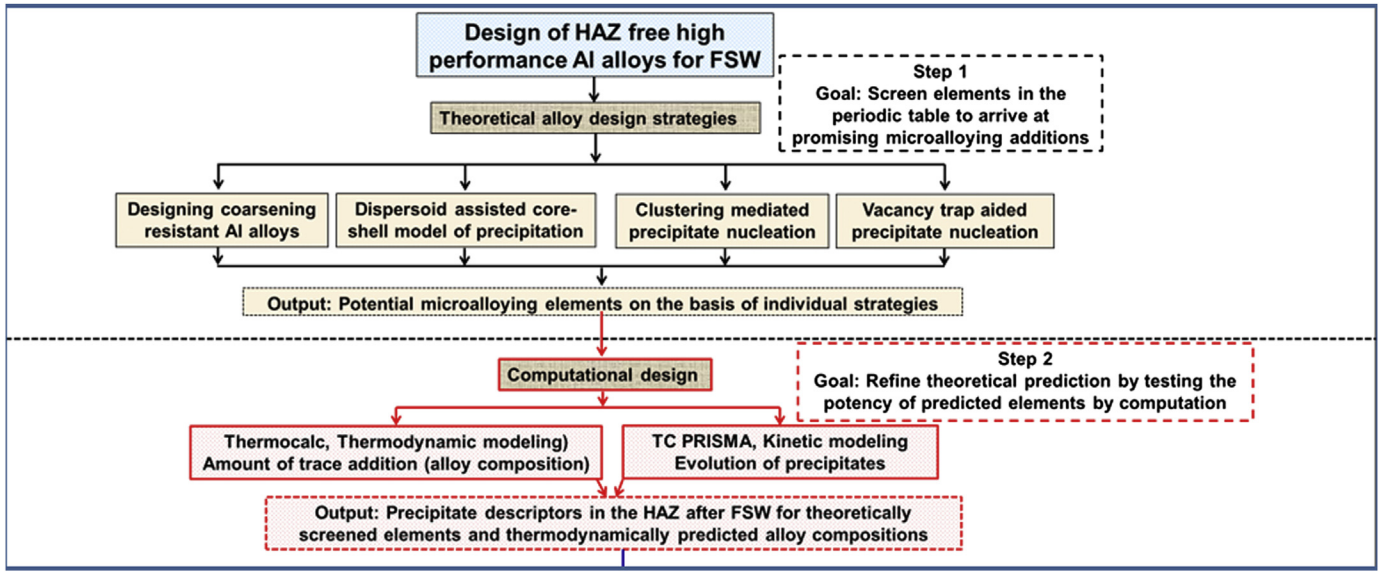


FIGURE 9.15

A multilevel, multidimensional, multitool research procedure is outlined for designing high joint performance heat affected zone free high-strength Al alloys for friction stir welding.

microalloying elements from a vast number that can be fed to the next level computation. In the case of double or multi-microalloying additions, theory and computational methods need to be combined to seek the prospective additions. Theoretical models can be constructed from the knowledge of the evolution of strengthening precipitates influenced by the physical mechanisms that are shown in Fig. 9.11. Also, care has to be taken so that other critical properties are not compromised. For the sake of simplified discussion, these models are explained for improving strength decoupling other important properties.

As detailed in Fig. 9.11, three physical mechanisms occur concurrently within the HAZ. These are coarsening, reprecipitation, and nucleation of the precipitates. The approach outlined here differs from the currently utilized approach in a way that it attempts to affect the physical mechanisms not by thermal cycling alone but by hybridizing it with the alloy chemistry. A general strategy arises from this hybridization to address the knockdown in the HAZ, which is to couple thermal cycle to the nucleation mechanism of the strengthening precipitate in a synergistic manner. Therefore, microalloying elements that trigger nucleation and enhance precipitate number density will be desired. Another approach is to incorporate elements that reduce the tendency of coarsening in these alloys. Obviously, the question is how to identify these elements?

In this section, four specific alloy design strategies are outlined that can serve as a guide for selecting the elements. For the sake of illustration, δ' (Al_3Li) and T_1 (Al_2CuLi) precipitates in an Al−Cu−Mg−Li alloy are taken to explain the design principles. Though further discussion is restricted to Al−Cu−Mg−Li alloys, these strategies are universal in nature and can be applied to other high-strength alloys to screen the microalloying elements. The following theoretical design approaches for architecting HAZ-free alloys are envisioned by integrating two separate concepts: alloy design and FSW process fundamentals under one umbrella.

9.2.3.1.1 Design of Coarsening Resistant High-Strength Al Alloys

Towards the goal of achieving very high joint efficiency welded structures using FSW, development of precipitate coarsening resistant aluminum alloys should be a significant part of alloy design strategy. Although significant progress has been made in the understanding of theoretical framework development concerning the coarsening behavior of precipitates, here the alloy design strategy is briefly discussed using the Lifshitz, Slyozov and Wagner (LSW) and Shiflet, Aaronson and Courtney (SAC) theories [48]. The volumetric diffusion controlled particle coarsening behavior is expressed as,

$$\overline{r}^3 - \overline{r}_o^3 = \left(\frac{8\sigma D C_o \Omega}{9RT}\right) t \tag{9.4}$$

where $\overline{r}$ and $\overline{r}_o$ are average precipitate size at time $t = t$ and $t = 0$. Other parameters σ, D, C_o, Ω, R, and T are interfacial energy, solute diffusivity in the matrix, solute content in the matrix at the beginning of the coarsening, atomic volume of the precipitate, universal gas constant, and temperature, respectively. For interface

controlled precipitate coarsening behavior, the following equation is used to describe the coarsening kinetics,

$$\bar{r}^2 - \bar{r}_o^2 = \left(\frac{64\sigma C_o \Omega k}{81RT}\right)t \tag{9.5}$$

where k is the interphase boundary reaction constant.

For the development of coarsening resistant precipitation strengthened alloy, Eqs. (9.4) and (9.5) provide many important qualitative suggestions. First, a low interfacial energy would be needed to keep coarsening kinetics low. Second, very low diffusivity of such alloying elements is desirable for having low coarsening kinetics.

Although Eqs. (9.4) and (9.5), based on LSW theory, provide invaluable insight in understanding coarsening behavior of precipitates, significant deviation between the theory and experimental results has been found. In this regard, SAC theory has acquired a special stature due to its better agreement with experimental results [47]. In the SAC model, interfacial structure has been given due importance and coarsening of precipitates are described in terms of migration of ledges. The SAC theory suggests that by proper alloying addition it is possible to control ledge migration. Microalloying additions may be effective in inhibiting the migration of ledges thereby improving the coarsening resistance of precipitates. In this context, it is worth mentioning the coarsening resistance of Ω precipitates in the Al−Cu−Mg−Ag system. Mg and Ag together promote the formation of Ω precipitates, which is not present in Al−Cu system, as already discussed in Chapter 4. The addition of Ag to Al−Cu−Mg system not only increases the density of Ω precipitates but also improves its coarsening resistance [49−51]. Hence, synergy and redistribution of Ag and Mg become the rate controlling step, which can be used as a microalloying strategy.

9.2.3.1.2 Dispersoid Assisted Core−Shell Model of Precipitation

The second strategy for screening microalloying elements is based on the ability to utilize the potential of dispersoids in nucleating strengthening precipitates. Unlike the first approach that was based on coarsening, this strategy rests on utilizing reprecipitation in the HAZ. The central principle of this strategy is best illustrated by considering the work of Gayle and Vander Sande [52]. They first observed that $L1_2$ δ' precipitate forms as a shell on the Al_3Zr core in an Al−Li−Zr alloy. This led to a series of efforts to understand the formation mechanism of the observed composite core−shell structure in Zr and Sc containing Al−Li alloys. Impressively, heat treatment schemes were developed to exploit this unique ability of enveloping Al_3Zr core with Al_3Li shell. Radmilovic et al. [53] had demonstrated a way for producing complex monodisperse Al_3(LiScZr) composite core−shell structure in an Al−Li−Sc−Zr alloy by devising a suitable heat treatment route that merits discussion. A two-step aging treatment was done to facilitate the formation of the core−shell structure. The first step was to age at a higher temperature (450°C, 4 h) to form Al_3Sc core (dispersoid) followed by low temperature second step aging (190°C,

19 h) to form the Al_3Li shell. When viewed closely, these heat treatment steps match with the thermal conditions prevalent during FSW.

Considering this observation from the perspective of FSW, the study by Radmilovic et al. [53] coupled with the core–shell composite structure provides the opportunity for altering the nucleation rate of strengthening δ' precipitates. To illustrate this point, consider a binary Al–0.05 wt% Zr alloy in which the solvus of Al_3Zr is 475°C [54]. During FSW, although the stir zone peak temperature is usually ≥450°C in Al–Cu–Li–Zr alloys [55], the hardness minimum is observed in the HAZ where temperature reaches between 325 and 375°C. Clearly, Al_3Zr dispersoids are stable at the critical temperature reached in HAZ during FSW. Therefore, Sc or Zr containing dispersoids can act as a template for δ' reprecipitation during the cooling cycle or postweld aging. Fig. 9.16 shows a schematic highlighting the principle of dispersoid assisted nucleation. The screening criterion for the microalloying elements are (1) the elements should form a precipitate with an $L1_2$ structure that should be stable at high temperature and (2) the dispersoid forming element should have negative enthalpy of mixing ($\Delta H < 0$) with the strengthening precipitate forming element.

9.2.3.1.3 Clustering-Mediated Precipitate Nucleation

The fundamental principle underlining this strategy is to use precipitate clusters in nucleating strengthening phases. Previously, such a strategy has been successfully applied for the development of conventional Al–Cu alloys where the addition of Sn, In, and Cd increased the number density of precipitates [56]. Rethinking in terms

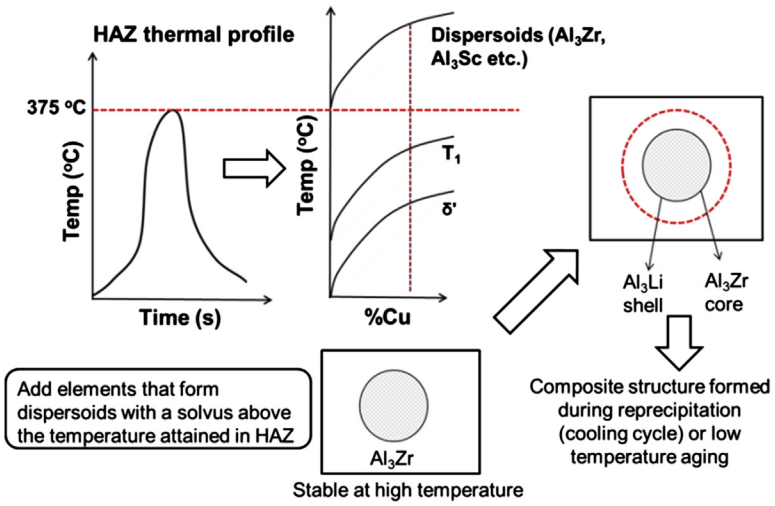


FIGURE 9.16

Schematic showing the principle for dispersoid (Al_3Zr) assisted nucleation δ' in an Al–Cu–Mg–Li alloy in the heat affected zone of a friction stir weld.

of FSW, the selection of elements that retain the clusters during the HAZ thermal cycle and act as sites for nucleation of strengthening precipitates will be highly desired. Mendis et al. [57] have proposed a qualitative thermo-kinetic criterion for choosing the microalloying elements (X). Adapting this approach with a slight modification for FSW, the following steps can be used to screen the microalloying elements:

1. Select elements that have a positive enthalpy of mixing ($\Delta H > 0$) with the Al matrix phase and negative enthalpy of mixing with the strengthening precipitate ($\Delta H < 0$).
2. Narrow the selected elements to those exhibiting higher diffusivity than the element forming the strengthening precipitate to form clusters during cooling cycle.

The hypothesis is that low-temperature aging after FSW should heterogeneously nucleate the strengthening precipitate on the pre-precipitate clusters and increase the nucleation density, thereby alleviating the reduction in joint performance.

9.2.3.1.4 Vacancy Trap Aided Precipitate Nucleation

Studies in the past have stressed on the nucleation of θ' and Ω precipitates in an Al−Cu and Al−Cu−Mg alloy assisted by Mg vacancy and Mg−Ag vacancy coclusters clearly indicating the beneficial effect of solute−vacancy complexes [58]. The concept in this final strategy is to utilize the large number of vacancies that are generated at high temperatures and retained depending on the cooling rate during FSW. Utilizing this model, the microalloying element can be selected on the basis of (1) trace element-vacancy (X-□, where □ represents vacancy) binding energy, (2) diffusivity, (3) size, and (4) enthalpy of mixing.

Further insight into this strategy is provided by two conceptual maps that are designed on the basis of the affinity of the strengthening alloying elements toward the vacancy. Consider the nucleation of T_1 precipitate in the presence of a vacancy and microalloying element. Two possible approaches are shown to increase the number density of T_1 precipitate. Fig. 9.17A shows the first approach where the X-□ > (Li-□ and Cu-□) binding energy. In this approach, the microalloying element is bound to the vacancy and has a higher interaction energy ($\Delta H < 0$) with the strengthening elements (Li and Cu). One kinetic requirement for locking of the vacancies by X is that the diffusivity of X should be faster than that of the strengthening alloying elements. In this case, X-□ clusters will form, enhancing the nucleation density by drawing in the strengthening alloying elements toward them. Another situation can arise and is more pertinent for the T_1 precipitate where binding energy of the strengthening element is greater than that of the trace element with the vacancy (Li-□ > X-□). Fig. 9.17B shows this option. During the FSW cooling cycle, Li will bind with the vacancy and draw X toward them forming □-Li-X clusters assisting T_1 precipitation and increasing their number density. Such maps can help in narrowing down the selection of microalloying elements.

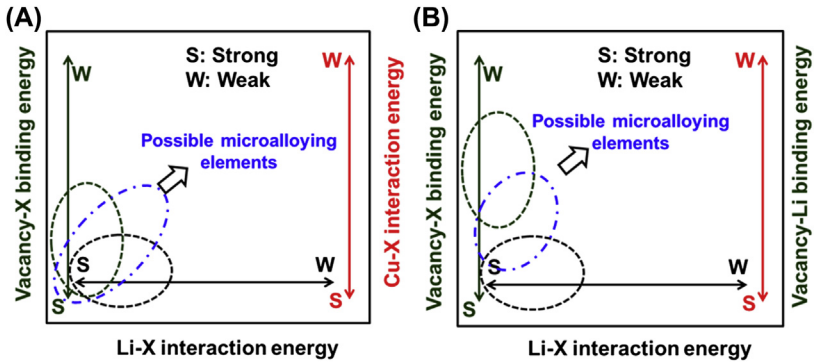


FIGURE 9.17

Schematic conceptual maps for designing alloys where (A) X-□ > (Li-□ and Cu-□) and (B) Li-□ > X-□. Note that the maps are illustrated for T_1 precipitation. In general, such maps can be plotted for several strengthening precipitate phases for different Al alloys and are universal in nature.

These four design strategies offer a holistic picture and describe the rationale for selecting prospective microalloying elements to architect HAZ-free high-performance alloys. The preference of any one strategy over the other or decision on integrating two of the above described strategies will depend on the precipitate under consideration.

9.3 ADDITIVE MANUFACTURING

AM, also referred to as three-dimensional printing, is considered "an enabling technology." The level of design flexibility it provides is unprecedented compared to other manufacturing techniques. The field has evolved significantly from early days when it was referred to as rapid prototyping. In their current forms, AM technologies are full production techniques. Since its origin, over the past 30 years, AM has started to facilitate a paradigm shift from the traditional manufacturing methods by reinventing the basics of product fabrication. The key factor driving the interest of the aerospace industries toward AM is the ability to produce light-weight structures. The aforementioned statement can be appreciated by considering the following estimate where reducing 1 pound on a fleet of 600 aircrafts can save 11,000 gallons of fuel [59]. Although, transportation industries contribute to the lion's share of AM revenue, when compared with the overall world market volume of $706 billion of aerospace industries, the current AM market share from these industries is marginal [60]. One key reason for the limited role of AM in these industries is associated with the inability to achieve structurally efficient metallic parts [61].

A recent article by Palanivel et al. [61] provided a comprehensive summary on the temporal evolution of additive technologies with their advantages and key issues. As

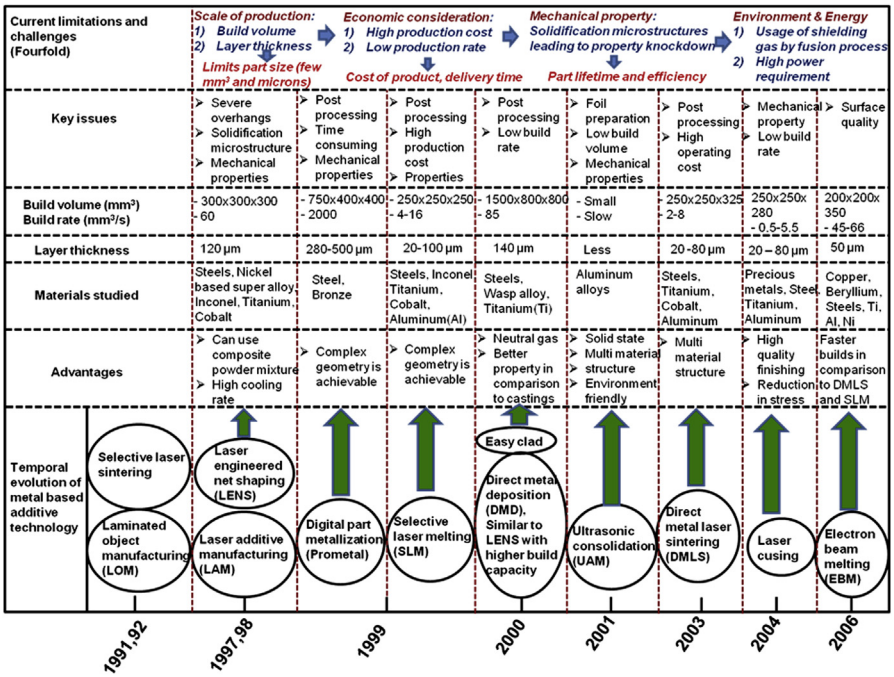


FIGURE 9.18

Temporal evolution of metal-based additive technologies highlighting structural performance as a grand challenge [61].

shown in Fig. 9.18, structural performance was identified as one of the four grand challenges faced by the fusion based additive techniques today. Why is structural performance a key challenge for fusion based techniques? The answer lies within the basic principle by which the components are fabricated. In fusion-based additive techniques, the conceptual basis for fabricating a build is melting that results in solidification microstructures. This process is similar to microcasting (or microwelding) where directional anisotropy becomes a major concern with the build direction exhibiting different properties than transverse direction. At a smaller length scale, such properties are an outcome of pronounced inhomogeneity in the microstructure. Also, another major drawback is that the knockdown in the final property is significant in comparison to the base material. Fig. 9.19A shows the knockdown in the build property for Ti, and Ni-based alloys fabricated by a few fusion-based AM techniques [62]. Fig. 9.19B highlights the severity of microstructural inhomogeneity in a Ti−6Al−4V alloy built by laser deposition and shows layer wise banding [63]. The spatial distribution of properties is further highlighted in Fig. 9.20 from a study of Ti−6Al−4V impeller using mini-tensile specimens [64]. Palanivel et al. [64] established the connection between site-specific microstructure and the corresponding strength and ductility values. The variation in microstructure comes from change in cooling rate and heat flow direction.

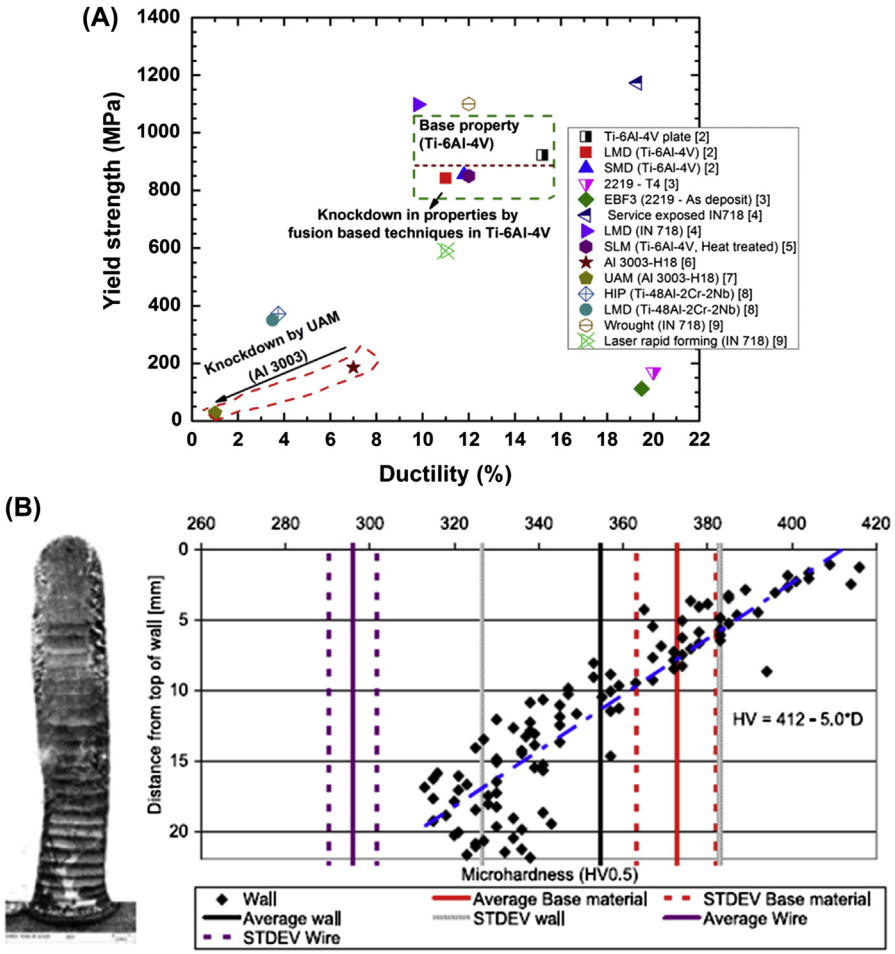


FIGURE 9.19

(A) Illustration of lower build properties achieved by fusion-based and solid-state ultrasonic additive manufacturing (UAM) technique when compared with base material [62] and, (B) spatially dependent hardness profile of laser deposited Ti–6Al–4V build [63]. A variation of 100 HV is seen over a spatial scale of 20 mm!

9.3.1 CURRENT ALLOYS USED FOR POWDER-BED AM PROCESSES

Just to give a broader perspective to facilitate discussions while not endorsing any system, alloys available from two commercial laser powder-bed AM systems producers, EOS and Concept Laser, are listed below. The alloys represent, aluminum, titanium, nickel including superalloys, steels, and cobalt alloys. The remainder of the discussion will consider only aluminum and titanium alloys, which are lightweight alloys and have the most potential for application in aircraft structures.

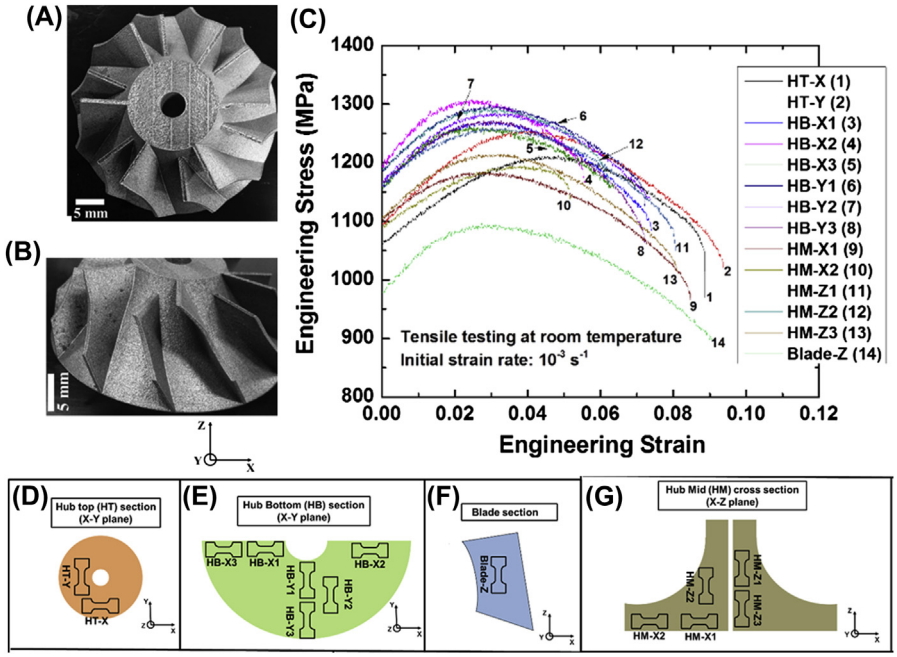


FIGURE 9.20

(A) Top view and (B) side view of Ti–6Al–4V impeller built by laser additive manufacturing (LAM). The vertical/build direction (Z) is perpendicular to the laser scanning direction (X–Y). (C) Engineering stress–strain curves of samples extracted from 14 different regions in the component. (D–G) Schematic illustration of the location and direction from which the samples were extracted for mini-tensile testing from the Ti–6Al–4V impeller [64].

For aluminum alloys, the most noteworthy aspect is that Al–10 wt% Si–Mg alloy is the primary alloy available for laser powder-bed AM machines. In fact, most of the research results are related to this alloy. The primary attribute of this alloy is its suitability for AM because of hot tear resistance. Chapter 4 covered aerospace aluminum alloys extensively and Al–Si alloys are not used in primary airframe structures. Castings are used to a limited extent for interior parts, which have low structural requirements. Al–10 wt% Si alloy is good for casting applications and the metal AM companies provide commercial alloys that can respond well to the microcasting process (it is also viewed as a microwelding process, which is essentially the same as for the fusion technique). Similarly, the titanium alloys are limited to commercially pure titanium and Ti–6Al–4V. As noted in Chapter 5, the rich variety of titanium alloys used in aircraft structure is based on the combination of properties that can be obtained. Obviously that range is limited by having only two compositions. The reviews by Frazier [65] and Sames et al. [66] are excellent foundation for this section. The summary statement from Sames et al. [66] is reproduced here as segue to the next section on alloy design: “New materials development is research intensive but necessary to increase the number of uses for metal AM.

New alloys will have uses for new industries and new parts. AM-specific alloys may be able to increase performance beyond what is capable with traditional wrought or cast alloys. The ability to manipulate grain and phase structures offers the potential for microstructural engineering and will likely see continued efforts."

Alloy powders available from EOS Company (the alloy application description is from the company Website).

EOS Aluminum AlSi10Mg—Light Metal for Motorsports and Aerospace Interior Applications
EOS Aluminum AlSi10Mg/200°C—Light Metal for Motorsports and Aerospace Interior Applications
EOS CobaltChrome MP1—CoCrMo Super Alloy for High-Temperature Engineering and Biomedical Applications
EOS CobaltChrome SP2—CE-Certified CoCrMo Super Alloy for Dental Applications
EOS MaragingSteel MS1—High-Performance Steel for Tooling and Mechanical Engineering
EOS NickelAlloy HX—Nickel-Alloy for Aerospace and Industry
EOS NickelAlloy IN625—Nickel-Chromium Alloy for Aerospace, Motorsports and Industry
EOS NickelAlloy IN718—Nickel Alloy for Aerospace and Industry
EOS StainlessSteel 17-4PH—Highly Abrasion Resistant Stainless Steel for Medical
EOS StainlessSteel CX—Corrosion Resistant Stainless Steel for Tooling
EOS StainlessSteel GP1—Stainless Steel for Mechanical Engineering and Medical
EOS StainlessSteel PH1—Hardenable Stainless Steel for Mechanical Engineering and Medical Technology
EOS StainlessSteel 316L—Corrosion-Resistant Stainless Steel Alloy for Medical, Lifestyle and Aerospace
EOS Titanium Ti64—Ti6Al4V Light Metal for Aerospace, Motorsports and Biomedical Applications
EOS Titanium Ti64ELI—Light Metal Alloy for Medical and Aerospace
EOS Titanium TiCP grade 2

Alloy powders available from Concept Laser Company

Stainless steel—X2CrNiMo 17-12-2, 316L/SUS 316L
Aluminum alloys—AlSi12(a), AlSi10Mg
Titanium alloys—TiAl6V4 ELI, Commercially Pure Titanium
Hot-work steel
Copper alloy—Bronze
Stainless hot-work steel—Stainless hot-work steel, precipitation hardening stainless steel, precipitation hardening stainless steel powder (17-4PH)
Nickel-based alloys—Inconel 718, Inconel 625
CoCrW-alloy

9.3.2 DESIGN OF ALUMINUM AND TITANIUM ALLOYS FOR HIGHER PERFORMANCE IN ADDITIVELY MANUFACTURED COMPONENTS

As mentioned in the last subsection, the best way to realize the full potential of AM and design opportunity is to develop specific alloys that embrace the attributes of the process. The challenges of qualification of materials and processes have to be accepted for accelerated progress. The use of ICME methodology to rapidly design Al and Ti alloys for enabling game-changing applications coupled with a predictive tool for guiding experiments can transform the AM field and reiterate the vision articulated in the Materials Genome Initiative (MGI); "to discover, manufacture, and deploy advanced materials twice as fast, at a fraction of the cost."

9.3.2.1 Build Variability and Inconsistency: Probabilistic Aspect

The details of laser powder-bed AM is beyond the scope of this section, but a top level discussion is warranted for understanding the need for new alloys. The inherent build variability comes from the probabilistic nature of the process. To take a simple sequence, a powder layer is spread, the laser rasters over the powder layer, the melt pool is formed, solidification proceeds epitaxially, the microstructure evolves during the multipass process and includes any phase transformation and precipitation. The packing density during powder spreading will vary based on the powder size distribution range and introduces the first probabilistic event. Then laser hits the powder particles and the details of laser−particle interactions dictate particle expulsion, particle melting, and splatter. This constitutes the second level of probability and the size of melt pool will vary along the track. The next step is solidification and this again has embedded probability because of the epitaxial nature and variation during multipass. As subsequent layers are added, previous layers go through additional thermal cycle and resultant phase transformation. From this it is clear that the final microstructural variation can be significant. The mechanical property variation derives from the microstructural distribution. Given this obvious narrative, are the optimization of the process parameters, powder development, and other process-related variables in combination with designing ways of powder addition adequate to reduce variability? Are the alloys being used capable of producing consistent and invariable microstructures along the build direction? Are the alloys capable of achieving exceptional mechanical properties in as-built AM parts? For example, it has been documented that immaterial of the precise control on thermal profile, it is impossible to avoid variation in Ti−6Al−4V alloy due to unintended phase transformations and morphological changes in the two phase of $\alpha+\beta$ field (see Ref. [64] for examples of microstructural variations).

Similarly, in the case of Al alloys, only Al−10Si−Mg has received attention mainly because of its good casting properties and hot tear resistance [67]. Typical values of yield strength in these alloys range from 220 to 275 MPa in as-built condition [68]. It can be noted that these strength values are far inferior to that high strength Al alloys (2XXX, 7XXX, and Al−Cu−Mg−Li) that have a yield strength

between 400 and 700 MPa. However, these high-strength Al alloys are considered nonweldable due to hot cracking issues and are unsuitable for AM. Furthermore, there is limited incentive for using 3XXX, 5XXX, and 6XXX series alloys, which have properties similar to Al−10Si−Mg alloy. Clearly, an "alloy chemistry" approach can be pursued to design suitable Ti and Al alloy compositions for powder-bed AM processes to mitigate the variability and enhance mechanical properties.

9.3.2.2 Framework for ICME Alloy Design for Powder-Based AM

To develop high-performance Ti and Al alloys, existing fundamentals about conventional alloy development can be coupled with the process specifics of powder-based AM (PBAM) and seamlessly blended into the computational and experimental tools. Because the physical metallurgy of Ti and Al alloys (as described in detail in Chapters 4 and 5) vastly differ from each other, the alloy design approach for them is discussed individually. The first part will focus on the design strategy for developing Ti alloys and the second part will detail the approach for developing AM appropriate Al alloy compositions. Fig. 9.21 provides the overview of ICME methodology that will be employed to design Ti and Al alloy chemistries for PBAM processes.

9.3.2.2.1 Theoretical Strategy for Designing High-Performance Ti Alloys Intended Toward PBAM Processes

As outlined in Chapter 5, the basic classification of Ti alloys are (1) α, (2) near-α, (3) α+ β, (4) near-β, and (5) β alloys. Section 5.2.1 gave the net effect of alloying elements expressed in terms of Al equivalent (Al_{eq}) and Mo equivalent (Mo_{eq}), which serve as a measure of α and β phase stability, respectively. The selection of Ti alloys for PBAM will be driven by three key aspects:

- Al_{eq} and Mo_{eq} linked to β stability index
- T_β, Beta transus temperature
- Time−temperature curves outlining the critical cooling rate for β to α+β transformation

Fig. 9.22A shows T_β as a function of Al_{eq} and Mo_{eq} for several Ti alloys. It can be noted that the currently used Ti−6Al−4V falls under the category of α/β alloys with higher Al_{eq}. This observation is supported from the β stability index plotted in Fig. 9.22B where, T_β for Ti−6Al−4V is close to 1000°C. Clearly, in such an alloy, two-phase microstructures will dominate with the morphology of the transformed microstructure playing the primary role in determining the final properties. In this alloy, the reason for variation in microstructure during PBAM is related to the multiple thermal cycles with each layer experiencing thermal fluctuations within the two-phase field for a substantial portion of time resulting in multiple variants and dissimilar scales and morphologies of α laths across the build. Hence, the first approach for Ti alloy design is to search for alloys that have relatively stable microstructures. Fig. 9.22A and B provide for initial screening for the selection of alloys that will fit into the aforementioned objective. To narrow down the search, the focus

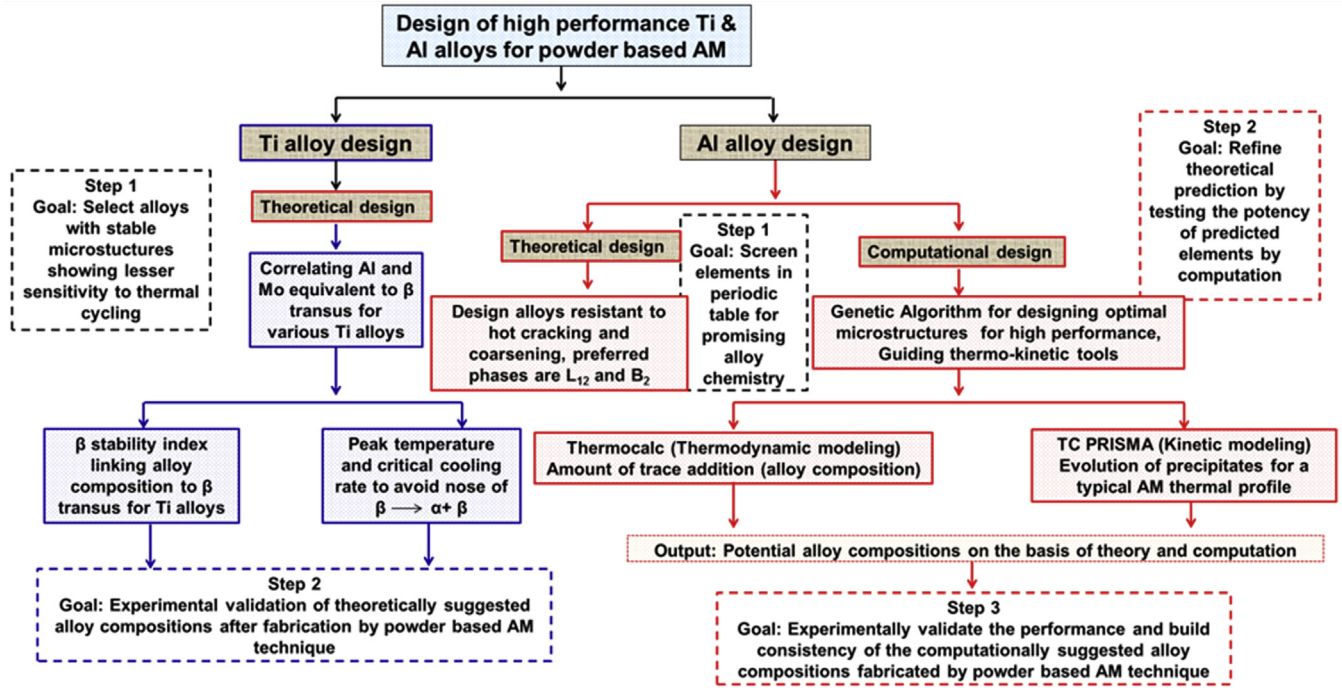


FIGURE 9.21

Overview of the Integrated Computational Materials Engineering approach to rapidly design high performance Ti and Al alloys for powder-based additive manufacturing (AM) technologies. This approach is outlined for gaining momentum in materials innovation for AM and will aid in their accelerated deployment.

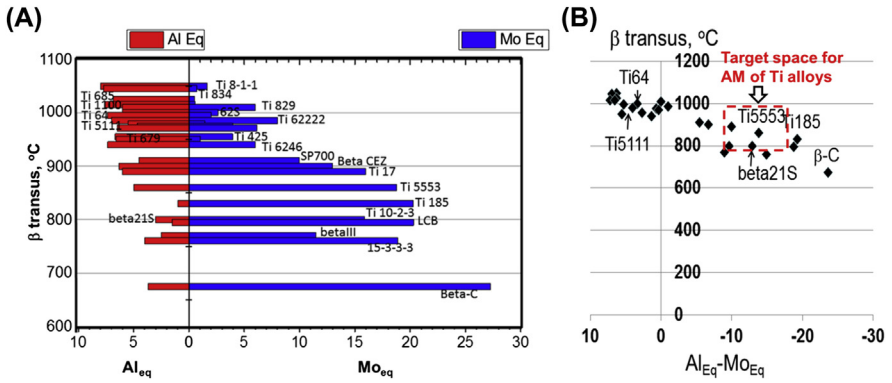


FIGURE 9.22

(A) Plot showing Al_{eq} and Mo_{eq} values for several titanium alloys and its relationship with T_β. (B) A beta stability map showing T_β for all the alloys shown in (A) [69]. For addressing the issues raised in this section, β alloys with a lower T_β can be selected for PBAM. Potential alloy design space for additive manufacturing is marked in (B).

should be on alloys with higher Mo_{eq} or in other words with lower T_β, which is typically the case for near-β or β alloys. The basis for choosing β alloys is the ability to enter a single-phase regime with greater ease in successive thermal passes. Such a case will reduce the chances of coarsening of α precipitates and lead to a greater microstructural tolerance with minimal variation in properties.

The selection of β alloys for PBAM is further substantiated by Fig. 9.23. In this figure, the key characteristic is the cooling rate required for avoiding the nose for β to α+β transformation in alloys with higher Mo_{eq}. On a qualitative note, very high cooling rates are experienced in the PBAM build at initial stages of fabrication. These cooling rates will be sufficient to retain the β phase due to low T_β in β alloys. Based on the martensitic start temperature, certain compositions will be susceptible to martensitic transformation. As more layers are deposited, the bottom layers will experience peak temperatures below T_β allowing for precipitation of α. For alloys with martensitic transformation, the repeated cycling would impact the annealing of martensite. At the same time, the middle and top layers will have a slower cooling rate and might undergo β to α+β transformation as the build cools down. The only difference in between these layers is in the mode of formation of α+β microstructure. Due to the fundamentals stated earlier, exploration of β alloys certainly appears promising for PBAM process.

9.3.2.2.2 Theoretical Strategy for Designing High-Performance Al Alloys Intended Toward PBAM Processes

To design Al alloys, the first and foremost criterion is to avoid elements that exhibit hot cracking tendency. Therefore, the possibility of using high-strength Al2XXX and 7XXX alloys is eliminated. Furthermore, coarsening can be a serious issue in prior layers during overlapping thermal passes in Al alloys. Hence, the strategy

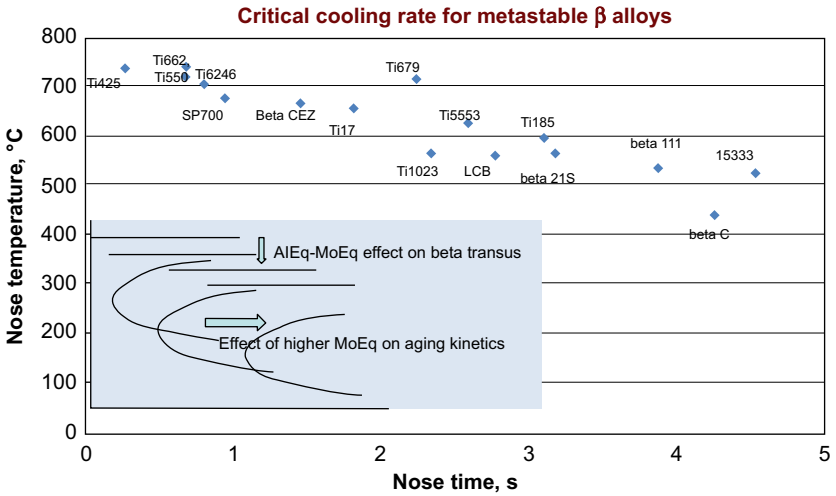


FIGURE 9.23

Variation of nose temperature and time for various titanium alloys. Note that near-α alloys like Ti–6Al–4V are not on this plot as the nose time calculation leads to negative values [69].

for developing Al alloys directed toward PBAM needs to focus on selecting elements that form phases resistant to coarsening.

Based on the approaches for aluminum alloys with stable phases, the literature suggests two such phases whose potential can be utilized for PBAM. These are (1) face centered cubic (FCC) like $L1_2$, and (2) Al_3X intermetallic phases. To provide coarsening resistance, addition of high temperature elements forming these phases is desired. Few example systems that can be focused on are Al–Mg–Sc–Zr and Al–Mg–Y–X termed as $L1_2$ formers and Al–Ni–X type systems with stable Al_3X intermetallic phases, with X being element like Cu that can form hierarchical precipitates. Because the FCC type $L1_2$ phase is more ductile, many such phases should be theoretically and thermodynamically evaluated for their applicability to AM. Table 9.1 outlines few probable $L1_2$ phases that can be considered for PBAM [70]. Among these Al_3Sc is very encouraging but an issue is the cost of Sc, which is $1400 for 100 g. Therefore, design of quaternary alloys with elements like Zr that can replace a portion of Sc in the precipitate to lower cost. Sc additions to Al–Mg alloys were also discussed for new alloy design in Chapter 4. Also, the addition of elements like Zn and Cu should be done with care as they can lead to hot shortness.

As a first step, theoretical screening of alloying elements can be done across the periodic table to further refine the search space leading to a few potential alloying elements. During the theoretical scan, expensive metals and elements with severe hot cracking tendency should be excluded. By imposing a set of simple boundary conditions into the theoretical approach, a vast majority of alloying elements can

Table 9.1 A Few $L1_2$ and Other Potential Al_3X Phases in Al Base Alloys [70,71]

$L1_2$ phases, (A_3B structure), FCC type	Al_3Sc, Al_2Ti_2, Al_2Zr_2, Al_2ZnZr, Al_2TiZn, Al_3Zr, Al_2ScZn, Al_2NbTi, Al_2CuTi, Al_2CuZr
Other coarsening resistant Al_3X intermetallic phases	Al_3Ni (DO_{20}), Al_3V (DO_{22})

be eliminated. Despite its simplicity, it lays a good initial foundation for accelerating materials innovation by subsequent computational approaches.

Fig. 9.24 shows a list of possible alloying elements to design Ti and Al alloys for the PBAM processes and are color coded in the periodic table. Further discussion on computational alloy design has been restricted to Al alloys primarily because a similar approach can be used for Ti alloys.

9.3.2.2.2.1 Computational Approach to Design of Al Alloys for PBAM Two computational approaches; genetic algorithm (GA) and CALculation of PHAse Diagrams (CALPHAD)-based simulations can be integrated with theory for designing Al alloys. In terms of sequence, after theoretically arriving at the alloying elements, GA can be used to predict the microstructural descriptors that are necessary to achieve the property of interest. Once these descriptors are known, CALPHAD calculations can be run on Thermo-Calc with support from kinetic software (TC-PRISMA) to develop an alloy ultimately leading to the requisite properties.

9.3.2.2.2.1.1 Genetic Algorithm: Principle for Alloy Design As mentioned earlier, once the set of possible alloying elements are predicted by theory, further

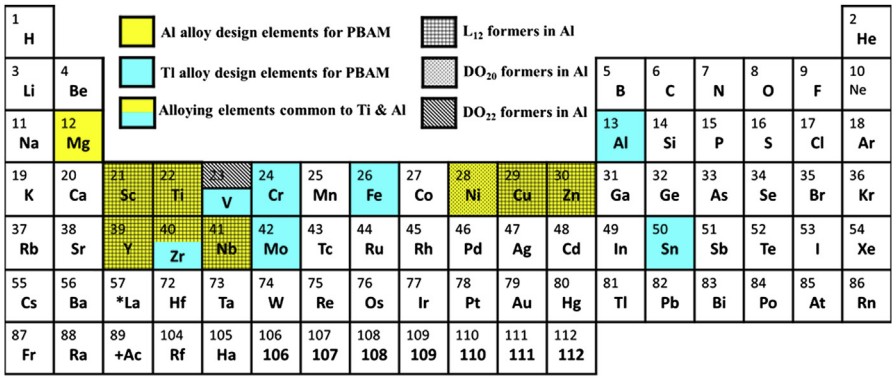


FIGURE 9.24

Theoretical selection of alloying elements to design Ti and Al alloys for PBAM. Each element is color coded and alloys either Al or Ti. Elements that form $L1_2$ or other Al_3X phases of interest when added to Al are also indicated. Lanthanide and actinide series are not shown due to their high cost.

microstructural optimization for achieving a good mix of mechanical properties in a specific alloy will be done by GA. For the present case of Al alloy design, a set of optimal properties can be set as yield strength greater than 400 MPa, ductility of 10% and minimum fracture toughness (K_{Ic}) value of 40 MPa $m^{1/2}$. Transitioning into the computational approach, GA is based on natural selection and genetics. Using this principle, GA combines survival of the fittest with a structured yet randomized information exchange to form a search algorithm [72,73]. Therefore, for GA to tailor the material properties directed toward a specific design criterion, the population is a set of microstructures.

The use of GA and CALPHAD approaches for Al alloy design is illustrated below by taking the example of $L1_2$ type Al_3Sc precipitate in an Al−Mg−Sc−Zr alloy. Excellent combination of properties like corrosion resistance, strength, and ductility makes this alloy a potential and interesting candidate to study for PBAM. Using the aforementioned alloy design principle in GA, optimal microstructure was obtained for achieving exceptionally high strength and ductility in an Al−Mg−Sc−Zr alloy [74]. By equally weighting strength and ductility, Kulkarni et al. [74] obtained the optimal microstructure for a desired strength of 900 MPa and ductility of 10%. These microstructural descriptors are as follows: (1) radius of particles = 15.8 nm; (2) volume fraction of the particles = 12.03%; and (3) amount of solute = 0.5 wt%. The predicted strength and ductility for this microstructure were 905 MPa and 10%, respectively, which are close to the desired values. Fig. 9.25A shows the change in strength and ductility with successive generations and, Fig. 9.25B shows the exploration of the parameter space for a possible solution.

9.3.2.2.2.1.2 CALPHAD Approach for Alloy Design In combination with GA, a CALPHAD-based thermodynamic tool (Thermo-Calc) can be used for executing two functions. These are, (1) phase diagram calculation for the elements predicted by theory to attain novel alloy systems and (2) use the optimal microstructure

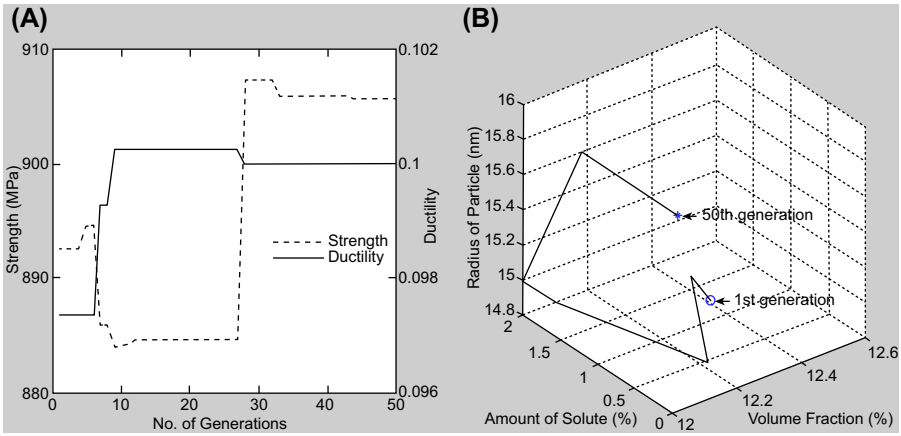


FIGURE 9.25

Genetic algorithm results showing, (A) evolution of strength and ductility, and (B) exploration of parameter space in Al−Mg−Sc−Zr alloy [73].

predicted by GA as the starting point for zeroing on the alloy composition for PBAM. Because the alloy system will be predominantly determined by theory with computation playing a secondary role, major portion of efforts should be directed toward the second objective, which is to arrive at the alloy composition for PBAM. For realizing this objective, Thermo-Calc can be used in combination with a tool capable of simulating precipitate evolution (TC-PRISMA). In Thermo-Calc, large number of compositions can be studied providing insight into the number and type of phases present along with reaction temperatures. Here, the major goal should be to stay within the region of interest. After the phase equilibria calculations, these alloy chemistries can be subjected to thermal cycles similar to the one experienced during PBAM in TC-PRISMA.

In TC-PRISMA, coarsening, reprecipitation, and dissolution mechanisms can be treated concurrently for the multiple interacting thermal profiles and initial microstructure input using the Langer−Schwartz theory and the Kampmann−Wagner numerical approach. Typical outputs from TC-PRISMA are the volume fraction, mean radius, size distribution, and number density of multiple precipitates. Fig. 9.26 shows two such outputs: mean radius and volume fraction of Al_3Sc in a simple binary Al-0.3 wt% Sc alloy isothermally aged at 350°C for 2777 h. Using such outputs for a non-isothermal profile in multicomponent systems, the alloy composition that results in matching precipitate descriptors with an error of 10% across the layers can be selected for PBAM. For example, consider one such precipitate descriptor; volume fraction. Adopting GA, volume fraction of precipitate predicted was 12.03% to achieve a strength of 900 MPa with 10% ductility. If the component in service needs a minimum of 10% Al_3Sc precipitates by volume to function without failure, the alloy composition should be such that it does not fall below this minimum number and in fact should be designed with a safety factor. Therefore, using CALPHAD approach, the chemistry of the alloy can be chosen in such a way that the volume fraction of Al_3Sc lies between 10.83% and 13.24% across the build volume.

Snyder [76] from QuesTek Innovations has summarized their effort on design of aluminum alloys for AM. In one example, the focus was on the critical trade-off between precipitate strengthening and AM processability. The approach is based on the systems approach of Olson [77]. Very promising early results have been reported for various concepts alloys that target strength (7XXX), high temperature strength (2XXX), and corrosion resistance (5XXX) as goals.

Overall, the goal for ICME-based approach should be to find answers to numerous critical questions. A few of these are: What is the optimum quantity of element that needs to be added? How is the stability of the precipitate affected by the addition of alloying elements? What is the microstructural response as a function of thermal cycling to these alloying additions? Which elements provide an optimum balance of properties with high-performance for PBAM? The idea behind coupling theory and computer-aided GA, thermodynamic, and kinetic calculations is to establish a synergistic pathway between these tools that elevates their individual capabilities and also the overall ability to design alloys for PBAM with minimum number of iterations. In this regard, with the accumulation of data on processing−microstructure−properties relations, informatics approaches, discussed in earlier chapters, can also used advantageously.

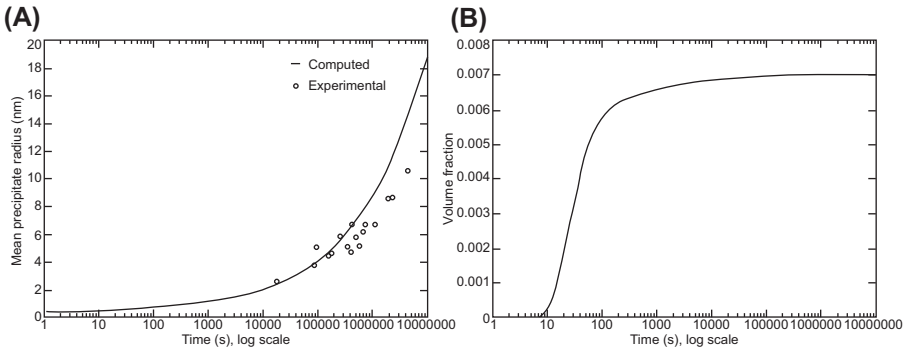


FIGURE 9.26

A typical output from tool capable of simulating precipitate evolution (TC-PRISMA) showing the plot of (A) mean radius and (B) volume fraction of Al_3Sc in binary Al—0.3 wt% Sc alloy isothermally aged at 350°C for 2777 h. Predictions by computation and the data from literature [75] are in good agreement for this simple binary system.

9.4 SUMMARY

This chapter discussed three different manufacturing processes with different level of maturity. SPF started in 1960s and is considered a mature technology with widespread aerospace applications. The alloy design examples are included to show the advantages of such approach. FSW was invented in 1991 and has been successfully implemented in wide-ranging applications because of its breakthrough capability for joining high-strength aluminum alloys. Even with all the successes, achieving high joint efficiency in high-strength Al—Zn—Mg and Al—Cu—Li alloys remains a challenge. Even though the process is more than 20 years old, no specific alloy has been designed to take advantage of the attributes of FSW. The final example is for AM. AM is quite recent in its current form, even though its roots go back to 1988. PBAM is opening up design spaces that were previously not possible. The best way to realize the full potential of AM and design opportunity is to develop specific alloys that can advantageously utilize the attributes of the process. The challenges of the qualification of materials and processes have to be recognized and overcome for accelerated progress. ICME-based examples of potential alloy design approaches are included for aluminum and titanium alloys.

REFERENCES

[1] New Materials for Next-Generation Commercial Transports, Committee on New Materials for Advanced Civil Aircraft, National Research Council, 1996, p. 33.
[2] National Critical Technologies Report, March 1995 (Chapter 6), Page 5, Available at: http://www.whitehouse.gov/WH/EOP/OSTP/CTIformatted/.
[3] Report of a Workshop on "Basic Research Needs for Environmentally Responsive Technologies of the Future", National Science Foundation and the Department of

Energy, New Orleans, January 4−6, 1996. Report available at: http://pmi.princeton.edu/conference/environmental/automotive.html.
[4] R. Martin, D. Evans, Reducing costs in aircraft: the metals affordability initiative consortium, Journal of Metals 52 (3) (2000) 24.
[5] R.S. Mishra, T.R. Bieler, A.K. Mukherjee, Superplasticity in powder metallurgy aluminium alloys and composites, Acta Metallurgica et Materialia 43 (1995) 877.
[6] D.A. Woodford, Strain rate sensitivity as a measure of ductility, Transaction of ASM 62 (1969) 291−293.
[7] O.D. Sherby, J. Wadsworth, Superplasticity − recent advances and future directions, Progress in Materials Science 33 (1989) 169.
[8] R.S. Mishra, M.W. Mahoney, S.X. McFadden, N.A. Mara, A.K. Mukherjee, High strain rate superplasticity in a friction stir processed 7075 Al alloy, Scripta Materialia 42 (2000) 163−168.
[9] Z.Y. Ma, R.S. Mishra, M.W. Mahoney, Superplastic deformation behavior of friction stir processed 7075Al alloy, Acta Materialia 50 (2002) 4419.
[10] I. Charit, R.S. Mishra, High strain rate superplasticity in a commercial 2024 Al alloy via friction stir processing, Materials Science and Engineering A A359 (2003) 290.
[11] Z.Y. Ma, R.S. Mishra, M.W. Mahoney, R. Grimes, High strain rate superplasticity in friction stir processed Al-Mg-Zr alloy, Materials Science and Engineering A A351 (2003) 148.
[12] I. Charit, R.S. Mishra, Evaluation of microstructure and superplasticity in friction stir processed 5083 Al alloy, Journal of Materials Research 19 (2004) 3329−3342.
[13] Z.Y. Ma, R.S. Mishra, M.W. Mahoney, R. Grimes, Effect of friction stir processing on the kinetics of superplastic deformation in an Al-Mg-Zr alloy, Metallurgical and Materials Transactions A 36A (2005) 1447−1458.
[14] I. Charit, R.S. Mishra, Low temperature superplasticity in a friction-stir-processed ultrafine grained Al-Zn-Mg-Sc alloy, Acta Materialia 53 (2005) 4211−4223.
[15] Z.Y. Ma, R.S. Mishra, Development of ultrafine-grained microstructure and low temperature (0.48 T_m) superplasticity in friction stir processed Al-Mg-Zr, Scripta Materialia 53 (2005) 75−80.
[16] Z.Y. Ma, F.C. Liu, R.S. Mishra, Superplastic deformation mechanism of an ultrafine-grained aluminum alloy produced by friction stir processing, Acta Materialia 58 (14) (2010) 4693−4704.
[17] R.S. Mishra, T.R. Bieler, A.K. Mukherjee, Mechanism of high strain rate superplasticity in aluminum alloy composites, Acta Metallurgica et Materialia 45 (1997) 561.
[18] R. Grimes, R.J. Dashwood, A.W. Harrison, H.M. Flower, Development of a high strain rate superplastic Al-Mg-Zr alloy, Materials Science and Technology 16 (11−12) (2000) 1334−1339.
[19] Z.Y. Ma, R.S. Mishra, Cavitation in superplastic 7075Al alloys prepared via friction stir processing, Acta Materialia 51 (2003) 3551.
[20] T.G. Nieh, J. Wadsworth, O.D. Sherby, Superplasticity in Metals and Ceramics, Cambridge University Press, Cambridge, UK, 1997.
[21] I. Charit, R.S. Mishra, Superplasticity and superplastic forming, in: J.R. Groza, J.F. Shackelford, E.J. Lavernia, M.T. Powers (Eds.), Materials Processing Handbook, Taylor and Francis, 2007, pp. 14-1−14-35.
[22] R.S. Mishra, V. V Stolyarov, C. Echer, R.Z. Valiev, A.K. Mukherjee, Mechanical behavior and superplasticity of a severe plastic deformation processed nanocrystalline Ti-6Al-4V alloy, Materials Science and Engineering A298 (2001) 44.

[23] E. Alabort, D. Putman, R.C. Reed, Superplasticity in Ti−6Al−4V: characterisation, modelling and applications, Acta Materialia 95 (2015) 428−442.
[24] A. Ogawa, H. Iizumi, K. Minakawa, Superplasticity and post-SPF properties of SP-700, in: Proceedings of the Conference Titanium'95, Science and Technology, Birmingham, 1995, pp. 588−595.
[25] J.R. Davis, ASM Specialty Handbook: Aluminum and Aluminum Alloys, ASM International, Materials Park, Ohio, 1993.
[26] W.M. Thomas, E.D. Nicholas, J.C. Needham, M.G. Murch, P. Templesmith, C.J. Dawes, Friction Stir Butt Welding, G.B. Patent Application No. 9125978.8, December 1991; U.S. Patent No. 5460317, October 1995.
[27] R.S. Mishra, Z.Y. Ma, Friction stir welding and processing, Materials Science and Engineering R 50 (2005) 1−78.
[28] A. Shrivastava, M. Krones, E. Pfefferkorn, Comparison of energy consumption and environmental impact of friction stir welding and gas metal arc welding for aluminum, CIRP Journal of Manufacturing Science and Technology 9 (2015) 159−168, http://dx.doi.org/10.1016/j.cirpj.2014.10.001.
[29] G.R. Cui, Z.Y. Ma, S.X. Li, The origin of non-uniform microstructure and its effects on the mechanical properties of a friction stir processed Al−Mg alloy, Acta Materialia 57 (2009) 5718−5729.
[30] C. Genevois, D. Fabrègue, A. Deschamps, W.J. Poole, On the coupling between precipitation and plastic deformation in relation with friction stir welding of AA2024 T3 aluminium alloy, Materials Science and Engineering A 441 (2006) 39−48.
[31] C. Genevois, A. Deschamps, A. Denquin, B. Doisneau-cottignies, Quantitative investigation of precipitation and mechanical behaviour for AA2024 friction stir welds, Acta Materialia 53 (2005) 2447−2458.
[32] B. Yang, J. Yan, M.A. Sutton, A.P. Reynolds, Banded microstructure in AA2024-T351 and AA2524-T351 aluminum friction stir welds: Part I. Metallurgical studies, Materials Science and Engineering A 364 (2004) 55−65.
[33] L. Fratini, S. Pasta, A.P. Reynolds, Fatigue crack growth in 2024-T351 friction stir welded joints: longitudinal residual stress and microstructural effects, International Journal of Fatigue 31 (2009) 495−500.
[34] T.S. Srivatsan, S. Vasudevan, L. Park, The tensile deformation and fracture behavior of friction stir welded aluminum alloy 2024, Materials Science and Engineering A 466 (2007) 235−245.
[35] O. Hatamleh, Effects of peening on mechanical properties in friction stir welded 2195 aluminum alloy joints, Materials Science and Engineering A 492 (2008) 168−176.
[36] H.R. Kroninger, A.P. Reynolds, R-curve behaviour of friction stir welds in aluminium-lithium alloy 2195, Fatigue & Fracture of Engineering Materials & Structures 25 (2002) 283−290.
[37] K.V. Jata, K.K. Sankaran, J.J. Ruschau, Friction-stir welding effects on microstructure and fatigue of aluminum alloy 7050-T7451, Metallurgical and Materials Transactions A 31 (2000) 2181−2192.
[38] A.P. Reynolds, W. Tang, Z. Khandkar, J.A. Khan, K. Lindner, Relationships between weld parameters, hardness distribution and temperature history in alloy 7050 friction stir welds, Science and Technology of Welding and Joining 10 (2005) 190−199.

[39] M.W. Mahoney, C.G. Rhodes, J.G. Flintoff, W.H. Bingel, R.A. Spurling, Properties of friction-stir-welded 7075 T651 aluminum, Metallurgical and Materials Transactions A 29 (1998) 1955−1964.
[40] C.B. Fuller, M.W. Mahoney, M. Calabrese, L. Micona, Evolution of microstructure and mechanical properties in naturally aged 7050 and 7075 Al friction stir welds, Materials Science and Engineering A 527 (2010) 2233−2240.
[41] L. Fratini, G. Buffa, R. Shivpuri, Mechanical and metallurgical effects of in process cooling during friction stir welding of AA7075-T6 butt joints, Acta Materialia 58 (2010) 2056−2067.
[42] A.H. Feng, D.L. Chen, Z.Y. Ma, Microstructure and cyclic deformation behavior of a friction-stir-welded 7075 Al alloy, Metallurgical and Materials Transactions A 41 (2010) 957−971.
[43] J.-Q. Su, T.W. Nelson, R. Mishra, M. Mahoney, Microstructural investigation of friction stir welded 7050-T651 aluminium, Acta Materialia 51 (2003) 713−729.
[44] R.S. Mishra, M. Komarasamy, Friction Stir Welding of High Strength 7XXX Aluminum Alloys, Butterworth-Heinemann, 2016, ISBN 978-0-12-809465-5.
[45] R.S. Mishra, H. Sidhar, Friction Stir Welding of 2XXX Aluminum Alloys Including Al-Li Alloys, Butterworth-Heinemann, 2016, ISBN 978-0-12-805368-3.
[46] H. Sidhar, N.Y. Martinez, R.S. Mishra, J. Silvanus, Friction stir welding of Al−Mg−Li 1424 alloy, Materials and Design 106 (2016) 146−152.
[47] H. Sidhar, R.S. Mishra, Aging kinetics of friction stir welded Al-Cu-Li-Mg-Ag and Al-Cu-Li-Mg alloys, Materials and Design 110 (2016) 60−71.
[48] G.J. Shiflet, J.A. Hawk, Interfacial structure consideration in coarsening, in: Y.W. Kim, W.M. Griffith (Eds.), Dispersion Strengthened Aluminum Alloys, TMS, 1988, pp. 123−141.
[49] C.R. Hutchinson, X. Fan, S.J. Pennycook, G.J. Shiflet, On the origin of the high coarsening resistance of Ω plates in Al−Cu−Mg−Ag alloys, Acta Materialia 49 (2001) 2827−2841.
[50] B.M. Gable, G.J. Shiflet, E.A. Starke Jr., Alloy development for the enhanced stability of Ω precipitates in Al-Cu-Mg-Ag alloys, Metallurgical and Materials Transactions A 37 (2006) 1091−1105.
[51] L. Sun, D.L. Irving, M.A. Zikry, D.W. Brenner, First-principles investigation of the structure and synergistic chemical bonding of Ag and Mg at the Al| Ω interface in a Al−Cu−Mg−Ag alloy, Acta Materialia 57 (2009) 3522−3528.
[52] F.W. Gayle, J.B. Vander Sande, Composite precipitates in an Al-Li-Zr alloy, Scripta Metallurgica 18 (1984) 473−478.
[53] V. Radmillovic, A. Tolley, E.A. Marquis, M.D. Rossell, Z. Lee, U. Dahmen, Monodisperse Al_3(LiScZr) core/shell precipitates in Al alloys, Scripta Materialia 58 (2008) 529−532.
[54] J.D. Robson, P.B. Prangnell, Modelling Al_3Zr dispersoid precipitation in multicomponent aluminium alloys, Materials Science and Engineering A 352 (2003) 240−250.
[55] P. Cavaliere, M. Cabibbo, F. Panella, A. Squillace, 2198 Al−Li plates joined by friction stir welding: mechanical and microstructural behavior, Materials and Design 30 (2009) 3622−3631.
[56] R. Sankaran, C. Laird, Effect of trace additions Cd, In and Sn on the interfacial structure and kinetics of growth of θ′ plates in Al-Cu alloy, Materials Science and Engineering A 14 (1974) 271−279.

[57] C.L. Mendis, C.J. Bettles, M.A. Gibson, S. Gorsse, C.R. Hutchinson, Refinement of precipitate distributions in an age hardenable Mg-Sn alloy through microalloying, Philosophical Magazine Letters 86 (2006) 443−456.
[58] L. Reich, M. Murayama, K. Hono, Evolution of Ω phase in an Al-Cu-Mg alloy: a three-dimensional atom probe study, Acta Materialia 46 (1998) 1315−1319.
[59] B. Lyons, in: Presentation on Additive Manufacturing in Aerospace; Examples and Research Outlook, The Boeing Company, September 2011. http://www.naefrontiers.org/File.aspx?id=31590.
[60] Global Aerospace and Defense Sector Financial Performance Study, Deloitte University Press, July 2014, pp. 1−52. https://www2.deloitte.com/content/dam/Deloitte/global/Documents/Manufacturing/gx-mfg-2014aandd-global-financial-performance-study.pdf.
[61] S. Palanivel, P. Nelaturu, B. Glass, R.S. Mishra, Friction stir additive manufacturing for high structural performance through microstructural control in an Mg based WE43 alloy, Materials & Design 65 (2015) 934−952.
[62] S. Palanivel, H. Sidhar, R.S. Mishra, Friction stir additive manufacturing: route to high structural performance, JOM (2015), http://dx.doi.org/10.1007/s11837-014-1271-x.
[63] E. Brandl, B. Baufeld, C. Leyens, R. Gault, Additive manufactured Ti-6Al-4V using welding wire: comparison of laser and arc beam deposition and evaluation with respect to aerospace material specifications, Physics Procedia 5 (2010) 595−606.
[64] S. Palanivel, A.K. Dutta, E.J. Faierson, R.S. Mishra, Spatially dependent properties in a laser additive manufactured Ti-6Al-4V component, Materials Science and Engineering A 654 (2016) 39−52.
[65] W.E. Frazier, Metal additive manufacturing: a review, Journal of Materials Engineering and Performance 23 (2014) 1917−1928.
[66] W.J. Sames, F.A. List, S. Pannala, R.R. Dehoff, S.S. Babu, The metallurgy and processing science of metal additive manufacturing, International Materials Reviews (2016) 1−46.
[67] E. Herderick, Additive manufacturing of metals: a review, Materials Science and Technology (MS&T) (2011) 1413−1425.
[68] Material Data Sheet EOS Aluminium $AlSi_{10}Mg$ for EOSINT M 270 EOS, 2017. https://www.anubis3d.com/documents/dmls/datasheets/Aluminum-AlSi10Mg.pdf.
[69] R.S. Mishra, P.S. De, N. Kumar, Friction Stir Welding and Processing: Science and Engineering, Springer, 2014. ISBN-13: 978-3-319-07043-8.
[70] T. Watson, High Strength Aluminum Alloy, United States Patent, Patent No.: US 6,248,453 B1, 2001.
[71] T.J. Bastow, C.T. Forwood, M.A. Gibson, Local site symmetry and electronic structure of trialuminide and related intermetallic alloys probed by solid-state NMR, Physical Review B 58 (1998) 2988−2997.
[72] J.H. Holland, Adaptation in Natural and Artificial Systems: An Introduction Analysis with Applications to Biology, Control and Artificial Intelligence, University of Michigan Press, Ann Arbor, MI, 1975.
[73] D.E. Goldberg, Genetic Algorithms in Search, Optimization and Machine Learning, Addison-Wesley, Reading, MA, 1989.
[74] A. Kulkarni, K. Krishnamurthy, S.P. Deshmukh, R.S. Mishra, Microstructural optimization of alloys using a genetic algorithm, Materials Science and Engineering A 372 (2004) 213.
[75] G.M. Novotny, A.J. Ardell, Precipitation of Al_3Sc in binary Al-Sc alloys, Materials Science and Engineering A 318 (1−2) (2001) 144−154.

[76] D. Snyder, ICME approach to additive manufacturing −modeling and alloy design, in: CHiMaD/SRG31 32nd Annual Meeting, March 22, 2016. http://www.questek.com/filebase/src/Presentations/Snyder-AdditiveMfgSRGV2.pdf.
[77] G.B. Olson, Computational design of hierarchically structured materials, Science 277 (1997) 1237.

CHAPTER

Insertion of New Alloys and Process Technologies 10

CHAPTER OUTLINE

Synopsis **451**
10.1 Insertion of New Technologies **451**
10.1.1 Traditional Approaches 452
10.1.2 Barriers to Insertion 453
10.2 Accelerated Insertion of Technologies **454**
10.3 Summary **456**
References **456**

SYNOPSIS

This chapter discusses the approaches used in practice to insert new materials and processes technologies whose metallurgy and design were described in the previous chapters. Despite the historic success of the commercialization of new technologies using traditional approaches, the increasing complexity of materials coupled with their longer development cycle time compared with those for products, has resulted in many missed opportunities for new materials and processes insertion. Examples are provided to emphasize the importance and necessity of integrating materials and processes design with product attributes and for the use of computational materials science tools to ensure the successful insertion of new technologies.

10.1 INSERTION OF NEW TECHNOLOGIES

The first chapter discussed the trends in new alloy design evolving from empirical approaches to those increasingly based on physics-based models of microstructure—property relationships with the goal of satisfying targeted structural performance requirements. Traditionally, new alloys with incremental improvements in property combinations that are continuously being developed are inserted into new products as needs and opportunities arise. Most of the commercial alloys discussed in the chapters on aluminum, titanium, and ultrahigh strength steel alloys were introduced this way. Often, new manufacturing processes that exploit alloy behavior and enable more efficient structures, e.g., superplastic forming discussed in the previous chapter, arise out

Metallurgy and Design of Alloys with Hierarchical Microstructures. http://dx.doi.org/10.1016/B978-0-12-812068-2.00010-2

Copyright © 2017 Elsevier Inc. All rights reserved.

of exploratory laboratory studies such as those conducted by Professor Walter Backofen's group at the Massachusetts Institute of Technology in the 1960s [1]. This process found immediate applications in products once its potential for improving structural performance and manufacturing efficiency and for reducing cost by unitization and reduction of part count was demonstrated and validated. These technology insertions have varying disruptive effects on the design and manufacturing aspects of new products as well as on the supply chain servicing them, as illustrated in Fig. 10.1.

Introduction of a new alloy to replace an incumbent alloy of the same family, e.g., 2524 for 2024, will generally have no practical effects on the manufacturing infrastructure and supply chain. The alloys will be produced in typically the same way by the same suppliers, and the design and manufacturing methods for structural components using these alloys will essentially remain the same. This is not the case, for example, for polymer−matrix composites replacing the traditional Al alloys for critical structures in the Boeing 787 and Airbus A350 airplanes. The material suppliers and the manufacturing methods and infrastructure will all be different. As discussed in the chapter on aluminum alloys, these changes often also result in additional design requirements necessitating changes in the material mix such as the increasing use of Ti alloys to ensure compatibility in factors such as thermal expansion and electrochemical characteristics. The subsequent sections of this chapter will discuss the traditional approaches to technology development and insertion, barriers to their successful implementation, and the recent progress in integrating materials and processes development with product design. Significant progress in this regard is facilitated by using computational materials science and integrated computational materials engineering of which many examples are provided in the recently launched open access journal *Integrating Materials and Manufacturing Innovation* [2].

10.1.1 TRADITIONAL APPROACHES

The history of the development of precipitation hardened Al alloys, discussed in detail in the fourth chapter, illustrates the success, to an extent, of the traditional approach to designing and inserting new alloys. This has been made possible by

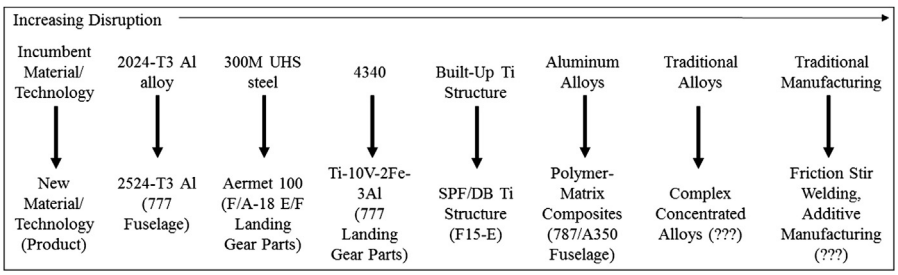


FIGURE 10.1

The relative disruptive effects of insertion of new technologies in airframes.

the evolutionary understanding of the metallurgy of microstructure—property relationships, their application to achieving targeted property combinations in materials required by the changing design drivers (Table 4.1), and the timely and simultaneous opportunities for insertions made possible by the continuous introduction of new products. Examples are the use of 7055-T77 for the upper wing and 2524-T3 for the fuselage skins of the Boeing 777, which along with other such replacements resulted in significant weight savings (Fig. 1.3). With some exceptions noted below, the alloys that were replaced were themselves from the same family. Similarly, the development in the 1970s of secondary hardening, high alloy steels with better strength—toughness—stress corrosion resistance combinations than possessed by the medium carbon, low alloy steels ensured their availability in the early 1990s for use in critical landing gear structures operating in marine environments. The replacement of many ultrahigh strength steel parts by near-β Ti alloys in the 777 in the 1990s resulting in weight reduction was made possible by their development in the earlier decades.

Several sequential steps are involved in ensuring that new alloys are ready for selection and use in structures when opportunities arise. These typically begin with the screening of many chemistries and processing trials to determine the specific alloy composition for scale up, followed by optimizing its production in the size range and product forms necessary for development of specifications and commercialization. Finally, the material properties "allowables" required for designing structures are determined by prescribed methods of statistical analysis of the results from the testing and evaluation of several material lots produced using the optimized practice. Although the entire process is aided by accumulated experience, much of which may be proprietary to material producers, and the use of physics-based models where feasible, the method of design, development, and qualification of alloys this way is still time consuming and expensive. Even small variations in alloy chemistries and processing may require extensive additional testing for their requalification.

It has been recognized that although the product development cycle time has decreased considerably by using computational design, analysis, and engineering tools, a corresponding reduction has not occurred in the time for materials development and qualification, with the result that new materials are not inserted frequently [3]. These and additional barriers to materials insertion are discussed next, followed by the approaches being developed and implemented to mitigating them.

10.1.2 BARRIERS TO INSERTION

There are many barriers to the insertion of new materials and manufacturing approaches. In discussing these, it is important to consider the competing forces of "technology push" and "requirements pull," which on balance help determine the overall benefits or lack thereof in introducing changes to existing or new products. The barriers to implementing and successfully commercializing new concepts have been captured in the term "valley of death" [4]. This term signifies the neglect and lack of use of promising technologies, often developed and demonstrated by spending

significant resources, for various reasons such as not being ready during the window of opportunity for insertion, not meeting all the product requirements, etc.

A very common barrier to the selection of new technologies is typically the adequacy of the existing and proven ones, and marginal benefits in performance improvements or cost reductions do not justify the expense and disruptions, even minor, caused by their replacement. The existing technologies often become entrenched along with the concurrent accumulation of service experience. There is a general reluctance to use new technologies without prior service experience, which of course is impossible to obtain without first being selected for service. The long cycle time for materials development vis-à-vis product development is also not commensurate with the relatively narrow window for materials selection for new products, as already discussed earlier.

Although every new airplane design potentially has opportunities for new materials insertion, they must "earn" their way in the framework of the overall cost of ownership and operation, of which the acquisition and fuel costs constitute the major portion [5]. Even with the high fuel costs of the 1980s, the promising second generation Al−Li alloys were not selected for many of the major new designs at the time. Despite their 8%−10% lower density compared with commonly used Al alloys, problems with manufacturing and the anisotropy of properties, among other factors [6] that were discussed in detail in the chapter on aluminum alloys, prevented their selection for many of the new airplanes being designed in that time frame. Significant weight savings were still achieved by using traditional Al alloys with improved damage tolerance (2524-T3) or compressive yield strength (7055-T77), for example, for various structural components of the Boeing 777. On the other hand, as already discussed, revolutionary changes to the materials mix were made by using polymer−matrix composites to replace Al alloys for the Boeing 787 and Airbus A350 resulting in significant performance improvements and other desirable attributes such as reduction of environmental impact and improved passenger comfort. Thus whether or not a new material or manufacturing technology is selected is determined by a complex combination of many factors that mostly are difficult to predict. This also highlights the benefits of materials design concurrently with product design using, for example, the "Systems Approach" and Integrated Computational Materials Engineering (ICME) in overcoming the barriers.

10.2 ACCELERATED INSERTION OF TECHNOLOGIES

The long cycle time for the development and qualification of new materials and the many missed opportunities for their insertion prompted several studies that recommended steps to overcome this trend [7,8]. Key among these was the integration of materials and product design with increasing use of multiscale modeling and simulation across the length scale, as in the ICME scheme. These were already discussed in the first three chapters with examples from the virtual aluminum castings [9] and

the "Atoms to Autos" [10] projects and by referring to the comprehensive textbook on ICME that discussed case studies in detail [11]. The "Accelerated Insertion of Materials" (AIM) projects sponsored by the US government's Defense Advanced Research Projects Agency demonstrated the feasibility of reducing the cycle time for materials development by the application of computational materials science in a collaborative environment between designers and materials engineers using digital tools and databases. The early efforts and the benefits of implementing the methodologies in industry have been described in many publications (e.g., Ref. [12] and additionally those available from repositories of technical information such as the Defense Technical Information Center).

It is noteworthy that Olson's "Systems Approach" [13], which links performance requirements with the design of materials with hierarchical microstructures in the framework of the processing−microstructure−properties−performance relationships, preceded the technology acceleration programs mentioned earlier by several years. Furthermore, the first success of this approach was demonstrated by the successful commercialization of the Ferrium steels, which belong to the class of structural materials that are also historically among the oldest. The science behind the development and application of this approach for steels has been described in an overview [14] and the details of the methods in a more recent publication [15]. The metallurgy of the Ferrium steels was discussed briefly in the sixth chapter. A recent review [16] describes the linking of QuesTek's Materials by Design approach and models used in computational alloy design with the qualification methods of the AIM program for the commercialization of the Ferrium steels. This Integrated Computational Materials Design framework and the hierarchical architecture of the ICME methods, materials genome initiative (MGI) framework, and fundamental models and databases on which it rests are schematically shown in Fig. 10.2 [17]. The linking of Materials by Design with the AIM methods and the transition across the concept, design and qualification phases for a new material are clearly shown. The acronym TRL in this figure denotes "technology readiness level," which is a measure of the maturity of the technology. A TRL of 1 refers to the observation and reporting of the basic principles of the technology and that of 9 refers to its proven use in practice. Numbers between 1 and 9 describe the progressive maturity of the technology [18].

The need for treating the target material or process with the desired attributes as a system whose successful development and insertion requires collaboration among materials and structural designers, materials producers, and end users, as initially envisioned in the "Systems Approach," is well recognized and embedded in all the current initiatives. One example is the collaborative effort among material suppliers and users in the development of the integrated models to design and process Ti alloy components with targeted properties in the framework of ICME, without having to incur significant cost and time for extensive experimental trials, as shown in Fig. 5.50. Another example is the integration of academic and industry groups to help accelerate the insertion of thermal spray technology into the manufacturing landscape, as documented in a recent case study [19].

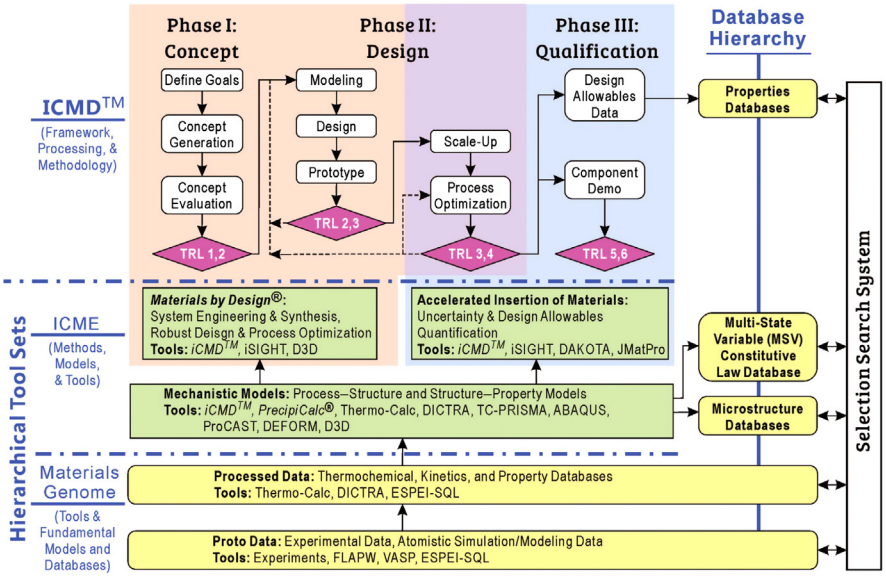


FIGURE 10.2

Hierarchical architecture of the Integrated Computational Materials Design (ICMD) methods, tools, and techniques resting on the Integrated Computational Materials Engineering (ICME) and MGI foundation [17].

10.3 SUMMARY

New materials and processes, discussed in the earlier chapters, with the potential to provide significant improvements in product performance are being developed at an accelerating pace. The ability to design rather than discover alloys to meet performance requirements has been known for several decades [20], but the development and implementation of formal strategies to ensure their accelerated insertion are relatively recent and barely more than a decade old. These initiatives are aided by the rapid advances in computational materials science tools and by the development of frameworks such as integrated computational materials engineering grounded in the MGI. The successful development and commercialization of computationally designed Ferrium steels is an example that bodes well for the ability to tailor alloys and processes rapidly, timely, and inexpensively in response to ever changing product requirements.

REFERENCES

[1] W.A. Backofen, I.R. Turner, D.H. Avery, Superplasticity in an Al-Zn alloy, Transactions of ASM 57 (4) (1964) 980–990.

[2] https://immijournal.springeropen.com/, Downloaded on January 24, 2017.

[3] A vision for integrated computational engineering, in: Integrated Computational Materials Engineering: A Transformational Discipline for Improved Competitiveness and National Security, The National Academies Press, Washington, DC, 2008, pp. 8−35.
[4] Capturing a culture for innovation and rapid technology transition, in: Accelerated Technology Transition, The National Academies Press, Washington, DC, 2004, pp. 8−23.
[5] Requirements and drivers, in: New Materials for Next-Generation Commercial Transports, Publication NMAB-476, The National Academies Press, Washington, DC, 1996, pp. 7−10.
[6] R.J. Rioja, J. Liu, The evolution of Al-Li products for aerospace and space applications, Metallurgical and Materials Transactions, A 43A (2012) 3325−3337.
[7] Accelerated Technology Transition, The National Academies Press, Washington, DC, 2004.
[8] Integrated Computational Materials Engineering: A Transformational Discipline for Improved Competitiveness and National Security, The National Academies Press, Washington, DC, 2008.
[9] J. Allison, M. Li, C. Wolverton, X. Su, Virtual aluminum castings: an industrial application of ICME, JOM 58 (11) (2006) 28−35.
[10] P.E. Krajewski, L.G. Hector Jr., Y. Qi, R.K. Mishra, A.K. Sachdev, "Atoms to autos": a multiscale approach to modeling aluminum deformation, JOM 63 (11) (2011) 24−32.
[11] M.F. Horstemeyer, Integrated Computational Materials Engineering (ICME) for Metals: Using Multiscale Modeling to Invigorate Engineering Design with Science, Wiley, 2012.
[12] D.G. Backman, D.Y. Wei, D.D. Whitis, M.B. buczek, P.M. Finnegan, D. Gao, ICME at GE: accelerating the insertion of new materials and processes, JOM 58 (11) (2006) 36−41.
[13] G.B. Olson, Computational design of hierarchically structured materials, Science 277 (5330) (1997) 1237−1242.
[14] G.B. Olson, Overview: science of steel, in: G.B. Olson, M. Azrin, E.S. Wright (Eds.), Innovations in Ultrahigh Strength Steel Technology, Proceedings of Sagamore Army Material Research Conference, Lake George, NY, 1987, pp. 3−66.
[15] G.B. Olson, Genomic materials design: the ferrous frontier, Acta Materialia 61 (2013) 771−781.
[16] W. Xiong, G.B. Olson, Cybermaterials: materials design and accelerated insertion of materials, npj/Computational Materials (February 2016). Open Access, Published Online 12, http://palgrave.nature.com/articles/npjcompumats20159.
[17] G.B. Olson, C.J. Kuehmann, Materials genomics: from CALPHAD to flight, Scripta Materialia 70 (2014) 25−30.
[18] Definition of Technology Readiness Levels. https://esto.nasa.gov/files/TRL_definitions.pdf, Downloaded January 27, 2017.
[19] S. Sampath, G. Dwivedi, A. Valarezo, B. Choi, Partnership for accelerated insertion of new technology: case study for thermal spray technology, Integrating Materials and Manufacturing Innovation 2 (1) (2013). Springer, Open Access Journal, https://immijournal.springeropen.com/articles/10.1186/2193-9772-2-1.
[20] R.F. Decker, Alloy design using second phases, Metallurgical Transactions 4 (11) (1973) 2495−2518.

Appendix 1

As discussed in the introductory chapters and in those describing specific alloy systems, new alloy design is increasingly being coupled with and tailored toward satisfying specific performance requirements along with the goal of achieving their accelerated and timely insertion in products. Although much of the alloy development has historically been aided by chance discoveries and followed by empirical approaches utilizing accumulated experience and knowledge, the ability to design multicomponent alloys for targeted property combinations using the tools of computational materials science is already demonstrated by the recent successes in ultrahigh strength steels. The foundations for "Modern Alloy Science" that made the latter achievement possible were based on the many developments starting with the application of thermodynamics to phase equilibria and the derivation of the phase rule by Gibbs [1]. Among the many subsequent vital developments in this regard are the studies on the kinetics of diffusion, crystallinity of metals and alloys, phase transformations, defects, and plastic deformation, density functional theory, modeling of multiphase systems, CALPHAD (CALculation of PHAse Diagrams), phase field methods, and of course, electron microscopy, atom probe tomography, and related characterization techniques. Extensive descriptions of these developments germane to alloy design can be found in many text books (e.g., see Refs. [1–3]).

The focus of this book has been on describing the materials phenomena occurring in the mesoscale region corresponding to the "microstructural" features that determine the properties of alloys. In this context, the chapters have emphasized the linkages among composition, processing, microstructure, and properties for the various alloys under consideration. In particular, the effect of processing on microstructural evolution and the way it responds to the environmental and loading conditions in service were used as the basis to describe the underlying physical metallurgy of commercial alloys and to provide guidance for new alloy development. Alloy design is essentially microstructural design. Computational alloy design uses models and simulations to determine the alloy chemistry and processing conditions, which will result in the microstructure that will provide the desired properties and performance. Examples of designing microstructures for engineering materials (see Ref. [4]) and that of the effects of thermomechanical processing (see Ref. [5]) are described in many publications. Application of computational materials science tools for the hierarchical multiscale modeling and simulation-based design of engineering structures, which is the basis for integrated computational materials engineering (ICME), has been described in detail in the textbook by Horstemeyer [6]. Key to the success of the ICME approach is the ability to integrate models and perform simulations across the length scale from atoms to continuum. A recent study [7] has assessed the state-of-the-art models and the methods for linking them across the entire length scale divided into three regions: (1) quantum and atomistic, (2) microstructural evolution and materials response, and (3) macroscopic. The study also discusses the gaps and challenges that must be addressed to achieve true integration and linkage of models.

"Computational Materials Science and Engineering" (CMSE) has been defined as the "computer based employment of modeling and simulation to understand materials behavior" [8]. A model is defined as "an idealization of real behavior, i.e., an approximate description based on some sort of empirical and/or physical reasoning" and simulation is defined as "a study of the response of the modeled system to external forces and constraints" [8]. The different types of models, e.g., mechanistic, empirical, or phenomenological, used to describe materials behavior were outlined in the introductory chapters. Many models linking parameters related to alloy composition, processing, microstructure, and properties for various alloy systems were described throughout the various chapters in this book. Although the intent of this book is not to provide detailed descriptions of all modeling and simulation techniques used in computational alloy design, a few concepts important for describing and applying the physical metallurgy of alloys are briefly described in the following to provide a context for their applications. These are covered under the headings of thermodynamic modeling, materials informatics, and the superposition of strengthening mechanisms. Thermodynamic modeling has advanced significantly to the stage that it is used routinely and its methods are covered in significant detail in many publications. The application of materials informatics methods to alloy design is relatively recent. The interactions of the features constituting the microstructure of alloys and the effects of their superposition in determining alloy properties have been recognized and studied in investigations of strengthening mechanisms, but are typically not discussed in detail while reporting alloy design efforts. The following discussion is by no means a comprehensive treatment of these topics. They are covered in detail in many textbooks and articles, which continue to appear in ever increasing numbers.

A.1 THERMODYNAMIC MODELING

Multicomponent alloys used in critical structural applications are typically not in a state of thermodynamic equilibrium, although, in practice, they are designed and processed to be stable at least for the duration of their anticipated service life, such as precipitation hardened aluminum alloys used in airframes. Nevertheless, thermodynamic modeling is essential for determining the occurrence and relative stability of the phases and, in conjunction with modeling of the kinetics, for the evolution of these phases that constitute the microstructure of alloys. Phase diagrams for multicomponent alloys are typically not available and their experimental determination is very difficult and time consuming, if not impossible. The effort required to determine the equilibrium conditions in these systems is reduced considerably by calculating the phase diagrams that entails minimizing the Gibbs free energy of all the possible phases present in the system [9]. The CALPHAD approach thus requires both reliable data for the thermodynamic parameters of each phase and a reliable computer software to carry out the calculations [10]. These data can be obtained from experimental measurements or by performing ab initio calculations, as

described for the density functional theory based on development of such data [11]. Thermodynamic information is generally available only for lower order (binary or ternary) systems, which are then used for calculating the phase equilibria for higher order systems.

The history of CALPHAD and its development over the first three decades leading up to its routine use has been summarized [12]. The CALPHAD abbreviation presently refers to "Computer Coupling of Phase Diagrams and Thermochemistry". In addition to calculating phase equilibria, this method has been extended to model atomic mobilities, molar volumes, and elastic coefficients [11] necessary for modeling diffusion processes and phase transformations. Among the aims stated in the CALPHAD website [13] are "promotion of computational thermodynamics through development of models to represent thermodynamic properties for various phases which permit prediction of properties of multicomponent systems, critical assessment of data and their incorporation into self-consistent databases, development of software to optimize and derive thermodynamic properties and development of databanks for performing calculations to understand industrial processes." CALPHAD developed under the leadership of Kaufman who has described the early use and applications of computational thermodynamics for alloy design [14]. That CALPHAD embedding the characteristics of the materials genome is illustrated by its thermodynamic database allowing phase equilibria calculations for engineering materials and its kinetic database allowing the determination of the response of materials to processing (Fig. A.1) [15].

Use of the CALPHAD approach and tools in the successful computational design and flight of Ferrium steels is described in a recent publication [16] and was discussed in the chapter on ultrahigh strength steels. Many of the commercial thermodynamic modeling softwares used to predict beta transus temperatures and

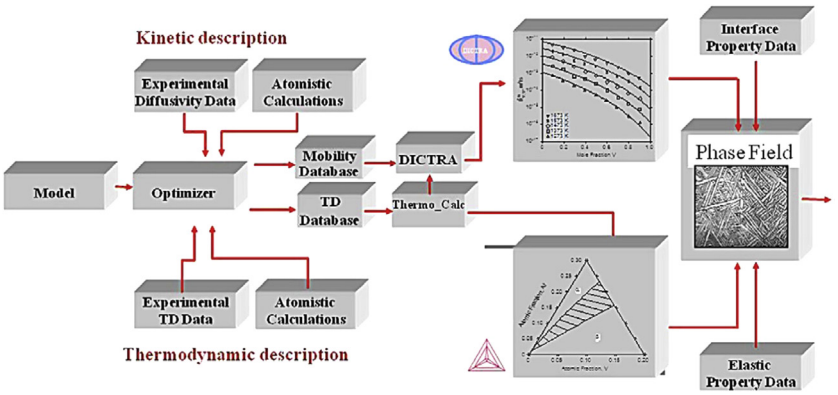


FIGURE A.1

CALPHAD: The roadmap of microstructure engineering—the materials genome [15]. Although the figure depicts ThermoCalc and DICTRA, any similar software can be used.

the beta approach curves discussed in the chapter on titanium alloys use databases assessed with the CALPHAD approach. In addition to predicting phase equilibria, these software products can also model solidification, diffusion, and phase transformation reactions. Both the abilities and the challenges of using thermodynamic modeling are illustrated by a study of the precipitation kinetics of the $Al_3(Sc,Zr)$ phase in an Al−Sc−Zr alloy [17]. This precipitate exhibits a core−shell structure due to the faster diffusion of Sc atoms resulting in the formation of Al_3Sc until the supersaturation of Sc reaches the equilibrium value. The precipitate then grows by the diffusion of Zr atoms forming a shell rich in this element. Although the measured and predicted values of the mean precipitate radii were in reasonable agreement, the predicted value of the volume fraction was twice that measured. This disagreement could be a combination of the assumptions made in formulating the model and/or the uncertainties in quantifying the experimental data from small angle X-ray scattering measurements.

Computational thermodynamic modeling and its integration with the ICME approaches to alloy design is facilitated by the rapidly increasing computing capability, advances in the ab initio methods to calculate properties and the accumulation of experimental data. There are, however, challenges to overcome in terms of the availability of mobility databases and models for the kinetics of phase transformations in alloys of commercial importance, the difficulty of simulation of the microstructural evolution, and the integration of models across length scales, as already mentioned [18]. A CALPHAD-based computational file repository containing evaluated data and other files for reproducing assessments from publications has been established [19,20]. Along with the developments in materials informatics (described next), thermodynamic modeling can be expected to play a vital and increasingly important role in the design and development of industrial alloys and processes.

B.1 MATERIALS INFORMATICS

Modeling of materials behavior using statistical methods was described briefly in the introductory chapters using examples of their applications in alloy design. As with thermodynamic modeling, the enormous increase in computing capabilities along with the availability of relatively large amounts of data, both calculated and experimentally acquired, is facilitating the increasing and advantageous use of statistics in uncovering relationships among composition, processing, microstructure, and properties not otherwise readily evident. This is especially important as these relationships are generally complex and not linear, especially for multicomponent alloys. Materials informatics "allows one to survey complex, multiscale information in a high-throughput, statistically robust, and yet physically meaningful manner, with significant impact in materials design and discovery" [21]. Although the basic concept of informatics has been used to describe materials behavior by capturing

empirical knowledge in the form of rules (e.g., Hume–Rothery rules), the advances in computation and data analysis capabilities have increased its applicability and usefulness tremendously [22].

Along with the methods of materials science and engineering, data acquisition, management, and analysis are integral components of materials informatics strategies, as shown in Fig. B.1 [23]. Data warehousing and management involve science-based selection and organization of data linked to a reliable search and management system, e.g., the CALPHAD file repository described earlier. Data mining enables correlation of multivariate data representative of the processing–microstructure–properties relationships and scientific visualization enables assessment of high-dimensionality information.

The role of informatics in materials design and engineering has been discussed in detail by many authors in a recently published book [24]. Informatics can optimize materials selection based on available data such as used in Ashby plots [25]. Where there is insufficient data, typical for the mechanical properties of alloys, informatics can account for inherent uncertainties and noise in data using stochastic analysis and increase the accuracy of models [26]. Thermochemical properties and crystal structures of phases have the most data available. Data relating to processing, microstructure, and properties are relatively sparse.

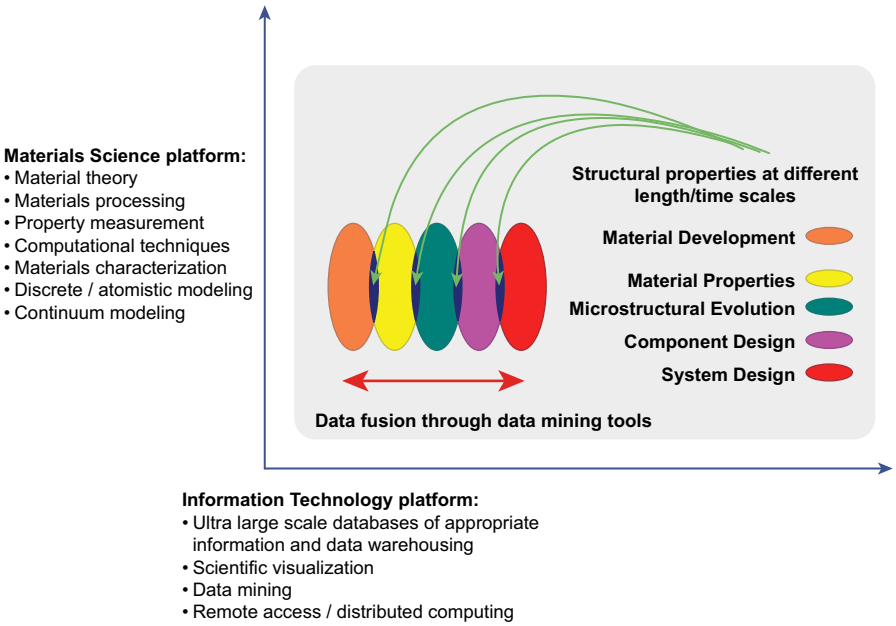


FIGURE B.1

The role of materials informatics across all aspects of materials science and engineering [23].

The advances in materials characterization in three dimensions through serial sectioning and by using techniques such as atom probe tomography have resulted in the ability to represent microstructural data digitally in forms amenable to statistical assessment of its stochastic nature and for its use as quantitative inputs for modeling of processing—microstructure—properties relationships. This was discussed in brief in the third chapter. The focus of microstructure informatics is to develop algorithms and computationally efficient protocols for mining large microstructural data sets and building robust knowledge systems [27], which can be shared by the materials community, as is the case with the CALPHAD file repository. The application of informatics to representing and quantifying hierarchical microstructures and for establishing robust processing—microstructure and microstructure—property linkages has been described in detail in a recent textbook [28]. The general concept is shown in Fig. B.2. All the relevant microstructures for a given alloy design goal are represented in the elliptical space and these evolve along the various processing directions, as encountered in industrial practice. The numbers 1, 2, 3, … N represent microstructural parameters, e.g., grain size or particle spacing, and the objective is to derive a rigorous mathematical description of the microstructures for finding the most appropriate processing path for targeted properties, which is essentially an inverse problem of finding the linkages [29]. The approach uses spatial correlation of microstructural features for their statistical quantification and can be integrated

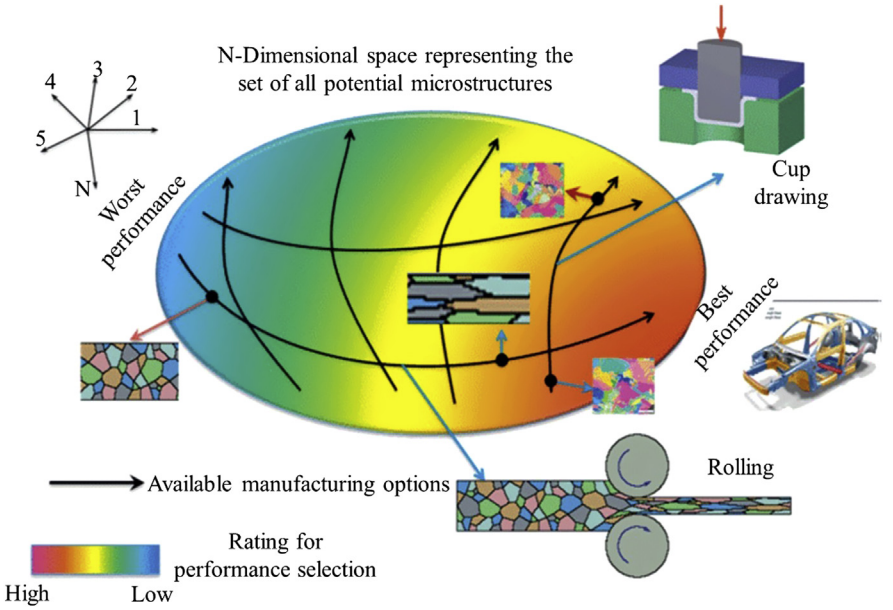


FIGURE B.2

Visualization of processing—microstructure—property linkages in the microstructure space [29].

with thermodynamic modeling and other components of the ICME framework. The use of spectral methods reduces computational requirements and enables inverse design [30]. It will be of significant use in alloys whose properties depend on many microstructural features with a multivariate dependence on processing parameters, for example, two-phase α/β Ti alloys discussed in detail in the fifth chapter.

C.1 SUPERPOSITION OF STRENGTHENING MECHANISMS

The microstructures of alloys used in structural applications generally contain many hierarchical features that interact in various ways with mobile dislocations. The observed strength of these alloys is a result of the superposition of the effects from the individual features that act as obstacles to dislocation motion and can include defects, solute atoms, dislocation substructure, subgrain, and grain structure, and second-phase particles. Modeling the strength of alloys requires a knowledge of the mechanisms that correspond to the microstructural features, as shown in Table C.1 [31].

Among the alloy systems used in airframes and discussed in this book, predicting the yield strength of commercial, precipitation hardened Al alloys is the easiest. All the microstructural features present in Al alloys are well characterized and their combined effects on yield strength can be modeled readily, as was shown in the fourth chapter by calculating the yield strength of alloy 7050. The accuracy of the predictive capability will depend on the rules used for superposition. Various additivity rules have been used to calculate the yield strength of alloys and the following generalized rule has been suggested [32]:

$$\tau^q = \tau_1^q + \tau_2^q + \ldots$$

where τ is the overall flow stress of the alloy, τ_1 is the flow stress contribution from feature 1, etc., and q is between 1 and 2, with its exact value depending on the relative strength of the obstacles. Obstacles are classified as "hard" or "soft" depending on the value of φ_c, the angle formed during their interaction with dislocations, as shown in Fig. C.1 [31]. Obstacles for which φ_c is close to 0 or 180° are considered hard or soft, respectively. The flow stress can be represented as the linear sum of contributions

Table C.1 Microstructural Features and Corresponding Strengthening Mechanisms [31]

Microstructural Feature	Strengthening/Hardening Mechanism
Solute/vacancies	Solid solution strengthening
Dislocations	Work hardening
(Sub-) grain/phase or twin boundaries	(Sub-) grain boundary hardening
Precipitates/dispersoids	Precipitation/dispersion strengthening

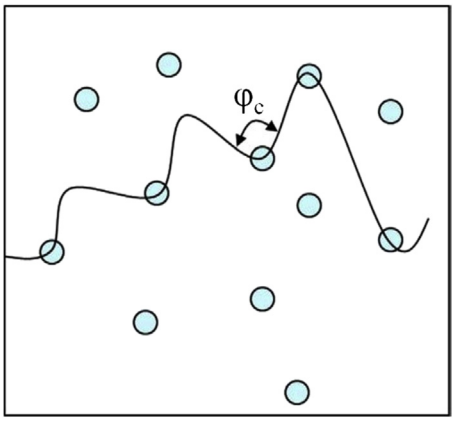


FIGURE C.1

Dislocation–obstacle interaction to illustrate soft and hard obstacles [31].

from soft and hard obstacles, whereas a Pythagorean superposition is used to combine effects of multiple hard obstacles.

Even for precipitation hardened Al alloys, flow stress has typically been modeled for the presence of only one type of monodispersed particles. These alloys often contain multiple types of strengthening phases (e.g., θ'', T_1, and δ' in Al–Cu–Li alloys) and some in multiple size distributions (e.g., bimodal) due to special aging treatments. Computer simulation of such alloys containing multiple precipitate phases has determined the exponent to be between 1 and 2 [33]. In contrast to Al alloys, there have been very few attempts to predictively model the strength of α/β Ti alloys, principally because of the presence of two ductile phases and the difficulty of quantifying the effects of the interphase morphologies and interfaces on the motion of dislocations. As discussed in the fifth chapter, neural networks have been used to delineate the contributions from the various microstructural features [34] and attempts have been made only recently to predict the yield strength using an additivity rule [35]. This effort is just beginning and enough data are not yet available to determine the feasibility of modeling the superposition of strengthening mechanisms in Ti alloys.

Compared with strength, the superposition of the effects of microstructural features on properties such as toughness and corrosion resistance has not received much attention. This is due to the difficulty of quantitatively delineating the individual effects of all these features on the properties. In many cases, the underlying mechanisms controlling the properties are also not known. However, a single microstructural feature can often be identified as predominantly controlling these properties. For example, the toughness of precipitation hardened Al alloys is related to the volume fraction of the constituent particles in otherwise identical alloys, providing some guidance for alloy design.

REFERENCES

[1] W. Pfeiler (Ed.), Alloy Physics, Wiley-VCH, 2007.
[2] Z.H. Barber (Ed.), Introduction to Materials Modeling, Maney Publishing, 2005.
[3] R. Lesar, Computational Materials Science: Fundamentals to Applications, Cambridge University Press, 2013.
[4] D.A. Molodov (Ed.), Microstructural Design of Advanced Engineering Materials, Wiley-VCH, 2013.
[5] B. Verlinden, J. Driver, I. Samajdar, R.D. Doherty, Thermo-Mechanical Processing of Metallic Materials, Elsevier, 2007.
[6] M.F. Horstemeyer, Integrated Computational Materials Engineering (ICME) for Metals − Using Multiscale Modeling to Invigorate Engineering Design with Science, Wiley-TMS, 2012.
[7] Modeling across scales: a roadmapping study for connecting materials models and simulations across length time scales, Report of a study organized by, The Minerals, Metals and Materials Society (2015).
[8] Introduction to materials modeling and simulation, in: R. Lesar (Ed.), Computational Materials Science: Fundamentals to Applications, Cambridge University Press, 2013, pp. 1−7.
[9] U.R. Kattner, The thermodynamic modeling of multicomponent phase equilibria, JOM 49 (12) (1997) 14−19.
[10] S.-L. Chen, F. Zhang, S. Daniel, F.-Y. Xie, X.-Y. Yan, Y.A. Chang, R. Scmid-Fetzer, W.A. Oates, Calculating phase diagrams using PANDAT and PanEngine, JOM 55 (12) (2003) 48−51.
[11] Y. Wang, S. Shang, L.-Q. Chen, Z.-K. Liu, Density functional theory-based database development and CALPHAD function, JOM 65 (11) (2013) 1533−1539.
[12] P.J. Spencer, A brief history of CALPHAD, Computer Coupling of Phase Diagrams and Thermochemistry 32 (2008) 1−8.
[13] www.calphad.org, downloaded February 19, 2017.
[14] L. Kaufman, Computational thermodynamics and alloy design, CALPHAD 25 (2) (2001) 141−161.
[15] L. Kaufman, J. Agren, CALPHAD, first and second generation − birth of the materials genome, Scripta Materialia 70 (2014) 3−6.
[16] G.B. Olson, C.J. Kuehmann, Materials genomics: from CALPHAD to flight, Scripta Materialia 70 (2014) 25−30.
[17] Q. Du, W.J. Poole, M.A. Wells, A mathematical model coupled to CALPHAD to predict precipitation kinetics for multicomponent aluminum alloys, Acta Materialia 60 (2012) 3830−3839.
[18] A.A. Luo, Material design and development: from classical thermodynamics to CALPHAD and ICME approaches, CALPHAD: Computer Coupling of Phase Diagrams and Thermochemistry 50 (2015) 6−22.
[19] C.E. Campbell, U.R. Kattner, Z.-K. Liu, File and data repositories for next generation CALPHAD, Scripta Materialia 70 (2014) 7−11.
[20] https://materialsdata.nist.gov/dspace/xmlui/handle/11256/2, downloaded February 29, 2017.
[21] K. Rajan, Materials informatics, Materials Today 8 (10) (2005) 38−45.

[22] Materials selection and design, in: Introduction to Computational Materials Science, Cambridge University Press, 2013, pp. 269−278.
[23] K. Rajan, Materials informatics: an introduction, in: K. Rajan (Ed.), Informatics for Materials Science and Engineering, Elsevier, 2013, pp. 1−16.
[24] K. Rajan (Ed.), Informatics for Materials Science and Engineering, Elsevier, 2013.
[25] M. Ashby, E. Cope, D. Cebon, Materials selection for engineering design, in: K. Rajan (Ed.), Informatics for Materials Science and Engineering, Elsevier, 2013, pp. 219−244.
[26] B. Ganapathysubramanian, Using data to account for lack of data: linking materials informatics with stochastic analysis, JOM 61 (1) (2009) 54−58.
[27] S.R. Kalidindi, Microstructure informatics, in: K. Rajan (Ed.), Informatics for Materials Science and Engineering, Elsevier, 2013, pp. 443−465.
[28] S.R. Kalidindi, in: Hierarchical Materials Informatics: Novel Analytics for Materials Data, Elsevier, 2015.
[29] Materials, data and informatics, in: Hierarchical Materials Informatics: Novel Analytics for Materials Data, Elsevier, 2015, pp. 1−32.
[30] D.T. Fullwood, S.R. Niezgoda, B.L. Adams, S.R. Kalidindi, Microstructure sensitive design for performance optimization, Progress in Materials Science 55 (2010) 477−562.
[31] N. Kumar, R.S. Mishra, Additivity of strengthening mechanisms in ultrafine grained Al-Mg-Sc alloy, Materials Science & Engineering, A 580 (2013) 175−183.
[32] A. de Vaucorbeil, W.J. Poole, C.W. Sinclair, The superposition of strengthening contributions in engineering alloys, Materials Science & Engineering, A 582 (2013) 147−154.
[33] A.W. Zhu, A. Csontos, E.A. Starke Jr., Computer experiment on superposition of strengthening effects of different particle, Acta Materialia 47 (1999) 1713−1721.
[34] P.C. Collins, S. Koduri, B. Welk, J. Tailey, H.L. Fraser, Neural networks relating alloy composition, microstructure, and tensile properties of α/β-Processed TIMETAL® 6-4, Metallurgical and Materials Transactions 44A (2013) 1441−1453.
[35] I. Ghamarian, P. Samimi, V. Dixit, P.C. Collins, A constitutive equation relating composition and microstructure to properties in Ti-6Al-4V: as derived using a novel integrated computational approach, Metallurgical and Materials Transactions 46A (2015) 5021−5037.

Appendix 2

PROBLEMS

CHAPTER 1

1.1 Referring to Fig. 1.2, elaborate on the statement "The development or selection of a material to meet given design requirements generally requires that a compromise be struck between several, usually conflicting, objectives" (M.F. Ashby, Acta Materialia 48 (2000) 359−369.). Besides the properties shown in the figure, what additional attributes need to be considered and traded in selecting materials?

1.2 The table below gives the density and Young's modulus for several metals (I. Polmear, Light Alloys, fourth ed., Butterworth-Heinemann, 2006, pp. 1−28.).

Metal	Al	Mg	Ti	Be	Fe	Cu
Density (mg/m^3)	2.70	1.74	4.51	1.85	7.87	8.96
Young's modulus (GPa)	70	45	120	295	211	130

a. What will be the relative weights of wing spars made from alloys based on these metals, if they are designed as I-beams of constant web thickness subjected to bending loads and limited by bending strain? Assume that the density and Young's modulus of alloys are the same as those of the respective pure metals.

b. Based on the answer to question 1.1, would the alloy that provides the least weight be chosen? Explain.

c. For similarly designed wing spars of equal weight, what will be their relative stiffness? Note that equal weight spars of different materials cannot have identical geometry. At least one dimension, for example, flange thickness, will be different.

1.3 The distribution of aerodynamic lift on an airplane wing results in a bending moment that causes compressive and tensile stresses on the upper and lower wing skin structure, respectively. For all the alloys listed in Table 1.4, what will be the relative weights of upper wing skin panels designed to withstand these compressive stresses? Use the values listed in Table 1.4 for compressive yield strength. For a given panel length and width, what will determine the extent to which the thickness can be reduced by using alloys of increasing strength? What properties will influence the selection of the alloy for lower wing skin?

1.4 For an aircraft landing gear cylinder (hollow beam) that needs to withstand high compressive stresses of a certain magnitude, what will be the relative weights of the component made from aluminum alloys 7050 and 7055, titanium alloys

Ti−6Al−V and Ti−10V−2Fe−3Al, and iron alloys 300M and Aermet 100 (use properties shown in Table 1.4)? Would the alloy that provides the least weight be chosen? Explain. Consider the tradeoff between weight and volume.

1.5 Hierarchical materials (e.g., biological tissue) occur in nature. How do they differ from microstructural hierarchy in engineering alloys discussed in this chapter? Consider factors such as the number and nature of elements in the materials, their formation, and how they function (e.g., see P. Fratzl, R. Weinkamer, Progress in Materials Science 52 (2007) 1263−1334.).

1.6 Hierarchy is also found in engineered materials and structures at various levels such as cellular solids, foams, etc., which can be designed and fabricated for improvements in structural performance and functionality (e.g., see R. Lakes, Nature 361 (February 11, 1993) 511−515.). How do these differ from alloys discussed in this chapter?

1.7 The "Systems Approach" to materials design is based on the philosophy of Cyril Stanley Smith who wrote extensively on structural hierarchy in materials (G.B. Olson, Journal of Computer-Aided Materials Design 4 (1997) 134−156.). Smith writes that "Structural change occurs by the formation of interfaces and/or by their movement." List some of the microstructural features listed in Figs. 1.4 and 1.7 that form such changes and discuss how they occur.

1.8 Fig. 1.9 illustrates the multivariate dependence of microstructural features on processing and that of properties on microstructural features. Given these complex linkages, describe the advantages and limitations, if any, of using the "Systems Approach" to designing alloys with multiple property requirements.

1.9 What specific hierarchical approaches (Fig. 1.6) are appropriate for modeling the various microstructural features of ultrahigh strength steels shown in Fig. 1.9? What mechanics models shown in Table 1.5 can be used to study the microstructure−property linkages?

CHAPTER 2

2.1 The wide range of property combinations in alloys is achieved by the manipulation of their microstructure by alloying and processing. As discussed in the first chapter there are also differences in the degree of sensitivity of individual properties to microstructure. Which of the properties listed in Table 2.1 are sensitive to microstructure and which are not? Which properties will be affected by the presence of texture (preferred orientation of grains)? In practice, can any property be completely insensitive to microstructure? Explain.

2.2 Grain size is one among the many microstructural parameters that affects the yield strength of alloys (Table 2.3). The average linear intercept obtained from two-dimensional micrographs is generally reported as the measure of grain

size in publications and is used in modeling its effects on strength using the Hall–Petch relationship.

- **a.** Given that microstructural features fill three-dimensional space (described in the first chapter), would the relationship be different if the average spatial diameter of the grains is used instead of the two-dimensional, linear intercept for materials with randomly oriented, equiaxed grains?
- **b.** What will be the effect of grain shape anisotropy, for example, shown in Fig. 1.7A? Assume the random orientation of grains.
- **c.** Although alloys with grain shape anisotropy need not exhibit texture (or vice versa), they usually do. What will be the effect of such anisotropy on the effects of grain size as described by the Hall–Petch relationship, particularly when comparing single-phase aluminum and magnesium alloys?
- **d.** Will the yield strength of two-phase α/β titanium alloys obey the Hall–Petch relationship? Explain.
- **e.** What will be the effects of subgrains on the strength of polycrystalline alloys in comparison to that of grains?

2.3 What are the microstructural features that contribute predominantly to the yield strength of each of the four families of alloy systems discussed in Tables 2.2 and 2.3? The yield strength of which of these alloy families is most amenable to modeling and why?

2.4 How would you rank the relative resistance of aluminum, titanium, and iron alloys used in airplane structures to the types of corrosion that occur in service? What are the contributing microstructural factors and why do titanium alloys exhibit superior corrosion resistance?

2.5 How can the fracture toughness of precipitation hardened alloys containing shearable precipitates (Fig. 2.4) be improved? What microstructural features affect the toughness and how can they be modified to improve this property? How do they correspond to the three different models of fracture toughness discussed in this chapter?

2.6 Predict the relative fracture toughness of similarly heat-treated alloys 7050 and 7055 solely from their compositions shown in Table 1.4. Explain the prediction.

2.7 Why does reduction of grain size and impurity content increase the fatigue crack initiation resistance of alloys? For two-phase α/β titanium alloys, how do the resistance to fatigue crack initiation and growth vary with changing proportions of equiaxed α and lamellar $\alpha+\beta$ components in the microstructure. What are the mechanisms responsible for this behavior?

2.8 Compare the approaches outlined in Figs. 1.9 and 2.8 to establishing the linkages, and for modeling and delineating the effects of processing on microstructure and properties. Comment on their suitability for designing and developing approaches to new alloys and processes.

CHAPTER 3

3.1 The 1973 Institute of Metals lecture titled "Alloy Design Using Second Phases" (Metallurgical Transactions, 4 (1973) 2495−2518.) by Raymond Decker starts with an earlier quote made in 1932 by Paul Merica that "the metallurgist has been obliged to discover rather than to design alloys." The lecture describes in detail the significant role second phases have played in alloy design and concludes with a summary of the progress made in the properties of steels and superalloys.

- **a.** From a review of the information in Figs. 3.1−3.3, what property combinations have been improved in aluminum, titanium, and iron alloys since the 1960s for use in airframe applications?
- **b.** What role have second phases played in the development of these alloys? Discuss in detail, the beneficial effects or otherwise of the second phases both by themselves and through their effects on the matrix microstructure.
- **c.** What is the role, if any, of second phases in titanium alloys and how does it compare with that in aluminum alloys?

3.2 In the context of designing rather than discovering alloys, how has the design of alloys shown in Figs. 3.1−3.3 evolved? What advances have made this evolution possible and what can be expected in the future? In this regard, what are the challenges involved in establishing quantitative, multivariate linkages among composition, processing, microstructure, and properties as described, for example, in Fig. 1.9 and Tables 2.2 and 2.3?

3.3 Is the approach to predicting the effects of compositional variations on the properties of aluminum alloy 3105 (Fig. 3.6), described in this chapter, applicable to the development of multicomponent alloys for airframe applications? What are the challenges involved?

CHAPTER 4

4.1 Precipitation reactions responsible for strengthening aluminum alloys begin with the nucleation of a second phase(s) from the supersaturated solid solution obtained by quenching.

- **a.** Identify and discuss the factors that determine the total free energy change associated with the nucleation process (Eq. 4.1).
- **b.** Identify sites for the heterogeneous nucleation of precipitates and explain how each affects the terms in Eq. (4.1).
- **c.** What factors determine the degree of coherency of homogeneously nucleated precipitates?
- **d.** Discuss the above for the sequence of precipitation in an Al−4 wt% Cu alloy, schematically shown in Fig. 4.4.

4.2 What are the requirements for precipitation hardenable aluminum alloys in terms of the choice of alloying elements? Why are some of the elements

with adequate maximum solid solubilities (shown in Table 4.7) not suitable individually, but are effective in combination with other solute elements?

4.3 Why are trace elements added to aluminum alloys? How do they affect the precipitation process? List the commercial alloys, discussed in this chapter, that have trace element additions and compare their properties with those of similar alloys, if available, without such additions.

4.4 Precipitates and dispersoids are two types of second-phase particles present in aluminum alloys. Discuss the similarities and differences in the characteristics of various types of these particles and their implications on the microstructure and properties of the alloys.

4.5 How do second phases determine the size, shape, and anisotropy of grains in aluminum alloys, such as shown in Fig. 4.21? What effects do these features have on various properties?

4.6 Discuss the mechanisms of formation of precipitate-free zones (PFZs) in aluminum alloys. What effect does the degree of recrystallization have on their formation? Is it possible in practice to achieve a completely unrecrystallized microstructure in these alloys? In what ways do dispersoids and their nature affect the formation of PFZs?

4.7 Why is cold working prior to aging effective in increasing the strength of only some families of aluminum alloys? Explain with examples from commercial alloys.

4.8 Explain the mechanisms of increasing hardness till the peak is achieved during the aging of aluminum alloys in terms of the effects of particle size, distribution, and volume fraction. What strengthening mechanism operates during aging past the peak? Explain the effects of precipitate size distribution on the observed peak strength, as shown schematically in Fig. 4.17D.

4.9 How does the quench rate from the solution heat treatment temperature affect the properties of aluminum alloys? What factors determine the desirable quench rate?

4.10 Why was Cr replaced by Zr as the dispersoid forming element in 7XXX series alloys? Why is a combination of Mn and Zr used as dispersoid elements for the more recently developed third-generation aluminum–lithium alloys?

4.11 Elucidate the metallurgical mechanisms underlying each of the processing–microstructure–property linkages described in Table 4.16, using a commercial alloy as an example and describing the role of each alloying and impurity element. Based on these linkages, discuss in detail the options available for improving strength, toughness, and stress corrosion cracking resistance in such alloys.

4.12 E. Hornbogen and E.A. Starke (Theory assisted design of high strength low alloy aluminum, Acta Materialia 341 (1993) 1–16.) discuss various approaches to designing an aluminum alloy having good strength while maintaining a high resistance to fracture.

a. The authors identify six mechanisms of hardening (from solid solution, dislocations, substructure, fine grains, precipitation, texture, and fiber reinforcements) as being relevant to aluminum alloys. Which of these six mechanisms operate in the alloys discussed in this chapter? Which of those operating is the most effective?
b. What is the theoretical upper limit to the strength of aluminum alloys and why it is not realized in commercial alloys?
c. The high stacking fault energy of aluminum is favorable for cross slip. On this basis, explain the effect of grain size on the yield strength of recrystallized 7475 alloy, shown in the table.

Grain Size (μm)	Aging Condition	Yield Strength (MPa)
18	Underaged	505
	Overaged	455
80	Underaged	451
	Overaged	445

4.13 For a given 7XXX series, aluminum alloy with a fixed size distribution and volume fraction of constituent particles, how will the fracture toughness vary with increasing strength during aging? What will be the trend with decreasing strength past peak aging? Why is the toughness of an overaged alloy lower than that of the underaged alloy of equal strength?
4.14 Explain the observation for a high strength 7XXX series alloy that the susceptibility to stress corrosion cracking is none, high, and low for as solution-treated, peak aged, and overaged by double aging conditions, respectively.
4.15 Why does the resistance to stress corrosion cracking decrease much more rapidly than the increase of strength during aging of the quenched alloy to peak strength (Fig. 4.45)?
4.16 Based on a comparison of the nominal compositions of alloys 2024 and 2524 (Table 4.19), explain the reasons for the higher toughness and resistance to fatigue crack growth observed in 2524.
4.17 What factors have previously limited the use of aluminum alloys in thicknesses beyond about 150 mm and what advances and metallurgical changes have overcome this limitation?
4.18 Why does alloy 7085 exhibit the least through-thickness anisotropy among all the thick section aluminum alloys? Why is this alloy used only in thickness above about 75 mm (3 in.)?
4.19 Discuss the metallurgical basis for the evolution of the 7XXX series alloys shown in Table 4.22. Consider factors such as the amounts of Zn, Mg, and Cu, the types of disperosid forming elements, levels of purity, and the development of special heat treatments. Why are these alloys generally not amenable to manufacturing processes such as welding?

4.20 Highest strength is achieved in aluminum alloys only by precipitation hardening. In this regard, what are the limitations to achieving high strength in alloys for commercial use by (1) precipitation hardening with Al_3Sc, (2) dispersion strengthening by a distribution of fine, incoherent particles, (3) severe plastic deformation, and (4) processing to achieve hierarchical nanostructures as discussed in this chapter.

4.21 Discuss the following:

- **a.** The early approach to aluminum alloy development based on the dictum that if a little of an alloying element is good, add more until something bad happens. How has alloy development evolved since?
- **b.** The statement made in 1976 that if the strength were the only criterion for aluminum alloy design, alloys available 40 years earlier would have been adequate.

4.22 Using commercial alloys and their properties as examples, discuss how aluminum alloy development has kept pace with the evolution of the design drivers shown in Table 4.2.

CHAPTER 5

5.1 What are the criteria for selecting alloying elements for designing titanium alloys used in airframes? Compare these with that for aluminum alloys.

5.2 Describe the underlying microstructures that impart each of the characteristics exhibited by the various classes of titanium alloys listed in Table 5.3.

5.3 Referring to Fig. 5.7, explain the sequence of microstructural changes that occur in α/β alloys with β stabilizer content (1) $< C_1$, (2) between C_1 and C_2, and (3) $> C_2$, quenched from a temperature T for (1) $T > T_\beta$, (2) $T_\beta > T > T_2$, (3) $T_2 > T > T_1$, and (4) $T_1 > T$. On this basis, explain the trend observed for the alloys shown in Fig. 5.9 in terms of the extent of their β stabilization. Do these observations correlate with the $[Al]_{eq}$ or $[Mo]_{eq}$ for the alloys?

5.4 What is the significance of the β approach curve for the processing of titanium alloys? Explain with examples from commercial alloys.

5.5 How is the thermomechanical processing of titanium alloys different from that for aluminum alloys? What is the rationale for selecting the range of processing temperatures for various alloys shown in Fig. 5.17?

5.6 How is a fully equiaxed microstructure achieved in Ti−6Al−4V? What are the challenges incurred during processing to achieve such a microstructure?

5.7 How are varying volume fractions of equiaxed and transformed β achieved in the microstructure? Under what conditions is the presence of two phases in the microstructure beneficial for processing?

5.8 Describe in detail the evolution of the microstructure of Ti−6Al−4V for each of the heat treatment conditions shown in Fig. 5.19.

5.9 Is the "aging" of Ti−6Al−4V during which secondary α forms, a precipitation hardening treatment as in aluminum alloys? What is the difference? Explain.

5.10 Explain the variations in the properties of Ti−6Al−4V and Ti−10V−2Fe−3Al, shown in Fig. 5.38 and Table 5.10, respectively, with changing microstructural types and parameters. How are these microstructures achieved?

5.11 What strengthening mechanisms operate in Ti−6Al−4V and Ti−10V−2Fe−3Al with the microstructures shown in Fig. 5.38 and Table 5.10, respectively. Are they amenable to modeling to predict the overall yield strength from their superposition? What are the challenges involved?

5.12 Why is it not possible in practice to achieve full hardening in Ti−6Al−4V in products thicker than about 25 mm (1 in.)? Why are near-β alloys more amenable to fabrication of thick products?

5.13 Why do higher-β stabilized α/β alloys (e.g., Ti−6Al−2Sn−4Zr−6Mo) have better forgeability and slightly higher temperature capability than Ti−6Al−4V?

5.14 From a consideration of the relative compositions of the α and β phases and the processing windows, explain the observation that the highest possible strength in α/β titanium alloys at room temperature is achieved in near-β and not in metastable β alloys (Fig. 5.36)? Why do metastable β alloys respond to cold work prior to aging as observed in 2XXX series aluminum alloys?

5.15 Explain the trend in the variation of the properties of Ti−6Al−2Sn−4Zr−2Mo alloy shown for three different conditions in the table. What are the microstructures resulting from the processing and how are the properties affected?

Thermomechanical Processing	Heat Treatment	Yield Strength (MPa)	Tensile Strength (MPa)	Elongation (%)	K_{Ic} (MPa $m^{1/2}$)
β field	885°C, air cool + 600°C, 4 h	1048	1200	7	57
High α/β field		1117	1214	13	34
α/β field	900°C, air cool + 540°C, 4 h	1151	1241	14	26

5.16 Explain the trend in the variation of the properties of Ti−10V−2Fe−3Al alloy shown for three different conditions in the table. What are the microstructures resulting from the processing and how are the properties affected for alloys thermomechanically processed similarly but heat treated differently and thermomechanically processed differently but heat treated similarly? What would be the estimated amount of primary α in each of the above conditions based on the data in Table 5.10?

Thermomechanical Processing	Heat Treatment	Yield Strength (MPa)	Tensile Strength (MPa)	Elongation (%)	K_{Ic} (MPa $m^{1/2}$)
β field	760°C, water quench + 500°C, 8 h	1262	1338	8	46
	760°C, water quench + 540°C, 4 h	1145	1200	11	64
	760°C, water quench + 600°C, 4 h	945	993	17	102
α−β field	760°C, water quench + 500°C, 8 h	1220	1269	11	56
	760°C, water quench + 540°C, 4 h	1131	1179	14	64
	760°C, water quench + 600°C, 4 h	1007	1089	17	78

5.17 Explain the trend in the variation of the high cycle fatigue behavior of Ti−6 Al−4V and Ti−10V−2Fe−3Al alloys shown Figs. 5.41 and 5.42, respectively, based on the microstructural features.

5.18 What microstructural features affect the fracture toughness of α/β titanium alloys and how can this property be maximized for alloys thermomechanically processed in the two-phase field? Discuss with examples from commercial alloys.

5.19 What is the mechanism responsible for the higher toughness of Ti−5Al−5 Mo−5V−3Cr in the beta annealed, slow cooled, and aged condition (Table 5.19)?

5.20 Why are the properties of α/β titanium alloys more difficult to model than those of precipitation hardened aluminum alloys. A recent attempt at delineating the contributions of various microstructural features to the yield strength of Ti−6Al−4V estimated that solid solution hardening of the phases contributed to 80% of the yield strength (Metallurgical and Materials Transactions 46A (2015) 5021−5037.). Comment on this estimate vis-à-vis contributions from other features.

5.21 Why is Ti−6Al−4V the predominantly used titanium alloy? What factors have limited the development of new higher strength, near-β, and metastable β alloys.

CHAPTER 6

6.1 What are the criteria for selecting alloying elements for designing ultrahigh strength steels used in airframes? Compare these with that for aluminum and

titanium alloys. For any one alloy in each of the medium carbon-low alloy, secondary hardening-high alloy and precipitation hardening stainless steel families, identify the role of each of the alloying elements.

6.2 Table 6.3 compares the general processing−microstructure linkages for aluminum, titanium, and ultrahigh strength iron alloys. Using commercial alloys (e.g., 7050, Ti−6Al−4V, Ti−10V−2Fe−3Al, 300M, and Aermet 100) identify some of the similarities and differences in the way microstructural features evolve in these alloys and how they affect the final properties such as strength and fracture toughness.

6.3 Explain the metallurgical basis for the trends in the variation of the properties of 300M steel (Fig. 6.5) compared with that of 4340 (Figs. 6.3 and 6.4).

6.4 What is the role, beneficial or otherwise, of second-phase particles in various steels (Table 6.4) in determining properties. Identify any similarities with the formation and effects of second phase particles in aluminum alloys.

6.5 Why is the martensitic transformation very effective in strengthening Fe−C alloys but not titanium alloys? What factors are considered in selecting the alloying elements to achieve the desired M_S temperature and hardenability?

6.6 The medium carbon, low-alloy steels 4130, 4140, and 4340 have generally similar compositions except that 4130 has 0.3 wt% C, 4140 and 4340 have 0.4 wt% C, and 4340 additionally has 1.85 wt% Ni. The properties of these alloys quenched in oil from the austenitization temperature and tempered at two different temperatures are shown in the table. Explain the observed property trends based on microstructural changes.

Alloy	Tempering Temperature (°C)	Yield Strength (MPa)	Tensile Strength (MPa)	Elongation (%)	Reduction of Area (%)
4130	650	607	786	22	59
4140	205	1641	1772	8	38
	650	655	758	18	53
4340	205	1641	1951	11	48
	650	1379	1531	12	47

6.7 What is the difference between retained and reverted austenite? How do they form and what are their effects on the properties of steels in which they occur?

6.8 Explain the effects of the systematic additions of alloying elements to Fe−10Ni steel on strength (Fig. 6.23). Are these individual and cumulative effects amenable to modeling? Based on the observations, discuss the basis of selecting the compositions for the carbide strengthened steels shown in Table 6.8.

6.9 For predicting the yield strength of alloys like AF1410, what additional strengthening contributions need to be added to the equations for 4340 steel discussed in this chapter? Would such an approach be feasible?

6.10 Explain the trends in the properties of the ultrahigh strength steels shown in Fig. 6.24. What microstructural features are responsible for the observed properties?

6.11 What compositional changes have been made to martensitic precipitation hardening stainless since the introduction of 17-4 PH (Table 6.8)? Relate these changes to the relative properties of the alloys shown in Fig. 6.26.

6.12 For any of the ferrium steels listed in Table 6.6, describe in detail the role of the alloying elements, the processing—microstructure linkages (Fig. 6.29) and the use of computational models to achieve the targeted properties in commercial alloys with reduced amounts of qualification testing. Discuss the challenges, if any, associated with utilizing this approach for designing α/β titanium alloys.

CHAPTER 7

7.1 Both magnesium and the α phase of titanium possess the hexagonal close packed (HCP) crystal structure. Use this as a basis to explain the plasticity of magnesium alloys in terms of their limited formability, anisotropy of properties, and low fracture toughness. In comparison, how does the HCP α phase affect the overall plastic deformation behavior and properties of two-phase α/β alloys?

7.2 What are the criteria for selecting alloying elements for designing magnesium alloys to render them competitive for potential application in airframes? Use examples of commercial alloys to explain the role of each alloying element.

7.3 Compared with aluminum alloys, what are the mechanisms of strengthening available for magnesium alloys? Explain how these are utilized in the evolution of wrought magnesium alloy families shown in Figs. 7.2 and 7.3.

7.4 Why is precipitation hardening the most effective for strengthening magnesium alloys, although it is not as effective as in aluminum alloys? Explain on the basis of the nature of the precipitates and the alloying efficiency discussed in this chapter. How is alloying efficiency improved in aluminum alloys and what are the effects on property combinations? Comment on whether such an approach is feasible for magnesium alloys.

7.5 What types of second-phase particles are present in wrought magnesium alloys? How do they affect the deformation behavior? Compare the behavior with that of aluminum alloys given the different mechanisms of plastic deformation.

7.6 What are the challenges in developing a framework for the prediction of the strength of wrought magnesium alloys by a superposition of contributions from various mechanisms? Explain with examples.

7.7 Consider the concept of microstructural efficiency. Assume that only basal slip is active and you are trying to block this deformation mode. For volume

fraction of 2%, 5%, and 10% of second-phase particles, how would the maximum strength vary with particle size and shape?

7.8 Using Fig. 7.18C, discuss the role of orientation on the activation of nonbasal slip. How does this help with work hardening? From the data in Table 7.5, plot (UTS-YS) versus elongation. Given the theoretical relationship between work hardening rate and uniform elongation, why a pattern does not emerge from this data set? Discuss the role of microstructural features.

CHAPTER 8

8.1 Write Hume–Rothery rules from the introduction to materials course. What rules are violated by the high entropy alloys (HEAs) or complex concentrated alloys? Discuss the importance of Fig. 8.1 in terms of alloy design and compositional search space.

8.2 How are four core effects of HEAs connected with mechanical behavior of these alloys? Discuss your thoughts in the context of current definition of these core effects. Can you propose specific tests to validate these core effects?

8.3 In comparison with aluminum and titanium alloys, what level of properties HEAs need to compete for aircraft structural applications?

CHAPTER 9

9.1 What is the main advantage of using superplastic forming? Which microstructural features impact the superplastic deformation? Discuss the role of each microstructural feature on the overall kinetics of superplastic flow.

9.2 Refer to Fig. 9.5. Why did friction stir processing enhance superplastic behavior of Al–Mg–Zr alloy?

9.3 Superplastic temperature of titanium alloys depends of the proportion of α and β phases. Assuming that 50:50 ratio of α and β is best for superplasticity, how would you predict the superplastic temperature? Discuss with the help of β transus temperature and refer to Chapter 5 for information regarding the change in volume fraction of β phase with temperature.

9.4 Draw a typical thermal cycle for friction stir welding and discuss the microstructural change in the nugget for a high-strength precipitation strengthened aluminum alloy. What type of precipitate distribution would be expected after friction stir welding? How would the microstructure respond to post-weld aging treatment? Should the aging temperature for the nugget be the same as the conventional aging temperature for T6?

9.5 Why does the joint efficiency differ for various alloy series in aluminum alloys? Consider at least one nonheat treatable alloy series and one which uses precipitation strengthening.

9.6 What are the steps involved in the design of a new aluminum alloy for friction stir welding? Discuss the approach for high-strength aluminum alloys and what type of alloy chemistry would eliminate heat affected zone? What elements would you consider to develop hierarchical microstructure?

9.7 What is the major rationale behind using powder-bed additive manufacturing when the cost of starting material is high and the build rates are slow?

9.8 Discuss major concerns in using conventional high-strength aluminum alloy compositions for additive manufacturing.

9.9 What would be the impact of multiple thermal cycles on the microstructure evolution in different alloy groups? Consider at least two precipitation strengthened aluminum alloys and two titanium alloys.

9.10 What leads to build variability and inconsistencies? Discuss at least three factors and how these can be mitigated.

9.11 Design a conceptual aluminum alloy for laser powder-bed additive manufacturing. What would you do to maximize strength with at least 5% ductility? Discuss each element that you would consider adding and what impact it will have on the microstructural evolution?

Index

'*Note*: Page numbers followed by "f" indicate figures and "t" indicate tables.'

A

Accelerated Insertion of Materials (AIM) projects, 454–455
Additive manufacturing (AM)
  computational approach, Al alloys design
    CALPHAD approach, 442–443, 444f
    genetic algorithm, 441–442, 442f
  fusion-based additive techniques, 431–432, 433f
  high-performance Al alloys, 439–443, 441f, 441t
  high-performance Ti alloys, 437–439, 439f–440f
  ICME methodology, 436
  integrated computational materials engineering approach, 437, 438f
  metal-based additive technologies, temporal evolution, 431–432, 432f
  powder-bed AM processes, 433–435
  solid-state ultrasonic additive manufacturing (UAM) technique, 431–432, 433f
  spatial distribution, 431–432, 434f
  variability and inconsistency, 436–437
Aermet 100, 330
Aerospace propulsion systems, 2–3
AF1410 alloy, 329
Airbus A350, 58–59
Airbus A380, 44–46
Airframes structures, 43–44
Al7475 alloy, 410–412
Al–Cu alloys, 81–82, 82f
Al–Cu–Li alloys, 84, 84t
Al–Cu–Mg alloys, 82–84, 83f
Al–Cu–Mg–Li alloys, 84, 85f
Al–Cu–Mg system, 69, 70f
Al–Li alloys, 102, 102f, 155, 454
  2060 and 2199 properties, 153, 154t
  compositions, third-generation alloys, 150–152, 151t
  Li-containing alloys, nominal compositions, 150–152, 152t
Al–Mg–Sc alloys properties, 161–164, 163t
Al–Mg–Si alloys, 84–85, 85t
Al–Mg system, 68–69
Aluminum alloys
  airframe structures
    design drivers, 59, 60t
    Hall–Heroult process, 60
    materials distribution, 58–59, 59t
    microstructural diversity, 60
    processing sequence, 61, 62f
    tensile strength, 60–61
    yield strength, 60–61
Al–Li alloys, 155
  2060 and 2199 properties, 153, 154t
  compositions, third-generation alloys, 150–152, 151t
  Li-containing alloys, nominal compositions, 150–152, 152t
cavity volume fraction variation, 413, 415f
corrosion resistance, 32–33, 33f
design
  Al–Mg–Sc alloys properties, 161–164, 163t
  computational alloy design, 159–161
  computational design, 164–165
  data mining, 165
  dispersion strengthening, 157–158
  manufacturing and performance efficiencies, 155
  nontraditional processing approach, 156
  rapid solidification processed alloys, 158–159, 160t
  SCC Index, 158
  solidification rates, 164
  solid solution strengthening, 157
  strain hardening exponent, 164
  strengthening phase, 161
  trace elements, 158
  work hardening, grain refinement, 156–157
elongation variation, 413, 414f
evolution of, 44–46, 45f
fatigue properties, 29, 30t
fracture toughness, 27, 28f
friction stir welding (FSW)
  clustering-mediated precipitate nucleation, 429–430
  coarsening, reprecipitation and nucleation mechanisms, 427
  coarsening resistant high-strength Al alloys, 427–428
  computational prediction, 425
  dispersoid assisted core–shell model of precipitation, 428–429, 429f
  experimental validation, 425
  microalloying elements, 425–427

Aluminum alloys (*Continued*)
multilevel, multidimensional, multitool research procedure, 425, 426f
theoretical prediction, 425
vacancy trap aided precipitate nucleation, 430–431, 431f
grain refinement effect, 410–412, 411f
grain size and grain boundary misorientation distribution, 411, 412f
hot- and cold-working mill processes, 66–67
impurity elements
compositions, 104–105, 105t
fracture process, 105–106, 106f
fracture toughness, 106
ingot processing, 105–106
localized corrosion, 107, 107f
solute elements, 106
integrated aluminum alloy/product design, 165–166
matrix microstructure control
Al–Li alloys, 102, 102f
coherent dispersoids, 101
continuous dynamic recrystallization (CDRX), 99
crack nucleation, 104, 105f
dispersoid compositions, 100, 100t
features, 103
Hall–Petch equation, 104
incoherent dispersoids, 101
microsegregation patterns, 102
nonheat treatable (NHT) alloys, 101–103
pancake-shaped grains, 101, 101f
particle stimulated nucleation, 99
quench sensitivity, 102–103
stacking fault energy (SFE), 99
thermomechanical processing, 103–104
Zener mechanism, 99
microstructural features, 6–7, 7f
microstructure and properties, 65–66, 66t
particle size and volume fraction, 412, 413f
precipitation hardened (PH) aluminum alloys. *See* Precipitation hardened (PH) aluminum alloys
processing–microstructure–property relations
anisotropy, 115, 115f
contributions estimation, 114, 114t
ductility and strain hardening behavior, 117–138
durability and damage tolerance (DADT) properties. *See* Durability and damage tolerance (DADT) properties; aluminum alloys
flat rolled products orientations, 115, 116f
friction stress, 114
grain/subgrain boundaries, 113–114
microstructural features, 107–108, 108t
PH aluminum alloys, 109–111, 112f
porosity and constituent particles, 109, 110f
precipitate evolution, 109, 111f
superposition of strengthening, 112
Taylor factor, 115–116
thermomechanical processing, 109
yield strength, 111–112, 113t
recrystallization and grain size, 138
structural materials, 2–3
thermomechanical processing, 155
wrought aluminum alloys. *See* Wrought aluminum alloys
2XXX series alloys, 139–142, 140t, 141f, 141t
6XXX series alloys, 142, 142t
7XXX series alloys. *See* 7XXX series alloys
Aluminum mill products, 66–67
Al–Zu–Mg–Cu alloys, 85–87, 86f, 88t
Ashby's theory, 121–122
Austenite, 303–305, 304f–305f
AZ91 alloy, 357
scanning electron microscope (SEM) micrographs, 357, 358f
transmission electron microscopy (TEM) micrographs, 357, 359f

B

Bayesian neural network modeling, 49–50
Boeing 777, 3, 4f, 4t
Boeing 787, 58–59

C

Calcium bearing alloys, 346–347
Carbide forming steels, 295–296, 296t
Clustering-mediated precipitate nucleation, 429–430
Coarsening resistant high-strength Al alloys, 427–428
Complex concentrated alloys (CCAs)
airframe structural applications, 386
CALPHAD approach, 401–403
constituent element based classification, 391–392
crystal structure-based classification, 392
density-based classification, 393
elements, 390–391, 391f
fault energy driven approach, 401–403
Hume–Rothery rules, 394
microstructure-based classification, 392, 393f

mixing enthalpy, 394, 395f
plastic deformation, 390–391
processing-microstructure-properties
deformation micromechanisms, 395–396
fatigue response, 400–401, 402f
mechanical properties, 394
strength–ductility response, 396–397, 397f–398f, 398t, 399f
toughness response, 398–400, 400f–401f
Computational Materials Science and Engineering (CMSE), 460
Continuous dynamic recrystallization (CDRX), 99
Crack growth mechanisms, 31
Crack growth rates, 31
Creep-limited design, 386
Critical resolved shear stress (CRSS), 92, 348–349, 352t

D

"Damage Tolerance" approach, 29
Disk-shaped precipitates, 351, 354f
Dislocation-mediated precipitation, 358–360
Durability and damage tolerance (DADT) properties, 138–139, 139f
aluminum alloys
Ashby's theory, 121–122
corrosion types, 128
crack nucleating feature, 127
dipsersoid decohesion, 120
exfoliation corrosion, 131–133, 132f
fatigue crack growth, 123–127, 125f–126f
fatigue strength/life, 122–123, 124f
fracture toughness, 117–118
high cycle fatigue, 122
impurity levels, toughness, 119, 119f
intergranular corrosion, 131
low cycle fatigue, 122
pitting corrosion, 128–131, 129f–130f
plane stress toughness, 122
shear deformation, 120
specimen configuration, 118, 118f
stress concentrations, 127–128
stress corrosion cracking (SCC). *See* Stress corrosion cracking (SCC)
stress intensity factor, 122
tensile properties, 117
transgranular and intergranular modes, 118–119
titanium alloys
dwell fatigue phenomenon, 249
FCG behavior, 253, 254f
fracture toughness, 253–255, 255t–256t, 257f
high cycle fatigue (HCF) behavior, 250–251, 250f–251f
low cycle fatigue (LCF) behavior, 251–253, 252f
microcracks and macrocracks, 249

E

Electron backscatter diffraction (EBSD), 237–238
Engineering alloys
commercial aluminum alloys, 9–10, 9f
hierarchical microstructural features and material properties, 10–12, 11t
multicomponent aluminum and steel alloys, 9–10
nickel-based superalloy, 10
processing–microstructure–property relationships, 12, 13f
structural elements, 9

F

Fatigue crack growth (FCG), 99
Fatigue-limited design, 386
Federal Aviation Administration (FAA), 346
Ferrium steels, compositions, 335, 336t
Friction stir welding (FSW)
advantages, 419
aluminum alloys. *See* Aluminum alloys
compositional dependence, 422–425, 424f
configuration, 418–419, 418f
joint efficiency, Al alloys, 419–420, 419f
precipitate evolution, 422, 424f
precipitate structure, 422, 423f
precipitation strengthening mechanism, 421
two-phase aluminum alloy, 421–422
zones of, 420–421, 420f
Fusion-based additive techniques, 431–432, 433f

G

Gibbs free energy, 89–90
Guinier–Preston/zones, 75–77, 77t

H

Hall–Heroult process, 60
Hall–Petch equation, 104
Heavy-weight CCAs, 393
Hierarchical modeling methods, 7–9, 8f
Hierarchical multiscale modeling and simulation-based design, 459
High cycle fatigue (HCF) behavior, 250–251, 250f–251f

High entropy alloys (HEAs)
  alloy design paradigm shift, 386–387, 387f
  four core effects, 387–388
    "cocktail" effect, 390
    high entropy effect, 388
    lattice distortion effect, 388–389, 388f–389f
    sluggish diffusion effect, 389–390
  solid-solution face centered cubic (FCC) alloys, 386–387
High-performance Al alloys, 439–443, 441f, 441t
High-performance Ti alloys, 437–439, 439f–440f
Hume–Rothery rules, 394

I

Integrated CALPHAD-phase field modeling approach, 279–280
Integrated computational materials engineering approach, 437, 438f
Integrated Computational Materials Engineering (ICME) system, 12, 14, 17f, 52, 454–455, 456f

J

Johnson–Mehl–Avrami–Kolmogorov relationship, 236

L

Light-weight CCAs, 393
Low cycle fatigue (LCF) behavior, 251–253, 252f

M

Magnesium alloys
  alloying elements, 349–351
  AZ91 alloy, 357
    scanning electron microscope (SEM) micrographs, 357, 358f
    transmission electron microscopy (TEM) micrographs, 357, 359f
  calcium bearing alloys, 346–347
  composition-based classification, 348, 350f
  corrosion resistance, 33
  critical resolved shear stress (CRSS), 348–349, 352t
  disk-shaped precipitates, 351, 354f
  dislocation-mediated precipitation, 358–360
  fatigue properties, 31
  Federal Aviation Administration (FAA), 346
  fracture toughness, 29
  grain size and intensity variation, 356, 357f
  manufacturing routes, 347–348, 350f
  Mg–Sn system model, 363, 364f
  microstructural efficiency
    composite strengthening, 355
    definition, 351
    grain boundary strengthening, 355
    Peierls/lattice friction stress, 352
    precipitation strengthening, 355–356, 356f
    solid solution strengthening, 352–355
    texture strengthening, 355
  microstructural features, 348–349, 351, 354t
  nucleation and growth, 356–357
  nucleation density, 361–363
  plasticity, 347
  precipitation-hardenable casting and wrought magnesium alloys, 347, 348f
  precipitation sequence, 349–351, 353t
  processing–microstructure–properties
    ductility, 373–374, 373f–374f
    fatigue response, 376, 377f–378f
    hardness measurement, 363–364
    low formability, composition effect, 367, 369f
    second-phase particles, 371
    superposition, 374–376, 375f
    tensile properties, 365–367, 368t–369t
    tensile yield strength *vs.* ductility, 365–367, 366f
    tension–compression yield asymmetry, 370–371, 370f
    thermomechanical processing, 364–365, 366f
    toughness response, 376, 377f
    twinning and strengthening, 371–373, 372f
  rare earth (RE) alloys, 346–347
  rod-shaped precipitates, 351
  slip and twinning systems, 348–349, 351f
  spherical precipitates, 351
  temper designations, 347, 349t
  thermomechanically processed alloys, 358–360
  WE 43 alloy
    bright field (BF) transmission electron microscopy (TEM), 357–358, 360f
    transmission electron microscopy (TEM), 357–358, 361f–362f
Martensite, 301–303, 302f–303f
Material manufacturability, alloy design, 15–17
Material properties
  ICME system, 14, 17f
  integrated systems approach, 14, 16f
  length and time scales, 14, 15t
  materials genome timeline, 14–15, 16f
  revolutionary manufacturing process, 15
  second-phase morphologies, 12–14
  structural applications, 12–14

Materials informatics, 462–465, 463f–464f
Materials models, 37
Medium carbon, low alloy (MC-LA) steels
  strength, 312f, 313–314
  tempering temperature effects
    properties, 297, 299f
    tensile properties, 296, 297f
    toughness, 297, 298f
  toughness, 319–320, 320f
Medium-weight CCAs, 393
Metal-based additive technologies, 431–432, 432f
Mg–Sn system model, 363, 364f
Microstructure–properties relationships, 451–452
  aluminum alloys. *See* Aluminum alloys
  anisotropy effects, 34
  critical stress concentration, 27
  "Damage Tolerance" approach, 29
  fatigue crack growth behavior, 31, 32f
  fatigue crack growth rate, 31, 32f
  magnesium alloys. *See* Magnesium alloys
  microstructural features, 24, 25t
  modeling
    cause-and-effect relationships, 34
    fatigue, 36
    fracture toughness, 35–36
    strength, 35
    strength–corrosion resistance tradeoff, 36, 37f
  "Safe Life" approach, 29
  steel alloys. *See* Steel alloys
  strength, 24–27, 26f
  stress intensity, 29
  titanium alloys. *See* Titanium alloys
Model-based alloy and product design, 50–52, 52f–53f
Model-based approaches
  adaptive numeric modeling, 49
  alloy 3105, 49, 50f
  Al–Zn–Mg–Cu alloys, 49–50
  Bayesian neural network modeling, 49–50
  CALPHAD tools and databases, 49
  data mining methods, 49
  materials behavior, 47–48
  materials design level, 48, 48f
  products and performance requirements, 48–49
Multilevel spatial hierarchy, 7, 8f

N

Nonheat treatable (NHT) alloys, 101–103

O

Orowan bowing mechanism, 91–94, 93f

P

Physics-based models, 451–452
Polymer–matrix composites, 58–59, 452
Powder-bed AM processes, 433–435
Precipitate-free zones (PFZs), 75
Precipitation hardened Al alloys, 452–453
Precipitation hardened (PH) aluminum alloys
  Al–Cu alloys, 81–82, 82f
  Al–Cu–Li alloys, 84, 84t
  Al–Cu–Mg alloys, 82–84, 83f
  Al–Cu–Mg–Li alloys, 84, 85f
  Al–Mg–Si alloys, 84–85, 85t
  Al–Mg system, 68–69
  Al–Zu–Mg–Cu alloys, 85–87, 86f, 88t
  binary alloy, 67, 68f
  defects and trace elements, 77–79
  dispersoid forming elements, 66
  fatigue crack growth (FCG), 99
  ferrous and nonferrous alloys, 74
  Gibbs free energy, 89–90
  impurity elements, 75
  integrated process modeling
    continuous cooling curve, 96
    isothermal conditions, 97
    nonisothermal treatments, 97
    quench factor analysis (QFA) method, 95
    quenching media, 94–95
    time–temperature–property (TTP), 95–97, 95f–96f
  intragranular and grain boundary effects, 98
  matrix microstructural features, 91
  mechanisms
    coarsening, 77
    growth, 77
    heat treatment conditions, 75
    heterogeneous nucleation, 76
    homogeneous nucleation, 76
    matrix interface, 76
    shape, 77, 77t
  mesoscale modeling approach, 89–90
  nonhomogeneous spatial distribution, 89
  Orowan bowing mechanism, 91–94, 93f
  PFZs formation and effects, 79–81, 79f
  phase equilibria
    Al–Cu–Mg system, 69, 70f
    binary phase diagrams, characteristics, 73, 73t
    intermetallic phases, 70
    multicomponent phases, 73
    phase relationships, 70–71, 71f

Precipitation hardened (PH) aluminum alloys (*Continued*)
postsolidification treatments, 73–74
S phase, 71, 72f
thermodynamic modeling, 69–70
precipitate characteristics, 75
precipitate-free zones (PFZs), 75
precipitate shape, 94
predictive and quantitative modeling, 87
requirements, 67–68
secondary alloying additions, 75
shearable precipitates, 92
small angle neutron scattering and transmission electron microscopy, 89, 90f
solid solubilities, 68, 69t
solid state precipitation, 74
stages, 87–89
thermodynamic and kinetic parameters, 91
toughness–yield strength relationships, 97–98, 98f
Precipitation hardening stainless steels (PH-SS), 299–300
strength, 317
toughness, 323
Process design, 38–39
Process models, 37–38, 38f

Q

Quench factor analysis (QFA) method, 95
QuesTek, 327

R

Rod-shaped precipitates, 351

S

"Safe Life" approach, 29
Secondary hardening, high alloy (SH-HA) steels, 298–299
Aermet 100, 330
AF1410 alloy, 329
Fe–10Ni steel, 328–329, 329f
mechanical properties, Aermet series steels, 330–331, 330f
strength, 314–317, 315f–316f
tensile strength levels, 328
toughness, 320–322, 321f, 323f
toughness index, 330–331
Solid solution hardening, 194
Solid-state ultrasonic additive manufacturing (UAM) technique, 431–432, 433f
Solution heat treatment (SHT), 189
β-Stabilized polycrystalline titanium alloy, 52–54, 53f
Stacking fault energy (SFE), 99
Steel alloys
corrosion resistance, 33
fatigue properties, 29
fracture toughness, 27–28
Stiffness-limited design, 386
Strength-limited design, 386
Stress corrosion cracking (SCC), 59, 257
compositions, 136–137, 137t
heat treatment schemes, 136, 137f
relative resistance, 133, 134f
resistance with aging time, 135, 136f
slip concentrations, 135
source of, 133
stress-corrosion tests, 135, 135f
stress intensity factor, 133–134
stress intensity *vs.* growth rate curves, 133–134, 134f
susceptibility, 138
Structural alloys, development timeline, 47, 47f
Structural materials
aerospace propulsion systems, 2–3
airframe design, 5
airplane structures, property requirements, 3, 3f
aluminum alloys, 2–3
Boeing 777, materials distribution, 3, 4f, 4t
design applications, 5
elastic modulus, 6
electrochemical properties, 23–24, 23t
evolution of, 2–3, 2f
flat plate buckling loading, 5–6, 6t
mechanical properties, 22–23
physical properties, 22
polymer–matrix composite materials, 2–3
refractory metals, 2–3
selection, 5
structural weight, 5, 5t
Superplastic forming (SPF)
additive manufacturing (AM). *See* Additive manufacturing (AM)
aerospace components, 408–409
aluminum alloys
cavity volume fraction variation, 413, 415f
elongation variation, 413, 414f
grain refinement effect, 410–412, 411f
grain size and grain boundary misorientation distribution, 411, 412f
particle size and volume fraction, 412, 413f
applications, 408

friction stir welding (FSW)
advantages, 419
aluminum alloys. *See* Aluminum alloys
compositional dependence, 422–425, 424f
configuration, 418–419, 418f
joint efficiency, Al alloys, 419–420, 419f
precipitate evolution, 422, 424f
precipitate structure, 422, 423f
precipitation strengthening mechanism, 421
two-phase aluminum alloy, 421–422
zones of, 420–421, 420f
grain boundary character distribution, 410
microstructural requirement, 409–410, 410f
titanium alloys
advantage, 417–418
body-centered cubic structure, 414–417
hcp structure, 414–417
normalized stress variation, 414–417, 416f
simulation results, 417–418, 417f
Superposition, 374–376, 375f, 465, 465t, 466f
Systems Approach, 455

T

Taylor factor, 115–116, 237
Theory-based alloy design, 54–55, 54f
Thermodynamic equilibrium, 7
Thermodynamic modeling, 460–461, 461f
Thermomechanical processing (TMP), 215–217, 218f–219f
Ti–5Al–5Mo–5V–Cr, 275–276, 277f
Ti–6Al–2Sn–2Zr–2Mo–2Cr–0.15Si (Ti-6-22-22), 267
Ti–6Al–4V, 205, 205f, 264–265, 266t
Ti–Al–V alloys, 202, 203f
Ti–6Al–4V ELI, 264–265, 266t
Ti–6Al–4V microstructure, 207–208, 208f
Ti–6Al–6V–2Sn, 266–267, 268t
TIMETAL 18, 276
TIMETAL 54M, 269
TIMETAL 62S, 266
Titanium alloys
advantage, 417–418
airframe structures
applications, 179–181
mill products and structural components, 179
properties, 181
structural materials distribution, 179, 179t
α/β alloys, 196
β-annealed microstructures, 227
attributes, 265
bilamellar microstructures, 243–244
bimodal microstructures, 244
diffusion rates, 267
equiaxed microstructures, 244
heat treatment conditions, 227, 229f
intermediate temperature applications, 269, 270f, 270t
lamellar, bimodal and equiaxed microstructures, 226f, 227
lamellar microstructures, 243
mill annealed condition, 227–229
processing–microstructure relationships, 229, 230t
processing parameters, 242–243
processing steps, 227, 228t
process parameters, 226
self-diffusion coefficients, 229
SP-700, 269
tensile properties, 241, 243f
thermomechanical processing and heat treatment, 244, 245f
Ti–6Al–2Sn–2Zr–2Mo–2Cr–0.15Si (Ti-6-22-22), 267
Ti–6Al–6V–2Sn, 266–267, 268t
TIMETAL 54M, 269
TIMETAL 62S, 266
water quenched alloys, 241–242
Widmanstatten (basketweave) type structure, 227
yield strength and ductility, 244, 245f
β alloys, 196, 244–246, 247t, 248f
β-annealed microstructures, 232
bimodal structures, 232
microstructure types, 229–231
processing–microstructure relationships, 232, 234t
processing steps, 231–232, 231t
solution heat treatment, 232, 233f
alloy strength, 241, 242f
attributes, 264, 265f
body-centered cubic structure, 414–417
characteristics, 189–191, 190t
classification
aging, 189
Al and Mo concentrations, 184
heat treatment operations, 188–189, 188f
phase diagrams, 182, 183f
processing steps, 187–188, 187f
pseudobinary diagram, Ti-β stabilizer element system, 184–187, 187f
solution heat treatment (SHT), 189
α stabilizers, 182
β stabilizers, 182
structural alloys, 184–187, 185t–186t, 192–193

Titanium alloys (*Continued*)
composition− processing−microstructure−properties relationships
fracture toughness modeling, 262−263
ICME framework, 259
integrated modeling, 263−264, 263f
linear addition rule, 261
mechanism-based models, 260
neural network modeling, advantage, 261−262
strengthening mechanisms, 260−261
tensile properties, 260
yield strength, 260, 261f
yield stress, 261−262, 262f
corrosion resistance, 33
cost-affordable titanium alloys, 217−220, 220f
cost reduction, 278
defects, 225−226, 225f
deformation behavior, 239
deformation mode and temperature, 237, 237f
deformation texture, 236
ductility, 246−249
durability and damage tolerance (DADT) properties. *See* Durability and damage tolerance (DADT) properties; titanium alloys
dynamic coarsening, 235
effective slip length, 240
electron backscatter diffraction (EBSD), 237−238
equilibrium phases, 197−198, 198f
evolution of, 44, 45f, 46, 264, 265f
fatigue properties, 31
fracture toughness, 28
hcp structure, 414−417
heat treatment
aging response, 212−213
air cooling, 213, 214f
phases *vs.* quenching temperatures, 213, 214f
quench delay, 215
residual stresses, 212
Ti−6Al−4V phases, 213, 213f
transformation products, 213
TTT curves, 215, 216f
yield and tensile strengths, 215
high temperature properties, 257−258
historical development, 191−192
ingot conditioning, 207
integrated CALPHAD-phase field modeling approach, 279−280
intergranular phase, 222
Johnson−Mehl−Avrami−Kolmogorov relationship, 236
lamellar microstructures, 207
lamellar morphology, 221−222
metallurgical phenomena, 232−233, 235t
metastable β alloys, 258, 276−277
microstructure−property relationships, 259
microstructure timeline of, 220, 221f
multivariate relationships, 238
near-α alloys, 195−196
applications, 269−271
diffusion and stabilization, 273
IMI 679, 271
IMI 685, 271
IMI 829, 271
mechanical properties, 271, 272t
microstructure type, ORL characteristics, 273, 273f
Ti-1100, 271
near-β alloys
aging parameters, 274
mechanical properties, 274, 275t−276t
SHT and quenching, 275−276
strength and toughness, 274
Ti−5Al−5Mo−5V−Cr, 275−276, 277f
TIMETAL 18, 276
neural network models, 238
nonequilibrium phases, 201f
alloys quenching, 199−200, 199f
composition and cooling rates, 198−199
Fe-based alloys, 198
microstructure, 198−199
pseudobinary phase diagram, 200, 200f
normalized stress variation, 414−417, 416f
parameters, 222, 223f
PH Al alloys, 220−221
phase relationships
β approach curve, 202, 204f
multicomponent commercial alloys, 207
multicomponent systems, 200−201
phase disappearance, 204−205
phase equilibria, 205−206, 206f
ThermoCalc, 205−206
thermodynamic and neural network modeling, 203−204
Ti−Al−V alloys, 202, 203f
Ti−6Al−4V and Ti−10V−2Fe−3Al, 205, 205f
volume fractions, 205−206, 206f
phase stability, 195
phase transformations and mechanical behavior, 232−233
primary/secondary phase, 221−222
primary working stage, 208−210, 210f

processing sequences, 226
properties, 194
quenched alloys, 241
recrystallization and grain growth, 236–237
secondary working stage, 211–212, 211f
sheet—basal orientation, 237, 237f
sheet—prismatic orientation, 237, 237f
simulation results, 417–418, 417f
size range, 238, 239t
solid solubility, 195
specific *vs.* multiple microstructure types, 240–241
spheroidization, 235, 236f
static coarsening, 235
stress corrosion cracking (SCC), 257
Taylor factor, 237
and texture, 222–225, 224f
thermomechanical processing (TMP), 215–217, 218f–219f
Ti–6Al–4V forged component, 208, 209f
Ti–6Al–4V and Ti–6Al–4V ELI, 264–265, 266t
Ti–6Al–4V microstructure, 207–208, 208f
twinning, 239
yield strength–toughness relationships, 239, 240f
Ti-10V-2Fe-3Al, 205, 205f
Toughness-limited design, 386

U

Ultrahigh strength (UHS) steels
advantages, computational methods, 335
airframe structures, 290–291, 300, 339, 339t
austenite, 303–305, 304f–305f
carbide forming steels, 295–296, 296t
classification, 291–292, 293t
composition–processing–microstructure relationships
austenite grain boundaries, 307
hardenability, 309
M_2C carbides, characteristics, 310–312, 311f
MC-LA steels, 307, 307t
M_s Temperature modeling, 308–309
secondary hardening steels, 310, 310f
corrosion damage, 333–335
evolution of, 44, 46–47, 46f
ferrium steels, compositions, 335, 336t
fracture toughness and fatigue properties, 294
martensite, 301–303, 302f–303f
medium carbon, low alloy (MC-LA) steels, 295–296, 327–328. *See also* Medium carbon, low alloy (MC-LA) steels
microstructural features, 335–337
microstructure evolution, aluminum, titanium and steel alloys, 301, 301t
modeling and complementary characterization tools, 338
multicomponent alloys, 292
phase relationships, 295, 295f
phase transformations, 294–295
plain carbon steels, 296
precipitation hardening stainless steels (PH-SS), 299–300, 331–332, 332f–334f. *See also* Precipitation hardening stainless steels (PH-SS)
processing–microstructure–properties relationships, 337–338, 337f
processing sequence, 294, 294f
properties
carbides/intermetallic compounds, 325
carbide strengthened steels, 326, 327f
cybersteels, 326
ductility, 317, 318f
embrittlement, 324
fatigue properties, 323
ferrous alloys, 326
resistance, 312–313
strength, 312f, 313–317, 315f–316f
stress corrosion cracking behavior, 324, 325f
toughness, 312–313, 319–323, 320f–321f, 323f
wrought stainless steels, 326
QuesTek, 327
secondary hardening, high alloy (SH-HA) steels, 298–299, 328–331, 329f–330f. *See also* Secondary hardening, high alloy (SH-HA) steels
second-phase particles, 306, 306t
systems approach, 338, 338t
vacuum induction melting/vacuum arc remelting (VIM/VAR), 294

V

Vacancy trap aided precipitate nucleation, 430–431, 431f
Vacuum arc remelting (VAR), 294
Vacuum induction melting (VIM), 294
Virtual Aluminum Castings (VAC) project, 51

W

WE 43 alloy
bright field (BF) transmission electron microscopy (TEM), 357–358, 360f
transmission electron microscopy (TEM), 357–358, 361f–362f

Widmanstatten (basketweave) type structure, 227
Wrought aluminum alloys
  classification, 62, 63f
  compositions, 62, 64t
  heat treatable, 62
  mill products, 67
  nonheat treatable, 62
  numbering system, 62, 64t
  temper designation system, 65, 65t
  wrought precipitation hardenable aluminum alloy families, 62, 63f

X

2XXX series alloys, 139–142, 140t, 141f, 141t
6XXX series alloys, 142, 142t
7XXX series alloys
  Al–Zn–Mg–Cu system, 142
  anisotropy minimization, 149
  compositions, 143, 144t
  computational modeling tools, 150
  controlled toughness, higher purity alloys, 145–146
  evolution and service, 149–150, 150f
  high strength and SCC resistance, 146, 146f, 147t
  mid-plane defects elimination, 146–147
  properties, 147, 147f
  residual stresses, 147
  7075-T6 strength improvements, 143–145
  T73 temper development, 145, 145t
  ultrahigh strength alloys, 148, 148f, 148t

Z

Zener mechanism, 99